Modeling, Design, Identification, Drive, and Control of a Rotary Actuator with Magnetic Restoration

by

Sajjad Mohammadi Yangijeh

B.S., Kermanshah University of Technology (2011)
M.S., Amirkabir University of Technology (2014)
M.S., Massachusetts Institute of Technology (2019)

Submitted to the Department of Electrical Engineering and Computer Science

in partial fulfillment of the requirements for the degree of

Doctor of Philosophy in Electrical Engineering and Computer Science

at the

MASSACHUSETTS INSTITUTE OF TECHNOLOGY

February 2022

© Massachusetts Institute of Technology 2022. All rights reserved.

Author . . . .
Department of Electrical Engineering and Computer Science
September 20, 2021

Certified by . . . .
James L. Kirtley
Professor of Electrical Engineering and Computer Science
Thesis Supervisor

Certified by . . . .
Jeffrey H. Lang
Professor of Electrical Engineering and Computer Science
Thesis Supervisor

Accepted by . . . .
Leslie A. Kolodziejski
Professor of Electrical Engineering and Computer Science
Chair, Department Committee on Graduate Students

Modeling, Design, Identification, Drive, and Control of a Rotary Actuator with Magnetic Restoration

by
Sajjad Mohammadi

Submitted to the Department of Electrical Engineering and Computer Science
on Sep 20, 2021, in partial fulfillment of the
requirements for the degree of
Doctor of Philosophy in Electrical Engineering and Computer Science

Abstract

Rotary actuators have been widely used in the industry. This thesis investigates the design, modeling, identification, drive, and control of an actuator with magnetic restoration. The design considerations are explained, FEM is used in the analysis, and a prototype is built for lab experiments. A design-oriented analytical model is developed for the actuator, in which the coil torque is obtained using the solution of Laplace's equation in the elliptical coordinates, and the reluctance torque is derived by an approach named differential flux tubes. In addition, nonlinear and linearized electromechanical models are developed for control system designs and dynamic studies. To obtain higher accuracy, the eddy-currents in the laminations and the magnet are also modeled using an analytical solution of 1-D and 2-D diffusion equation and extracting a lumped-element circuit for system-level analysis. It adds to the accuracy of the model to a large degree. The impact of the pre-sliding friction on the mechanical dynamic is studied as well. Then, identification of the model is performed. Next, an op-amp-based drive circuit for the current control loop is proposed, modeled, and designed. Then, three DSP-based position control techniques are implemented: pole placement with voltage drive, pole placement with current drive, and nonlinear control with feedback linearization. State observers are employed to estimate the unmeasured states. The control techniques are evaluated and compared through time response indices such as rise time, overshoot, steady-state error, and large-signal tracking, as well as by frequency domain indices like bandwidth, robustness, phase margin, sensitivity, disturbance rejection. A method of eddy-current plated is also proposed for inductance reduction. In the end, a new effectiveness index is proposed.

Thesis Supervisor: James L. Kirtley
Title: Professor of Electrical Engineering and Computer Science

Thesis Supervisor: Jeffrey H. Lang
Title: Professor of Electrical Engineering and Computer Science

بسم الله الرحمن الرحيم

وقل رب زدني علما

And say, "My Lord, increase me in knowledge."

Quran [20:114]

Acknowledgment

I am delighted to acknowledge everyone who contributed to my thesis or provided me with any kind of support and motivation. First, I would like to express my sincere appreciation to professor James Kirtley and professor Jeffrey Lang for their encouragement, guidance, and support as the supervisors of this thesis. Their knowledge and experience in the field of electric machines, electromagnetic systems, and electromechanical devices provided me an opportunity to gain considerable expertise. They gave me the freedom to explore different areas related to my Ph.D. thesis, from electromagnetics to drives and control systems. They always had time for discussions about anything. I had a fantastic course on the Advanced Design of Electric Machines with prof. Kirtley, and I were the teaching assistant of the course later. I took a class on Electromagnetic Fields, Forces, and Motion with prof. Lang; I took this course three times as I enjoyed his passion for teaching.

Next, I would like to thank the other committee members of my Ph.D. thesis: professor David Trumper at the mechanical engineering department at MIT, and Professor Arijit Banerjee at the electrical engineering department at the University of Illinois at Urbana-Champaign. I enjoyed and learned from their challenging comments on my Ph.D. thesis. I also had a course on Control System Design with prof. Trumper, in which I learned a lot.

I would also like to thank others who contributed to my knowledge during the journey. I would like to thank William Benner for the deep knowledge in various fields of engineering that he provided to us. We enjoyed collaborating with him and learned from his comments from an industrial point of view. Next, I would like to thank Professor Steven Leeb and professor David Perreault. I had several power electronics courses with them, and I learned how to design and analyze such circuits.

Also, I would like to thank all my colleagues at the Grainger Energy Machines Facility (GEM) at MIT, formerly known as the laboratory of electromagnetic and electronic systems (LEES): Mohammad, Krishan, Colm, Lukasz, Tommy, Tony, Nelson, Donna, Erik, Mostafa, William, Mark, Jei, and Mike. I want to thank my friends at MIT with whom I enjoyed my life as a graduate student: Asma, Ardavan, Sepideh, Ali V, Mehrdad, Amir, Soroush, Shahab, Alborz, Ali F, Alireza, Zahra R, Maryam, Arash, Pouya, Behrouz, Morteza, and Khashayar. I would also like to thank the Iranian community in the Boston area, who provided a positive and supportive environment.

I also want to express my appreciation for the masterpiece of the great Persian poet Mowlana Balkhi Rumi. His poetry, especially his renowned book *Masnavi*, has inspired my soul to seek eternal values beyond day-to-day life.

Words can never do justice to express my gratitude to my family, especially my father Jamshid and my mother Zohreh, for the sacrifice they have always made, just like a candle that burns itself to light the way of others. After the favor of God, the Compassionate, my family has always been the unconditional source of love, endless care, and continuous support.

Contents

List of Figures

List of Tables

Chapter 1

Introduction and Literature Review

1.1 Literature Review of Limited-Angle Rotary Actuators

Electric machines and electromagnetic devices have an important role in energy conversion between electrical and mechanical forms. Limited-angle rotary actuators, sometimes called limited-angle torque motors, have been employed widely in the industry, from automotive manufacturing and biomedical applications to robotics, aerospace, fluid valves, and 3D printers. Therefore, their study has been of great interest among researchers.

1.1.1 FEM-Based Studies of Electric Machines and Rotary Actuators

The finite element method (FEM) as a powerful technique has been employed widely in the study and design of a range of electromagnetic devices from Eddy-Current Couplers [1]-[3] and induction machines [4] to Line-Start Permanent Magnet Motors [5]-[7] and Switched Reluctance Motors [8]- [10]. And Vernier motors [11]. The following studies have been employed FEM in the analysis, design, and model verification of rotary actuators and limited-angle torque machines.

In [12], the finite element method (FEM) is employed in the torque ripple suppression of a 4-pole slotted limited angle torque motor. The configuration of the motor is shown in Figure 1.1.

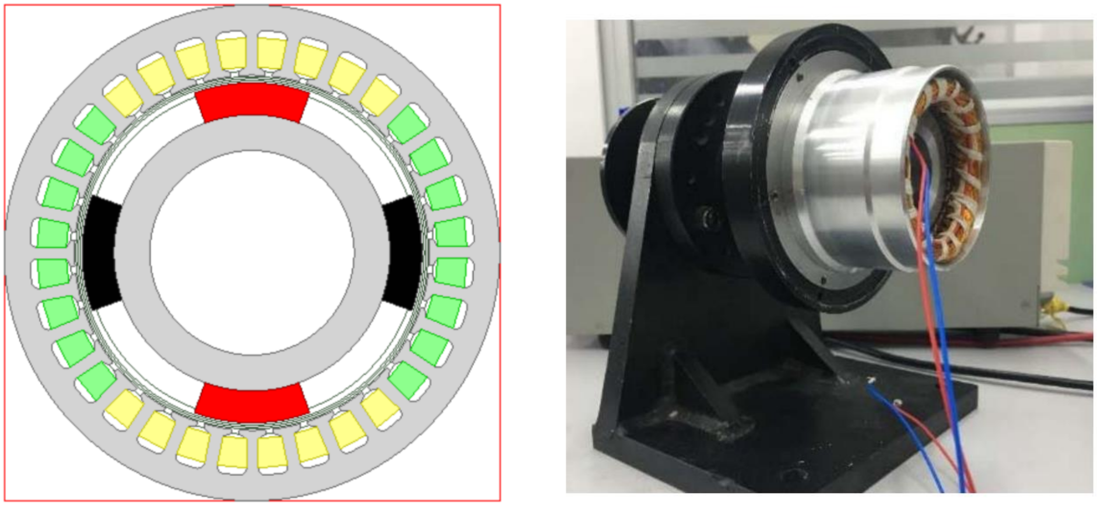

Figure 1. 1: The configuration of the studied LATM.

In [13], the finite element method (FEM) is employed in the torque performance improvement for 4-pole slotted limited-angle torque motors with concentrated winding whose configuration and geometry are shown in Figure 1.2.

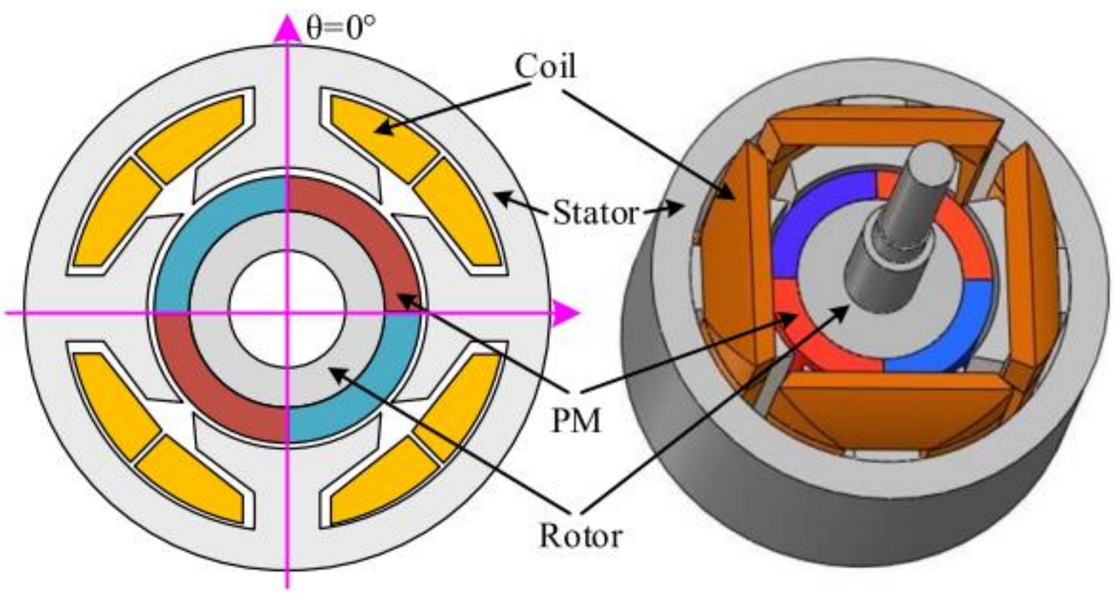

Figure 1. 2: The configuration of the studied slotted limited-angle torque motors.

In [14], a slotless limited-angle torque motor for the reaction wheels torque measurement system is proposed. The finite element method (FEM) is also employed in the study. The configuration of the studied motor is shown in Figure 1.3.

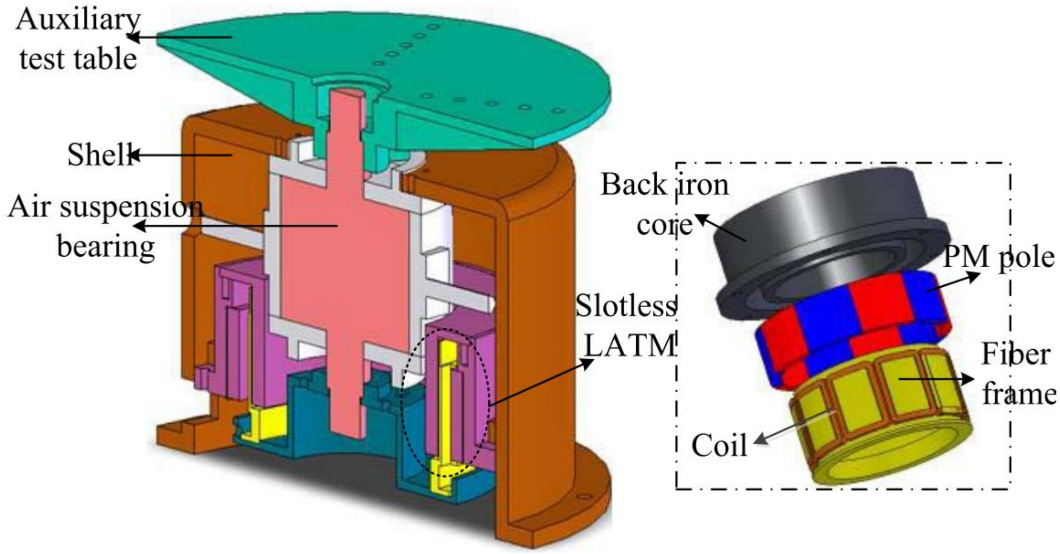

Figure 1. 3: The configuration of the slotless LATM for reaction wheels torque measurement

In [15], finite element method (FEM) and basic formulations are employed in the analysis of limited angle torque motors with irregular slot numbers for performance improvement. The configuration of the motor is shown in Figure 1.4.

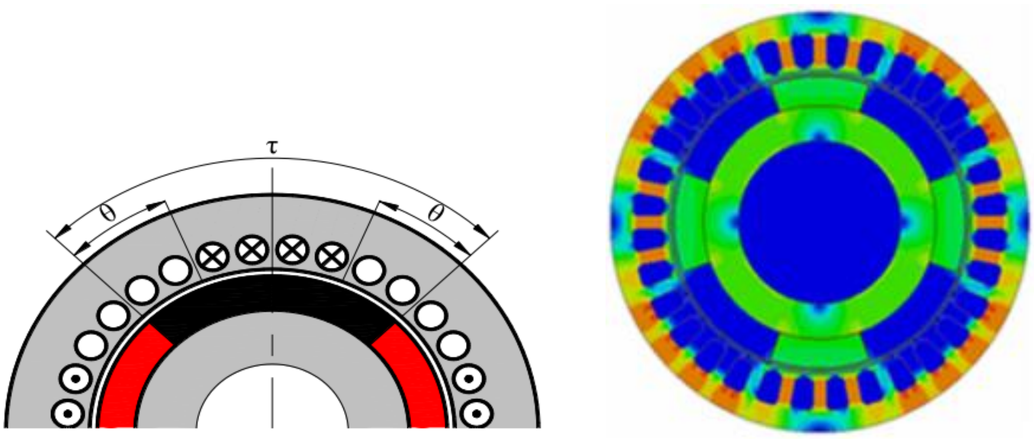

Figure 1. 4: The configuration of the studied LATM.

In [16], torque performance improvement of a radial-flux slotted limited-angle torque motor by tapered tooth-tip is studied. The finite element method (FEM) is also employed in the analysis. The configuration of the motor is shown in Figure 1.5.

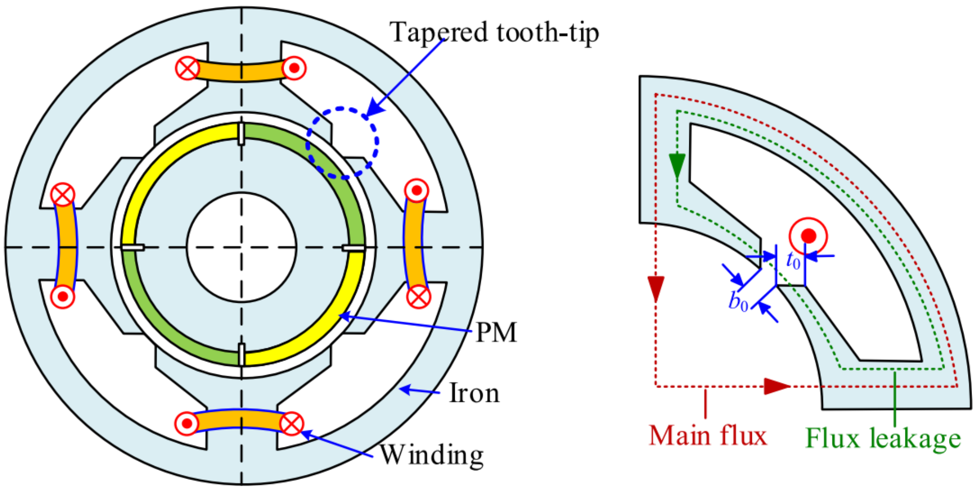

Figure 1. 5: The configuration of the studied LATM with tapered tooth-tip

1.1.2 Electric Machine Modeling Using Laplace's Equation

The solution of Laplace's and Poisson's equations [17]- [18] is a powerful approach in field calculation and modeling of electromagnetic devices from magnetic couplers [19] to rotary actuators. Such studies have been done in elliptical coordinates in [20]-[24], in which general frameworks for the solution of Laplace's and Poisson's equations in different coordinates have been studies.

In [25], based on the solution of Laplace's and Poisson's equations, a voice coil having a double-layer Halbach array is studied. The results are verified by FEM and an experimental prototype. The configuration of the studied actuator is shown in Figure. 1.6.

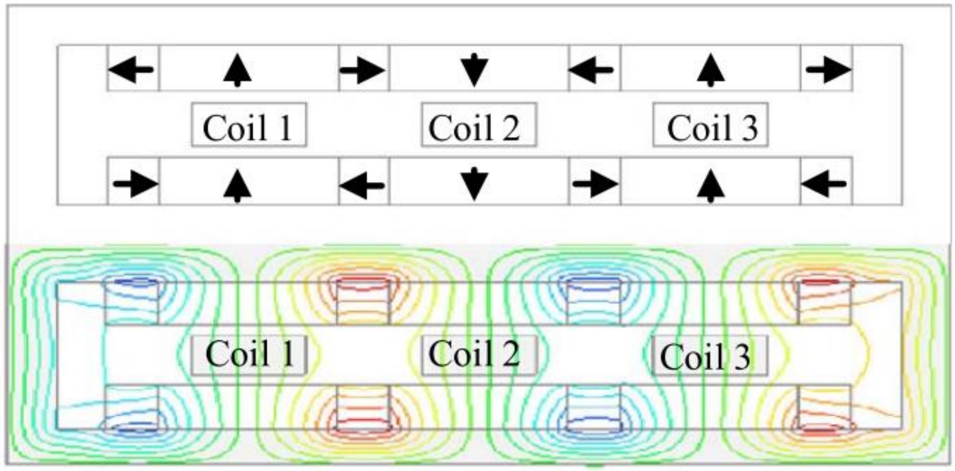

Figure 1. 6: The geometry of the studied LATM.

In [26], a solution based on Laplace's equation is employed in the analysis and estimation of the maximum angular operation range of a permanent-magnet slotted limited-angle torque motor. The configuration of the studied actuator is shown in Figure. 1.7.

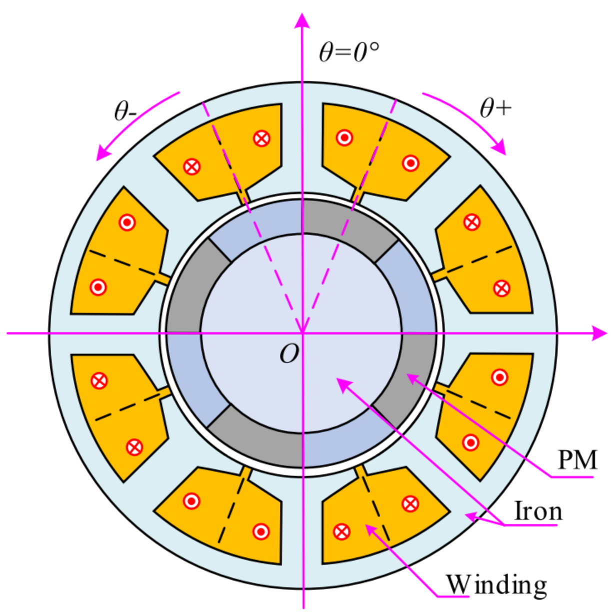

Figure 1. 7: The geometry of the studied LATM.

1.1.3 MEC-Based Studies of Electric Machines and Rotary Actuators

Magnetic equivalent circuits (MEC) and flux tube-based approaches are powerful modeling techniques that are widely used in a variety of electromagnetic devices and electric machines from eddy-current couplers [27]-[31] and switched reluctances motors (SRMs) [32]-[33] to permanent magnet synchronous motors [34]- [35] and magnetically-geared machines [36]- [38]. In the following, some papers are reviewed in which MEC is employed in the model and design of rotary actuators, voice coil motors, and limited-angle torque motors.

In the old paper [39], performance prediction of a limited-angle rotary actuator, named Law's relay actuator, is studied using a simple magnetic equivalent circuit. The structure and the employed MEC are shown in Figure 1.8. This actuator does not have any permanent magnet and works based on the reluctance alignment of the rotor.

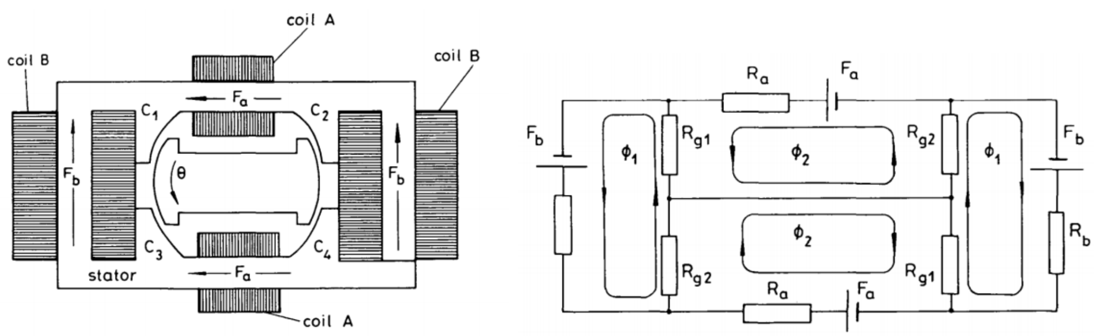

Figure 1. 8: The geometry and magnetic equivalent circuit of a Law's relay.

In [40], an equivalent magnetic circuit (MEC) is developed for a radial-flux slotted limited-angle torque motor with asymmetrical teeth aimed at torque performance improvement. The configuration of the studied actuator and the developed MEC is shown in Figure. 1.9.

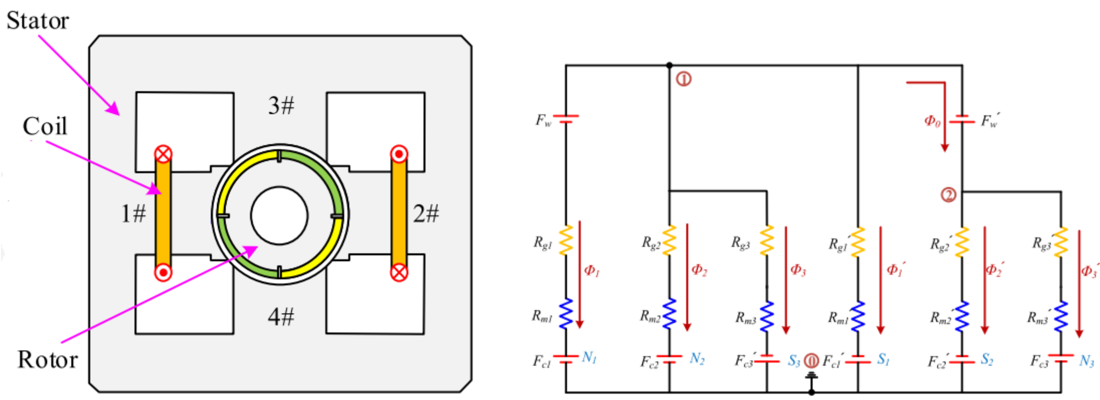

Figure 1. 9: The geometry and the developed MEC of the studied LATM.

In [41], magnetic equivalent circuit (MEC) and finite element method (FEM) are employed in the analysis, optimization, and design of a limited-angle torque-motor with segmented rotor pole tip structure and toroidal winding. The configuration of the studied actuator and the developed MEC are shown in Figure. 1.10.

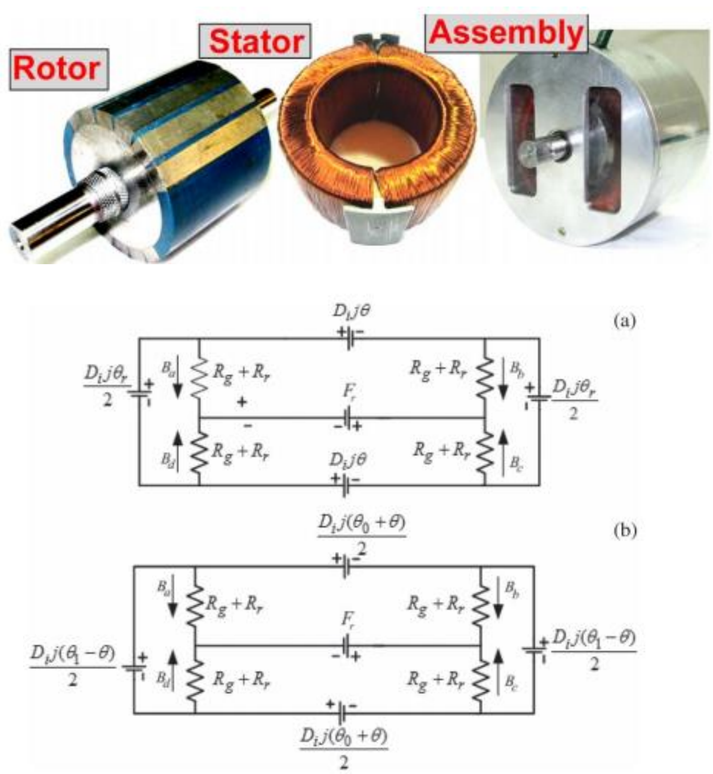

Figure 1. 10: The geometry and the developed MEC of the studied LATM.

In [42], a nonlinear magnetic equivalent circuit is proposed for a permanent-magnet slotted limited-angle torque motor. The model is also employed for multi-objective design optimization of the device. The configuration of the motor and the developed MEC are shown in Figure 1.11.

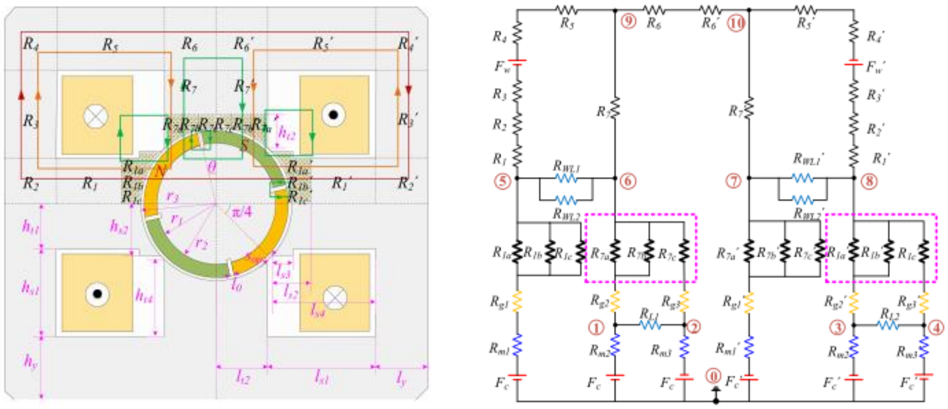

Figure 1. 11: The configuration and the developed nonlinear MEC of the studied LATM.

In [43], a comprehensive magnetic equivalent circuit is developed for a toroidally-wound limited-angle torque motor having Halbach permanent magnet array as the rotor. The model is also employed for multi-objective design optimization of the device. The configuration of the motor and the developed MEC are shown in Figure 1.12.

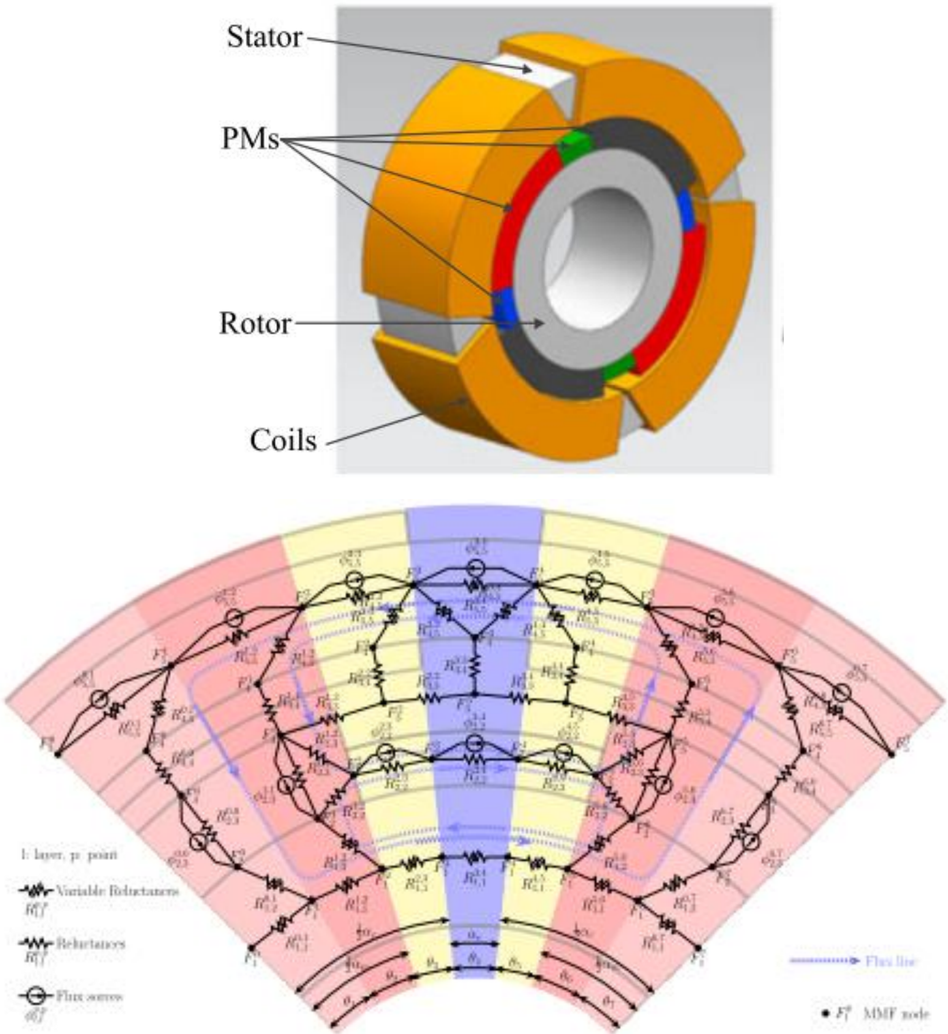

Figure 1. 12: The configuration and the developed nonlinear MEC of the studied LATM.

In [44], a magnetic equivalent circuit (MEC) and FEM are employed in the analysis and design of a limited-angle torque motor with a moving coil. The configuration of the studied actuator is shown in Figure. 1.13.

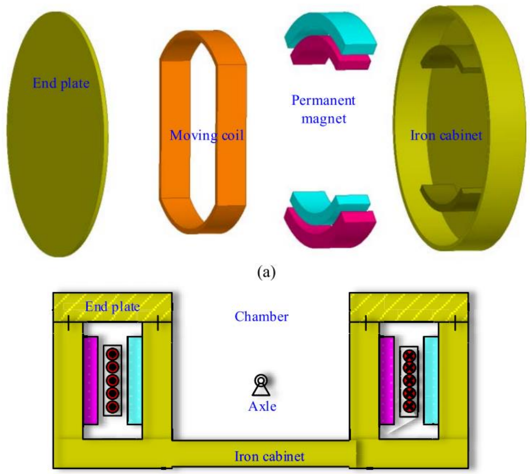

Figure 1. 13: The geometry of the studied limited-angle torque motor with a moving coil

The paper [45] presents simple calculations for the inductance prediction of a toroidally-wound limited angle torque motor having a permanent magnet as the rotor. Its configuration is shown in Figure. 1.14.

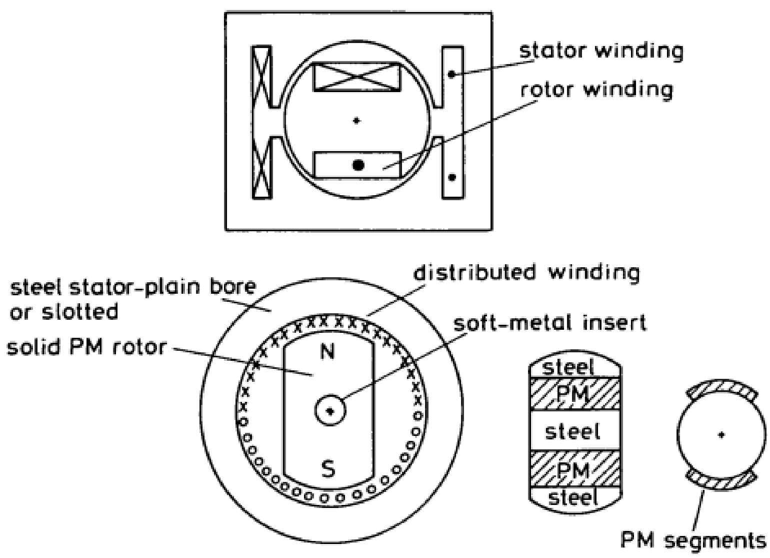

Figure 1. 14: The geometry of the studied toroidally-wound limited-angle torque motor.

1.1.4 Restoration torque Techniques in Rotary Actuators

For many applications, for example, in fail-safe operations, the rotor is needed to return to the initial position when the stator excitation is removed. This restoration force is traditionally provided by a mechanical stiffness or spring. Also, there have been some actuator designs offering a magnetic mechanism to replace the mechanical spring with a magnetic restoration force. It is more reliable and does not have the problem of traditional springs like mechanical fatigue.

In the papers [46]-[47], simplified modeling and dynamic analysis of a Laws's relay, including a stiffness, is studied. The stiffness is a nonlinear function of rotor angular position (tangent function of position) and provides a restoration torque that attempts to bring the rotor back to the initial position. The geometry of the device and stiffness as a nonlinear function of the angular position of the rotor is shown in Figure 1.15. The stiffness is represented by a nonlinear equation as well. Finally, a nonlinear dynamic model is established to study the dynamic behavior of the actuator.

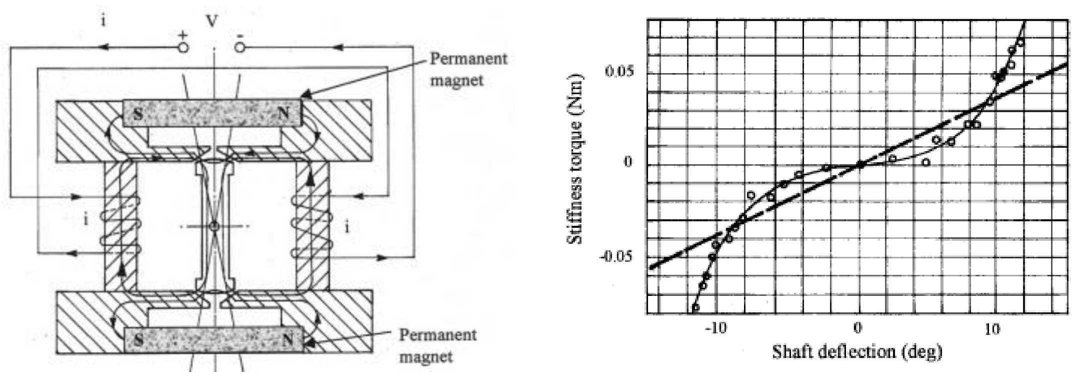

Figure 1. 15: The structure of Laws's relay and the nonlinear stiffness function

In the papers [48], a self-aligning limited-angle rotary torque PM motor for the control valve is studied. In addition to the stator poles, alignment poles are added to the device, such that the rotor returns to its original position when the current is cut off without requiring a separate mechanism to control the position. The structure of the device is shown in Figure 1.16.

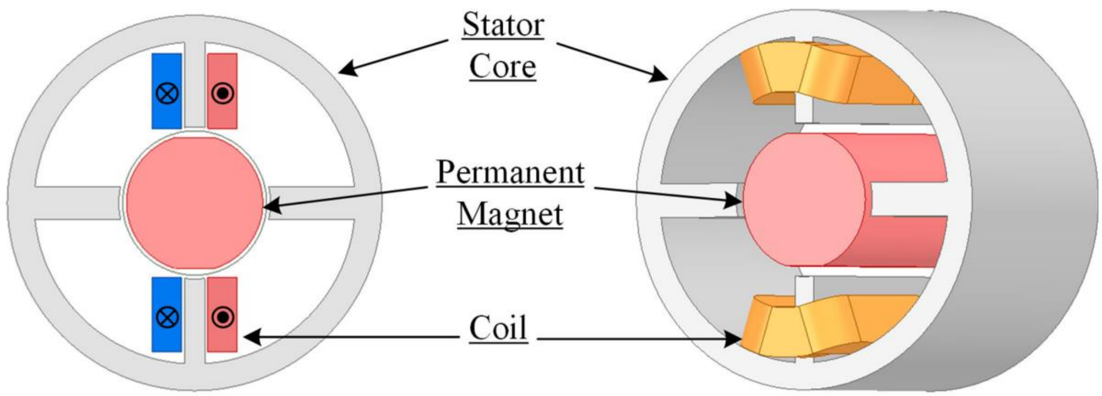

Figure 1. 16: The structure of the LATM having self-alignment or restoration torque

In the papers [49], a zero-returner limited-angle torque motor is proposed, in which the restoration torque is provided by a separate electromagnetic device connected to the LATM. The structure of the device is shown in Figure 1.17. The restoration torque developed by the zero-returner system is shown in Figure 1.18.

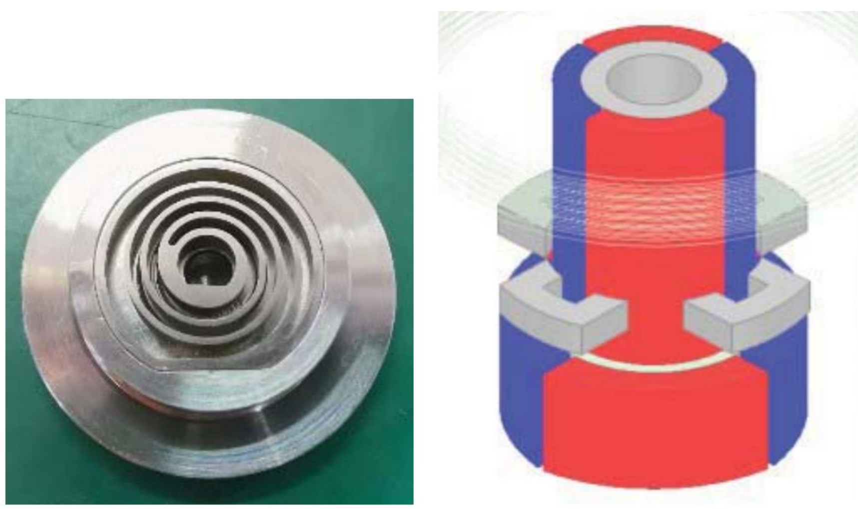

Figure 1. 17: Restoration torque mechanisms: the traditional mechanical spring (left) and magnetic spring (right)

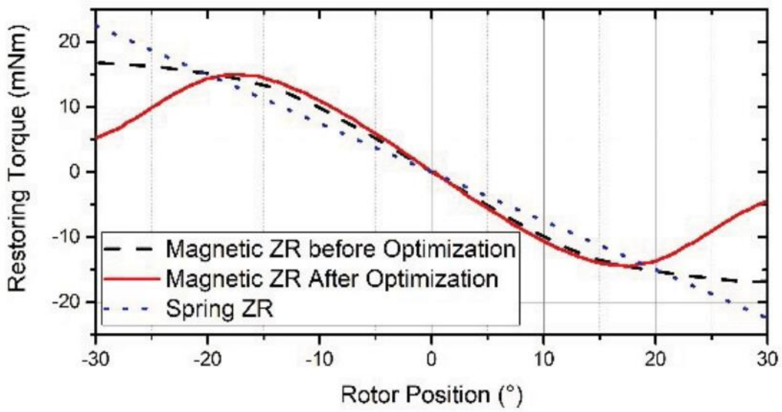

Figure 1. 18: The restoration torque developed by the zero-returner system.

The patents, e.g., [50]- [55], provides a variety of structures of rotary actuators with and without magnetic restoration torque. This thesis presents generalized studies applicable to such actuators while certain aspects of the physical implementations of the actuator with magnetic restoration described herein in this thesis, as well as other interesting topologies, are covered by patents, among others. In Figure 1.19 and Figure 1.20 a number of such actuators along with physical embodiments are presented.

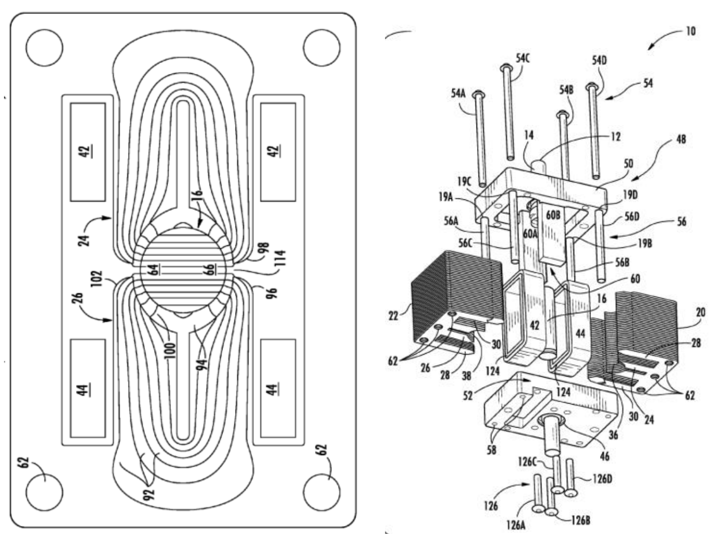

Figure 1. 19: Topology and embodiments of an actuator with magnetic restoration.

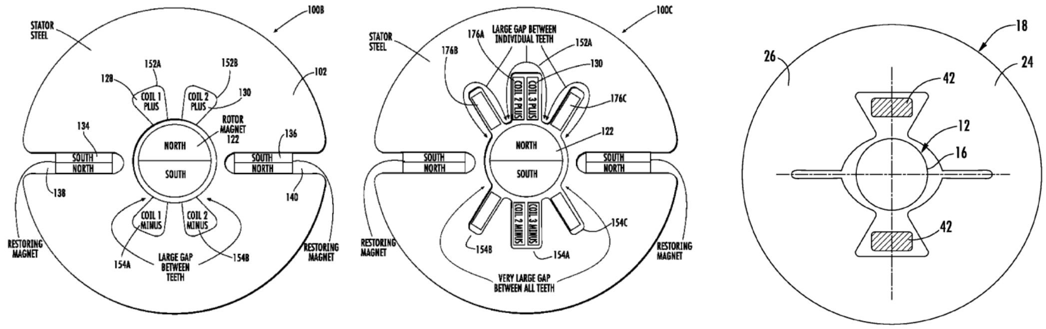

Figure 1. 20: Topology and embodiments of actuators with magnetic restoration.

1.1.5 Dynamic Behavior and Control Studies

High-performance control of electric machines requires accurate models and an effective identification rather than conventional lumped models. The identification can be offline [56] or even online [57] when there are variations in the parameters of the device. Among modeling techniques, the finite element method (FEM), although powerful in the numerical modeling and design of electromagnetic devices, is too slow to be used in dynamic studies. Magnetic equivalent circuits [58]-[59] and subdomain models [60]-[61] provide fast yet accurate analytical frameworks that can be employed in developing electromechanical models. MEC-based models are developed to study the design of LATMs [58] and magnetic cores [59]. The subdomain approach is employed to study the diffusion in eddy current brakes [60] and cylindrical ferrite cores [61]. In [62], the finite difference method is employed to find the numerical solution of 2-D diffusion in a rectangular sheet. As eddy currents can highly impact the dynamic and thus control system design of an electromagnetic device, incorporating their impact in the model can be very crucial. In the interesting works [63]-[64], an analytical solution of 1-D diffusion in thin laminations or magnetic materials is used to modify the electrical circuit of an electromagnetic device. Friction is another factor affecting the mechanical dynamics of electromechanical devices, whose impact can be studied by LuGre model [65]-[68]. High bandwidth current loops are widely employed to drive actuators and electromagnetic devices in order to eliminate the electrical dynamic so that the torque can be directly commanded by the outer control loops. It also provides a faster response and higher robustness by making the system independent of temperature-dependent elements like the stator resistance. The current drives may be developed using analog architectures like opamps circuits [69]-[71] or FPGA-based switching devices [72]. Advanced current controllers are also studied in [73]. A push-pull-based drive is also implemented in [74].

The position control system of rotary actuators can be implemented by voltage drives [75]-[76] or current drives [69]-[71]. The former, although cheap and simple, have disadvantages like a slower response, weak robustness, and even more uncertainties in the model. The latter, by eliminating the electrical dynamic of the actuator using a high-bandwidth current loop, can offer a faster response, higher robustness, and even simplicities in the model. Among others, feedback linearization has been employed as a powerful yet simple nonlinear control technique for the control of electromechanical devices if a precise model is available [77]-[78]. Also, unmeasured states can be estimated using observers [79]-[80]. Model-based observers, especially those which are based on state-space models, can be easily discretized to be implemented in a DSP [81]. In addition, advanced observers can be developed for special purposes [82]. Advanced position control techniques are implemented in [83]- [85].

1.2 Outline and Contributions of the Thesis

Analytical models are useful in the design of electromagnetic devices. In this thesis, a model is developed for a rotary actuator whose stator curvature is elliptically shaped to have a reluctance torque that restores the rotor to the maximum torque per ampere position. The total torque is decomposed to the coil torque as well as a reluctance torque. The rotor's permanent magnet is represented by equivalent Amperian currents. The stator geometry is simplified to an ellipse having surface current densities at the interpolar regions which are equivalent to the stator currents. Then, the field solution within the ellipse is obtained using Laplace's equation in the elliptical coordinates, so that the coil torque can be obtained by Lorentz force. The reluctance torque is derived by the energy method and an approach named differential flux tubes, which is similar to the conventional flux tubes in magnetic equivalent circuits. A rotating reference frame on the rotor is also adopted to simplify mathematics. The finite element method is also used in the field analysis and development of the proposed model. In the end, the actuator is prototyped whose experimental results are employed to evaluate the results obtained from the analytical model and finite element method.

Modeling, identification, drive, and current control loop of a limited-rotation actuator is studied. The stator pole faces are elliptically shaped to obtain a restoration torque. A nonlinear electromechanical model is developed for analysis and nonlinear control for large signals. It is also linearized to be used in the linear control for small signals. To get higher accuracy and an efficient design, the eddy-currents in the laminations and the magnet are included in the model by analytically solving the diffusion equation and extracting a lumped-element circuit. The impact of the pre-sliding friction on the mechanical dynamic is studied as well. Finite element analysis is also used in the study. The lab experiments are performed using a prototype actuator. Torque-angle and back-emf characteristics are obtained, and the identification of the model is carried out. Then, an op-amp-based drive circuit for the current control loop is proposed and designed. Using a third-order model of the op-amps, a very accurate model for the drive and the current loop is developed to be used for prediction and evaluation purposes, while its simplified version is also obtained for the design procedure.

Also, the accuracy of the modeling of the actuator and the drive circuit is evaluated in control studies. The importance of eddy current modeling is shown as well. Also, the effectiveness of the designed current loop and its practical trade-offs are investigated. Then, three DSP-based position control techniques are implemented and compared: pole placement with voltage drive, placement with current drive, and nonlinear control with feed linearization. Full-order and reduced-order observers are also employed to estimate the unmeasured states. The control system designs are evaluated through indices like rise time, overshoot and steady-state error, and large-signal tracking in the step response as well as bandwidth, robustness, phase margin, sensitivity, disturbance rejection, and noise rejection in the frequency domain.

An eddy-current-based technique is proposed that may reduce the coil inductance at high frequencies. However, it is an initial examination by two-dimensional FEM, while more tests and optimizations may be done by researchers on various aspects of the technique, how to optimize the strategy, what penalties do we pay for using this method, the effectiveness of this approach, etc. It is just a conceptual study, for which a typical geometry of the actuator is picked. The default values of the conductivity of laminations and the magnet given by the software are employed. Although close, they do not accurately simulate experimental studies or even three-dimensional finite element analysis.

A new effectiveness index is proposed that may represent the effectiveness of an actuator with oscillational behavior in a better way. Like the previous chapter, more investigations and discussions can be done on the proposed effectiveness index herein.

.

Chapter 2

Electromagnetics and Energy Conversion

2.1 Introduction

In this chapter, first, we start with an overview of *electromagnetic field theory* and Maxwell's equations [17]-[18]. Then, we continue with *quasi-static field theory*, i.e., magneto-quasi-static (MQS) field theory and electro-quasi-static (EQS) field theory. Also, we review static field theory, i.e., magneto-static (MS) field theory and electrostatic (ES) field theory. The, we talk about energy conversion and calculations of force and torque.

2.2. Maxwell's Equations and Charge Conservation in Free Space

Differential and integral forms of *Maxwell's equations in free space* or *microscopic formulation of Maxwell's equations*, as well as *continuity equation* are as in below:

	Differential Form	Integral Form	Boundary Conditions
Ampere's law	$\nabla \times \frac{B}{\mu_0} = J_f + \frac{\partial \varepsilon_0 E}{\partial t}$	$\oint_C \frac{B}{\mu_0}.dl = \iint_S \left(J_f + \frac{\partial \varepsilon_0 E}{\partial t} \right).ds$	$n \times (\frac{B_1}{\mu_0} - \frac{B_2}{\mu_0}) = K_f$ $\frac{1}{\mu_0}(B_{1t} - B_{2t}) = K_f$
Gauss's law of magnetic	$\nabla.B = 0$	$\oiint_S B.ds = 0$	$n.(B_1 - B_2) = 0$ $B_{1n} = B_{2n}$
Faraday's law	$\nabla \times E = -\frac{\partial B}{\partial t}$	$\oint_C E.dl = -\iint_S \frac{\partial B}{\partial t}.ds$	$n \times (E_1 - E_2) = 0$ $E_{1t} = E_{2t}$
Gauss's law	$\nabla.\varepsilon_0 E = \rho_f$	$\oiint_S \varepsilon_0 E.ds = \iiint_{vol} \rho_f \, dv$	$n.(\varepsilon_0 E_1 - \varepsilon_0 E_2) = \sigma_{sf}$ $\varepsilon_0 (E_{1n} - E_{2n}) = \sigma_{sf}$
Continuity equation	$\nabla.J_f + \frac{\partial \rho_f}{\partial t} = 0$	$\oiint_S J_f.ds + \iiint_{vol} \frac{\partial \rho_f}{\partial t} dv = 0$	$n.(J_{f1} - J_{f2}) + \nabla.K_f$ $= -\frac{\partial \sigma_{sf}}{\partial t}$

where B is magnetic flux density, E is the electric field, J_f is free current density, K_f is free surface current density, ρ_f is free charge density, σ_{sf} is free surface charge density. Also, t and n stand for tangential and normal, respectively.

2.3. Maxwell's Equations in Matter

Employing two new quantities of magnetic field intensity H and electric displacement field D, *constitutive relations* are given below:

$B=\mu_0(H+M)$
$D=\varepsilon_0 E+P$
$J=\sigma E$

where M and P are *magnetization* and *polarization* vectors of the matter. Also, σ is the conductivity of the matter.

Then, the differential and the integral form of *Maxwell's equations in matter* or *macroscopic formulation of Maxwell's equations* are as in below:

	Differential Form	Integral Form	Boundary Condition
Ampere's law	$\nabla\times H=J_f+\dfrac{\partial D}{\partial t}$	$\oint_C H.dl=\iint_S\left(J_f+\dfrac{\partial D}{\partial t}\right).ds$	$n\times(H_1-H_2)=K_f$ $H_{1t}-H_{2t}=K_f$
Gauss's law of magnetic	$\nabla.B=0$	$\oint\!\!\oint_S B.ds=0$	$n.(B_1-B_2)=0$ $B_{1n}=B_{2n}$
Faraday's law	$\nabla\times E=-\dfrac{\partial B}{\partial t}$	$\oint_C E.dl=-\iint_S\dfrac{\partial B}{\partial t}.ds$	$n\times(E_1-E_2)=0$ $E_{1t}=E_{2t}$
Gauss's law	$\nabla.D=\rho_f$	$\oint\!\!\oint_S D.ds=\iiint_{vol}\rho_f\,dv$	$n.(D_1-D_2)=\sigma_{sf}$ $D_{1n}-D_{2n}=\sigma_{sf}$
Continuity equation	$\nabla.J_f+\dfrac{\partial\rho_f}{\partial t}=0$	$\oint\!\!\oint_S J_f.ds+\iiint_{vol}\dfrac{\partial\rho_f}{\partial t}dv=0$	$n.(J_{f1}-J_{f2})+\nabla.K_f$ $=-\dfrac{\partial\sigma_{sf}}{\partial t}$

2.3.1. Employing Charge Model of Magnetization

By substituting for $B=\mu_o(H+M)$ and $D=\varepsilon_o E+P$ from constitutive relations, we can get a new formulation. It should be noted that, in this model, the equations and the boundary conditions are in terms of *H*, and then we obtain *B* with $B=\mu_0(H+M)$. Using the *charge model of magnetization*, we have:

	Differential Form	**Boundary Condition**
Ampere's law	$\nabla\times H = J_f + \dfrac{\partial(\varepsilon_0 E+P)}{\partial t} \Rightarrow$ $\nabla\times H = J_f + \dfrac{\partial P}{\partial t} + \varepsilon_0 \dfrac{\partial E}{\partial t}$ $\nabla\times H = J_f + J_p + \varepsilon_0 \dfrac{\partial E}{\partial t}$ $J = J_f + J_p$ polarization current density: $J_p = \dfrac{\partial P}{\partial t}$	$n\times(H_1-H_2)=K_f$ $H_{1t}-H_{2t}=K_f$ *note:* boundary conditions are in terms of *H*
Gauss's law of magnetic	$\nabla.\mu_0(H+M)=0 \Rightarrow \nabla.\mu_0 H = -\nabla.\mu_0 M$ $\nabla.\mu_0 H = \rho_m$ (surface) magnetic-charge density: $\rho_m = -\mu_0\nabla.M \;\; ; \;\; \sigma_{sm} = -n.(M_1-M_2)$	$n.(\mu_0 H_1-\mu_0 H_2)=\sigma_{sm}$ $\mu_0(H_{1n}-H_{2n})=\sigma_{sm}$ *note:* boundary conditions are in terms of *H*
Faraday's law	$\nabla\times E = -\dfrac{\partial\mu_0(H+M)}{\partial t} \Rightarrow$ $\nabla\times E = -\mu_0\dfrac{\partial H}{\partial t} - \mu_0\dfrac{\partial M}{\partial t}$ $\nabla\times E = -\mu_0\dfrac{\partial H}{\partial t} - J_m^*$ magnetic-current density: $J_m^* = \mu_0\dfrac{\partial M}{\partial t}$	$n\times(E_1-E_2)=0$ $E_{1t}=E_{2t}$
Gauss's law	$\nabla.(\varepsilon_0 E+P)=\rho_f \Rightarrow$ $\nabla.\varepsilon_0 E = \rho_f - \nabla.P$ $\nabla.\varepsilon_0 E = \rho_f + \rho_p$ (surface) polarization charge density: $\rho_p = -\nabla.P \;\; ; \;\; \sigma_{sp} = -n.(P_1-P_2)$	$n.(D_1-D_2)=\sigma_{sf}+\sigma_{sp}$ $D_{1n}-D_{2n}=\sigma_{sf}+\sigma_{sp}$

Continuity equation	$\nabla.J_f + \frac{\partial \rho_f}{\partial t} = 0$ $\nabla.J_m^* + \frac{\partial \rho_m}{\partial t} = 0$ $\nabla.J_p + \frac{\partial \rho_p}{\partial t} = 0$	$n.(J_1 - J_2) + \nabla.K$ $= -\frac{\partial \sigma_s}{\partial t}$

2.3.2. Employing Amperian Current Model of Magnetization

Also, we can employ the *Amperian current model of magnetization* to get a new formulation for Maxwell's equation mater. In this case, we need to remove $J_m^* = \mu_0 \frac{\partial M}{\partial t}$ and $\rho_m = -\mu_0 \nabla.M$, and instead, employ $J_m = \nabla \times M$ as a free current in Ampere's law. It should be noted that, in this model, the equations and <u>the boundary conditions are in terms of *B*, and then we obtain *H*</u> with $H = \frac{B}{\mu_0} - M$. We have:

	Differential Form	**Boundary Condition**
Ampere's law	$\nabla \times \frac{B}{\mu_0} = J_f + J_p + J_m + \varepsilon_0 \frac{\partial E}{\partial t}$ $\underline{J = J_f + J_m + J_p}$ polarization current density: $\underline{J_p = \frac{\partial P}{\partial t}}$ Amperian current model of magnetization: $J_m = \nabla \times M \;\; ; \;\; K_m = n \times (M_1 - M_2)$	$n \times \frac{1}{\mu_0}(B_1 - B_2) = K_f + K_m$ $\frac{B_{1t} - B_{2t}}{\mu_0} = K_f + K_m$ *note:* boundary conditions are in terms of *B*
Gauss's law of magnetic	$\nabla.B = 0$	$n.(B_1 - B_2) = 0$ $B_{1n} = B_{2n}$ *note:* boundary conditions are in terms of *B*
Faraday's law	$\nabla \times E = -\frac{\partial B}{\partial t}$ or $\nabla \times E = -\frac{\partial \mu_0 (H + M)}{\partial t}$ or $\nabla \times E = -\frac{\partial \mu H}{\partial t}$	$n \times (E_1 - E_2) = 0$ $E_{1t} = E_{2t}$

Gauss's law	$\nabla.\varepsilon_0 E = \rho_f + \rho_p$ $\underline{\rho = \rho_f + \rho_p}$ (surface) polarization charge density: $\rho_p = -\nabla.P \;\; ; \;\; \sigma_{sp} = -n.(P_1 - P_2)$	$n.(D_1 - D_2) = \sigma_{sf}$ $D_{1n} - D_{2n} = \sigma_{sf}$
Continuity equation	$\nabla.J_f + \dfrac{\partial \rho_f}{\partial t} = 0$ $\nabla.J_p + \dfrac{\partial \rho_p}{\partial t} = 0$	$n.(J_1 - J_2) + \nabla.K$ $= -\dfrac{\partial \sigma_s}{\partial t}$

The net electric current I_{enc} enclosed in closed lines C encompassing surface S corresponding to current density J, as well as the net electric charge Q_{enc} enclosed in volume *vol* corresponding to volume charge density ρ are as in below:

Current	$I_{enc} = \iint\limits_S J.ds$
Charge	$Q_{enc} = \iiint\limits_{vol} \rho \, dv$

Magnetic flux and electric flux through a surface S are defined as in below:

Magnetic flux	$\varphi_B = \iint\limits_S B.ds$
Electric flux	$\varphi_E = \iint\limits_S E.ds \; , \;\; \varphi_D = \iint\limits_S D.ds$

The macroscopic formulation of Maxwell's equations is as in below:

	Integral Form
Ampere's law	$\oint\limits_C H.dl = I_{enc} + \dfrac{d\varphi_D}{dt}$ $I_{enc} = \iint\limits_S J_f.ds$
Gauss's law of magnetic	$\oiint\limits_S B.ds = 0$

Faraday's law	$\oint_C E.dl = -\frac{d\varphi_B}{dt}$
Gauss's law	$\oiint_S D.ds = Q_{e.enc}$ $Q_{e.enc} = \iiint_{vol} \rho_f \, dv$
Continuity equation	$\oiint_S J.ds + \frac{dQ_{e.enc}}{dt} = 0$

Using the charge model of magnetization, we can also rewrite as in below:

	Integral Form
Ampere's law	$\oint_C H.dl = I_{enc} + \varepsilon_0 \frac{d\varphi_E}{dt}$ electric current: $I_{enc} = \iint_S (J_f + J_p).ds$
Gauss's law of magnetic	$\oiint_S \mu_0 H.ds = Q_m$ magnetic charge: $Q_{m.enc} = \iiint_{vol} \rho_m \, dv$
Faraday's law	$\oint_C E.dl = -\frac{d\varphi_B}{dt} - I_m^*$ magnetic current: $I_m^* = \iint_S J_m^*.ds$
Gauss's law	$\oiint_S \varepsilon_0 E.ds = Q_{e.enc}$ Electric charge: $Q_{e.enc} = \iiint_{vol} (\rho_f + \rho_p) \, dv$
Continuity equation	$\oiint_S J.ds + \frac{dQ_{e.enc}}{dt} = 0$ $\oiint_S J_m.ds + \frac{dQ_{m.enc}}{dt} = 0$

Using the Amperian current model of magnetization, we can also rewrite as in below:

	Integral Form
Ampere's law	$\oint_C \frac{B}{\mu_0}.dl = I_{enc} + \varepsilon_0 \frac{d\varphi_E}{dt}$ electric current: $I_{enc} = \iint_S (J_f + J_p + J_m).ds$
Gauss's law of magnetic	$\oiint_S B.ds = 0$
Faraday's law	$\oint_C E.dl = -\frac{d\varphi_B}{dt}$
Gauss's law	$\oiint_S \varepsilon_0 E.ds = Q_{e.enc}$ electric charge: $Q_{e.enc} = \iiint_{vol} (\rho_f + \rho_p)\, dv$
Continuity equation	$\oiint_S J.ds + \frac{dQ_{enc}}{dt} = 0$

Notes:

- There is a duality in the four of Maxwell's equations. The duality between Ampere's law and Faraday's law (in the charge model of magnetization) is as in below:

$$\nabla \times H - \varepsilon_0 \frac{\partial E}{\partial t} = J_f + J_p \tag{2.1}$$

$$\nabla \times E + \mu_0 \frac{\partial H}{\partial t} = -J_m^* \tag{2.2}$$

  The duality between magnetic and electric Gauss's laws is as in below:

$$\nabla . \mu_0 H = \rho_m \tag{2.3}$$

$$\nabla . \varepsilon_0 E = \rho_f + \rho_p \tag{2.4}$$

- The rate of change of magnetic flux $\frac{d\varphi_B}{dt}$ is the induced electro-motive force (EMF) which can be seen in Faraday's law.

- The rate of change of electric flux $\frac{d\varphi_D}{dt}$ is the displacement current or the induced magneto-motive force (MMF), which can be seen in Ampere's law.

- The coupling between electric and magnetic fields, i.e., the magnetic induction in Faraday's law ($\partial D / \partial t$) and the displacement current in Ampere's law ($\partial B / \partial t$), gives rise to electromagnetic waves.

- **Derivation of continuity equation:** by employing Ampere's law, Gauss's law, and the fact that divergence of the curl of a vector H is always zero, we have:

$$\nabla.(\nabla \times H) = 0 \xrightarrow{\nabla\times H = J + \frac{\partial D}{\partial t}} \nabla.(J + \frac{\partial D}{\partial t}) = 0 \Rightarrow \nabla.J + \frac{\partial(\nabla.D)}{\partial t} = 0 \xrightarrow{\nabla.D=\rho} \nabla.J + \frac{\partial \rho}{\partial t} = 0$$

(2.5)

- In Maxwell's equations written using the magnetic charge model of magnetization, the relationships and the boundary conditions are written in terms of H and then $B = \mu_0 (H + M)$. In Maxwell's equations written using the Amperian current model of magnetization in which the magnets are treated as free currents, the relationships and the boundary conditions are written in terms of B and then $H = \frac{B}{\mu_0} - M$.

2.3.3. Linear Isotropic Material

For magnetically linear isotropic homogeneous materials, magnetization M can be buried in permeability μ by using magnetic susceptibility χ_m. Also, for electrically linear isotropic materials, polarization P can be buried in permittivity ε by using electric susceptibility χ_e.

magnetization $M = \chi_m H$	**permeability** $\mu = \mu_0 \mu_r$, $\mu_r = (1 + \chi_m)$	$B = \mu_0 (1 + \chi_m) H = \mu H$
polarization $P = \varepsilon_0 \chi_e E$	**permittivity** $\varepsilon = \varepsilon_0 \varepsilon_r$, $\varepsilon_r = (1 + \chi_e)$	$D = \varepsilon_0 (1 + \chi_e) E = \varepsilon E$

The equations $B = \mu H$ and $D = \varepsilon E$ are helpful in media like iron and can be employed instead of $B = \mu_0(H + M)$ and $D = \varepsilon_0(E + P)$.

For example, it is true for iron in the linear region, i.e., when field H is small. Figure 2.1 shows a simple comparison of permeability for ferromagnetic, paramagnetic, and diamagnetic materials.

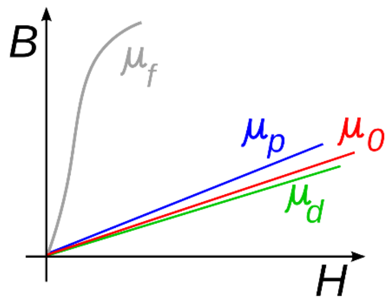

Figure 2. 1. Comparison of permeability for ferromagnetic, paramagnetic, and diamagnetic materials [source: wikipedia].

For nonlinear isotropic homogeneous materials, μ, ε, and σ depends on the field as in below:

$B = \mu(H)H$
$D = \varepsilon(E)E$
$J = \sigma(E)E$

In anisotropic material, $\mu(H)$, $\varepsilon(E)$ and $\sigma(E)$ are independent of the direction of the field, while in anisotropic material μ, ε and σ depend on the direction as in below:

$$\begin{bmatrix} B_x \\ B_y \\ B_z \end{bmatrix} = \begin{bmatrix} \mu_{11} & \mu_{12} & \mu_{13} \\ \mu_{21} & \mu_{22} & \mu_{23} \\ \mu_{31} & \mu_{32} & \mu_{33} \end{bmatrix} \begin{bmatrix} H_x \\ H_y \\ H_z \end{bmatrix} \tag{2.6}$$

In a homogeneous material, μ, ε and σ do not depend on position, while in an inhomogeneous material, they do as in below:

$\mu = \mu(x, y, z)$
$\varepsilon = \varepsilon(x, y, z)$
$\sigma = \sigma(x, y, z)$

2.4. Vector and Scalar Potentials

The fields can be obtained in two ways:

- Maxwell's equations can be solved directly for the fields. In this case, we deal with *four coupled first-order field equations*. Maxwell's equation in a stationary, homogeneous, isotropic and linear medium with constitutive relations $B=\mu H$, $D=\varepsilon E$ and $J=\sigma E$ are as in below:

Magnetic	$\nabla \times H = J + \dfrac{\partial \varepsilon E}{\partial t}$
	$\nabla . B = 0$
	$B = \mu_0 (H + M)$
Electric	$\nabla \times E = -\dfrac{\partial B}{\partial t}$
	$\nabla . \varepsilon E = \rho$
	$D = \varepsilon_0 (E + P)$

- Also, it might be more convenient to employ scalar and vector potentials. In this case, we deal with *two uncoupled second-order field equations*.

Magnetic Vector Potential:

It is worth noting that the divergence of the curl of a vector is zero $\nabla .(\nabla \times A) = 0$. In other words, if the divergence of a vector is zero, it can be defined by a vector potential. According to magnetic Gauss's law in the Amperian current model of magnetization, a magnetic vector potential can be defined as in below:

$$\nabla . B = 0 \quad \Rightarrow \quad B = \nabla \times A \tag{2.7}$$

As shown in Figure 2.2(a), the net flux passing through a surface S enclosed by closed line C is the surface integral of magnetic flux density vector B over surface S, or is the closed line integral of the magnetic vector potential A over line C as in below:

$$\varphi = \oiint_S \vec{B} . d\vec{s} = \oint_c \vec{A} . d\vec{l} \tag{2.8}$$

It is obtained by substituting B in terms of A and employing Stokes' theorem. In a 2D problem where A is only in the z-direction, flux is easily calculated as in below:

$$\varphi = L(A_{z1} - A_{z2}) = L\,\Delta A_z \tag{2.9}$$

where A_{z1} and A_{z1} are values of A_z at the two points in the xy-plane as shown in Figure 2.2(b), and L is the axial length of the problem in the z-direction. In case of having a uniform magnetic flux density B or in approximations, we have:

$$\varphi = L\,w\,B_{av} \tag{2.10}$$

Combining the last two equations, we have:

$$\Delta A_z = w\,B_{av} \tag{2.11}$$

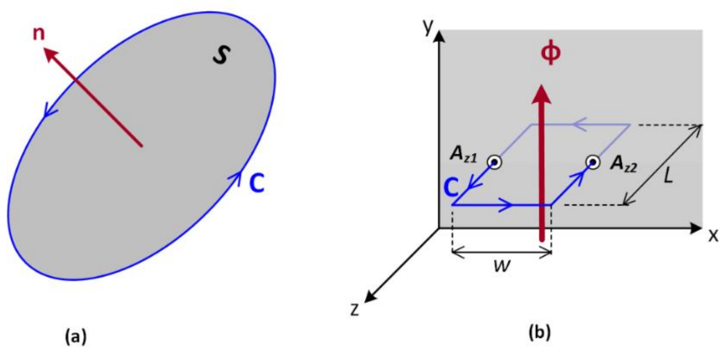

Figure 2. 2. Closed line C enclosed by open surface S in (a) 3D problem and (b) 2D problem.

Magnetic Scalar Potential (current-free region):

In a current-free region, the magnetic field is solenoidal. We know that the curl of gradient of a scalar function is zero, so according to Faraday's law, a magnetic scalar potential can be defined as in below:

$$\nabla \times H = 0 \rightarrow \quad H = -\nabla \psi \tag{2.12}$$

By employing the identity $\nabla.\nabla\psi = \nabla^2\psi$ in the magnetic Gausses' law with charge model of magnetization and substituting the fields in terms of the potentials, we obtain a second-order scalar Poison's equation governing as in below:

$$\nabla.\mu(-\nabla\psi) = \rho_m \Rightarrow \nabla^2\psi = -\rho_m \tag{2.13}$$

Electric Scalar Potential:

Also, the curl of gradient of a scalar function is zero, i.e., the rotation of the maximum variation of the scalar field at any point in space is zero. In other words, if the curl of a vector is zero, it can be defined by a scalar potential. According to Faraday's law, an electric scalar potential can be defined as in below:

$$\nabla\times E=-\frac{\partial B}{\partial t}\xrightarrow{B=\nabla\times A}\nabla\times(E+\frac{\partial A}{\partial t})=0\Rightarrow E+\frac{\partial A}{\partial t}=-\nabla\varphi\Rightarrow\quad E=-\nabla\varphi-\frac{\partial A}{\partial t} \tag{2.14}$$

Two Uncoupled Equations in Terms of Potentials:

Magnetic: By substituting $B=\nabla\times A$ and $E=-\nabla\varphi-\partial A/\partial t$ in Ampere's law and Gauss's law, we obtain uncoupled equations in terms of vector and scalar potentials. By employing the identity $\nabla\times\nabla\times A=\nabla(\nabla.A)-\nabla^2 A$ in the Ampere's law, we have:

$$\begin{aligned}
&\nabla\times\frac{\nabla\times A}{\mu}=J+\varepsilon\frac{\partial(-\nabla\varphi-\partial A/\partial t)}{\partial t}\Rightarrow\\
&\nabla^2 A-\nabla(\nabla.A)=-\mu J+\mu\varepsilon\frac{\partial(-\nabla\varphi-\partial A/\partial t)}{\partial t}\Rightarrow\\
&\nabla^2 A-\mu\varepsilon\frac{\partial^2 A}{\partial t^2}-\nabla(\nabla.A+\mu\varepsilon\frac{\partial\varphi}{\partial t})=-\mu J
\end{aligned} \tag{2.15}$$

By imposing the *Lorentz gauge condition* $\nabla.A=-\mu\varepsilon\frac{\partial\varphi}{\partial t}$, we obtain:

$$\nabla^2 A-\mu\varepsilon\frac{\partial^2 A}{\partial t^2}=-\mu J\quad ;\ J=J_f+J_m+J_p \tag{2.16}$$

In the Cartesian coordinates, it can be simplified in terms of the vector components as in below:

$$\vec{A}=A_x\hat{x}+A_y\hat{y}+A_z\hat{z}\ ,\ \vec{J}=J_x\hat{x}+J_y\hat{y}+J_z\hat{z}\Rightarrow\begin{cases}\nabla^2 A_x-\mu\varepsilon\frac{\partial^2 A_x}{\partial t^2}=-\mu J_x\\ \nabla^2 A_y-\mu\varepsilon\frac{\partial^2 A_y}{\partial t^2}=-\mu J_y\\ \nabla^2 A_z-\mu\varepsilon\frac{\partial^2 A_z}{\partial t^2}=-\mu J_z\end{cases} \tag{2.17}$$

Electric: By employing the identity $\nabla.\nabla\varphi=\nabla^2\varphi$ in the Gausses' law and substituting the fields in terms of the potentials, we have:

$$\nabla.\varepsilon(-\nabla\varphi-\frac{\partial A}{\partial t})=\rho \Rightarrow \nabla^2\varphi+\frac{\partial(\nabla.A)}{\partial t}=-\frac{\rho}{\varepsilon} \tag{2.18}$$

By imposing the Lorentz gauge condition $\nabla.A=-\mu\varepsilon\frac{\partial\varphi}{\partial t}$, we obtain:

$$\nabla^2\varphi-\mu\varepsilon\frac{\partial^2\varphi}{\partial t^2}=-\frac{\rho}{\varepsilon} \tag{2.19}$$

Using the charge model of magnetization, the potential relationships and their solutions can be summarized as follow:

	Potentials	**Poison's equation**	**Solutions**
Magnetic $\nabla.B=0$	$B=\nabla\times A$	current model of magnetization $\nabla^2 A-\mu\varepsilon\frac{\partial^2 A}{\partial t^2}=-\mu J$ $J=J_f+J_m+J_p$	$A(x,t)=\frac{\mu}{4\pi}\int_{V'}\frac{J(x',t-\frac{\lvert x-x'\rvert}{u})}{\lvert x-x'\rvert}dv'$
Magnetic (current free) $\nabla\times H=0$	$H=-\nabla\psi$	charge model of magnetization $\nabla^2\psi=\nabla.M=-\rho_m$	
Electric $\nabla\times(E+\frac{\partial A}{\partial t})=0$	$E=-\nabla\varphi-\frac{\partial A}{\partial t}$	$\nabla^2\varphi-\mu\varepsilon\frac{\partial^2\varphi}{\partial t^2}=-\frac{\rho}{\varepsilon}$	$\varphi(x,t)=\frac{1}{4\pi\varepsilon}\int_{V'}\frac{\rho(x',t-\frac{\lvert x-x'\rvert}{u})}{\lvert x-x'\rvert}dv'$
Lorentz gauge	$\nabla.A=-\mu\varepsilon\frac{\partial\varphi}{\partial t}$		

where $u=1/\sqrt{\varepsilon\,\mu}=3\times10^8\ m/s$ is the speed of light in the medium.

2.5. Quasistatic Field Theory

Quasi-static fields are obtained by ignoring either the magnetic induction in Faraday's law ($\partial B/\partial t$) or the displacement current in Ampere's law ($\partial D/\partial t$) when the dimension of the studied device is small enough compared to the wavelength ($\lambda=c/f$) of the electromagnetic wave.

Magnetoquasistatic (MQS) fields: by ignoring the displacement current in Ampere's law ($\partial D/\partial t$), we have:

$$\nabla \times H = J \tag{2.20}$$

$$\nabla . B = 0 \tag{2.21}$$

$$\nabla \times E = -\frac{\partial B}{\partial t} \tag{2.22}$$

According to magnetic Gauss's law, a magnetic vector potential is still $B = \nabla \times A$. By employing Ampere's law and the fact that divergence of the curl of a vector H is always zero, we have:

$$\nabla .(\nabla \times H) = 0 \xrightarrow{\nabla \times H = J} \nabla . J = 0 \tag{2.23}$$

In other words, the current density distribution of magnetoquasistatic is solenoidal, that is, it does not have sources or sinks.

By employing the identity $\nabla \times \nabla \times A = \nabla(\nabla . A) - \nabla^2 A$ in Ampere's law, we obtain one second-order equation governing magnetoquasistatic fields:

$$\nabla \times \frac{\nabla \times A}{\mu} = J \Rightarrow \nabla^2 A - \nabla(\nabla . A) = -\mu J$$

To determine a vector A uniquely, we need to know both the curl and divergence of it. In MQS systems, we take the vector a to be solenoidal for the sake of convenience, i.e., zero divergences $\nabla . A = 0$, which is called the *Coulomb's gauge*. It is worth noting that this choice is arbitrary. By imposing Coulomb's gauge condition, we obtain the second-order vector Poison's equation governing magnetoquasistatic fields:

$$\nabla^2 A = -\mu J \tag{2.24}$$

In the Cartesian coordinates, it can be simplified in terms of the vector components as in below:

$$\vec{A} = A_x \hat{x} + A_y \hat{y} + A_z \hat{z} \ , \ \vec{J} = J_x \hat{x} + J_y \hat{y} + J_z \hat{z} \Rightarrow \begin{cases} \nabla^2 A_x = -\mu J_x \\ \nabla^2 A_y{}^2 = -\mu J_y \\ \nabla^2 A_z = -\mu J_z \end{cases} \tag{2.25}$$

Electroquasistatic (EQS) fields: by ignoring the magnetic induction in Faraday's law ($\partial B / \partial t$), we have:

$$\nabla \times E = 0 \tag{2.26}$$

$$\nabla . \varepsilon E = \rho \tag{2.27}$$

The continuity equation is there with full terms because we only ignored ($\partial B / \partial t$), not ($\partial D / \partial t$).

$$\nabla.(\nabla\times H)=0 \xrightarrow{\nabla\times H=J+\frac{\partial D}{\partial t}} \nabla.(J+\frac{\partial D}{\partial t})=0 \Rightarrow \nabla.J+\frac{\partial(\nabla.D)}{\partial t}=0 \xrightarrow{\nabla.D=\rho} \nabla.J+\frac{\partial\rho}{\partial t}=0 \tag{2.28}$$

We know that the curl of gradient of a scalar function is zero, so according to Faraday's law, an electric scalar potential can be defined as in below:

$$\nabla\times E=0 \rightarrow \quad E=-\nabla\varphi \tag{2.29}$$

By employing the identity $\nabla.\nabla\varphi=\nabla^2\varphi$ in the Gausses' law and substituting the fields in terms of the potentials, we obtain the second-order scalar Poison's equation governing electroquasistatic fields:

$$\nabla.\varepsilon(-\nabla\varphi)=\rho \Rightarrow \nabla^2\varphi=-\frac{\rho}{\varepsilon} \tag{2.30}$$

The equations governing quasistatic fields can be summarized in the table below:

	Magnetoquasistatic $\frac{\partial D}{\partial t}=0$	**Electroquasistatic** $\frac{\partial B}{\partial t}=0$
Field equations	$\nabla\times H=J \quad , \quad \nabla.J=0$ $\nabla.B=0$ $\nabla\times E=-\frac{\partial B}{\partial t}$ $J=J(E,B)$	$\nabla\times E=0$ $\nabla.\varepsilon E=\rho$ $\nabla.J+\frac{\partial\rho}{\partial t}=0$ $J=J(E)$
Potentials	$B=\nabla\times A$ current-free: $H=-\nabla\psi$	$E=-\nabla\varphi$
Poison's equation	$\nabla^2 A=-\mu J$ current-free: $\nabla^2\psi=\nabla.M=-\rho_m$	$\nabla^2\varphi=-\frac{\rho}{\varepsilon}$
Potential solutions	$A(x,t)=\frac{\mu}{4\pi}\int_{V'}\frac{J(x',t)}{\lvert x-x'\rvert}dv'$	$\varphi(x,t)=\frac{1}{4\pi\varepsilon}\int_{V'}\frac{\rho(x',t)}{\lvert x-x'\rvert}dv'$
Coulomb's gauge	$\nabla.A=0$	

Note:

Conservative Vector Field: Closed-line integral of an irrational field is zero, and it can be represented by the gradient of a scalar potential, e.g., E in EQS and H in a current-free region. Such fields are called conservative because the line integral of the field vector between two points in space is path independent. In EQS where $\nabla \times E = 0, E = -\nabla \varphi$ we have:

$$\oint_C E.dl = 0 \Rightarrow \int_{a,\, path\, A}^{b} E.dl = \int_{a,\, path\, B}^{b} E.dl = \varphi(b) - \varphi(a) \tag{2.31}$$

In current-free MQS where $\nabla \times H = 0, H = -\nabla \psi$, we have:

$$\oint_C H.dl = 0 \Rightarrow \int_{a,\, path\, A}^{b} H.dl = \int_{a,\, path\, B}^{b} H.dl = \psi(b) - \psi(a) \tag{2.32}$$

2.6. Static Field Theory

In static field theory, there are no time variations, and the time-dependent terms ($\partial / \partial t = 0$) will be removed from Maxwell's equations. The currents are steady in magnetostatic (MS), and the charges have stationary distributions in electrostatic (ES).

	Magnetostatic	**Electrostatic**
Field equations	$\nabla \times H = J$ $\nabla.B = 0$ $B = \mu_0 \left(H + M \right)$ or $B = \mu H$ $\nabla.J = 0$	$\nabla \times E = 0$ $\nabla.\varepsilon E = \rho$ $D = \varepsilon_0 \left(E + P \right)$ or $D = \varepsilon E$ $\nabla.J = 0$
Potentials	$B = \nabla \times A$ current-free: $H = -\nabla \psi$	$E = -\nabla \varphi$
Poison's equation	$\nabla^2 A = -\mu J$ current-free: $\nabla^2 \psi = \nabla.M = -\rho_m$	$\nabla^2 \varphi = -\dfrac{\rho}{\varepsilon}$
Potential solutions	$A(x) = \dfrac{\mu}{4\pi} \int_{V'} \dfrac{J(x')}{\vert x - x' \vert} dv'$	$\varphi(x) = \dfrac{1}{4\pi\varepsilon} \int_{V'} \dfrac{\rho(x')}{\vert x - x' \vert} dv'$
Coulomb's gauge	$\nabla.A = 0$	

2.7. Toque Calculations Using Maxwell Stress Tensor

Maxwell stress tensor is usually employed in microscopic field description of forces—the way Poynting's theorem is used in field discretion of energy flow. Maxwell stress tensor is the rewritten form of Lorenz law and is solely in terms of magnetic fields, so it can be used to calculate the force in situations in which the currents (charged particles) are not available or hard to calculate to be used in Lorentz force. In cylindrical coordinates *(r, θ, z)*, the Maxwell stress tensor is as in below:

$$T = \begin{bmatrix} T_{rr} & T_{r\theta} & T_{rz} \\ T_{\theta r} & T_{\theta\theta} & T_{\theta z} \\ T_{zr} & T_{z\theta} & T_{zz} \end{bmatrix} \tag{2.33}$$

where stress tensor T_{ij} in electromagnetics is as in the following:

$$T_{ij} = \varepsilon_0 E_i E_j + \frac{1}{\mu_0} B_i B_j - \frac{1}{2}(\varepsilon_0 E^2 + \frac{1}{\mu_0} B^2)\,\delta_{ij} \tag{2.34}$$

where i and j can be r, θ or z, and δ_{ij} is the Kronecker's delta which is 1 if $i=j$, otherwise *0*. For magnetic fields, e.g., in electric machines, we have:

$$T_{ij} = \frac{1}{\mu_0} B_i B_j - \frac{1}{2\mu_0} B^2\,\delta_{ij} \tag{2.35}$$

where

$$\begin{aligned} B^2 &= B_r^{\,2} + B_\theta^{\,2} + B_z^{\,2} \\ \vec{B} &= B_r\,\hat{a}_r + B_\theta\,\hat{a}_\theta + B_z\,\hat{a}_z \end{aligned} \tag{2.36}$$

Maxwell stress tensor can be rewritten as in below:

$$T = \frac{1}{\mu_0}\begin{bmatrix} \dfrac{B_r^{\,2} - B_\theta^{\,2} - B_z^{\,2}}{2} & B_r\,B_\theta & B_r\,B_z \\ B_\theta\,B_r & \dfrac{B_\theta^{\,2} - B_r^{\,2} - B_z^{\,2}}{2} & B_\theta\,B_z \\ B_z\,B_r & B_z\,B_\theta & \dfrac{B_z^{\,2} - B_r^{\,2} - B_\theta^{\,2}}{2} \end{bmatrix} \tag{2.37}$$

Similar to the role of Poynting vector S in field description of energy flow in Poynting's theorem, the divergence of the sensor in cylindrical coordinates is the vector of *volume force density* (with the dimension of N/m^3) as in the following:

$$
\begin{aligned}
f_v = \nabla . T = & \left(\frac{\partial A_{rr}}{\partial r} + \frac{1}{r}\frac{\partial A_{r\theta}}{\partial \theta} + \frac{\partial A_{rz}}{\partial z} + \frac{A_{rr} - A_{\theta\theta}}{r} \right) \hat{a}_r \\
& + \left(\frac{\partial A_{\theta r}}{\partial r} + \frac{1}{r}\frac{\partial A_{\theta\theta}}{\partial \theta} + \frac{\partial A_{\theta z}}{\partial z} + \frac{A_{\theta r} + A_{r\theta}}{r} \right) \hat{a}_\theta \\
& + \left(\frac{\partial A_{zr}}{\partial r} + \frac{1}{r}\frac{\partial A_{z\theta}}{\partial \theta} + \frac{\partial A_{zz}}{\partial z} + \frac{A_{zr}}{r} \right) \hat{a}_z
\end{aligned}
\tag{2.38}
$$

Then, force (with the dimension of N) on an object surrounded by closed surface S having the volume *vol* can be obtained as in below:

$$
F = \begin{bmatrix} F_r \\ F_\theta \\ F_z \end{bmatrix} = \iiint_{vol} \nabla . T \, dv \tag{2.39}
$$

Using Stokes' theorem, we have:

$$
F = \begin{bmatrix} F_r \\ F_\theta \\ F_z \end{bmatrix} = \oint\!\!\oint_S T . \hat{n} \, dA \tag{2.40}
$$

As shown in Figure 2.3, the stress on a surface has two components: the normal component, which is called normal stress, and the parallel component, which is called shear stress. There are actually three stresses operating on a surface, two of which are parallel to the surface, whose resultant is the shear stress. The normal stress, which is actually the normal force per unit area, will be as in below:

$$
\vec{\sigma}_n = (\vec{\sigma} . \hat{n}) \, \hat{n} \tag{2.41}
$$

The shear stress, which is actually the tangential force per unit area, is then remaining as in below:

$$
\vec{\tau} = \vec{\sigma} - (\vec{\sigma} . \hat{n}) \hat{n} \tag{2.42}
$$

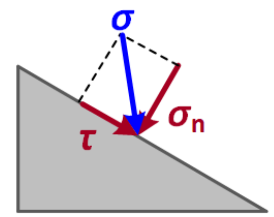

Figure 2. 3. Stress, shear stress, and normal stress

Then, the developed torque on a lever arm vector ***r*** is as in below:

$$T^e = \oiint_S \vec{r} \times (T.\hat{n})\, dA \tag{2.43}$$

Generally, for a surface having the normal unit vector of $n=(n_r, n_\theta, n_z)$, the *surface force density* (with the dimension of N/m^2) is as in below:

$$\vec{f} = \begin{bmatrix} f_r \\ f_\theta \\ f_z \end{bmatrix} = T.\hat{n} = \begin{bmatrix} T_{rr} & T_{r\theta} & T_{rz} \\ T_{\theta r} & T_{\theta\theta} & T_{\theta z} \\ T_{zr} & T_{z\theta} & T_{zz} \end{bmatrix} . \begin{bmatrix} n_r \\ n_\theta \\ n_z \end{bmatrix} = \begin{bmatrix} T_{rr}\,\hat{a}_r + T_{r\theta}\,\hat{a}_\theta + T_{rz}\,\hat{a}_z \\ T_{\theta r}\,\hat{a}_r + T_{\theta\theta}\,\hat{a}_\theta + T_{\theta z}\,\hat{a}_z \\ T_{zr}\,\hat{a}_r + T_{z\theta}\,\hat{a}_\theta + T_{zz}\,\hat{a}_z \end{bmatrix} \tag{2.44}$$

In a two-dimensional analysis of radial-flux rotating machines having an internal rotor, the magnetic field does not have any z-component ($B_z=0$), so $T_{iz}=T_{zi}=0$. As shown in Figure 2.4, for a cylinder of radius R encompassing the rotor, normal vector of the side surface (S_{r+}), top surface (S_{z+}) and bottom surface (S_{z-}) are $n=(1, 0, 0)$, $n=(0, 0, 1)$ and $n=(0, 0, -1)$, respectively.

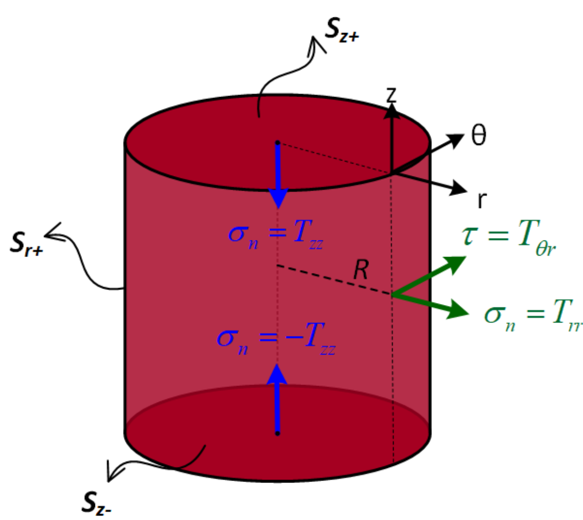

Figure 2. 4. Stresses on a cylinder encompassing the rotor of a radial-flux rotating machine.

The force density on the closed surface integral over a cylinder surrounding the rotor can be separated into three open surface integrals of the side surface, the top surface, and the bottom surface as in below:

$$F = \oiint_{S} (T.\hat{n})\, dA = \iint_{S_r} (T.\hat{a}_r)\, R\, d\theta\, dz + \iint_{S_{z+}} (T.\hat{a}_z)\, r\, dr\, d\theta + \iint_{S_{z-}} (T.-\hat{a}_z)\, r\, dr\, d\theta \qquad (2.45)$$

As shown in Figure 2.4, the tensor (force density vector) operating on the three surfaces of the cylinder are calculated as below:

$$\vec{f}_{S_{r+}} = T.\hat{a}_r = \begin{bmatrix} T_{rr} = \dfrac{B_r^{\,2} - B_\theta^{\,2}}{2\mu_0} & T_{r\theta} = \dfrac{1}{\mu_0} B_r\, B_\theta & 0 \\ T_{\theta r} = \dfrac{1}{\mu_0} B_\theta\, B_r & T_{\theta\theta} = \dfrac{B_\theta^{\,2} - B_r^{\,2}}{2\mu_0} & 0 \\ 0 & 0 & T_{zz} = \dfrac{-B^2}{2\mu_0} \end{bmatrix} . \begin{bmatrix} 1 \\ 0 \\ 0 \end{bmatrix} = \begin{bmatrix} T_{rr} \\ T_{\theta r} \\ 0 \end{bmatrix} = T_{rr}\, \hat{a}_r + T_{\theta r}\, \hat{a}_\theta$$

(2.46)

$$\vec{f}_{S_{z+}} = T.\hat{a}_z = \begin{bmatrix} T_{rr} = \dfrac{B_r^{\,2} - B_\theta^{\,2}}{2\mu_0} & T_{r\theta} = \dfrac{1}{\mu_0} B_r\, B_\theta & 0 \\ T_{\theta r} = \dfrac{1}{\mu_0} B_\theta\, B_r & T_{\theta\theta} = \dfrac{B_\theta^{\,2} - B_r^{\,2}}{2\mu_0} & 0 \\ 0 & 0 & T_{zz} = \dfrac{-B^2}{2\mu_0} \end{bmatrix} . \begin{bmatrix} 0 \\ 0 \\ 1 \end{bmatrix} = \begin{bmatrix} 0 \\ 0 \\ T_{zz} \end{bmatrix} = T_{zz}\hat{a}_z \qquad (2.47)$$

$$\vec{f}_{S_{z-}} = T.-\hat{a}_z = \begin{bmatrix} T_{rr} = \dfrac{B_r^{\,2} - B_\theta^{\,2}}{2\mu_0} & T_{r\theta} = \dfrac{1}{\mu_0} B_r\, B_\theta & 0 \\ T_{\theta r} = \dfrac{1}{\mu_0} B_\theta\, B_r & T_{\theta\theta} = \dfrac{B_\theta^{\,2} - B_r^{\,2}}{2\mu_0} & 0 \\ 0 & 0 & T_{zz} = \dfrac{-B^2}{2\mu_0} \end{bmatrix} . \begin{bmatrix} 0 \\ 0 \\ -1 \end{bmatrix} = \begin{bmatrix} 0 \\ 0 \\ -T_{zz} \end{bmatrix} = -T_{zz}\hat{a}_z$$

(2.48)

Therefore, the three integrals can be rewritten as in below:

$$F = \iint_{S_r} (T_{rr}\,\hat{a}_r + T_{\theta r}\,\hat{a}_\theta)\,R\,d\theta\,dz + \iint_{S_{z+}} T_{zz}\hat{a}_z\,r\,dr\,d\theta + \iint_{S_{z-}} (-T_{zz}\hat{a}_z)\,r\,dr\,d\theta \tag{2.49}$$

The last two terms will cancel. In fact, the negative sign in T_{zz} shows that the last two terms are just the forces that tend to keep the rotor within the stator region, produced by fluxes that tend to take the shortest path with minimum reluctance. These normal stresses on these top and base surfaces are as in below:

$$S_{z+}: \quad \vec{\sigma}_n = \frac{-B^2}{2\mu_0}\vec{a}_z \tag{2.50}$$

$$S_{z-}: \quad \vec{\sigma}_n = \frac{B^2}{2\mu_0}\vec{a}_z \tag{2.51}$$

The stress on the side surface of the cylinder has two components: $T_{\theta r}$ in the tangential direction the contributes to the torque production and T_{rr} whose spatial average around the cylinder is zero because the normal force at any point on the cylinder will be canceled by a negative value on the opposite side. On the side surface, the shear stress and the normal stress can be obtained as:

$$S_{r+}: \quad \vec{\sigma}_n = (\vec{\sigma}.\hat{n})\,\hat{n} = [(T_{rr}\,\hat{a}_r + T_{\theta r}\,\hat{a}_\theta).\hat{a}_r]\,\hat{a}_r = T_{rr}\,\hat{a}_r = \frac{B_r{}^2 - B_\theta{}^2}{2\mu_0}\hat{a}_r \tag{2.52}$$

$$S_{r+}: \quad \vec{\tau} = \vec{\sigma} - (\sigma.\hat{n})\,\hat{n} = (T_{rr}\,\hat{a}_r + T_{\theta r}\,\hat{a}_\theta) - T_{rr}\,\hat{a}_r = T_{\theta r}\,\hat{a}_\theta = \frac{1}{\mu_0}B_r B_\theta\,\hat{a}_\theta \tag{2.53}$$

Therefore, the developed electromagnetic torque is as in below:

$$T^e = \iint_{S_{r+}} \vec{r} \times (T.\hat{n})\,dA \tag{2.54}$$

It leads to the following:

$$T^e = \int_0^L \int_0^{2\pi} R\,B_r H_\theta\,R\,d\theta\,dz = R^2 L \int_0^{2\pi} B_r(\theta) H_\theta(\theta)\,d\theta \tag{2.55}$$

where C can be any closed circle of radius R in the air-gap, as shown in Figure 2.5. In certain conditions where the shear stress on the surface has a spatial average of

$$< \tau >= \frac{1}{2\pi} \int_0^{2\pi} B_r(\theta) H_\theta(\theta)\, d\theta \tag{2.56}$$

the average toque will be

$$T^e = 2\pi R^2 L < \tau > \tag{2.57}$$

Observation:

- The clear observation in the above equation is that the developed torque is just the average shear stress $<\tau>$ (average force density) times the surface area $2\pi RL$ times the torque leg R.

- We know that this equation leads to the same torque regardless of the circle path C of radius R we take, so the stress should be larger for lower radii.

$$R_1 < R_2 \;\Rightarrow\; \tau_1 > \tau_2 \tag{2.58}$$

- The torque is independent of R and can be calculated from the closed line integral over ANY circle C in the air-gap region.

$$< \tau >= \frac{1}{2\pi} \oint_C B_r(\theta) H_\theta(\theta)\, dl \tag{2.59}$$

$$T^e = R^2 L \oint_C B_r(\theta) H_\theta(\theta)\, d\theta \tag{2.60}$$

- Since the shear stress and the torque are independent of the radius of the cylinder, they can be obtained from averaging over air-gap volume (or air-gap area in 2D analysis). It is useful in FEM when the meshed air gap is not very fine.

$$T^e = \frac{1}{R_o - R_i} \int_0^L \int_{R_i}^{R_o} \int_0^{2\pi} r\, B_r(\theta) H_\theta(\theta)\, r\, dr\, d\theta\, dz \tag{2.61}$$

so

$$T^e = \frac{1}{R_o - R_i} \int_0^L \int_{R_i}^{R_o} \int_0^{2\pi} r\, B_r(\theta) H_\theta(\theta)\, r\, dr\, d\theta\, dz = \frac{L}{R_o - R_i} \oint\!\!\oint_{S_g} B_r(\theta) H_\theta(\theta)\, r^2 dr\, d\theta \tag{2.62}$$

where R_i and R_o can be inner and outer radii of the air-gap region (hollow cylinder). The arbitrary circle C in the air-gap and the air-gap surface area S_g (yellow area) is shown in Figure 2.5.

- If the normal and tangential components of the field are orthogonal, the average shear stress will be zero. The following trigonometric pairs are orthogonal:

➢ $\sin p_1\theta \quad and \quad \sin p_2\theta \quad where \quad p_1 \neq p_2$

➢ $\sin p_1\theta \quad and \quad \cos p_2\theta \quad where \quad p_1 \neq p_2$

➢ $\sin p\theta \quad and \quad \cos p\theta$

Therefore, the pair that results in nonzero average shear stress is:

➢ $\sin p\theta \quad and \quad \sin(p\theta - \theta_0) \quad where \quad \theta_0 \neq \dfrac{\pi}{2}$

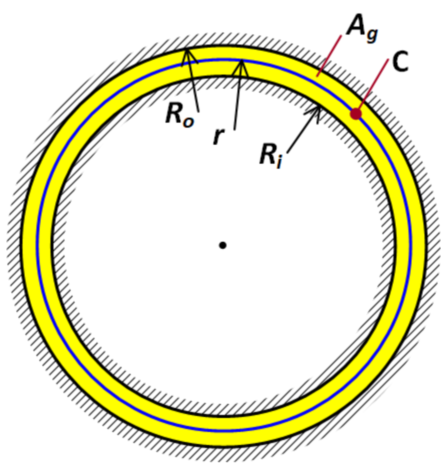

Figure 2. 5. Arbitrary closed line C and air-gap surface area Ag employed in torque calculations using Maxwell stress tensor.

It is worth noting that the developed electromagnetic torque can be obtained from the shear stress on either the stator or the rotor. As illustrated in Figure 2.6., it can be shown that the shear stresses on the two sides of the air gap are in opposite directions. The normal unit vector of the rotor surface is in +r direction, so we have:

$$T^{rotor}.\hat{a}_r = \begin{bmatrix} T_{rr} & T_{r\theta} & T_{rz} \\ T_{\theta r} & T_{\theta\theta} & T_{\theta z} \\ T_{zr} & T_{z\theta} & T_{zz} \end{bmatrix} . \begin{bmatrix} 1 \\ 0 \\ 0 \end{bmatrix} = \begin{bmatrix} T_{rr}\,\hat{a}_r + T_{r\theta}\,\hat{a}_\theta \\ 0 \\ 0 \end{bmatrix} \qquad (2.63)$$

The normal unit vector of the stator surface is in -r direction, so we have:

$$T^{stator}.-\hat{a}_r = \begin{bmatrix} T_{rr} & T_{r\theta} & T_{rz} \\ T_{\theta r} & T_{\theta\theta} & T_{\theta z} \\ T_{zr} & T_{z\theta} & T_{zz} \end{bmatrix} . \begin{bmatrix} -1 \\ 0 \\ 0 \end{bmatrix} = \begin{bmatrix} -(T_{rr}\,\hat{a}_r + T_{r\theta}\,\hat{a}_\theta) \\ 0 \\ 0 \end{bmatrix} \tag{2.64}$$

It is seen that both shear and normal stresses are in opposite directions.

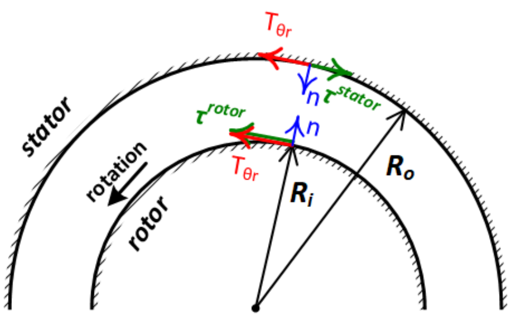

Figure 2. 6. Maxwell stress tensor and shear stress on the surfaces of rotor and stator

We should be careful about the fact that a minus sign comes in if the torque is calculated using the shear stress on the stationary part—the stator, so

$$T^e = 2\pi R_i^2 L < \tau_{rotor} > = -2\pi R_o^2 L < \tau_{stator} > \tag{2.65}$$

The point is that we take the one whose calculation is easier according to the situation we have. For example, in the case of having a surface current density on the surface of an infinitely permeable iron, the tangential magnetic field intensity is just equal to the surface current density. Since the calculated torque is constant regardless of the radius, the shear stress is larger on the surface of the rotor than on the surface of the stator for an inner-rotor radial-flux machine:

$$R_i < R_o \quad \Rightarrow \quad |\tau_{rotor}| > |\tau_{stator}| \tag{2.66}$$

It is also consistent with the fact that the fields B_r and H_θ are larger on the rotor surface (smaller radii) than on the stator surface (larger radii). Also, in cases where the air-gap length is very small compared to rotor radius ($g << R_i$), the torque can be calculated using the average radius, and the shear stress on either side, and also the shear stresses have equal amplitudes but opposite directions.

$$T^e = 2\pi R_{ave}{}^2 L < \tau_{rotor} > = -2\pi R_{ave}{}^2 L < \tau_{stator} > \tag{2.67}$$

$$< \tau_{rotor} > \approx - < \tau_{stator} > \tag{2.68}$$

2.8. Carter's Coefficient and Slot Modeling

In a slotted-stator machine, the slots can be modeled by carter's coefficient. Figure 2.7 shows the flux lines and magnetic flux density distribution in an air-gap having a slotted-stator on the bottom side and surface-mounted permanent magnets for the sake of modeling on the other side. It is seen that the flux lines which are facing the stator teeth take a shorter path—almost the air-gap length—, while those facing the stator slots take a longer path; therefore, the effective air gap is larger than the physical air gap.

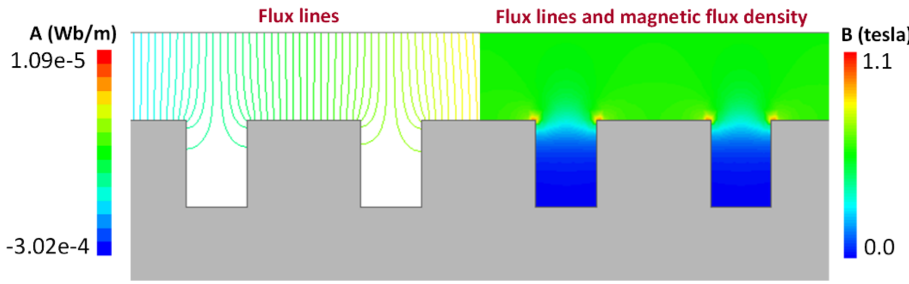

Figure 2. 7. flux lines and magnetic flux density distribution in an air-gap having slots.

In order to account for the effect of the two mentioned regions, we employ a slot pitch of the stator, including a tooth and a slot. The associated region is also modeled with proper boundary conditions as in Figure 2.8 to solve Poisson's equation for magnetic vector potential A in a region without any current. In a 2-D problem, vector potential as in below:

$$\nabla^2 A_z = \frac{\partial^2 A_z}{\partial x^2} + \frac{\partial^2 A_z}{\partial y^2} = 0 \tag{2.69}$$

It is worth noting that in a two-dimensional problem, magnetic vector potential $A_z(x,y)$ only has a z-component while magnetic flux density and magnetic field intensity have x- and y-components. We have:

$$\vec{A} = A_z \hat{a}_z \tag{2.70}$$

$$\vec{B} = B_x \hat{a}_x + B_y \hat{a}_y = \nabla \times \vec{A} \quad \Rightarrow \quad \vec{B} = (\frac{\partial A_z}{\partial y}, -\frac{\partial A_z}{\partial x}, 0) \tag{2.71}$$

$$\vec{H} = H_x \hat{a}_x + H_y \hat{a}_y = \frac{1}{\mu}\vec{B} \quad \Rightarrow \quad \vec{H} = (\frac{1}{\mu}B_x, \frac{1}{\mu}B_y, 0) \tag{2.72}$$

We have Neumann boundary conditions on the iron boundaries because the flux lines are perpendicular to the iron edges. In other words, magnetic field intensity *H* is zero in an infinitely permeable iron, and due to the continuity of the tangential components H_t where there isn't any surface current density on the boundary, H_t is also zero in the air gap and on the iron boundaries.

$$\vec{H}^{iron} = 0 \;\Rightarrow\; H_t^{air} = H_t^{iron} = 0 \;\Rightarrow\; \frac{\partial A_z}{\partial n} = 0 \tag{2.73}$$

where n is the normal component of the boundary. We also have Neumann boundary condition the bottom edge of the problem to which the flux lines, as well as the magnetic field intensity, are perpendicular.

$$H_x = 0 \;\Rightarrow\; \frac{\partial A_z}{\partial y} = 0 \tag{2.74}$$

There is a Dirichlet boundary condition on the left and right sides of the air gap. As in below:

$$A_z\big|_{left} = A_{z1} \tag{2.75}$$

$$A_z\big|_{right} = A_{z2} \tag{2.76}$$

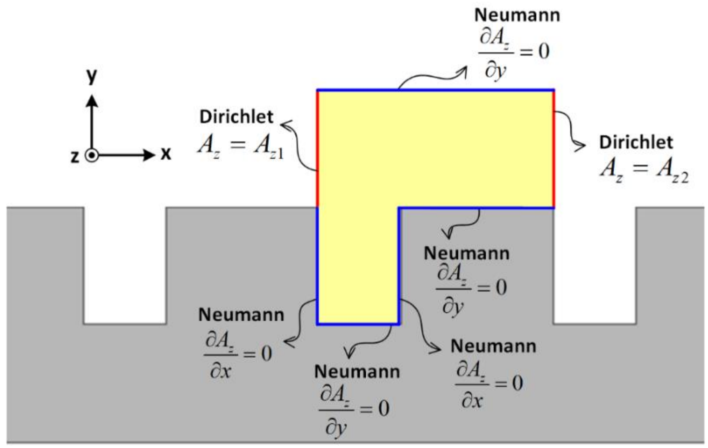

Figure 2. 8. (a) Dirichlet and Neumann boundary conditions of the problem

To solve the problem, it is needed to choose two reasonable values for A_{z1} and A_{z2}. Assuming an average magnetic flux density of *1 Tesla* in the air gap, it will be possible to come up with fine values. As shown in Figure 2.9(a), the net flux passing through a surface *S* enclosed by closed line *C* is the surface integral of magnetic flux density vector *B* over surface *S*, or is the closed line integral of the magnetic vector potential *A* over line C as in below:

$$\varphi = \oiint_S \vec{B}.d\vec{s} = \oint_c \vec{A}.d\vec{l} \tag{2.77}$$

It is obtained by substituting *B* in terms of *A* and employing Stokes' theorem. In a 2D problem where *A* is only in the z-direction, flux is easily calculated as in below:

$$\varphi = L\,(A_{z1} - A_{z2})\,L = L\,\Delta A_z \tag{2.78}$$

where A_{z1} and A_{z1} are values of A_z at the two points in the *xy*-plane as shown in Figure 2.9(b), and *L* is the axial length of the problem in the z-direction. In case of having a uniform magnetic flux density *B* or in approximations, we have:

$$\varphi = L\,w\,B_{av} \tag{2.79}$$

Combining the last two equations, we have:

$$\Delta A_z = w\,B_{av} \tag{2.80}$$

where $w = w_s + w_t$ in our case.

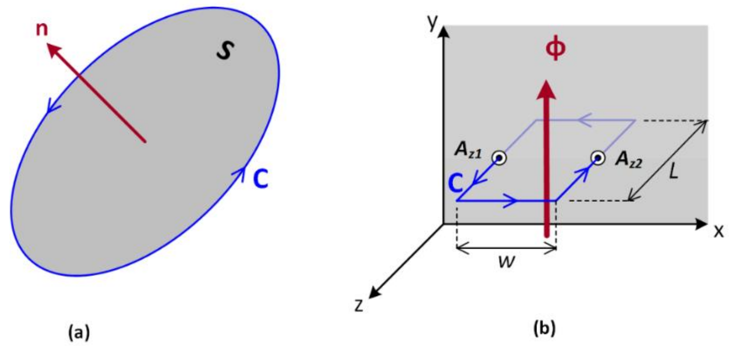

Figure 2. 9. Closed line C enclosed by open surface S in (a) 3D problem and (b) 2D problem.

We take $w_s=4\ mm$, $w_t=5\ mm$, and $g=4\ mm$, so for $B_{av}=1\ Tesla$ in the air-gap, we have $\Delta A_z=0.009\times 1=0.009\ wb/m$. We assign $A_{z1}=0$ to the left side and $A_{z2}=0.009\ wb/m$ to the right side of the air gap. As shown in Figure 2.10, flux lines have the expected values and behave the way that we expected, magnetic vector potential is in the z-direction, average magnetic flux density distribution in the air-gap is 1 *Tesla*, and magnetic flux density vectors have a downward direction that matches the flux pathing through the surface which is *-0.009 wb* per unit length.

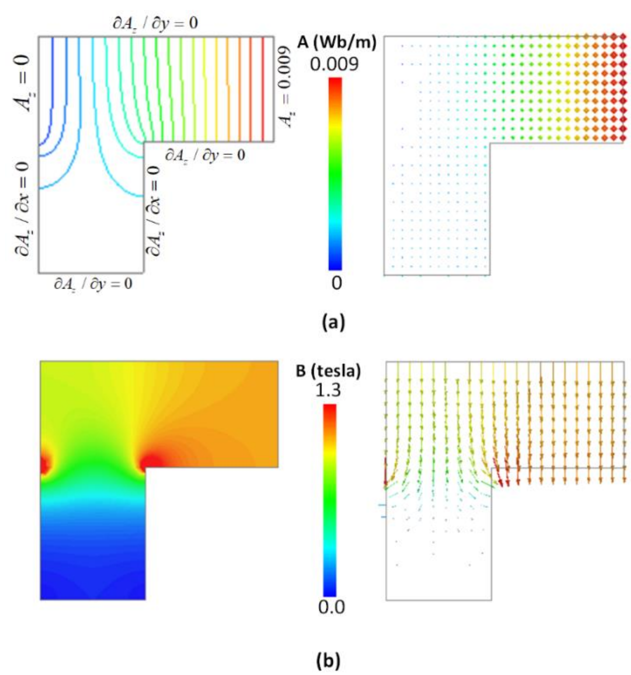

Figure 2. 10. Field simulation in one slot pitch region: (a) flux lines and magnetic vector potential and (b) magnetic flux density distribution and vectors.

It is worth noting that the slot depth h_s is large enough that no flux reaches the bottom of the slot, and all flux lines are attracted to the sides. Based on the flux lines in the region, the flux tube model is shown in Figure 2.11(a) is offered to determine the reluctance in an air gap facing a slotted stator. The permeance P_{g1} is calculated as in below:

$$P_{g1} = \int_0^{w_s/2} \frac{\mu_0 L\, dl}{g_i + \frac{\pi}{2} l} \tag{2.81}$$

We have:

$$P_{g1} = \frac{2\mu_0 L}{\pi} \ln\left(1 + \frac{\pi\, w_s}{4\, g_i}\right) \tag{2.82}$$

The permeance P_{g2} is calculated as in below:

$$P_{g2} = \frac{\mu_0\, w_t\, L}{g_i} \tag{2.83}$$

The total permeance is:

$$P_g = 2P_{g1} + P_{g2} \tag{2.84}$$

We have:

$$P_g = \mu_0\ L\left\{\frac{w_t}{g_i} + \frac{4}{\pi} \ln\left(1 + \frac{\pi\, w_s}{4\, g_i}\right)\right\} \tag{2.85}$$

In case of ignoring the fringing effect due to the slots, the air-gap permeance is:

$$P_g' = \frac{\mu_0\, w\, L}{g_i} \tag{2.86}$$

Therefore, Carter's coefficient is:

$$k_c = \frac{R_g}{R_g'} = \frac{P_g'}{P_g} = \left[1 - \frac{w_s}{w} + \frac{4\, g}{\pi\, w} \ln\left(1 + \frac{\pi\, w_s}{4\, g_i}\right)\right]^{-1} \tag{2.87}$$

It is seen that as long as the slot is deep enough, k_c is independent of h_s and is only a function of slot opening w_s, slot pitch w, and air-gap length g_{ie}. Finally, as shown in Figure 2.11(b), an equivalent slotless stator with efficient air-gap length g_{ie} can be employed where

$$g_{ie} = k_c\, g_i \quad ; \; k_c \geq 1 \tag{2.88}$$

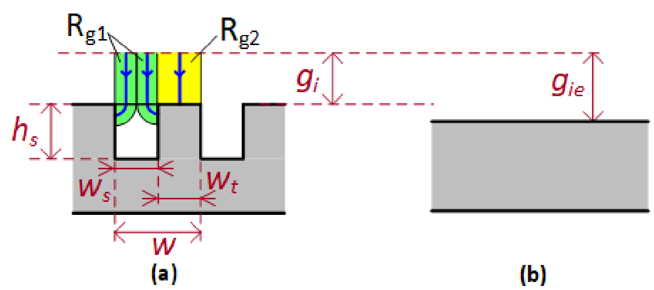

Figure 2. 11. (a) flux-tube modeling of an air-gap having slotted stator and (b) equivalent slotless stator with efficient air-gap length.

2.9. Modeling of the Stator

In this section, magnetomotive force, equivalent surface current density, and tangential magnetic field intensity of a stator are obtained. In the studied structure, the stator is the inner part, and the rotor is the outer part.

2.9.1. MMF Produced by Stator

In this section, we will obtain the magnetomotive force produced by the stator, which will be used in the calculation of the radial component of the magnetic field density in the air gap. Figure 2.12(a) shows a typical 2-pole ($P_s=1$) three-phase stator with concentrated windings. The positive direction of the pulsating fluxes produced by each phase is also depicted (negative currents produce flux in the opposite direction). The resultant of these three pulsating fluxes is a rotating field in the air gap.

Figure 2.11(b)-(d) show the flux lines (closed path of Ampere's law) and the corresponding spatial distribution of the magnetomotive forces (pulsating fluxes) for the three phases at time $t=0$ where $i_a=I_s$, $i_b=-I_s/2$, and $i_c=-I_s/2$. The resultant magnetomotive force, as shown in Figure 2.11(e), is a traveling wave for $t>0$. The amplitude of the MMF of each phase is obtained from Ampere's circuital law as in below:

$$\oint_C \vec{H}.d\vec{l} = I_{enc} \quad \Rightarrow \quad g\,H + g\,H = \frac{Ni_a}{p_s} \quad \Rightarrow \quad H = \frac{Ni_a}{2\,g\,p_s} \tag{2.89}$$

Also,

$$MMF = g\,H \quad \Rightarrow \quad MMF = \frac{Ni_a}{2\,p_s} \tag{2.90}$$

where N is the number of turns per phase and N/p_s is the number of turns per phase per pole, and phase currents are:

$$i_a(t) = I_s \cos(\omega t) \tag{2.91}$$

$$i_b(t) = I_s \cos(\omega t - \frac{2\pi}{3}) \tag{2.92}$$

$$i_c(t) = I_s \cos(\omega t + \frac{2\pi}{3}) \tag{2.93}$$

The Fourier series representation of the spatial distribution of the three magnetomotive forces are as in below:

$$F_a(\theta,t) = -\sum_{\substack{n=1\\odd}}^{+\infty} \frac{4}{n\pi}\frac{N\,i_a(t)}{2\,p_s}\sin\left(np_s\theta\right) \tag{2.94}$$

$$F_b(\theta,t) = -\sum_{\substack{n=1\\odd}}^{+\infty} \frac{4}{n\pi}\frac{N\,i_b(t)}{2\,p_s}\sin\left(np_s(\theta - \frac{2\pi}{3})\right) \tag{2.95}$$

$$F_c(\theta,t) = -\sum_{\substack{n=1\\odd}}^{+\infty} \frac{4}{n\pi}\frac{N\,i_c(t)}{2\,p_s}\sin\left(np_s(\theta + \frac{2\pi}{3})\right) \tag{2.96}$$

The Fourier representation series of the spatial distribution of the total magnetomotive forces can be obtained directly from the step-wise waveform in Figure 2.11(e) directly or by mathematical calculations as in below:

$$F_s(\theta,t) = F_a(\theta,t) + F_b(\theta,t) + F_c(\theta,t) \tag{2.97}$$

By substitution of the magnetomotive forces and the currents, we have:

$$
\begin{aligned}
F_s(\theta,t) = & -\sum_{\substack{n=1\\odd}}^{+\infty} \frac{4}{n\pi}\frac{N\,I_s}{2p_s}\cos(\omega t)\sin\left(np_s\theta\right) \\
& -\sum_{\substack{n=1\\odd}}^{+\infty} \frac{4}{n\pi}\frac{N\,I_s}{2p_s}\cos(\omega t-\frac{2\pi}{3})\sin\left(np_s(\theta-\frac{2\pi}{3})\right) \\
& -\sum_{\substack{n=1\\odd}}^{+\infty} \frac{4}{n\pi}\frac{N\,I_s}{2p_s}\cos(\omega t+\frac{2\pi}{3})\sin\left(np_s(\theta+\frac{2\pi}{3})\right)
\end{aligned} \tag{2.98}
$$

We have,

$$
\begin{aligned}
F_s(\theta,t) = -\frac{4}{n\pi}\frac{N\,I_s}{2p_s}\sum_{\substack{n=1\\odd}}^{+\infty} \Big\{ & \sin\left(np_s\theta-\omega t\right)+\sin\left(np_s\theta+\omega t\right) \\
& +\sin\left(np_s\theta-\omega t-(n-1)\frac{2\pi}{3})\right)+\sin\left(np_s\theta+\omega t-(n+1)\frac{2\pi}{3})\right) \\
& +\sin\left(np_s\theta-\omega t+(n-1)\frac{2\pi}{3})\right)+\sin\left(np_s\theta+\omega t+(n+1)\frac{2\pi}{3})\right)\Big\}
\end{aligned} \tag{2.99}
$$

For *n=1, 7, 13, etc.*, we have the first part of each pair in the three lines of the equation above, resulting in a forward traveling wave in the air gap. The n^{th} component is as in below:

$$
F_{sn}(\theta,t) = -\frac{3}{2}\frac{4}{n\pi}\frac{NI_s}{2p_s}\sin\left(np_s\theta-\omega t\right) \tag{2.100}
$$

while for *n=5, 11, etc.*, we have the first part of each pair in the three lines of the equation above, resulting in a backward traveling wave in the air gap. The n^{th} component is as in the following:

$$
F_{sn}(\theta,t) = -\frac{3}{2}\frac{4}{n\pi}\frac{NI_s}{2p_s}\sin\left(np_s\theta+\omega t\right) \tag{2.101}
$$

Therefore, the fundamental component (*n=1*) is:

$$
F_s(\theta,t) = -\frac{3}{2}\frac{4}{\pi}\frac{NI_s}{2p_s}\sin\left(p_s\theta-\omega t\right) \tag{2.102}
$$

In reality, usually, we do not employ full-pitched concentrated windings, so to account for the winding configuration, the winding factor k_{w} can be included in the above relationship as in below:

$$F_s(\theta,t) = F_{s1}\sin\left(p_s\theta - \omega t - \delta\right) \tag{2.103}$$

$$F_{s1} = -\frac{3}{2}\frac{4}{\pi}\frac{NI_s}{2p_s}k_w \tag{2.104}$$

where δ is the current angle, and the winding factor is defined as in below:

$$k_w = k_p\, k_d \tag{2.105}$$

where k_p and k_b are pitch and distribution factors, respectively. In a short-pitched winding, the pitch factor for the n^{th} harmonic is as in below:

$$k_{pn} = \sin\frac{n\alpha}{2} \tag{2.106}$$

where α refers to the angular displacement between the two sides of a coil in electrical degrees. For a full-pitched coil $\alpha=\pi$.

In a distributed winding, the distribution factor for the n^{th} harmonic is given below:

$$k_{dn} = \frac{\sin\frac{nm\gamma}{2}}{m\sin\frac{n\gamma}{2}} \tag{2.107}$$

where γ is the slot angular pitch in electrical degrees and m is the number of slots per pole per phase. For a concentrated winding, $m=1$ and so $k_d=1$.

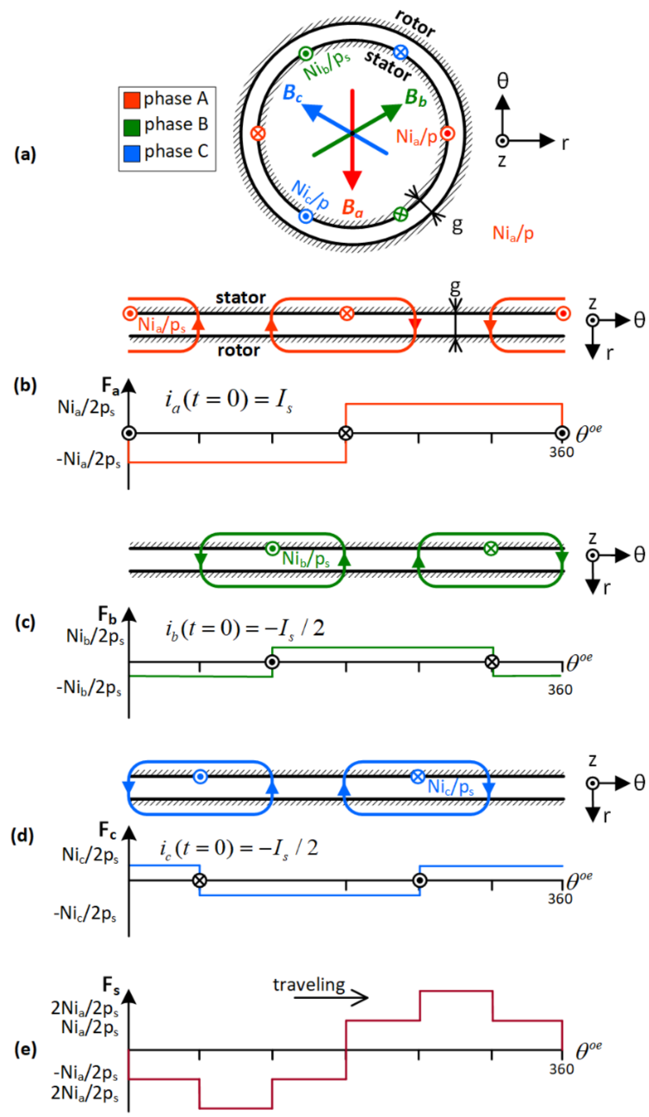

Figure 2. 12. A typical three-phase two-pole stator with concentrated windings: (a) stator phases and field axis of each phase, (b) flux lines and MMF produced by phase a, (c) flux lines, and MMF produced by phase b, (d) flux lines and MMF produced by phase c, and (e) the resultant traveling MMF in the air-gap

2.9.2. Equivalent Surface Current Density of Stator

In this section, we obtain the equivalent surface current density of the stator that plays the role of the stator winding embedded in the slots in the slotless winding after employing the carter's coefficient. It will be used in torque calculations on the stator as well as in extracting the tangential component of the magnetic field intensity on the surface of the stator. Using Ampere's circuital law for the closed curve C in Figure 2.13, we have:

$$\oint_C \vec{H}.d\vec{l} = K_z\, R_i \Delta\theta \tag{2.108}$$

Magnetic field intensity is zero in infinitely permeable irons, so it leads to:

$$g\,H_r\big|_{\theta-\Delta\theta/2} - g\,H_r\big|_{\theta+\Delta\theta/2} = K_z\,R_i\Delta\theta \;\Rightarrow\; K_z = -\frac{g}{R_i}\frac{H_r\big|_{\theta+\Delta\theta/2} - H_r\big|_{\theta-\Delta\theta/2}}{\Delta\theta} \tag{2.109}$$

The limit of the difference quotient above as *Δθ* approaches to zero leads to the derivative of H_r with respect to θ as in below:

$$K_z = \lim_{\Delta\theta\to 0} -\frac{g}{R_i}\frac{H_r\big|_{\theta+\Delta\theta/2} - H_r\big|_{\theta-\Delta\theta/2}}{\Delta\theta} = -\frac{g}{R_i}\frac{\partial H_r}{\partial\theta} \tag{2.110}$$

On the other hand, we know that

$$F_s = g\,H_r \tag{2.111}$$

Combining the two leads to:

$$K_z(\theta,t) = \frac{-1}{R_i}\frac{\partial F_s}{\partial\theta} \tag{2.112}$$

By substitution of F_s, we obtain the fundamental component as in below

$$K_z(\theta,t) = \frac{3}{2}\frac{4}{\pi}\frac{NI_s}{2R_i}k_w\cos\left(p_s\theta - \omega t - \delta\right) \tag{2.113}$$

It can be written as in below:

$$K_z(\theta,t) = K_{z1}\cos\left(p_s\theta - \omega t - \delta\right) \tag{2.114}$$

$$K_{z1} = \frac{3}{2}\frac{4}{\pi}\frac{NI_s}{2R_i}k_w \tag{2.115}$$

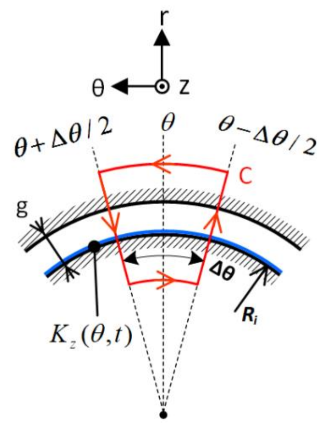

Figure 2. 13. Closed line of Ampere's law enclosing the surface current density of the stator.

2.9.3. Tangential Component of Field Intensity on Surface of Stator

The tangential component of the magnetic field intensity on the surface of the stator will be used in determining the shear stress on the stator surface using the Maxwell stress tensor. Using Ampere's law over the contour *C* shown in Figure 2.14, and knowing that magnetic intensity within infinitely permeable iron of stator is zero, we have:

$$H_\theta - 0 = K_z \;\Rightarrow\; H_\theta = K_z \tag{2.116}$$

By substituting K_z, we obtain the fundamental component as in below:

$$H_\theta(\theta,t) = H_{\theta 1}\cos\left(p_s\theta - \omega t - \delta\right) \tag{2.118}$$

$$H_{\theta 1} = \frac{3}{2}\frac{4}{\pi}\frac{NI_s}{2R_i}k_w \tag{2.119}$$

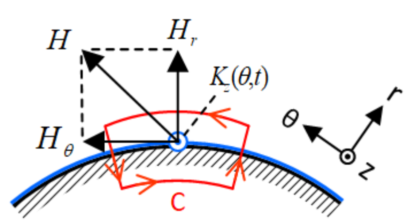

Figure 2. 14. Closed line of the Ampere's law around the boundary of stator surface

2.10. Permanent Magnet Modeling

This part is devoted to the calculation of the magnetomotive force, equivalent magnetic charge, and equivalent Amperian current of the PMs.

2.10.1. MMF Produced by PMs

The magnetomotive force produced by permanent magnets, which will be used in the calculation of the radial component of the magnetic flux density distribution, can be written as in below:

$$F_m(\theta) = h_m\, M(\theta) \tag{2.120}$$

where h_m is the PM height and the magnetization density of permanent magnets $\boldsymbol{M}$, shown in Figure 2.15(a), is related to PM's residual flux density B_r as in below:

$$M = \frac{1}{\mu_0} B_r \tag{2.121}$$

We also know that

$$\vec{H} = \mu_0(\vec{B} + \vec{M}) \tag{2.122}$$

The permanents magnets are alternating in the polarity and have an arc angle of θ_m, so Fourier series representation of the demagnetization density distribution can be written as in below:

$$M(\theta) = \sum_{\substack{n=1 \\ odd}}^{+\infty} \frac{B_r}{\mu_0} \frac{4}{n\pi} \sin\frac{n\, p_m \theta_m}{2} \cos n\, p_m(\theta - \theta_0) \tag{2.123}$$

Then, the fundamental component leads to a continuous magnetization sheet, as shown in Figure 2.16(a). It can be represented as in the following:

$$M(\theta, t) = M_0 \cos p_m(\theta - \theta_0) \tag{2.124}$$

where

$$M_0 = \frac{4}{\pi}\frac{B_r}{\mu_0}\sin\frac{p_m\theta_m}{2} \tag{2.125}$$

In the case of rotating magnets, we have:

$$\theta_0 = \omega_m t + \zeta \tag{2.126}$$

where ω_m is the mechanical speed of the rotor and ξ is the initial position at time $t=0$. When the modulators are the rotating part, and PMs are stationary, we have $\theta_0=0$ and then,

$$M(\theta) = M_0 \cos p_m\theta \tag{2.127}$$

2.10.2. Coulombian Magnetic Charge Model of PMs

Using the so-called Coulombian model, the permanent magnets can be represented by fictitious magnetic charges that can be used in torque calculation by employing Kelvin magnetization force density. The magnetization density ***M*** results in the fictitious charge density ρ_m as in below:

$$\rho_m = -\nabla.\mu_0\vec{M} \tag{2.128}$$

In radially magnetized permanent magnets, we have:

$$\rho_m = -\mu_0\frac{\partial M_r}{r} \tag{2.129}$$

In a permanent magnet having a uniform magnetization, the divergence of ***M*** is zero throughout the volume. In this case, a magnetic surface charge density is defined as in the following:

$$\sigma_m = -\hat{n}.\mu_0(M^a - M^b) \tag{2.130}$$

where ***n*** is the normal unit vector of the surface boundary. It is worth noting that positive and negative magnetic surface charge densities should be assigned to the surface boundaries of a permanent magnet such that *M* vectors originate from negative charges and terminates on positive charges—the rule. As shown in Figure 2.15(b), the surfaces magnetic charges on the two sides of PMs, whose normal vectors are in the radial direction, are obtained as in below:

$$\sigma_m = \pm \mu_0 M \tag{2.131}$$

The fundamental component, as shown in Figure 2.16(b), obtained from the fundamental component of the surface charge density distribution shown in Figure 2.16(a), is obtained as:

$$\sigma_m(\theta, t) = -\mu_0 M_0 \cos p_m(\theta - \theta_0) \tag{2.132}$$

When modulators are the rotating part, and PMs are stationary, we have $\theta_0=0$ and then,

$$\sigma_m(\theta) = -\mu_0 M_0 \cos p_m \theta \tag{2.133}$$

Torque on PMs using Kelvin force and magnetic charge model of PMs:

Kelvin magnetization force density can be used in finding the force on a magnetic charge in the presence of a magnetic field. Force density acting on magnetic charge density ρ_m in a magnetic field of ***H*** can be obtained as in the following:

$$\vec{f} = \rho_m \vec{H} \tag{2.134}$$

Also, force density acting on magnetic surface charge density σ_m in a magnetic field of ***H*** can be obtained as in the following:

$$\vec{f} = \sigma_m \vec{H} \tag{2.135}$$

where the magnetic field ***H*** has two components as in below:

$$\vec{H} = H_r \hat{a}_r + H_\theta \hat{a}_\theta \tag{2.136}$$

2.10.3. Amperian Current Model of PMs

Magnetization of permanent magnets can be modeled by an equivalent current density called Amperian currents which can be used in torque calculations by employing Lorentz force. The equivalent current density of magnetization ***M*** can be extracted as in below:

$$\vec{J}_m = \nabla \times \vec{M} \tag{2.136}$$

For radially magnetized PMs, the equivalent current is in the z-direction is obtained as in the following:

$$J_m = -\frac{1}{r}\frac{\partial M}{\partial \theta} \tag{2.137}$$

In a permanent magnet having a uniform magnetization, the curl of ***M*** is zero throughout the volume. In this case, a surface current density is defined as in the following:

$$\vec{K}_m = \vec{M} \times \hat{n} \tag{2.138}$$

where ***n*** is the normal unit vector of the surface boundary. It is worth noting that positive (in +z direction) and negative (in -z-direction) surface current densities should be assigned to the surface boundaries of a permanent magnet such that they produce flux in the same direction as *M*—right-hand rule in Ampere's law. As shown in Figure 2.15(c), the surfaces current densities on the two sides of PMs, whose normal vector are in the θ direction, are obtained as in below:

$$K_m = \pm M \tag{2.139}$$

This is a singularity at the side surfaces of a radially-magnetized PM. The radius *r* in the curl representation of Amperian currents can be seen by looking at the nature of an impulse. If θ_0 is the left side position of the right PM, on which there is a singularity, according to the definition of an impulse, we have:

$$\int_{\theta_{0-}}^{\theta_{0+}} J_m(\theta)\,dl = M \Rightarrow \int_{\theta_{0-}}^{\theta_{0+}} J_m(\theta)\,r\,d\theta = M \Rightarrow \int_{\theta_{0-}}^{\theta_{0+}} J_m(\theta)\,d\theta = \frac{M}{r} \qquad (2.140)$$

The fundamental component, as shown in Figure 2.16(c), obtained from the fundamental component of the magnetization density distribution shown in Figure 2.16(a), is obtained as:

$$J_m(r,\theta,t) = -\frac{1}{r}\frac{\partial M}{\partial \theta} = \frac{M_0 p_m}{r}\sin p_m(\theta - \theta_0) \qquad (2.141)$$

When the modulators are rotating part and PMs are stationary, we have $\theta_0=0$ and then,

$$J_m(r,\theta) = \frac{M_0 p_m}{r}\sin p_m\theta \qquad (2.142)$$

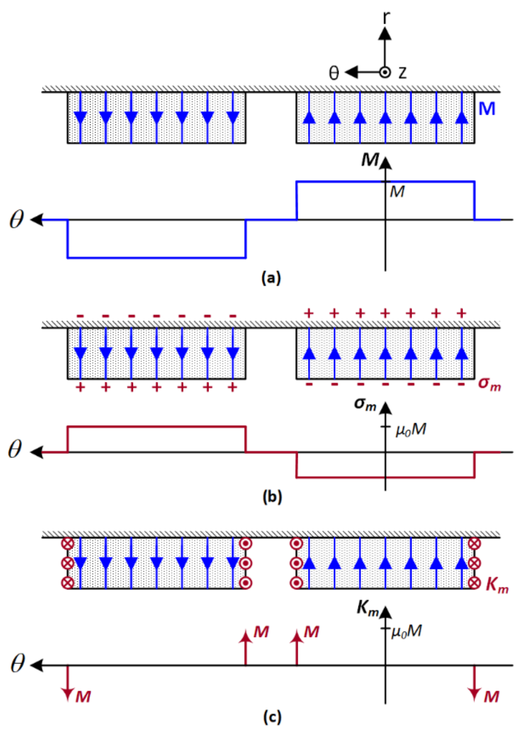

Figure 2. 15. Permanent magnet modeling: (a) magnetization, (b) equivalent fictitious charge and (c) equivalent surface current density

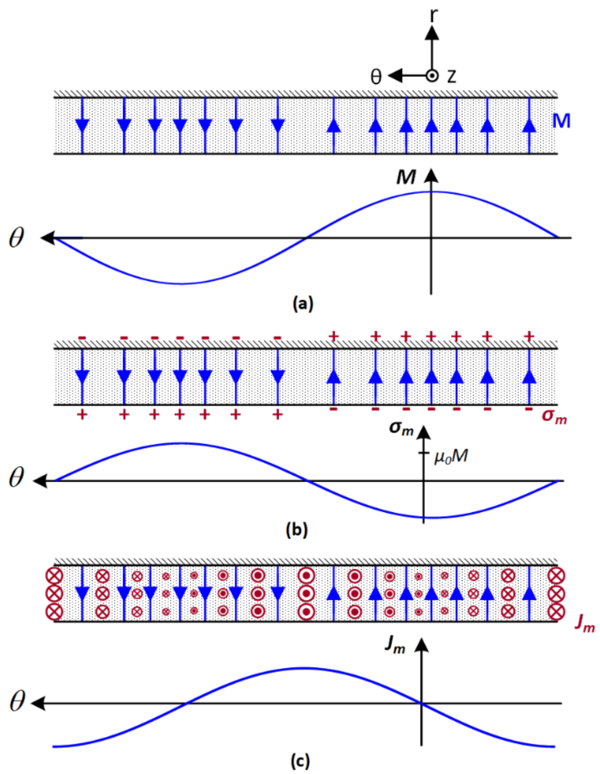

Figure 2. 16. Permanent magnet modeling using the fundamental component: (a) magnetization, (b) equivalent fictitious charge, and (c) equivalent surface current density

2.10.4. Tangential Component of Field Intensity on Surface of PMs

The tangential component of the magnetic field intensity on the surface of the PMs will be used in determining the shear stress on the surface of PMs using Kelvin force density. The tangential component of the field H_θ can be approximated based on the radial component of the field H_r. The field is perpendicular to the surface of the infinitely permeable iron, so

$$H_\theta\big|_{r=R_o+h_m} = 0 \tag{2.143}$$

As shown in Figure 2.17, using a linear approximation of H_θ in the PM region, H_θ can be represented as a linear function of r with the rate of $\partial H_\theta/\partial\theta$.

$$H_\theta\big|_{r=R_o} - H_\theta\big|_{r=R_o+h_m} = \frac{\partial H_\theta}{\partial r}[R_o - (R_o + h_m)] \tag{2.144}$$

It leads to:

$$H_\theta\big|_{r=R_o} = -h_m \frac{\partial H_\theta}{\partial r} \tag{2.145}$$

Ampere's law in a current-free region says that:

$$\nabla \times H = 0 \;\; \Rightarrow \;\; (0-0)a_r + (0-0)a_\theta + (\frac{\partial H_\theta}{\partial r} - \frac{1}{r}\frac{\partial H_r}{\partial \theta})a_z = 0 \tag{2.146}$$

so,

$$\frac{\partial H_\theta}{\partial r} = \frac{1}{r}\frac{\partial H_r}{\partial \theta} \tag{2.147}$$

We obtain H_θ as a function of H_r on the surface of the PM ($r=R_o$):

$$H_\theta\big|_{r=R_o} = -\frac{h_m}{R_o}\frac{\partial H_r}{\partial \theta} \tag{2.148}$$

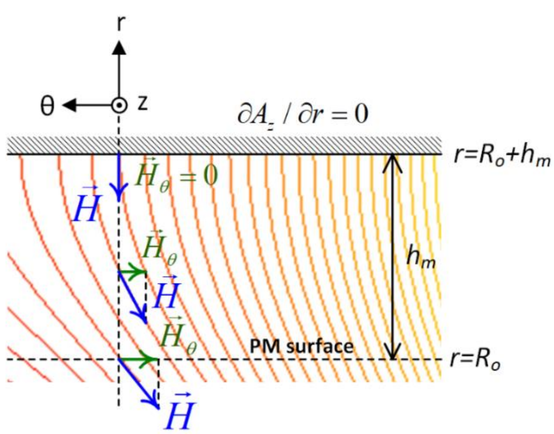

Figure 2. 17. Linear approximation of the flux lines at the surface of PMs

Chapter 3

Flux Tubes and Magnetic Equivalent Circuits

3.1 Introduction

Both numerical or analytical techniques may be used in the analysis of electrical machines. Numerical approaches like the finite element method [86], although accurate, are usually expensive and too time-consuming to be used in the design optimizations, while analytical models by providing fast yet accurate solutions are a very good trade-off between accuracy and the required time—useful in preliminary design stages.

Analytical frameworks for analysis of electrical machines may be performed using the solution of Laplace's and Poison's equations, or by employing flux-tube-based techniques [87] The former, although very powerful, might be complicated for many geometries, incapable of taking iron saturation into account, while the latter is usually simpler and effective in many configurations without any symmetry and is able to account for iron saturation and most material properties, e.g., both PM characteristics. In this chapter, flux-tube-based models for eddy-current couplers and switched reluctance motors, as very good examples, have been developed. Analytical models are the best candidates for design optimization and parametric analysis of electric machines. In this chapter, this method is studied for two topologies od electric machines.

3.2. Example I: Eddy Current Couplers

In this section, a flux-tube model for axial-flux eddy-current couplers is offered [31], which is on the basis of a three-dimensional magnetic equivalent circuit combined with Faraday's and Ampere's laws to account for the reaction field produced by induced eddy-currents. The proposed framework provides good flexibility and simplicity and is able to consider all geometrical parameters and material properties, e.g., saturation and permeability of the iron parts, remanence and coercivity of PMs, and actual current paths.

Moreover, it is capable of handling complicated geometries since there is no need for boundary conditions. A number of design-related considerations are analytically derived as well and accounted for practical concerns. Three-dimensional FEM has also been employed in the analyses of the device as well as evaluations of the model. Advantages of the proposed model in terms of accuracy and effectiveness are shown.

3.2.1. Proposed model

Geometry and specifications of the studied axial-flux eddy-current coupler are illustrated in Figure 3.1 and Table 3.1. Axially-polarized surface-mounted PMs alternating in the direction of magnetization are placed on the surface of the primary rolled back-iron, and the conductive sheet (CS) is located on the surface of the secondary part. The prime mover is attached to one part while the load is fixed to the other. Currents are induced in the CS due to a relative speed between the two parts, from which the reaction field is developed that produces an electromagnetic torque from the interaction with the primary magnetic field. The active region associated with PMs and back irons are limited by R_i and R_o, while the conductive sheet is extended by overhangs of length H from both sides to provide a return path for the induced current.

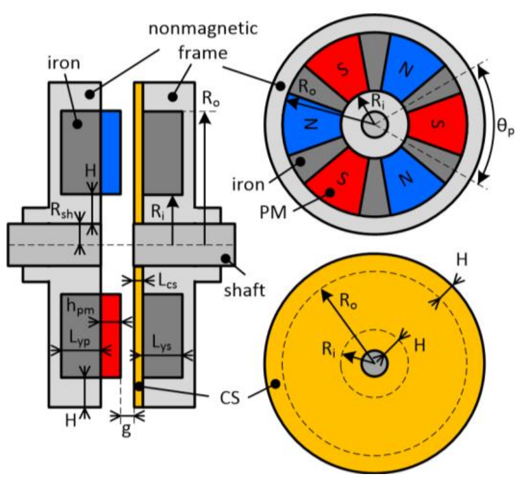

Figure 3. 1. Geometry of the studied eddy-current coupler

Table 3. 1 Specifications of the case-study coupler

parameter	value	parameter	value
active inner radius, R_i	30 mm	primary-yoke, L_{yp}	6.5 mm
active outer radius, R_o	50 mm	secondary-yoke, L_{ys}	6.1 mm
PM height, h_{pm}	7 mm	PM grade	N35
air-gap length, g	1 mm	PM remanence	1.19 T
CS thickness, L_{cs}	1 mm	PM corecity	-872 kA/m
overhang length, H	10 mm	CS conductivity (Cu)	58 MS
PM arc, θ_m	30 deg	steel grade	M15
number of PMs, N_{pm}	8	frame material	Aluminum

To simplify some calculations, the device geometry may linearly be expanded along with the average radius of the active part given below:

$$R_{av} = (R_i + R_o)/2 \tag{3.1}$$

Then, the pole pitch, the equivalent effective length and the translational speed of the linearized structure could be defined respectively as in the following:

$$\tau_p = R_{av}\theta_p \quad ; \quad L = R_o - R_i \quad ; \quad v = R_{av}\omega \tag{3.2}$$

3.2.2. Field Calculations:

First, the magnetic flux produced by PMs is determined using the implemented nonlinear MEC. The induced current in the conductive sheet is then calculated through Faraday’s law. Finally, the impact of the reaction field on the original air-gap field is taken into account by Ampere’s law. The flux paths and the 3D MEC of one flux loop associated with the machine are depicted in Figure 3.2.

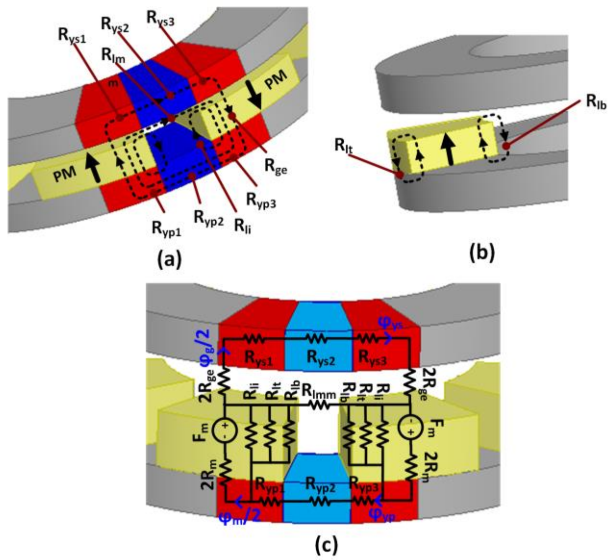

Figure 3. 2. Magnetic equivalent circuit: **(a)** Flux paths within the machine, **(b)** Flux paths within the machine, **(c)** The corresponding 3D MEC

The equivalent MMF of a PM is as follows:

$$F_m = H_c \, h_{pm} \tag{3.3}$$

The reluctance of a PM, and the total reluctance of the effective air-gap (including CS) are calculated as follows:

$$R_m = \frac{h_{pm}}{\mu_0 \, \mu_r \int_0^{\theta_m} \int_{R_i}^{R_o} r \, dr \, d\theta} = \frac{2h_{pm}}{\mu_0 \, \mu_r (R_o{}^2 - R_i{}^2)\theta_m} \tag{3.4}$$

$$R_{ge} = \frac{g + L_{cs}}{\mu_0 \int_0^{\theta_m} \int_{R_i}^{R_o} r \, dr \, d\theta} = \frac{2(g + L_{cs})}{\mu_0 (R_o{}^2 - R_i{}^2)\theta_m} \tag{3.5}$$

where $g_e = g + L_{cs}$ is the effective air-gap, and $\mu_r = -B_r/\mu_0 H_c$ is the relative recoil permeability of PMs through which both PM characteristics are accounted for in the proposed model. It is worth noting that only B_r is accounted for in the models that are based on Laplace's equations. The flux tube associated with the leakage permeance between the two adjacent PMs is shown in Figure 3.3(a), whose corresponding permeance can be found as follows:

$$P_{mm} = \int_0^{g_e} \frac{\mu_0 (R_o - R_i) dl}{\pi l + (1-\alpha_m)\tau_p} \tag{3.6}$$

Finally, we obtain:

$$P_{mm} = \frac{\mu_0 (R_o - R_i)}{\pi} ln\left(1 + \frac{\pi (g + L_{cs})}{(1-\alpha_m)\tau_p}\right) \tag{3.7}$$

According to Figure 3.3(b), the magnet to iron leakage permeance can be calculated from the following:

$$P_{li} = \mu_0 \int_0^{L_1} \frac{(R_o - R_i) dl}{\pi l + h_{pm}} \tag{3.8}$$

Executing the integration yields:

$$P_{li} = \frac{\mu_0 (R_o - R_i)}{\pi} Ln\left(1 + \frac{\pi L_1}{h_{pm}}\right) \tag{3.9}$$

where the thickness of the flux tube L_1 is the minimum of half of the inter-polar length and the effective air gap as follows:

$$L_1(\alpha_m) = \min\left(g_e, (1-\alpha_m)\tau_p / 2\right) \tag{3.10}$$

According to Figure 3.3(c), magnet leakage from the top surface is calculated as:

$$P_{lt} = \int_0^{g_e} \frac{\mu_0 (R_o \theta_m / 2) dl}{\frac{3\pi}{2} l + h_{pm}} \tag{3.11}$$

We obtain

$$P_{lt} = \frac{\mu_0 R_o \theta_m}{3\pi} Ln\left(1 + \frac{3\pi g_e}{2 h_m}\right) \tag{3.12}$$

According to Figure 3.3(d), the bottom leakage flux is obtained as:

$$P_{lb} = \int_0^{g_e} \frac{\mu_0 (R_i \theta_m / 2)\, dl}{\frac{3\pi}{2} l + h_{pm}} \tag{3.13}$$

We obtain

$$P_{lb} = \frac{\mu_0\, R_i \theta_m}{3\pi} Ln\left(1 + \frac{3\pi g_e}{2h_m}\right) \tag{3.14}$$

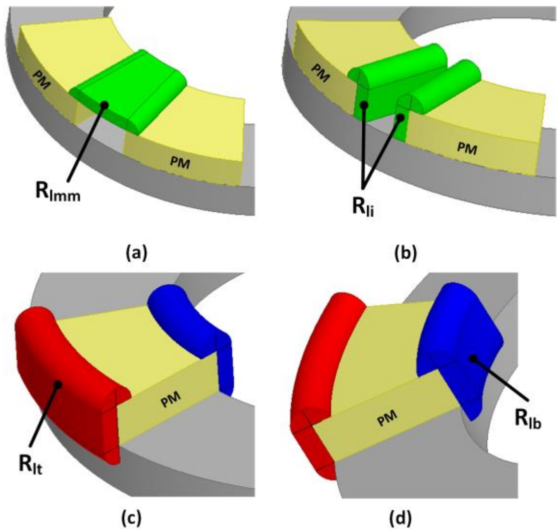

Figure 3. 3. Flux tubes: **(a)** PM to PM leakage permeance, **(b)** PM to iron leakage permeance in the interpolar region, **(c)** PM to iron leakage permeance on the top surface, **(d)** PM to iron leakage permeance on the bottom surface

Since the flux density within the iron yokes are higher behind the inter-polar regions, to obtain higher accuracy, as shown in Figure 3.4(a) and Figure 3.5(a), reluctance of either primary or secondary iron yokes are considered to be formed from three separate components. In addition, a mean area, defined as the average of the areas through which the flux paths as shown in Figure 3.4(b)-(d), is considered to calculate reluctances of the primary iron as in below:

$$R_{yp1} = R_{yp3} = \frac{l_{yp1}}{\mu_0\, \mu_{iyp1} A_{yp1}} = \frac{0.5\,(R_i + R_o)(\theta_m / 2)}{0.5\,\mu_0\, \mu_{iyp1} \left\{ (R_o - R_i) L_{yp} + \int_0^{\theta_m/2} \int_{R_i}^{R_o} r\, dr\, d\theta \right\}} \tag{3.15}$$

$$R_{yp1} = R_{yp3} = \frac{0.5\,(R_i + R_o)\theta_m}{\mu_0\,\mu_{iyp1}\left\{(R_o - R_i)L_{yp} + (R_o^{\,2} - R_i^{\,2})\theta_m / 4\right\}} \tag{3.16}$$

$$R_{yp2} = \frac{l_{yp2}}{\mu_0\,\mu_{iyp2} A_{yp2}} = \frac{0.5\,(R_i + R_o)\,(\theta_p - \theta_m)}{0.5\,\mu_0\,\mu_{iyp2}\left\{(R_o - R_i)L_{yp} + (R_o - R_i)L_{yp}\right\}} \tag{3.17}$$

$$R_{yp2} = \frac{0.5\,(R_i + R_o)\,(\theta_p - \theta_m)}{\mu_0\,\mu_{iyp2}\,(R_o - R_i)L_{yp}} \tag{3.18}$$

According to Figure 3.5(b)-(d), reluctances of the secondary iron is obtained similarly as in below:

$$R_{ys1} = R_{ys3} = \frac{l_{ys1}}{\mu_0\,\mu_{iys1} A_{ys1}} = \frac{0.5\,(R_i + R_o)(\theta_m / 2)}{\mu_0\,\mu_{iys1}\,0.5\left\{(R_o - R_i)L_{ys} + \int_0^{\theta_m/2}\int_{R_i}^{R_o} r\,dr\,d\theta\right\}} \tag{3.19}$$

$$R_{ys1} = R_{ys3} = \frac{0.5\,(R_i + R_o)\theta_m}{\mu_0\,\mu_{iys1}\left\{(R_o - R_i)L_{ys} + (R_o^{\,2} - R_i^{\,2})\theta_m / 4\right\}} \tag{3.20}$$

$$R_{ys2} = \frac{l_{ys2}}{\mu_0\,\mu_{iys2} A_{ys2}} = \frac{0.5\,(R_i + R_o)\,(\theta_p - \theta_m)}{0.5\,\mu_0\,\mu_{iys2}\left\{(R_o - R_i)L_{ys} + (R_o - R_i)L_{ys}\right\}} \tag{3.21}$$

$$R_{ys2} = \frac{0.5\,(R_i + R_o)\,(\theta_p - \theta_m)}{\mu_0\,\mu_{iys2}\,(R_o - R_i)L_{ys}} \tag{3.22}$$

$$\begin{bmatrix} 4R_{ge} + R_{ys1} + R_{ys2} + R_{ys3} + R_{mm} & 0 & -2R_{mm} & 0 \\ 0 & 2R_m + \dfrac{R_{li}R_{lt}R_{lb}}{R_{li}R_{lt} + R_{li}R_{lb} + R_{lt}R_{lb}} & \dfrac{-2R_{li}R_{lt}R_{lb}}{R_{li}R_{lt} + R_{li}R_{lb} + R_{lt}R_{lb}} & 0 \\ -R_{mm} & \dfrac{-2R_{li}R_{lt}R_{lb}}{R_{li}R_{lt} + R_{li}R_{lb} + R_{lt}R_{lb}} & 2(R_{yp1} + R_{yp2} + R_{yp3} + \dfrac{2R_{li}R_{lt}R_{lb}}{R_{li}R_{lt} + R_{li}R_{lb} + R_{lt}R_{lb}} + R_{mm}) & 0 \\ -1 & 0 & 0 & 2 \end{bmatrix} \begin{bmatrix} \varphi_g \\ \varphi_m \\ \varphi_{yp} \\ \varphi_{ys} \end{bmatrix} = \begin{bmatrix} 0 \\ 2F_m \\ 0 \\ 0 \end{bmatrix} \tag{3.23}$$

where, μ_{ip1}, μ_{ip2}, μ_{ip3}, μ_{is1}, μ_{is2}, and μ_{is3} are relative permeabilities of the iron components determined by the *B*-*H* characteristic of the utilized steel. Finally, solving the circuit shown in Figure 3.2(c) yields the system of equations in (3.23), from which circuit fluxes can be calculated.

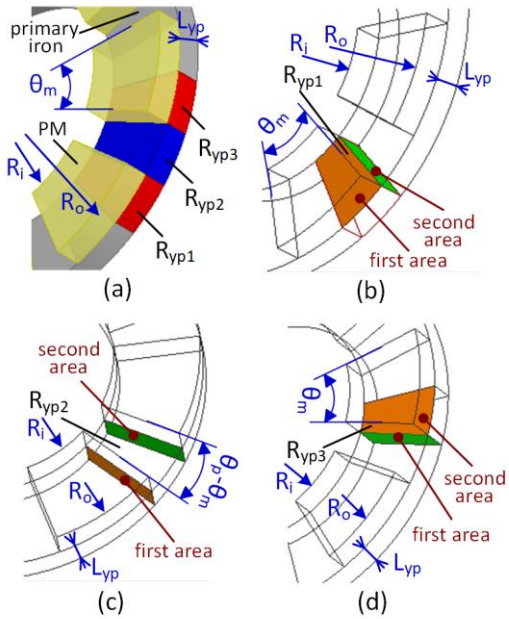

Figure 3. 4. Reluctances calculations for the primary iron: **(a)** Reluctance elements, **(b)** Calculations of R_{yp1}, **(c)** calculations of R_{yp2}, **(d)** Calculations of R_{yp3}

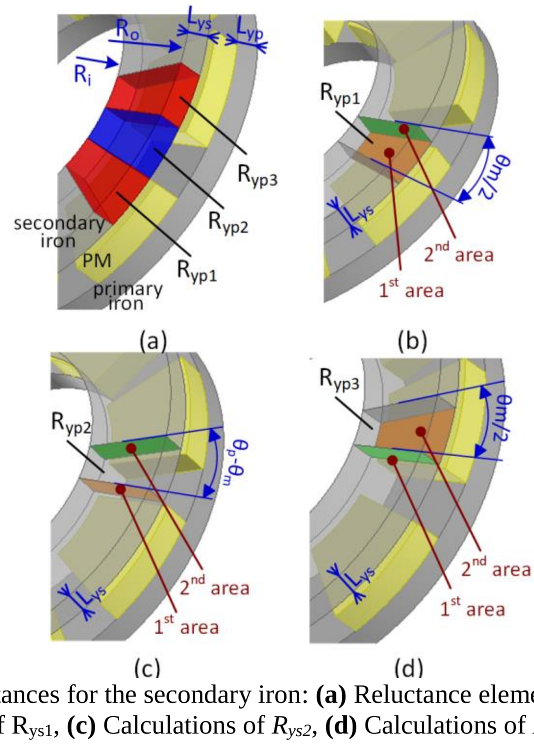

Figure 3. 5. Reluctances for the secondary iron: **(a)** Reluctance elements, **(b)** Calculations of R_{ys1}, **(c)** Calculations of R_{ys2}, **(d)** Calculations of R_{ys3}

An iterative procedure is employed to calculate the permeability of the saturable permeances. The unsaturated values are initially assigned to the relative permeability of iron reluctance to determine the reluctance network and solve the circuit. Afterward, the associated magnetic flux densities are calculated as in the following:

$$B_{yp1} = B_{yp3} = \frac{\varphi_{yp}}{A_{yp1}} = \frac{\varphi_{yp}}{\left\{(R_o - R_i)L_{yp} + (R_o^2 - R_i^2)\theta_m / 4\right\}/2} \tag{3.24}$$

$$B_{yp2} = \frac{\varphi_{yp}}{A_{yp2}} = \frac{\varphi_{yp}}{(R_o - R_i)L_{yp}} \tag{3.25}$$

$$B_{ys1} = B_{ys3} = \frac{\varphi_{ys}}{A_{ys1}} = \frac{\varphi_{ys}}{\left\{(R_o - R_i)L_{ys} + (R_o^2 - R_i^2)\theta_m / 4\right\}/2} \tag{3.26}$$

$$B_{ys2} = \frac{\varphi_{ys}}{A_{ys2}} = \frac{\varphi_{ys}}{(R_o - R_i)L_{ys}} \tag{3.27}$$

Then, through the *B*-*H* curve of the utilized iron, new permeabilities are updated. To this end, auxiliary permeabilities are obtained by:

$$\hat{\mu}_{iyp1}^{(k)} = B_{yp1}^{(k-1)} / \mu_0 H_{yp1}^{(k-1)} \tag{3.28}$$

$$\hat{\mu}_{iyp2}^{(k)} = B_{yp2}^{(k-1)} / \mu_0 H_{yp2}^{(k-1)} \tag{3.29}$$

$$\hat{\mu}_{iys1}^{(k)} = B_{ys1}^{(k-1)} / \mu_0 H_{ys1}^{(k-1)} \tag{3.30}$$

$$\hat{\mu}_{iys2}^{(k)} = B_{ys2}^{(k-1)} / \mu_0 H_{ys2}^{(k-1)} \tag{3.31}$$

Then, new permeabilities are calculated through:

$$\mu_{iyp1}^{(k)} = [\hat{\mu}_{iyp1}^{(k)}]^d \, [\mu_{iyp1}^{(k-1)}]^{1-d} \tag{3.32}$$

$$\mu_{iyp2}^{(k)} = [\hat{\mu}_{iyp2}^{(k)}]^d \, [\mu_{iyp2}^{(k-1)}]^{1-d} \tag{3.33}$$

$$\mu_{iys1}^{(k)} = [\hat{\mu}_{iys1}^{(k)}]^d \, [\mu_{iys1}^{(k-1)}]^{1-d} \tag{3.34}$$

$$\mu_{iys2}^{(k)} = [\hat{\mu}_{iys2}^{(k)}]^{d}\,[\mu_{iys2}^{(k-1)}]^{1-d} \tag{3.35}$$

where k is the iteration number, and d denotes a damping constant set to 0.1. The process lasts until the following criterion is independently satisfied for all permeabilities as in below:

$$\left|[\mu_{iyp1}^{(k)} - \mu_{iyp1}^{(k-1)}]/\,\mu_{iyp1}^{(k-1)}\right| \le \varepsilon \tag{3.36}$$

$$\left|[\mu_{iyp2}^{(k)} - \mu_{iyp2}^{(k-1)}]/\,\mu_{iyp2}^{(k-1)}\right| \le \varepsilon \tag{3.37}$$

$$\left|[\mu_{iys1}^{(k)} - \mu_{iys1}^{(k-1)}]/\,\mu_{iys1}^{(k-1)}\right| \le \varepsilon \tag{3.38}$$

$$\left|[\mu_{iys2}^{(k)} - \mu_{iys2}^{(k-1)}]/\,\mu_{iys2}^{(k-1)}\right| \le \varepsilon \tag{3.39}$$

where ε is the termination factor assigned based on the required accuracy (0.01 herein). The distribution of the radial component of the flux density produced by PMs in the air gap and the CS can be expressed as below:

$$B_{pm}(x) = \begin{cases} 0 & ;-\tau_p/2 \le x \le -\alpha_m\tau_p/2 \\ B_m = \dfrac{\varphi_g}{\alpha_m\tau_p L} & ;-\alpha_m\tau_p/2 \le x \le \alpha_m\tau_p/2 \\ 0 & ;\alpha_m\tau_p/2 \le x \le \tau_p/2 \end{cases} \tag{3.40}$$

3.2.3. The Induced Currents

Once the flux density is calculated, the induced current density in the conductive sheet is determined by Ampere's law as in below:

$$J(x) = \sigma\ \vec{v} \times \vec{B} = \sigma\, v\, B_z(x) = R_{av}\,\sigma\,\omega\, B_z(x) \tag{3.41}$$

where v, ω, B, and B_z are respectively the relative velocity vector, relative angular velocity, and the total magnetic flux density vector and its axial component.

3.2.4. The Reaction Field

The resultant flux density distribution in air-gap and the conductive sheet is defined as the resultant of the fields produced by PMs and the reaction field as in below:

$$B_z(x) = B_{pm}(x) + B_{cs}(x) \tag{3.42}$$

where $B_{cs}(x)$ denotes the reaction flux density issued from the induced current in the conductive sheet, whose associated flux lines are shown in Figure 3.6. This can be calculated by applying Ampere's law to the depicted path, as in below:

$$2\left(h_m + g + L_{cs}\right) B_{cs}(x) / \mu_0 = \int_{x_1}^{x_2} \int_0^{L_{cs}} \left(\sigma\, R_{av}\, \omega\, B_z(x)\right) dz\, dx \tag{3.43}$$

where, x_1 and x_2 are the positions of the left and right sides of the path, respectively. The term after the equality is the total current enclosed in the closed path. Since the reaction flux mainly flows across the unsaturated iron parts, the corresponding MMF drops are negligible, and PM recoil permeability is assumed unity compared to the iron parts, all of which help avoid excessive calculations. Finally, the substitution of (3.42) yields:

$$B_{cs}(x) = \frac{\mu_0\, \sigma\, v\, L_{cs}}{2(g + L_{cs} + h_{pm})} \int_{x_1}^{x_2} [B_{pm}(x) + B_{cs}(x)]\, dx \tag{3.44}$$

Differentiating (44) with respect to x yields an ordinary differential equation as in the following:

$$\frac{dB_{cs}(x)}{dx} = \frac{\mu_0\, \sigma\, v\, L_{cs}}{2(g + L_{cs} + h_{pm})} \left\{B_{pm}(x) + B_{cs}(x)\right\} \tag{3.45}$$

whose general solution can be obtained according to the definition intervals of $B_{pm}(x)$ given in (40), as follows:

$$B_{cs}(x)=\begin{cases} B_{cs1}=k_1\exp\left\{\dfrac{\mu_0\,\sigma\,v\,L_{cs}}{2(g+L_{cs}+h_{pm})}x\right\} & ;\dfrac{-\tau_p}{2}<x<\dfrac{-\alpha_m\tau_p}{2} \\ B_{cs2}=k_2\exp\left\{\dfrac{\mu_0\,\sigma\,v\,L_{cs}}{2(g+L_{cs}+h_{pm})}x\right\}-B_m & ;\dfrac{-\alpha_m\tau_p}{2}\le x\le\dfrac{\alpha_m\tau_p}{2} \\ B_{cs3}=k_3\exp\left\{\dfrac{\mu_0\,\sigma\,v\,L_{cs}}{2(g+L_{cs}+h_{pm})}x\right\} & ;\dfrac{\alpha_m\tau_p}{2}<x<\dfrac{\tau_p}{2} \end{cases} \tag{3.46}$$

Given in the Appendix, constants k_1, k_2, and k_3 are determined by the conditions below:

$$B_{cs2}(x_0)=0 \;\;\Rightarrow\;\; \int_{-\tau_p/2}^{x_0}\int_0^{L_{cs}} J\,dA=\int_{x_0}^{\tau_p/2}\int_0^{L_{cs}} J\,dA \tag{3.47}$$

$$B_{cs1}(x=-\frac{\alpha_m\tau_p}{2})=B_{cs2}(x=-\frac{\alpha_m\tau_p}{2}) \tag{3.48}$$

$$B_{cs2}(x=\frac{\alpha_m\tau_p}{2})=B_{cs3}(x=\frac{\alpha_m\tau_p}{2}) \tag{3.49}$$

where the first equation denotes the main condition referring to the point $x=x_0$ where total currents enclosed in the intervals $[-\tau_p/2,x_0]$ and $[x_0,\tau_p/2]$ are the same, so the magnetic field at the point x_0 is zero. Equations (3.48) and (3.49) denote the continuity of $B_{cs}(x)$ at the margins of the PMs. The significant point x_0 is thus determined through the following equation:

$$R_{av}\,\sigma\,\omega\int_{-\tau_p/2}^{x_0}\int_0^{L_{cs}} B_z(x)\,dz\,dx=R_{av}\,\sigma\,\omega\int_{x_0}^{\tau_p/2}\int_0^{L_{cs}} B_z(x)\,dz\,dx \tag{3.50}$$

x_0 is obtained by solving the above equation as in below:

$$x_0=-\frac{1}{m}Ln\left(\cosh[(1-\alpha_m)\frac{m\,\tau_p}{2}]/\cosh[\frac{m\,\tau_p}{2}]\right) \tag{3.51}$$

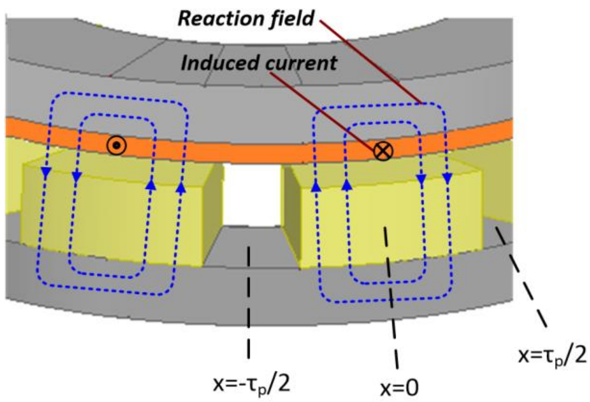

Figure 3. 6. Flux lines of the reaction field

3.2.5. The Developed Torque

Finally, the developed torque is calculated by the total ohmic losses dissipated by the induced currents in the conductive sheet, as in below:

$$T = P/\omega = (L/\sigma\omega)\iint_{CS} |J(x)|^2 \, dx\, dz \tag{3.52}$$

3.2.6. The Actual Current Distribution

Here, a 3D correction of the equivalent 2D model is carried out to consider the actual current paths in the conductive sheet, including the return paths in the overhangs. Figure 3.7 illustrates the induced current paths in the conductive sheet. Figure 3.7(a) illustrates the condition in which return paths are neglected, and induced currents are considered to flow only in the r-direction, while actual induced currents, including the return paths, are depicted in Figure 3.7(b). Finally, Russel's coefficient, given below, is employed in order to take into account the actual current paths.

$$K_s = 1 - \frac{\tanh(pL/4R_{av})}{(pL/4R_{av})(1+\lambda)} \tag{53.3}$$

where λ is the overhang coefficient defined as in below:

$$\lambda = \tanh(pL/4R_{av})\ \tanh(\alpha_L pL/4R_{av}) \tag{3.54}$$

where $\alpha_L=2H/L$ is the ratio of the total overhang length to the active length. The developed torque is finally modified by the correction of the CS conductivity, as in below:

$$\sigma^* = K_s\,\sigma \tag{3.55}$$

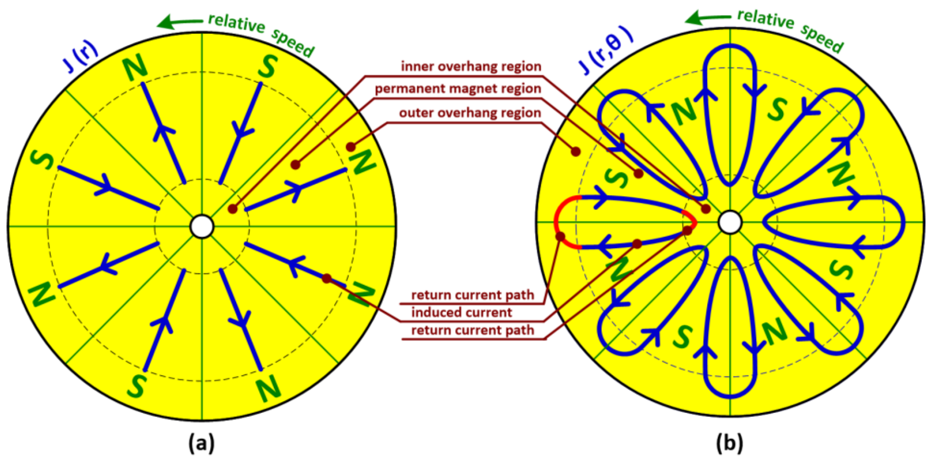

Figure 3. 7. Induced currents in the conductive sheet: **(a)** Simplified current paths in the conductive-sheet by neglecting the return paths, **(b)** Real current paths by considering the return paths in the overhangs

3.2.7. Design Considerations

A constraint should be placed on the maximum current density in the conductive sheet to avoid an excessive temperature rise that substantially affects the PMs and the adhesive holding them to the rotor surface. The average current density is calculated as in below:

$$J_{av} = \int_0^{L_{cs}} \int_{-\tau_p/2}^{\tau_p/2} J(x)\,dx\,dz \,/\, L_{cs}\,\tau_p \tag{3.56}$$

Also, the following relationship should also be satisfied to limit the flux flowing into the back irons and avoid saturation.

$$L_{yp} \geq \varphi_{yp} / L\,B_{knee} \quad ; \quad L_{ys} \geq \frac{\varphi_{ys}}{L\,B_{knee}} \tag{3.57}$$

Moreover, it is essential to limit the ratio of the field intensity inside the PMs to its coercivity in order to keep the operating point conservatively above the knee of the demagnetization curve to prevent irreversible demagnetization due to the reaction field or high temperature. A H_m/H_c ratio of 0.75 is acceptable. We have:

$$H_m / H_c = 1 - B_m / B_r \tag{3.58}$$

where B_m is the flux density within PMs.

3.2.8. Evaluations

This section is devoted to the evaluation of the main characteristics of the device obtained by FEM, the implemented analytical model, and the prototyped coupler. Figure 3.8 shows the *B-H* characteristic of the utilized steel. Figure 3.9 illustrates the resultant magnetic flux density in the air-gap and the current density distribution in the conductive sheet, from which a close agreement with FEM is seen as well. A full-meshed model of the utilized 3D FEM is shown in Figure 3.10(a), in which relatively smaller elements are considered in the CS and the PMs wherein there is a higher field variation. As flux density on the surface of iron parts and PMs is shown in Figure 3.10(b), the flux density within the secondary iron behind the inter-polar region corresponding to R_{yp1} and R_{ys1} is 1.5 T, i.e., the knee point of the *B-H* curve, as designed, and the adjacent portions associated with R_{yp2} and R_{ys2} magnetically operate at a lower flux density, as expected. Flux density distribution on the air-gap side of the conductive sheet is presented in Figure 3.10(c).

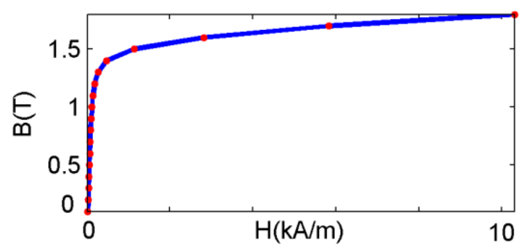

Figure 3. 8. B-H characteristic of the utilized steel grade M15.

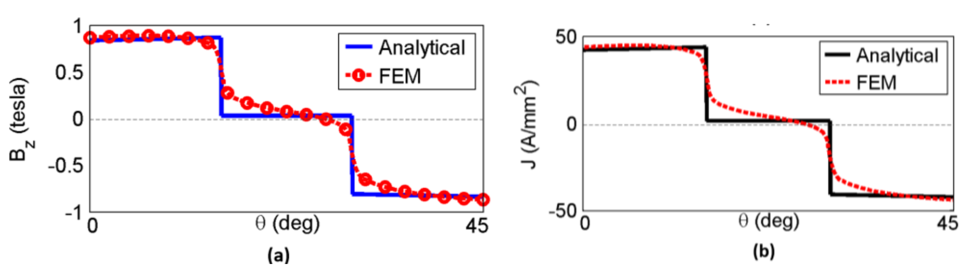

Figure 3. 9. Field calculations at speed of 400 rpm: **(a)** Air-gap magnetic flux density and **(b)** Current density distributions

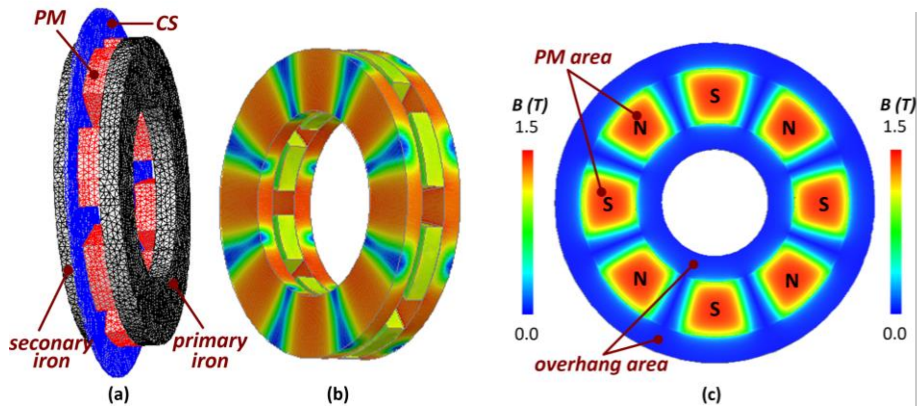

Figure 3. 10. 3D FEM: **(a)** Full meshed model, **(b)** Flux density distribution on the surface of iron parts and PMs, **(c)** Flux density distribution on the surface of the conductive sheet

The torque-speed characteristic of the coupler is shown in Figure 3.11, from which a maximum torque limitation of *4.4 N.m* via the allowed maximum current density of *50 A/mm²* can be determined. Also, it can be observed that a close agreement between the analytical, the experimental, and the FEM results are obtained. It is worth noting that in the eddy-current couplers since the induced current only exists in a solid conductive sheet without any insulation, the current density can be much higher (here 50 A/mm^2) compared to conventional machines (about 5 A/mm^2).

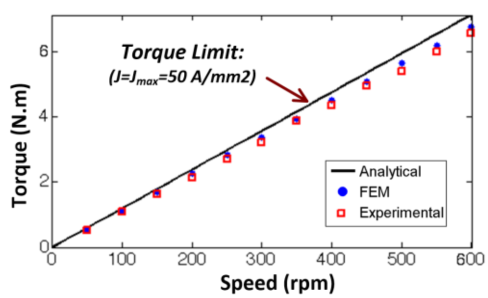

Figure 3. 11. Torque-speed characteristics of the machine

3.3. Example II: A Switched Reluctance Motor with Hybrid Excitation

In this section, modeling, design, and experimental study of a two-phase SRM with Hybrid excitation and self-starting capability is accomplished. The geometry of the motor is based on C-core modules, whose advantages are shortened flux paths leading to smaller core losses and reduced hysteresis losses as the direction of the flux within the stator core do not reverse; the required MMF is also smaller, resulting in a reduction in the copper losses. Thanks to this configuration, a number of PMs can be incorporated into the motor to get the hybrid excitation leading to a higher torque density. In addition, by adding several teeth on the two poles of the C-cores, the desired number of stator/rotor teeth can be obtained, as well as the winding area, and thus, the electrical loading of the motor goes up. Also, a new technique is employed to bring a self-starting capability and a pre-determined direction of rotation, which has superiorities over the previously proposed methods. A MEC-based model for analysis and design of the motor is implemented. It includes precise flux tubes for modeling the air gap and the core permeances by dividing the rotation range into five different regions according to the observed flux pattern. To attain higher accuracy, core saturation is also considered. Another superiority of the proposed model over the previous techniques is that it provides a continuous analytical model over the five regions as well as on the boundary between them, whose merit is clear in the numerical differentiation in torque calculations. Also, FEM is employed in the design and the analysis of the motor, as well as verifications of the model.

3.3.1. Proposed SRM

As shown in Figure 3.12, in the proposed two-phase SRM ($N_{ph}=2$), the stator is made up of separated C-cores called modules, there are a number of teeth on each pole of a C-core, and PMs are embedded in the structure to provide a hybrid excitation. Also, a technique is used to obtain a self-starting capability. Table 3.2 summarizes the specifications of the proposed structure with and without PMs, i.e., hybrid-excited modular SRM (HEMSRM) and modular SRM (MSRM).

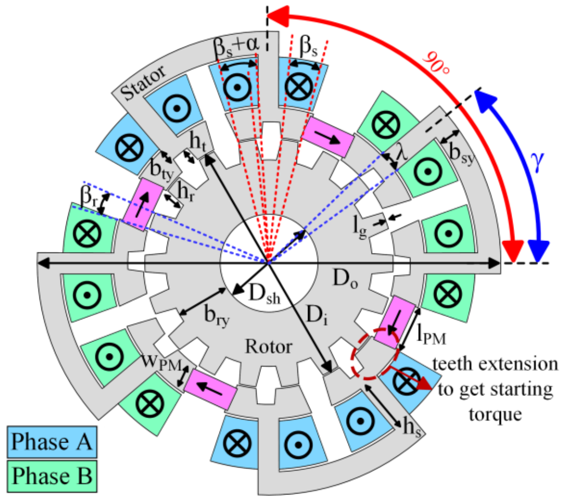

Figure 3. 12. Topology of the proposed HEMSRM.

Table 3. 2 Dimensions of HEMSRM and MSRM

Parameter	Symbol	HEMSRM	MSRM
Number of phases	N_{ph}	2	2
Number of stator teeth	N_s	16	16
Number of rotor teeth	N_r	18	18
Number of C-core per phase	n	2	2
Number of teeth per pole of a C-core	m	2	2
Rotor pole pitch (deg)	θ_{rp}	20	20
C-core angle (deg)	γ	40	40
Stator pole arc (deg)	λ	8	8
Stator tooth arc (deg)	β_s & $\beta_s+\alpha$	8.4 & 11.9	8.4 & 11.9
Rotor pole arc (deg)	β_r	8.4	8.4
Stator outer diameter (mm)	D_o	94	94
Stator yoke thickness (mm)	b_{sy}	4.7	4.7
Stator inner diameter (mm)	D_i	51.2	51.2
Stator pole length (mm)	h_s	10.7	10.7
Stator tooth yoke thickness (mm)	b_{ty}	3	3
Stator tooth length (mm)	h_t	3	3
Air-gap length (mm)	l_g	0.3	0.3
Rotor outer diameter (mm)	d	50.6	50.6
Rotor pole length (mm)	h_r	4.55	4.55
Shaft diameter (mm)	D_{sh}	20	20
Stack length (mm)	L	20	20
PM width & length (mm)	W_{PM} & l_{PM}	5 & 10	-
Available windings space (mm^2)	a_c	112	112
Fill factor	F_f	0.64	0.64
Current density (A/mm2)	J_c	5.5	5.5
Number of turns per pole of a C-core	T_{pole}	90	90
Type of PM	-	NdFe42	-

3.3.1.1. C-Core Stator

Each stator phase is made up of a number of C-cores. Each C-core has two poles. There is a concentrated winding around each pole. The stator flux goes to the rotor from one pole and returns from the other pole. There are three main advantages compared to the conventional structures:

1. Compared to conventional SRMs, the flux path in the rotor and stator back irons is shorter, so the required magnetomotive force and the following copper and core losses are reduced.
2. The direction of the flux in the C-cores does not reverse and is always the same, which results in a significant reduction in the core losses.
3. As the C-cores are magnetically isolated, we can incorporate PMs to have a hybrid-excited stator.

We know that each C-core produces an attraction force on the shaft, so an important point is the number of C-core per phase. As it will be explained later, having only one C-core per phase ($n=1$) results in a radial force on the shaft of the motor, which is destructive, can damage the ball bearing, and can cause eccentricity. Therefore, $n=2$ is picked so that the radial forces on the shaft are canceled out.

3.3.1.2. The Stator and Rotor Teeth Design

The stator is designed such that there are m teeth on each pole of a C-core. The number of stator teeth N_s is the number of phases N_{ph} times the number of C-core per phase n times the total number teeth per C-core $2m$:

$$N_s = N_{ph} \times n \times 2m \tag{3.59}$$

The number of rotor teeth N_r is given as follows, where $2m$ is the number of teeth required for the aligned phase, and $2m+1$ is the number of teeth required for the unaligned phase.

$$N_r = n[2m + (2\,\mathrm{m}{+}1)] \tag{3.60}$$

3.3.1.3. Hybrid Excitation by Embedding PMs

By adding PMs between the C-core modules of the MSRM, we obtain a HEMSRM. The direction of the magnetization of the PMs should be determined such that the direction of the PM flux is the same as the direction of the stator flux in the air gap when a phase is excited. Consequently, the air-gap flux is strengthened, resulting in higher torque. Therefore, the direction of the PMs should be clockwise or counterclockwise, which is based on the direction of currents in the stator windings. Here, the clockwise direction is selected.

3.3.1.4. Self-Starting Capability

A big drawback of two-phase SRMs is that they do not have a self-starting torque and thus a pre-determined direction of rotation. To obtain a starting torque, one of the left or the right tooth of each pole of a C-core needs to be extended by an amount of α from one side. It can be seen that when phase B is aligned (the right flux loop), phase A (the left flux loop), which is in an unaligned position, can develop a starting torque if excited. This technique of developing a staring torque by making an asymmetry in the torque-angle characteristic can be observed in Figure 3.13. If the extension is made on the right side of the teeth, the direction of the rotation of the rotor is counterclockwise; also, if the extension is made on the left side of the teeth, the direction of the rotation of the rotor is clockwise.

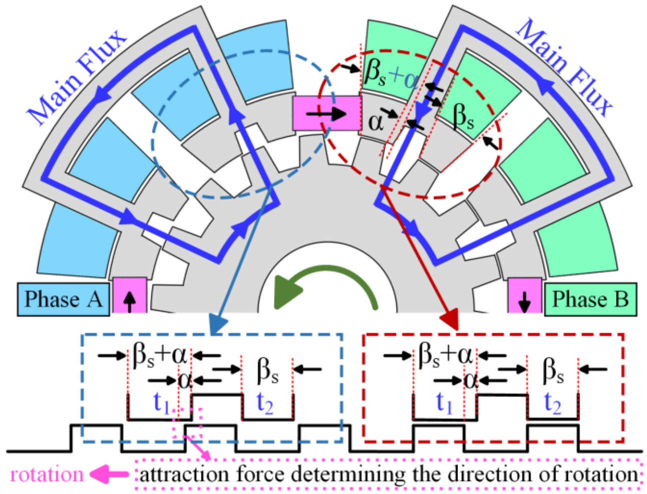

Figure 3. 13. Teeth extension in the proposed self-starting technique.

3.3.1.5. Flux Analysis

Figure 3.14(a) shows flux loops and flux density distribution due to only stator excitation (MSRM). It can be seen that, compared to conventional SRMs, there are no flux reversals and the flux paths are shorter (smaller required MMF), resulting in lower core and copper losses. As flux paths and flux density distribution due to only PM excitation are shown in Figure 3.14(b), it is observed that nearly all of the PM flux closes its pass through the stator C-cores at zero current, resulting in almost zero cogging torque. As shown in Figure 3.14(c), as the current goes up in HEMSRM, the stator core gets close to the knee point of the saturation, and core reluctance goes up, thus more PM flux tends to pass the air-gap and close its path through the rotor; it is how the PM flux reinforces the air-gap flux density, leading to an increase in the developed torque. It is worth noting that the thickness of the C-cores should be designed such that they get close to the knee point of the saturation curve at the nominal current so that most of the PM flux passes the air gap to contribute to the energy conversion.

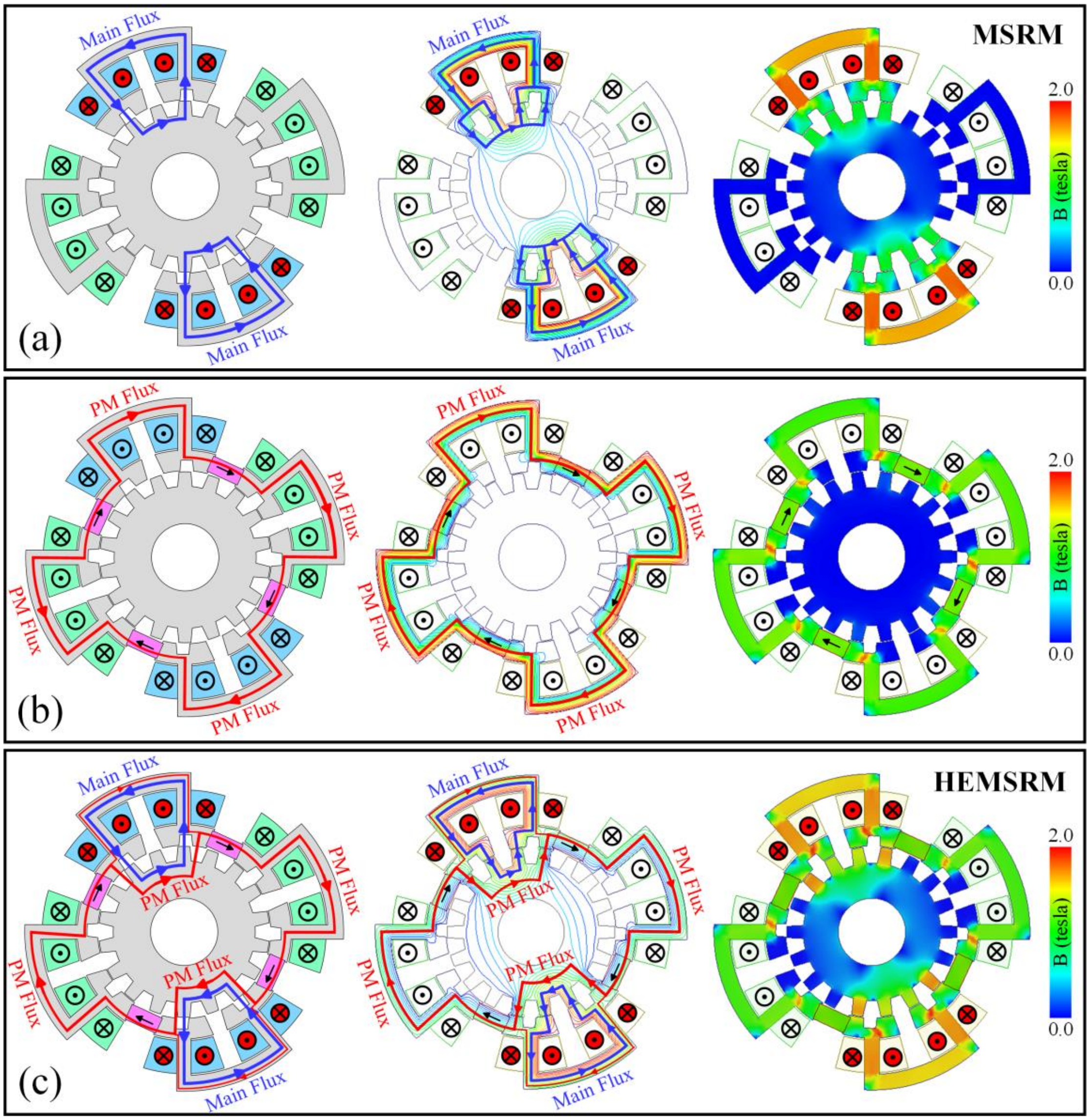

Figure 3. 14. Flux paths, flux lines, and flux density due to (a) only current (MSRM), (b) only PMs, and (c) both current and PMs (HEMSRM).

3.3.2. Flux Tube Modeling

This section is devoted to MEC and torque derivation.

3.3.2.1. Magnetic Equivalent Circuit

The implemented MEC, is given in Figure 3.15. The circuit, which has 32 nodes, can be solved using Kirchhoff's current law to obtain the node MMFs. It leads to the following 32-by-32 system of equations:

$$\left[P_{i,j}\right]_{32\times32}\left[F_i\right]_{32\times1}=\left[\varphi_i\right]_{32\times1} \tag{3.61}$$

where the node MMFs F_i are the unknowns. The flux sources φ_i are obtained using the Norton equivalent of the MMF sources of the stator F_s and the PMs F_{pm} as in below:

$$\varphi_s=(2P_{sp}+P_{sy})(2F_s) \tag{3.62}$$

$$\varphi_{pm}=(2P_{PM}+P_{sy})(2F_{pm}) \tag{3.63}$$

Then, the flux source φ_i is φ_{sp} for $i=2$ and 31, $-\varphi_{sp}$ for $i=3$ and 30, φ_{pm} for $i=1$ and 32, and $-\varphi_{pm}$ for $i=4$ and 28. Otherwise, φ_i is zero. The element $P_{i,j}$ is the sum of the permeances connected to the node i if $i=j$, and it is minus the permeance between the nodes i and j if $i\neq j$.

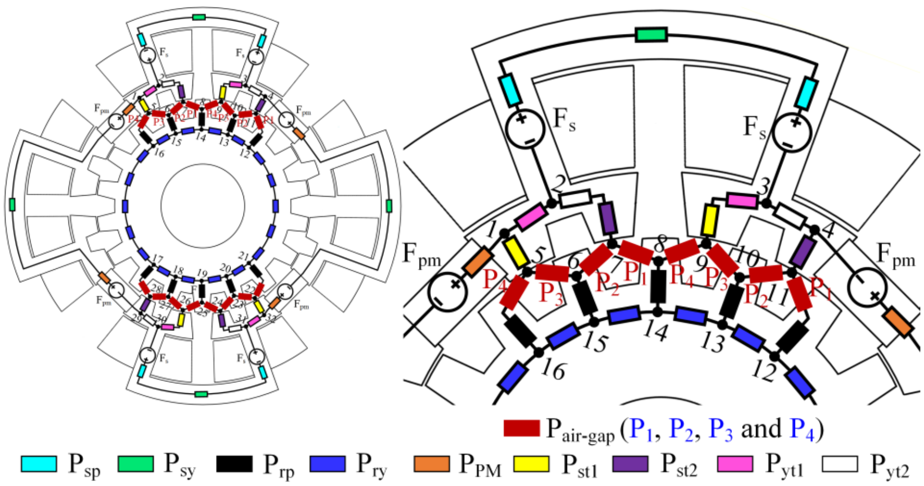

Figure 3. 15. Magnetic Equivalent Circuit.

3.3.2.2. Air-Gap Flux Tubes and Permeances

As shown in Figure 3.16, based on the observation of the flux lines and the fact that the flux pattern changes as the rotor rotates from an unaligned position ($\theta=0$) to a fully-aligned position ($\theta=\theta_{rp}/2$), five different regions are considered for the flux tube modelling and permeance calculation of the air-gap. The boundary between the regions is also specified. The highest number of flux tubes (the most complicated model) exists in region one, and this number decreases with disappearing some flux tubes as the rotor gets close to the end of region 5 (the simplest model). Each flux tube can be calculated using:

$$P_{gi} = \int_a^b \frac{\mu_0 L\, dx}{l_{gi}} \tag{3.64}$$

where the integration interval [a,b], the flux tube length l_{gi}, and the obtained permeance relationships are given in Table 3.3. For simplicity, $k=\mu_0 L/\pi$ is used. Other geometrical parameters are given in the Appendix.

Comparing the MEC in Figure 3.15 and the air-gap flux tubes in Figure 3.16, we understand that the four air-gap permeances P_1, P_2, P_3, and P_4 shown in Figure 3.15 are constituted from several parallel flux-tubes (P_{g1} to P_{g13}), calculated as in below:

$$P_1 = P_{g1} + P_{g2} + P_{g3} + P_{g12} \tag{3.65}$$

$$P_2 = P_{g4} + P_{g5} + P_{g6} \tag{3.66}$$

$$P_3 = P_{g7} + P_{g8} + P_{g9} + P_{g13} \tag{3.67}$$

$$P_4 = P_{g5} + P_{g10} + P_{g11} \tag{3.68}$$

It is worth noting that the value of P_{gi} is zero in some regions, as shown in Table 3.3.

3.3.2.3. Core and PM Permeances

The permeances of the rotor and the stator cores, as well as the PMs, as shown in Figure 3.16, can be obtained using the following relationship:

$$P = \frac{\mu A}{l} \tag{3.69}$$

where the values of permeability μ, length l, area A, and the obtained relationships are given in the Table 3.3.

Table 3. 3 Permeance Calculations for Different Regions

Air-gap Permeances					
P_{gi}	Region (R_i)	Integration interval		Flux tube length	Permeance Relationship
		a	*b*	$l_i(x)$	
P_{g1}	R_1	$\theta_1-\theta$	$\tau_r+\theta_1-\theta$	$l_g+(\pi/2)x$	$2k\times ln\left(1+(\pi\tau_r)/\left(2l_g+\pi(\theta_1-\theta)\right)\right)$
	R_2, R_3, R_4, R_5	0	$\tau_r+\theta_1-\theta$	$l_g+(\pi/2)x$	$2k\times ln\left(1+\pi(\tau_r+\theta_1-\theta)/(2l_g)\right)$
P_{g2}	R_1	0	$\theta_1-\theta$	$l_g+\pi x$	$k\times ln\left(1+\pi(\theta_1-\theta)/(l_g)\right)$
	R_2, R_3, R_4, R_5	-	-	-	0
P_{g3}	R_1	$\theta_1-\theta$	$\tau_r/2+\theta_1$	$l_g+(\pi/2)x$	$2k\times ln\left(\left(4l_g+\pi(\tau_r+2\theta_1)\right)/\left(4l_g+2\pi(\theta_1-\theta)\right)\right)$
	R_2, R_3	0	$\tau_r/2+\theta_1$	$l_g+(\pi/2)x$	$2k\times ln\left(1+\pi(\tau_r+\theta_1)/(2l_g)\right)$
	R_4, R_5	0	$\tau_r+\theta_1-\theta$	$l_g+(\pi/2)x$	$2k\times ln\left(1+\pi(\tau_r+\theta_1-\theta)/(2l_g)\right)$
P_{g4}	R_1, R_2, R_3	$\theta_1+\theta$	$\tau_r/2+\theta_1$	$l_g+(\pi/2)x$	$2k\times ln\left(\left(4l_g+\pi(\tau_r+2\theta_1)\right)/\left(4l_g+2\pi(\theta_1+\theta)\right)\right)$
	R_4, R_5	-	-	-	0
P_{g5}	R_1, R_2, R_3	0	$\theta_1+\theta$	$l_g+\pi x$	$k\times ln\left(1+\pi(\theta_1+\theta)/(l_g)\right)$
	R_4, R_5	-	-	-	0
P_{g6}	R_1, R_2	$\theta_1+\theta$	$\tau_r-\tau_{s1}/2+3\theta_1/2$	$l_g+(\pi/2)x$	$2k\times ln\left(\left(4l_g+\pi(2\tau_r-\tau_{s1}+3\theta_1)\right)/\left(4l_g+2\pi(\theta_1+\theta)\right)\right)$
	R_3, R_4, R_5	-	-	-	0
P_{g7}	R_1, R_2	0	$\tau_r-\tau_{s1}/2+\theta_1/2$	$l_g+(\pi/2)x$	$2k\times ln\left(1+\pi(2\tau_r-\tau_{s1}+\theta_1)/(4l_g)\right)$
	R_3, R_4	0	$2\tau_r-\tau_{s1}+\theta_1-\theta$	$l_g+(\pi/2)x$	$2k\times ln\left(1+\pi(2\tau_r-\tau_{s1}+\theta_1-\theta)/(2l_g)\right)$
	R_5	-	-	-	0
P_{g8}	R_1, R_2, R_3, R_4	0	$\tau_{s1}-\tau_r-\theta_1+\theta$	l_g	$\mu_0 L(\tau_{s1}-\tau_r-\theta_1+\theta)/(l_g)$
	R_5	0	τ_r	l_g	$\mu_0 L(\tau_r)/(l_g)$
P_{g9}	R_1, R_2, R_3	0	$\tau_r/2+\theta_1$	$l_g+(\pi/2)x$	$2k\times ln\left(1+\pi(\tau_r+2\theta_1)/(4l_g)\right)$
	R_4, R_5	0	$\tau_r+\theta_1-\theta$	$l_g+(\pi/2)x$	$2k\times ln\left(1+\pi(\tau_r+\theta_1-\theta)/(2l_g)\right)$
P_{g10}	R_1, R_2, R_3	$\theta_1+\theta$	$\tau_r/2+\theta_1$	$l_g+(\pi/2)x$	$2k\times ln\left(\left(4l_g+\pi(\tau_r+2\theta_1)\right)/\left(4l_g+2\pi(\theta_1+\theta)\right)\right)$
	R_4, R_5	-	-	-	0
P_{g11}	R_1	$\theta_1+\theta$	$\tau_r+\theta_1+\theta$	$l_g+(\pi/2)x$	$2k\times ln\left(1+(\pi\tau_r)/\left(2l_g+\pi(\theta_1+\theta)\right)\right)$
	R_2, R_3	$\theta_1+\theta$	$\tau_r+2\theta_1$	$l_g+(\pi/2)x$	$2k\times ln\left(2l_g+\pi(\tau_r+2\theta_1)/\left(2l_g+\pi(\theta_1+\theta)\right)\right)$
	R_4, R_5	-	-	-	0
P_{g12}	R_1	-	-	-	0
	R_2, R_3, R_4, R_5	0	$\theta-\theta_1$	l_g	$\mu_0 L(\theta-\theta_1)/l_g$
P_{g13}	R_1, R_2, R_3, R_4	-	-	-	0
	R_5	0	$\tau_{s1}-2\tau_r-\theta_1+\theta$	$l_g+(\pi/2)x$	$2k\times ln\left(1+\pi(\tau_{s1}-2\tau_r-\theta_1+\theta)/(2l_g)\right)$

Core and PM Permeances				
P_{core}	μ	Area A	Length l	Permeance Relationship
P_{sy}	μ_{sy}	$b_{sy} L$	$\gamma (D_o-b_{sy})/2$	$\mu_{sy}(b_{sy}L)/((\gamma)(D_o-b_{sy})/2)$
P_{sp}	μ_{sp}	$\tau_s L$	h_s	$\mu_{sp}(\tau_s L)/h_s$
P_{rp}	μ_{rp}	$\tau_r L$	h_r	$\mu_{rp}(\tau_r L)/h_r$
P_{ry}	μ_{ry}	$b_{ry} L$	τ_{rp}	$\mu_{ry}(b_{ry}L)/\tau_{rp}$
P_{st1}	μ_{st1}	$\tau_{s1} L$	h_t	$\mu_{st1}(\tau_{s1}L)/h_t$
P_{st2}	μ_{st2}	$\tau_{s2} L$	h_t	$\mu_{st2}(\tau_{s2}L)/h_t$
P_{yt1}	μ_{yt1}	$b_{ty} L$	$(\tau_{rp}+\tau_r-\tau_{s1})/2$	$\mu_{yt1}(b_{ty}L)/((\tau_{rp}+\tau_r-\tau_{s1})/2)$
P_{yt2}	μ_{yt2}	$b_{ty} L$	$\tau_{rp}/2$	$\mu_{yt2}(b_{ty}L)/(\tau_{rp}/2)$
P_{PM}	μ_{PM}	$w_{PM} L$	l_{PM}	$\mu_{PM}(w_{PM}L)/l_{PM}$

3.3.2.4. Core Saturation

The core saturation is accounted for using an iterative procedure in which the permeabilities of the core permeances updates in each iteration as in below:

$$\hat{\mu}_{ri}^{(k)} = B_i^{(k-1)} / \mu_0 H_i^{(k-1)}, \;\; \mu_{ri}^{(k)} = (\hat{\mu}_{ri}^{(k)})^d . (\mu_{ri}^{(k-1)})^{1-d} \tag{3.70}$$

where B_{iron} and H_{iron} are obtained from the BH curve. The damping d is set to 0.1. This iterative process repeats until the following stop criterion is satisfied for ε=0.001.

$$\mu_{ri}^{(k)} - \mu_{ri}^{(k-1)} \le \delta \tag{3.71}$$

3.3.2.5. Torque Calculation

Having the node MMFs calculated, the flux passing a pole of a C-core φ_{sp}, and then the flux linkage and the inductance of a phase can be obtained as in below:

$$\begin{aligned} L(\theta,i) &= \frac{\lambda(\theta,i)}{i} \\ \lambda(\theta,i) &= 2\,n\,T_{pole}\,\varphi_{sp}(\theta,i) \end{aligned} \tag{3.72}$$

Then, the coenergy and the torque are obtained as in below:

$$W_c(\theta,i) = \frac{1}{2} L(\theta,i)\, i^2 \tag{3.73}$$

Having the coenergy, the developed torque can be obtained by numerical differentiation using the following relationship:

$$T(\theta,i) = \left. \frac{\partial W_c(\theta,i)}{\partial \theta} \right|_{i=const} = \frac{1}{2} i^2 \frac{dL(\theta,i)}{d\theta} \tag{3.74}$$

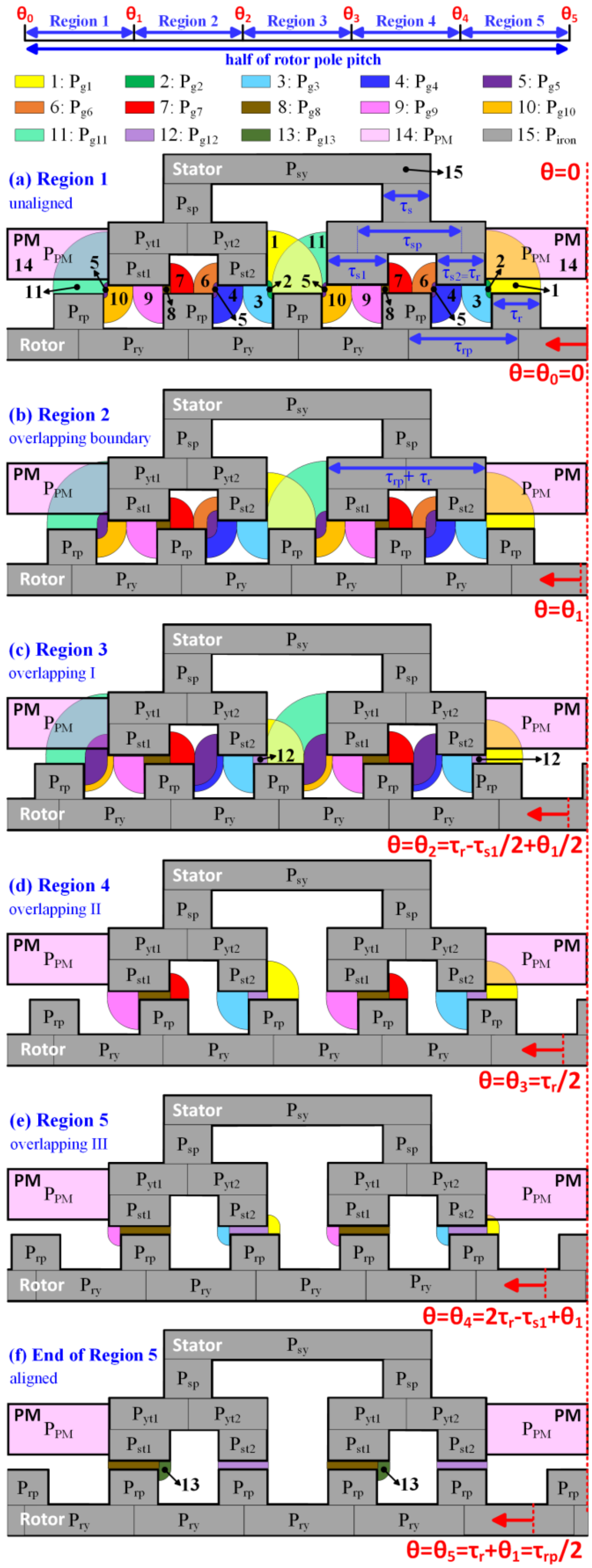

Figure 3. 16. Flux tubes for permeances calculations in different regions.

3.3.3. Results and Discussions

As shown in Figures 3.17(a)-(b), there is a starting torque in both HEMSRM and MSRM. The PMs have increased the torque in HEMSRM. As summarized in Table 3.4, the higher the current, the larger the impact of PM deployment on the torque increase; as it was shown in Figure 3.14, as the current goes up, the core gets closer to the knee point of saturation and the core reluctance goes up, so more PM flux tends to pass the air-gap so as to contribute to the energy conversion and finally torque production. Figures 3.19(c) illustrates the total torque (T_{HEMSRM}) at the nominal current of 6 A and its components, i.e., the parts produced by stator flux (T_{MSRM}) and PM flux (T_{PM}), respectively; it is seen that almost half of the total torque is produced by the PMs. As shown in Figures 3.17(d), the magnitude of the cogging torque is almost zero (less than 5 mN.m) as almost all of the PM flux passes the C-cores, as can also be observed in Figure 3.14(b). Also, a great correlation is observed between analytical, FEM, and experimental results, proving the accuracy of the model. As given in Figure 3.18, the rate of change of flux linkage versus position is higher in HEMSRM compared to MSRM, which is the reason behind its larger torque capability.

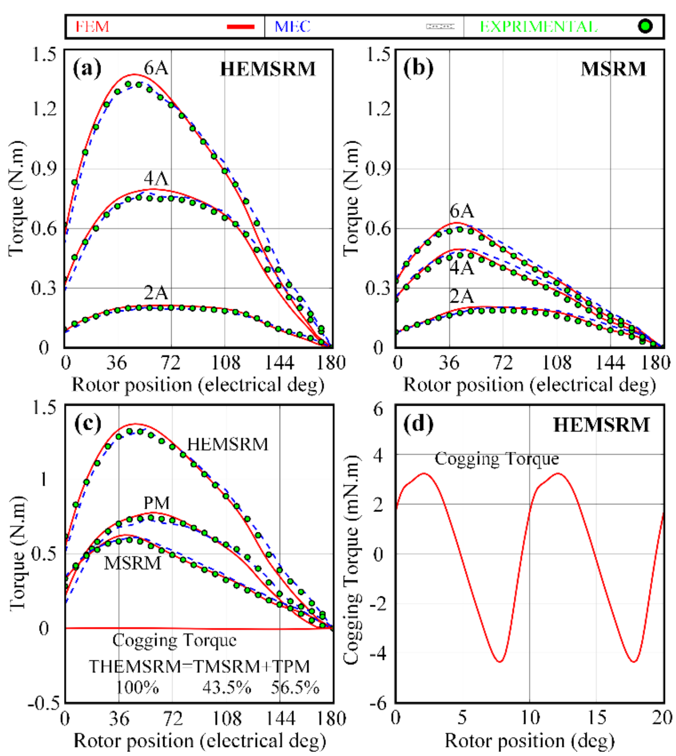

Figure 3. 17. (a) and (b) torque-angle characteristics at different currents for HEMSRM and MSRM, (c) total torque of HEMSRM and its components at the current of 6A, and (d) cogging torque of HEMSRM.

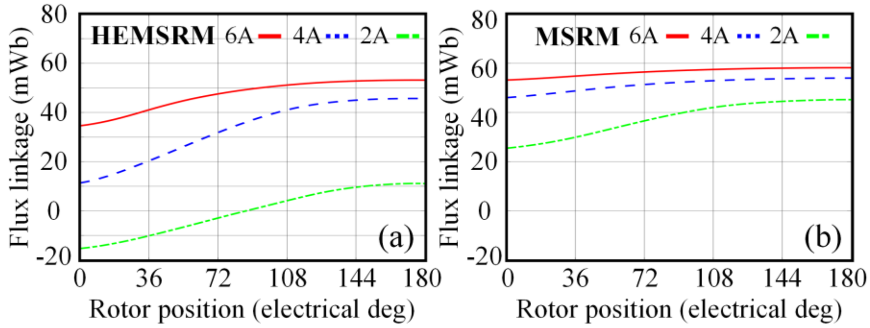

Figure 3. 18. Flux linkage versus position characteristics for the two motors at the currents of 2, 4, and 6 A.

Table 3. 4 Comparison of Mean and Peak Torque

Phase current (A)	Torque of HEMSRM (N.m)		Torque of MSRM (N.m)		Mean torque of HEMSRM compared to MSRM (%)	Peak torque of HEMSRM compared to MSRM (%)
	Mean	peak	Mean	peak		
1	0.038	0.056	0.038	0.054	0.00	3.70
2	0.150	0.212	0.140	0.206	7.14	2.91
3	0.328	0.471	0.234	0.392	40.17	20.15
4	0.534	0.797	0.291	0.496	83.50	60.68
5	0.704	1.116	0.330	0.570	113.33	95.79
6	0.833	1.374	0.363	0.628	129.47	118.79

Chapter 4

A Rotary Actuator with Magnetic Restoration and an Experimental Prototype

4.1 The Topology of the Actuator

In this chapter, an electromechanical model incorporating eddy currents is developed for a limited-angle rotary actuator with a magnetic restoration torque to be employed in identification, drive, and control studies. By elliptically shaping the stator curvature, the reluctance torque is produced to restore the rotor to the maximum torque position if the coil current is removed.

The geometry and the exploded view of the actuator, whose specifications are listed in Table 4.1, are shown in Figure 1(a)-(b). The rotor PM has diametral magnetization. The interaction of stator flux and the magnet produces the main torque. The stator inner surface is shaped to have an elliptical curvature whose interaction with the magnet produces a reluctance torque which tends to restore the rotor back to the maximum torque per ampere position (MTPAP).

Table 4. 1 Specifications of the Studied Motor

parameter	value	parameter	value
outer diameter, D_o	13.716 mm	PM remnant, B_r	1.37 Tesla
lamination height d	0.35	total turns, N	100
# of laminations, m	12	wire gauge	AWG33
stack length, L	4.191 mm	torque constant, k_t	1.906 mN.m/A
pole width, w_p	4.72 mm	Mag. spring k_s	0.636 mN/rad
PM length, L_{pm}	9 mm	total stiffness, K_s	1.3 mN/rad
rotor diameter, D_r	3.048 mm	total damping, k_d	4.49e-7 Ns/rad
minor radius, R_1	1.71 mm	inertia, J	1.65e-9 kg.m^2
major radius, R_2	1.9665 mm	inductance, L_{c0}	280 uH
PM conductivity	0.6 MS/m	resistance, R_c	1.76 ohm
lamination conduct.	2 MS/m	sense resistor, R_s	0.1 ohm

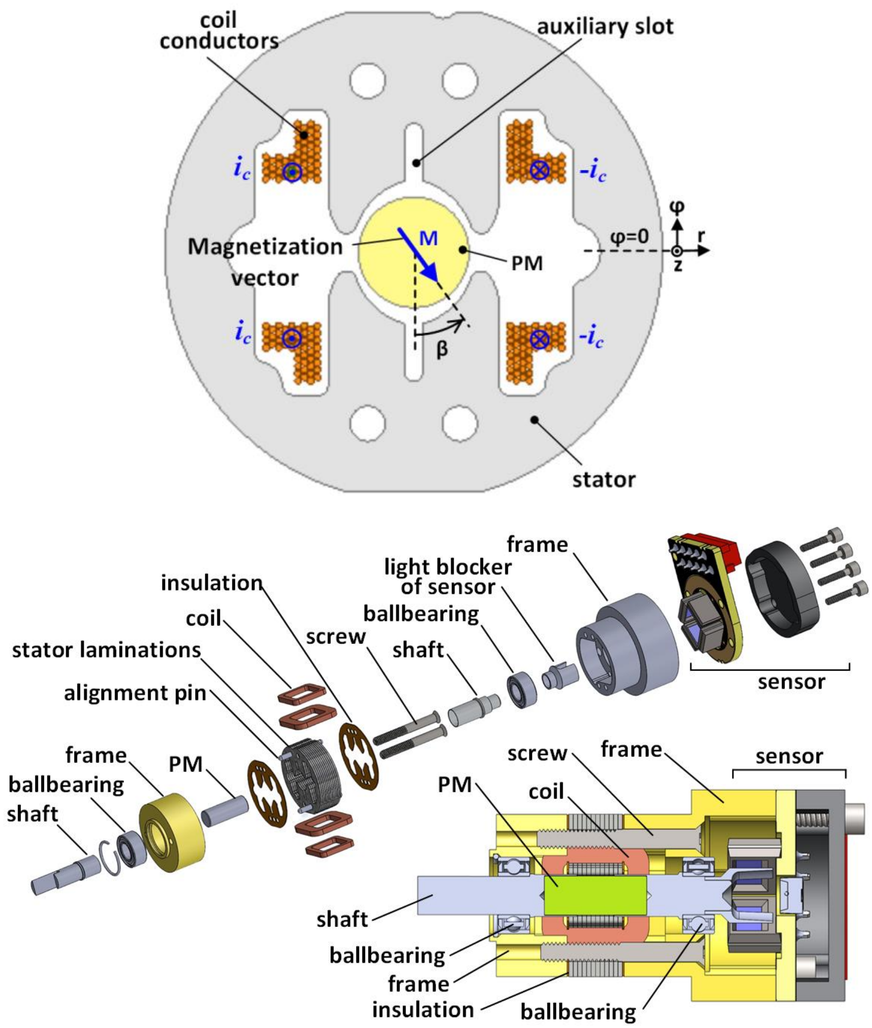

Figure 4. 1. (a) exploded view of the actuator, (b) geometry of the actuator, (c) Amperian current model of PM, and (d) lumped-element models of the PM

4.2. Design Considerations

In this section, some design aspects of the actuator are explained:

1. The rotor radius R_r and thus the overall sizing is obtained based on torque/power requirements.

2. The inner radius of the stator is designed to provide enough space for the stator winding according to the required electrical loading (Ampere turn).

3. The outer diameter of the stator D_o is designed such that the back iron operates at the knee point of the magnetic saturation curve; too small values result in saturation while

a large value causes the excessive use of iron and oversizing. A value around half of the pole face is a good design.

4. There is a compromise between k_t and k_{res}; a larger restoration can be achieved by a higher saliency, but k_t goes down as the saliency increase the effective air-gap length, which causes a reduction in the average flux density of air-gap; therefore, the saliency should be designed to provide the minimum required restoration.

5. There are two auxiliary slots to divide the pole faces into two sections in order to aid in restoration by suppressing hysteresis effects. As the rotor goes back and forth around MTPAP, the direction of the flux produced by the PM within each half of the stator pole faces changes without the auxiliary slots. By separating the two halves of a pole face, the magnet flux turns the auxiliary slot; thus, one section always stays North and the other one always stays South, guaranteeing that the rotor restores to the MTPAP when the current is removed from the coil. As illustrated in Figure 4.2, without the auxiliary slots, there could be a hysteresis effect making one-half of the pole face more or less North/South if the current is removed when the rotor is not at the MTPAP; as a result, the rotor restores to position with a small deviation from MTPAP. The opening of these two slots should be small enough so that its fringing effect can be ignored.

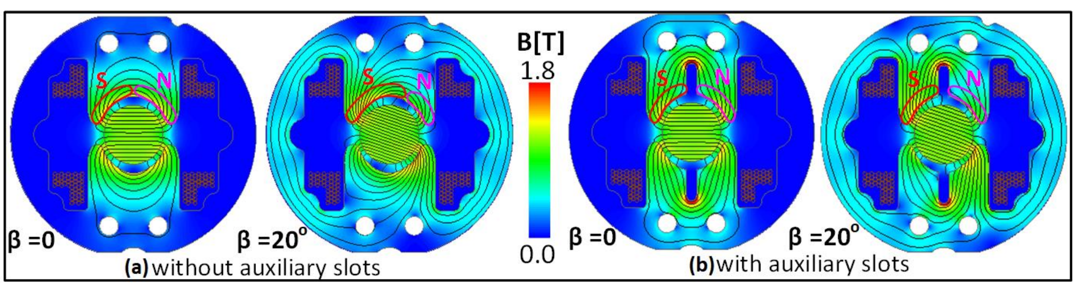

Figure 4. 2. PM flux and hysteresis effect: (a) without and (b) with auxiliary slots.

4.3. Field Analysis

Figure 4.3(a) shows flux lines, flux density distribution, the radial component B_r and its fundamental B_{r1} on the rotor surface due to the stator current. The left sides of Figures. 4.3(b)-(d) show the magnetic flux density distribution due to the PM at different rotor positions, while the right sides illustrate the PM Amperian currents K_m together with B_{r1}—the torque producing. At $\beta=0$, $K_m B_{r1}$ integrates to zero, *so* $T_{coil}=0$; also, $T_{rest}=0$, because the PM is faced with the minimum permeance, which is an unstable equilibrium as the slope of the curve is positive. At $\beta=45$, T_{rest} is maximum. At MTPAP, i.e., $\beta=0$, $K_m B_{r1}$ integrates to a maximum value; also, $T_{rest}=0$ as the PM is faced with the maximum permeance, which is a stable equilibrium as the slope of the curve is negative. The meshed models used in finite element analysis are shown in Figure 4.4.

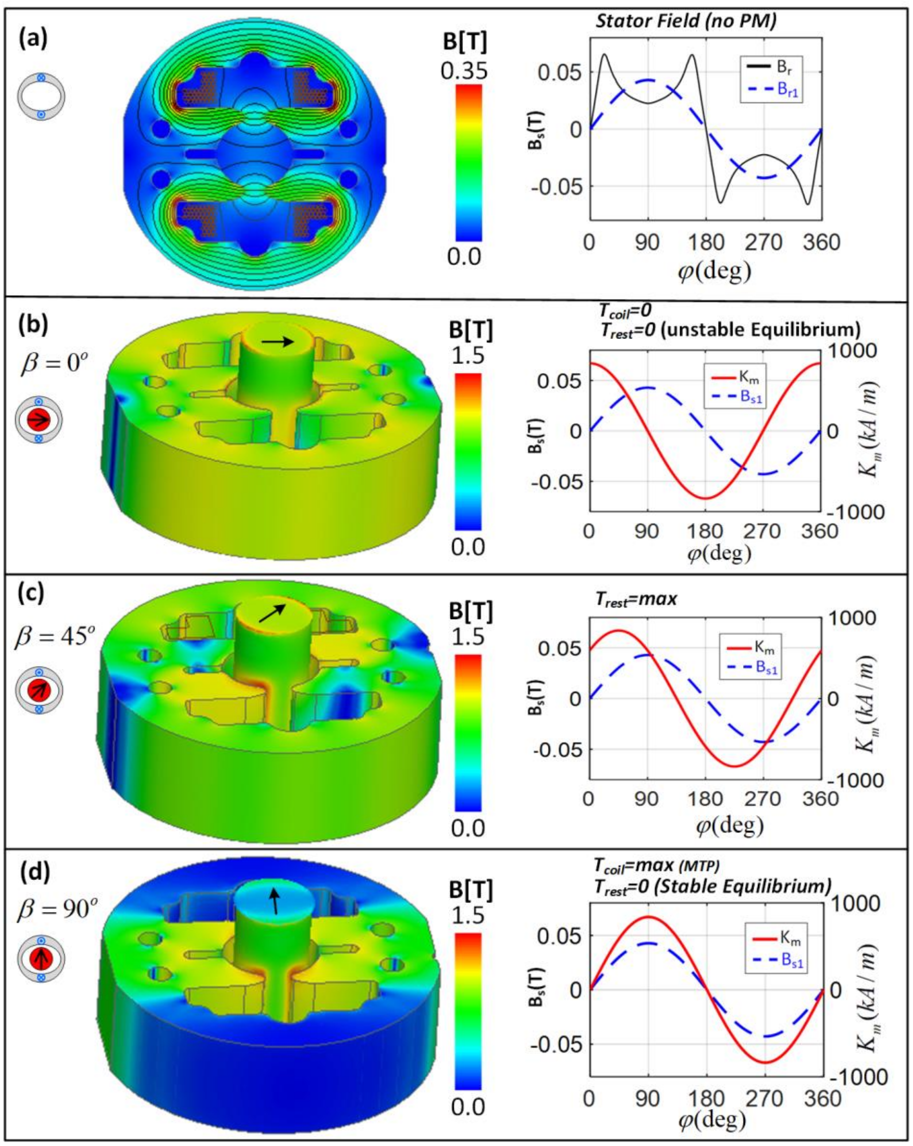

Figure 4. 3. (a) 2D distribution of magnetic flux density and flux lines (left), and radial component of magnetic flux density B_r and its fundamental B_{r1} due to stator current of *1A*, and (b)-(d) 3D distribution of magnetic flux density (left), and Amperian current distribution of PM together with B_{r1} (right) at rotor positions $\beta=0$, $\beta=45^o$ and $\beta=90^o$.

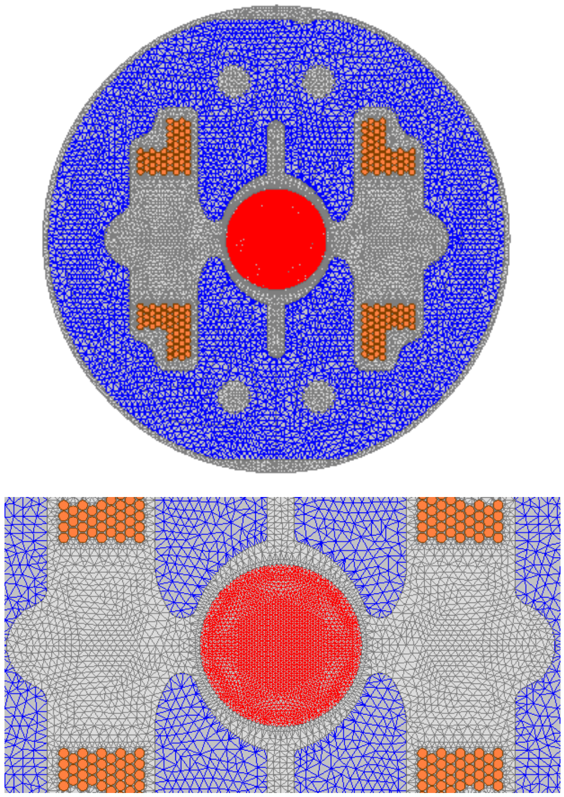

Figure 4. 4. Meshed models for original geometry used for FEM.

4.3. Experimental Prototype

Figure 4.5 shows the prototyped actuator and the torque-angle measurement setup. The torque-angle characteristics at zero coil currents (the restoration torque) as well as the coil torque and the total torque at a current of *1A* are given in Figure 4.6(a). The torque constant is obtained as k_t=1.906 *m N.m/A* by experiment and 1.953 *m N.m/A* by 3D FEM and, i.e., less 2.5% of error. Also, the restoration constant is obtained as k_{rest}=0.318 by experiment and 0.28 by FEM and, i.e., an error of 11%. Among the sources of the discrepancies might be prototyping issues, misalignments, inaccurate material characteristics, etc. The coil torque is obtained by subtracting the restoration torque from the total torque as it cannot directly be measured. The back-emf waveform at a velocity around *100 rad/sec* is shown in Figure 4.6(b), where the peak divided by the velocity is obtained as k_b=*1.91 volt.sec/rad* by experiment and *1.96 volt.sec/rad* by FEM and, i.e., an error of less than 3%. It is seen that all waveforms have a sinusoidal pattern, as expected from the nonlinear electromechanical model that will be explained in a future chapter.

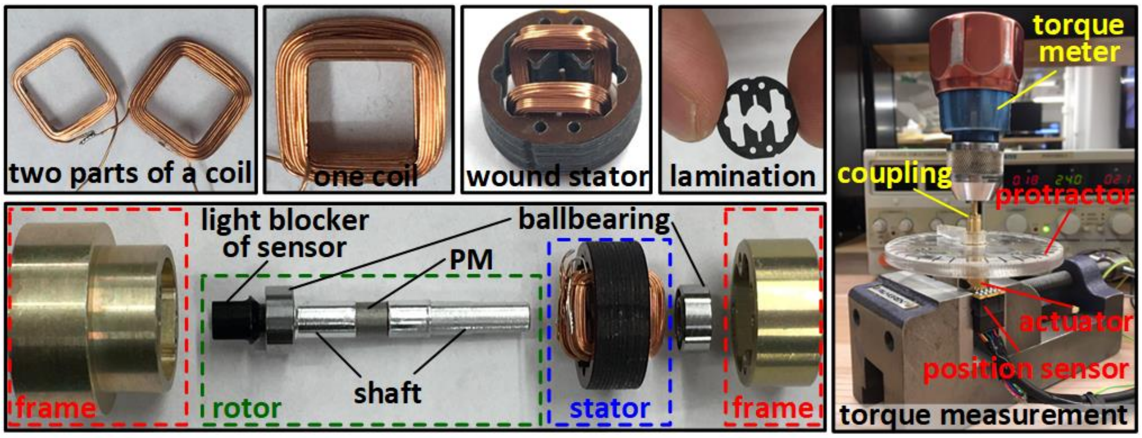

Figure 4. 5. The prototype actuator (left), and torque-angle measurement (right).

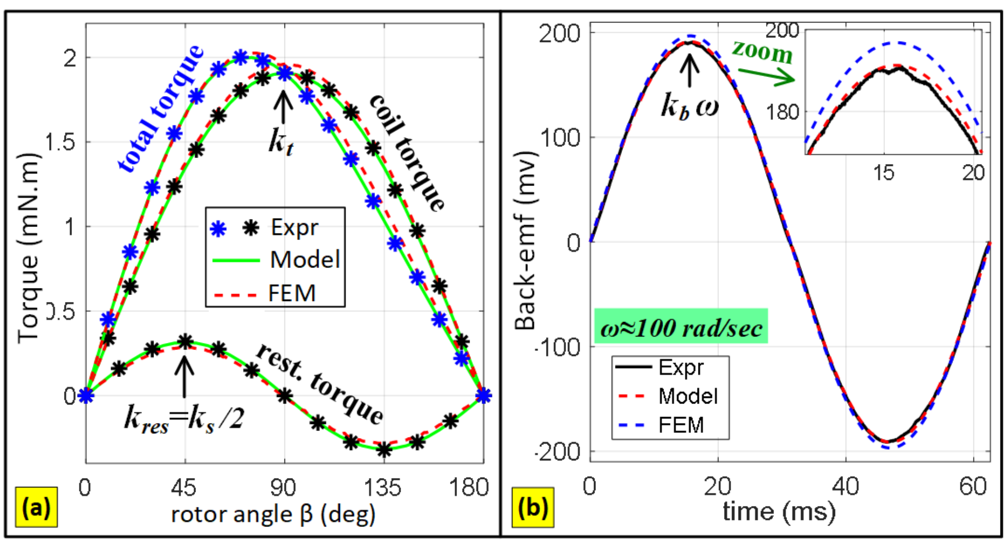

Figure 4. 6. (a) Coil, restoration and total torques, and (b) back-emf waveform

4.4. Conclusions

In the studied actuator, the coil torque is produced by the interaction of the fluxes produced by the coil current, and the restoration torque is produced by the interaction of the magnet with the saliency of the stator poles. The penalty of having the restoration torque is that the coil torque goes down to a small degree, which is a point to have in mind for the design of such devices. In some applications, the restoration torque might not be needed, and so a circular crosssection might is adopted for the stator pole faces. It is also true for the auxiliary slots; if the restoration does not matter, they may be eliminated from the topology of the actuator.

Chapter 5

Electromagnetic Model

5.1 Introduction

Modeling of electric machines and provides very useful tools for design, analysis, and optimization purposes. Due to advantages like simple structure, cheap maintenance, high reliability, low cost, and uncomplicated control, rotary actuators have been employed widely in the industry from automotive manufacturing and biomedical applications to robotics, aerospace, fluid valves, optical scanning, and 3D printers. They are sometimes called limited-angle torque motors, especially when designed to provide a constant torque over an angular region. Voice coil motors have the same behavior.

The finite element method (FEM) is a very powerful numerical technique in the analysis of electromagnetic devices, e.g., in limited-angle torque motors and actuators; however, FEM can be expensive and time-consuming, making them very slow in the design optimizations. On the other hand, analytical approaches, by providing closed-form solutions, are very fast yet accurate alternatives for preliminary designs and optimizations. Electric machines may be successfully modeled based on the solution of Laplace's and Poisson's equations; this powerful approach provides precise field solutions and torque calculations, yet their major drawback is that several boundary conditions are required to solve the system of equations, so severe challenges can be faced in complicated geometries. This approach has been used in the modeling of many electromagnetic devices in different coordinates, e.g., magnetic couplers in cylindrical coordinates [19], a voice coil actuator in cartesian coordinates [25], and limited-angle torque motors in cylindrical coordinates [26]. General solutions in cartesian, cylindrical, and spherical coordinates can be found in [17] -[18]. However, Laplace's equation in elliptical coordinates, whose general solutions can be found in [20] and [24], have rarely been used in the modeling of electric machines. In [21]-[23], such studies have been done in the realm of physics and accelerator magnets.

In this chapter, an analytical model is developed for a rotary actuator with a magnetic restoration torque that replaces the traditional mechanical springs having a shorter lifetime and mechanical fatigue problems. The rotor is a permanent magnet (PM) with diametral magnetization. The restoration torque is produced by shaping the stator to have an approximately elliptical curvature such that a reluctance torque is obtained. To model the actuator, the stator geometry is simplified to an ellipse having surface current densities on the interpolar regions which are equivalent to stator coils. Also, the PM is represented with Amperian currents on the surface of the rotor.

To obtain the coil torque, the field solutions within the stator are obtained by solving Laplace's equation in the elliptical coordinates in which the equivalent surface current is used as a boundary condition. Afterward, the magnetic flux density on the PM boundary are obtained and converted to the cylindrical coordinates. Then, the coil torque is calculated by the Lorentz force operating on the Amperian currents. As the stator boundary is an ellipse and the rotor boundary is a circle, the reluctance torque cannot be derived by solving Laplace's equation in one coordinate system, so the flux tube method is employed. Also, a rotating reference frame on the rotor is adopted to simplify the mathematics. It is shown that the conventional flux tubes used in lumped-element MECs do not work, and thus a method named differential flux tubes is adopted in which, instead of lumped permeances for different regions, differential permeances are utilized. Then, the corresponding differential co-energy is integrated to calculate the co-energy at any rotor position, whose derivative with respect to rotor position gives the reluctance torque.

The finite element method is also employed in the field analysis and development of the proposed model. Field distribution, flux lines, and torque profiles are obtained and analyzed. The actuator is also prototyped. Finally, it is shown that there is close agreement among the results obtained from the analytical model, FEM in the simplified geometry, FEM in the original geometry, and experimental results obtained from the prototype.

5.2. The Actuator and The Proposed Model

5.2.1 The Actuator

The geometry and the exploded view of the actuator are shown in Figure 5.1. The specifications are also listed in Table 5.1. For this study, the length of the magnet is shorter than the one used in the previous chapter and the one used in the dynamic studies. It is a two-pole machine. The stator has two coils that are in series, and each of them includes half of the total number of turns. The rotor PM has diametral magnetization. The magnetic field developed by the stator current interacts with the PM to produce a torque which will be obtained by Lorentz force. Changing the direction of stator current results in back and forth rotation of the rotor. The stator inner surface has an elliptical shape to create a reluctance difference seen by the PM to develop a reluctance torque to bring the rotor back to the maximum torque per ampere position. Also, there are two auxiliary slots in the pole faces to aid in rotor restoration to maximum torque per ampere position by suppressing hysteresis effects in the stator laminations.

The total developed torque of the actuator is constituted from the coil torque, which is the interaction of the field produced by the stator current with the PM, and the restoration torque, which is a reluctance torque developed from the interaction of the PM with the variable reluctance of the air-gap. The total torque is a function of stator current and rotor position as in below:

$$T_t(\beta, i_c) = T_{coil}(\beta, i_c) + T_{res}(\beta) \tag{5.1}$$

The coil torque is obtained by solving Laplace's equation in simplified geometry of the stator in the elliptical coordinates, and the restoration torque is derived by differential flux tubes.

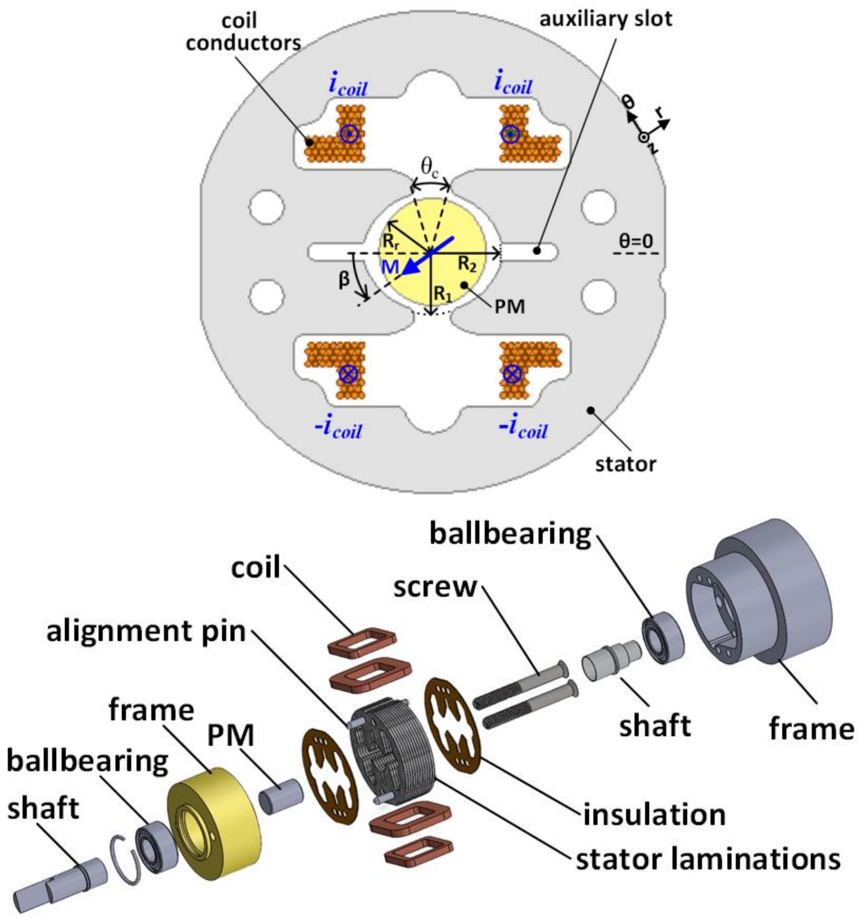

Figure 5. 1. Geometry (top) and exploded view (bottom) of the actuator.

Table 5. 1 Specifications of the Studied Motor

parameter	Value
stator outer diameter D_o	13.716 mm
stack length L	4.191 mm
outer diameter of rotor $D_r=2R_r$	3.048 mm
minor radius of elliptical surface of stator R_1	1.71 mm
major radius of elliptical surface of stator R_2	1.9665 mm
PM remnant flux B_r	1.37 Tesla
total number of turns, N	100
wire gauge	AWG33
interpolar angle θ_c	38 degrees
fringing angle θ_f	50 degrees

5.2.2 Equivalent Geometry of Stator in Elliptical Coordinates

The solution of Laplace's equation cannot straightforwardly be obtained for the complicated geometry of the stator where the boundary conditions cannot easily be applied. As shown in Figure 5.2, in the proposed model, the stator is simplified into a hollow ellipse whose semi-major and semi-minor axes are R_2 and R_1. The two foci F_1 and F_2 are also located at ($\pm c$, 0). The ellipse is represented in Cartesian coordinates as in below:

$$x^2 / R_2^{\,2} + y^2 / R_1^{\,2} = 1;\; c = \sqrt{R_2^{\,2} - R_1^{\,2}} \tag{5.2}$$

The advantage of the simplified geometry is that the boundaries of Laplace's equation can be easily applied in elliptical coordinates (η, ψ, z). However, the main challenges are how to form the boundary conditions and how to reproduce the stator coils in the new geometry. As shown in Figure 5.2, the stator coils are represented as equivalent surface current densities $K_c=\pm K_{cm}$ with an angular span of θ_c on the boundary of the ellipse where the interpolar region is located in the original geometry. It will be shown that this new boundary produces the same field distribution in the region inside the ellipse with very good accuracy.

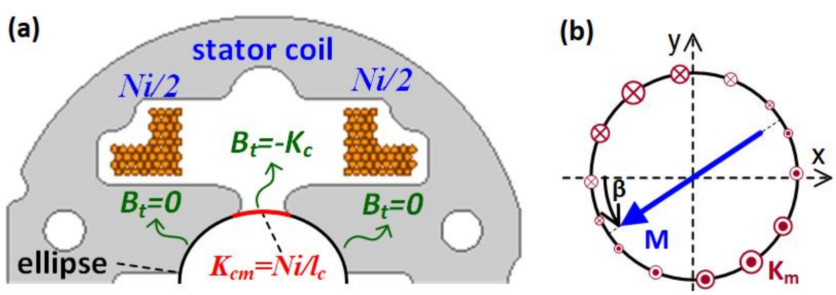

Figure 5. 2. An ellipse as an equivalent geometry for the stator curvature and a surface current density K_c in the interpolar region as an equivalent for the coils.

Figure 5.3 shows the new geometry in the elliptical coordinates (η,ψ,z) whose relationship with cartesian coordinates (x,y,z) is $x + \mathrm{j}\,y = c\cosh(\eta + \mathrm{j}\,\psi)$ in the complex plane and. Deriving real and imaginary parts leads to:

$$\begin{cases} x = c\ \cosh\eta\cos\psi \\ y = c\ \sinh\eta\sin\psi\ ; \quad \eta\in[0,+\infty],\ \psi\in[0,2\pi] \\ z = z \end{cases} \tag{5.3}$$

where constant η gives elliptic cylinders and constant ψ gives hyperbolic cylinders, as shown in Figure 5.3 with the green lines. A line between the two foci is obtained by $\eta=0$. With the simplified geometry, the flux lines and the flux density vectors have the same behavior on the ellipse boundary, i.e., perpendicular to the iron surface (zero tangential component $B_\psi=0$) where the is no surface current, and non-perpendicular to the boundary on the interpolar region where there is a surface current density ($B_\psi=-K_c$). The small impact of auxiliary slots on the field distribution is also ignored.

The stator boundary can be represented as an ellipse $\eta=\eta_0$ where $\eta_0=tanh^{-1}(R_1/R_2)$ which is obtained from $R_1 = c\sinh\eta_0$ divided by $R_2 = c\cosh\eta_0$.

Now, the interpolar region angular span θ_c in the cylindrical coordinates need to be translated into ψ_c in elliptical coordinates. According to point $A(x_c,y_c)$ in Figure 5.3, the angular span in the cylindrical coordinates can be obtained $\mathrm{x}_c / y_c = \tan(\theta_c/2)$. Also, dividing the two equations (3) at the point A results in $\mathrm{x}_c / y_c = \coth\eta_0 \cot(\mathrm{pi}/2-\psi_c/2)$. Mathematical manipulations result in:

$$\psi_c = 2\tan^{-1}\left(\frac{\tan(\theta_c/2)}{\coth\eta_0}\right) \tag{5.4}$$

The equivalent current density of the stator coils K_c, assumed to be uniformly distributed, is the total current Nic over the length lc in the interpolar region is obtained as:

$$K_c = Ni_c / l_c \tag{5.5}$$

The length l_c is obtained by integrating over the differential length $dl=h_t\, d\psi$ where ht is the scale factor given in the appendix. The length lc is obtained as in below:

$$l_c = \int_{pi/2-\psi_c/2}^{pi/2+\psi_c/2} h_t d\psi = \int_{pi/2-\psi_c/2}^{pi/2+\psi_c/2} c\sqrt{\cosh^2\eta_0 - \cos^2\psi}\, d\psi \tag{5.6}$$

It could also be determined in cartesian coordinates but with much more calculations.

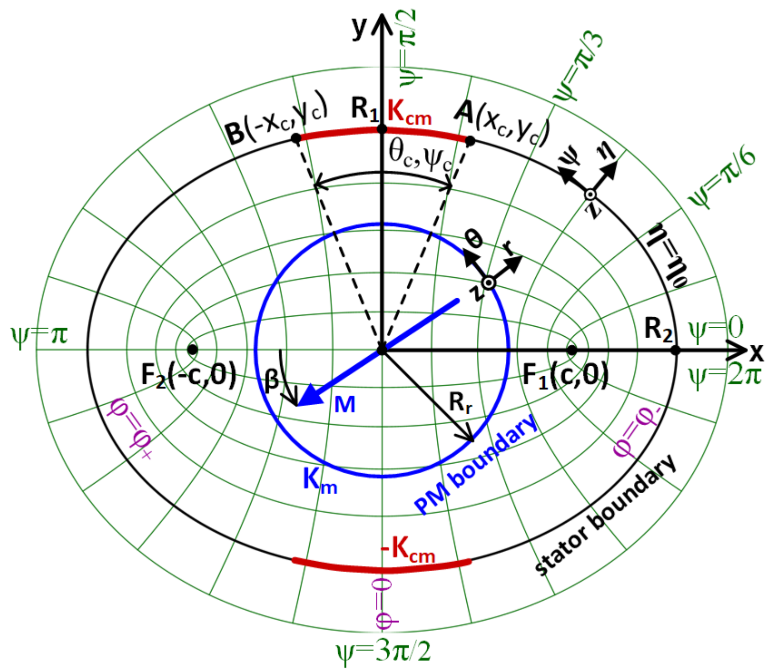

Figure 5. 3. Simplified geometry of the actuator in elliptical coordinates.

5.2.3 Amperian Current Representation of PM in Cylindrical Coordinates

As the PM has a circular shape, it is easier to be modeled in cylindrical coordinates (*r*, *θ, z*). The magnetization vector *M* in the PM region in terms of azimuth *θ* and rotor angular position β can be represented as in below:

$$\vec{M}(\theta,\beta) = -M\cos(\theta-\beta)\ \hat{r} + M\sin(\theta-\beta)\ \hat{\theta};\ r \le R_r \tag{5.7}$$

Having the residual flux density B_r, magnetization is obtained as $M=B_r/\mu_0$. A magnetization vector can be represented as Amperian current density J_m, and since the magnetization is uniform inside the PM, there is only a surface current density Km on the surface of the rotor as in below:

$$\vec{J}_m = \nabla \times \vec{M}; \quad \vec{K}_m = \vec{M} \times \hat{n} \tag{5.8}$$

where n=r is the unit vector normal to the surface of the rotor. By substituting the magnetization M in (7), Km on the surface of the PM is obtained as in below:

$$\vec{K}_m(\theta,\beta) = \vec{M} \times \hat{r} = -M\sin(\theta-\beta)\ \hat{z};\ r = R_r \tag{5.9}$$

As shown in Figure 5.2(b), it is also seen that the Amperian currents are in the z-direction because the magnetization vector is always in the rφ-plane.

5.3. Coil Torque

To obtain the coil torque using the Lorentz force, the flux density distribution produced by stator current on the surface of the rotor, where the Amperian currents exist, is obtained through the solution of Laplace's equation in elliptical coordinates.

5.3.1 Laplace's Equations in Elliptical Coordinates

As inside the ellipse is a current free region and the surface currents can be employed as boundary condition of flux density B or field intensity H, the Ampere' law can be reduced as:

$$\nabla \times H = J \xrightarrow{J=0} \nabla \times H = 0 \tag{5.10}$$

As the curl of gradient of a scalar field is zero, a magnetic scalar potential can be defined as in below:

$$H = -\nabla\varphi \tag{5.11}$$

By employing the identity $\nabla.\nabla\varphi = \nabla^2\varphi$ in the magnetic Gausses' law results in the Laplacian equation below:

$$\nabla.B = 0 \xrightarrow{B=\mu_0 H} \nabla.\mu_0(-\nabla\varphi) = 0 \ \rightarrow\ \nabla^2\varphi = 0 \tag{5.12}$$

Laplace's equation in elliptical coordinates is [20]:

$$\nabla^2\varphi(\eta,\psi) = \frac{1}{c^2\cosh^2\eta - \cos^2\psi}\left(\frac{\partial^2\varphi}{\partial\eta^2} + \frac{\partial^2\varphi}{\partial\psi^2}\right) = 0 \tag{5.13}$$

Employing the separation of variables $\varphi(\eta,\psi) = \Gamma(\eta)\Psi(\psi)$ leads to the following relationships:

$$\frac{1}{\Gamma(\eta)}\frac{d^2\Gamma(\eta)}{d\eta^2} = -\frac{1}{\Psi(\psi)}\frac{d^2\Psi(\psi)}{d\psi^2} = p^2 \tag{5.14}$$

This equation can be satisfied independent of η and ψ if they are constant and equal to a separation constant p^2 where p is usually the number of pole pairs of the electric machine (here $p=1$). Then, this PDE is reduced to two ODEs as in below:

$$\Gamma'' - p^2\Gamma = 0, \quad \Psi'' + p^2\Psi = 0 \tag{5.15}$$

For $p\neq 0$, as Ψ must be periodic in ψ, the solutions of $\Psi(\psi)$ are the followings sets:

$$e^{jp\psi},\ e^{-jp\psi} \quad or \quad \sin(\mathrm{p}\psi),\ \cos(\mathrm{p}\psi) \tag{5.16}$$

The exponential ones are helpful for problems with infinite half-space. Also, the solutions of $\Gamma(\eta)$ are as in below:

$$e^{p\eta},\ e^{-p\eta} \quad or \quad \sinh(\mathrm{p}\eta),\ \cosh(\mathrm{p}\eta) \tag{5.17}$$

For $p=0$, the solution for uniform fields is as follows:

$$\Gamma_0(\eta) = \mathrm{a}_0 + \mathrm{b}_0\eta, \quad \Psi_0(\psi) = 1 \tag{5.18}$$

However, it is not the solution to the problem as it is not periodic in ψ. It is shown in [21]-[23] that, due to the Green's function of the potential, the solution of Laplace's equation in elliptical coordinates is comprised of either odd or even functions as in below:

$$\sinh(\mathrm{p}\eta)\sin(\mathrm{p}\psi), \quad \cosh(\mathrm{p}\eta)\cos(\mathrm{p}\psi); \ \ \mathrm{p} = 1,2,3... \tag{5.19}$$

In other words, odd functions come together, and even functions come together as well. The flux lines originate from the positive potentials at the left side of the ellipse (centered at $\psi=\pi$) and end in the negative equipotential line at the right side of the ellipse (centered at $\psi=0$), showing an even function $\varphi(\eta,\psi)$. As the potential is an even function of ψ, the second term in (5.19) is picked and thus $\varphi_n=A_n \cosh(np\eta) \cos(np\psi)$ where $p=1$. Finally, the general solution of $\varphi_n(\eta,\psi)$ can be written as:

$$\varphi(\eta,\psi) = \sum_{n=1}^{+\infty} \mathrm{A}_n \cosh(\mathrm{n}\,\eta)\cos(\mathrm{n}\,\psi) \tag{5.20}$$

5.3.2. Boundary Conditions and the Solution

At the ellipse boundary ($\eta=\eta_0$), the boundary condition for the solution of the vector field H can be obtained as in below:

$$\hat{\eta}\times(\vec{H}_{iron}-\vec{H}_{air}) = K_c \Rightarrow H_{\psi,iron} - H_{\psi} = K_c \tag{5.21}$$

As the field intensity H_ψ,iron inside infinitely permeable iron is zero, the tangential component of the field intensity inside the ellipse at the boundary is obtained as

$$H_\psi(\eta_0,\psi) = -K_c(\psi) \tag{5.22}$$

In Figure 5.4, the flux lines and the distribution of K_c and H_ψ on the boundary of the stator ellipse are shown.

$$K_c(\psi) = \begin{cases} +K_{cm}\,; & \pi/2-\psi_c/2 < \psi < \pi/2-\psi_c/2 \\ -K_{cm}\,; & -\pi/2-\psi_c/2 < \psi < -\pi/2-\psi_c/2 \\ 0\,; & o.w. \end{cases} \tag{5.23}$$

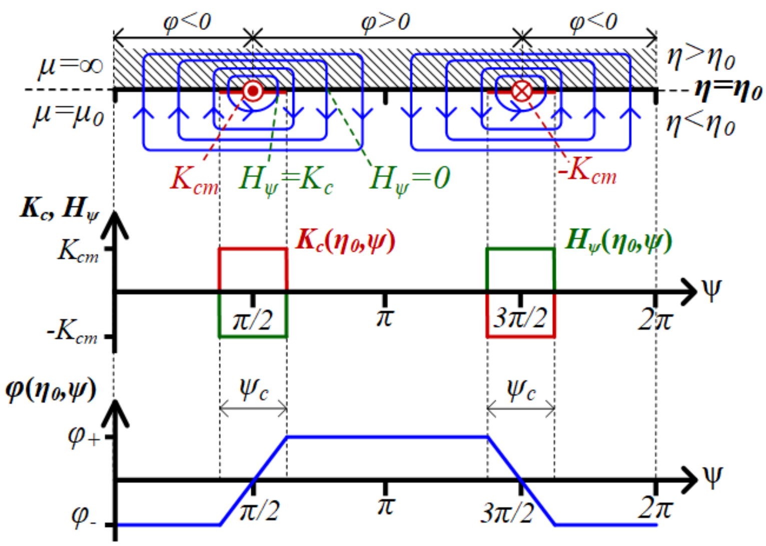

Figure 5. 4. Flux lines as well as surface current density K, tangential field intensity H_ψ and scalar potential φ on the surface of ellipse $\eta=\eta_0$.

The field intensity H can be obtained as:

$$\vec{H} = H_\eta \hat{\eta} + H_\psi \hat{\psi} = -\nabla\varphi = -\frac{1}{h_t}\left(\frac{\partial\varphi}{\partial\eta}\hat{\eta} + \frac{\partial\varphi}{\partial\psi}\hat{\psi}\right) \tag{5.24}$$

Thus, the normal and tangential components H_η and H_ψ are obtained as in the following:

$$H_\eta = \frac{-1}{c\sqrt{\cosh^2\eta - \cos^2\psi}} \sum_{n=1}^{+\infty} n\,\mathrm{A}_n \sinh(\mathrm{n}\,\eta)\cos(\mathrm{n}\,\psi) \tag{5.25}$$

$$H_\psi = \frac{1}{c\sqrt{\cosh^2\eta - \cos^2\psi}} \sum_{n=1}^{+\infty} n\,\mathrm{A}_n \cosh(\mathrm{n}\,\eta)\sin(\mathrm{n}\,\psi) \tag{5.26}$$

From the boundary condition (21), the following equality is obtained.

$$\frac{1}{c\sqrt{\cosh^2\eta_0 - \cos^2\psi}} \sum_{n=1}^{+\infty} n\,\mathrm{A}_n \cosh(\mathrm{n}\,\eta_0)\sin(\mathrm{n}\,\psi) = -K_c(\psi) \tag{5.27}$$

It is worth noting that a big mistake would be trying to calculate the coefficients An based on the Fourier series expansion of -$K_c(\psi)$ because the coefficient of $sin(n\psi)$ in the left side should not be a function of ψ; any coefficient of $sin(n\psi)$ which is a function of ψ

should be taken to the right side before finding the Fourier series coefficients. Taking $c\sqrt{\cosh^2\eta_0 - \cos^2\psi}$ to the right side, the following Fourier series expansion is obtained:

$$-c\sqrt{\cosh^2\eta_0 - \cos^2\psi}\,K_c(\psi) = \sum_{n=1}^{+\infty} a_n \sin n\psi \tag{5.28}$$

whose Fourier coefficients are obtained as in below:

$$a_n = \frac{2}{\pi}\int_0^{\pi} -c\sqrt{\cosh^2\eta_0 - \cos^2\psi}\; K_c(\psi)\sin n\psi\,\mathrm{d}\psi \tag{5.29}$$

As $n\,\mathrm{A}_n\cosh(\mathrm{n}\,\eta_0) = a_n$, the coefficients An are obtained as:

$$A_n = \frac{-2cK_{cm}}{n\pi\cosh(\mathrm{n}\,\eta_0)}\int\limits_{\pi/2-\psi_c/2}^{\pi/2+\psi_c/2}\sqrt{\cosh^2\eta_0 - \cos^2\psi}\,\sin n\psi\,\mathrm{d}\psi \tag{5.30}$$

It can easily be obtained by numerical integration. Having the tangential component $H_\psi(\eta_0,\psi)$ at the ellipse $\eta=\eta_0$, the scalar potential $\varphi(\eta_0,\psi)$ can be obtained by integration as follows:

$$\begin{gathered} H_\psi(\eta_0,\psi) = \frac{-1}{h_t(\eta_0,\psi)}\frac{\partial\varphi}{\partial\psi} \Rightarrow \\ \varphi(\eta_0,\psi) = -\int\limits_{\psi_0}^{\psi} h_t(\eta_0,\psi)H_\psi(\eta_0,\psi)\,\mathrm{d}\psi + \varphi_0(\psi_0) \end{gathered} \tag{5.31}$$

For simplicity, the initial point can be taken at the middle of the surface current density where the potential is zero, i.e., $\varphi_0(\psi_0=\pi/2)=0$. As shown in Figure 5.4, it is also seen that the flux lines originate on positive potentials and terminate on negative potentials. The field direction can also be observed by the right-hand rule. The relationship (5.31) is very useful for obtaining the scalar potential from magnetic flux density vector B obtained from FEM to be compared to analytical results (Figure 5.5).

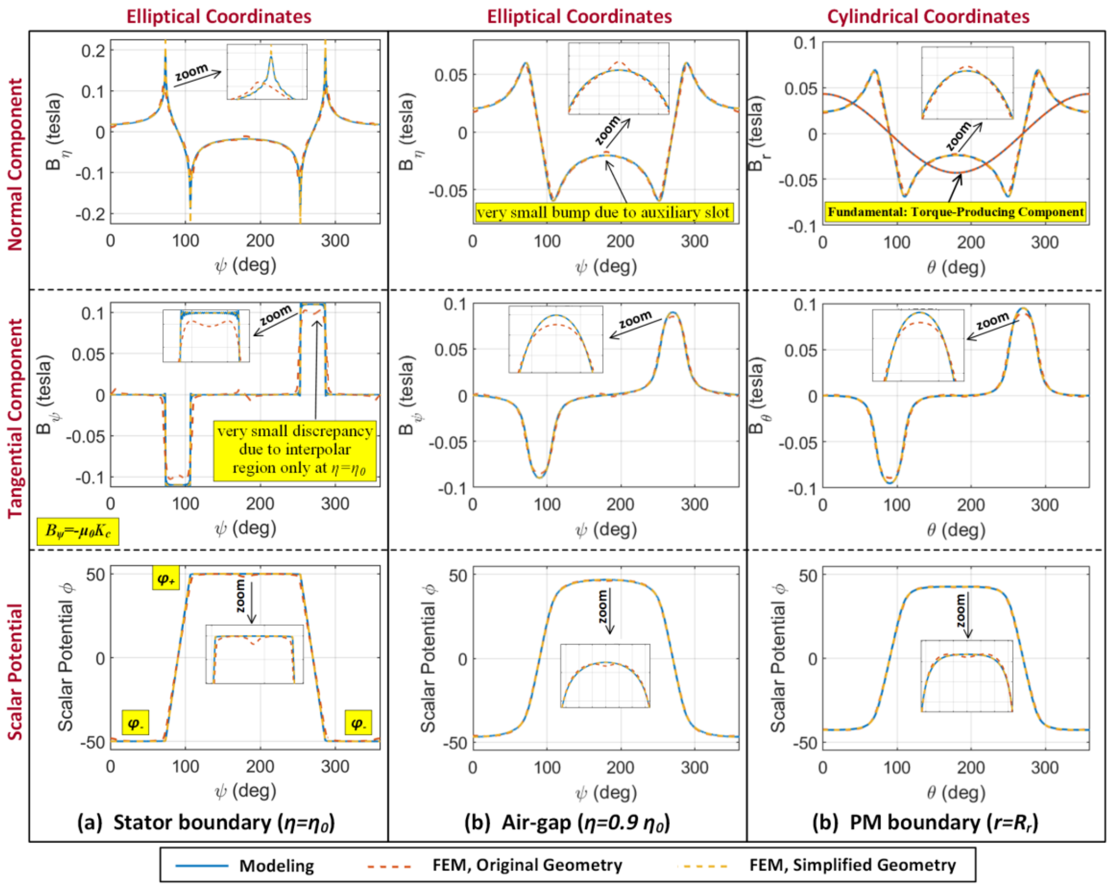

Figure 5. 5. Normal and tangential components of magnetic flux density distribution as well as the scalar magnetic potential (a) on the stator boundary, i.e. ellipse $\eta=\eta_0$, (b) in the air-gap, i.e. ellipse $\eta=0.9\ \eta_0$, and (c) on PM boundary, i.e. circle $r=R_r$.

As given in the Appendix, instead of the magnetic scalar potential, field solutions can be obtained using Laplace's equation in terms of the z-component of magnetic vector potential A_z. Unlike the scalar potential φ, A_z must have a sine behavior, so the general solution of $A_z(\eta,\psi)$ can be written as:

$$A_z(\eta,\psi) = \sum_{n=1}^{+\infty} D_n \cosh(n\,\eta)\cos(n\,\psi) \tag{5.32}$$

The relationship between the coefficients A_n and D_n is as:

$$D_n = -\mu_0 A_n \tag{5.33}$$

5.3.3. Torque Calculation by Lorentz Force

To calculate the developed torque, the radial component of magnetic flux density distribution B_r on the surface of the PM is required. The circle $r=R_r$ is represented as:

$$x = R_r \cos\theta,\ \ y = R_r \sin\theta\ ; \qquad 0 < \theta < 2\pi \tag{5.34}$$

This trajectory can be translated into elliptical coordinates as:

$$\eta = \mathrm{Re}\left\{\cosh^{-1}\left(\frac{x+\mathrm{j}\,y}{c}\right)\right\} \tag{5.35}$$

$$\psi = \mathrm{Im}\left\{\cosh^{-1}\left(\frac{x+\mathrm{j}\,y}{c}\right)\right\} \tag{5.36}$$

After obtaining the vector fields (B_η, B_ψ) on the circle $r=R_r$, it can be converted into cartesian coordinates as in below:

$$B_x + jB_y = \frac{h_t(\eta,\psi)}{c\sinh(\eta+\mathrm{j}\psi)}(B_\eta + jB_\psi) \tag{5.37}$$

After obtaining B_x and B_y through real and imaginary parts, it can be converted to cylindrical coordinates as follows:

$$\begin{bmatrix} B_r \\ B_\theta \end{bmatrix} = \begin{bmatrix} \cos\theta & \sin\theta \\ -\sin\theta & \cos\theta \end{bmatrix} \begin{bmatrix} B_x \\ B_y \end{bmatrix} \tag{5.38}$$

Having the radial component of the magnetic flux density B_r on the surface of the PM, the developed torque can be obtained by Lorentz force over the Amperian currents as:

$$T_{coil}(\beta,i_c) = L\int_0^{2\pi} R_r K_m(\theta,\beta)\, B_r(\theta)\, R_r\, d\theta \tag{5.39}$$

Since Km is a sinusoidal waveform, only the fundamental component of the magnetic flux density B_{r1} participates in the torque production.

$$B_{r1}(\theta,i_c) = B_1\cos\theta;\ \ B_1(i_c) = \frac{1}{\pi}\int_0^{2\pi} B_r(\theta,i_c)\cos\theta\, d\theta \tag{5.40}$$

By substituting for B_{r1} and K_m in (5.39) and expressing the trigonometric product in sums, the torque equation is obtained as in below:

$$T_{coil}(\beta, i_c) = R_r^2 L\pi\, B_1 M \sin\beta \tag{5.41}$$

where the torque constant, i.e., the maximum coil torque at a stator current of 1 A, is obtained as $k_t = R_r^2 L\pi\, B_1 M / i_c$.

5.3.4. Field Analysis

Figure 5.5 illustrates normal and tangential components of magnetic flux density distribution as well as scalar magnetic potential on the stator boundary (ellipse $\eta=\eta_0$), in the air-gap (ellipse $\eta=0.9\,\eta_0$) and on PM boundary (circle $r=R_r$). The results derived from the analytical model, FEM in the simplified geometry, and FEM in the original geometry, are compared. A great agreement is observed between the analytical and numerical results with a very small discrepancy. The analytical results from the model and those extracted from FEM in the simplified geometry exactly match with almost zero error. As shown in Figure 5.5(a), a small discrepancy is observed between the simplified geometry (analytical or FEM) and the original geometry on the stator surface ($\eta=\eta_0$) at the interpolar region, which makes sense as this section was the most challenging part of generating the equivalent geometry. The boundary condition $B_\psi=-K_c$ can also be observed on the stator surface ($\eta=\eta_0$). A very small bump is also observed at the auxiliary slots, as expected. As shown in Figure 5.5(c), very good accuracy is observed in the analytical results for the torque-producing component of the magnetic flux density, i.e., the radial component B_r.

It is worth noting that the employed FEM is based on the solution of the z-component of vector magnetic potential Az and only produces the normal and tangential components of the B or H. To obtain the FEM results for the magnetic scalar potential φ in the elliptical coordinates, the relationship (30) is used to numerically integrate over B_ψ. To obtain scalar magnetic potential in cylindrical coordinates $\varphi(r,\theta)$ from the tangential component B_θ, the relationship of a gradient in cylindrical coordinates is employed as follows:

$$H_\theta(R_r,\theta) = \frac{-1}{r}\frac{\partial\varphi}{\partial\theta} \Rightarrow \varphi(R_r,\theta) = -\int_{\theta_0}^{\theta} r\, H_\psi(R_r,\theta)\,\mathrm{d}\theta + \varphi_0(\theta_0) \tag{5.42}$$

where the initial point $\varphi_0(\theta_0=\pi/2)=0$ is taken for simplicity. As expected, the scalar magnetic potential is positive on the left side of the y-axis, zero on the y-axis, and negative on the right side of the y-axis. It is $\varphi_+=50$ on the left pole face of the stator and $\varphi_-=-50$ on the right pole face of the stator. At the interpolar region, where there is a surface current density, there is a transition between φ_+ and φ_- which is equal to the integration of the surface current density (or minus tangential component of field intensity) times the scale factor of the coordinate system.

Figure 5.6(a) shows flux density vectors B and scalar potentials contours φ obtained by the analytical model. It can be seen that the flux density vectors are perpendicular to the equipotential lines φ as expected from the gradient relationship (5.24). Also, the field vectors depart from the positive equipotential lines and end on the negative ones. It is also seen that flux density vectors and flux lines are perpendicular to the infinitely permeable iron where there is no surface current density. As shown in Figure 5.6(b) and Figure 5.6(c), the field distribution within the stator curvature obtained from the equivalent geometry is the same as the one extracted from the original geometry (inside dotted ellipse). It is how geometry simplification is useful by simplifying the field solution in the region where the field distribution is important to perform torque calculations.

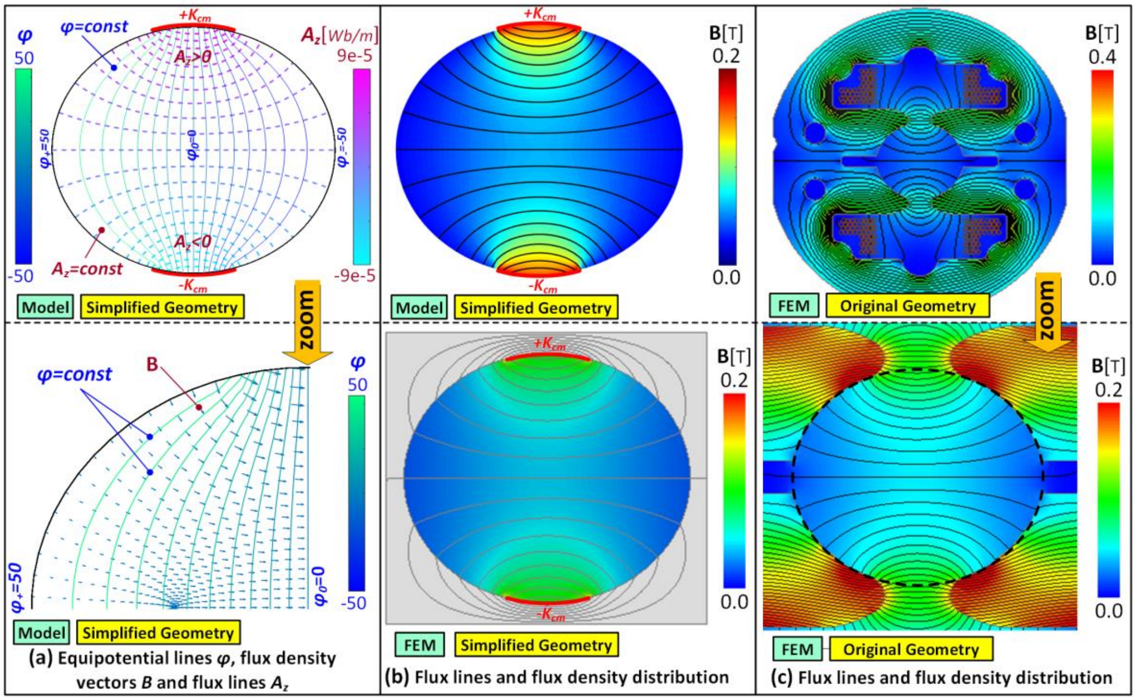

Figure 5. 6. Fields produced by stator current: (a) flux density vectors and scalar potentials contours obtained by model, (b) flux density distribution and flux lines in the simplified geometry obtained by the model and FEM, and (d) flux density distribution and flux lines within the original geometry obtained by FEM.

5.4. Reluctance Torque

The stator pole faces elliptically shaped such that the air-gap permeance seen by the PM varies by the rotation of the rotor, producing a reluctance torque that restores the rotor to the maximum torque per ampere position. It acts as a magnetic spring. Since the stator boundary is an ellipse and the PM boundary is a circle, neither elliptical coordinates nor cylindrical coordinates can be employed to solve Laplace's equation; thus flux tube method is employed to calculate the reluctance torque by energy method.

5.4.1. Differential Flux Tubes

Figure 5.7 presents magnetic flux density distribution and flux lines due to the PM in equivalent and original geometries at rotor positions of β=0 (M is aligned with major axis), β=45, and β=90 (M is aligned with minor axis). It can be observed that, within the PM, the flux lines are parallel to the magnetization. The flux lines deviate at the PM boundary due to the Amperian currents as $H_{1\theta}$-$H_{2\theta}$=K_m (counter-clockwise turn at positive currents and clockwise turn at negative currents). Also, the flux lines are perpendicular to the infinitely permeable boundary of the stator (H_θ=0). No energy is stored within the infinitely permeable iron. The flux within the PM and the air-gap lines are approximated with straight lines. In Figure 5.8, the Amperian currents and the flux lines employed in the modeling are illustrated at the same rotor angles of 0, 45, and 90 degrees. The air-gap flux tubes and the corresponding permeances of the air-gap and the PM are also shown.

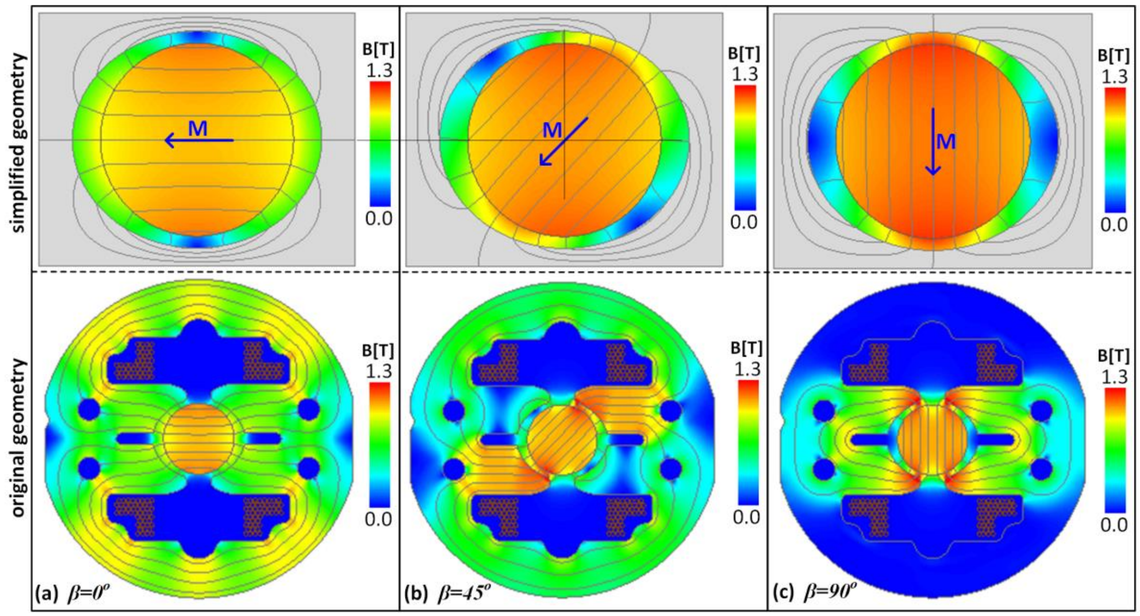

Figure 5. 7. Magnetic flux density and flux lines due to the PM in equivalent (top) and original (bottom) geometries at rotor positions of: (a) $\beta=0$ (M is aligned with major axis), (b) $\beta=45$ and $\beta=90$ (M is aligned with minor axis).

In the conventional MEC methods, to develop a lumped-element model, flux tubes are employed for different regions, and MMF sources are adopted for the regions having magnetization or current. The conventional flux tubes are not useful in our case as, according to the flux lines shown in Figure 5.8, the conventional flux tubes do not incorporate the variation of stored co-energy whose derivative with respect to β is the reluctance torque. Integrating the flux lines and Amperian currents of the PM gives permeance and an MMF for the PM. However, it can be seen that integrating over the flux lines within the air-gap leads to equal air-gap permeances if the PM magnetization is aligned with either the major axis or the minor axis. As shown in Figure 5.8, the lumped-element values of the permeances P_{g0} and P_{g90} are equal; visually describing, just relocate the bottom right part of P_{g90} to the top of its left part to obtain P_{g0}. In other words, this lumped MEC model does not reflect the rate of change of co-energy, which is the torque.

What is missing in this lumped model? It can be observed in Figure 5.8 that the total current enclosed in the closed path of Ampere's law for different flux loops is different, which is ignored in the lumped permeances in which it is integrated over flux lines. For example, looking at Figures 5.8(a) and (b) carefully, it can be observed that the currents enclosed in the flux loops with the shortest length in the air-gap are different for β=0 and β=90; this fact, which is missing in the lumped MEC model, makes a difference in the stored co-energy in the two cases, resulting in a reluctance torque. When the PM magnetization is aligned with the minor axis (β=90), the enclosed current and thus stored co-energy is larger; it can also be seen that the magnitude of the flux density distribution is relatively larger.

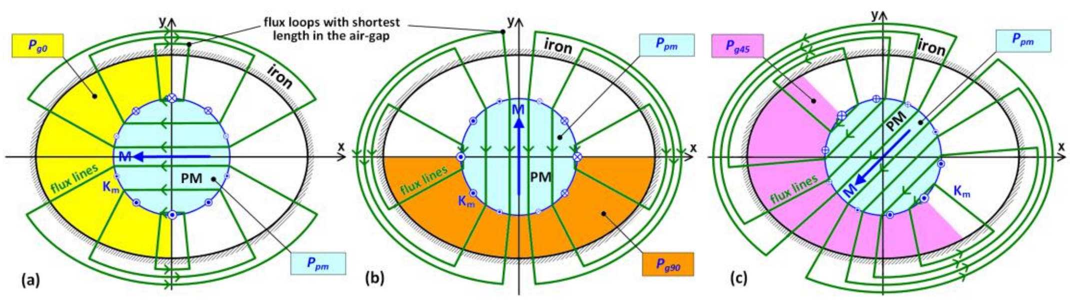

Figure 5. 8. Flux lines due to PMs at rotor positions of: (a) $\beta=0$ (M is aligned with major axis), (b) $\beta=45$ and (c) $\beta=90$ (M is aligned with major axis).

In Figure 5.9, a differential flux tube having a differential thickness d_{yr}, i.e. a differential area $L\ d_{yr}$, enclosing a current as a function of y^r is depicted. Its total length is $l(y^r)$. Two strategies can be taken here:

In the conventional flux tubes, integrating over y^r from 0 to R_r gives a lumped permeance to be employed in a lumped-element MEC to obtain the co-energy, multiplied by 2 for the other half, gives the total co-energy at the rotor angle β. It was explained that it does not reflect the reluctance torque as this lumped permeance is the same for β=0 degrees and β=90 degrees.

With a strategy that we would name differential flux tubes (DFT), differential permeance is employed in further analysis, and it is not integrated over y^r to get a lumped permeance. This differential flux tube encloses a total current which is a function of y^r. Next, the differential co-energy associated with this differential permeance is calculated as a function of y^r. Afterward, integrating this differential co-energy with respect to y^r from 0 to R_r, multiplied by 2 for the other half, gives the total co-energy at the rotor angle β. Contrary to the conventional method, the DFT-based approach makes a difference between the two cases of β=0 or β=90 degrees as it understands that the total currents enclosed in the flux loops with the shortest length in the air-gap are different for β=0 and β=90 (refer to Figures 8(a) and (b)). The whole process can be performed over a rotor rotation to obtain the stored co-energy W_c as a function of β. Finally, the reluctance torque can be determined as the derivative of the co-energy with respect to β.

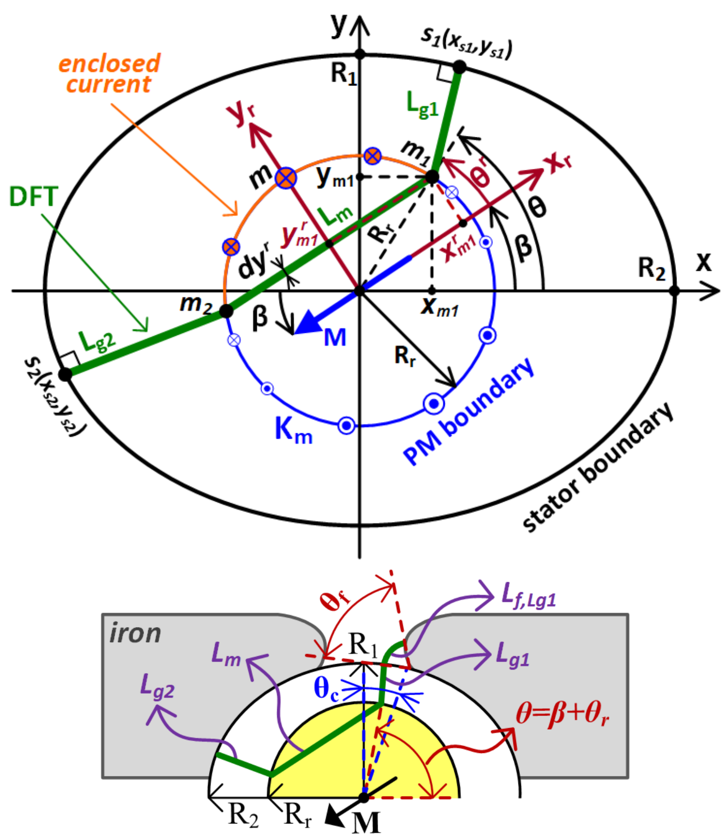

Figure 5. 9. Differential flux tubes to calculate reluctance torque: (a) within the ellipse boundary and (b) including fringing length at the interpolar regions.

5.4.2. Rotor Reference Frame

To simplify calculations, a rotating reference frame $\{(x^r, y^r); (r,\theta_r)\}$ on the rotor is used, as shown in Figure 5.9. The axis x^r is set parallel to the magnetization vector M, and thus the perpendicular axis y^r is the integration variable for the DFTs. The rotation angle of the rotating frame with respect to the stationary frame $\{(x, y), (r,\theta)\}$ is β and thus $\theta = \beta + \theta^r$. The following relationships are obtained for any point on the PM boundary:

$$\begin{cases} x = R_r \cos\theta = R_r \cos(\beta + \theta^r) \\ y = R_r \sin\theta = R_r \sin(\beta + \theta^r) \end{cases}; \begin{cases} x^r = R_r \cos\theta^r \\ y^r = R_r \sin\theta^r \end{cases} \tag{5.43}$$

By converting the sine and cosine of $\beta+\theta_r$ to products, the transformation matrix between the two frames is obtained as:

$$\begin{bmatrix} x \\ y \end{bmatrix} = \begin{bmatrix} \cos\beta & -\sin\beta \\ \sin\beta & \cos\beta \end{bmatrix} \begin{bmatrix} x^r \\ y^r \end{bmatrix} \tag{5.44}$$

5.4.3. Current Enclosed by the Differential Flux Tubes

In the rotor reference frame, the Amperian current density (5.9) is independent of rotor rotation β and can be simplified to:

$$K_m(\theta^r) = -M \sin\theta^r \tag{5.45}$$

Then, the total magnetomotive force F_m associated with the DFT at y^r or θ_r is obtained by the total current enclosed in the closed path of the Ampere's law obtained as in below:

$$F_m(\theta^r) = \int_{\theta^r}^{\pi-\theta^r} |K_m(\theta^r)| R_r d\theta^r = 2R_r M \cos\theta^r \tag{5.46}$$

It can be written as a function of y^r as in below:

$$F_m(\theta^r) = 2M\sqrt{R_r^{\,2} - (y^r)^2} \tag{5.47}$$

5.4.4. Differential Permeance, Differential Co-energy, and Reluctance Torque

The co-energy associated with a differential permeance $d\wp$ is:

$$d\wp = \mu_0 L\, dy^r \,/\, l(y^r) \tag{5.48}$$

The differential energy associated with the DFT is:

$$dW_c = \frac{1}{2} F_m^2(y^r)\, d\wp = \frac{1}{2} \mu_0 L \frac{F_m^2(y^r)}{l(y^r)} dy^r \tag{5.49}$$

where $l(y^r)$ is the total length of the flux tube within the PM and air-gap regions. By substituting F_m and $d\wp$, and integrating over y^r from 0 to R_r, the total co-energy stored in the system (i_{coil}=0) at any rotor angle β is obtained as in below:

$$W_{c,tot}(\beta) = 2 \int_{W_c(y^r=0)}^{W_c(y^r=R_r)} dW_c = 2\int_0^{R_r} \frac{1}{2} \mu_0 L \frac{F_m^2(y^r)}{l(y^r)} dy^r \tag{5.50}$$

Then, the developed restoration torque is obtained as follows:

$$T_{rest} = \frac{\partial W_{c,tot}(\beta)}{\partial \beta} = \frac{1}{2} F_m{}^2 \frac{\partial \wp(\beta)}{\partial \beta} \tag{5.51}$$

Its frequency is double the frequency of the coil torque as the PM faces the stator saliency twice per revolution. It is simplified to the fundamental component as in below:

$$T_{rest} = T_1 \sin 2\beta; \;\; T_1 = \frac{2}{\pi} \int_0^{\pi} T_{rest}(\beta) \sin 2\beta \, d\beta \tag{5.52}$$

5.4.5. Length of the Differential Flux Tubes

The total length of the flux tube $l(y^r)$ needs to be calculated as a function of y^r as in the following:

$$l(y^r) = (L_{g1} + L_{f,\mathrm{Lg1}}) + L_m + (L_{g2} + L_{f,\mathrm{Lg2}}) \tag{5.53}$$

where L_m is the length within the magnet, L_{g1} and L_{g2} are the lengths within the air-gap, and $L_{f,Lg1}$ and $L_{f,Lg2}$ are the lengths due to the fringing effect at the interpolar regions.

The length of the line L_m inside the PM, which is between the points m_1 and m_2 is obtained as below:

$$L_m(y^r) = 2x^r = 2R_r \cos\theta^r = 2\sqrt{R_r^{\,2} - (y^r)^2} \tag{5.54}$$

Obtaining the coordinates of the point pairs m_1-s_1 and m_2-s_2 in the stationary frame, the lengths L_{g1} and L_{g2} in the air-gap can be obtained as:

$$L_{g1} = \sqrt{\left(x_{m1} - x_{s1}\right)^2 + \left(y_{m1} - y_{s1}\right)^2} \tag{5.55}$$

$$L_{g2} = \sqrt{\left(x_{m2} - x_{s2}\right)^2 + \left(y_{m2} - y_{s2}\right)^2} \tag{5.56}$$

However, these lengths are required to be obtained in terms of y^r to be employed in co-energy calculations (5.50). The point $m_1(x_{m1},y_{m1})$ in which $\theta^r_{m1} = \theta^r$ and $\theta_{m1} = \beta + \theta^r$ is obtained in the stationary and rotor reference frames as:

$$m_1 : \begin{cases} x_{m1} = R_r \cos(\beta + \theta^r) \\ y_{m1} = R_r \sin(\beta + \theta^r) \end{cases}; \quad m_1^r : \begin{cases} x^r_{m1} = R_r \cos\theta^r \\ y^r_{m1} = R_r \sin\theta^r \end{cases} \tag{5.57}$$

The point $m_2(x_{m2}, y_{m2})$ where $\theta^r_{m2} = \pi - \theta^r$ and $\theta_{m2} = \beta + \pi - \theta^r$ is obtained in the stationary and rotor reference is as follows:

$$m_2 : \begin{cases} x_{m2} = -R_r \cos(\beta - \theta^r) \\ y_{m2} = -R_r \sin(\beta - \theta^r) \end{cases}; \quad m_2^r : \begin{cases} x^r_{m2} = -R_r \cos\theta^r \\ y^r_{m2} = R_r \sin\theta^r \end{cases} \tag{5.58}$$

The points s_1 and s_2 are the intersections of the ellipse with the lines L_{g1} and L_{g2}, which are determined based on the fact that the flux lines are perpendicular to the infinitely permeable boundary of the ellipse. The normal vector to the ellipse is the gradient of the ellipse trajectory as in below:

$$\hat{n} = \nabla f = \frac{2x}{R_2^2}\hat{x} + \frac{2y}{R_1^2}\hat{y}; \quad f = \frac{x^2}{R_2^2} + \frac{y^2}{R_1^2} - 1 \tag{5.59}$$

Thus, the slope of the perpendicular line at point (x,y) is as:

$$m = \frac{n_y}{n_x} = \frac{R_2^2}{R_1^2}\frac{y}{x} \tag{5.60}$$

Having the slop and the two points $m_1(x_{m1},y_{m1})$ and $s_1(x_{s1},y_{s2})$, line L_{g1} is obtained as:

$$y_{s1} - y_{m1} = \frac{R_2^2}{R_1^2}\frac{y_{s1}}{x_{s1}}(x_{s1} - x_{m1}) \tag{5.61}$$

By writing y_{s1} in terms of x_{s1}, and substituting it into the ellipse equation $x_{s1}^2 / R_2^2 + y_{s1}^2 / R_1^2 = 1$, the following polynomial is achieved.

$$a_4 x_{s1}^4 + a_3 x_{s1}^3 + a_2 x_{s1}^2 + a_1 x_{s1} + a_0 = 0 \tag{5.62}$$

whose coefficients a_0 to a_4 are given in the Appendix. Two of the four roots of the above polynomial are complex conjugate which is not the solution. One of the two remaining roots is positive, and the other one is negative, one of which should be picked based on the sign of x_{m1}, i.e., if $x_{m1}>0$, then $x_{s1}>0$, and if $x_{m1}<0$, then $x_{s1}<0$. Afterward, y_{s1} is obtained as in below:

$$y_{s1} = \pm R_1 \sqrt{1 - x_{s1}^2 / R_2^2} \tag{5.63}$$

The sign of ys1 is picked based on the sign of y_{m1}, i.e. if $y_{m1}>0$, then $y_{s1}>0$, and if $y_{m1}<0$, then $y_{s1}<0$. The general rule is that s_1 is in the same quadrant as m_1. The same procedure is taken to obtain the line L_{g2} and its intersection with the ellipse, i.e., point $s_2(x_{s2},y_{s2})$.

5.4.6. The Fringing Lengths in the Interpolar Regions

As observed in Figure 5.7, in the original geometry, the flux produced by the PM includes a fringing effect in the interpolar region which is not is incorporated in the equivalent elliptical geometry. It was negligible in the derivation of the stator field and the coil torque, but it needs to be accounted for in the calculation of the PM flux and the reluctance torque a reach higher accuracy. As shown in Figure 5.9, the fringing length L_f is model as a circular arc with a fringing angle θ_f if the point is in the interpolar region; otherwise, L_f is zero. We have:

$$L_f(\theta)=\begin{cases} R_1\theta_f\times\left|\theta_c/2-|\theta-\pi/2|\right| \;;\; |\theta-\pi/2|<\theta_c/2 \\ R_1\theta_f\times\left|\theta_c/2-|\theta-3\pi/2|\right|;\; |\theta-3\pi/2|<\theta_c/2 \\ 0;\; o.w. \end{cases} \tag{5.64}$$

in which θ is substituted with θ_{m1} for $L_{f,Lg1}$, and θ_{m2} for $L_{f,Lg2}$. Also, θ_{m1} and θ_{m2} can be obtained in terms of y^r.

5.5. Experimental Study and The Results

The actuator is prototyped whose experimental results are compared with those obtained from the analytical model and FEM. Figure 5.10 shows the component of the prototyped actuator and the torque-angle measurement setup. Figure 5.11 presents the coil torque, the restoration torque, and the total toque extracted from the model, FEM, and experiment. It can be seen that there is a close agreement among the analytical, numerical, and experimental results. It is observed that the frequency of the reluctance torque is twice the coil torque, and the equilibrium point of the restoration torque is at the maximum torque per ampere position, i.e., β=90 degrees. In other words, the reluctance torque acts as a magnetic spring that restores the rotor to the maximum torque per ampere position. The meshed models used for FEM are given in Figure 5.12 and Figure 5.13.

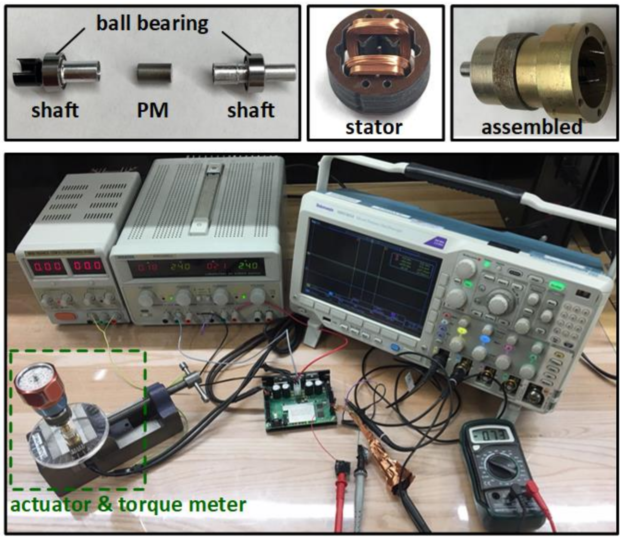

Figure 5. 10. The prototype (top), and torque-angle measurement setup (bottom).

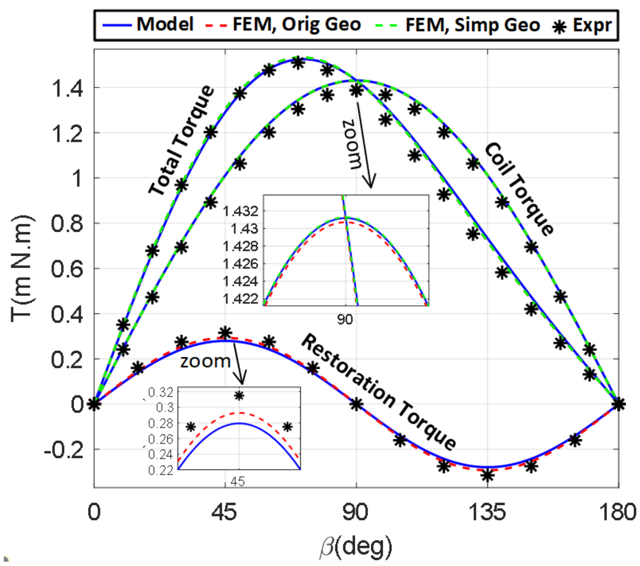

Figure 5. 11. Restoration, coil and total torque profiles obtained by model, FEM in the original geometry, FEM in the simplified geometry and experiment.

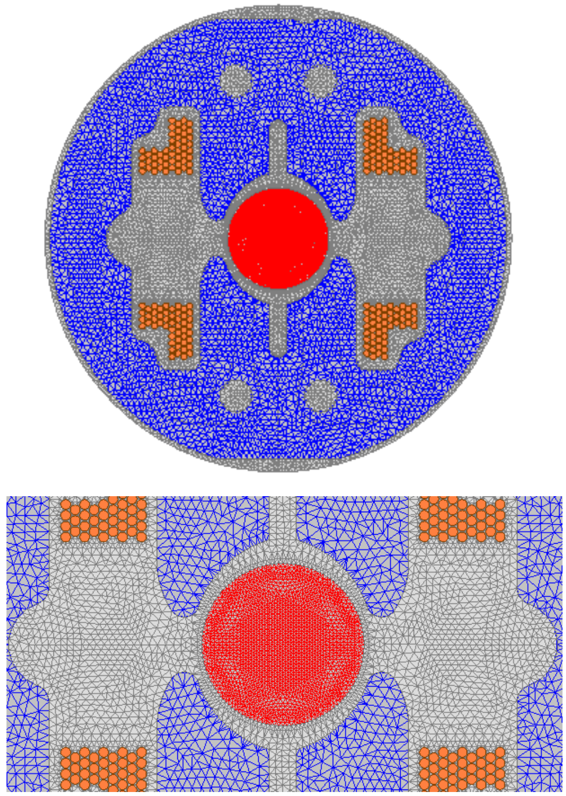

Figure 5. 12. Meshed models for original geometry used for FEM.

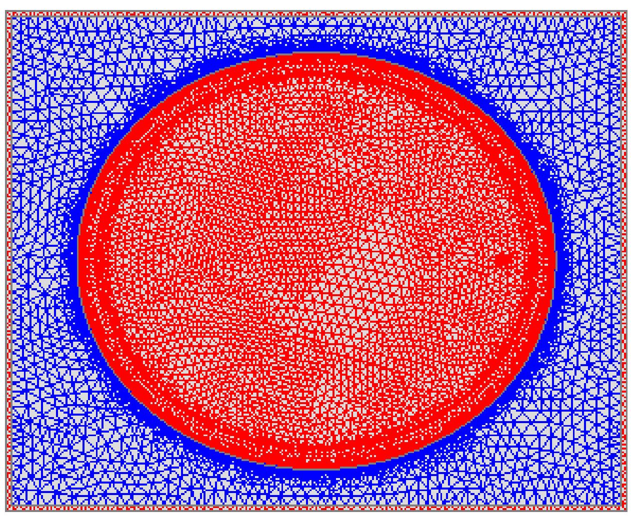

Figure 5. 13. Meshed models for simplified geometry used for FEM.

5.6. Conclusion

In this chapter, an analytical model is developed for an actuator whose stator curvature is nonuniformly shaped to have a reluctance torque in addition to the coil torque. The rotor's permanent magnet is incorporated in the model through equivalent Amperian currents. To model the actuator, the complicated geometry of the stator is substituted with an equivalent ellipse having a surface current density representing the stator current. The coil torque is obtained using the Lorentz force and the solution of Laplace's equation in terms of both scalar and vector potentials in the elliptical coordinates. The reluctance torque is obtained using the energy method and differential flux tubes that incorporate the variation of current enclosed in the flux loops. In addition to the detailed explanations, an attempt is made to visualize the modeling procedure and the field distributions so that the readers can clearly understand the ideas and utilize them in their research. Also, the finite element method is employed in the field analysis and development of the model. In the end, the actuator is prototyped.

The model produces the results in a few seconds while, depending on the desired accuracy, it could take a couple of hours up to a few days using a FEM. It is shown that the equivalent geometry produces the same field solution within the rotor area as the original geometry. Normal and tangential components of magnetic flux density, flux lines, magnetic scalar potential, magnetic vector potential, coil torque, reluctance torque, and total torque are extracted and analyzed. A very close agreement is observed among the results obtained from the analytical model, FEM in the simplified geometry, FEM in the original geometry, and experimental results from the prototyped device.

Chapter 6

Electromechanical Model, Eddy-Currents and Identification

6.1 Introduction

Rotary actuators have been widely employed in the industry, from robotics and aerospace to fluid valves and optical scanning, due to advantages like simple structure, cheap maintenance, high reliability, low cost, and uncomplicated control. They are sometimes called limited-angle torque motors (LATMs) when designed to provide a constant torque over an angular range. In many applications, such as fail-safe operations, a restoration torque is required to return the rotor to the initial position, such as a nonlinear stiffness used in Laws's relays, and a magnetic restoration created by adding alignment poles to the stator. This paper presents generalized studies applicable to such actuators while certain aspects of the physical implementations of the actuator described herein are covered by patents.

High-performance control of electric machines requires accurate models and an effective identification rather than conventional lumped models. The identification can be offline [56] or even online [57] when there are variations in the parameters of the device. Among modeling techniques, the finite element method (FEM), although powerful in the numerical modeling and design of electromagnetic devices, is too slow to be used in dynamic studies. Magnetic equivalent circuits [58]-[59] and subdomain models [60]-[61] provide fast yet accurate analytical frameworks that can be employed in developing electromechanical models. MEC-based models are developed to study the design of LATMs [58] and magnetic cores [59]. The subdomain approach is employed to study the diffusion in eddy current brakes [60] and cylindrical ferrite cores [61]. In [62], the finite difference method is employed to find the numerical solution of 2-D diffusion in a rectangular sheet. As eddy currents can highly impact the dynamic and thus control system design of an electromagnetic device, incorporating their impact in the model can be very crucial. In the interesting works [63]-[64], an analytical solution of 1-D diffusion in thin laminations or magnetic materials is used to modify the electrical circuit of an electromagnetic device. Friction is another factor affecting the mechanical dynamics of electromechanical devices, whose impact can be studied by LuGre model [65]-[68].

In this chapter, an electromechanical model incorporating eddy currents is developed for a limited-angle rotary actuator with a magnetic restoration torque to be employed in identification, drive, and control studies. By elliptically shaping the stator curvature, the reluctance torque is produced to restore the rotor to the maximum torque position if the coil current is removed. The relationship of the restoration torque is obtained using the co-energy method and a lumped-parameter model of the magnet, while the relationship of the torque component developed by the coil current is obtained using the Lorentz force and the Amperian current model of the magnetization. The back-emf relationship is also obtained. Then, a nonlinear electromechanical model, including governing electrical and mechanical equations and its nonlinear state-space representation, is developed for large-signal studies and nonlinear control. Then, the nonlinear model is linearized around the preferred equilibrium point, i.e., the maximum torque position per Ampere, to reach a linear electromechanical model and a linear state-space model for linear control system designs.

As the eddy-currents in the laminations and the magnet largely distort the electrical dynamic from a simple RL circuit, in order to obtain a higher precision and a more efficient control system design, the eddy-currents are included in the model by solving 1-D diffusion in the laminations and 2-D diffusion in the magnet; then, from the microscopic field solutions, lumped-element magnetic and electric circuits having frequency dependant reluctance and inductance are obtained which are more useful for system-level designs and control purposes. It brings a near-zero discrepancy in estimating the phase margin of the current loop, while this error could be very large if eddy currents are ignored. Its accuracy is much better compared to the case where only 1-D diffusion in laminations is considered. The impact of the pre-sliding friction on the mechanical dynamic is also studied using the LuGre model. Also, 2D and 3D FEM are employed in the analysis, and the actuator is prototyped. Torque-angle and back-emf characteristics are obtained. The identification of the model is carried out as well. A close agreement is observed between the results obtained from the experiment, model, and FEM.

6.2. The Actuator

The geometry and the exploded view of the actuator, whose specifications are listed in Table 6.1, are shown in Figure 6.1. The rotor PM has diametral magnetization. The interaction of stator flux and the magnet produces the main torque. The stator inner surface is shaped to have an elliptical curvature whose interaction with the magnet produces a reluctance torque which tends to restore the rotor back to the maximum torque per ampere position (MTPAP).

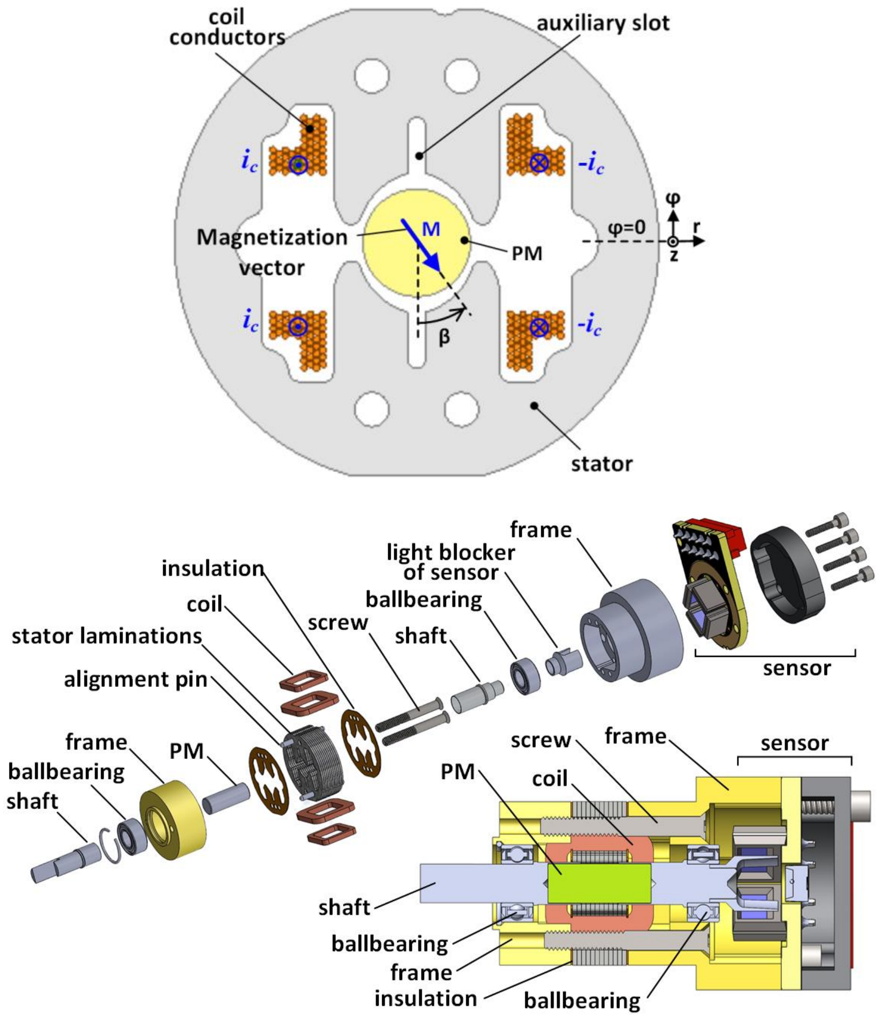

Figure 6. 1. (a) exploded view of the actuator, (b) geometry of the actuator, (c) Amperian current model of PM, and (d) lumped-element models of the PM

Table 6. 1 Specifications of the Studied Motor

parameter	value	parameter	value
outer diameter, D_o	13.716 mm	PM remnant, B_r	1.37 Tesla
lamination height d	0.35	total turns, N	100
# of laminations, m	12	wire gauge	AWG33
stack length, L	4.191 mm	torque constant, k_t	1.906 mN.m/A
pole width, w_p	4.72 mm	Mag. spring k_s	0.636 mN/rad
PM length, L_{pm}	9 mm	total stiffness, K_s	1.3 mN/rad
rotor diameter, D_r	3.048 mm	total damping, k_d	4.49e-7 Ns/rad
minor radius, R_1	1.71 mm	inertia, J	1.65e-9 kg.m^2
major radius, R_2	1.9665 mm	inductance, L_{c0}	280 uH
PM conductivity	0.6 MS/m	resistance, R_c	1.76 ohm
lamination conduct.	2 MS/m	sense resistor, R_s	0.1 ohm

6.3. Torque and Back-EMF Calculations

6.3.1. Permanent Magnet Models

The magnetization vector M of the PM in terms of azimuth φ and rotor angular position β can be represented as in below:

$$\vec{M}(\varphi,\beta) = -M\sin(\varphi-\beta)\ \hat{r} - M\cos(\varphi-\beta)\ \hat{\varphi};\ r \le R_r \tag{6.1}$$

A magnetization M can be represented as Amperian current density J_m. As shown in Figure 6.2(a), since M is uniform inside the PM, there is only a surface current density K_m as:

$$\vec{J}_m = \nabla\times\vec{M};\qquad \vec{K}_m = \vec{M}\times\hat{n} \tag{6.2}$$

where n=r is the unit vector normal to the surface. Thus:

$$\vec{K}_m(r,\varphi,\beta) = \vec{M}\times\hat{r} = M\cos(\varphi-\beta)\ \hat{z};\ r = R_r \tag{6.3}$$

As shown in Figure 6.2(b), the lumped-element model of the PM consists of a permeance $\wp_m$ and a magneto-motive force F_m which is the total current enclosed in the Amperian loop as:

$$F_m = \int_{\varphi=-\pi/2+\beta}^{\varphi=\pi/2+\beta} \left|K_m(\varphi,\beta)\right| R_r\, d\varphi = 2R_r M \tag{6.4}$$

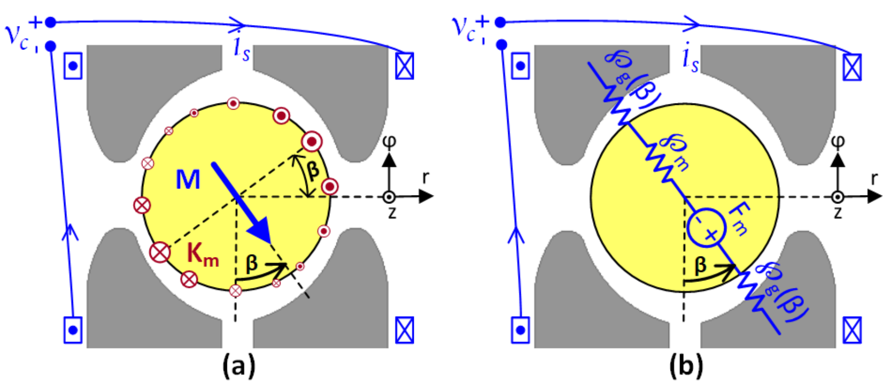

Figure 6. 2. (a) Amperian current and (b) lumped-element models of the PM.

6.3.2. Stator Field

Through Ampere's law, the current in the stator coils produces a magnetic field as in below:

$$\nabla \times \vec{B} = \mu_0 \mu_r \vec{J} \tag{6.5}$$

The radial component of magnetic flux density distribution on the surface of the PM, which is the torque-producing component, can be represented in Fourier series as in below:

$$B_r(\varphi) = \sum_{n=1,3,5}^{+\infty} B_n \sin n\varphi = B_1 \sin\varphi + B_3 \sin 3\varphi + \ldots \tag{6.6}$$

As long as the stator iron is not saturated, the coefficients B_n are linearly proportional to the coil current i_s, so:

$$B_r(\varphi) = \sum_{n=1,3,5}^{+\infty} k_n\, i_c \sin n\varphi = k_1\, i_c \sin\varphi + k_3\, i_c \sin 3\varphi + \ldots \tag{6.7}$$

6.3.3. Coil Torque

The stator flux interacts with the PM to produce an electromagnetic torque which is obtained by Lorentz force as:

$$T_{coil} = L \int_0^{2\pi} R_r K_m(\varphi, \beta)\, B_r(\varphi)\, R_r\, d\varphi \tag{6.8}$$

By substitution of K_m and B_r, we have:

$$\begin{cases} \dot{x}_1 = x_2 = f_1 \\ \dot{x}_2 = \{-k_d\, x_2 + k_t\, x_3 \sin x_1 + k_{rest} \sin 2x_1 - T_L\} / J = f_2 \\ \dot{x}_3 = \{-R_c\, x_3 - k_t\, x_2 \sin x_1 + v_c\} / L_{co} = f_3 \end{cases} \tag{6.9}$$

Except for $n=1$, the integration of the product of $cos(\varphi-\beta)$ and $sin\ n\varphi$ is zero, i.e., only the fundamental component of B_r contributes to the torque production. It simplifies as in below:

$$T_{coil}(\beta, i_c) = L\, R_r^2 M_0 k_1 i_c \int_0^{2\pi} \cos(\varphi - \beta)\sin(\varphi)\, d\varphi \tag{6.10}$$

By expressing the trigonometric product in sums, it yields:

$$T_{coil}(\beta, i_c) = \pi L\, R_r^2\, k_1 M_0\, i_c \sin\beta = k_t\, i_c \sin\beta \tag{6.11}$$

where k_t is the torque constant [Nm/A].

6.3.4. Restoration Torque

The elliptical curvature of the stator causes a reluctance torque. The PM is faced maximum permeance at MTPAP ($\beta=90$). The total permeance can be expressed as in below:

$$\wp(\beta) = \wp_0 - \wp_1 \cos 2\beta \tag{6.12}$$

The stored co-energy and the restoration torque are as:

$$W_c(\theta) = \frac{1}{2} {F_m}^2 \wp(\beta) \tag{6.13}$$

$$T_{rest} = \frac{\partial W_c(\beta)}{\partial \beta} = \frac{1}{2} {F_m}^2 \frac{\partial \wp(\beta)}{\partial \beta} = k_{rest} \sin 2\beta;\ k_{rest} = \wp_1 {F_m}^2 \tag{6.14}$$

where k_{rest} is the maximum restoration torque.

6.3.5. Total Torque

The total electromagnetic torque can be expressed as:

$$T_e(\beta, i_c) = k_t\, i_c \sin\beta + k_{rest} \sin 2\beta \tag{6.15}$$

whose small-signal model around MTPAP ($\theta=\beta-\pi/2$) is:

$$T_e(\theta, i_c) = k_t\, i_c - k_s \theta \tag{6.16}$$

where $k_s=2\ k_{rest}$ can be defined as the magnetic spring constant.

6.3.6. Back Electromotive Force

The flux linked by the stator coil is:

$$\lambda(\beta, i_c) = L_{co}\, i_c + \lambda_m(\beta); \quad \lambda_m(\beta) = -\lambda_0 \cos\beta \tag{6.17}$$

where λ_m and λ_0 are PM flux and its maximum, and L_{c0} is the frequency-independent coil inductance. As PM flux is in the opposite direction of the unit normal vector of coil area at $\beta=0$, there is a negative sign. The back-emf is as in below:

$$E(\omega_r, \beta) = \frac{d\lambda_m}{dt} = \frac{d\lambda_m}{d\beta}\frac{d\beta}{dt} = \omega_r \frac{d\lambda_m}{d\beta} = \lambda_0 \omega_r \sin\beta \tag{6.18}$$

where $\beta = \omega_r t$ and $\omega_r = d\lambda_m/d\beta$ is the angular velocity of the rotor. Defining the back EMF constant k_b [volt.sec/rad] as the amplitude of the back EMF at *1 rad/sec*, we have:

$$E(\omega_r, \beta) = k_b \omega_r \sin\beta \tag{6.19}$$

In the linearized model around MTPAP, $E=k_b\,\omega_r$. Due to energy conservation in the conversion of electrical power ($E\ i_s$) to mechanical form ($T_{coil}\ \omega_r$), so $k_b=k_t$.

6.4. Electromechanical Model

6.4.1. Nonlinear Electromechanical Model

The governing electromechanical dynamic, whose block diagram is shown in Figure 6.3, is as in the following:

$$v_c(t) = R_c\, i_c(t) + \frac{d\lambda(\beta, i_c)}{dt} = E(t) + R_c\, i_c(t) + L_{co}\frac{di_c(t)}{dt} \tag{6.20}$$

$$J\frac{d^2\beta}{dt^2} + k_d\frac{d\beta}{dt} = T_e(\beta, i_c) - T_L \tag{6.21}$$

where k_d is the viscous damping constant, and T_L is the load torque. It leads to a nonlinear differential equation as in below:

$$J\ddot{\beta} + k_d\dot{\beta} - k_{rest}\sin 2\beta = k_t\, i_c \sin\beta \tag{6.22}$$

The states are defined as angular position, angular velocity, and coil current. The inputs are coil voltage and load torque:

$$x(t) = [x_1, x_2, x_3]^t = [\beta, \omega_r, i_c]^t;\ u(t) = [u_1, u_2]^t = [v_c, T_L]^t \tag{6.23}$$

Substitution for E and T_t yields the nonlinear system below:

$$\begin{cases} \dot{x}_1 = x_2 = f_1 \\ \dot{x}_2 = \{-k_d\ x_2 + k_t\ x_3 \sin x_1 + k_{rest} \sin 2x_1 - T_L\} / J = f_2 \\ \dot{x}_3 = \{-R_c\ x_3 - k_t\ x_2 \sin x_1 + v_c\} / L_{co} = f_3 \end{cases} \tag{6.24}$$

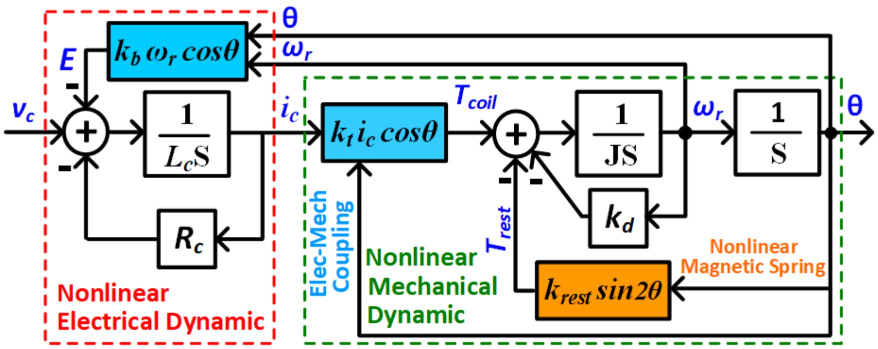

Figure 6. 3. The developed nonlinear electromechanical model.

6.4.2. Equilibrium Point

The equilibrium points, i.e., the solution of the system of equation [f_1=0; f_2=0; f_3=0] at zero input, are obtained as:

$$\bar{\beta} = 0,\ \pi/2,\ \pi,\ 3\pi/2; \quad \bar{\omega}_r = 0; \quad \bar{i}_c = 0 \tag{6.25}$$

where $\pi/2$ and $3\pi/2$ are stable equilibriums, and 0 and π are unstable ones. The position $\beta=\pi/2$ is taken as MTPAP.

6.4.3. Electromechanical and State Space Models

The system is linearized around the equilibrium point below:

$$\bar{x} = [\bar{x}_1,\ \bar{x}_2,\ \bar{x}_3]^t = [\pi/2,\ 0,\ 0]^t;\ \ \bar{u} = [\bar{u}_1, \bar{u}_2]^t = [0, 0]^t \tag{6.26}$$

Then, the states and the inputs are as in the following:

$$x = \bar{x} + \delta x \Rightarrow [\beta,\ \omega_r,\ i_c]^t = [\pi/2 + \delta\beta,\ \delta\omega_r,\ \delta i_c]^t \tag{6.27}$$

$$u = \bar{u} + \delta u \Rightarrow [v_c, T_L]^t = [\delta v_c, \delta T_L]^t \tag{6.28}$$

All variables are the same as their deviations except β, for which new variable $\theta=\delta\beta$ is defined as deviations of angular position around MTPAP. The linearized state-space system is:

$$\frac{d}{dt}\delta x(t) = A\delta x(t) + B\delta u(t); \quad y(t) = C\,\delta x(t) \tag{6.29}$$

$$A = \begin{bmatrix} \frac{\partial f_1}{\partial x_1} & \frac{\partial f_1}{\partial x_2} & \frac{\partial f_1}{\partial x_3} \\ \frac{\partial f_2}{\partial x_1} & \frac{\partial f_2}{\partial x_2} & \frac{\partial f_2}{\partial x_3} \\ \frac{\partial f_3}{\partial x_1} & \frac{\partial f_3}{\partial x_2} & \frac{\partial f_3}{\partial x_3} \end{bmatrix}, \; B = \begin{bmatrix} \frac{\partial f_1}{\partial u_1} & \frac{\partial f_1}{\partial u_2} \\ \frac{\partial f_2}{\partial u_1} & \frac{\partial f_2}{\partial u_2} \\ \frac{\partial f_3}{\partial u_1} & \frac{\partial f_3}{\partial u_2} \end{bmatrix} \; at \;\; x = \bar{x}, u = \bar{u} \tag{6.30}$$

It leads to the following linear state-space system:

$$\begin{bmatrix} \dot{\theta} \\ \dot{\omega}_r \\ \dot{i}_c \end{bmatrix} = \begin{bmatrix} 0 & 1 & 0 \\ -k_s / J & -k_d / J & k_t / J \\ 0 & -k_t / L_{co} & -R_c / L_{co} \end{bmatrix} \begin{bmatrix} \theta \\ \omega_r \\ i_c \end{bmatrix} + \begin{bmatrix} 0 & 0 \\ 0 & -1/J \\ 1/i_c & 0 \end{bmatrix} \begin{bmatrix} v_c \\ T_L \end{bmatrix} \tag{6.31}$$

The linear electromechanical dynamic is as in below:

$$\begin{gathered} v_c = k_t \omega_r + L_c \frac{di_c}{dt} + R_c\, i_c \\ J \frac{d^2\theta}{dt^2} + k_d \frac{d\theta}{dt} + k_s \theta = k_t\, i_c - T_L \end{gathered} \tag{6.32}$$

where $k_s=2k_{rest}$. The output is angular position, so $C=[1\ 0\ 0]^t$. The block diagram of the linearized model is shown in Figure 6.4.

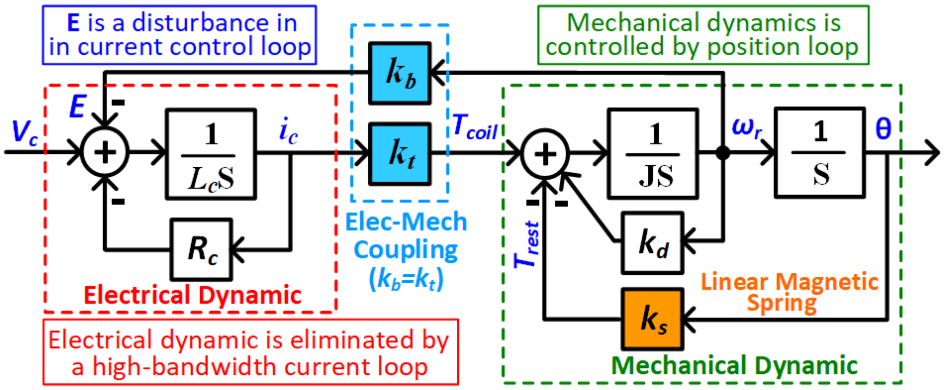

Figure 6. 4. The linearized electromechanical model.

6.4.4. Transfer Function of Electrical and Mechanical Dynamics

The mechanical dynamics of the actuator is as in below:

$$H_m(\mathrm{s}) = \frac{\theta(\mathrm{s})}{I_c(\mathrm{s})} = \frac{k_t}{Js^2 + k_d s + k_s} = \frac{k_t / J}{s^2 + 2\xi\omega_n s + \omega_n{}^2} \tag{6.33}$$

where natural frequency and damping ratio are $\omega_n = \sqrt{k_s / J}$ and $\xi = k_d / 2J\omega_n$. The electrical dynamic can be written as:

$$H_e'(\mathrm{s}) = \frac{I_c}{V_c} = \frac{Js^2 + k_d s + k_s}{L_{co} Js^3 + (R\,J + L_{co} k_d)\mathrm{s}^2 + (R\,k_d + k_s k_d + k_t{}^2)\mathrm{s} + R\,k_s} \tag{6.34}$$

where R is the total resistance of coil R_c and current sensor R_s. It includes an anti-resonance at the natural frequency of mechanical dynamic. Ignoring the back-emf leaves an RL circuit as:

$$H_e(\mathrm{s}) = \frac{I_c}{V_c} = \frac{1}{L_{co} s + R} \tag{6.35}$$

The back-emf is treated as a disturbance in the current loop. The electrical time constant is $\tau_e \approx L_{c0}/R$.

6.5. Eddy-Current Impact on the Electrical Dynamic

To obtain higher accuracy in the electrical dynamic, eddy currents in the laminations and the magnet are modeled, which adds two more degrees of freedom in addition to L_{c0} and R_c. As shown in Figure 6.5, according to Ampere's law, the stator current Ni_c produces an initial flux φ_0 whose time variations induce eddy currents in the iron laminations and the magnet ($I_{e.i}$ and $I_{e.m}$) according to Faraday's law which causes a secondary flux attenuating the initial flux. It reduces the coil inductance. A combination of Ampere's and Faraday's laws leads to the diffusion equation $\nabla^2 B = \mu\sigma \partial B / \partial t$.

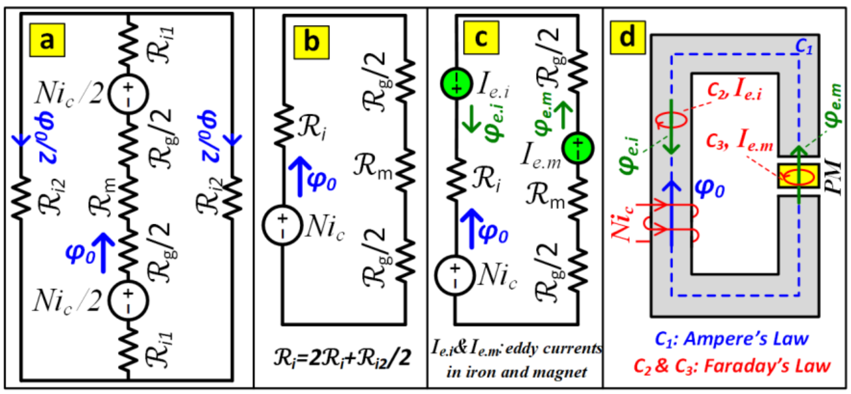

Figure 6. 5. (a)-(b) MEC and simplified MEC without eddy currents, (c) simplified MEC with eddy currents, and (d) paths of Ampere's and Faraday's laws.

To avoid unneeded complexities, the magnet cylinder is simplified to a cube with a rectangular cross-section. The width of the rectangle is the same as the pole width w_p. The length of the magnet l_m along the flux loop is obtained such that the cross-sectional areas and thus the volumes are kept the same:

$$w_p l_m = \pi R_r^2 \Rightarrow l_m = \pi R_r^2 / w_p \tag{6.36}$$

The average air-gap length is as follows:

$$l_g = 2\times\{(R_1 - R_r) + (R_2 - R_r)\}/2 = R_1 + R_2 - 2R_r \tag{6.37}$$

The average length of the flux loop within the iron core l_i can be approximated as a half-circle plus pole lengths as in below:

$$l_i = \pi\left(\frac{D_o}{2} - \frac{w_p}{4}\right) + \left\{\left(\frac{D_o}{2} - \frac{w_p}{4}\right) - \left(\frac{l_m}{2} + \frac{l_g}{2}\right)\right\} \tag{6.38}$$

The reluctances of air-gap, magnet, and iron are obtained as:

$$R_g = \frac{l_g}{\mu_0 A};\ R_m = \frac{l_m}{\mu_0 A};\ R_i = \frac{l_i}{\mu_0 \mu_{ri} A};\ (A_p = w_p L) \tag{6.39}$$

where μ_{ri} is the relative permeability of iron. The area of the left and right return paths, including half of the air-gap flux $\varphi_0/2$, is almost $w_pL/2$. The total reluctance R_{t0} and its approximation based on the low-frequency inductance L_{c0} is as follows:

$$R_{t0} = R_g + R_m + R_i = \frac{l_i + \mu_r(l_g + l_m)}{\mu_0 \mu_{ri} A_p}; \quad R_{t0} \approx \frac{N^2}{L_{co}} \tag{6.40}$$

The initial flux and flux density are obtained as $\varphi_0 = Ni_c/R_{t0}$ and $B_0 = \varphi_0 A_p$. Employing Ampere’s law over a flux loop leads to:

$$\oint_c \frac{B}{\mu}.dl = I_{enc} \Rightarrow \frac{Bl_g}{\mu_0} + \frac{Bl_m}{\mu_0} + \frac{Bl_i}{\mu_0 \mu_{ri}} = Ni_c + I_{e.i} + I_{e.\mathrm{m}} \tag{6.41}$$

It can be rewritten to obtain the effective permeability to solve diffusion in the laminations and magnets as in below:

$$Bl_i = \mu_{eff}^i (Ni_c + I_{e.i} + I_{e.\mathrm{m}});\ \mu_{eff}^i = \frac{\mu_0 \mu_{ri} l_i}{l_i + \mu_r(l_g + l_m)} = \frac{l_i}{R_t A_p} \approx \frac{l_i L_{co}}{N^2 A_p} \tag{6.42}$$

$$Bl_m = \mu_{eff}^m (Ni_c + I_{e.i} + I_{e.\mathrm{m}});\ \mu_{eff}^m = \frac{\mu_0 \mu_{ri} l_m}{l_i + \mu_{ri}(l_g + l_m)} = \frac{l_m}{R_t A_p} \approx \frac{l_m L_{co}}{N^2 A_p} \tag{6.43}$$

6.5.1. 1-D Diffusion for Eddy Currents in the Laminations

As shown in Figure 6.6(a), since the laminations are thin, the eddy-currents in the laminations can be modeled by one-dimensional diffusion as in below:

$$\begin{aligned} &\frac{\partial^2 B_y}{\partial z^2} = \mu_{eff}^i \sigma_i \frac{\partial B_y}{\partial t} \\ &B_y(z,t) = \mathrm{Re}\left\{\hat{B}_y(z)\,\mathrm{e}^{j\omega t}\right\} \end{aligned} \tag{6.44}$$

In phasor domain, it leads to:

$$\frac{\partial^2 \hat{B}_y}{\partial z^2} = j\omega\mu_{eff}^i \sigma_i \hat{B}_y \tag{6.45}$$

The solution is obtained as in below:

$$s = \pm\sqrt{j\omega\mu_{eff}^i \sigma_i} = \pm\alpha \Rightarrow \hat{B}_y(\mathrm{z}) = A_+ e^{+z} + A_- e^{-z} \tag{6.46}$$

As the initial field B_0 on the boundaries of the magnet is not disturbed by the flux produced by the eddy currents, the boundary conditions are $\hat{B}_z(x, \mathrm{z} = \pm d/2) = B_0$ which result in:

$$\begin{bmatrix} e^{\alpha d/2} & e^{-\alpha d/2} \\ e^{-\alpha d/2} & e^{\alpha d/2} \end{bmatrix} \begin{bmatrix} A_+ \\ A_- \end{bmatrix} = \begin{bmatrix} B_0 \\ B_0 \end{bmatrix} \Rightarrow \begin{cases} A_+ = e^{\alpha d/2} / (1 + e^{\alpha d/2}) \\ A_- = e^{\alpha d/2} / (1 + e^{\alpha d/2}) \end{cases} \tag{6.47}$$

By substituting *A*+ and *A*-, the solution is obtained as:

$$\hat{B}_y(\mathrm{z}, \omega) = B_0 \frac{\cosh \alpha z}{\cosh \alpha d/2} \tag{6.48}$$

The flux passing all lamination is obtained as follows:

$$\begin{aligned} \hat{\varphi}(\omega) &= 2m \int_{-w_p/4}^{w_p/4} \int_{-d/2}^{d/2} \hat{B}_y(\mathrm{z}, \omega)\, \mathrm{dxdz} = \varphi_0 \frac{\tanh \alpha z/2}{\alpha d/2} \\ \varphi_0 &= \frac{N i_c}{R_{t0}} \end{aligned} \tag{6.49}$$

where m is the number of laminations such that $L=md$, and 2 is for the two flux loops. Using the approximation $\tanh x = 1/(1+x)$ and substituting for φ_0, the following MEC is obtained:

$$\begin{aligned} \varphi(j\omega) &= \frac{N\, I_c(j\omega)}{R_{t0} + R_{e.i}(j\omega)} \\ R_{e.i}(j\omega) &= R_{t0}\, Q_i(\mathrm{j}\omega)\ ; \quad Q_i(\mathrm{j}\omega) = 0.5d\sqrt{j\omega\mu_{eff}^i \sigma_i} \end{aligned} \tag{6.50}$$

The eddy-impedance $R_{e.i}$ is a half-order complex reluctance that is zero at $\omega=0$. It goes up with frequency, causing a magnitude reduction and a phase lag in the flux $\varphi(t)$ with respect to the magnetomotive force or coil current. The associated magnetic circuit is shown in Figure 6.7(a). The induced eddy current density in one lamination is obtained as follows:

$$\hat{J}(z,\omega) = \frac{1}{\mu_{eff}^{i}} \nabla \times \hat{B}_y \Rightarrow J_x = \frac{1}{\mu_{eff}^{i}} \frac{\partial \hat{B}_y}{\partial z} = B_0 \frac{\alpha}{\mu_{eff}^{i}} \frac{\sinh \alpha z}{\cosh \alpha t / 2} \tag{6.51}$$

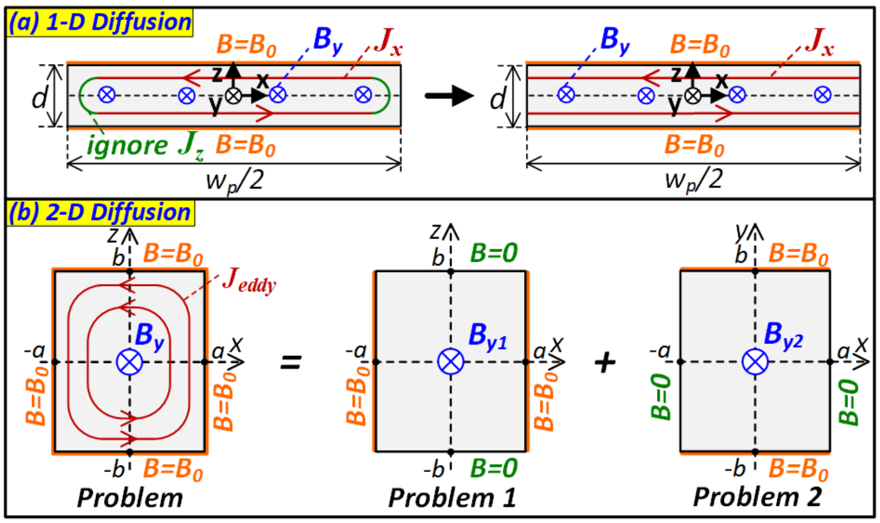

Figure 6. 6. (a) 1-D diffusion in laminations, and (b) 2-D diffusion in magnet.

6.5.2. 2-D Diffusion for Eddy Currents in the Magnet

As shown in Figure 6.6(b), the eddy-currents in the magnet can be modeled using two-dimensional diffusion as in below:

$$\frac{\partial^2 B_y}{\partial x^2} + \frac{\partial^2 B_y}{\partial z^2} = \mu_{eff}^{m} \sigma_m \frac{\partial B_y}{\partial t}; \quad B_y(x,z,t) = \mathrm{Re}\left\{\hat{B}_y(x,z)\, e^{j\omega t}\right\} \tag{6.52}$$

where $\hat{B}_y$ is a complex number. In phasor domain, it leads to:

$$\frac{\partial^2 \hat{B}_y}{\partial x^2} + \frac{\partial^2 \hat{B}_y}{\partial z^2} = j\omega\mu_{eff}^m \sigma_m \hat{B}_y \tag{6.53}$$

Using the separation of variables, we have:

$$\hat{B}_z(x,z) = X(x)\,\mathrm{Z}(z) \Rightarrow \frac{X''}{X} + \frac{Z''}{Z} = j\omega\mu_{eff}^m \sigma_m \tag{6.54}$$

The boundary conditions are $\hat{B}_y(\pm a, z) = \hat{B}_y(x, \pm b) = B_0$ where $a=w_p/2$, $b=L/2$. By superposition, the problem can be divided into two problems as shown in Figure 6.6(b) with boundary conditions:

$$P1: \hat{B}_y(\pm a, \mathrm{z}) = B_0; \;\; \hat{B}_y(x, \mathrm{z} = \pm b) = 0 \tag{6.55}$$

$$P2: \hat{B}_y(\pm a, \mathrm{z}) = 0; \quad \hat{B}_y(x, \mathrm{z} = \pm b) = B_0 \tag{6.56}$$

The solution of equation (54) for problem 1 is as follows:

$$P1\begin{cases} \dfrac{X''}{X} = k_{1n}^2 \Rightarrow s = \pm k_{1n} \Rightarrow X(\mathrm{x}) \sim \sinh k_{1n}x,\ \cosh k_{1n}x \\ \dfrac{Z''}{Z} = -(\dfrac{n\pi}{2b})^2 \Rightarrow s = -j(\dfrac{n\pi}{2b}) \Rightarrow Z(\mathrm{z}) \sim \sin\dfrac{n\pi}{2b}\mathrm{z},\ \cos\dfrac{n\pi}{2b}z \\ k_{1n}^2 - (\dfrac{n\pi}{2b})^2 = j\omega\mu_0\sigma_m \Rightarrow k_{1n} = \sqrt{(\dfrac{n\pi}{2b})^2 + j\omega\mu_{eff}^m\sigma_m} \end{cases} \tag{6.57}$$

Satisfying $\hat{B}_y(x, \pm b) = 0$, the solution is obtained as follows:

$$\hat{B}_{y1}(x, \mathrm{z}, \omega) = \sum_{n=1,3,\ldots}^{+\infty} a_n \cos\frac{n\pi}{2b}z \,\frac{\cosh k_{1n}x}{\cosh k_{1n}a} \tag{6.58}$$

where a_n is obtained as the coefficients of the Fourier series of the boundary condition $\hat{B}_z(\pm a, \mathrm{z}) = B_0$ as follows:

$$a_n = \frac{1}{b}\int_{-b}^{b} B_0 \cos\frac{n\pi z}{2b}\,\mathrm{dz} = \frac{4}{n\pi}\sin\frac{n\pi}{2} \tag{6.59}$$

The solution of equation (6.48) for problem 2 is as follows:

$$P2\begin{cases} \dfrac{X''}{X} = -(\dfrac{n\pi}{2a})^2 \Rightarrow s = -j(\dfrac{n\pi}{2a}) \Rightarrow X(\mathrm{x}) \sim \sin\dfrac{n\pi}{2a}x,\ \cos\dfrac{n\pi}{2a}x \\ \dfrac{Z''}{Z} = k_{2n}^2 \Rightarrow s = \pm k_{2n} \Rightarrow Z(\mathrm{z}) \sim \sinh k_{2n}z,\ \cosh k_{2n}z \\ -(\dfrac{n\pi}{2a})^2 + k_2^2 = j\omega\mu_0\sigma_m \Rightarrow k_{2n} = \sqrt{(\dfrac{n\pi}{2a})^2 + j\omega\mu_{eff}^m\sigma_m} \end{cases} \tag{6.60}$$

Satisfying $\hat{B}_z(\pm a, 0) = 0$, the solution is obtained as follows:

$$\hat{B}_{z2}(x, z, \omega) = \sum_{n=1,3,...}^{+\infty} b_n \cos\frac{n\pi}{2a}x\,\frac{\cosh k_{2n}z}{\cosh k_{2n}b} \tag{6.61}$$

where b_n is Fourier series coefficients of the boundary condition $\hat{B}_y(\pm a, \mathrm{z}) = B_0$ as $b_n=a_n$. Thus $B_y=B_{y1}+B_{y2}$ is obtained as:

$$\hat{B}_y = \sum_{n=1,3,...}^{+\infty} \frac{4}{n\pi}\sin\frac{n\pi}{2}\left\{\cos\frac{n\pi}{2b}z\,\frac{\cosh k_{1n}x}{\cosh k_{1n}a} + \cos\frac{n\pi}{2a}x\,\frac{\cosh k_{2n}z}{\cosh k_{2n}b}\right\} \tag{6.62}$$

By integrating over the area, the flux is obtained as follows:

$$\hat{\varphi}(\omega) = \int_{-b}^{b}\int_{-a}^{a} \hat{B}_y(x, z, \omega)\,\mathrm{dxdz} = \sum_{n=1,3,..}^{+\infty} \frac{8}{n^2\pi^2}\varphi_0\left\{\frac{\tanh k_{1n}a}{k_{1n}a} + \frac{\tanh k_{2n}b}{k_{2n}b}\right\} \tag{6.63}$$

where $\varphi_0 = 4abB_0$. As $a \approx b$, for simplicity of calculations, the rectangle is approximated with a square whose side width w is picked such that the area is the same, i.e. $w = \sqrt{a\,b}$. Only the fundamental component (n=1) is employed to obtain a lumped-element model. The approximation $\tanh x=1/(1+x)$ is used as well. As the series terms for n=3,5,… are ignored, the DC gain should be matched such that $\varphi(\omega=0)=\varphi_0$. Substituting for $\varphi_0=Ni_c/R_{t0}$ and writing the rest in format $1/(1+func(\omega))$ leads to:

$$\hat{\varphi}(\omega) = \frac{N\,I_c(j\omega)}{R_{t0} + R_{e.\mathrm{m}}(j\omega)} \tag{6.64}$$

$$R_{e.\mathrm{m}}(j\omega) = R_{t0}\,Q_m(j\omega);\ \ Q_m(j\omega) = \frac{w\sqrt{(\pi/2\mathrm{w})^2 + j\omega\mu_{eff}^m\sigma_m} - \pi/2}{1 + \pi/2} \tag{6.65}$$

The eddy-impedance $R_{e.m}$ is zero at $\omega=0$. The associated magnetic circuit is shown in Figure 6.7(b). The induced eddy current density in the magnet is as follows:

$$\hat{J}(x,z,\omega)=\frac{1}{\mu_{eff}^{m}}\nabla\times\hat{B}_y=\frac{1}{\mu_{eff}^{m}}\left(\frac{\partial\hat{B}_y}{\partial z}\hat{a}_x-\frac{\partial\hat{B}_y}{\partial x}\hat{a}_z\right) \tag{6.66}$$

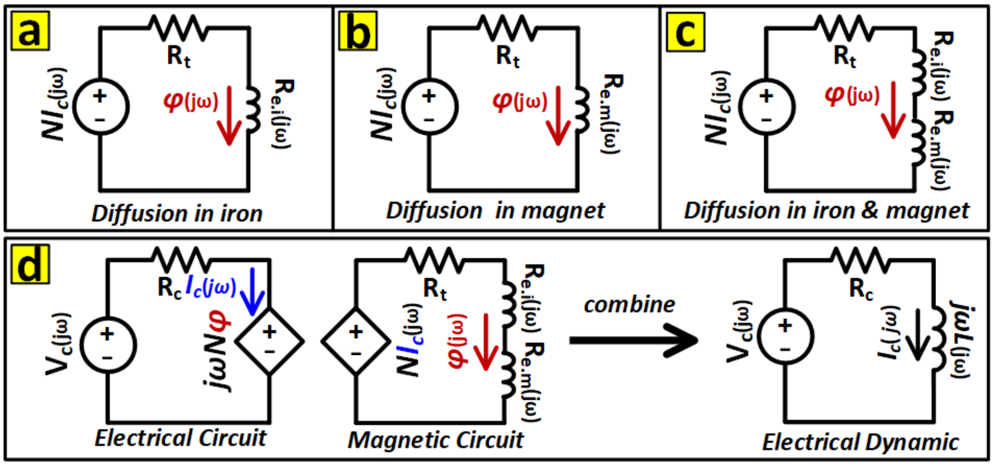

Figure 6. 7. (a)-(c) MEC with eddy current in iron and magnet, and (d) coupled electric-magnetic circuit to obtain electrical dynamic including eddy currents.

6.5.3. The Coupled Electric-Magnetic Circuit

As shown in Figure 6.7(c), the MEC incorporating eddy currents in both laminations and the magnet, whose total reluctance is $R_t(j\omega)=R_{t0}+R_{e.i}(j\omega)+R_{e.m}(j\omega)$. Combining magnetic and electric circuits as in Figure 6.7(d) results in the system of equations below:

$$\begin{cases} V_c = R_c I_c + j\omega N\varphi \\ NI_c = (R_{t0}+R_{e.\mathrm{i}}+R_{e.\mathrm{m}})\varphi \end{cases} \Rightarrow \begin{bmatrix} R_c & j\omega N \\ -N & R_{t0}+R_{e.\mathrm{i}}+R_{e.\mathrm{m}} \end{bmatrix}\begin{bmatrix} I_c \\ \varphi \end{bmatrix}=\begin{bmatrix} V_c \\ 0 \end{bmatrix} \tag{6.67}$$

The electrical dynamic can be obtained by solving the above system of equation, or simply by finding φ from the magnetic equation and substituting it into the electric equation:

$$\begin{aligned} H_e(j\omega) &= \frac{1+Q(j\omega)}{R_c+j\omega L_{co}+R_c Q(j\omega)} \\ Q(j\omega) &= Q_i(j\omega)+Q_m(j\omega) \end{aligned} \tag{6.68}$$

where $Q(j\omega)\geq 0$. The low-frequency inductance is $L_{c0}=N^2/R_{t0}$, as expected. There are four parameters to be found in identification: R_c, L_{c0}, $\mu^i_{eff}\sigma_i$ and $\mu^m_{eff}\sigma_m$. The frequency-dependent inductance can also be obtained as:

$$L_c(j\omega)=\frac{N^2}{R_t(j\omega)}=\frac{N^2}{R_{t0}(1+Q(j\omega))}\xrightarrow{L_{c0}=N^2/R_{t0}}L_c(j\omega)=\frac{L_{c0}}{(1+Q(j\omega))} \tag{6.69}$$

Using the above relationship, (35) can be rewritten as:

$$H_e(j\omega)=\frac{1}{R_c+j\omega L_c(j\omega)} \tag{6.70}$$

Figure 6.8 illustrates the distribution of the flux density as well as current density vectors within the laminations and the magnet. It is seen that, at zero frequency, no eddy current is induced, and flux density distributions are uniform, while eddy currents are induced at higher frequencies, causing a reduction in the flux density at the center of the material.

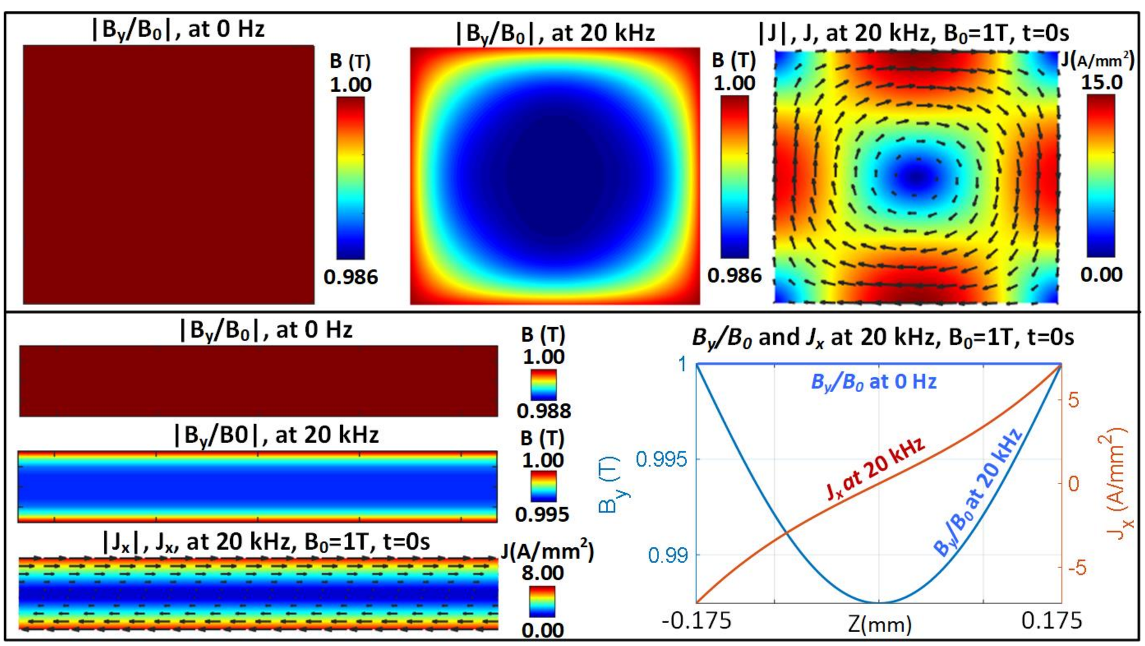

Figure 6. 8. Flux density distribution, current density distributions and current density vectors within magnet (top) and laminations (bottom).

6.5.4. Fractional-Order System

The square roots, including $s=j\omega$, illustrate a fractional dynamic which may be written as in the following:

$$H_e(s) = \left\{ \sum_{j=0}^{m} b_j s^{\beta_j} \right\} / \left\{ \sum_{i=0}^{n} a_i s^{\alpha_i} \right\} \tag{6.71}$$

where s^α and s^β correspond to fractional derivatives. Here Q_i is in the above format, and Q_m can be rewritten using Taylor expansion as in below:

$$\begin{aligned} Q_i(s) &= \frac{d}{2}\sqrt{\mu_{eff}^{i}\sigma_i}\, s^{0.5} \\ Q_m(s) &= \frac{w\{\frac{\pi}{2w} + \frac{w}{\pi}\mu_{eff}^{m}\sigma_m s + \frac{w^3}{\pi^3}(\mu_{eff}^{m}\sigma_m)^2 s^2\} - \frac{\pi}{2}}{1+\pi/2} \end{aligned} \tag{6.72}$$

6.6. Experimental Evaluation and Identification

Figure 6.9 shows the prototyped actuator and the torque-angle measurement setup. Figure 6.10 shows the experimental setup, including the drive and the current control loop.

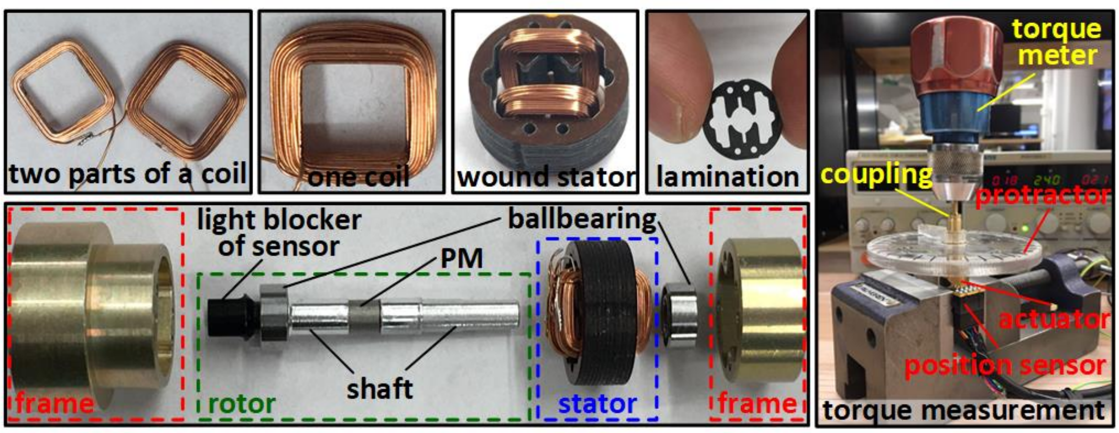

Figure 6. 9. The prototype actuator (left), and torque-angle measurement (right).

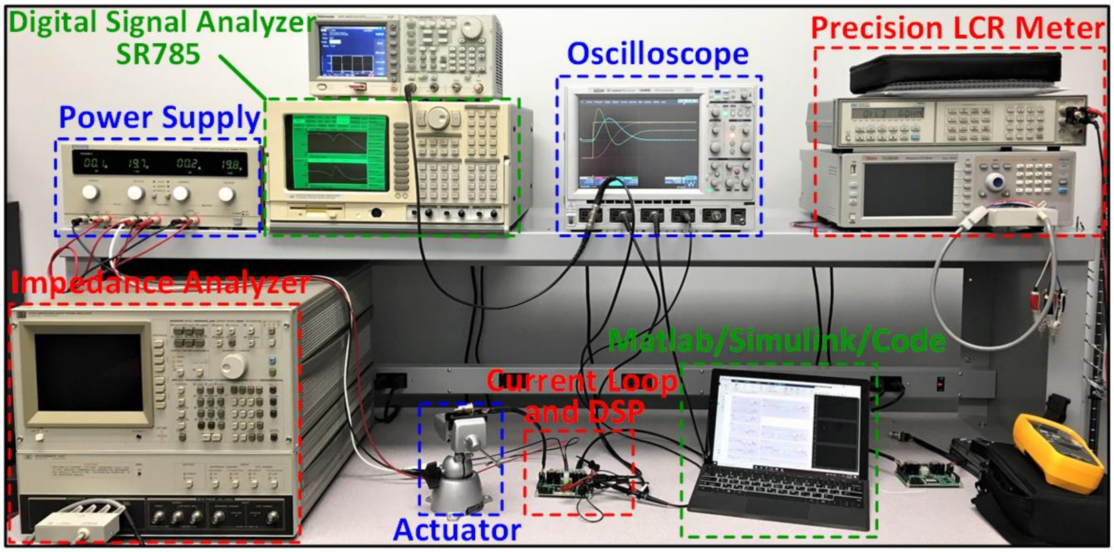

Figure 6. 10. The setup for identification and analysis of actuator and current loop.

6.6.1. Torque and Back-EMF Profiles

The torque-angle characteristics at zero coil currents (the restoration torque) as well as the coil torque and the total torque at a current of *1A* are given in Figure 6.11(a). The torque constant is obtained as k_t=1.906 *m N.m/A* by experiment and 1.953 *m N.m/A* by 3D FEM and, i.e., less 2.5% of error. Also, the restoration constant is obtained as k_{rest}=0.318 by experiment and 0.28 by FEM and, i.e., an error of 11%. Among the sources of the discrepancies might be prototyping issues, misalignments, inaccurate material characteristics, etc. The experimental values are used in the identification. The coil torque is obtained by subtracting the restoration torque from the total torque as it cannot directly be measured. The back-emf waveform at a velocity around *100 rad/sec* is shown in Figure 6.11(b), where the peak divided by the velocity is obtained as k_b=*1.91 volt.sec/rad* by experiment and *1.96 volt.sec/rad* by FEM and, i.e., an error of less than 3%. It is seen that all waveforms have a sinusoidal pattern, as expected from the nonlinear model.

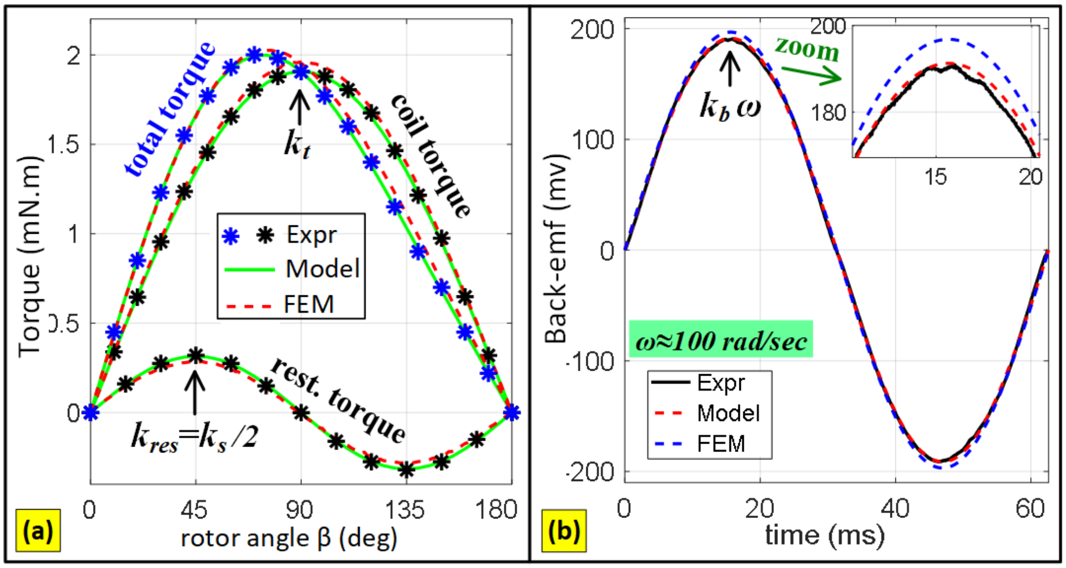

Figure 6. 11. (a) Coil, restoration and total torques, and (b) back-emf waveform

6.6.2. Identification of the Mechanical Dynamics and Friction Impact

The actuator is excited with the current control loop as a current source to obtain the frequency response of the mechanical dynamic H_m. In Figure 6.12(a)-(d), the waveforms of the coil current i_c and the rotor position θ, as well as frictional hysteresis loops in the torque-position plane for different amplitudes of coil current, are extracted. The hysteresis loops can be approximated as a straight line whose slope is almost the total stiffness seen by the system. It is observed that, for smaller amplitudes of current, the total stiffness is larger, and the hysteresis band is wider. Figure 6.12(e) shows the frequency response of *H*m for different amplitudes of the injected signal. A value of 10 mv at the input of the current loop corresponds to a coil current of about 20 mA as the DC gain of the current loop is almost 2. The DC gain of H_m is smaller than the value of k_t/k_s, i.e., the total stiffness of the system is a bit larger than the stiffness of the magnetic spring. It is caused by hysteresis behavior of the pre-sliding friction as described by LuGre model [20]-[21]:

$$\begin{cases} F_f = \sigma_s\, z + \sigma_d\, \dot{z} \\ \dfrac{dz}{dt} = v - \dfrac{\sigma_s\,|v|}{g(v)}\, z \\ g(v) = F_c + (F_s - F_c)\, \mathrm{e}^{-(v/v_s)^2} \end{cases} \tag{6.73}$$

where σ_s is the bristle stiffness, σ_d is the bristle damping, z is the internal state of bristle deflection, $v=d\theta/dt$ is the relative velocity between the two surfaces. Also, $g(v)$ is the Stribeck curve for steady-state velocities, F_c is the Coulomb friction force, F_s is the static friction force, and v_s is Stribeck velocity. A term for viscosity may also be added to F_f. Linearization around $z=0$ and $v=0$ results in [65]- [68]:

$$F_f = \sigma_s \theta + \sigma_d \dot{\theta} \tag{6.74}$$

In other words, the friction looks like a stiffness σ_s and a damping σ_d. Thus, the mechanical dynamics is modified to:

$$J\ddot{\theta} + k_d\dot{\theta} + k_s\theta = k_t i_c - F_f \quad \Rightarrow \quad H_m(\mathrm{s}) = \frac{\theta}{I_c} = \frac{k_t}{Js^2 + K_d s + K_s} \tag{6.75}$$

where $K_d=k_d+\sigma_d$ and $K_s=k_s+\sigma_s$ are the total damping and stiffness. As expected, the DC gain of H_m in Figure 6.12(e) is smaller for smaller amplitudes. There is also a phase delay at low frequencies, which is caused by the frictional hysteresis. This delay gets smaller for larger amplitudes of current as the hysteresis band gets smaller. The profiles of the total stiffness and the low-frequency lag versus current are shown in Figure 6.12(f). The identification is performed using the frequency response for currents around 80-120 mA where the actuator operates, and the values of K_s and K_d do not have big variations. Having the DC gain G_{m0} from the magnitude response and k_t from the previous section, the spring factor $k_s = k_t / G_{m0}$ is obtained. At a high-frequency ω_{hf} where the slope is -40 *dB/dec*, the inertia dominates the dynamic as $H_m(s) = k_t / Js^2$ so $J = k_t / \omega_{hf}^2 \, |H_m(\omega_{hf})|$ which is also close to the value obtained by Solid Works. Then, the natural frequency ω_n is obtained by $\omega_n = \sqrt{k_s / J}$. According to the resonance peak, an initial value for ζ is guessed. Finally, the parameters are re-adjusted such that the closest match is obtained. Having ζ, the damping factor is derived as $k_d = 2J\omega_n\xi$. A close agreement between the model and the experimental results is observed up to a sufficiently large frequency.

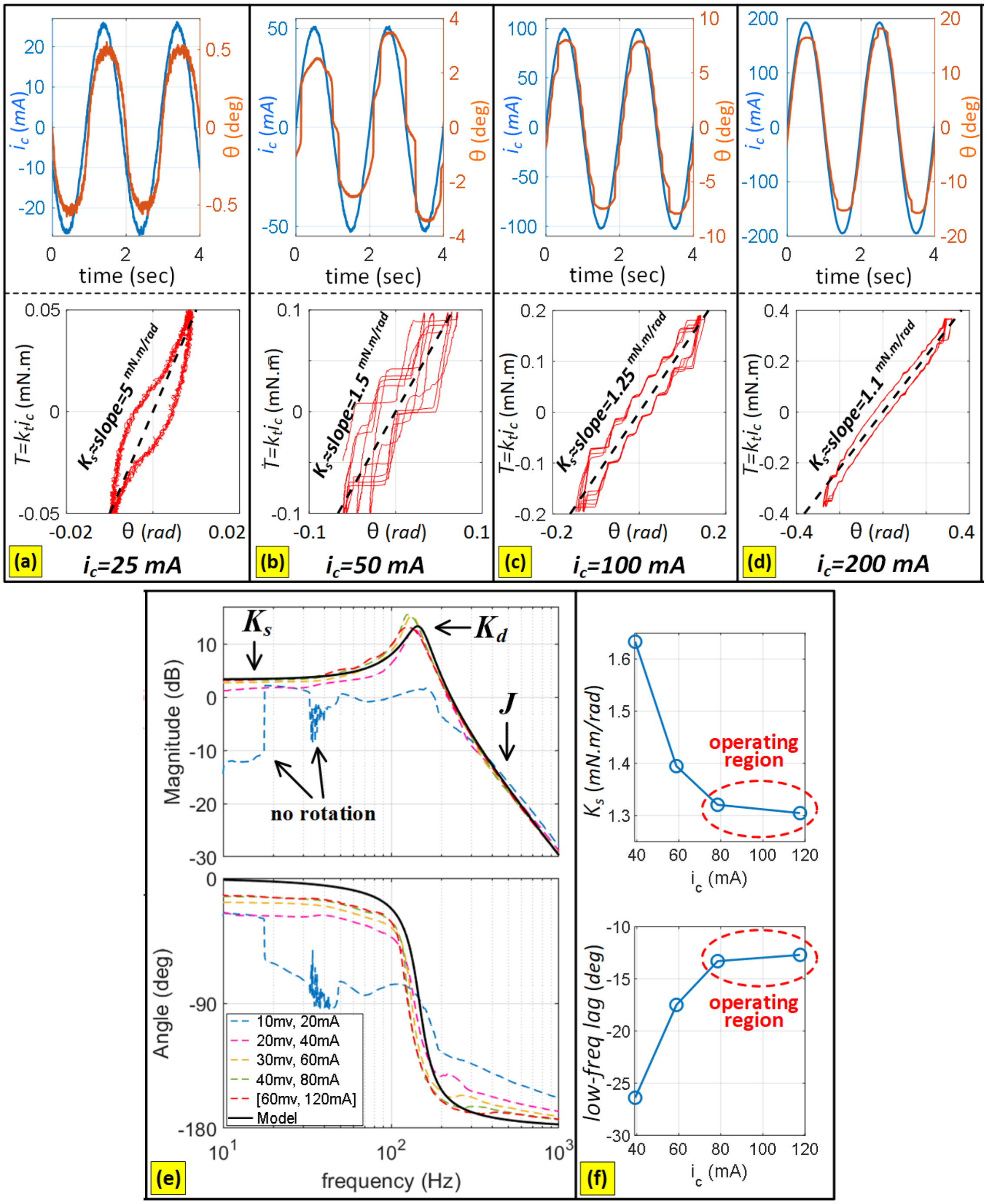

Figure 6. 12. Mechanical dynamic: (a)-(d) profiles of the coil current i_c and the position θ as well as frictional hysteresis loops in the torque-position plane for different amplitudes of current, (e) frequency response of the mechanical dynamics H_m for different amplitudes of injected signal, and (f) total stiffness and low-frequency lag due to the hysteresis loop for different amplitudes of injected signal.

6.6.3. Identification of the Electrical Dynamics

In Figure 6.13(a), the 2-DoF conventional RL model of the electrical dynamic and the proposed4-DoF model including eddy currents are compared with experimental results. The parameters of the RL model are simply measured by an LCR meter, as given in Table 6.1. From the DC gain, the resistance $R= R_c+R_s$ and then R_c is obtained. At high frequency, the dynamic is reduced to the inductance as $H_e(s)=1/L_{c0}s$, so at a higher frequency ω_{hf} where the slope is -20 *dB/dec*, the inductance can be obtained as $L=1/\omega_{hf}\,|H_e(\omega_{hf})|$. These are pretty close to those obtained by LCR meter. The accuracy of this model drops drastically at mid frequencies, causing problems in the design of the current loop. As observed, the phase asymptote of the experimental result, instead of -90°, gets close to -45° due to eddy currents which affect the frequency response by nature of half order (45 degrees).

The phase error at a frequency of 20 kHz (crossover frequency of the current loop) is around 15 degrees in the 2-DoF RL model, while it is reduced to 9 degrees for the 3-DoF model with eddy currents in only laminations, and 0.4 degrees for the 4-DoF model with eddy currents in both laminations and magnets. The approximated parameters of the 3-DoF model are R_c=1.76 Ω, L_{c0}=295 μH, $\mu_{eff}^{i}\sigma_i=6.4071$. The approximated parameters of the 4-DoF model are R_c=1.76 Ω, L_{c0}=295 μH, $\mu_{eff}^{i}\sigma_i=3.2035$ and $\mu_{eff}^{m}\sigma_m=2.8227$. The magnetic reluctance without and with the impact of eddy currents in the laminations and the magnet are shown in Figure 6.13(b), illustrating that the reluctance of the flux loop goes up due to eddy currents at higher frequencies, resulting in an inductance reduction. The ratio of the flux to the initial flux is also shown in Figure 6.14, due to eddy currents, from which it can be observed that the flux goes down at high frequencies.

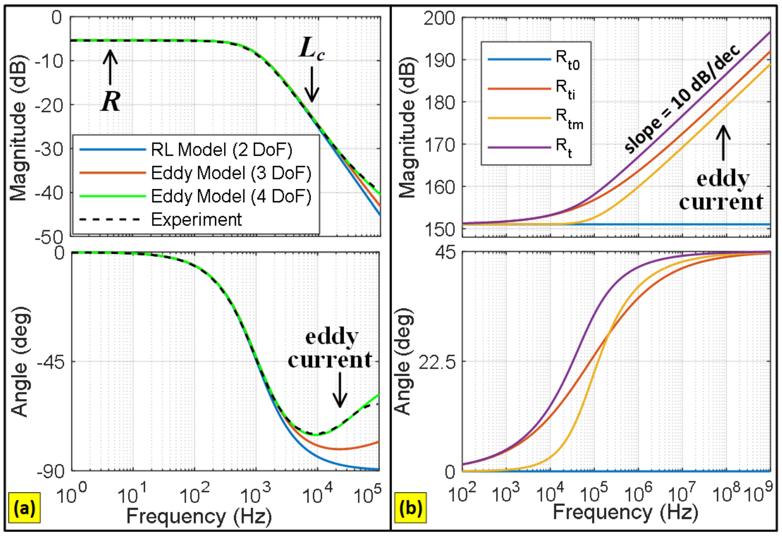

Figure 6. 13. (a) electrical dynamic and (b) ferequency-dependant magnetic reluctances.

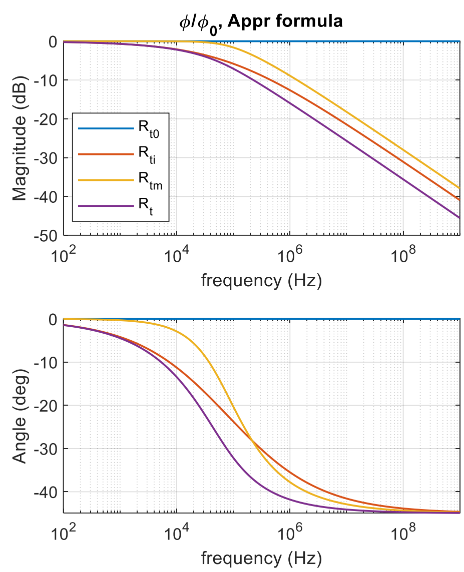

Figure 6. 14. Ratio of flux to the initial flux versus frequency.

6.7. Conclusions

Nonlinear and linear modeling of the actuator is developed. The eddy currents in the laminations and the magnet are included in the model by extracting a lumped-element framework from the analytical solution of the diffusion equation, which provides very high accuracy for dynamic and control studies of the device. As the field solutions are not preferred for system-level designs, a lumped-element model is extracted that incorporates eddy currents. Without including the eddy-current in the model, it could result in large inaccuracies in the frequencies around the crossover frequency of the current loop, which can cause misleading predictions of the phase margin design. By including the eddy current in the laminations using the solution of 1-D diffusion, a part of the inaccuracy issue is solved, and by including the eddy current in the magnet using the solution of 2-D diffusion, most part of the inaccuracy issue is solved. The impact of friction on the mechanical dynamic is investigated. The friction acts like stiffness and damping in the pre-sliding regime. The lab experiments are performed using a prototype actuator, whose results illustrate a very good correlation with the results obtained by modeling and FEM. Torque and back-emf profiles are obtained, and the identification of the model is carried out, which will be used in the control system designs.

Chapter 7

Modeling and Design of Drive Circuit and Current Control Loop

7.1 Introduction

High bandwidth current loops are widely employed to drive actuators and electromagnetic devices in order to eliminate the electrical dynamic so that the torque can be directly commanded by the outer control loops. It also provides a faster response and higher robustness by making the system independent of temperature-dependent elements like the stator resistance. The current drives may be developed using analog architectures like op-amps circuits [69]-[71] or FPGA-based switching devices [72].

In this chapter, n op-amp-based drive circuit for the current control loop is proposed, modeled, and designed. Using a third-order model of the op-amps estimated from the datasheet, a very accurate model for the drive and the current control loop is developed to be used for prediction and evaluation purposes. In addition, the simplified version of the model is obtained for design purposes and high-level intuitive analysis. The accuracy and effectiveness of the modeling of the actuator and the drive circuit are evaluated in control studies. The importance of eddy current modeling is demonstrated as well. Also, the effectiveness of the designed current loop and various practical trade-offs are investigated. The control system designs are evaluated and compared through indices like rise time, overshoot, and steady-state error in the step response, as well as bandwidth, phase margin, sensitivity, disturbance rejection, and noise rejection in the frequency domain.

7.2. Drive Circuit and Modeling Approach

The electromagnetic torque is proportional to the current which is developed in the coil within an electrical time constant. By implementing a high bandwidth current loop as the most inner loop, the whole electrical dynamic can be eliminated. Thus, instead of coil voltage, the current or torque can be commanded directly from the outer loops. Also, the complexities such as fractional dynamics of eddy currents are removed, resulting in the simplicity and accuracy of the position control. In addition, the robustness of the drive is increase by making the system independent of temperature-dependent elements such as coil resistance. As the drive circuit is shown in Figure 7.1, an analog control system is employed for the current loop whose advantage is that an immediate response to the current command is achieved. The desired closed-loop response is obtained by a lead-lag compensator.

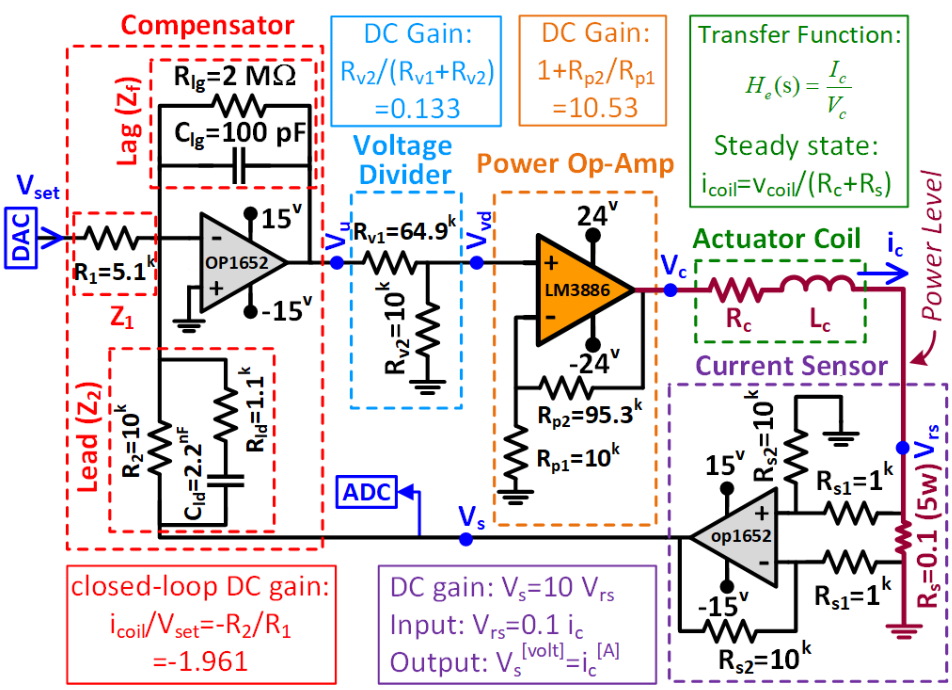

Figure 7. 1. Drive circuit and current control loop

A very accurate model for the drive circuit is developed using a non-ideal model of the op-amps. According to the frequency response of the op-amps given in the datasheet, a third-order model for the gain *A(s)* can be approximated as in below:

$$A(s) = \frac{A_{OL}}{(1+\mathrm{s}/2\pi\,\mathrm{f}_1)(1+\mathrm{s}/2\pi\,\mathrm{f}_2)(1+\mathrm{s}/2\pi\,\mathrm{f}_3)} \qquad (7.1)$$
$$\mathrm{f}_1 \approx GBP / A_{OL}$$

where the open-loop gain A_{oL}, gain-bandwidth product *GBP*, $f_1=GBP/A_{OL}$, and frequencies f_2 and f_3 can be approximated from the datasheet. The approximated specifications and frequency responses of LM3886 and OP1652 op-amps used in the drive are shown in Figure 7.2. Lower order models can also be obtained by ignoring the dynamics of f_2 and f_3. Then, by writing the differential input voltage V_d in terms of output voltage V_o and inputs V_+ and V_-, the op-amp circuit can be modeled.

$$V_o = A_s(\mathrm{s})V_d \qquad (7.2)$$
$$V_d = V_+ - V_-$$

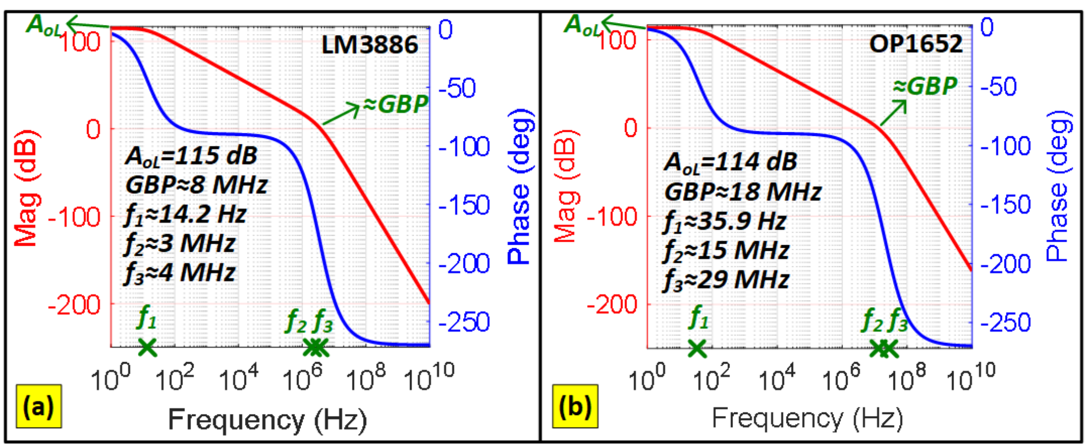

Figure 7. 2. (a) Torque and (b) back-emf waveforms

The developed model is very precise for simulations and performance prediction. However, for the design procedure, an ideal model is obtained when the gain *A(s)* approaches infinity. This simplified version is written in terms of conventional control system architectures. There are two main points on how to pick mid-range resistances for op-amp circuits. First, the resistances should not be too small to avoid drawing a large current that causes heating and loss. For example, if R_{p1} and R_{p2} are too small, they can draw a big current from the output of the power op-amp to the ground. Second, the resistances should not be too large to cause non-ideal op-amp behavior as input impedances are not infinite in reality. Also, bypass capacitors of 0.1uF are used for power rails of op-amps connected very close to the power pins.

7.3. Modeling of the Power Op-Amp and Voltage Divider

To drive the actuator, an LM3886 power op-amp with an open-loop gain of A_1(s) is used, which can provide a current of ±10 A and a large instantaneous and continuous power capability. Generally, in op-amp circuits, the higher the closed-loop gain, the lower the bandwidth; thus, the lowest possible gain is preferred. Based on the datasheet of LM3886, the lowest closed-loop gain to have a stable circuit and to get a phase margin of around 15 degrees in open-loop gain A(s) is 10. In smaller gains, the phase margin gets lost. Therefore, mid-range values for R_{p1} and R_{p2} are picked to have a gain of 10.53. Another consideration is that the impedances at the inverting and noninverting inputs (10||64.9 and 10||95.3) should be close; it is satisfied as the 10 kΩ resistance dominates the large parallel ones. A voltage divider with a gain of 0.133 is used to adjust the maximum output of the compensator (±14.7) to the maximum output of the power op-amp (±14.7 volt×0.133×10.53=±20.6 volt). The transfer function of the voltage divider is just a gain as in below:

$$H_{vd}(s) = \frac{V_{vd}}{V_u} = \frac{R_{v2}}{R_{v1} + R_{v2}} \tag{7.3}$$

The differential input voltage of the power op-amp is:

$$\begin{aligned} v_{dp} &= V_{vd} - \frac{R_{p1}}{R_{p1} + R_{p2}} V_c \\ V_c &= A_1(s)\, v_{dp} \end{aligned} \tag{7.4}$$

The transfer function of the ideal model is just a gain as follows:

$$H_p(s) = \frac{V_c}{V_{vd}} = \frac{A_1(s)}{1 + \frac{R_{p1}}{R_{p1} + R_{p2}} A_1(s)}$$
$$\lim_{A_1(s)\to\infty} H_p(s) = 1 + \frac{R_{p2}}{R_{p1}} \quad (7.5)$$

The block diagrams of the ideal and non-ideal models are shown in Figure 7.3. Its bandwidth is large enough compared to the current loop bandwidth that can be treated as a gain in the design process.

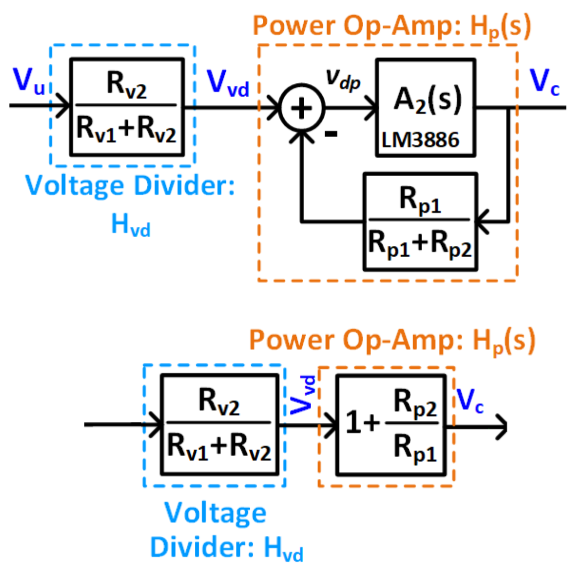

Figure 7. 3. The non-ideal (top) and the ideal (bottom) models of the power op-amp

7.4. Modeling of the Current Sensor

A low-noise high-bandwidth OP1652 op-amp with an open-loop gain of $A_2(s)$ is used for compensator and current measurement. The coil current is measured by the voltage across a Metal Element 5-watt resistance R_s =0.1 Ω in series with the coil, whose voltage is buffered so that it is not loaded. The advantage of this open-air resistor is to keep the hot spot safely off the PCB and improve the heat dissipation. Its parasitic inductance is much smaller than the metal film resistors. Also, the sense circuitry should be as close as possible to the sense resistor to avoid large loop areas by the PCB tracks, which can form parasitic inductances. The buffer gain is set to $1/R_s$, i.e., R_{s2}/R_{s1}=10, so the DC gain of H_s is unity (V_s=i_c). The differential input voltage of the op-amp is:

$$\begin{aligned} v_{ds} &= \frac{R_{s1}}{R_{s1}+R_{s2}}\left\{V_{rs} - \frac{R_{s1}}{R_{s2}}V_s\right\} \\ V_{rs} &= R_s i_c \\ V_s &= A_2(\text{s})\, v_{ds} \end{aligned} \tag{7.6}$$

The transfer function of the ideal model is just a gain as follows:

$$\begin{aligned} H_s(\text{s}) &= \frac{V_s}{I_c} = R_s \frac{\frac{R_{s1}}{R_{s1}+R_{s2}} A_2(s)}{1+\frac{R_{s1}}{R_{s1}+R_{s2}}\frac{R_{s1}}{R_{s2}} A_2(s)} \\ \lim_{A(s)\to\infty} H_s(\text{s}) &= R_s \frac{R_{s2}}{R_{s1}} = 1 \end{aligned} \tag{7.7}$$

As its bandwidth is large enough compared to the current loop, it is treated as a gain in the design process. The block diagrams of the non-ideal and ideal models are shown in Figure 7.4.

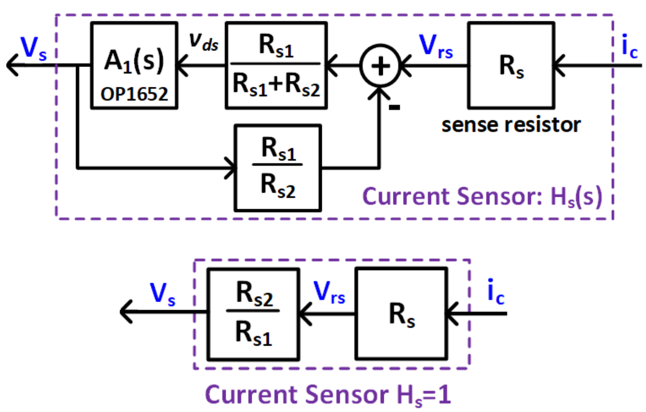

Figure 7. 4. The non-ideal (top) and the ideal (bottom) models of the current sensor

7.5. Modeling of the Lead-Lag Compensator

The lag compensator provides a large low-frequency gain to eliminate steady-state error. The lead compensator provides a fairly large phase margin to limit the overshoot of the time response and to increase the robustness of the control system.

The lead compensator is put in the feedback path so as to reduce overshoot and thus saturation in the output of the power op-amp. The differential input of the op-amp V_{dc} is as follows:

$$-v_{dc} = \frac{Z_f \parallel Z_2}{Z_1 + Z_f \parallel Z_2} V_{set} + \frac{Z_f \parallel Z_1}{Z_2 + Z_f \parallel Z_1} V_s + \frac{Z_1 \parallel Z_2}{Z_f + Z_1 \parallel Z_2} V_u \tag{7.8}$$

It can be simplified to:

$$\begin{aligned} v_{dc} &= -\frac{Z_1 Z_2 Z_f}{Z_1 Z_2 + Z_1 Z_f + Z_2 Z_f} \left\{ \frac{V_{set}}{Z_1} + \frac{V_s}{Z_2} + \frac{V_u}{Z_f} \right\} \\ V_u &= A_2(s) v_{dc} \end{aligned} \tag{7.9}$$

The transfer function of the lag compensator is obtained as:

$$H_{\lg}(s) = \frac{V_u}{e_i} = \frac{\dfrac{Z_1 Z_2 Z_f}{Z_1 Z_2 + Z_1 Z_f + Z_2 Z_f} A_2(s)}{1 + \dfrac{Z_1 Z_2 Z_f}{Z_1 Z_2 + Z_1 Z_f + Z_2 Z_f} \dfrac{1}{Z_f} A_2(s)} \tag{7.10}$$

With the ideal model of op-amps ($A_2(s) \to \infty$), it reduces to:

$$\begin{aligned} & H_{\lg}(s) = Z_f = \frac{R_{\lg}}{R_{\lg} C_{\lg} s + 1}; \\ & \lim_{R_{\lg} \to \infty} H_{\lg}(s) = \frac{1}{C_{\lg} s} \end{aligned} \tag{7.11}$$

The role of very large resistor R_{lg} is to limit the DC gain of the closed-loop system to avoid overcurrent in the coil in unexpected scenarios. However, if R_{lg} is very large, a pure integrator is obtained as $1/C_{lg}S$. As the value of R_{lg}=2 MΩ is picked, the pure integrator approximation can be used in the design process. The transfer function of the lead compensator using the ideal model of the op-amp is:

$$H_{ld}(s) = \frac{1}{Z_2} = \frac{1}{R_2}\frac{(R_2+R_{ld})C_{ld}s+1}{R_{ld}C_{ld}s+1} = \frac{1}{R_2}\frac{\alpha\tau s+1}{\tau s+1} \tag{7.12}$$

where the time constant is $\tau=R_{ld}C_{ld}$, and the pole-zero ratio is $\alpha=1+R_2/R_{ld}$. The lead compensator provides a maximum phase of ϕ_m at the frequency of ω_m as in below:

$$\phi_m = \sin^{-1}\left(\frac{\alpha-1}{\alpha+1}\right) \quad at \quad \omega_m = \frac{1}{\tau\sqrt{\alpha}} \tag{7.13}$$

The value of α is set according to the required phase compensation. Too big values can amplify high-frequency noise. The value of ω_m is usually set at the gain crossover frequency ω_c of the loop transmission so that the highest phase margin is obtained. The non-ideal and the ideal model of the compensator are shown in Figure 7.5.

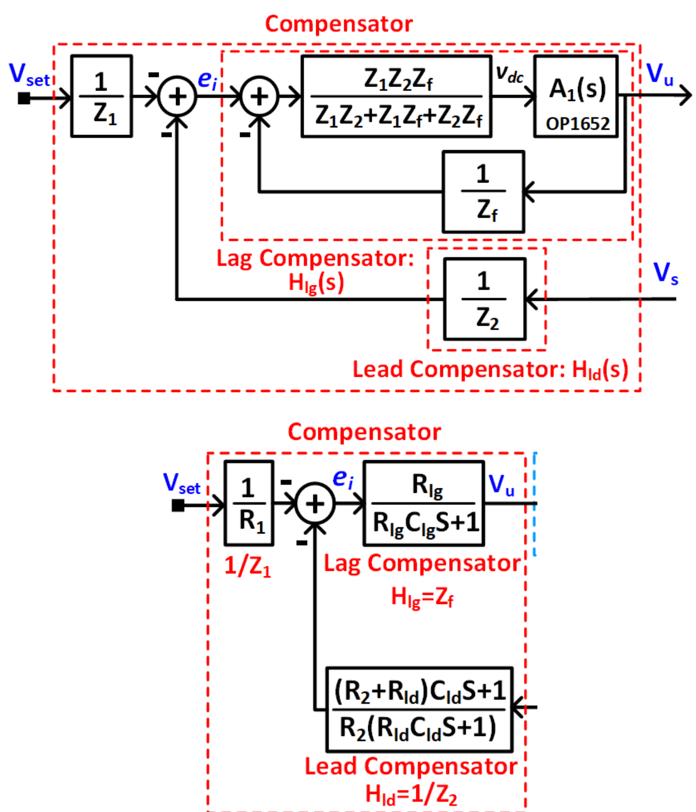

Figure 7. 5. The non-ideal (top) and the ideal (bottom) models of the compensator

7.6. Model of the Drive Circuit and Current Control Loop

In Figure 7.6, the non-ideal and the ideal models of the drive circuit and the current control loop are shown. The non-ideal model is employed for simulations and predictions, while the ideal model can be used for initial discussions and design purposes, as in the following section.

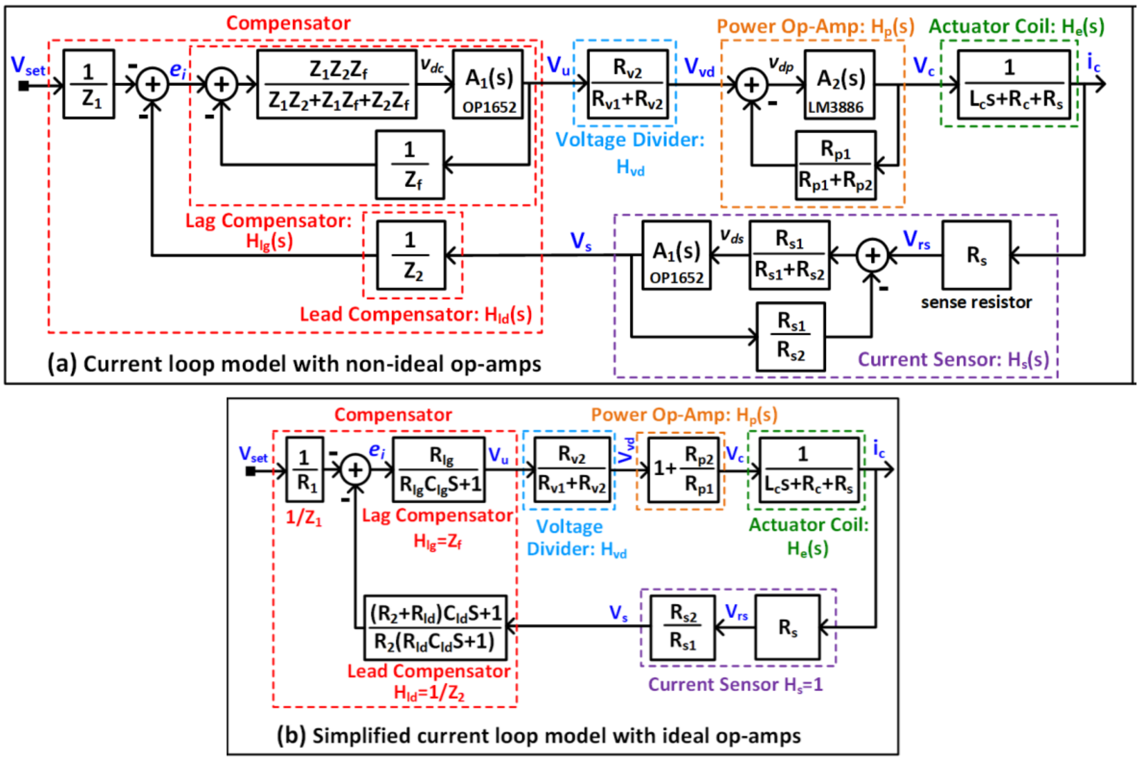

Figure 7. 6. The non-ideal (top) and the ideal (bottom) models of the drive circuit and the current control loop

7.7. Design of Lead-Lag Compensator

The design steps are as in below:

1. The closed-loop DC gain is almost R_2/R_1, whose value is picked such that bounds of V_{set} (±5V from DAC of DSP) are matched to the current capability of the power op-amp (±5×10/5.1=±9.8A). The resistor R_1 should not be smaller than 1 kΩ as it can cause heating and damaging the DAC with overloading and drawing a large current. Picking R_1=5.1 kΩ, leaves R_2=10 kΩ.

2. Next, the typical pole-zero ratio of α=10 is used, which provides a maximum phase of $\phi_m \approx 55^o$ to the loop. Therefore, R_{ld} is obtained as:

$$\alpha = 1 + R_2 / R_{ld} \quad \Rightarrow \quad R_{ld} = R_2 / (\alpha - 1) \approx 1.1\ k\Omega \tag{7.14}$$

3. The 10%-90% rise time of the closed-loop response is $t_r \approx 2.2/\omega_{bw}$, where ω_{bw} is the closed-loop bandwidth in rad/sec. To have a t_r<50µs, at least a bandwidth of 7 kHz is required. The crossover frequency must be much larger than $1/\tau_e$ to provide a very fast time response with a small rise time. The crossover frequency of the loop transmission is set to f_c=20 kHz which gives a closed-loop bandwidth around f_{bw}=7.8 kHz. Setting $\omega_m=\omega_c=2\pi f_c$, the value of C_{ld} is obtained as follows:

$$\omega_m = \frac{1}{R_{ld} C_{ld} \sqrt{\alpha}} \quad \Rightarrow \quad C_{ld} = \frac{1}{\omega_m R_{ld} \sqrt{\alpha}} \approx 2.2\, nF \tag{7.15}$$

4. The last component to be determined is C_{lg} which is set such that the gain of loop transmission is unity at ω_c.

$$\left| \frac{1}{\mathrm{j}\omega_c C_{\mathrm{lg}}} H_{ld}(\mathrm{j}\omega_c) H_e(\mathrm{j}\omega_c) \frac{R_{v2}}{R_{v1}+R_{v2}} \left(1+\frac{R_{p2}}{R_{p1}}\right) \right| = 1 \quad \Rightarrow \quad C_{\mathrm{lg}} \approx 100\, pF \tag{7.16}$$

where H_v, H_p, and H_s are just the simple gains of the ideal models of the voltage divider, power op-amp, and current sensor. The electrical dynamic, including eddy currents, is used here.

5. Figure 7.7 shows the loop transmission and its components as designed in part I of the paper, as well as the Nyquist of the loop. The results of the developed model are in very close agreement with the experiment. A sufficient phase margin of φ_m=72.5^o is obtained. It is seen that the phase margin is estimated with an error less than 1^o with the electrical dynamic including eddy current, while the error is around 16^o if eddy currents are ignored in the RL model. The Nyquist is a well far away from -1.

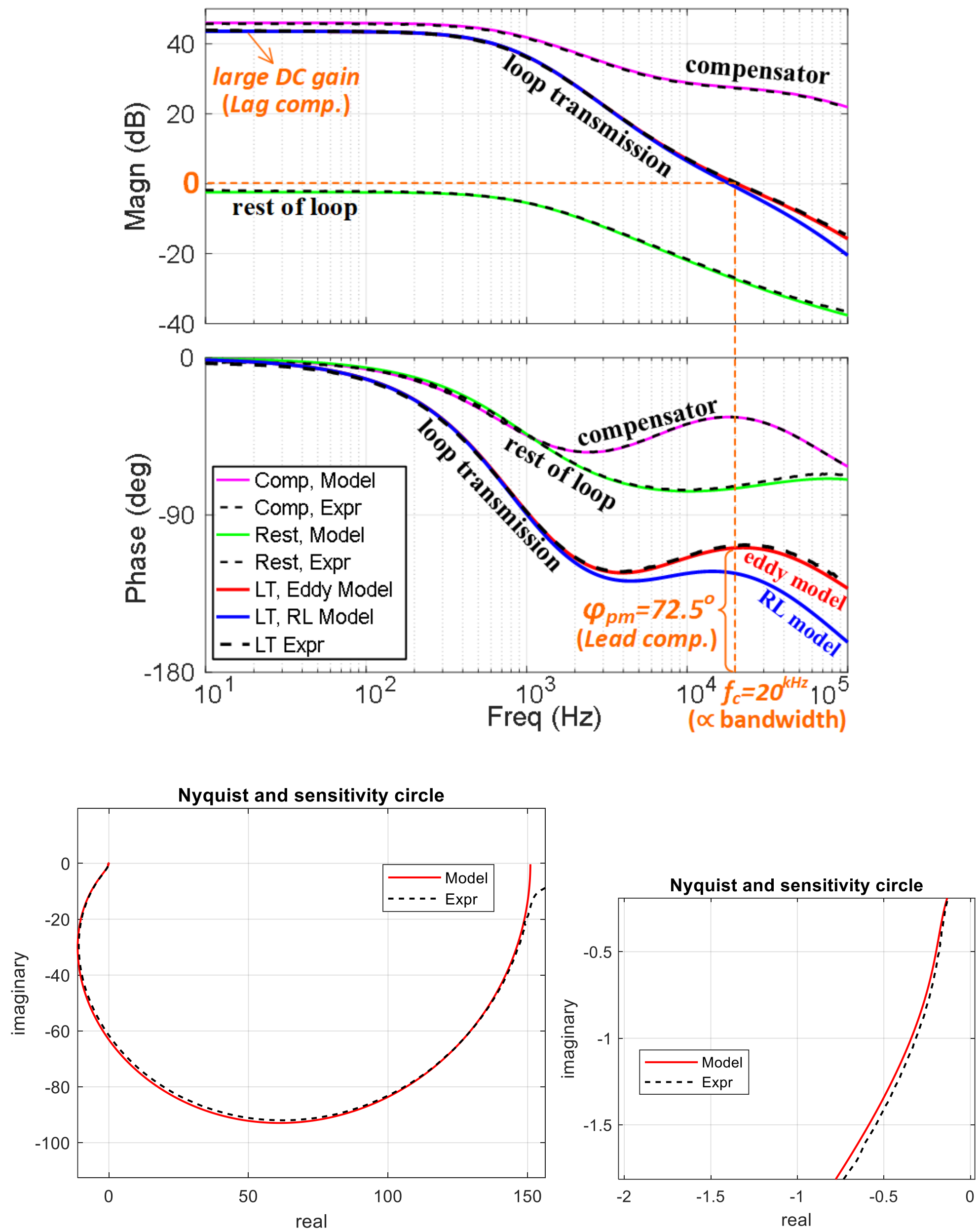

Figure 7. 7. Frequency response of loop components: (top) loop transmission, compensator, and rest of loop (loop transmission excluding compensator), and (bottom) Nyquist

7.8. The Six Gangs: Design Trade-Offs of Drive and Current loop

The design trade-off of the current control loop is studied in this section. As shown in the block diagram given in Figure 7.8, the three important inputs of the current loop are reference R (current command V_{set}), disturbance D, and measurement noise N. Also, the three outputs are the plant output x (position θ), measured output y, and drive output u. The loop transmission is $L=PCH$. It can be represented as a MIMO system as follow:

$$\begin{bmatrix} x \\ y \\ u \end{bmatrix} = \begin{bmatrix} \frac{P}{1+PCH} & \frac{-PCH}{1+PCH} & \frac{PCF}{1+PCH} \\ \frac{P}{1+PCH} & \frac{1}{1+PCH} & \frac{PCF}{1+PCH} \\ \frac{PCH}{1+PCH} & \frac{CH}{1+PCH} & \frac{CF}{1+PCH} \end{bmatrix} \begin{bmatrix} D \\ N \\ R \end{bmatrix} \tag{7.17}$$

There are six district transfer functions known as the six gangs [88]. The experimental frequency responses are obtained by SR785 Digital Signal Analyzer, whose maximum frequency is 100 kHz. Easily obtaining the frequency responses of loop transmission $L=PCH$, Gang 1, Gang 2 and Plant P, the Gangs 3-6 can easily be obtained as $G3$=P/(1+L), $G4$=1/(1+L), $G5$=(L/P)/(1+L) and $G6$=L/(1+L). The high precision of the developed models for the actuator and the drive circuit is illustrated in comparison with the experimental data. It is also shown that the RL model of the electrical dynamic in which the eddy currents are ignored may cause misleading inaccuracies in the design process.

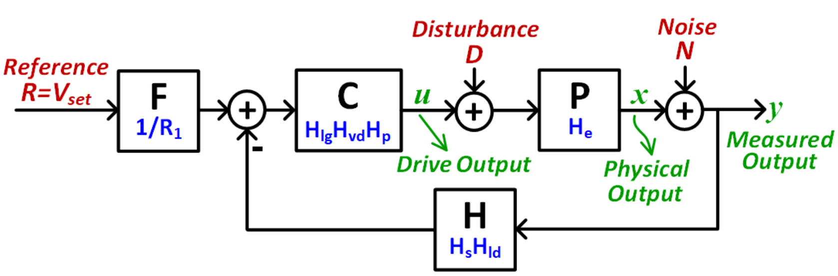

Figure 7. 8. The six gangs: block diagram, inputs and outputs

7.8.1. Gang 1: Reference Tracking

This is the reference tracking transfer function from the current command (DAC) to the coil current as in below:

$$T = \frac{Y}{R} = \frac{FPC}{1+PCH} \tag{7.18}$$

$$T_{DC} = \lim_{C\to\infty} T(0) = \frac{F(0)}{H(0)} = \frac{R_2}{R_1} \approx 5.96\,dB \tag{7.19}$$

Frequency and step responses of T are shown in Figure 7.9 and Figure 7.10. Provided by the crossover frequency of ω_c=20 kHz, as $\omega_{bw} \propto \omega_c$, a sufficient bandwidth of around f_{bw}=7.86 kHz is obtained, which provides a fast response with a small rise time t_r≈2.2/ω_{bw}=45 us as expected. Also, the bandwidth is not excessively large to introduce high-frequency noise to the system. Thanks to the sufficient phase margin of the loop, the closed-loop response is well damped ($\zeta \approx \varphi_m/100$) without a significant resonance peak. Provided by the lag compensator, if the loop gain at low frequency is large enough, the steady-state error converges to zero, and the D.C. gain is R_2/R_1=1.961, that is, a current command of V_{est}=1 produces a current of 1.961 A in the coil.

7.8.2. Gang 2: Voltage Capability of the Drive

This is the transfer function from the current setpoint R to the output of the power op-amp U as in below:

$$\frac{U}{R} = \frac{FC}{1+PCH} \tag{7.20}$$

$$\lim_{C\to\infty} \frac{FC}{1+PCH} = \frac{F(0)}{P(0)H(0)} = \frac{R_2}{R_1} R \approx 11.26dB \tag{7.21}$$

A design criterion is the D.C. gain which converts the current setpoint (DAC voltage) to the steady-state coil voltage. The DC gain of 11.26 dB converts the ±5 volt at the DAC to ±18 volt at the coil terminal—a bit below the maximum voltage capability of drive. Also, a comparison is made with a case where the lead compensator is placed in the forward path. As shown in Figure 7.9, it can be observed that the resonance peak of the frequency response and the overshoot of the step response is larger, which can result in saturation of the voltage op-amp whose output voltage cannot go beyond ±20.6 volts. Therefore, putting the lead compensator in the feedback path is a wise decision that enhances the voltage capability of the drive in the transient regime. The step response is also shown in Figure 7.10.

7.8.3. Gang 3: Disturbance Rejection or Load Sensitivity

This is the transfer function from the disturbance D to the output y (coil current) as in below:

$$\frac{Y}{D} = \frac{P}{1+PCH} \tag{7.22}$$

$$\lim_{C\to\infty} \frac{P}{1+PCH} = 0 \tag{7.23}$$

The disturbance operates at low frequency as the reference command. The back-emf $E=k_b\omega_r$ is treated as a disturbance in the current loop. A large loop gain in low frequencies provided by the lag compensator brings a good disturbance rejection whose capability needs a compromise with reference tracking capability and robustness as increasing the low-frequency gain comes at the expense of a decrease in the magnitude slope and thus in the phase margin of the loop transmission around the crossover frequency. In other words, pushing down the output response to the disturbance (Gang 3) comes at the cost of an overshoot in the output response to the setpoint (Gang 1). The disturbances are effectively attenuated at low to high frequencies, as it can be observed in Figure 7.9 that the magnitude peak is around -30 dB.

To obtain time responses of Gangs 3 to 6, extra equipment is not required to inject D and N signals to the specified locations. As the input impedance of the power op-amp is very large and the output impedance of the compensator op-amp is very low, according to the circuit shown in Figure 7.10(c), approximated responses of Gangs 3 and 4 can be obtained by injecting the input signal to the non-inverting input of the power op-amp through a 10 kΩ resistor. If the inverse gains of the voltage divider (v_{in} to v_+) and power op-amp (v_+ to v_c) are applied to the responses, i_c and v_c give the approximate responses for $G3=P/(1+PCH)$ and $G4=1/(1+PCH)$, respectively. The inverse of the total gain from v_{in} to v_c is 0.2, so if the magnitude of injected signal v_{in} is 0.2 volt, the signals i_c and v_c give the unit step responses of Gangs 3 and 4. It is seen that the unit step response to the disturbance signal is effectively suppressed to 6 mv.

7.8.4. Gang 4: Sensitivity

The sensitivity is the transfer function from the noise N to the output y, or reference R to the error for F=1.

$$S = \frac{Y}{N} = \frac{1}{1 + PCH} \tag{7.24}$$

Typically, S is zero at low frequencies, has a peak M_s at a mid-frequency ω_{ms}, and converges to unity at high frequencies. Sensitivity is a measure of the robustness of the control system to the variations of the parameters of the plant H_e as the impact of variations of T to P is proportional to sensitivity S as follows:

$$\frac{dT}{dP} = S\frac{T}{P} \;\Rightarrow\; \frac{dT}{T} = S\frac{dP}{P} \tag{7.25}$$

If the sensitivity curve is harshly pushed down at low frequencies to obtain a smaller steady-state error and robust disturbance rejection, it pops up at mid frequencies resulting in a larger M_s; it is called waterbed effect and needs a trade-off. It is also reflected in the fact that S+T=1 if F=H=1. Usually, a value of M_s smaller than 2dB or 3dB shows a satisfying design. Thanks to the sufficient phase margin of the loop, $M_s=1$ is obtained, as shown in Figure 7.9. It can also be seen that if the RL model without eddy current dynamic is used, the value of M_s has a significant discrepancy which can be misleading in the design trade-offs. According to Figure 7.10, the unit step response to the noise signal is effectively suppressed to 10 mv. It is also a measure of steady-state error elimination, which is largely satisfying.

7.8.5. Gang 5: Noise Sensitivity

The noise sensitivity is the transfer function from the noise N to the drive output U.

$$S_N = \frac{U}{N} = \frac{CH}{1 + PCH} \tag{7.26}$$

The system should be designed such that noise sensitivity is as small as possible so that the measurement noise is not amplified by the power op-amp, causing loss and drive saturation. As S_n=CH×S, at high frequencies S=1 and so S_n=CH; thus, the pole-zero ratio of the lead compensator α should not be very large to avoid noise amplification. As shown in Figure 7.9, a sufficient noise attenuation is obtained at high frequencies by a value of α=10.

7.8.6. Gang 6: Complementary Sensitivity

Complementary sensitivity is the transfer function from the disturbance D to the drive output U.

$$S_{cm} = \frac{U}{D} = \frac{PCH}{1+PCH} \tag{7.27}$$

If F=H=1, S_{cm}=T. As S+S_{cm}=1, there is a compromise between S and S_{cm}. It is shown in Figure 7.9.

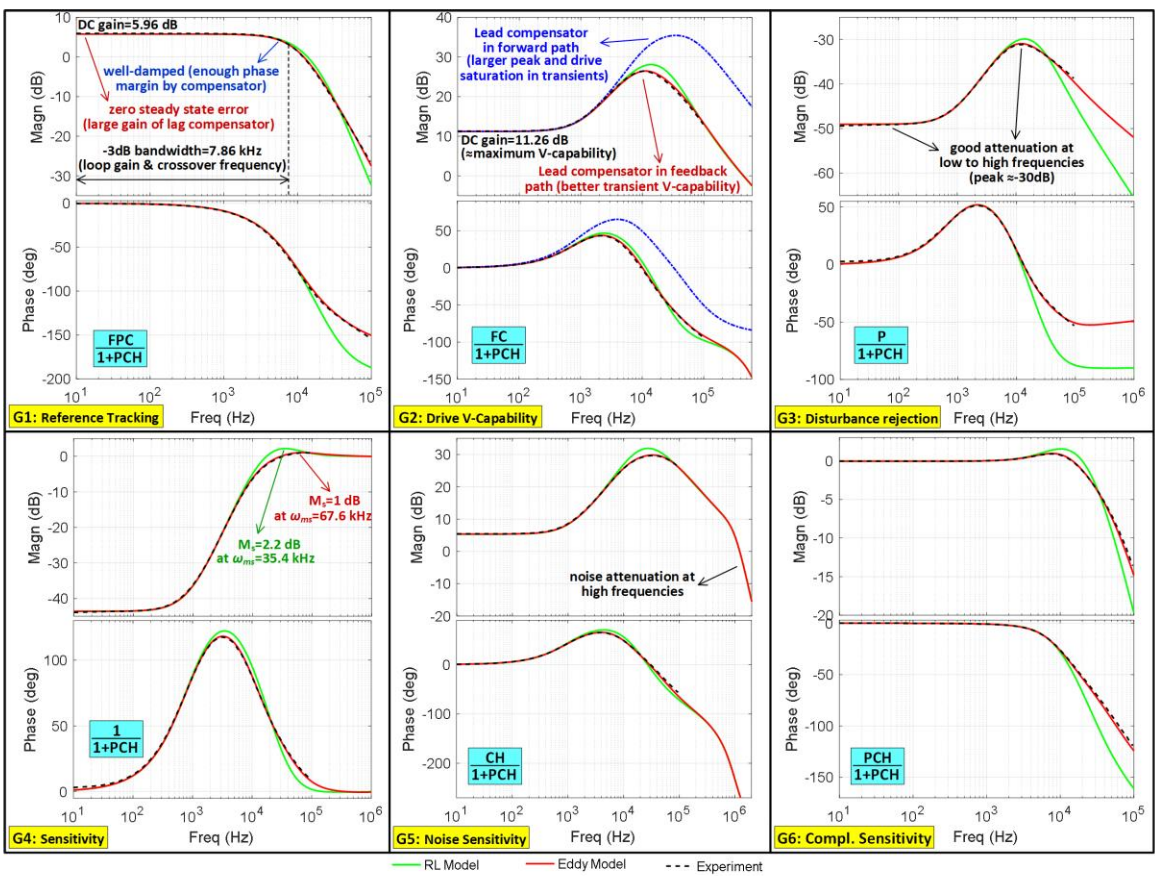

Figure 7. 9. Frequency response of the six gangs.

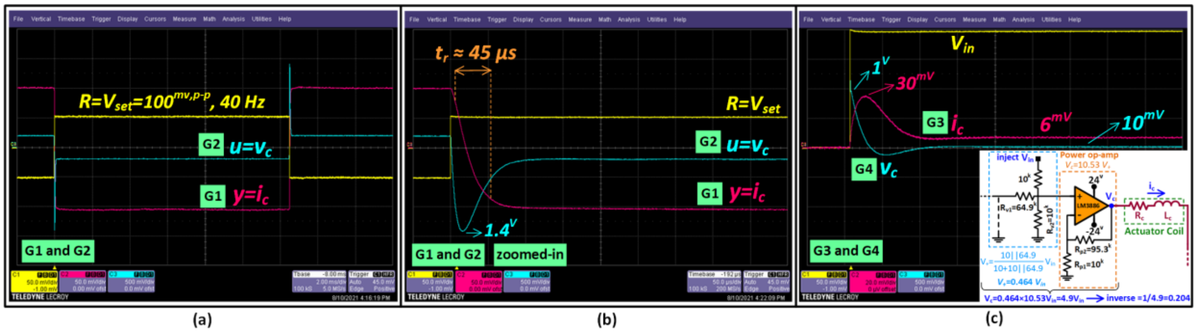

Figure 7. 10. Step responses of (a) Gang 1and Gang 2, (b) Gang 1and Gang 2 zoomed-in, and (c) Gang 3 and Gang 4.

7.9. Conclusion

An op-amp-based analog drive circuit is proposed, designed, and precisely modeled by a third-order model of the op-amps. It provides a very accurate simulation platform to predict the performance of the drive circuit and the current control loop. In addition, an ideal model using the ideal model of op-amps is then developed to be employed in the design of the current control loop. The accuracy of the ideal model is a bit lower than the non-ideal model, but its diagram is in the form of the conventional lea-lag control systems, which provides a good platform for the design of the current loop. The design trade-offs are analyzed through six important performance indices called the six gangs, including tracking capability, voltage capability of drive, disturbance rejection, sensitivity, noise sensitivity, and complementary sensitivity. Among the six gangs, the first four are the most important ones. Tracking with sufficient bandwidth (small rise time) and enough phase margin (small overshoot) is significant. The sensitivity is the second important one whose peak needs to be smaller than 2 or 3 dB to have good robustness. A good disturbance rejection is also helping to suppress the back-emf in the current control loop. Checking the saturation level of the power op-amp is important; for example, by placing the lead compensator, a larger head room is provided for the overshoot of the output of the power op-amp.

The accuracy of the drive modeling, as well as the effectiveness of the actuator model, are studied in the tests of the current control loop. The developed models for the actuator and the drive are employed in position control studies, and the significance of eddy current modeling in the effectiveness and accuracy of the control system designs and predictions is demonstrated. Also, various aspects and practical trade-offs of the current loop are investigated. Then, three DSP-based position control techniques are implemented.

Chapter 8

Pole-Placement Position Control with Voltage Drive

8.1 Introduction

The position loop can be digitally implemented in a DSP. The Zero-Order-Hold (ZOH) sampling is performed at the frequency of f_s up to 160 kHz. Bipolar ADCs with 16 bits of resolution is employed. If unipolar ADCs are used, it is required to deal with an offset by an extra op-amp circuit. The position sensor returns a voltage as a function of position, and its inverse function is implemented in the DSP. As the bandwidth of the position loop should be around or not much larger than the bandwidth of the actuator to avoid drive saturation, pole placement position control is employed for desired poles having a natural frequency of $\omega_n=2\pi 500\ rad$. The experimental control setup is shown in Figure 8.1. As shown in Figure 8.2, the pole placement control is performed using the power op-amp as a voltage drive. To effectively use the resolution of the DAC, a voltage divider with a gain of 0.4 is used such that ±5v at the DAC translates to ±21v at the output of power op-amp (±5×0.4×10.53=±21). The coil voltage is measured by ADC through a voltage divider. Also, the current can be measured using the output of the buffer sent to an ADC, or it can be estimated by a state observer. The circuits gains are canceled out in the DSP by their inverse values so that the physical model of the actuator can be used for control system design without requiring any gain modification.

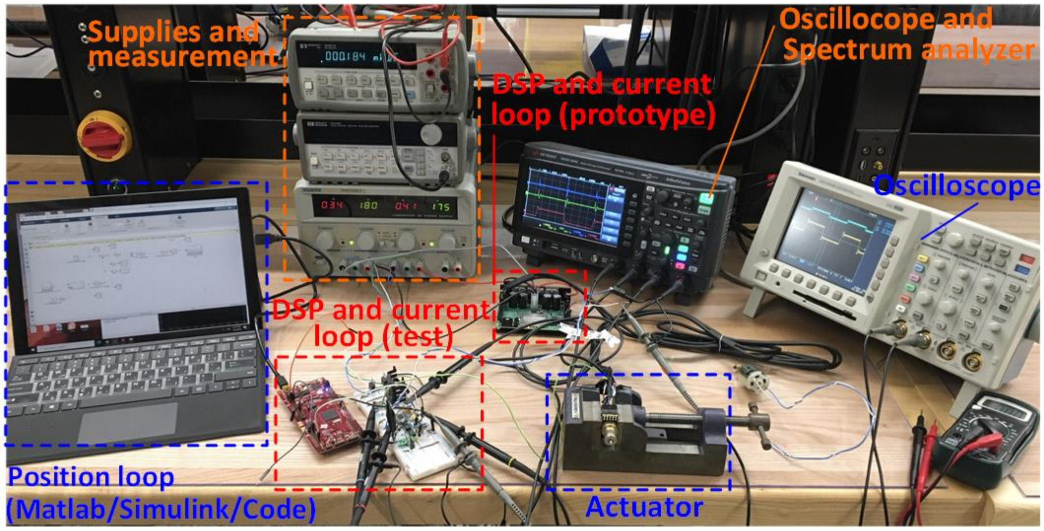

Figure 8. 1. Experimental control setup

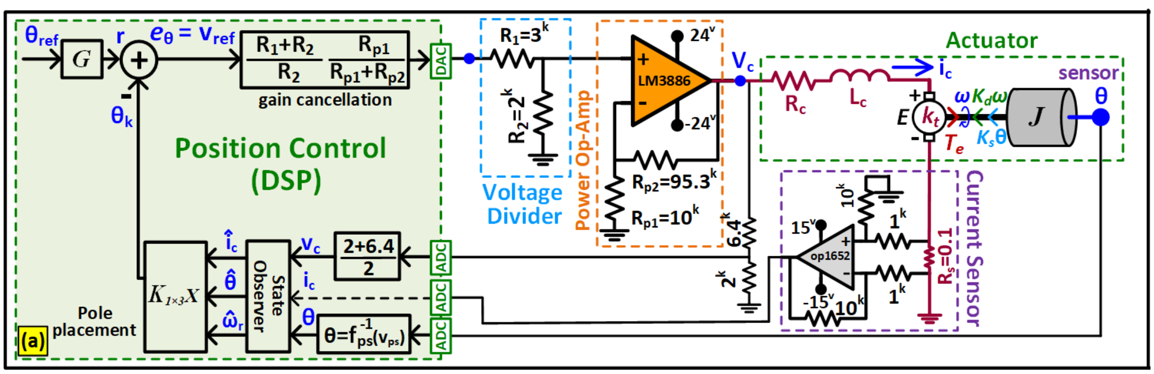

Figure 8. 2. Pole placement with voltage drive

8.2. Employed Model

By ignoring the fractional-order dynamic of eddy currents, an integer-order linearized model, whose block diagram is shown in Figure 8.3, is obtained to be used in pole placement control:

$$v_c = k_t \omega_r + L_{c0} \frac{di_c}{dt} + R i_c \,; \qquad J \frac{d^2\theta}{dt^2} + K_d \frac{d\theta}{dt} + K_s \theta = k_t \, i_c \tag{8.1}$$

It can be represented as a third-order state-space model as:

$$\begin{bmatrix} \dot{\theta} \\ \dot{\omega}_r \\ \dot{i}_c \end{bmatrix} = \begin{bmatrix} 0 & 1 & 0 \\ -K_s / J & -K_d / J & k_t / J \\ 0 & -k_t / \mathrm{L}_{c0} & -R_c / L_{c0} \end{bmatrix} \begin{bmatrix} \theta \\ \omega_r \\ i_s \end{bmatrix} + \begin{bmatrix} 0 \\ 0 \\ 1/L_{c0} \end{bmatrix} v_c \tag{8.2}$$

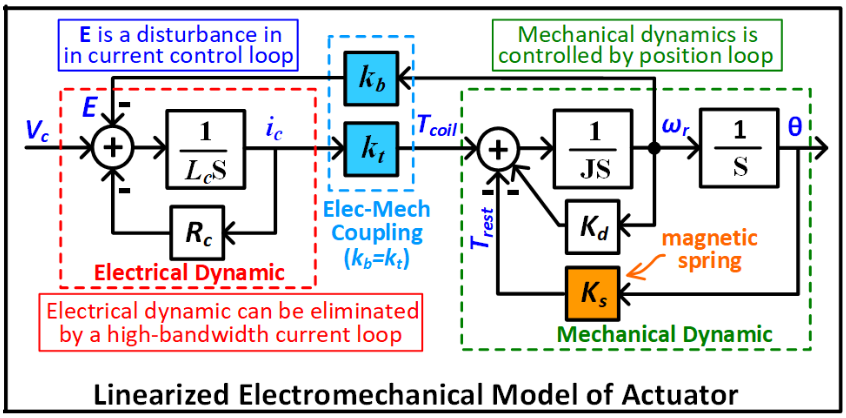

Figure 8. 3. Block diagram of the linearized electromechanical model.

8.3. Full-State Feedback Control in Time Domain

As shown in Figure 8.2, full-state feedback is obtained by substituting $u=r-K\,\delta x$ and $r=G\,\theta_{ref}$ as in below:

$$\frac{d}{dt}\delta x(t) = (A - BK)\,\delta x(t) + B\,r(t) \tag{8.3}$$

The eigenvalues of matrix $A_{cl}=A\text{-}BK$ determine the closed-loop dynamic. The gain vector $K=[k_1, k_2, k_n]$ is obtained by pole-placement using Ackermann's formula as in below:

$$K = [0\ 0\ 1]_{1\times 3}\, M_c^{-1}\, \phi_d(A_{3\times 3});\ \ M_c = [\mathrm{B\ AB\ A^2B}] \tag{8.4}$$

where M_c is the controllability matrix and φ_d is the desired characteristic polynomial whose roots are the desired eigenvalues λ_1, λ_2 and λ_3 of closed-loop dynamic $A_{cl}=A\text{-}BK$ which are chosen to be on a circle with a radius of $\omega_n=2\pi f_n$ and with damping of ζ as $-\omega_n$ and $-\xi\omega_n \pm j\omega_n\sqrt{1-\xi^2}$. It leads to the following desired characteristic polynomial:

$$\varphi_d(\lambda) = (\lambda - \lambda_1)(\lambda - \lambda_2)(\lambda - \lambda_3) = (\lambda^2 + 2\zeta\omega_n\lambda + \omega_n{}^2)(\lambda + \omega_n) \tag{8.5}$$

The input gain for position tracking (C=[1 0 0]^t) is obtained as:

$$G = -[C\left(A - BK\right)^{-1} B]^{-1} \tag{8.6}$$

8.4. Full-Order State Estimator

Position and current can be directly measured or estimated, and velocity is estimated. When there are noise problems and unmodeled dynamics, as in our case where eddy current dynamics are ignored, a full-order observer might be preferred over a reduced-order one. The estimator dynamics are as follows:

$$\frac{d}{dt}\delta\hat{x}(t) = A\delta\hat{x}(t) + Bu(t) + L(y(t) - \hat{y}(t)) \tag{8.7}$$

$$\hat{y}(t) = C\,\delta\hat{x}(t) \tag{8.8}$$

Substituting for $\hat{y}$ in (15) results in:

$$\frac{d}{dt}\delta\hat{x}(t) = (A - LC)\,\delta\hat{x}(t) + [B\,L]\begin{bmatrix} u(t) \\ y(t) \end{bmatrix} \tag{8.9}$$

where A_e=A-LC forms the closed-loop dynamics of the estimator. The pole placement can be done for the estimator using Ackermann's formula to obtain the gain vector L=[L_1 L_2 L_3]^t:

$$L = \phi_e(A) M_o^{-1}\left[0\ 0\ 1\right]_{1\times 3}^{t};\ M_o = \begin{bmatrix} C \\ CA \\ CA^2 \end{bmatrix} \tag{8.10}$$

where M_o is the observability matrix, and $\varphi_e(\lambda)$ is the desired characteristic polynomial whose roots are the desired eigenvalues of estimator dynamic A_e=A-LC which are chosen to be around 5 to 10 times faster than the controller. For example, locating them at $-10\omega_n$, can be a good choice as it is still within the bandwidth of the sensors. It leads to the following characteristic polynomial:

$$\varphi_e(\lambda) = (\lambda + 10\omega_n)^3 \tag{8.11}$$

Using the Forward Euler method, by substituting *d/dt* with (*z-1*)/T_s, the Z-transform and the discrete-time equation of the estimator is obtained as in below:

$$\hat{x}(k) = (I + T_s A_e)\,\hat{x}(k-1) + T_s B v_c(k-1) + T_s L\, y(k-1) \tag{8.12}$$

where $T_s = 1/f_s$ is the sampling time. It can be easily implemented into the DSP. Another state estimation technique is to employ a full-order observer where only the unmeasured states (velocity) are taken from the observer and the measured states (position and current) are directly taken from the sensor. In this method, model uncertainties can be more efficiently suppressed in velocity estimations.

8.5. Design of the Compensator

The compensator is the combined controller and estimator with input *y*(*t*) and outputs *u*(*t*). If *r=0*, the dynamics is obtained by substituting $u = -K\,\delta\hat{x}$ and $\hat{y} = C\,\delta\hat{x}$ in (15) as in below:

$$\frac{d}{dt}\delta\hat{x}(t) = (A - BK - LC)\delta\hat{x}(t) + L\,y(t);\; u = -K\,\delta\hat{x}(t) \tag{8.13}$$

where $A_c = A-BK-LC$, $B_c = L$ and $C_c = -K$. Its dynamics are obtained as eigenvalues of $A_c = A-BK-LC$, which need to be checked for stability. The closed-loop dynamic is as follows:

$$\frac{d}{dt}\begin{bmatrix} \delta x(t) \\ \delta\hat{x}(t) \end{bmatrix} = \begin{bmatrix} A & -BK \\ LC & A - BK - LC \end{bmatrix}\begin{bmatrix} \delta x(t) \\ \delta\hat{x}(t) \end{bmatrix} \tag{8.14}$$

The characteristic polynomial of the compensator is $|\lambda I-(A-BK)|\times|\lambda I-(A-LC)|=0$, and so the 6 eigenvalues of the above system are the same as the 3 eigenvalues of $A_{cl} = A-BK$ and the 3 eigenvalues of A_e=A-LC taken together. This fact is called the separation principle that enables us with the independent design of controller and estimator.

8.6. Design, Simulation, and Experiment

The plant is controllable and observable as M_c and M_o are full rank matrices. The eigenvalues of A_{cl} are chosen by $\omega_n=2\pi f_n=2\pi 500$ rad/sec and damping of ζ=0.8. The feedback and the input gains are obtained as K=[5.3636, 0.0031, 0.3437] and G=6.8664. The eigenvalues of estimator dynamic A_e are chosen to be around 5 to 10 times faster than the controller. For a response that is 10 times faster, the value of estimator gain L is obtained as [8.73e4, 2.34e9, 1.15e7]. Also, the compensator is stable as the eigenvalues of A-BK-LC are -42069 and -26703±11066i.

Figure 8.4(a)-(d) shows both simulation and experimental results for a square wave reference with a magnitude of ±5 degrees and a frequency of 20 Hz. The steady-state error is almost zero, voltage and current are within limits, and the experimental results are close to those expected from simulations. As shown in Figure 8.4(a), a small discrepancy is observed in the reference tracking results; the simulation predicted a small overshoot which is expected from the desired damping, while the experiment does not illustrate any overshoot. It can also be explained by the closed-loop frequency response given in Figure 8.5(a) that the experimental result shows a more damped system. This discrepancy can probably be explained by non-modeled dynamics such as friction as well as eddy-currents; as shown in Figure 8.5(b), the phase margin of the real system is a bit larger than the model, i.e., a smaller overshoot. Although the obtained phase margin looks good, the closed-loop response is a function of temperature-dependent elements such as coil resistance.

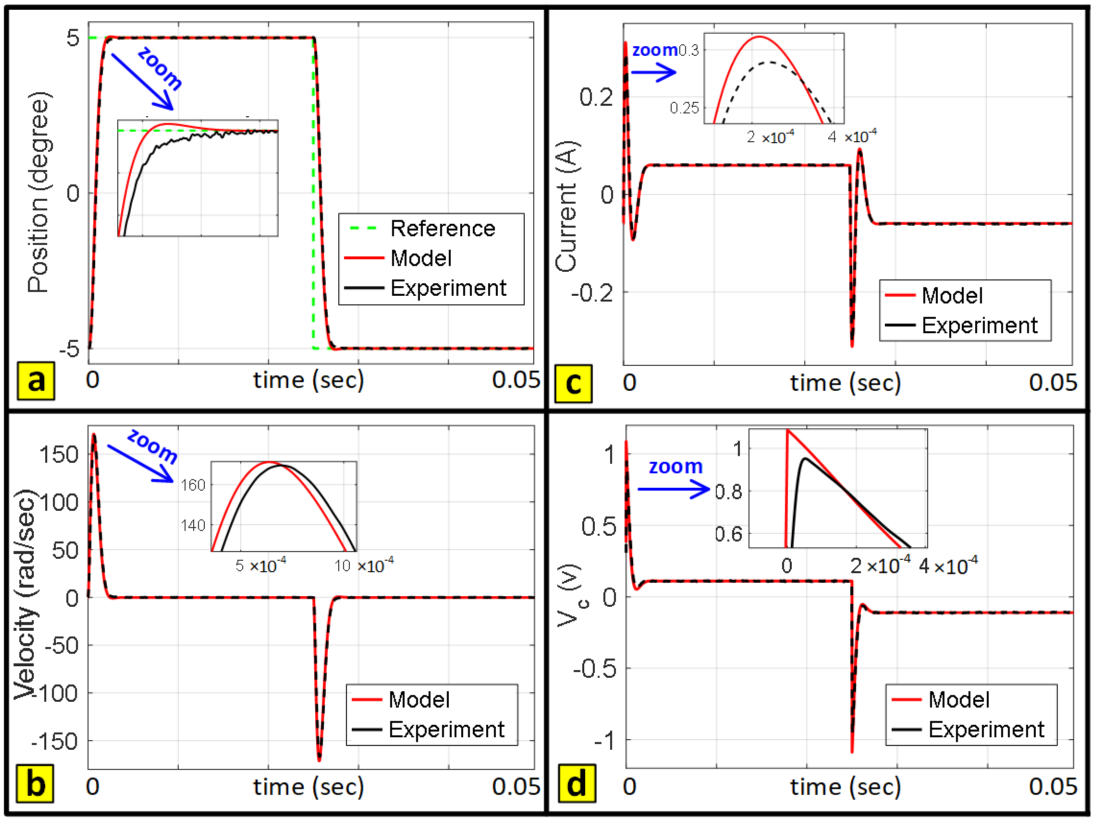

Figure 8. 4. Step response of pole placement with voltage drive: (a) position, (b) velocity, (c) current and (d) voltage

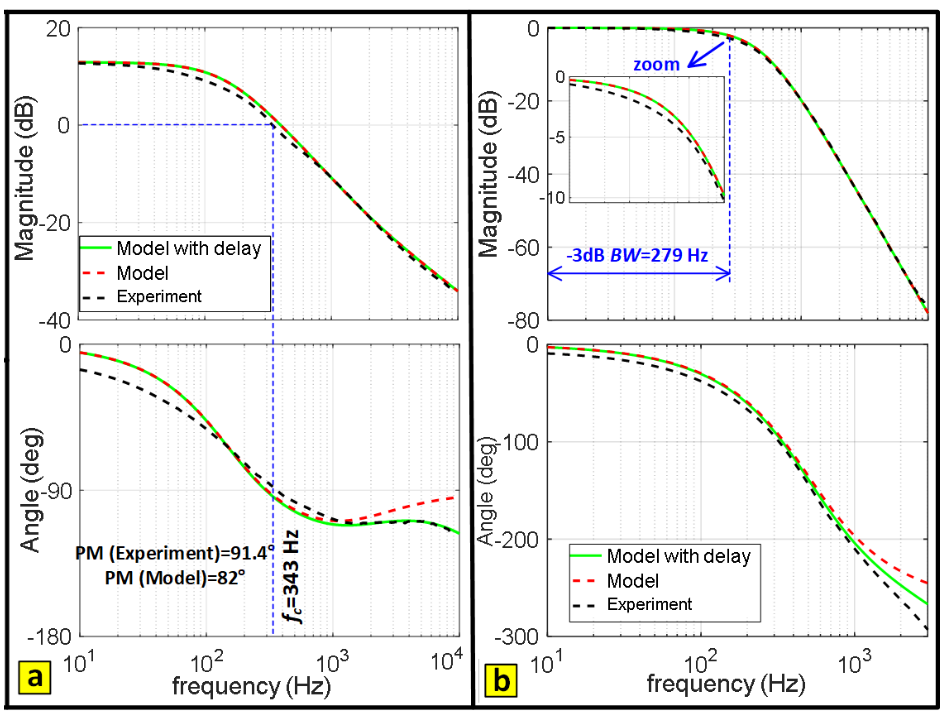

Figure 8. 5. Frequency Response of pole placement with voltage drive: (a) loop transmission, and (b) closed-loop system.

8.7. Extra Math

The relationship of the closed-loop transfer function (r to θ) is obtained as:

$$T = GC(SI - [A - BK])^{-1} B \tag{8.15}$$

Also, the loop transmission, which is the transfer function from u to the comparison point θ_k is obtained as:

$$L = \frac{\theta_k}{I_{ref}} = K(SI - A)^{-1} B \tag{8.16}$$

Corrections of the delays due to ADC and computation time can be performed by the term e^{-sT_d} where T_d is the delay. The dynamic of the current loop can be reduced to a simple gain for controller design; however, it can be included in the model to gain a higher accuracy in the designs and simulations. If the transfer function H_{CL} is the closed-loop response of the current loop (Gang 1) multiplied by the inverse of its D.C. gain to have a unity D.C. gain on total, the control effort, instead of being $U= G\theta_{ref} -K\ \delta X$, will be $U=H_{CL}(R-K\ \delta X)$. The transfer function of the plant from u to the states as outputs is the 1-input 2-output system $G_m=C(SI-A)^{-1}B$ where $C=I_{2\times 2}$. The difference between G_m and H_m is that G_m is a 2-by-1 matrix that outputs both position and velocity. Thus, a closed-loop system incorporating the current-loop dynamic is obtained as:

$$X = G_m H_{CL}(G\theta_{ref} - KX) \Rightarrow \frac{X}{\theta_{ref}} = (I_{2\times 2} + G_m H_{CL} K)^{-1} G_m H_{CL} G \tag{8.17}$$

8.8. Conclusion

In this chapter, a pole placement position control with voltage drive is developed. The drive circuit is cheap and simple. It shows acceptable performance for simple applications, but it lacks accuracy and robustness for advanced control requirements. The source of inaccuracies could be uncertainties or unmodeled dynamics like eddy-currents. A source of the lack of robustness could be the fact that the control system is dependent on the temperature-dependent resistor of the coil. In the next chapter, this issue is solved by employing a high-bandwidth current loop which eliminates the electrical dynamic, including uncertainties like eddy-currents.

Chapter 9

Pole-Placement Position Control with Current Drive

9.1 Introduction

As shown in Figure 9.1(a), using a high-bandwidth current loop as the most inner loop, the electrical dynamic of the actuator, including its time constant and complicated dynamics such as eddy currents, can be eliminated, leaving a faster plant having fewer complexities. Then, instead of the coil voltage, the current or torque can instantaneously be commanded by the position loop. The bandwidth of the current loop is around 7.86 kHz, while the desired bandwidth of the position loop is less than 500 Hz. Therefore, as shown in Figure 9.1(b), the current loop can be seen as its D.C. gain from the position loop. This gain is canceled out by its inverse in the DSP to avoid requiring to add extra gain to the plant.

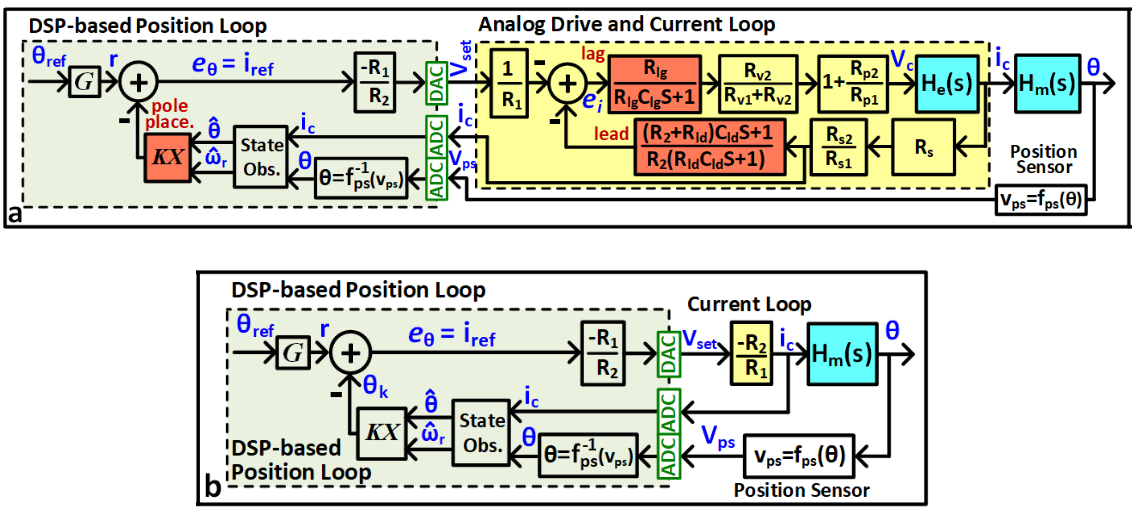

Figure 9. 1. Pole placement with current drive: (a) current and position control loops, (b) simplifying the high bandwidth current loop to its DC gain

9.2. Employed Model

As shown in Figure 9.2, eliminating the electrical dynamic by the current loop and canceling its DC gain in the DSP, the model is reduced to the second-order mechanical dynamic as follows:

$$\begin{bmatrix} \dot{\theta} \\ \dot{\omega}_r \end{bmatrix} = \begin{bmatrix} 0 & 1 \\ -K_s / J & -K_d / J \end{bmatrix} \begin{bmatrix} \theta \\ \omega_r \end{bmatrix} + \begin{bmatrix} 0 \\ k_t / J \end{bmatrix} i_c \tag{9.1}$$

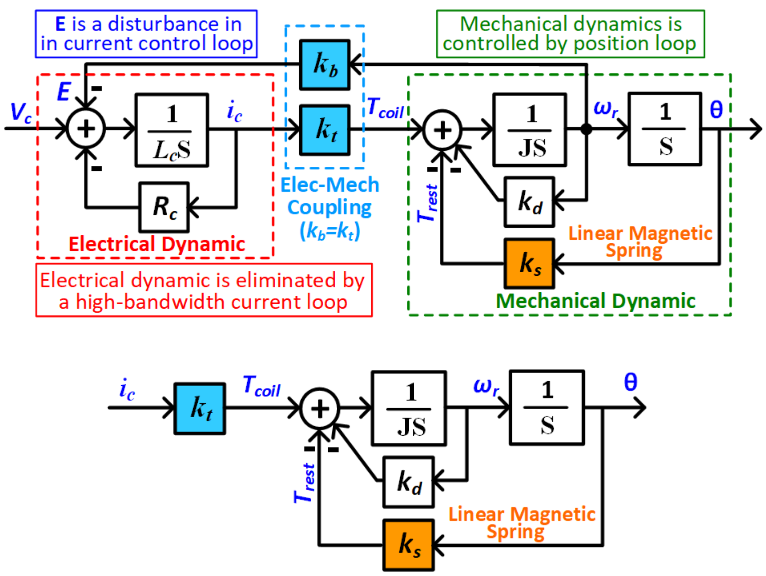

Figure 9. 2. Order reduction of the electromechanical model from three (top) to two (bottom)

9.3. Full-State Feedback Control in Time Domain

The feedback gains K=[k_1 k_2] and the unitary input gain G are obtained where C=[1 0]^t.

$$K = [0\ 1]_{1\times 2} M_c^{-1} \phi_d (A_{2\times 2});\ M_c = [\mathrm{B\ AB}] \tag{9.2}$$

$$G = -[C(A - BK)^{-1} B]^{-1} \tag{9.3}$$

9.4. Reduced-Order Estimator

The available states do not need to be estimated by the observer. Reduced-order observers are computationally more efficient, may converge faster, and have higher bandwidth. For the current drive, a reduced-order observer is employed to estimate velocity. The model can be partitioned based on the measured states $X_1=\theta$ and unmeasured ones $X_2=\omega_r$ as follows:

$$\begin{bmatrix} \dot{X}_1 \\ \dot{X}_2 \end{bmatrix} = \begin{bmatrix} A_{11} & A_{12} \\ A_{21} & A_{22} \end{bmatrix} \begin{bmatrix} X_1 \\ X_2 \end{bmatrix} + \begin{bmatrix} B_1 \\ B_2 \end{bmatrix} i_c \tag{9.4}$$

$$y = [\mathrm{I}\ 0] \begin{bmatrix} X_1 \\ X_2 \end{bmatrix} \tag{9.5}$$

The estimator in terms of the new state z can be expressed as:

$$\dot{Z} = \hat{A} Z + \hat{B}\, y + \hat{F}\, i_c \tag{9.6}$$

$$X_2 = Z + L\, y \tag{9.7}$$

whose parameters are obtained as:

$$\hat{A} = A_{22} - L\, A_{12} \tag{9.8}$$

$$\hat{B} = \hat{A} L + A_{21} - L\, A_{11} \tag{9.9}$$

$$\hat{F} = B_2 - L\, B_1 \tag{9.10}$$

Thus, the characteristic polynomial of $\hat{A}=-k_d/J-L$ has been obtained whose characteristic polynomial is $\varphi(\lambda)=|\lambda I-\hat{A}|=\lambda+k_d/J+L$. Also, the bandwidth of the estimator is λ_0, so the desired pole is $-\lambda_0$ and the desired characteristic polynomial is $\varphi_e(\lambda)=\lambda+\lambda_0$. Thus, the estimator gain is obtained as $L=\lambda_0-k_d/J$. Also, Ackermann's formula can be used to obtain estimator's gain by substituting A with A_{22} and C with A_{12} as:

$$L = \phi_e(A_{22}) M_o^{-1} [1]^t \tag{9.11}$$

$$M_o = [A_{12}] \tag{9.12}$$

It gets to the same value for L. Substituting L in (29) leads to:

$$\hat{A} = -\lambda_0 \tag{9.13}$$

$$\hat{B} = -(\lambda_0^{\ 2} - k_d \lambda_0 / J + k_s / \mathrm{J}) \tag{9.14}$$

$$\hat{F} = k_t / J \tag{9.15}$$

Finally, the velocity is obtained as $\omega_r = z + L\theta$. Using the Forward Euler, the discrete-time equations are obtained for DSP implementation as in below:

$$Z(k) = (I + T_s \hat{A}) Z(k-1) + T_s \hat{B}\,\theta(k-1) + T_s \hat{F}\, i_c(k-1) \tag{9.16}$$

$$\omega_r(k) = Z(k) + L\,\theta(k) \tag{9.17}$$

The estimator bandwidth is set to $\lambda_0 = 10\omega_n$.

9.5. Compensator

It can be shown that the characteristic equation of the compensator $|\lambda I-(A-BK)|\times|\lambda I-(A_{22}-LA_{12})|=0$, so the controller dynamic $A_{cl}=A-BK$ and the estimator dynamic $\hat{A}= A_{22}-LA_{12}$ can be designed independently.

9.6. Design, Simulation, and Experiment

The desired closed-loop poles λ_1 and λ_2 are chosen to have a natural frequency of $\omega_n=2\pi f_n=1000\pi$ rad/sec, and damping of $\zeta=0.8$ as $-\xi\omega_n \pm j\omega_n\sqrt{1-\xi^2}$, so the desired characteristics polynomial is as follows:

$$\varphi_d(\lambda) = (\lambda - \lambda_1)(\lambda - \lambda_2) = \lambda^2 + 2\zeta\omega_n \lambda + \omega_n^{\ 2} \tag{9.18}$$

The feedback gains and the unitary gain are obtained as K=[7.124, 0.0037] and G=7.806. Then, the estimator gain L is obtained as 31118.

The step responses of position, velocity, current command (scaled DAC output), and coil current are shown in Figure 9.3. The reference tracking and the performance of the current loop are very good. Not only are the results as expected from the experiment, but also, they correlate well with the simulations from the model. It can be observed that, compared to voltage drive control, the control system design using the current drive is more accurate, which is due to the elimination of electrical dynamics, including eddy currents and back-emf impact. Also, the elimination of the temperature-dependent resistance of the coil adds to the robustness of the system.

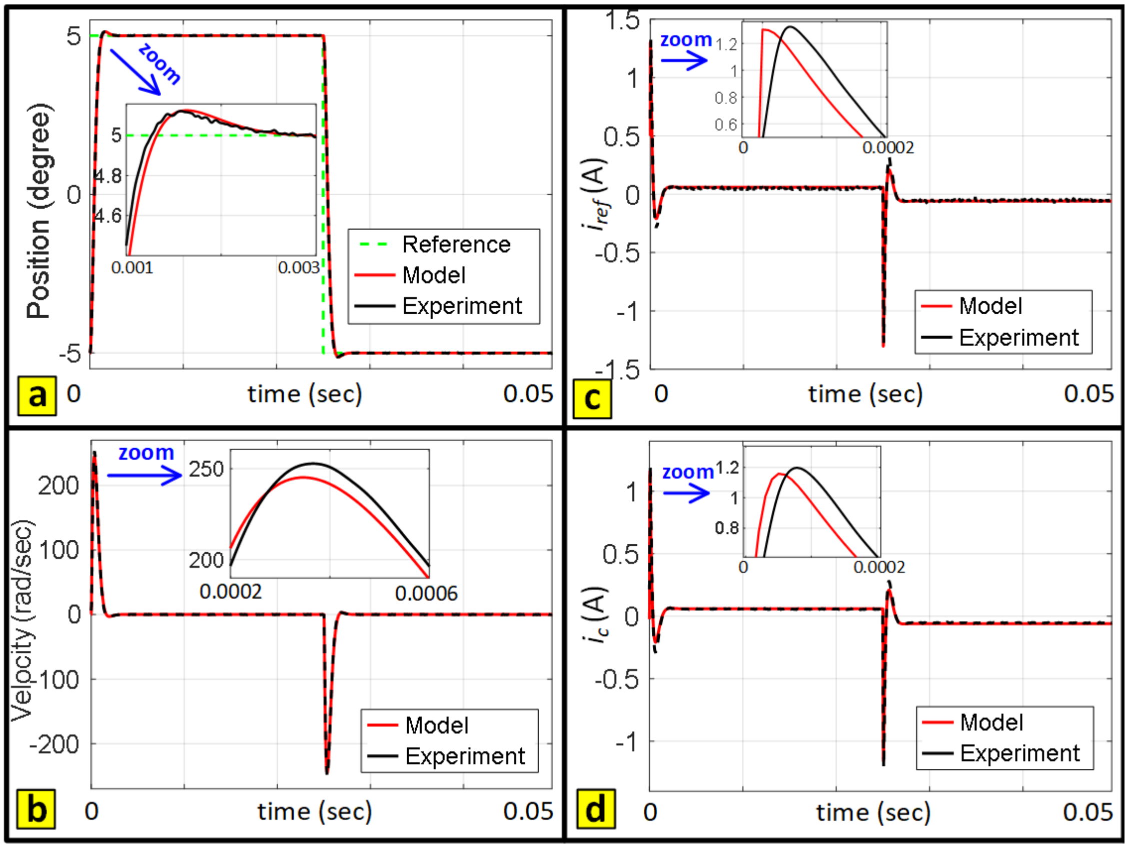

Figure 9. 3. Step response of the pole placement with current drive: (a) position, (b) velocity, (c) current command, and (d) coil current.

As shown in Figure 9.4, the performance of the system is checked in the frequency domain, illustrating a sufficient phase margin of 70 degrees and a -3dB bandwidth of 455 Hz, which is higher than the bandwidth of the pole placement control with voltage drive.

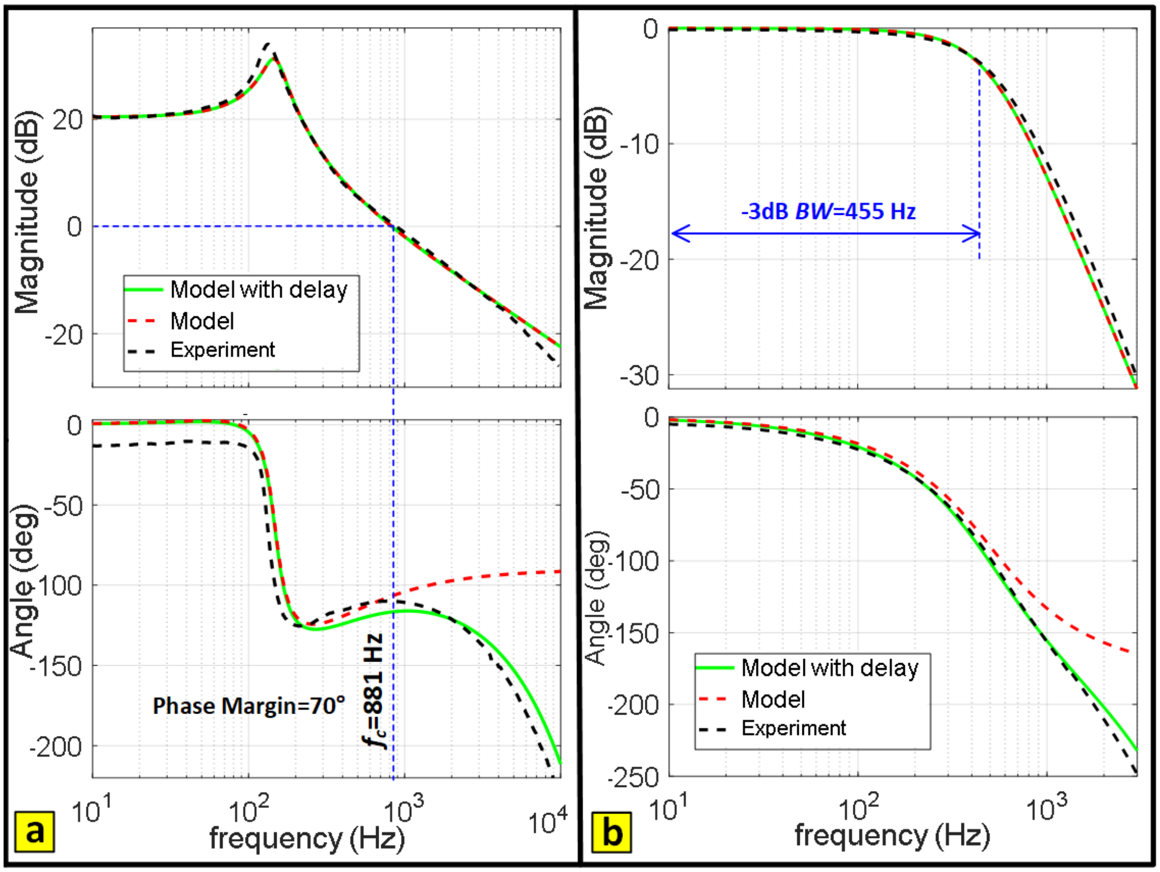

Figure 9. 4. Frequency response of (a) loop transmission, and (b) closed-loop system

As shown in Figure 9.5, there is a steady error and a bit larger overshoot in the large-signal reference tracking result of the control system for a reference amplitude of 10 degrees. It is expected as the control system was designed using the linearized model of the actuator to be employed for small-signal maneuvers. This issue can be solved using a nonlinear control system.

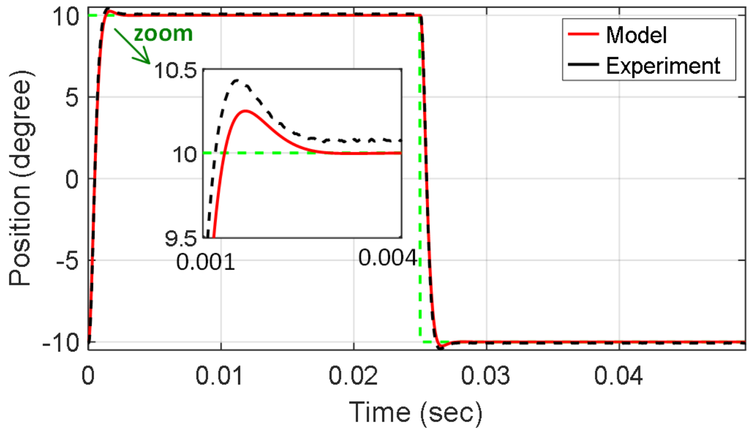

Figure 9. 5. Large-signal response of the pole placement with current drive.

9.7. Conclusion

The pole placement position control using the current drive is more accurate and more effective compared to the position control with voltage drive. It is also more robust. Also, the current or torque can be commanded directly. These advantages are provided by the high bandwidth current control loop that eliminated the electrical dynamic. Therefore, implementing a current loop as the most inner loop is always recommended. The only significant problem with the control system was large-signal control in which showed some lack of performance like steady-state error and a larger overshoot. It was expected because the linear control system design was carried out using the linearized version of the electromechanical model for small-signal deviations around the equilibrium point. The issue is solved by nonlinear control in the next chapter.

Chapter 10

Nonlinear Control by Feedback Linearization

10.1 Introduction

The linear control system techniques, as in the previous sections, work well for small-signal setpoints while, for large-signal maneuvers, they can result in unwanted inaccuracies like steady-state error, large overshoots, and even instability in severe cases. Nonlinear control provides an opportunity to work with large-signal inputs. Feedback linearization is a nonlinear technique that can be powerful in eliminating the nonlinearities of the system, yet it requires a very accurate model of the plant as well as measuring or estimating the state variable. Thanks to the accuracy of the developed nonlinear model, effective nonlinear control can be established. The current loop is employed to get a faster response and to get rid of the complexities and fractional-order elements of the electrical dynamic. Then, we only deal with the nonlinear model of the mechanical dynamic, including the nonlinear profiles of the electromagnetic torque and the magnetic spring, as shown in Figure 10.1. As the restoration torque and the electromagnetic torque are functions of the position, by substituting $\theta=\beta-\pi/2$, the nonlinear electromechanical model is obtained as follows:

$$\begin{cases} Elec: \ v_c = k_b \omega_r \cos\theta + R_c\, i_c + L_c \dfrac{di_c}{dt} \\ Mech: \ J\dfrac{d^2\theta}{dt^2} + K_d \dfrac{d\theta}{dt} + k_{rest} \sin 2\theta = k_t\, i_c \cos\theta \end{cases} \tag{10.1}$$

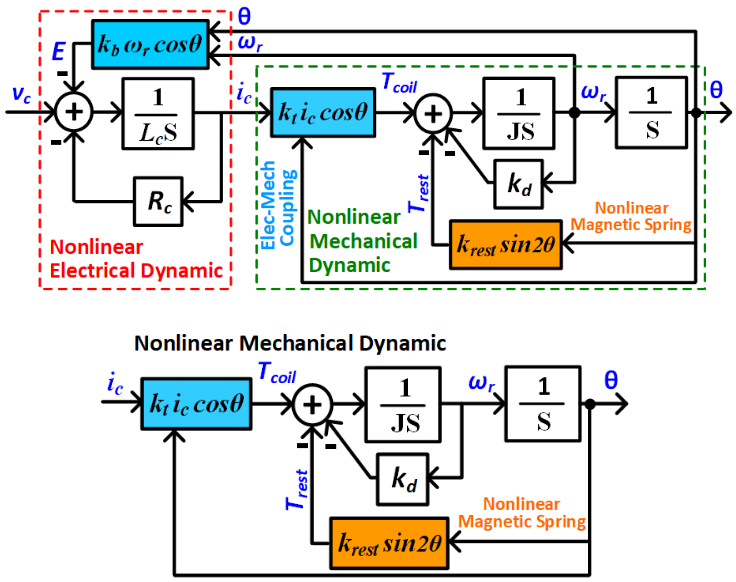

Figure 10. 1. Eliminating of the nonlinear electrical dynamic from the nonlinear mechanical dynamic (top) to reduce the system to the nonlinear mechanical dynamic (bottom)

10.2. Feedback Linearization

Feedback linearization can be implemented for a plant if its state-space model can be written in the companion form as follows:

$$\begin{cases} \dot{x}_1 = x_2 \\ \dot{x}_2 = x_3 \\ \dots \\ \dot{x}_n = f(\mathrm{x}_1,\dots,\mathrm{x}_n) + \mathrm{g}(\mathrm{x}_1,\dots,\mathrm{x}_n)\,\mathrm{u(t)} \;=\; v(\mathrm{t}) \end{cases} \tag{10.2}$$

where functions $f(x)$ and $g(x)$ are nonlinear functions of the states. $u(t)=i_c(\mathrm{t})$ is the input. In addition to a very accurate model, all of the states need to be measured or estimated in order to evaluate functions f and g. Then, the following nonlinear transformation is used at the input to cancel out the nonlinearities.

$$u(t) = \frac{1}{\mathrm{g}(\mathrm{x}_1,\dots,\mathrm{x}_n)}\left[v(\mathrm{t}) - f(\mathrm{x}_1,\dots,\mathrm{x}_n)\right] \tag{10.3}$$

It results in a linear system having n poles at the origin and with the new input $v(t)$, to which linear control techniques can be applied. The nonlinear mechanical dynamic can be written as in below:

$$\begin{cases} \dot{\theta} = \omega_r \\ \dot{\omega}_r = -\dfrac{k_d \omega_r + k_{rest} \sin 2\theta}{J} + \dfrac{k_t \cos\theta}{J} i_c = f + g\, i_c = v \end{cases} \tag{10.4}$$

Where functions f and g are obtained as:

$$f(\theta, \omega_r) = -\frac{k_d \omega_r + k_{rest} \sin 2\theta}{J} \tag{10.5}$$

$$g(\theta, \omega_r) = \frac{k_t \cos\theta}{J} \tag{10.6}$$

The nonlinear transformation at the input is as follows:

$$i_c(t) = \frac{1}{g(\theta, \omega_r)} [v(t) - f(\theta, \omega_r)] \tag{10.7}$$

Then, the remaining system is a double integrator with the new input $v(t)$, which can be designed using linear control techniques yet having a good performance in large-signal analysis and maneuvers. The new linear system is as follows:

$$\ddot{\theta} = v \;\Rightarrow\; H'_m = \frac{\theta(\mathrm{s})}{v(s)} = \frac{1}{s^2} \tag{10.8}$$

The state-space form is obtained as follows:

$$\begin{bmatrix} \dot{\theta} \\ \dot{\omega}_r \end{bmatrix} = \begin{bmatrix} 0 & 1 \\ 0 & 0 \end{bmatrix} \begin{bmatrix} \theta \\ \omega_r \end{bmatrix} + \begin{bmatrix} 0 \\ 1 \end{bmatrix} v \tag{10.9}$$

The block diagram of the feedback linearization control is shown in Figure 10.2. The current loop is treated as its D.C. gain because its bandwidth is much larger than the bandwidth of the position loop. However, like pole placement with current drive, its dynamic is accounted for in the simulations to get higher accuracy.

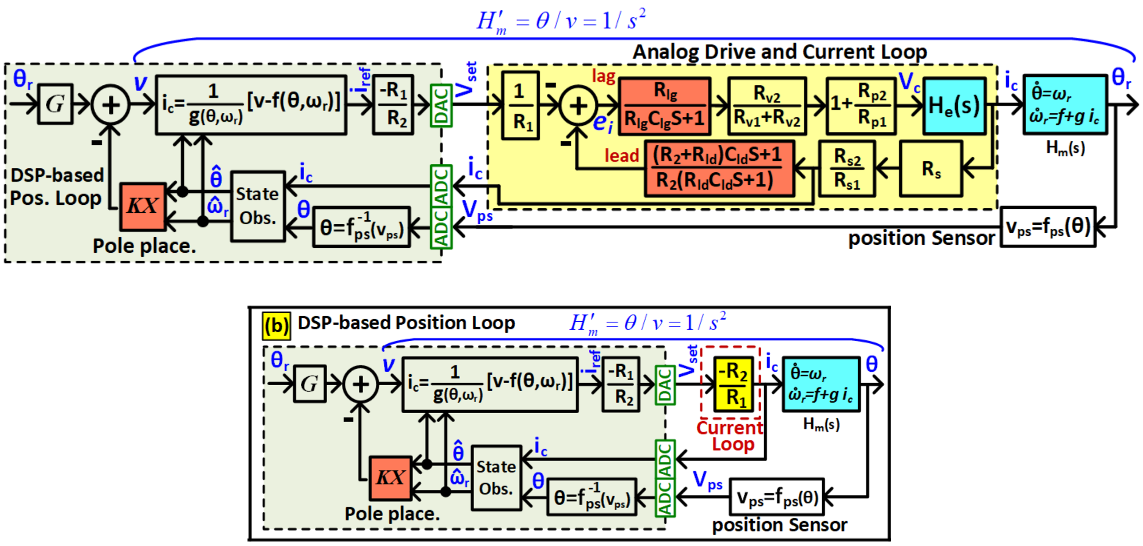

Figure 10. 2. Block diagram of the nonlinear control system using feedback linearization and pole-placement: (a) current and position control loops, (b) simplifying the high-bandwidth current loop to its DC gain

10.3. Pole Placement in Time Domain

The desired closed-loop poles λ_1 and λ_2 are chosen to have a natural frequency of $\omega_n=2\pi f_n$ and damping of ζ as $-\xi\omega_n \pm j\omega_n\sqrt{1-\xi^2}$, so the desired characteristics polynomial is as follows:

$$\varphi_d(\lambda) = \lambda^2 + 2\zeta\omega_n\lambda + \omega_n^{\ 2} \tag{10.10}$$

The matrices *A*, *B*, and *C* are obtained as:

$$A = \begin{bmatrix} 0 & 1 \\ 0 & 0 \end{bmatrix} \tag{10.11}$$

$$B = \begin{bmatrix} 0 \\ 1 \end{bmatrix} \tag{10.12}$$

$$C = [1 \;\; 0] \tag{10.13}$$

The feedback gains $K=[k_1\ k_2]$ for position and velocity obtained by Ackermann's formula as well, as the unitary input gain is obtained as follows:

$$k_1 = \lambda_1 \lambda_2 = \omega_n{}^2 \tag{10.14}$$

$$k_2 = -(\lambda_1 + \lambda_2) = 2\xi\omega_n \tag{10.15}$$

$$G = \omega_n{}^2 \tag{10.16}$$

The velocity observation is done using a derivate plus a low-pass filter which is kind of like the reduced-order observer used in the pole placement with the current drive.

10.4. The Equivalent System

Also, as shown in Figure 10.3, it can be proved by mathematical manipulations that the transfer function of the loop transmission is almost the double integrator (linearized system from v to θ) in series with a P.D. compensator in the feedback loop as in below:

$$L \approx \frac{\theta_k}{v} = \frac{\omega_n{}^2 + 2\xi\omega_n s}{s^2} \tag{10.17}$$

Therefore, the closed-loop system is obtained as:

$$\frac{\theta}{\theta_{ref}} = \frac{G/s^2}{1+L} = \frac{\omega_n{}^2}{s^2 + 2\xi\omega_n s + \omega_n{}^2} \tag{10.18}$$

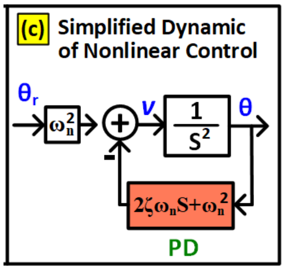

Figure 10. 3. Equivalent system of double integrator plus a PD controller in the feedback path

10.5. Design, Simulation, and Experiment

The desired closed-loop poles have a natural frequency of $\omega_n=2\pi f_n=1000\pi$ rad/sec and damping of $\zeta=0.8$. The step responses of position, velocity, current command (scaled DAC output), and coil current for a large-signal command with an amplitude of 10 degrees are shown in Figure 10.4. A comparison is also made with the simulations obtained using the model. Thanks to the accuracy of the developed nonlinear model, the nonlinear control technique works as expected, and it correlates well with the simulation results. Contrary to the linear control system, the developed nonlinear control technique works well with a large-signal input without any steady-state error.

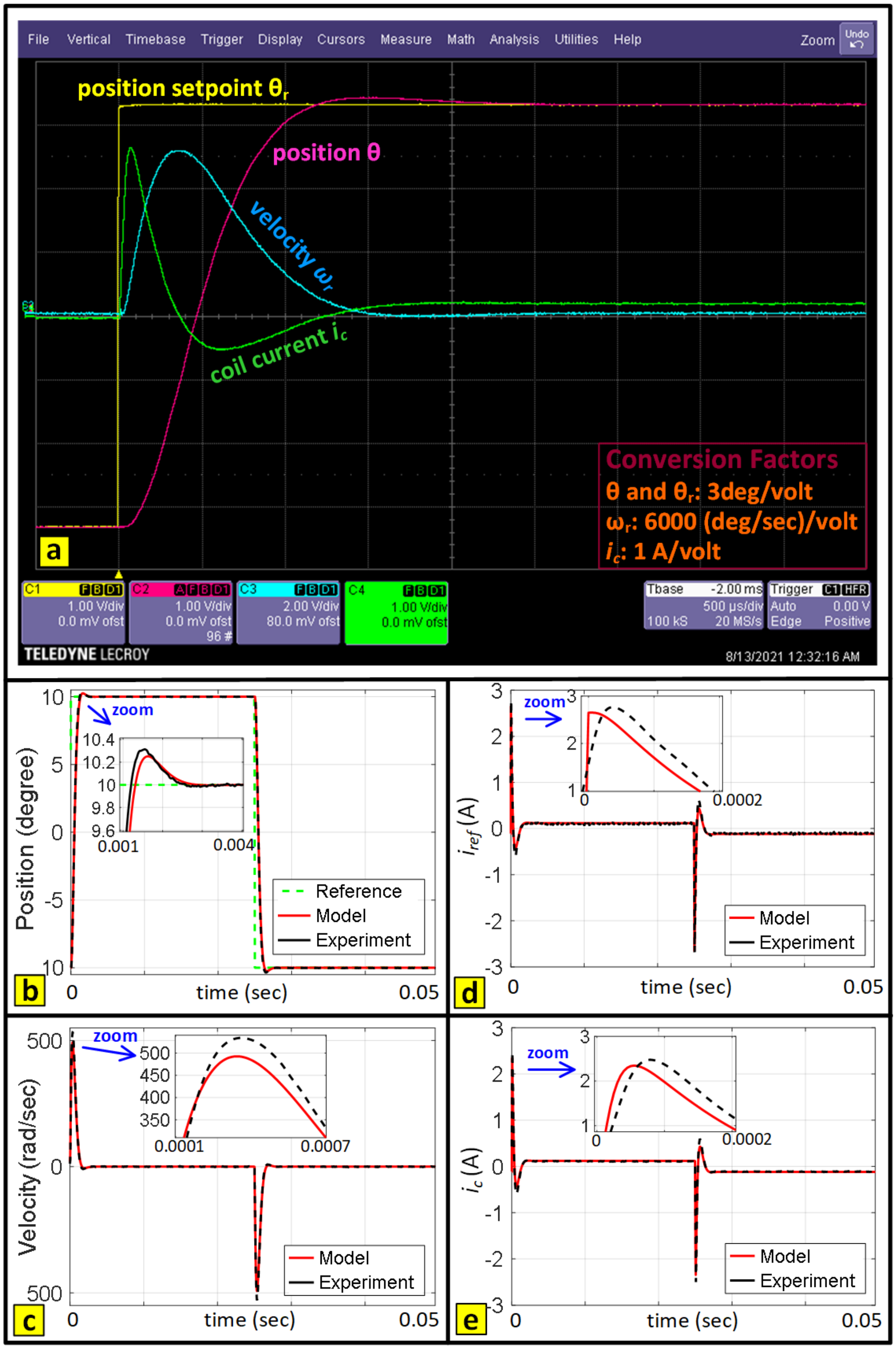

Figure 10. 4. Nonlinear control: (a) time responses, and (b)-(e) full-period waveforms and comparison with model for position, velocity, current command, and coil current.

The system performance is also checked in the frequency domain given in Figure 10.5. The frequency response of the system from the signal *v* to the position is very close to a double integrator given in Figure 10.5(a); it should be noted that its gain is attenuated for measurements by SR785 digital signal analyzer, and also a delay is observed in the phase which due to sampling and computations. It can also be seen in Figure 10.5(b)-(c) that the loop transmission is kind of a double integrator in series with a P.D. compensator. A sufficient phase margin of 59 degrees is obtained as well. As shown in Figure 10.5(d), a bandwidth of 413 Hz is obtained, which is closed to the one obtained by the linear control system with the current drive as the sensitivity is shown in Figure 10.5(e), the maximum sensitivity of the control loop is M_s=2.4 dB, showing sufficient robustness.

10.6. Conclusion

Thanks to the accuracy of the developed model, the feedback linearization technique is then used in nonlinear control for large-signal applications. It showed almost zero steady-state error. Full-order and reduced-order observers are also employed to estimate the unmeasured states. The control system designs in the thesis are evaluated through indices like rise time, overshoot, and steady-state error in the time response, as well as bandwidth, phase margin, sensitivity, disturbance rejection, and noise rejection in the frequency domain. In Table 10.1, the three position control systems are compared and ranked for different indices.

Table 10. 1 Comparison and Ranking of the Position Control Techniques

	Voltage Drive	Current Drive	Nonlinear
Bandwidth	2	1	1
Robustness	2	1	1
Accuracy	3	2	1
Small Signal	2	1	1
Large Signal	3	2	1
Simplicity/Cost	1	2	3

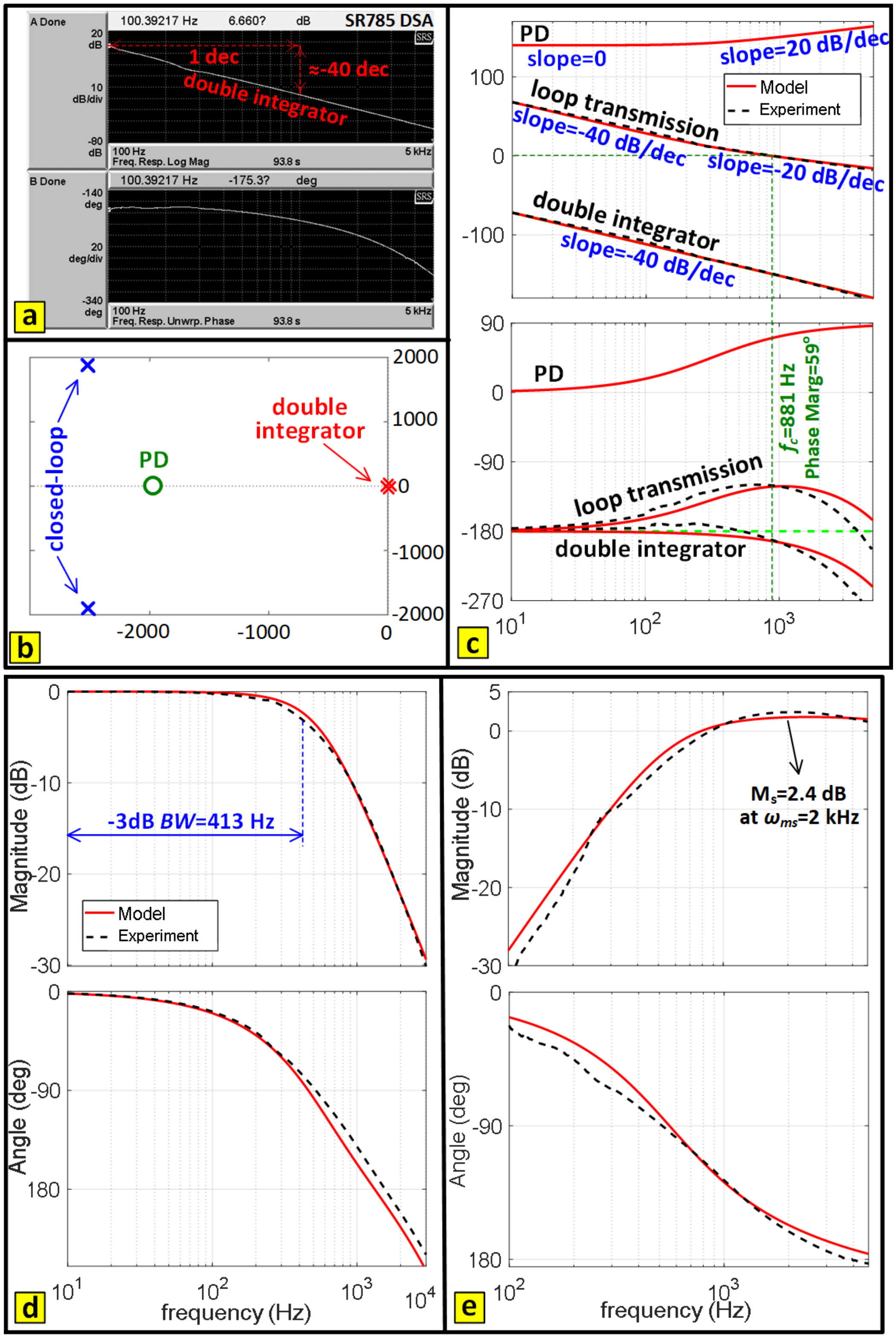

Figure 10. 5. Frequency domain analysis of nonlinear control: (a) double integrator, (b) pole locations, (c) loop components, (d) closed loop, and (e) sensitivity.

Chapter 11

Eddy-Current Plates to Reduce Leakage Inductances

11.1. Introduction

An eddy-current-based technique is proposed that may reduce the coil inductance at high frequencies. However, it is an initial examination by two-dimensional FEM, while more tests and optimizations may be done by researchers on various aspects of the technique, how to optimize the strategy, what penalties do we pay for using this method, the effectiveness of this approach, etc. It is just a conceptual study, for which a typical geometry of the actuator is picked. The default values of the conductivity of laminations and the magnet given by the software are employed. Although close, they do not accurately simulate experimental studies or even three-dimensional finite element analysis.

11.2. The Design Strategy

There are **three rules** on where to place eddy-current plates:

Rule 1: Place eddy-current plates in the regions where there exists a leakage flux that does not contribute to the torque production and only adds to the coil inductance. The plates should be placed perpendicular to the leakage fluxes to kill them through the opposing flux produced by eddy-currents induced in them.

The slot areas and the region between the edges of the two stator poles seem to be such areas.

Rule 2: Do NOT Place eddy-current plates in the region where the main flux exists. Main flux is the portion of the flux that interacts with the magnet to produce torque.

Rotor area or pole faces of the stator are such regions. A shorted turn around a pole of the stator lamination would do the same thing: killing the main flux.

Rule 3: Do NOT place eddy-current plates in regions where there is a varying flux from the rotor because it causes an eddy-current brake that acts as a damper on the rotor.

The region between the edges of the two stator poles seems to be such an areas. Also, pole faces of the stator are such regions.

11.3. Leakage Fluxes of Stator: Where to Place Eddy-Current Plates

Figure 11.1 shows the flux lines within the motor due to the coil current (no PM). It helps us find the leakage fluxes: the portion of the flux that does not interact with the magnet to produce torque and only adds to the inductance value.

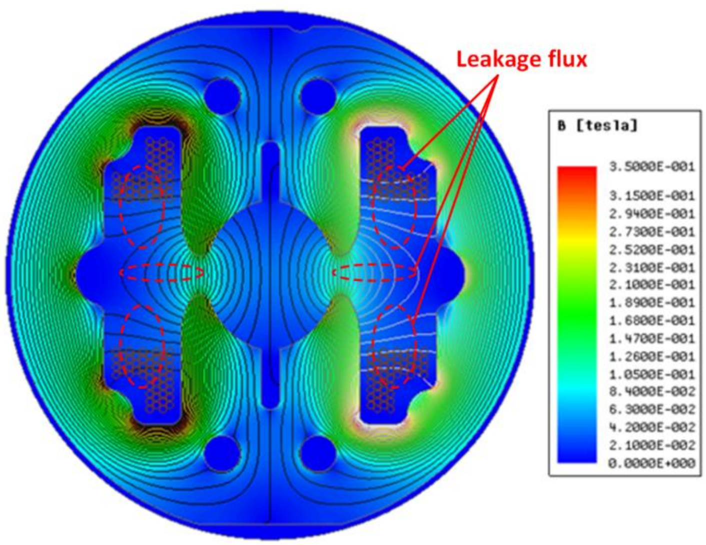

Figure 11. 1. Leakage fluxes within the actuator due to coil current: where to put eddy current plates

Most portion of the flux goes through the magnet to contribute to torque production. However, it is seen that a part of the flux lines is only a *leakage flux* that does not pass the magnet and close their path through the slots—that is to say, they do not contribute to the torque production and only add to the coil inductance. We can place eddy-current plates perpendicular to these leakage fluxes to kill them through the opposite flux produced by eddy currents induced in the plates.

11.4. Magnetic Field Produced by Rotor

Figure 11.2 shows flux lines within the motor due to the magnet (zero current) at different directions (0, 45, and 90 degrees). Watching the stray fluxed of the PM helps us to find the wrong locations to place the eddy-current plates. The eddy-current plates should not be placed where there is a varying flux from the magnet because it causes *eddy-current brake*, which is like *extra damping* on the rotor.

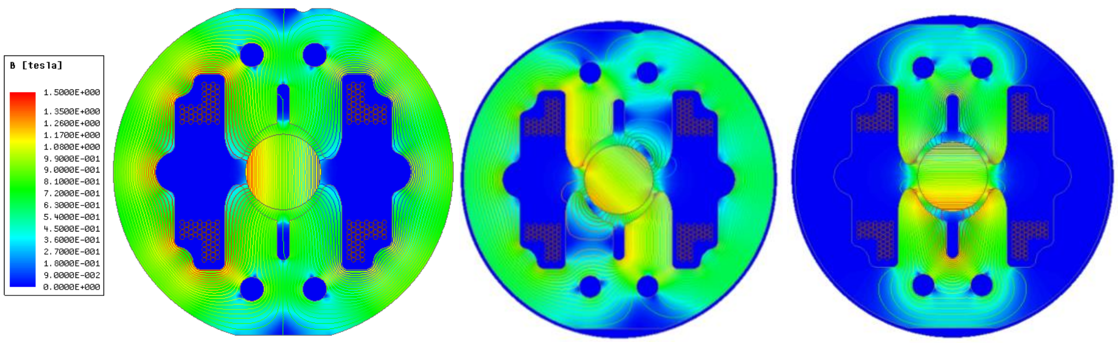

Figure 11. 2. Fluxed to the PM: where NOT to put eddy current plates

11.5. The Inductance-Frequency Profile without Eddy-Current Plates

The stator coil inductance versus frequency up to around 1 MHz is in Figure 11.3. It is seen that the inductance is about 225 µH at low frequencies while it goes down as frequency goes up. It is seen that the inductance is about **227 micro Henry** which is close but smaller than the experimental result we obtained by LCR meter. Among the sources of discrepancy could be ignoring the 3-D effects, end turns, and inaccuracy of material properties. It is observed that the inductance goes down to around **5 micro Henry** in very high frequencies. What is the reason for inductance reduction at higher frequencies? Eddy-currents in the motor elements, i.e., the magnet, the laminations, the copper coils (skin and proximity effects). In the next section, it is compared with the cases including eddy-current plates.

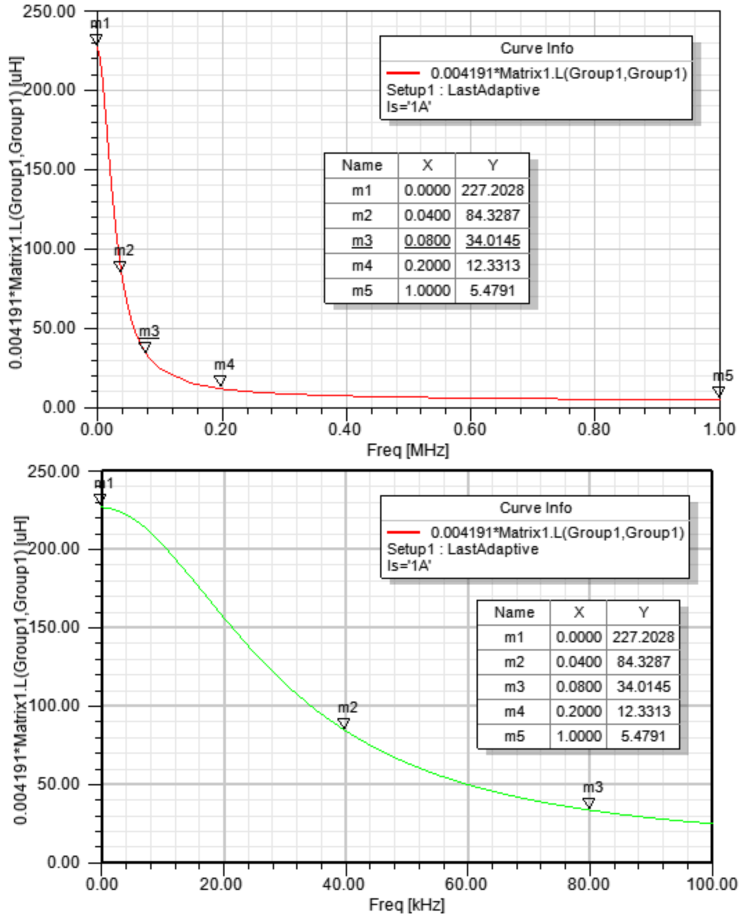

Figure 11. 3. The inductance-frequency profile without eddy-current plates obtained by FEM

11.6. Eddy-Current Plates

11.6.1. Case 1: Placing Eddy-Current Plates in Slots

In case 1, as shown in Figure 11.4, the eddy-current plates are placed in the slots perpendicular to the leakage fluxes to kill the leakage flux in the slots. The inductance versus frequency up to 1 MHz is obtained as in Figure 11.5. Some reduction is observed in the inductance profile of the device just by placing the four plates.

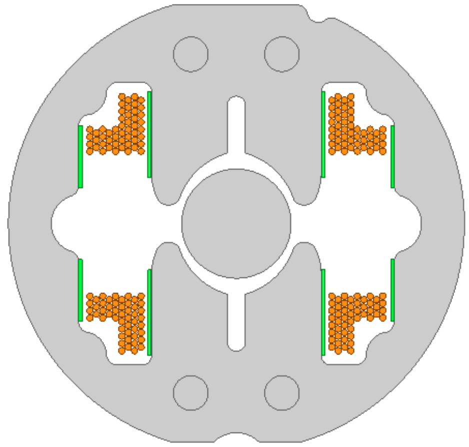

Figure 11. 4. Placing the eddy-current plates in the slots obtained by FEM

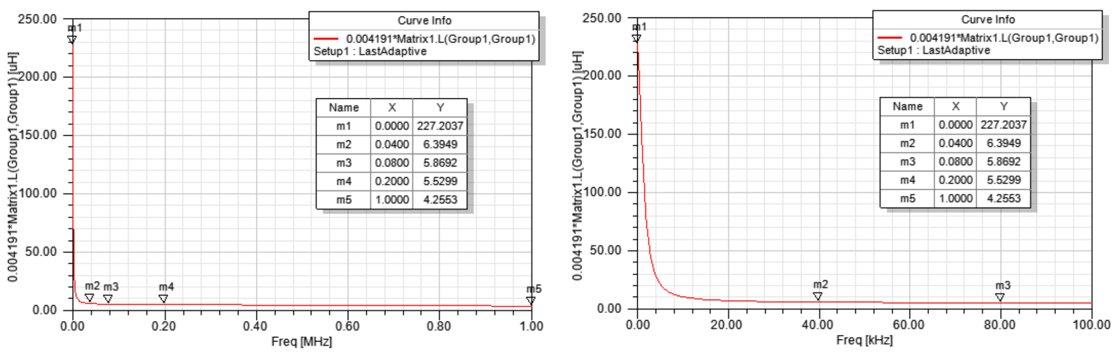

Figure 11. 5. The inductance-frequency profile when eddy-current plates are placed in the slots

11.6.2. Case 2: Placing Eddy-Current Plates in Slots and Interpolar Regions

In case 2, as shown in Figure 11.6, two more eddy-current plates are placed in the interpolar region to kill the leakage fluxes between the two edges of each of the two-pole faces. The inductance versus frequency up to 1 MHz is shown in Figure 11.7. There is not a significant improvement compared to case 1 by adding these to plates. As shown in Figure 11.8, the two eddy-current plates are thickened and moved toward the center such that they have more interaction with the leakage fluxes in the interpolar region. Almost no impact on inductance reduction is observed.

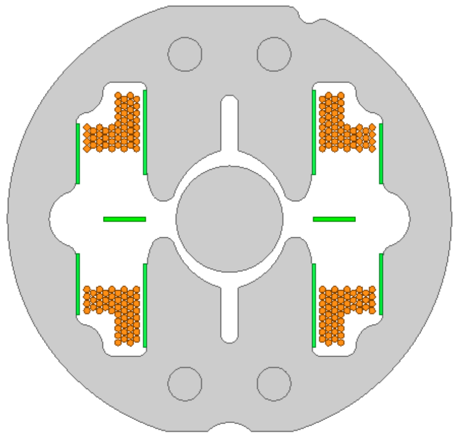

Figure 11. 6. Placing the eddy-current plates in the slots and the interpolar regions

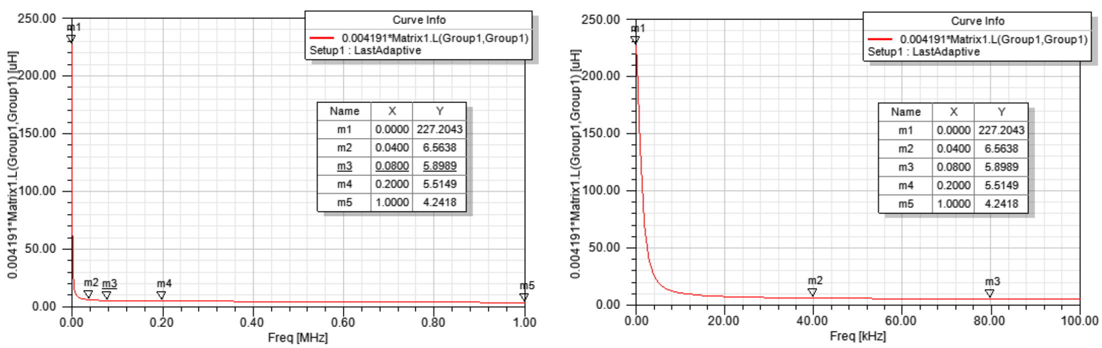

Figure 11. 7. The inductance-frequency profile when eddy-current plates are placed in the slots and the interpolar regions obtained by FEM

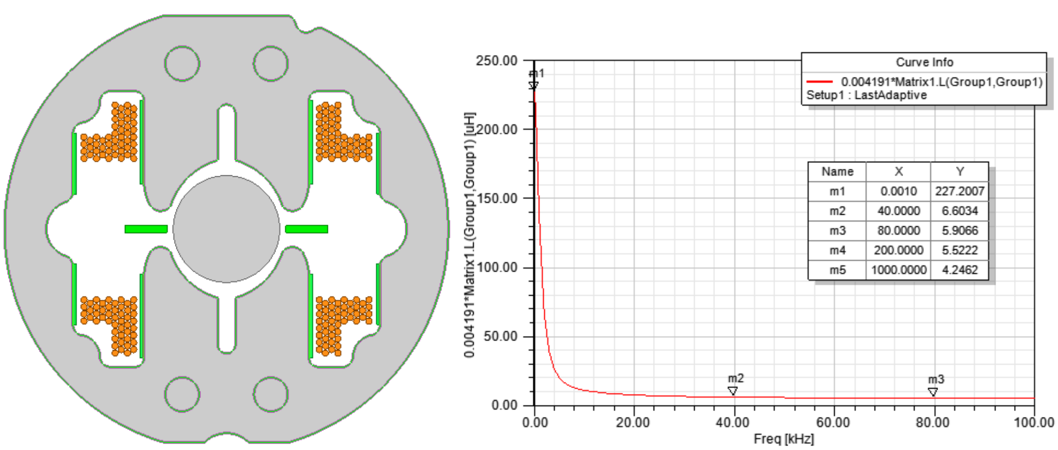

Figure 11. 8. Increasing the thickness of eddy current plates and moving them toward the center

11.7. Conclusion

An elementary conceptual study is carried out to study the feasibility of reducing the coil inductance using eddy current operations in some conductive plates called eddy-current plates. A strategy is explained on where to or not to place the plates. It is observed that it can kill the leakage fluxes and reduce the inductance. The penalty for placing the eddy current plates can be limiting the coil area or producing more heat due to the induced eddy currents. One may study the impact of the material and thickness of the plates, the best locations to places the, etc. Performing several experiments could also be helpful. In an elementary test that we performed, there was a difference ib the results. The inductance reduction happened at higher frequencies compared to simulations. However, optimations and more concrete experiments are needed to test and verify the idea.

Chapter 12

A Proposed Effectiveness Index

12.1 Introduction

A new effectiveness index is proposed that may represent the effectiveness of an actuator with oscillational behavior in a better way. Like the previous chapter, more investigations and discussions can be done on the proposed effectiveness index herein.

13.2 Power Flow Inside an Electric Motor

In the motoring operation, the electrical power is the input to the coil terminals. Then, energy conversion from electrical to mechanical occurs in the air-gap through the magnetic field media, and finally, mechanical power is produced on the shaft as the output. We also have losses with the path from input to output. The electric power terms are as in below

Instantaneous power:

$$p_e(t) = v(t)\, i(t) \tag{12.1}$$

Apparent Power S_e:

$$|S_e| = \frac{1}{2} V_m\, I_m = V_{rms}\, I_{rms} \tag{12.2}$$

$$V_{rms} = \frac{V_m}{\sqrt{2}} \quad and \quad V_{rms} = \frac{I_m}{\sqrt{2}} \tag{12.3}$$

The apparent Power has two components: *active power P* and *reactive power Q*.

Active Power P_e:

It is the portion of power flow that, averaged over a complete cycle of the AC waveform, results in a net transfer of energy in one direction is known as real power (also referred to as active power). This is the real power (average power) we usually talk about and is the component that does the work. It is the power in the resistive part of the circuit. The unit of P is Watt.

$$P_e = \frac{1}{T}\int_0^T p_e(t)dt = \frac{1}{T}\int_0^T v(t)\, i(t)dt = \frac{1}{2} V_m\, I_m \cos\varphi_e \tag{12.4}$$

where the angle φ is the angle between voltage and current

$$P_e = |S_e|\cos\varphi_e = \frac{1}{2}V_m I_m \cos\varphi_e = V_{rms} I_{rms} \cos\varphi_e \tag{12.5}$$

Reactive Power Q_e:

That portion of power flow due to stored energy that returns to the source in each cycle is called reactive power. It is the power in the reactive part of the circuit (inductor or capacitor). The unit of Q is Var.

$$Q_e = |S_e|\sin\varphi_e = \frac{1}{2}V_m I_m \sin\varphi_e = V_{rms} I_{rms} \sin\varphi_e \tag{12.6}$$

Note:

- For a resistive load, $\varphi=0$ and so $\cos\varphi=1$, $\sin\varphi=0$, i.e., we only have active power
- For a reactive load (inductor or capacitor), $\varphi=+90$ or -90 and so $\cos\varphi=0$, $\sin\varphi=1$, i.e., we only have reactive power—no work is done.

12.3. Traditional Notion of Mechanical Power:

In linear-motion systems, mechanical power is force (N) times linear speed (m/sec):

$$p_m(t) = F(t)\, v(t) \tag{12.7}$$

In rotational systems, mechanical power is torque (N.m) times rotational speed (rad/sec):

$$p_m(t) = T(t)\, \omega(t) \tag{12.8}$$

Average Mechanical Power:

We know that p(t) oscillates with time. The average power is the average of p(t) over a period as in below:

$$P_m = \frac{1}{T}\int_0^T p_m(t)dt = \frac{1}{T}\int_0^T T(t)\,\omega(t)dt = \frac{1}{2}T_m\,\omega_m \cos\varphi_m \tag{12.9}$$

where φ_m is the angle between torque and velocity.

12.4. New Definition: Apparent, Active and Reactive Mechanical Power

- **Problem:** For evaluating an actuator with oscillating rotation, the traditional power definition might not always reflect the satisfactory performance of the actuator.
- For example, when a torque *T* is applied to a pure inertia *J*, the output velocity $\boldsymbol{\omega}$ is lagging the torque by 90 degrees. Thus, the average mechanical power, which is the integration of a sine waveform times a cosine, is zero. However, it is doing something for us by rotating the rotor, so we may define a new power index!

$$P_m = \frac{1}{T}\int_0^T p_m(t)dt \; = \frac{1}{T}\int_0^T sin\left(\frac{2\pi}{T}t\right) cos(\frac{2\pi}{T}t)dt \qquad (12.10)$$

- As another example, when there is a lag (e.g., 20 degrees in an inertia plus damper system) between the torque and velocity, there are instances when instantaneous power is negative. What should we think about that? Should we take the absolute value before calculating the average?!
- **Proposed Solution:** To solve this issue, we can define the counterpart of apparent electrical power for mechanical power. Then, we can calculate the efficiency as the ratio of apparent mechanical power on the rotor shaft (output) to apparent electrical power at the coil terminal (input).

Apparent Mechanical Power:

$$S_m = \frac{1}{2}T_m \; \omega_m = \; T_{rms} \; \omega_{rms} \qquad (12.11)$$

$$T_{rms} = \frac{T_m}{\sqrt{2}} \quad and \quad \omega_{rms} = \frac{\omega_m}{\sqrt{2}} \qquad (12.12)$$

Apparent Power *S* has two components: ***active power*** $\boldsymbol{P_m}$ and ***reactive power*** $\boldsymbol{Q_m}$

Active Mechanical Power:

It has properties as in below:

- The portion of power flow that, averaged over a complete cycle, results in a net transfer of energy in one direction, which is known as real power (also referred to as active power)

- This is the *real power (average power)* we usually talk about and is the component that is doing work.

$$P_m = \frac{1}{T}\int_0^T p_m(t)dt = \frac{1}{T}\int_0^T T(t)\omega(t)\,dt = \frac{1}{2}T_m\,\omega_m\,cos\varphi_m \qquad (12.13)$$

where the angle φ_m is the angle between torque and velocity.

- It is the power in the **damper** part of the circuit. A damper in a mechanical circuit is like a resistor in an electrical circuit. They both dissipate energy.

$$P_m = S_m\,cos\varphi_m = \frac{1}{2}T_m\,\omega_m\,cos\varphi_m = T_{rms}\,\omega_{rms}\,cos\varphi_m \qquad (12.14)$$

- The unit of P_m is *Watt***.**

Reactive Mechanical Power:

- That portion of power flow due to stored energy that returns to the source in each cycle is known as reactive power.
- It is the power in the reactive part of the circuit (inertia or spring)**.**

$$Q_m = S_m\,sin\varphi_m = \frac{1}{2}T_m\,\omega_m\,sin\varphi_m = T_{rms}\,\omega_{rms}\,sin\varphi_m \qquad (12.15)$$

- The unit of Q is *Var***.**

12.5. The Traditional Efficiency and the New effectiveness Index:

Traditional Definition of Efficiency:

- Efficiency is the ratio of output power to input power.

$$Efficiency = \frac{P_{out}}{P_{in}} \qquad (12.16)$$

- By substitution, we have:

$$Efficiency = \frac{P_{out}}{P_{in}} = \frac{\frac{1}{2}T_m\,\omega_m\,cos\varphi_m}{\frac{1}{2}V_m\,I_m\,cos\varphi_e} = \frac{\frac{1}{2}K_t\,I_m\,\omega_m\,cos\varphi_m}{\frac{1}{2}V_m\,I_m\,cos\varphi_e} = \frac{K_t\,\omega_m}{V_m}\,\frac{cos\varphi_m}{cos\varphi_e} \qquad (12.17)$$

- Here, P_{in} is the *Average Electrical Power (Active Electrical Power)* at the coil terminals, and P_{out} is the *Average Mechanical Power (Active Mechanical Power)* on the shaft

- **Issue:** For evaluating an actuator with oscillating rotation, the traditional power definition might not always reflect a satisfactory performance of the actuator.
- For example, when a torque *T* is applied to a pure inertia *J*, the output velocity $\boldsymbol{\omega}$ is lagging the torque by 90 degrees ($cos\varphi_m = 0$). Thus, the average mechanical power, which is the integration of a sine waveform times a cosine, will be zero. However, it is doing something for us by rotating the rotor, so we may define a new efficiency index!

The Proposed Definition for Effectiveness:

- The **solution** we propose for the mentioned problem is to define efficiency as the ratio of the apparent mechanical power to the apparent electrical power, i.e., removing $\boldsymbol{cos\varphi_m}$ and $\boldsymbol{cos\varphi_e}$ from the traditional notion of efficiency.

$$Effectiveness = \frac{|S|_{out}}{|S|_{in}} \tag{12.18}$$

- It may be called *Apparent Efficiency* or *Apparent-Power Efficiency*.
- By substitution, we have:

$$Effectiveness = \frac{S_{out}}{S_{in}} = \frac{\frac{1}{2} T_m\ \omega_m}{\frac{1}{2} V_m\ I_m} = \frac{\frac{1}{2} K_t\ I_m\ \omega_m}{\frac{1}{2} V_m\ I_m} = \frac{K_t\ \omega_m}{V_m} \tag{12.19}$$

- It is seen that it leads to efficiency as the ratio of back-EMF over terminal Voltage because $E = K_t$ ω.

$$Effectiveness = \frac{E_m}{V_{rms}} \tag{12.20}$$

- This is very interesting because the back-EMF is also zero at zero velocity, where mechanical power is also zero.

- It can also be represented with *RMS* values as in below:

$$Effectiveness = \frac{K_t\ \omega_{rms}}{V_{rms}} \tag{12.21}$$

12.6. Frequency-Domain Analysis of Efficiency (New Definition by Reactive Power):

For the new definition of effectiveness defined as the ratio of the amplitude of back-EMF ($k_t\omega$) to the terminal voltage amplitude, a *transfer function* can be defined whose input and output are terminal voltage and back-EMF, respectively.

$$Effectiveness = \frac{E_m}{V_{rms}} = \frac{K_t\ \omega_{rms}}{V_{rms}} \tag{12.22}$$

We can obtain the transfer function from terminal voltage to the position as follows:

$$\frac{\theta\,(s)}{V(S)} = \frac{K_t}{L\ J\ s^3 + (R\ J + L\ K_d)\ s^2 + \left(R\ K_d + K_s\ K_d + {k_t}^2\right)s + R\ K_s} \tag{12.23}$$

Therefore, just by taking a derivative (multiplying numerator by S), we can get the transfer function from terminal voltage to the velocity:

$$\frac{\omega\,(s)}{V(S)} = \frac{k\ s}{L\ J\ s^3 + (R\ J + L\ K_d)\ s^2 + \left(R\ K_d + K_s\ K_d + {k_t}^2\right)s + R\ K_s} \tag{12.24}$$

Then by multiplying by torque constant k_t, we can get the transfer function from terminal voltage to the back-EMF, which is the proposed effectiveness index as follows:

$$Effectiveness(s) = \frac{E\,(s)}{V(S)} = \frac{{k_t}^2\ s}{L\ J\ s^3 + (R\ J + L\ K_d)\ s^2 + \left(R\ K_d + K_s\ K_d + {k_t}^2\right)s + R\ K_s} \tag{12.25}$$

If we multiply the two sides by current, it gives effectiveness as the ratio of the input power to the converted power.

$$Effectiveness(s) = \frac{E\,(s)I(s)}{V(S)I(s)} = \frac{input\ power}{converetd\ power} \tag{12.26}$$

The absolute and logarithmic values of the new effectiveness index as a function frequency are shown in Figure 12.1. It is seen that the peak happens at a mid-frequency around the natural frequency of the mechanical dynamic. It makes sense as the back-emf gets its peak value around that frequency. At zero frequency, where the velocity and so back-EMF are zero, there is no output mechanical power, and thus the effectiveness value is zero. At a mid-frequency, a resonance happens, which corresponds to the maximum power conversion and maximum effectiveness.

This frequency can be understood by *Maximum power transfer theory* if we define an equivalent impedance for the back-EMF as in below:

$$Z_E(s) = \frac{E\,(s)}{I(S)} = \frac{{k_t}^2\, s}{J\, s^2 + K_d s + K_s} \tag{12.27}$$

The maximum happens around a frequency where $Z_{coil} \approx Z_{emf}^{*}$. In other words, if coil resistance is close to the equivalent back-emf resistance ($R_c \approx R_{emf}$), and coil reactance is close to the negative back-emf reactance ($X_c \approx -X_{emf}$), i.e., emf reactance looks capacitive. In Figure 12.2, the magnitude-phase, as well as the real-imaginary components of the impedances of the coil (Zcoil=R+jω), back-emf and total impedance, are plotted.

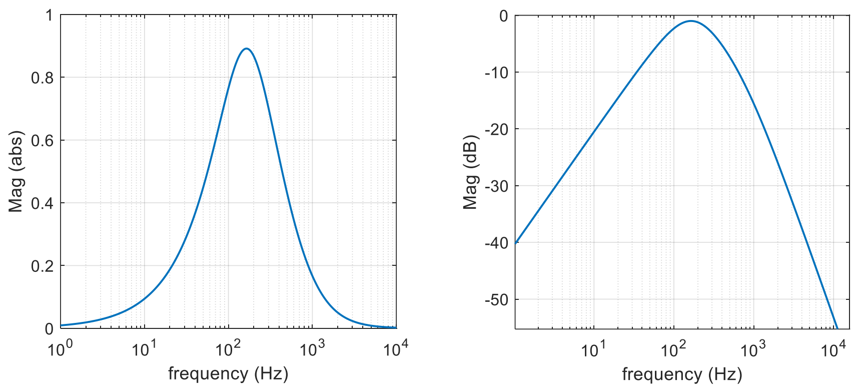

Figure 12. 1. Effectiveness index versus frequency

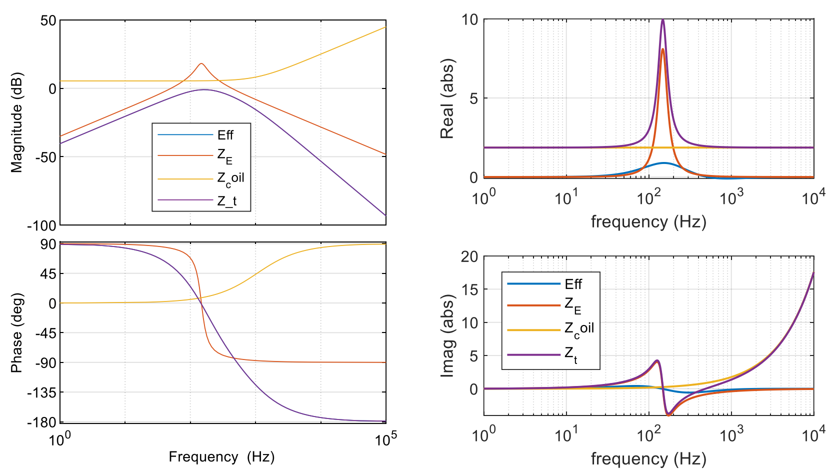

Figure 12. 2 Impedances of coil Z_{coil}, back-emf Z_E and the total Z_t

12.7. Conclusion

In this chapter, an effectiveness index is proposed that may evaluate the performance of oscillating actuators in a better way. However, more analysis and experiments may be carried out about it. To this end, apparent mechanical power is defined whose concept is like apparent electrical power. Therefore, the effectiveness index is defined as the ratio of apparent mechanical power as the output of the actuator to the apparent electrical power as the input of the device. A new parameter is defined as the equivalent impedance of the back-emf, representing the converted energy. Then, a discussion is made with the theory of maximum power transfer.

Chapter 13

Conclusion and Future Works

13.1 Conclusions

An electromechanical model is developed for an actuator whose stator curvature is nonuniformly shaped to have a reluctance torque in addition to the coil torque. The rotor's permanent magnet is incorporated in the model through equivalent Amperian currents. To model the actuator, the complicated geometry of the stator is substituted with an equivalent ellipse having a surface current density representing the stator current. The coil torque is obtained using the Lorentz force and the solution of Laplace's equation in terms of both scalar and vector potentials in the elliptical coordinates. The reluctance torque is obtained using the energy method and differential flux tubes that incorporate the variation of current enclosed in the flux loops. In addition to the detailed explanations, an attempt is made to visualize the modeling procedure and the field distributions so that the readers can clearly understand the ideas and utilize them in their research. Also, the finite element method is employed in the field analysis and development of the model. In the end, the actuator is prototyped. The model produces the results in a few seconds while, depending on the desired accuracy, it could take a couple of hours up to a few days using a FEM. It is shown that the equivalent geometry produces the same field solution within the rotor area as the original geometry. Normal and tangential components of magnetic flux density, flux lines, magnetic scalar potential, magnetic vector potential, coil torque, reluctance torque, and total torque are extracted and analyzed. A very close agreement is observed among the results obtained from the analytical model, FEM in the simplified geometry, FEM in the original geometry, and experimental results from the prototyped device.

In addition, a nonlinear and linear electromechanical model of an actuator with magnetic restoration is developed for dynamic and control studies. The eddy currents in the laminations and the magnet are included in the model by extracting a lumped-element framework from the analytical solution of the diffusion equation, which provides very high accuracy for dynamic and control studies of the device. The impact of friction on the mechanical dynamic is investigated. The design considerations of the actuator are explained as well. The lab experiments are performed using a prototype actuator, illustrating a very good correlation with the results obtained by modeling and FEM. Torque and back-emf profiles are obtained, and the identification of the model is carried out. Then, an analog drive circuit is proposed, designed, and precisely modeled by a third-order model of the op-amps, whose ideal version is then employed in the design of the current control loop. The accuracy of the drive modeling, as well as the effectiveness of the actuator model in the current loop, is studied, and the design trade-offs are analyzed. Then, three DSP-based position control techniques are implemented. First, a pole placement position control with voltage drive is developed, showing acceptable performance for simple applications but lacking accuracy and robustness for advanced control requirements. Second, by employing the developed current control loop, the complexities of the electrical dynamic are eliminated, and then a pole placement position control with the current drive is implemented whose accuracy and robustness are improved while still lacking effectiveness for large-signal purposes. Thanks to the accuracy of the developed model, the feedback linearization technique is then used in nonlinear control for large-signal applications. Full-order and reduced-order observers are also employed to estimate the unmeasured states. The control system designs are evaluated through indices like rising time, overshoot, and steady-state error in the time response, as well as bandwidth, phase margin, sensitivity, disturbance rejection, and noise rejection in the frequency domain. The three-position control systems are compared and ranked for different indices.

Also, an elementary conceptual study is carried out to study the feasibility of reducing the coil inductance using eddy current operations in some conductive plates called eddy-current plates. A strategy is explained on where to or not to place the plates. It is observed that it can kill the leakage fluxes and reduce the inductance. The penalty for placing the eddy current plates can be limiting the coil area or producing more heat due to the induced eddy currents. One may study the impact of the material and thickness of the plates, the best locations to places the, etc. Performing several experiments could also be helpful. At the end, an effectiveness index is proposed that may evaluate the performance of oscillating actuators in a better way. However, more analysis and experiments may be carried out about it. To this end, apparent mechanical power is defined whose concept is like apparent electrical power. Therefore, the effectiveness index is defined as the ratio of apparent mechanical power as the output of the actuator to the apparent electrical power as the input of the device. A new parameter is defined as the equivalent impedance of the back-emf, representing the converted energy. Then, a discussion is made with the theory of maximum power transfer.

13.2 Future Works and Recommendations for the Designers

- Other control techniques for position control might be studied. Input shaping or prefilters to make the step setpoint smoother to avoid overshoots and thus saturation in the power op-amp can be a good investigation.

- Design and implementation of a loop-shaping control with higher bandwidth for the position loop can be studied. Its design procedure is presented in the Appendix.

- Developing a switching drive would be an interesting subject. It can provide a higher voltage and current capability, plus a smaller copper loss compared to the op-amp-based analog drive. However, it may introduce noise and switching ripple to the system.

- Modeling the switching drive would be an interesting case study as well. It provides a simulation platform to study the input shaping and prefilters and auto-tuning systems. Then, it can be compared with the modeling and design of the op-amp-based current control loop and drive.

- The switching drive can be implemented by an op-amp-based current control loop just by substituting the power op-amp with an H-bridge, including an extra circuit to convert the output of the compensator to a PWM to drive the gates of the MOSFETs. It can be done by comparing the output of the compensator with a sawtooth wave. Also, filters may be used at the H-bridge to filter out the high-frequency stuff.

- The switching current control loop may also be implemented digitally by DSPs or FPGAs. For example, both current and position loops may be implemented in one DSP, or the current loop may be implemented by an FPGA to have a faster dynamic while the position loop is implemented in a DSP as the outer loop.

- A high-precision friction model may also be important, especially if the device is going to work in low frequencies where the stiffness of the system matters. It can also be an interesting research direction.

- If the device works at a sufficiently high frequency where the inertia is dominant, the magnetic spring and the friction stiffness might not be a significant matter in the dynamic behavior of the device. However, the magnetic spring might still be required as a fail-safe operation. For example, in laser projection applications, the magnetic spring provides safety for situations when the current is removed from the stator or when the actuator is going to start from turn-off mode; it avoids projecting the laser beam at unwanted locations that can damage the people or the equipment.

- Flux feedback can be an interesting control strategy that may be studied. Actually, in electric machines, the coil current produces a magnetic flux in the air gap, then the magnetic flux interacts with the rotor (here the PM), and finally, a torque is produced. If eddy currents are ignored, there is no phase shift between flux and torque. Therefore, by eliminating the electrical dynamic using a high-bandwidth current loop, torque is related to the current with a torque constant k_t. Then, the current loop is just the torque loop, and commanding the current is just commanding the torque. However, if we have significant eddy currents in the device, torque and current are not related by just a simple gain k_t because the reluctance is a function of frequency. Therefore, the torque constant k_t, instead of being a simple gain, will be frequency-dependent. The torque constant k_t will have a frequency response that relates torque to current with magnitude and a phase at any frequency. In this case, the current loop might not be as effective as the normal cases. As a solution, having a flux loop can be helpful because commanding the flux is like commanding the torque. The diagram is given in Figure. 13.1.

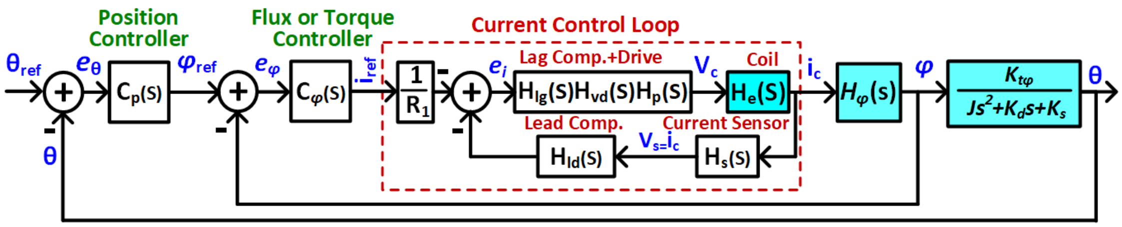

Figure 13. 1. Impedances of coil Z_{coil}, back-emf Z_E and the total Z_t

Measurement or Estimation of Magnetic Flux:

Four methods for estimating or measuring the flux are proposed, as given in Figure. 13.2.

1. Measurement by an extra coil around pole faces

Having an extra coil (maybe one or two turns) around the pole faces can be used for flux measurement to be employed in feedback control.

$$E_\varphi = N_\varphi \frac{d\varphi}{dt} \Rightarrow \varphi = \frac{1}{N_\varphi}\int E_\varphi \, dt \tag{13.1}$$

2. Flux Estimation by the Eddy-Current Model

A method to estimated flux would be the eddy current modeling using the diffusion equation. In chapter 6, we obtained the relationship of flux and current as a function of terminal voltage as n below:

$$\begin{cases} V_c = R_c I_c + j\omega N\varphi \\ NI_c = (R_{t0} + R_{e.i} + R_{e.m})\varphi \end{cases} \Rightarrow \begin{bmatrix} R_c & j\omega N \\ -N & R_{t0} + R_{e.i} + R_{e.m} \end{bmatrix} \begin{bmatrix} I_c \\ \varphi \end{bmatrix} = \begin{bmatrix} V_c \\ 0 \end{bmatrix} \tag{13.2}$$

According to the above equation, a model-based flux estimator can be implemented if the coil current is available.

3. Flux estimation by Coil Current

Current can be directly measured or estimated by the last equation. To clarify, having the terminal voltage measured, the coil current and the core flux can be estimated using the above equation.

$$\varphi(s) = \frac{N\, I_c(s)}{R_{t0} + R_{e.i}(s) + R_{e.m}(s)} \tag{13.3}$$

4. Flux Estimation by voltage and current of the coil

Also, if identification of the frequency-dependent reluctances were difficult, a flux estimator may be implemented using the measured values of the terminal voltage and the coil current as follows:

$$v_c(t) = R\, i_c(t) + N \frac{d\varphi}{dt} \quad \Rightarrow \quad \varphi = \frac{1}{N} \int [v_c(t) - R\, i_c(t)\, dt \tag{13.4}$$

Having the flux measured or estimated, a flux loop may be implemented around the current loop to eliminate the frequency-dependent torque constant or the delay between current and flux. Then, the output of the position loop is just the torque input to the mechanical dynamics of the device. It will be a simple yet accurate flux estimation. Just the value of the coil resistance is required.

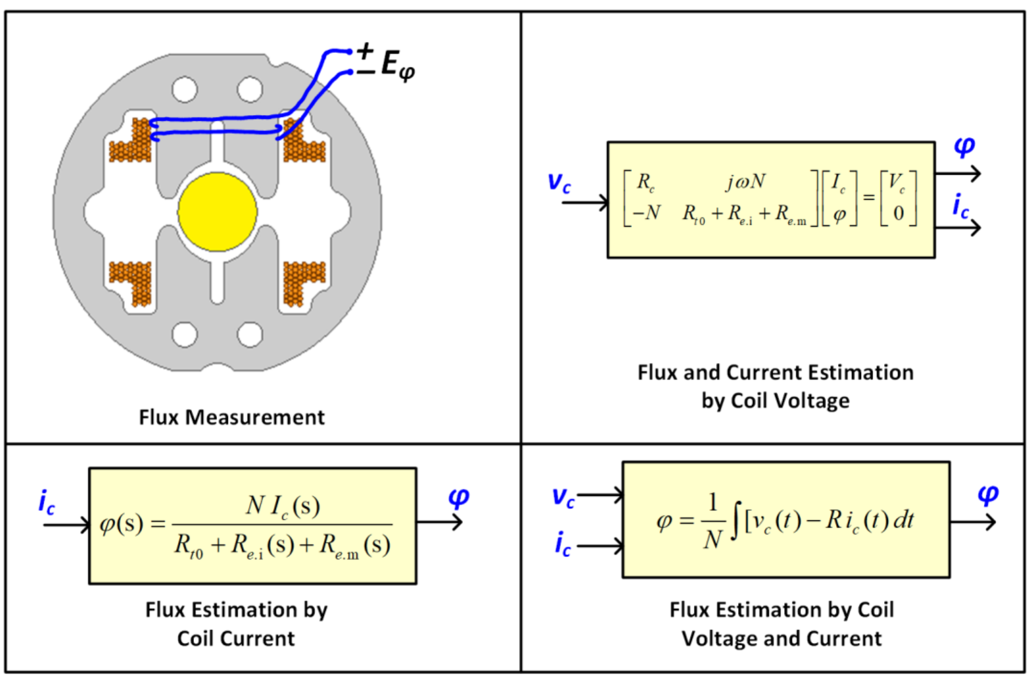

Figure 13. 2. The methods for measurement or estimation of the flux

Appendix A

Experimental Results of Identification of Mechanical and Electrical Dynamics

Identification of Mechanical Dynamics and Friction Test

The current loop is used as a current source to excite the transfer function of the mechanical dynamic H_m, and the voltage from the sensor is measured. The result obtained from Dynamic Signal Analyzer SR785 is shown in Figure A.1. The sensor voltage is 10 volt/25 degrees. In other words, there is the following extra gain in the magnitude of the frequency response that needs to be subtracted at the end:

$$G_{sensor} = 20\log_{10}\left\{\frac{10\,volt}{25\,\text{degress}} \times \frac{180\,\text{deg}\,rees}{\pi\; radians}\right\} \tag{A.1}$$

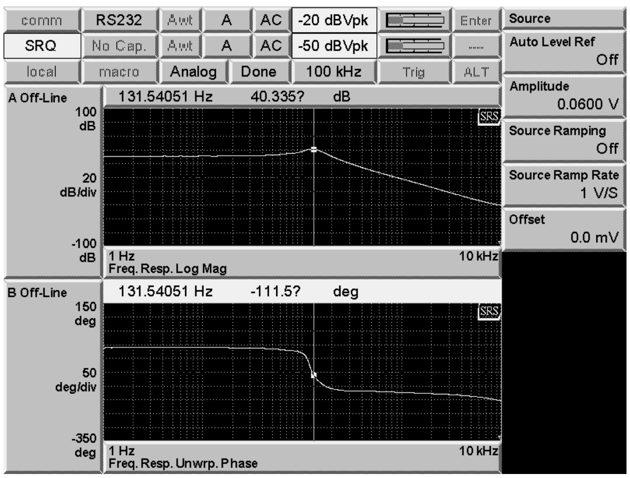

Figure A. 1. The Mechanical Dynamic obtained by SR785

Friction Test:

The impact of the friction in the pre-sliding regime can be modeled by damping and stiffness. This impact is a function of the amplitude of the position. Figure A.2 shows the bode plot and the time responses of the mechanical dynamics of the actuator, i.e., coil current as input and position as output. It can be observed that for smaller amplitudes, the DC gain goes down. In other words, as the torque constant k_t is constant, the total stiffness goes up for smaller amplitudes. It can be seen that, for a very small amplitude of 10 mv, the friction of bearing becomes significant as the rotor stops rotating at some frequencies. In the plots, when the amplitude is decreased, the faint curve is the one from the previous test, which is left there for comparison. The time profiles of coil current (almost double the setpoint of the current loop) and position for different amplitudes of current are shown in Figure A.3. There is a voltage offset at the position sensor, which is caused by misalignment of the light blocker of the sensor on the rotor, which should be canceled out.

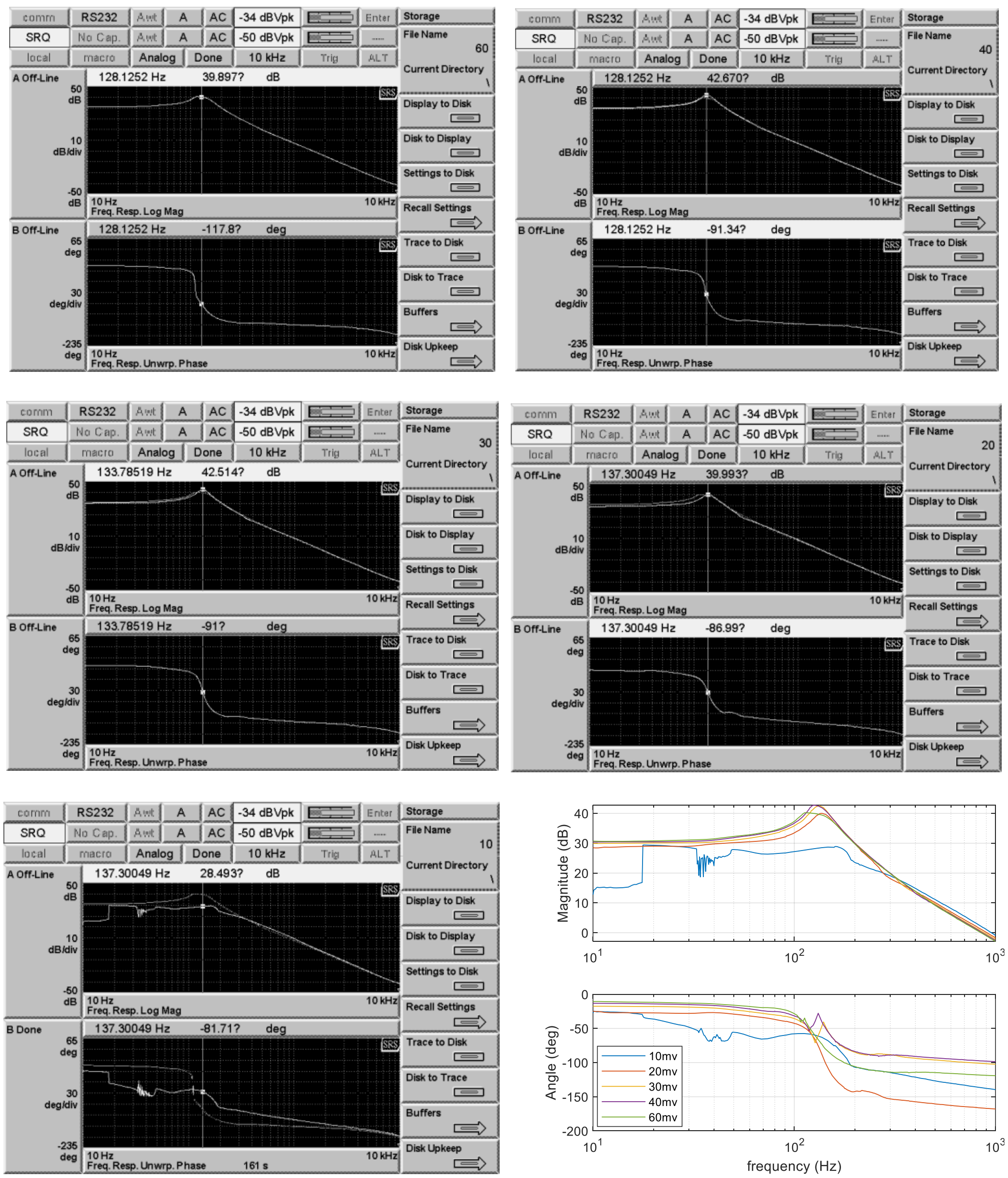

Figure A. 2. The frequency response of the mechanical dynamic for different amplitudes of the injected signal which is the setpoint of the current loop: (a) 60 mv, (b) 40 mv, (c) 30 mv, (d) 20 mv, (e) 10 mv, and (f) all together.

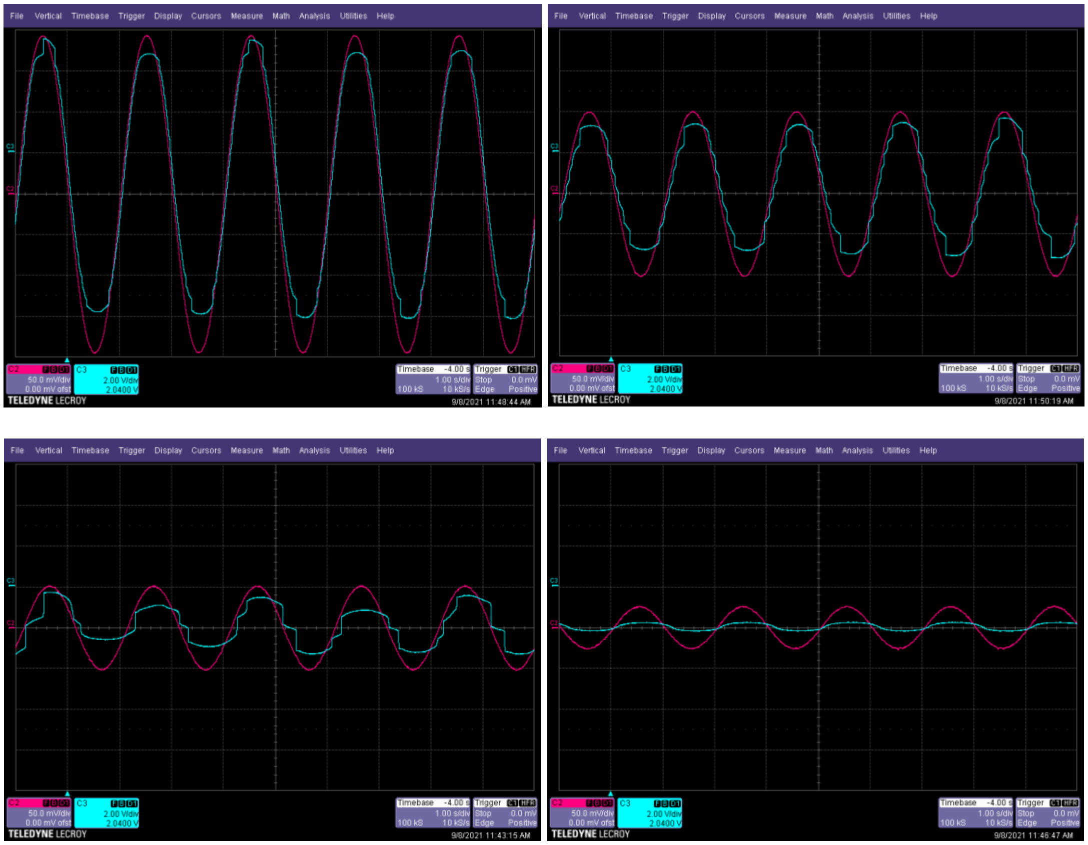

Figure A. 3. The frequency response of the mechanical dynamic for different amplitudes of the injected signal which is the setpoint of the current loop: (a) 200 mA, (b) 100 mA, (c) 50 mA, and (d) 25 mA.

Identification of Electrical Dynamics

The result is shown in Figure A.4. For frequencies above 10 kHz, the magnetic coupling between the position sensor and coil comes in, which ruins the frequency response. When the rotor is free to move, the resonance frequency is exactly at the natural frequency of the mechanical dynamic, as it is caused by the effect of back-emf, which is proportional to the mechanical velocity.

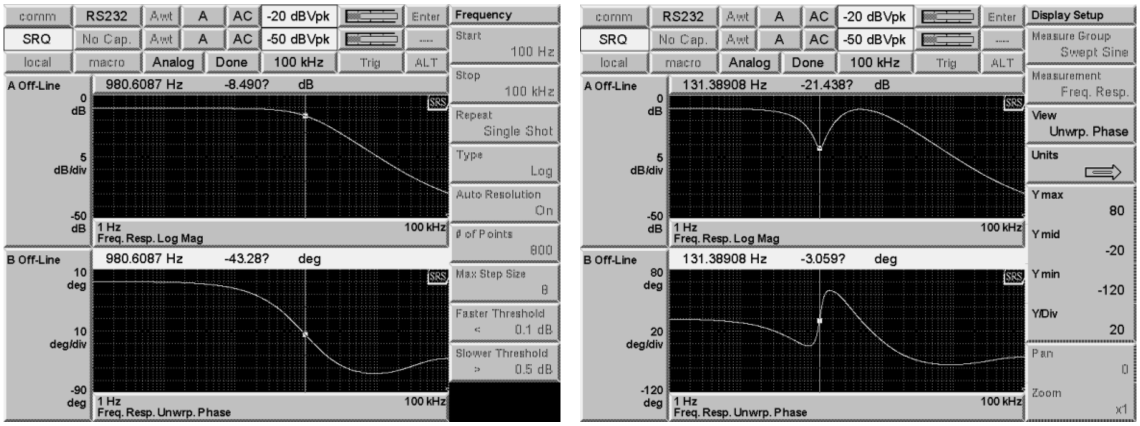

Figure A. 4. The frequency response of the electrical dynamic: with rotor free to move H_m' (left) and with locked rotor H_m (right) obtained by SR785.

Appendix B

Experimental Results of Drive and Current Loop

Frequency Response of Compensator and Loop Transmission

To obtain the frequency response of the loop transmission, the total gain of the loop needs to be attenuated so that the coil winding is not damaged by a very large current. This attenuation can be obtained by attenuator pads or adding a parallel resistor to the grounded resistor of the voltage divider. This attenuation gain should be canceled out at the end. The results are given in Figure B.1.

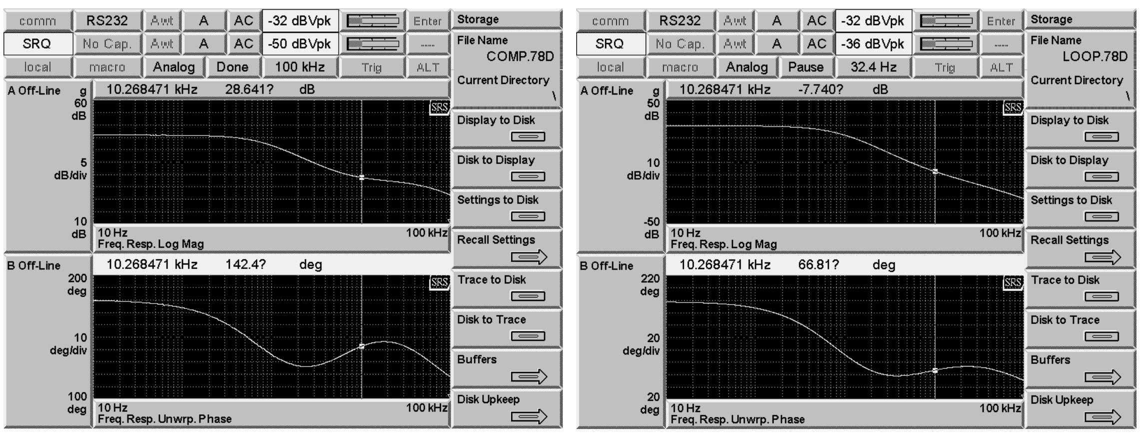

Figure B. 1. Frequency response of compensator (left) and loop transmission (right).

Frequency Responses of Gangs 3 to Six Using the Frequency Responses of the Loop Transmission and the Plant

Having the experimental results for the loop transmission $L=PCH$ and the plant $P=H_e$, the gangs 3 to 6 can be obtained as:

$$G3 = \frac{P}{1+L} = \frac{P}{1+PCH} \tag{B.1}$$

$$G4 = \frac{1}{1+L} = \frac{1}{1+PCH} \tag{B.2}$$

$$G5 = \frac{(L/P)}{1+L} = \frac{CH}{1+PCH} \tag{B.3}$$

$$G6 = \frac{L}{1+L} = \frac{PCH}{1+PCH} \tag{B.4}$$

The results obtained using the above method are given in Figure B.2. However, they can directly be measured or approximated by injecting signals to the appropriate points. It is possible with op-amp circuits as the input impedance of an op-amp is infinite, and the output impedance is zero. However, in our drive circuit, calculating them using the loop transmission and the plant was more accurate.

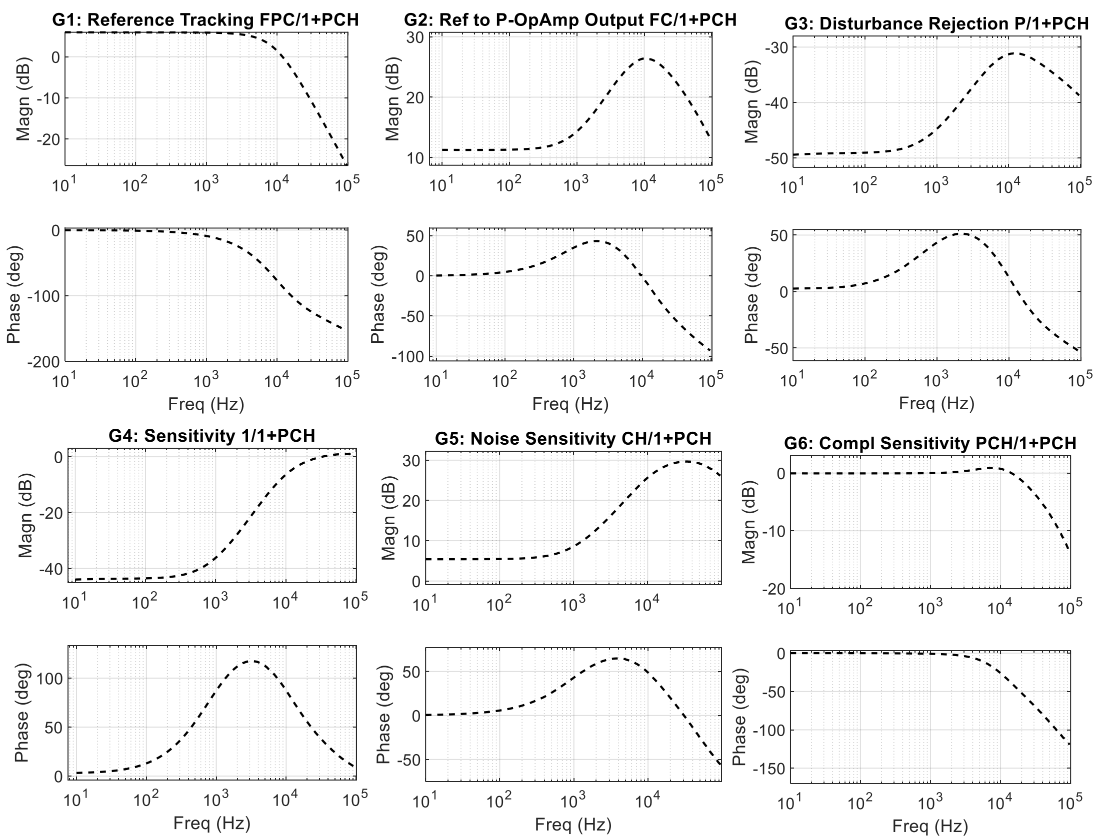

Figure B. 2. Frequency response of compensator (left) and loop transmission (right).

Frequency and Step Responses of Gang 1 and Gang 2

The inverted input of the current loop is excited. The coil current is measured at the output of the current sensor buffer to get Gang 1. The output of the power op-amp is measured to get Gang 2. The results for locked and unlocked rotor cases are shown in

Figure B.3 and Figure B.4. For the unlocked case, there is a hump at the natural frequency of the mechanical dynamic, which is caused by back-emf as observed in the electrical dynamic of the actuator when back-emf is included:

$$H_e{}'(s) = \frac{I_c}{V_c} = \frac{Js^2 + k_d s + k_s}{L_{co} Js^3 + (R\,J + L_{co} k_d)s^2 + (R\,k_d + k_s k_d + k_t{}^2)s + R\,k_s} \tag{B.5}$$

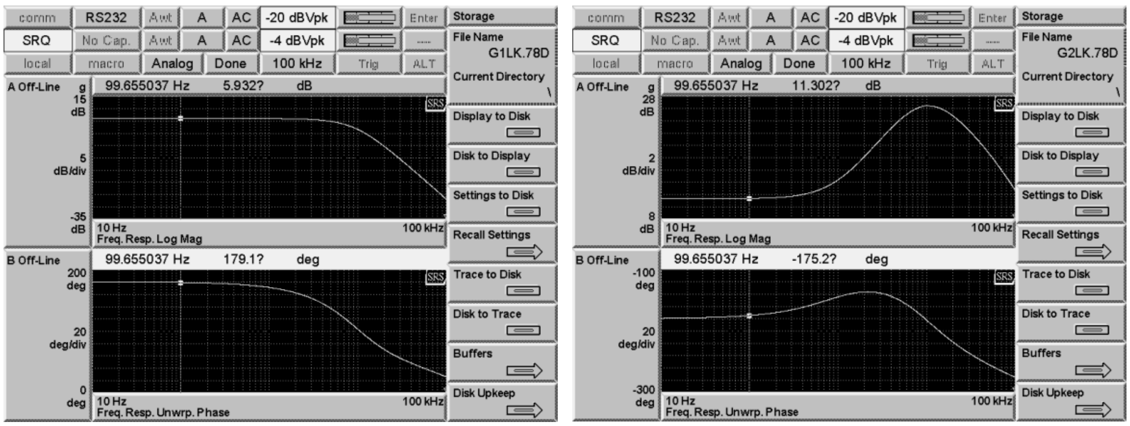

Figure B. 3. Frequency Response of Gang 1 (left) and Gang 2 (right) when the rotor is locked.

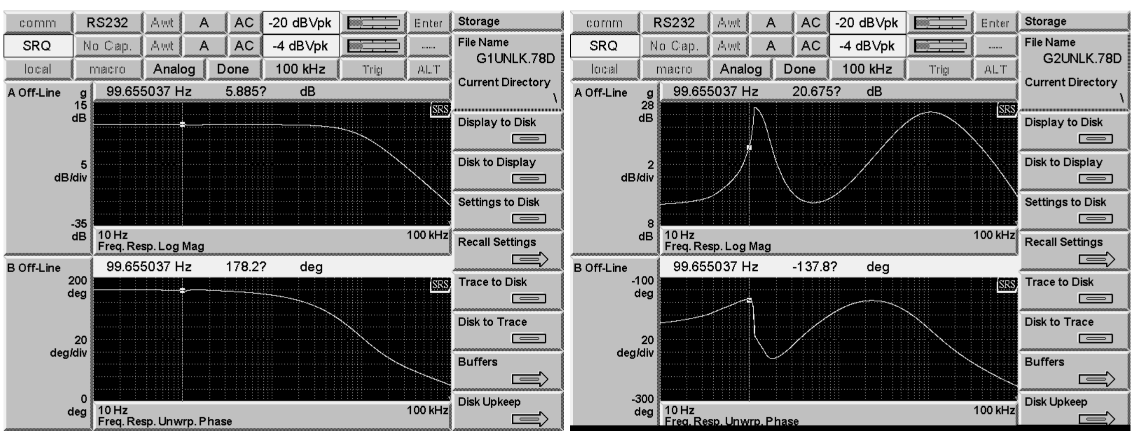

Figure B. 4. Frequency Response of Gang 1 (left) and Gang 2 (right) when the rotor is free to move.

The time responses are sent to the DAC of DSP and measured, so the conversion ratios should be applied. The results for locked and unlocked rotor cases are shown in Figure B.5 and Figure B.6.

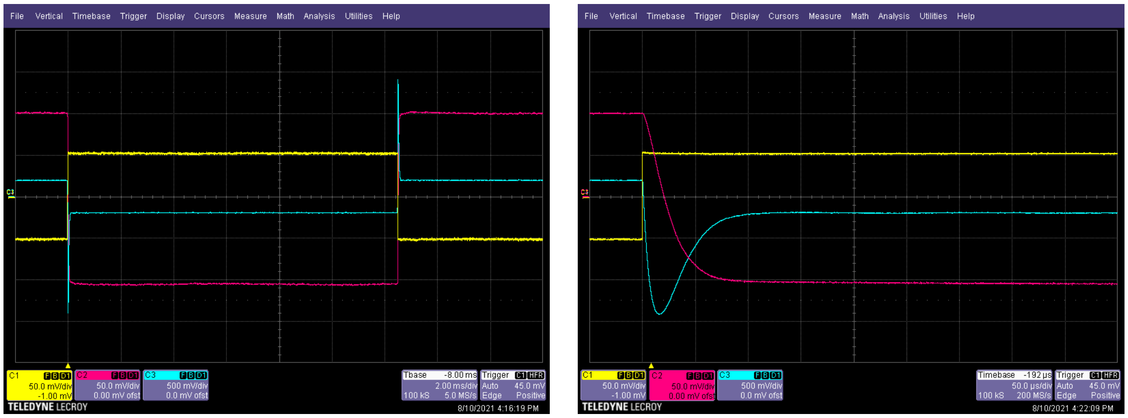

Figure B. 5. Step Response of Gang 1 and Gang 2 when the rotor is locked.

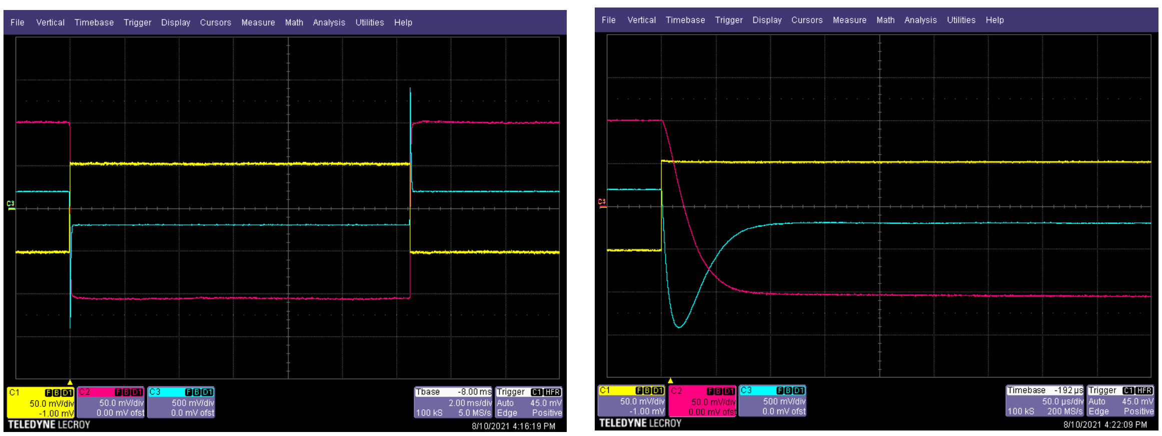

Figure B. 6. Step Response of Gang 1 and Gang 2 when the rotor is free to move.

Frequency and Step Responses of Gang 3 and Gang 4

To measure the frequency responses of Gang 3 and gang 4, a resister R_d=10k is connected to the positive input of the power op-amp to inject disturbance. It is fine as the power op-amp input has a high impedance. Also, the output of the compensator op-amp is very low (almost zero), so the voltage dividers are paralleled, which, together with R_d form a voltage divider whose middle voltage is V_+ of the op-amp. This gain should cancel out at the end. The Gang 3 (Disturbance Rejection) is measured at the coil current (output of current sensor op-amp). Gang 4(sensitivity) is measured at the output of power op-amp, but the gain of Power op-amp should be canceled out at the end. The frequency and time responses are shown in Figure B.7 and Figure B.8. If the inverse gains of the voltage divider (v_{in} to v_+) and power op-amp (v_+ to v_c) are applied to the responses, i_c and v_c give the approximate responses for $G3=P/(1+PCH)$ and $G4=1/(1+PCH)$, respectively. The inverse of the total gain from v_{in} to v_c is 0.2, so if the magnitude of injected signal v_{in} is 0.2 volt, the signals i_c and v_c give the unit step responses of Gangs 3 and 4. This injection method has distortions in the obtained bode plot and step response, so the results calculated based on the frequency response of loop transmission and the plant are more accurate.

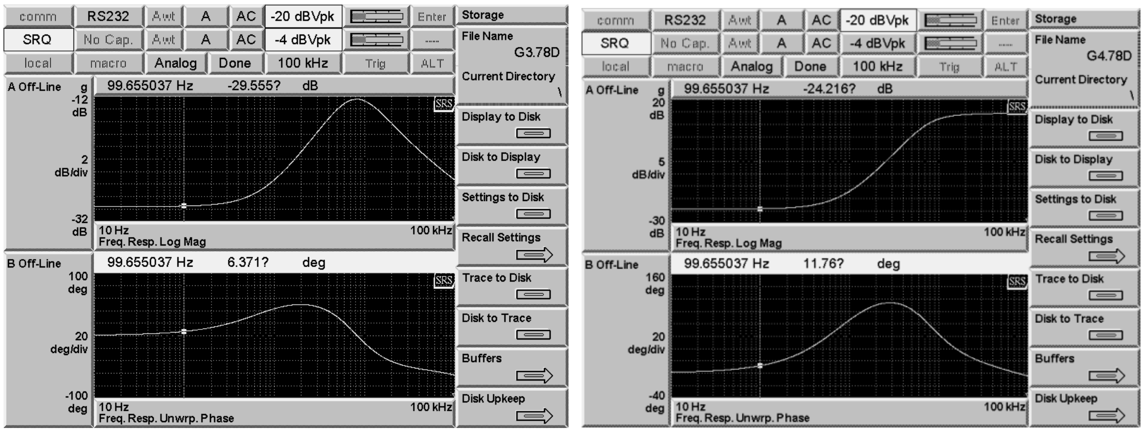

Figure B. 7. Frequency Response of Gang 3 (left) and Gang 4 (right).

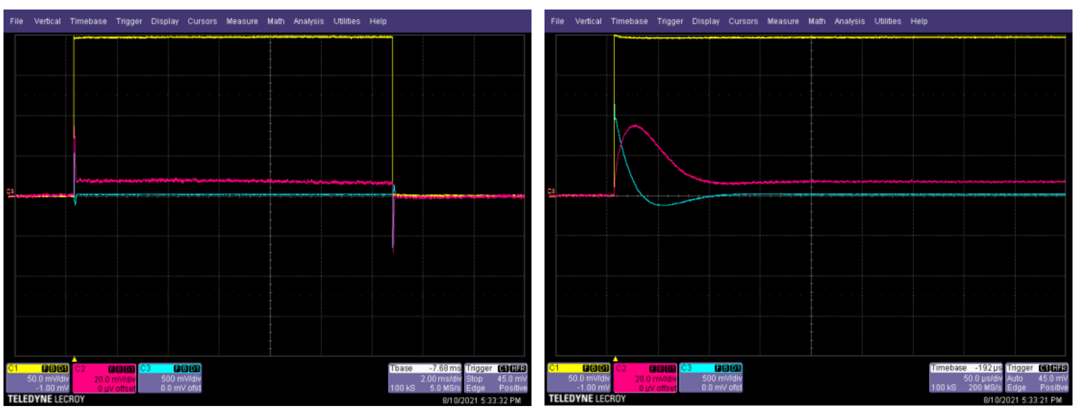

Figure B. 8. Step response of Gang 3 and Gang 4.

Frequency Response and Step Response of Gang 4, Gang 5, and Gang 6

The input signal is injected into the positive input of the current sensor op-amp with a resistance of R_n=10k (the same feedback resistance) so that we have the same signal at the output of the op-amp (gain=1). Gang 4 (sensitivity) can be measured at the output of the current sensor op-amp as an alternative method. The Gang 5, i.e., $CH/1+PCH$, can be obtained by measuring the output of the coil voltage (output of power op-amp). The Gang 6, i.e., $PCH/1+PCH$, can be obtained by measuring the coil current. As we exited the buffer op-amp, the coil current could not be measured at the output of the buffer op-amp or at the top of the sense resistor. *Solution:* We measure the coil current with a "current probe." The gain of the current probe should be canceled out, which is 0.1 *Volt/A*. The results are shown in Figure B.9. The time responses are also given in Figure B.10.

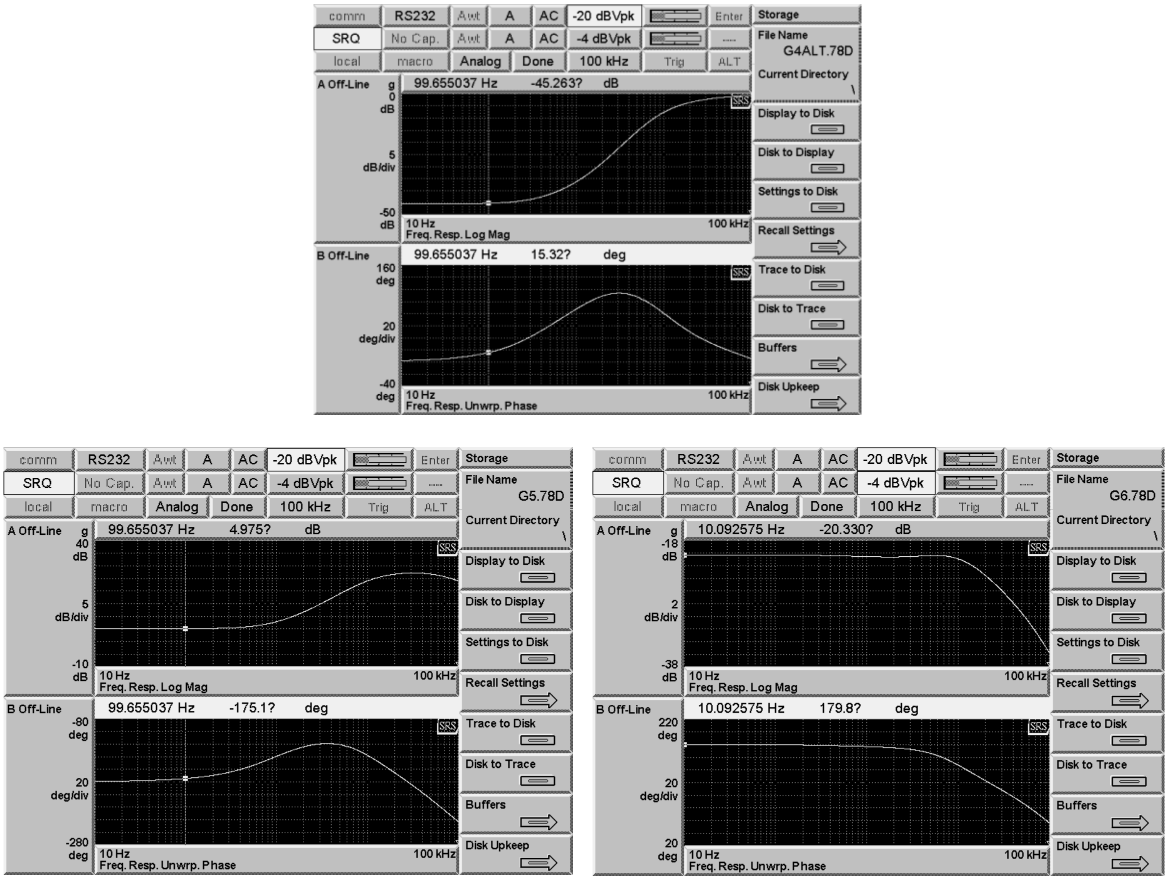

Figure B. 9. Frequency Response of Gang 4 (top), gang 5 (bottom left) and Gang 6 (bottom right).

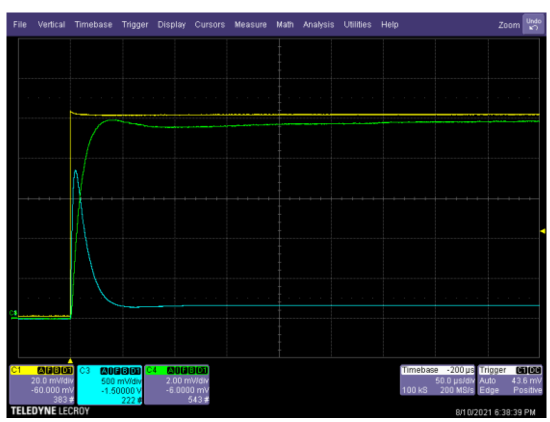

Figure B. 10. Step response of Gang 4, gang 5 and Gang 6.

Appendix C

Initial Designs of Drive and Control Loops

The initial design on the breadboard, together with a Texas Instrument LAUNCHXL-F28379D, as well as the final PCB, including the DSP, are given in Figure C.1. It is seen that the results obtained from the PCB-based circuit match better with the model as there are all kinds of parasitic like capacitors in the breadboard circuit.

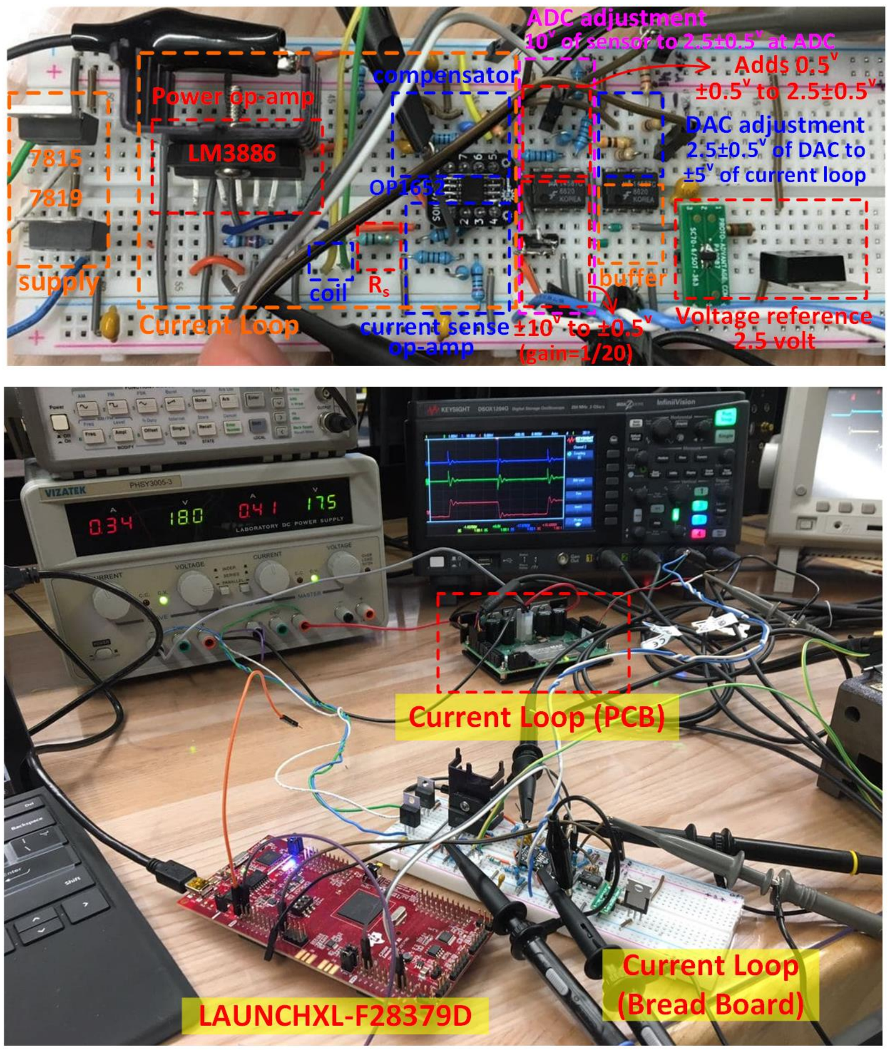

Figure C. 1. Initial design and test of the drive, current loop and position loop

More pictures from the experimental setup, the prototypes, and the equipment are given in Figure C.2 and Figure C.3.

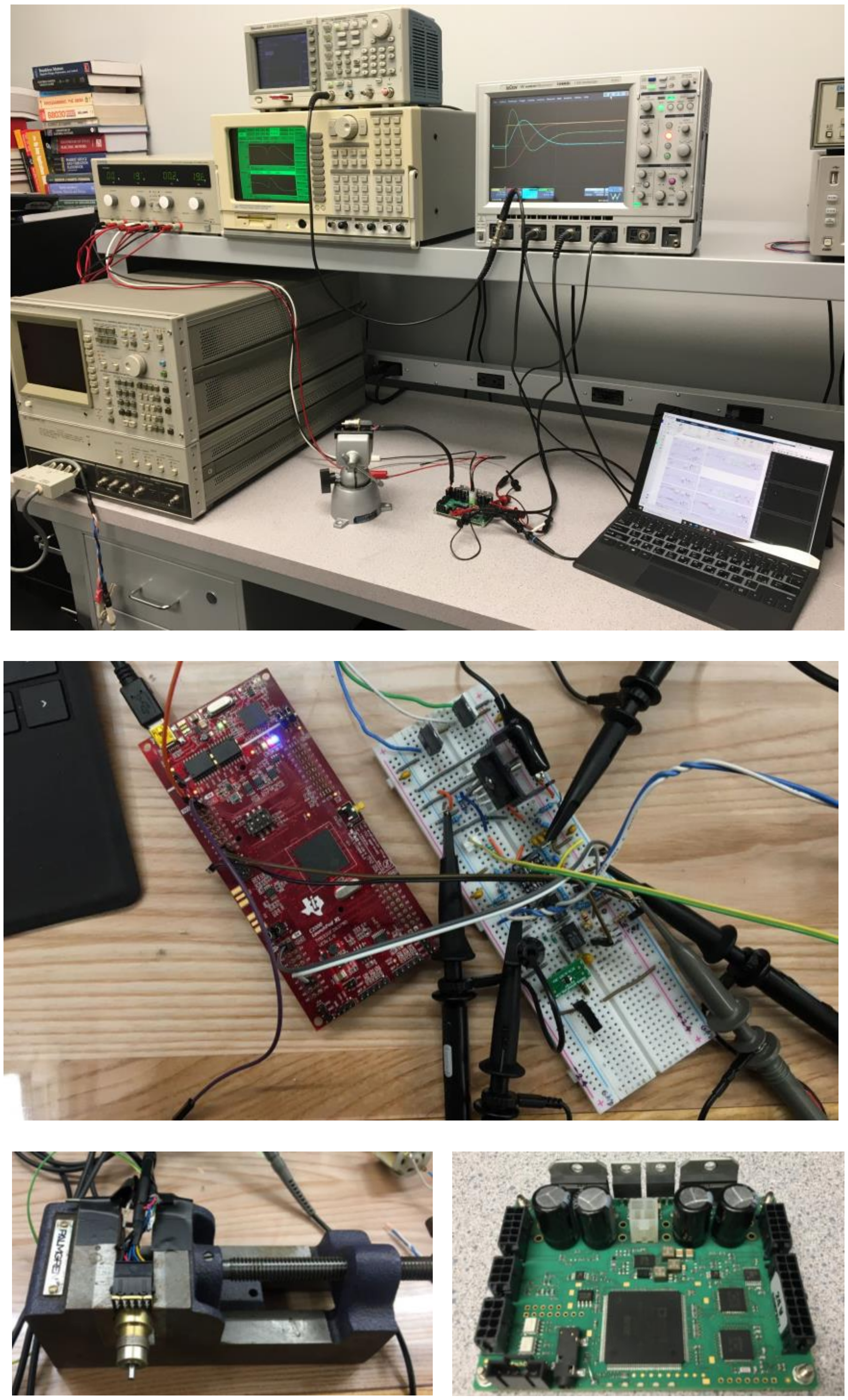

Figure C. 2. More pictures from experimental setups and tests

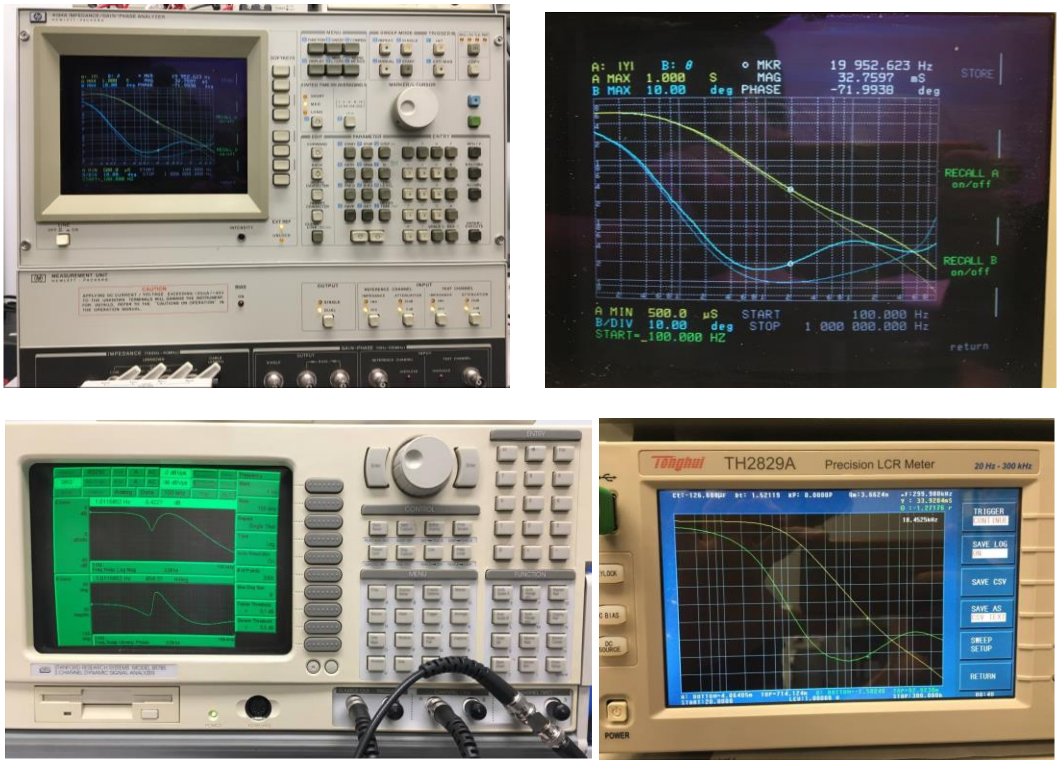

Figure C. 3. More pictures from experimental setups and tests

Appendix D

Experimental Results of Position Control with Voltage Drive

Step Response

The step reference of position for the small signal of ±5 as well as the step responses position, velocity, and current are given in Figure D.1. and Figure D.2. The quantities are measured at the DAC of the DSP, so the conversion ratios should be applied.

Figure D. 1. Step response results: reference position (±5 degrees), output position, velocity, current

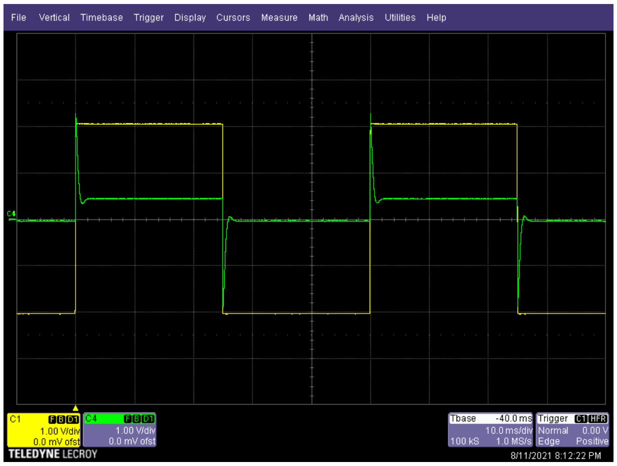

Figure D. 2. Step response results: reference position (±5 degrees), and coil voltage

Frequency Response of Gang 1 and Gang 2

The reference position is excited. For Gang 1, the output position is measured. The gain of the position sensor needs to be canceled out. For Gang 2, the output of the power op-amp (coil voltage) is measured. The results are given in Figure D.3.

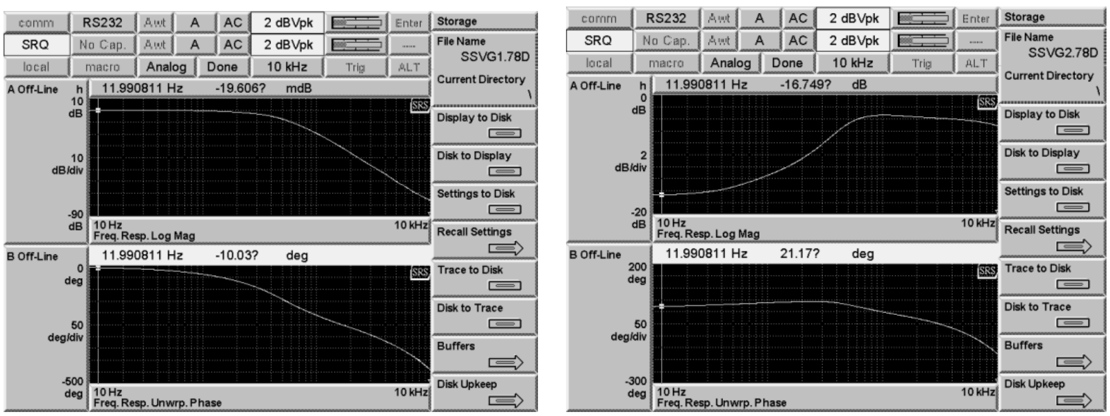

Figure D. 3. Frequency responses of Gang 1 (left) and Gang 2 (right)

Frequency Response of Gang 3 and Gang 4

A resister R_d=10k is connected to the positive input of the power op-amp to inject disturbance which is fine as the power op-amp input has high impedance. The power op-amp gain, which is around 20dB, needs to be canceled out at the end. Gang 3 (Disturbance Rejection) is measured at the position sensor. The position sensor gain should also be canceled out. The measured output is position sensor voltage (25 degrees/10 volt), so this gain should be considered, which is 20*log10((25/10)*(pi/180)) = -27.2037. The Gang 4 (sensitivity) is measured at the output of power op-amp. Note that the gain of power op-amp should be canceled out. The results are shown as in Figure D.4.

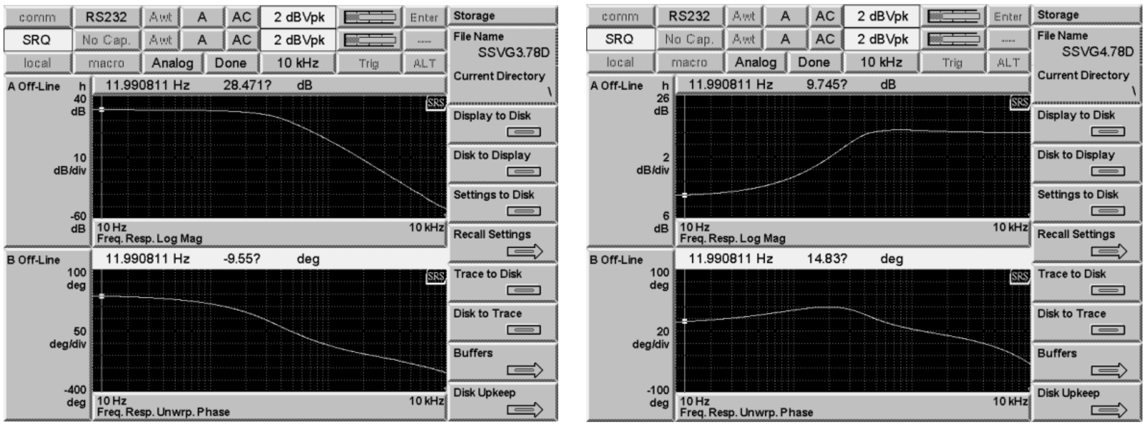

Figure D. 4. Frequency Response of Gang 3 (left) and Gang 4 (right)

Frequency Response of Gang 5 and Gang 6

The input signal is injected into the positive input of the current sensor op-amp with a resistance of R_n=10k (the same feedback resistance) so that we have the same signal at the output of the op-amp (gain=1). The Gang 5, i.e., CH/1+PCH, can be obtained by measuring the coil voltage (output of power op-amp). Gang 6, i.e., PCH/1+PCH, can be obtained by measuring the coil current. By exciting the buffer op-amp, the coil current cannot be measured at the output of the buffer op-amp or at the top of the sense resistor. Solution: the coil current can be measured with a "current probe." The gain of the current probe should be canceled out (0.1Volt/A). The results are given in Figure D.5.

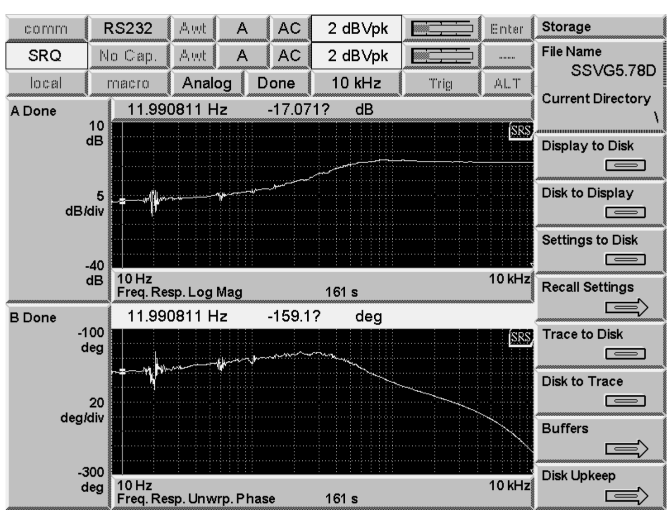

Figure D. 5. Frequency Response of Gang 5 (left). Gang 6 missing.

Having loop transmission L and the plant $P=H_e$, the gangs 3 to 6 can be obtained as:

$$G3 = \frac{P}{1+L} = \frac{P}{1+PCH} \tag{D.1}$$

$$G4 = \frac{1}{1+L} = \frac{1}{1+PCH} \tag{D.2}$$

$$G5 = \frac{(L/P)}{1+L} = \frac{CH}{1+PCH} \tag{D.3}$$

$$G6 = \frac{L}{1+L} = \frac{PCH}{1+PCH} \tag{D.4}$$

These results are more accurate than the method of injecting to the high-impedance inputs of the op-amps.

Frequency Response of Loop Transmission of the Position

The results are given in Figure D.6.

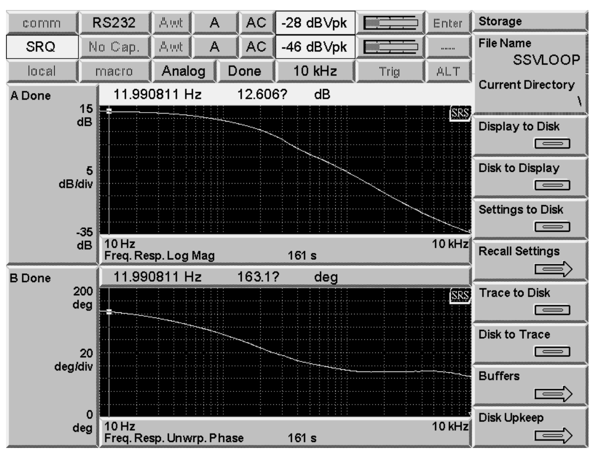

Figure D. 6. Frequency response of the loop transmission for the pole placement with voltage drive

Frequency Response of Voltage to Position

The frequency response of the plant, i.e., voltage to position, for different amplitudes of the injected signal is given in Figure D.7. The gain of the position sensor (27.2 dB) should be canceled out. It can be observed that as the amplitude of the injected signal goes up, the DC gain goes up; it is the impact of variations of stiffness K_s due to the friction. As we know that the DC gain is $(1/R)*(k_t/K_s)$. For larger amplitudes, the stiffness goes down, and thus the DC gain goes up. For the last case (200 mv), the expected DC gain is 20*log10((1/R)*(kt/ks)) + 20*log10((180/pi)*(10/25)) = 25.1384 which is close.

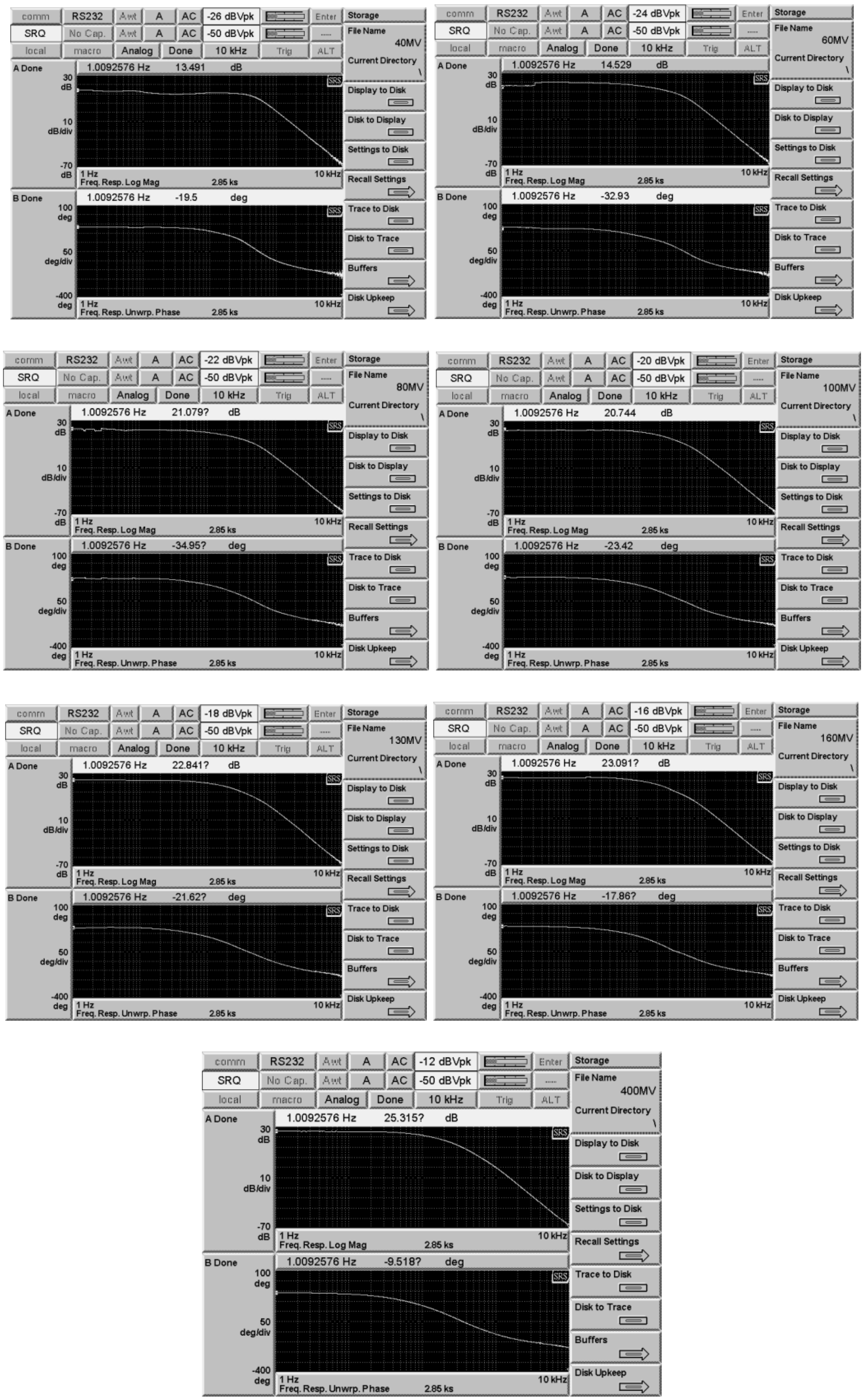

Figure D. 7. Frequency response of voltage to position for amplitudes of injected signal as 20 mv, 30 mv, 40 mv, 50 mv, 65 mv, 80 mv and 200 mv

Appendix E

Experimental Results of Position Control with Current Drive

Frequency Response of Gang 1 and Gang 2

The reference position is excited. For Gang 1, the output position is measured, so the gain of the position sensor needs to be canceled out. The results are given in Figure E.1.

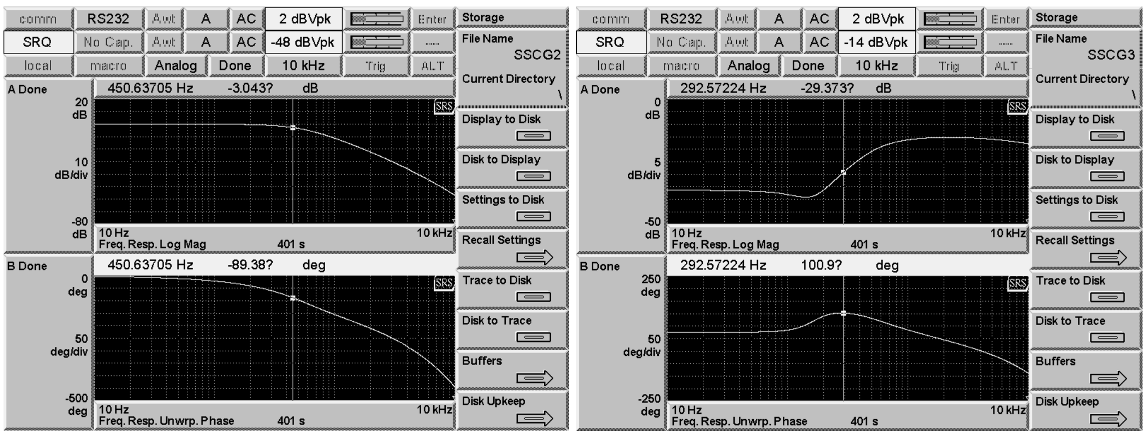

Figure E. 1. Frequency response of Gang 1 (left) and Gang 2 (right)

Frequency Response of Gang 3 and Gang 4

An R_d=10k resister is connected to the positive input of the compensator to inject the input signal. Gang 3 is measured at the position. The position sensor gain should also be canceled out. Gang 4 is measured at the coil current. The DC gain of the current loop should be canceled out. The results are shown as in Figure E.2. Note that these results can also be obtained using the frequency responses of the loop transmission and the plant, which are more accurate.

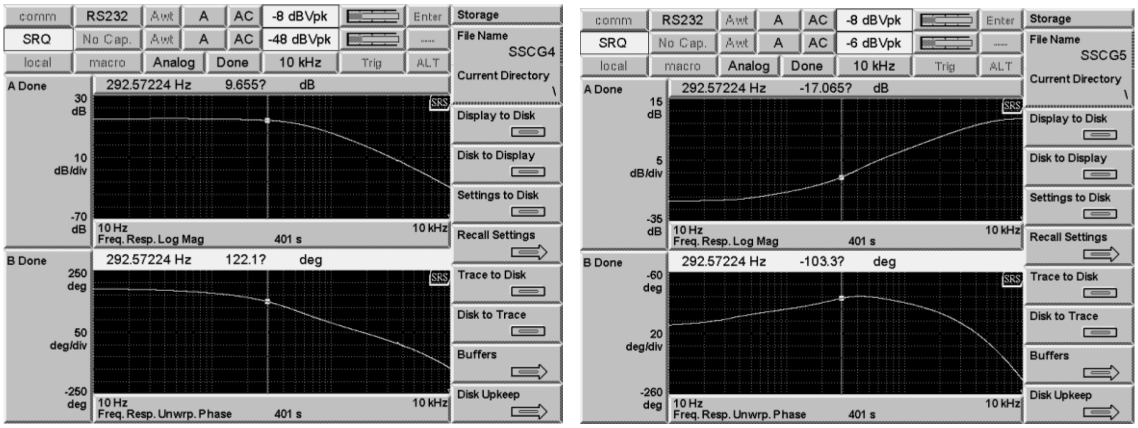

Figure E. 2. Frequency response of Gang 3 (left) and Gang 4 (right)

Loop Transmission

The loop is broken at the DAC. Then, the power op-amp input is excited, and the voltage is measured at the DAC. The results are given in Figure E.3.

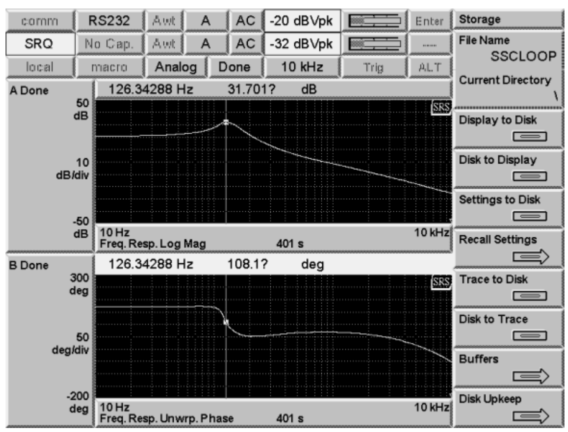

Figure E. 3. Frequency response of Gang 5 (left). Gang 6 missing.

Having loop transmission L and the plant $P{=}H_e$, the gangs 3 to 6 can be obtained as:

$$G3 = \frac{P}{1+L} = \frac{P}{1+PCH} \tag{E.1}$$

$$G4 = \frac{1}{1+L} = \frac{1}{1+PCH} \tag{E.2}$$

$$G5 = \frac{(L/P)}{1+L} = \frac{CH}{1+PCH} \tag{E.3}$$

$$G6 = \frac{L}{1+L} = \frac{PCH}{1+PCH} \tag{E.4}$$

These results are more accurate than the method of injecting to the high-impedance inputs of the op-amps.

Appendix F

Experimental Results of Nonlinear Position Control with Feedback Linearization

Step Response

The step reference of position for the large signal of ±10 as well as the step responses position, velocity, and current are given in Figure F.1. and Figure F.2. The quantities are measured at the DAC of the DSP, so the conversion ratios should be applied.

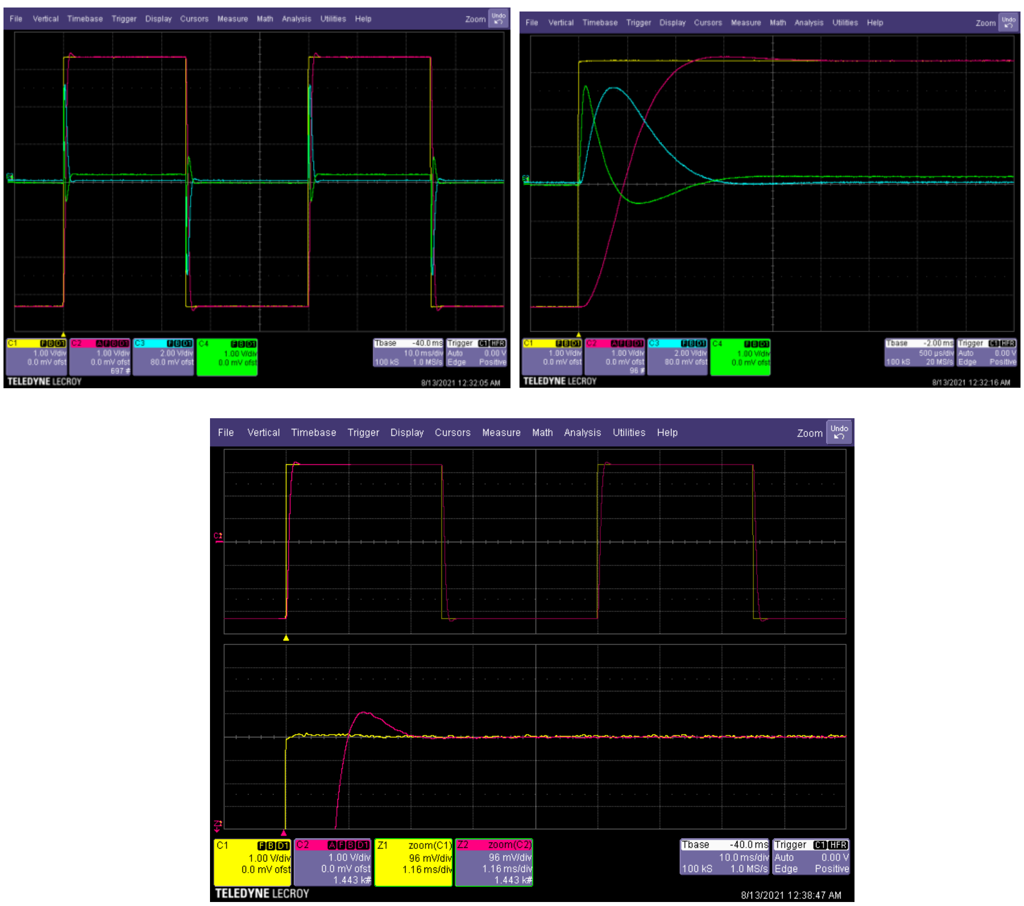

Figure F. 1. (top) Step response (plus zoomed-in version) of reference position (±10 degrees), position, velocity, current, and (bottom) the zoomed-in version of the step response of position

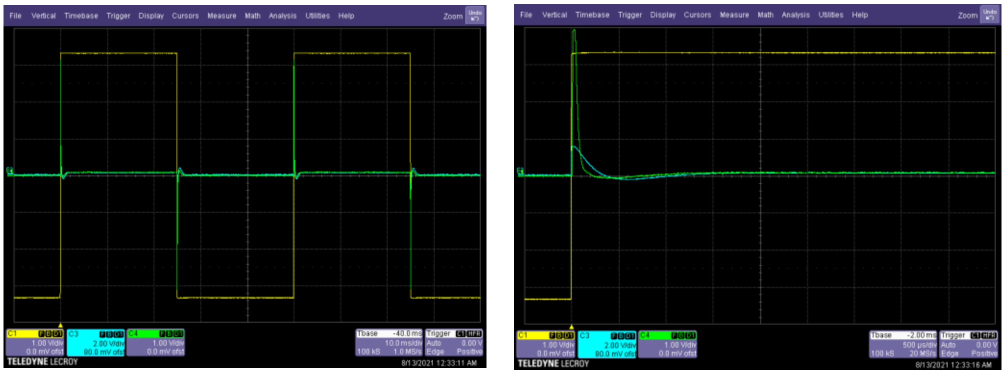

Figure F. 2. Step response results: reference position (±5 degrees), and coil voltage

Frequency Response of Gang 1 and Gang 2

The reference position is excited. For Gang 1, the output position is measured. The gain of the position sensor needs to be canceled out. The results are given in Figure F.3.

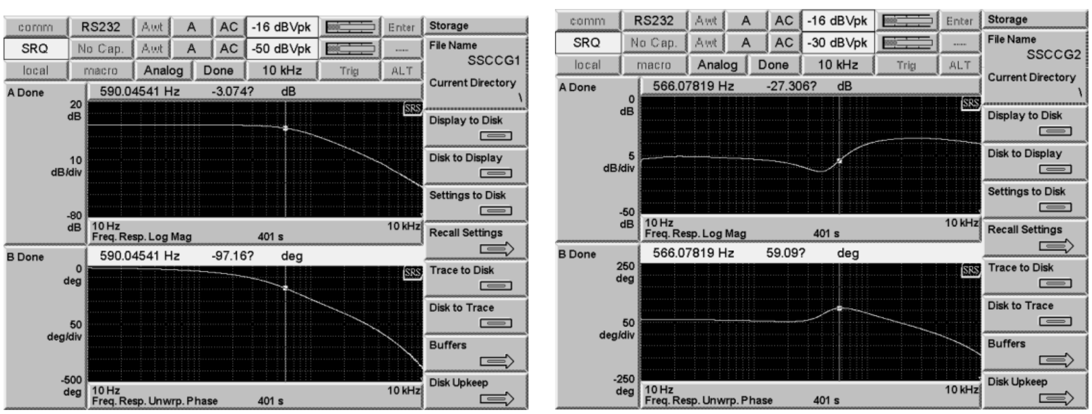

Figure F. 3. Frequency Response of Gang 1 (left) and Gang 2 (right)

Frequency Response of Gang 3 and Gang 4

A resister R_d=10k is connected to the positive input of the power op-amp to inject disturbance which is fine as the power op-amp input has high impedance. The power op-amp gain, which is around 20dB, needs to be canceled out at the end. Gang 3 (Disturbance Rejection) is measured at the position sensor. The position sensor gain should also be canceled out. The measured output is position sensor voltage (25 degrees/10 volt), so this gain should be considered, which is 20*log10((25/10)*(pi/180)) = -27.2037. The Gang 4 (sensitivity) is measured at the output of power op-amp. Note that the gain of power op-amp should be canceled out. The results are shown as in Figure F.4.

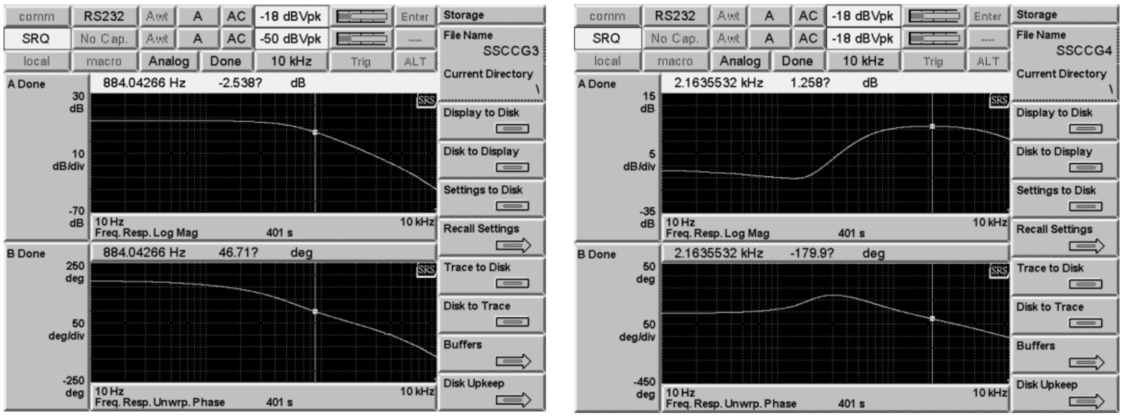

Figure F. 4. Frequency Response of Gang 3 (left) and Gang 4 (right)

Having loop transmission L and the plant $P\!=\!H_e$, the gangs 3 to 6 can be obtained as:

$$G3 = \frac{P}{1+L} = \frac{P}{1+PCH} \tag{F.1}$$

$$G4 = \frac{1}{1+L} = \frac{1}{1+PCH} \tag{F.2}$$

$$G5 = \frac{(L/P)}{1+L} = \frac{CH}{1+PCH} \tag{F.3}$$

$$G6 = \frac{L}{1+L} = \frac{PCH}{1+PCH} \tag{F.4}$$

These results are more accurate than the method of injecting to the high-impedance inputs of the op-amps.

Frequency Response of Double Integrator from *v* to position θ

The frequency response of the system from the signal *v* to the position is very close to a double integrator. It should be noted that its gain is attenuated for measurements by SR785 digital signal analyzer, and also, a delay is observed in the phase due to sampling and computations. The results are given in Figure F.5.

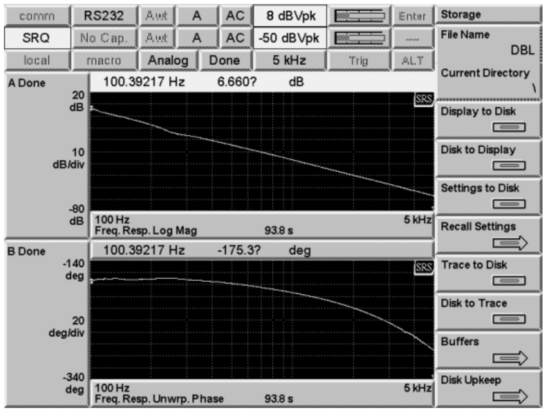

Figure F. 5. Frequency response of the double integrator from v to θ

Appendix G

Extension on Formulations of the Electromagnetic Model in Chapter 5

G.1 Coefficient of Polynomial (5.62)

The coefficient of the polynomial (5.62) are as below:

$$a_0 = -R_2^6 x_{m1}^2 \tag{G.1}$$

$$a_1 = 2R_2^4 x_{m1} (R_2^2 - R_1^2) \tag{G.2}$$

$$a_2 = R_2^4 x_{m1}^2 + R_1^2 R_2^2 y_{m1}^2 - R_2^2 (R_1^2 - R_2^2)^2 \tag{G.3}$$

$$a_3 = 2R_2^2 x_{m1} (R_1^2 - R_2^2) \tag{G.4}$$

$$a_4 = (R_1^2 - R_2^2)^2 \tag{G.5}$$

G.2. Scale Factors of Elliptical Coordinates

The scale factor $h_t = h_\eta = h_\psi$ can be obtained using orthogonal curvilinear theory. Having the coordinate system (u,v,w) expressed in cartesian coordinates (x,y,z), the scale factor h_u, h_v, and h_w can be obtained as:

$$h_u = \left| \left(\frac{\partial x}{\partial u}, \frac{\partial y}{\partial u} \right) \right|; \; h_v = \left| \left(\frac{\partial x}{\partial v}, \frac{\partial y}{\partial v} \right) \right|; \; h_w = \left| \left(\frac{\partial x}{\partial w}, \frac{\partial y}{\partial w} \right) \right| \tag{G.6}$$

The differential lengths, differential area, and differential volume are obtained as:

$$dl_u = h_u du; \; dl_v = h_v dv; \; dl_w = h_w dw \tag{G.7}$$

$$dA_u = h_v h_w \, dv \, dw; \; dA_v = h_u h_w \, du \, dw; \; dA_w = h_u h_v \, du \, dv \tag{G.8}$$

$$dv = h_u h_v h_w \, du \, dv \, dw \tag{G.9}$$

In elliptical coordinates, for example, h_η is obtained as:

$$h_\eta = \left| \left(\frac{\partial x}{\partial \eta}, \frac{\partial y}{\partial \eta} \right) \right| = \sqrt{\left(\frac{\partial x}{\partial \eta} \right)^2 + \left(\frac{\partial y}{\partial \eta} \right)^2} \tag{G.10}$$

Manipulations leads to:

$$h_t = h_\eta = h_\psi = c\sqrt{\cosh^2 \eta - \cos^2 \psi} \tag{G.11}$$

It is also clear that $h_z = 1$.

G.3. Solutions by Magnetic Vector Potential

Instead of using magnetic scalar potential ψ for a current-free region, field solutions within the ellipse could be obtained based on the magnetic vector potential. As the divergence of the curl of a vector field is zero, according to Ampere's law, a magnetic vector potential A can be defined as in below:

$$\nabla . B = 0 \rightarrow B = \nabla \times A \tag{G.12}$$

By employing the identity $\nabla \times \nabla \times A = \nabla(\nabla.\mathrm{A}) - \nabla^2 A$ in Ampere's law, we obtain one second-order equation governing magnetoquasistatic fields:

$$\nabla \times H = J \rightarrow \nabla \times \frac{\nabla \times A}{\mu_0} = J \rightarrow \nabla^2 A - \nabla(\nabla.A) = -\mu_0 J \tag{G.13}$$

To determine the vector A uniquely, its curl and divergence are required to be known. In magnetoquasistatic systems, the vector is taken to be solenoidal for the sake of convenience, i.e., zero divergence $\nabla.\mathrm{A} = 0$, which is called the Coulomb's gauge. It is worth noting that this choice is arbitrary. By imposing Coulomb's gauge condition, a second-order vector Poison's equation is obtained. Since it's a 2D problem, the vector A only has a z-component. Also, as the region within the ellipse is current-free, and the surface currents are treated as boundary conditions, the Poison's equation is reduced to Laplace's equation as:

$$\nabla^2 A = -\mu_0 J \xrightarrow{A=A_z\hat{z}} \nabla^2 A_z = -\mu_0 J_z \xrightarrow{J_z=0} \nabla^2 A_z = 0 \tag{G.14}$$

In elliptical coordinates, the solution can be one of the expressions in (5.19). The net flux passing through a surface *S* enclosed by closed line *C* is the surface integral of magnetic flux density vector *B* over surface *S*, or according to Stoke's theorem, is the closed line integral of the magnetic vector potential *A* over line *C* as in below:

$$\varphi = \oiint_s \vec{B}.d\vec{s} = \oint_c \vec{A}.d\vec{l} \tag{G.15}$$

In 2D problems, the flux is easily calculated as in below:

$$\varphi = L(\mathrm{A}_{z2} - \mathrm{A}_{z2}) \tag{G.16}$$

where A_{z1} and A_{z1} are values of A_z at the two points in the xy-plane. As shown in Figure G.1, according to Ampere's law for the surface currents, the magnetic flux is flowing within the ellipse from left to right. Then, as the curl of vector potential is the *B*, A_z must have positive values above the x-axis and negative values below the x-axis. Also, as minus gradient scalar potential is the magnetic field, the magnetic flux flows from positive potentials to negative potentials. In other words, unlike scalar potential φ, which is an even function with a *cosine* behavior, the vector potential A_z must be an odd function with a *sine* behavior, so the first term is in (5.19) is picked and thus $A_{zn}=D_n\, sinh(n\eta)\, sin(n\psi)$. Finally, the general solution of $A_z(\eta,\psi)$ can be written as:

$$A_z(\eta,\psi) = \sum_{n=1}^{+\infty} D_n \sinh(\mathrm{n}\,\eta)\sin(\mathrm{n}\,\psi) \tag{G.17}$$

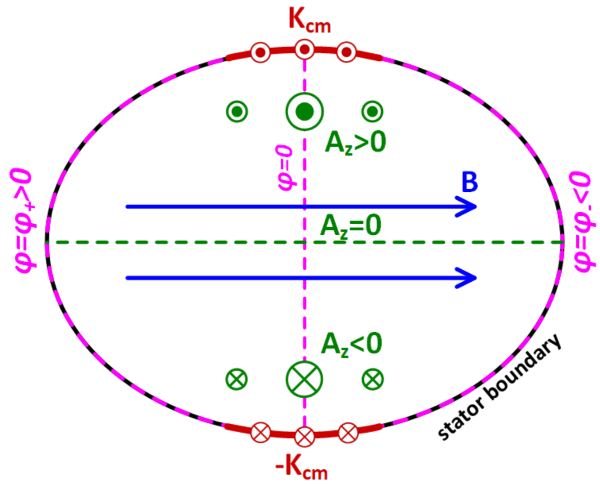

Figure G. 1. Sine behavior of vector potential A and cosine behavior of scalar potential φ.

The boundary condition can be applied by finding B or H field as in below:

$$B = B_\eta \hat{\eta} + B_\psi \hat{\psi} = \frac{1}{h_t^2} \begin{bmatrix} h_t \hat{\eta} & h_t \hat{\psi} & \hat{z} \\ \partial/\partial\eta & \partial/\partial\psi & \partial/\partial z \\ h_t \times 0 & h_t \times 0 & A_z \end{bmatrix} \tag{G.18}$$

Thus, the normal and tangential components H_η and H_ψ are obtained as in the following:

$$B_\eta = \frac{1}{h_t} \sum_{n=1}^{+\infty} n D_n \sinh(n\eta)\cos(n\psi) \tag{G.19}$$

$$B_\psi = \frac{-1}{h_t} \sum_{n=1}^{+\infty} n D_n \cosh(n\eta)\sin(n\psi) \tag{G.20}$$

The boundary condition $B_\psi(\eta_0, \psi) = -\mu_0 K_c(\psi)$ leads to:

$$\sum_{n=1}^{+\infty} nD_n \cosh(n\eta_0)\sin(n\psi) = \mu_0 h_t K_c(\psi) \tag{G.21}$$

The term $nD_n \cosh(n\eta_0)$ is the coefficients of the Fourier series expansion of the right side as in below:

$$nD_n \cosh(n\eta_0) = \frac{2}{\pi} \int_0^{\pi} \mu_0 h_t(\eta_0, \psi) K_c(\psi) \sin n\psi \, d\psi \tag{G.22}$$

As $nD_n \cosh(\mathrm{n}\,\eta_0) = a_n$, the coefficients D_n are obtained as:

$$D_n = \frac{2\mu_0 c K_{cm}}{n\pi \cosh(\mathrm{n}\,\eta_0)} \int_{\pi/2-\psi_c/2}^{\pi/2+\psi_c/2} \sqrt{\cosh^2\eta_0 - \cos^2\psi}\, \sin n\psi \,\mathrm{d}\psi \tag{G.23}$$

It is seen that the solutions of scalar potential φ and vector potential A_z are exactly the same with the following relationship between the coefficients A_n and D_n:

$$D_n = -\mu_0 A_n \tag{G.24}$$

G.4. Transformation Matrix

$$\begin{cases} x = R_r \cos\theta = R_r \cos(\beta + \theta^r) \\ y = R_r \sin\theta = R_r \sin(\beta + \theta^r) \end{cases} ; \begin{cases} x^r = R_r \cos\theta^r \\ y^r = R_r \sin\theta^r \end{cases} \tag{G.25}$$

For $\cos(\beta + \theta^r)$ and $\cos(\beta + \theta^r)$, we substitute the products as:

$$\begin{cases} x = R_r[\cos\beta \ \cos\theta^r - \sin\beta \ \sin\theta^r] \\ y = R_r[\sin\beta \ \cos\theta^r + \cos\beta \ \sin\theta^r] \end{cases} \tag{G.26}$$

It can be rewritten as in below:

$$\begin{cases} x = \cos\beta[R_r \cos\theta^r] - \sin\beta[R_r \sin\theta^r] \\ y = \sin\beta[R_r \cos\theta^r] + \cos\beta[R_r \sin\theta^r] \end{cases} \tag{G.27}$$

By substituting the terms in the bracket in x^r and y^r, we obtain:

$$\begin{cases} x = \cos\beta \ x^r - \sin\beta \ y^r \\ y = \sin\beta \ x^r + \cos\beta \ y^r \end{cases} \tag{G.28}$$

The transformation matrix is obtained as:

$$\begin{bmatrix} x \\ y \end{bmatrix} = \begin{bmatrix} \cos\beta & -\sin\beta \\ \sin\beta & \cos\beta \end{bmatrix} \begin{bmatrix} x^r \\ y^r \end{bmatrix} \tag{G.29}$$

It can be observed that, for $\beta=0$, the rotor reference frame falls on the stationary reference frame, i.e., $x=x^r$ and $y=y^r$.

G.5. Obtaining the Polynomial Coefficients

Having the slop and two points $m_1(x_{m1},y_{m1})$ and $s_1(x_{s1},y_{s2})$, the line L_{p1} is obtained as:

$$y_{s1} - y_{m1} = \frac{R_2^2}{R_1^2}\frac{y_{s1}}{x_{s1}}(x_{s1} - x_{m1}) \tag{G.30}$$

Then, y_{s1} can be obtained in terms of x_{s1} as in below:

$$y_{s1} = \frac{R_1^2 y_{m1} x_{s1}}{(R_1^2 - R_2^2)x_{s1} + R_2^2 x_{m1}} \tag{G.31}$$

By substituting y_{s1} into the ellipse equation:

$$\frac{x_{s1}^2}{R_2^2} + \frac{y_{s1}^2}{R_1^2} = 1 \tag{G.32}$$

Leads to:

$$\frac{x_{s1}^2}{R_2^2} + \frac{1}{R_1^2}\left\{\frac{R_1^2 y_{m1} x_{s1}}{(R_1^2 - R_2^2)x_{s1} + R_2^2 x_{m1}}\right\}^2 = 1 \tag{G.33}$$

Simplifying results in the following polynomial:

$$a_4 x_{s1}^4 + a_3 x_{s1}^3 + a_2 x_{s1}^2 + a_1 x_{s1} + a_0 = 0 \tag{G.34}$$

whose coefficients are:

$$a_0 = -R_2^6 x_{m1}^2 \tag{G.35}$$

$$a_1 = 2R_2^4 x_{m1}(R_2^2 - R_1^2) \tag{G.36}$$

$$a_2 = R_2^4 x_{m1}^2 + R_1^2 R_2^2 y_{m1}^2 - R_2^2 (R_1^2 - R_2^2)^2 \tag{G.37}$$

$$a_3 = 2R_2^2 x_{m1}(R_1^2 - R_2^2) \tag{G.38}$$

$$a_4 = (R_1^2 - R_2^2)^2 \tag{G.39}$$

Appendix H

Loop-Shaping Position Control in Frequency Domain

An advantage of the control in the frequency domain is that the stability and robustness of the system can be evaluated.

Control Architecture

As shown in Figure H.1, the position loop can be digitally implemented in a DSP around the current loop, which had analog implementation using op-amps. The current loop is much faster than the position loop so that the current loop is seen as a D.C. gain from the position loop; the inverse of this DC gain is placed before the DAC so that the output of the position compensator is exactly the current command i_{ref} sent to the current loop. In other words, the bandwidth of the current loop should be designed to be much larger than the bandwidth of the position loop. Also, the sampling frequency is large enough that the time delay (computational time and sampling by ZOH) can be ignored.

The desired bandwidth of the position loop is around $f_{bw}=500\ Hz$; this bandwidth provides a fast response with a rise time around $t_r=2.2/\omega_{bw}$. The phase compensation is around 55 degrees, providing a small overshoot in the step response, good robustness, and enough stability margin. The position sensor returns a voltage as a function of position, and its inverse function is implemented in the DSP so that they cancel out in the loop transmission. There can be a low-pass filter in the loop to reject the high-frequency content of the position sensor and other elements; its break frequency should be greater than the crossover frequency such that it does not add a negative phase to the system. The crossover frequency ω_c is related to the desired bandwidth of the closed-loop system, so it is set at $\omega_{bw} = 1000\pi\ Hz$ or higher.

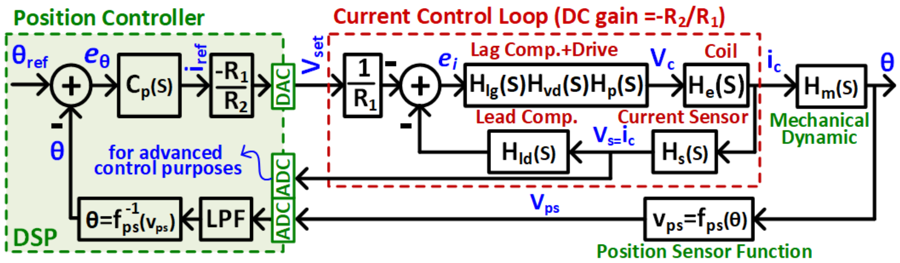

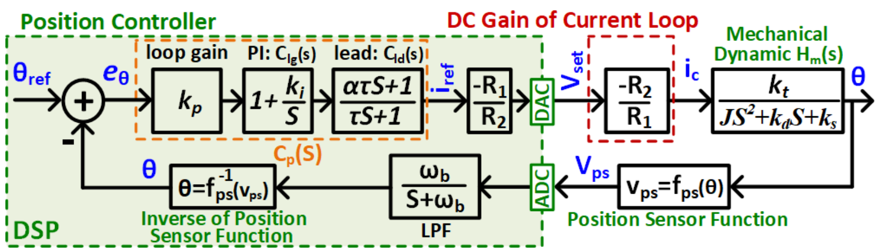

Figure H. 1. Position loop in the frequency domain: (a) with full dynamic of the current loop (top), and by replacing the current loop with its DC gain when its bandwidth is much larger than position loop (bottom).

A PI compensator, including an integrator, is used to null any steady-state error. A lead compensator is employed to achieve enough phase margin.

Design of Compensator and Low-Pass Filter

The transfer function of the lead-lag compensator is as in below:

$$C_p(s) = k_p C_{lg}(s) C_{ld}(s) = k_p (1 + \frac{k_i}{s})(\frac{\alpha \tau s + 1}{\tau s + 1}) \tag{H.1}$$

The lead compensator can provide a maximum phase compensation φ_m at the frequency of ω_m as in below:

$$\varphi_m = \sin^{-1}\left(\frac{\alpha - 1}{\alpha + 1}\right) \quad at \quad \omega_m = \frac{1}{\tau\sqrt{\alpha}} \tag{H.2}$$

The typical pole-zero ratio $\alpha = 10$ is picked for the lead compensator to get a maximum phase compensation of around $\varphi_m = 55$ degrees. Setting $\omega_m = \omega_c$, leads to $\tau = 10^{-4}$.

The integrator gain is set to one decade before the crossover frequency, i.e., $k_i=\omega_c/10=100\pi$, so that its impact on the reduction of the phase margin is limited to around 5 degrees.

The transfer function of the low-pass filter is as follow:

$$H_{LPF}(s)=\frac{\omega_b}{s+\omega_b} \tag{H.3}$$

The break frequency should be well below the noise frequency as well as at least one decade above ω_c to limit its impact on the reduction of the phase margin. Since the bandwidth of the position sensor is sufficiently high (100 kHz), it can even be removed.

Finally, the loop gain k_p is determined based on the fact that the gain of the loop transmission at ω_c should be unity:

$$k_p=1/\left|C_{\lg}(\mathrm{j}\omega_c)C_{ld}(\mathrm{j}\omega_c)H_m(\mathrm{j}\omega_c)H_{LPF}(\mathrm{j}\omega_c)\right| \tag{H.4}$$

whose unknown k_p can be obtained. Even the transfer function of the low-pass filter H_{LPF} can be ignored in the above equation as its magnitude is almost unity at ω_c. The DC gain of the current loop and its inverse, as well as the position sensor function and its inverse function, do not appear in the loop transmission as they are canceled out.

Digital Implementation of the Compensator

The sampling time $T_s=1/f_s$ where $f_s=160\ kHz$ is the sampling frequency of the DSP. Using the Tustin transformation, the z-transform of the discrete-time lag compensator is obtained as:

$$C_{\lg}(s)=1+\frac{k_i}{s}\ \overset{s=\frac{2}{T_s}\frac{z-1}{z+1}}{\Longrightarrow}\ C_{\lg}(\mathrm{z})=\frac{Y_{\lg}(\mathrm{z})}{X_{\lg}(\mathrm{z})}=1+\frac{k_iT_s}{2}\frac{z+1}{z-1} \tag{H.5}$$

The discrete-time implementation of the lag compensator is

$$y_{\lg}(t+1)=y_{\lg}(t)+[k_iT_s/2+1]x_{\lg}(\mathrm{t}+1)+[k_iT_s/2-1]x_{\lg}(\mathrm{t}) \tag{H.6}$$

By using shifting theorem, it leads to:

$$y_{\lg}(t) = y_{\lg}(t-1) + [k_i T_s / 2 + 1] x_{\lg}(\mathrm{t}) + [k_i T_s / 2 - 1] x_{\lg}(\mathrm{t}-1) \tag{H.7}$$

The z-transform of the discrete-time lead compensator is obtained as:

$$C_{ld}(s) = \frac{\alpha\tau s + 1}{\tau s + 1} \Rightarrow C_{ld}(\mathrm{z}) = \frac{Y_{ld}(\mathrm{z})}{X_{ld}(\mathrm{z})} = k_{ld}\,\frac{z + z_1}{\mathrm{z} + z_2} \tag{H.8}$$

where z_1, z_2, and k_{ld} are as follows:

$$k_{ld} = \frac{T_s + 2\alpha\tau}{T_s + 2\tau};\ z_1 = \frac{T_s - 2\alpha\tau}{T_s + 2\alpha\tau};\ z_2 = \frac{T_s - 2\tau}{T_s + 2\tau} \tag{H.9}$$

The discrete-time implementation of the lead compensator is:

$$y_{ld}(t+1) + z_2\, y_{ld}(t) = k_{ld}[x_{ld}(\mathrm{t}+1) + z_1\, x_{ld}(t)] \tag{H.10}$$

By using shifting theorem, it leads to:

$$y_{ld}(t) = -z_2\, y_{ld}(t-1) + k_{ld}[x_{ld}(\mathrm{t}) + z_1\, x_{ld}(t-1)] \tag{H.11}$$

Nonlinear Control by Feedback Linearization

Nonlinear control provides an opportunity to work with large input signals. Feedback linearization is nonlinear technique which can be a powerful in eliminating the nonlinearities of the system, yet it requires a very accurate model of the plant.

Since the inductance is a function of frequency due to eddy-currents and proximity effects, obtaining an accurate model for the electrical dynamic is complicated, so employing the current control loop is very useful to eliminate the electrical dynamics and all its nonlinearities. Then, for feedback linearization, we only deal with the mechanical dynamic whose model is relatively more accurate.

Feedback Linearization

If a nonlinear state space can be written in companion form as in below:

$$\begin{cases} \dot{x}_1 = x_2 \\ \dot{x}_2 = x_3 \\ \ldots \\ \dot{x}_n = f(\mathrm{x}_1, \ldots, \mathrm{x}_n) + \mathrm{g}(\mathrm{x}_1, \ldots, \mathrm{x}_n)\,\mathrm{u(t)} = v(\mathrm{t}) \end{cases} \tag{H.12}$$

where functions $f(x)$ and $g(x)$ are nonlinear functions of the states, and $u(t)$ is the input; it can be seen that all states should be measured or estimated to be able to evaluate f and g. Then, the following nonlinear transformation can be used at the input to cancel the nonlinearities.

$$u(t) = \frac{1}{\mathrm{g}(\mathrm{x}_1, \ldots, \mathrm{x}_n)}\left[v(\mathrm{t}) - f(\mathrm{x}_1, \ldots, \mathrm{x}_n)\right] \tag{H.13}$$

The result is a linear system with new input is v and n poles at the origin, to which linear control techniques can be applied.

As the restoration torque and the electromagnetic torque are functions of the position, by substituting $\theta = \beta - \pi/2$, the nonlinear electromechanical model is obtained as follows:

$$\begin{cases} Elec:\ v_c = k_b \omega_r \cos\theta + R_c\, i_c(t) + L_c \dfrac{di_c}{dt} \\ Mech:\ J\dfrac{d^2\theta}{dt^2} + k_d \dfrac{d\theta}{dt} + k_{rest}\sin 2\theta = k_t\, i_c \cos\theta \end{cases} \tag{H.14}$$

The nonlinear state-space form of mechanical dynamic is as:

$$\begin{cases} \dot{\theta} = \omega_r \\ \dot{\omega}_r = -\dfrac{k_d \omega_r + k_{rest}\sin 2\theta}{J} + \dfrac{k_t \cos\theta}{J} i_c = f + g\, i_c = v \end{cases} \tag{H.15}$$

The nonlinear transformation at the input is as follows:

$$i_c(t) = \frac{1}{g(\theta, \omega_r)}[v(t) - f(\theta, \omega_r)] \tag{H.16}$$

Then, the remaining system with the new input v is a double integrator linear system as in below:

$$\ddot{\theta} = v \;\Rightarrow\; H'_m = \frac{\theta(s)}{v(s)} = \frac{1}{s^2} \tag{H.17}$$

The state-space form is as follows:

$$\begin{bmatrix} \dot{\theta} \\ \dot{\omega}_r \end{bmatrix} = \begin{bmatrix} 0 & 1 \\ 0 & 0 \end{bmatrix} \begin{bmatrix} \theta \\ \omega_r \end{bmatrix} + \begin{bmatrix} 0 \\ 1 \end{bmatrix} v \tag{H.18}$$

Any kind of linear control can be designed for this system.

Nonlinear Control by Loop Shaping in Frequency Domain

The block diagram of the control architecture is shown in Fig. 6. The same lead-lag compensator as in section II is used. However, since the plant is changed, the loop gain k_p needs to be redesigned as in below:

$$k_p = 1 / \left| C_{\lg}(\mathrm{j}\omega_c) C_{ld}(\mathrm{j}\omega_c) H'_m(\mathrm{j}\omega_c) \right| \tag{H.19}$$

It is assumed that the state observer is fast enough that it does not have a big impact on the loop phase at the crossover frequency. The digital implementation of the controller is the same.

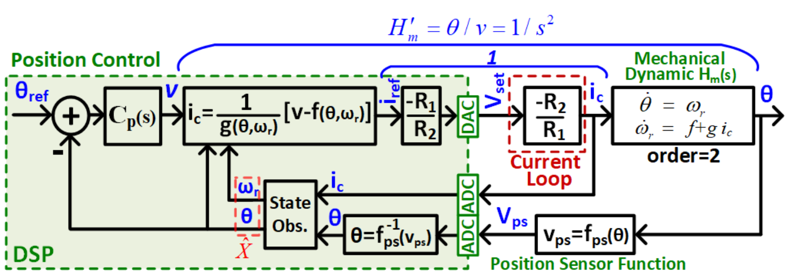

Figure H. 2. Nonlinear control by loop shaping

Appendix I

Matlab Code for the Electromagnetic Model in Chapter 5

The code is as in below:

```
%------------------------------------------------------------------------%
%   Actuator Model by Elliptical Coordinates and Differential Flux Tubes  %
%                 Sajjad Mohammadi, EECS, MIT, August 2021                %
%------------------------------------------------------------------------%
clear; clc;

%% [1] Parameters

N  = 100; % Number of turns
ic  = 1;   % current [A]
u0 = 4*pi*1e-7;
R1 = 1.71e-3; % semi-major axis of ellipse [m]
R2 = 1.15*1.71e-3; % semi-minor axis of ellipse [m]
Rr = 1.524e-3; % Rotor radius [m]
Br = 1.37; % residual flux of PMs (T)
M  = Br/u0; % PM Magnetization
LL = 4.191e-3; % axial length of actuator (m),  0.165 inch
theta_c = 38*(pi/180); % Interpolar angle Cylindrical [rad],
atand(0.564/1.63816169)


% Rotor Rotation
db   = pi/1000; % Increament of rotor rotation: beta
beta = 0:db:pi; % Rotor rotation: beta


% Elliptical Coordinates
eta0 = atanh(R1/R2); % Reference ellipse
c = sqrt(R2^2-R1^2); % Ellipse foci +c and -c
psi_c = 2*atan(tan(theta_c/2)/coth(eta0)); % Interpolar angle Elliptical11

% Coordinates of point A, right side of surface current Kc
x_A = c*cosh(eta0).*cos(pi/2 - psi_c/2)*1000
y_A = c*sinh(eta0).*sin(pi/2 - psi_c/2)*1000

% Calculation of lc
% Method 1: Cartesian Coordinates
t1 = atan((R2/R1)*cot(theta_c/2));
tt = linspace(t1,pi/2,1000);
Lc  = 2*trapz(tt,sqrt((R2*sin(tt)).^2+(R1*cos(tt)).^2)) % verttical ellipse
% Method 2: Ellipticals Coordinates
psi_L = linspace(pi/2-psi_c/2,pi/2+psi_c/2,1000);
Lc = trapz(psi_L, c*sqrt(cosh(eta0)^2-cos(psi_L).^2))
% Lc=1.140186e-3; % measured from FEM

% Load FEM data
run FEMresult_B_Current_eta0_eta9_Rr
```

```
%% [2] Field calculations, eta and psi components of B on elliplse eta=eta0

% The ellipse to calculate fields on it
eta = 0.999*eta0; % stator boundary

% Test for get point A
% x_c = c*cosh(eta0)*cos(pi/2-psi_c/2)
% y_c = c*sinh(eta0)*sin(pi/2-psi_c/2)
% theta_c = 2*atand(x_c/y_c)

psi = linspace(0,2*pi,10000); % 2*pi range of elliptical angle psi

phi   = zeros(1,length(psi));  % Magnetic Scalar  Potentian
Az    = zeros(1,length(psi));  % Magnetic Vector  Potentian
B_eta = zeros(1,length(psi));% eta-component of B (normal)
B_psi = zeros(1,length(psi));% psi-component of B (tangential)

for n=1:2:300
    % Caculation of Fourier Coefficients An
    psii = linspace(pi/2-psi_c/2,pi/2+psi_c/2,10000); % for integration
    An   = -(N*ic/Lc)*(2*c./(n*pi*cosh(n*eta0)))...
           *trapz(psii, sqrt(cosh(eta0)^2-cos(psii).^2).*sin(n*psii) );

    % Scalar Potential: phi=A cosh(n eta) cos(psi)
    phi = phi + An.*cosh(n*eta).*cos(n*psi); % Magnetic scalar potential

    % Vector Potential: phi=A sinh(n eta) sin(psi)
    Dn  = -u0*An;
    Az  = Az + Dn.*sinh(n*eta).*sin(n*psi);

    % Scale Factor
    ht = c*sqrt(cosh(eta).^2-cos(psi).^2); % Scale factor

    % Flux Density Vectors
    B_eta = B_eta+u0*(-1./ht)*n.*An.*sinh(n*eta).*cos(n*psi); % B_eta
    B_psi = B_psi+u0*(1./ht)*n.*An.*cosh(n*eta).*sin(n*psi);  % B_psi

end

% Magnetic Flux density: B_eta and B_psi
subplot(3,1,1)
   plot(psi*(180/pi),B_eta,...                   % Model
        psi_B_eta0_orig*(180/pi), Beta_B_eta0_orig,'--',... % FEM original
        psi_B_eta0_simp*(180/pi), Beta_B_eta0_simp,'--',... % FEM simplified
        'LineWidth',1); grid on
   legend('Model','FEM original','FEM simplified')
   xlabel('\psi (deg)')
   ylabel('B_\eta (tesla)')
   xlim([0,360])
   title('Ellipse Boundary \eta=\eta_0')
subplot(3,1,2)
   plot(psi*(180/pi),B_psi,...
        psi_B_eta0_orig*(180/pi), Bpsi_B_eta0_orig,'--',...
        psi_B_eta0_simp*(180/pi), Bpsi_B_eta0_simp,'--',...
        'LineWidth',1); grid on
   legend('Model','FEM original','FEM simplified')
   xlabel('\psi (deg)')
   ylabel('B_\psi (tesla)')
   xlim([0,360])
subplot(3,1,3)
   plot(psi*(180/pi),phi,...
        psi_B_eta0_orig*(180/pi), phi_B_eta0_orig,'--',...
        psi_B_eta0_orig*(180/pi), phi_B_eta0_simp,'--',...
```

```
        'LineWidth',1); grid on
    xlim([0,360]); ylim([-55,55])
    legend('Model','FEM original','FEM simplified')
    xlabel('\psi (deg)'); ylabel('Scalar Potential \phi')


       plot(psi*(180/pi),Az,...
         'LineWidth',1); grid on


% % Scalar Potential from H_psi
% B_psii =B_psi;
% psii = psi;
%
% zz = c*sqrt(cosh(eta).^2-cos(psii).^2).*B_psii/u0;
% phii = -cumtrapz(psii, zz); % Cumulative Integral
% phi0 = (1/(psii(end)-psii(1)))*trapz(psii, phii); % Averaging to find DC
value
% BB = phii - phi0; % Subtract DC value
%
% plot(psii*(180/pi), BB)
% xlabel('\psi'); ylabel('Scalar Potential \phi')
%



% Magnitude of B
% plot(psi*(180/pi),sqrt(B_eta.^2+B_psi.^2))
% xlim([0,360])
% xlabel('\psi')
% ylabel('|B|')

% % Test: H_psi = (1/ht)*dphi/dt
% db=psi(2)-psi(1);
% for kk=1:(length(psi)-1)
%     T(kk)=(phi(kk+1)-phi(kk))/db;
% end
% plot(psi(1:length(psi)-1)*(180/pi), u0*1./(c.*sqrt((cosh(eta0)^2-
cos(psi(1:length(psi)-1)).^2))).*T)


% Converting (B_eta, B_psi) to (Bx, By) and (Br, B_theta)
% ht = c*sqrt(cosh(eta).^2-cos(psi).^2);
% Bx = imag( (ht./(c*sinh(eta+j*psi))) .* (B_psi+j*B_eta));
% By = real( (ht./(c*sinh(eta+j*psi))) .* (B_psi+j*B_eta));
%
% x = c*cosh(eta).*cos(psi);
% y = c*sinh(eta).*sin(psi);
%
% for jj=1:length(x)
%     if x(jj)<=0
%        theta(jj)=atan(y(jj)./x(jj))+pi; % pi because atan in Matlab is in [-
pi/2,pi/2]
%     else
%        theta(jj)=atan(y(jj)./x(jj));
%     end
% end
%
% B_r = Bx.*cos(theta)+By.*sin(theta);
% B_theta = -Bx.*sin(theta)+By.*cos(theta);
%
% figure
% subplot(3,1,1)
%    plot(theta*(180/pi),B_r)
```

```matlab
%    xlabel('\theta'), ylabel('B_r')
% subplot(3,1,2)
%    plot(theta*(180/pi),B_theta)
%    xlabel('\theta'), ylabel('B_\theta')
% subplot(3,1,3)
%    plot(theta*(180/pi),sqrt(B_r.^2+B_theta.^2))
%    xlabel('\theta'), ylabel('|B|')



%% [3] Field calculations, eta and psi components of B in air-gap (elliplse
eta=0.9*eta0)

% The ellipse to calculate fields on it
eta = 0.9*eta0;

% For FEM, to measure fields on this line
R2p = c*cosh(eta)
R1p = c*sinh(eta)

% Test for get point A
% x_c = c*cosh(eta0)*cos(pi/2-psi_c/2)
% y_c = c*sinh(eta0)*sin(pi/2-psi_c/2)
% theta_c = 2*atand(x_c/y_c)

psi = linspace(0,2*pi,10000); % 2*pi range of elliptical angle psi

phi   = zeros(1,length(psi));  % Scalar Magnetic Potential
Az   = zeros(1,length(psi));  % Scalar Magnetic Potential
B_eta = zeros(1,length(psi));% eta-component of B (normal)
B_psi = zeros(1,length(psi));% psi-component of B (tangential)

for n=1:2:300
    % Caculation of Fourier Coefficients An
    psii = linspace(pi/2-psi_c/2,pi/2+psi_c/2,10000); % for integration
    An   = -(N*ic/Lc)*(2*c./(n*pi*cosh(n*eta0)))...
           *trapz(psii, sqrt(cosh(eta0)^2-cos(psii).^2).*sin(n*psii) );

    % Scalar Potential: phi=A cosh(n eta) cos(psi)
    phi = phi+An.*cosh(n*eta).*cos(n*psi); % Magnetic scalar potential

    % Vector Potential: phi=A sinh(n eta) sin(psi)
    Dn  = -u0*An;
    Az  = Az+Dn.*sinh(n*eta).*sin(n*psi);

    ht = c*sqrt(cosh(eta).^2-cos(psi).^2); % Scale factor

    % Flux Density Vectors
    B_eta = B_eta+u0*(-1./ht)*n.*An.*sinh(n*eta).*cos(n*psi); % B_eta
    B_psi = B_psi+u0*(1./ht)*n.*An.*cosh(n*eta).*sin(n*psi);  % B_psi

end

% Magnetic Flux density: B_eta and B_psi
subplot(3,1,1)
   plot(psi*(180/pi),B_eta,...
   psi_B_eta9_orig*(180/pi), Beta_B_eta9_orig,'--',...
   psi_B_eta9_simp*(180/pi), Beta_B_eta9_simp,'--',...
   'LineWidth',1); grid on
   legend('Model','FEM original','FEM simplified')
   xlabel('\psi (deg)'); ylabel('B_\eta (tesla)'); xlim([0,360])
   title('air-gap \eta=0.9\eta_0')
subplot(3,1,2)
```

```
   plot(psi*(180/pi),B_psi,...
   psi_B_eta9_orig*(180/pi), Bpsi_B_eta9_orig,'--',...
   psi_B_eta9_simp*(180/pi), Bpsi_B_eta9_simp,'--',...
   'LineWidth',1); grid on
   legend('Model','FEM original','FEM simplified')
   xlabel('\psi (deg)'); ylabel('B_\psi (tesla)')
   xlim([0,360])
subplot(3,1,3)
   plot(psi*(180/pi),phi,...
        psi_B_eta9_orig*(180/pi), phi_B_eta9_orig,'--',...
        psi_B_eta9_simp*(180/pi), phi_B_eta9_simp,'--',...
        'LineWidth',1); grid on
   xlim([0,360]); ylim([-55,55])
   xlabel('\psi (deg)'); ylabel('Scalar Potential \phi')



% Magnitude of B
% plot(psi*(180/pi),sqrt(B_eta.^2+B_psi.^2))
% xlim([0,360])
% xlabel('\psi')
% ylabel('|B|')



%% [4] Torque Calculations, eta and psi components of B on PM boundary (r=Rr)

% Cylindrical coordinates
theta = linspace(0,2*pi,1000);
r = Rr;

% Cylindrical to Cartesian coordinates
xx = r.*cos(theta);
yy = r.*sin(theta);

% Cartesian to elliptical coordinates
eta_cr = real(acosh((xx+j*yy)./c));
psi_cr = imag(acosh((xx+j*yy)./c));

phi   = zeros(1,length(psi_cr));
Az    = zeros(1,length(psi_cr));
B_eta = zeros(1,length(psi_cr));
B_psi = zeros(1,length(psi_cr));

for n=1:2:299

    % Caculation of Fourier Coefficients An
    psii = linspace(pi/2-psi_c/2,pi/2+psi_c/2,10000);
    An   = -(N*ic/Lc)*(2*c./(n*pi*cosh(n*eta0)))...
           *trapz(psii, sqrt(cosh(eta0)^2-cos(psii).^2).*sin(n*psii) );

    % Scalar Potential: phi=A cosh(n eta) cos(psi)
    phi = phi+An.*cosh(n*eta_cr).*cos(n*psi_cr); % Magnetic Scalar Potential

    % Vector Potential: phi=A sinh(n eta) sin(psi)
    Dn  = -u0*An;
    Az  = Az+Dn.*sinh(n*eta_cr).*sin(n*psi_cr);

    % Scale Factor
    ht  = c*sqrt(cosh(eta_cr).^2-cos(psi_cr).^2); % Scale factor

    B_eta = B_eta+u0*(-1./ht)*n.*An.*sinh(n*eta_cr).*cos(n*psi_cr); % B_eta
    B_psi = B_psi+u0*(1./ht)*n.*An.*cosh(n*eta_cr).*sin(n*psi_cr);  % B_psi
```

```
end

% acosh gives [0,pi], so it needs to be modified to get [0,2pi]
psi_crr = [psi_cr(1:length(psi_cr)/2) ,
2*pi+psi_cr(length(psi_cr)/2+1:length(psi_cr))];

% B_eta and B_psi on boundary of PM
subplot(3,1,1)
   plot(psi_crr*(180/pi),B_eta,'LineWidth',1); grid on
   xlabel('\psi (deg)'); ylabel('B_\eta (tesla)')
   xlim([0,360])
   title('PM Boundary r=Rr')
   legend('Model','FEM original','FEM simplified')
subplot(3,1,2)
   plot(psi_crr*(180/pi),B_psi,'LineWidth',1); grid on
   xlabel('\psi (deg)'); ylabel('B_\psi (tesla)')
   xlim([0,360])
   legend('Model','FEM original','FEM simplified')
subplot(3,1,3)
   % Scalar potential phi on boundary of PM as a function of psi
   plot(psi_crr*(180/pi),phi,'LineWidth',1); grid on
   xlim([0,360]); ylim([-55,55])
   xlabel('\psi (deg)'); ylabel('Scalar Potential \phi')
   legend('Model','FEM original','FEM simplified')


% plot(psi_crr*(180/pi),sqrt(B_eta.^2+B_psi.^2),'LineWidth',1); grid on
% xlim([0,360])
% xlabel('\psi (deg)')
% ylabel('|B| (tesla)')

% Plot Ellipse and PM boundaries
x_el = c*cosh(eta0).*cos(psi);
y_el = c*sinh(eta0).*sin(psi);

x_cr = c*cosh(eta_cr).*cos(psi_cr);
y_cr = c*sinh(eta_cr).*sin(psi_cr);
figure; plot(x_el,y_el,x_cr,y_cr,'LineWidth',1); grid on
legend('Ellipse boundary','PM boundary')
axis equal

% Covert Vector B from Elliptical to Cartesian
ht = c*sqrt(cosh(eta_cr).^2-cos(psi_cr).^2);
Bx = imag( (ht./(c*sinh(eta_cr+j*psi_cr))) .* (B_psi+j*B_eta));
By = real( (ht./(c*sinh(eta_cr+j*psi_cr))) .* (B_psi+j*B_eta));

% Covert Vector B from Cartesian to Cylindrical
B_r     =  Bx.*cos(theta)+By.*sin(theta);
B_theta = -Bx.*sin(theta)+By.*cos(theta);

% Fundamental Component of Br, Torque-Producing Component
Br1_model    = (2/(2*pi))*trapz(theta,B_r.*cos(theta)) % Model
Br1_FEM_orig =
(2/(2*pi))*trapz(theta_B_Rr_orig,Br_B_Rr_orig.*cos(theta_B_Rr_orig)) % Original
Geometry
Br1_FEM_simp =
(2/(2*pi))*trapz(theta_B_Rr_simp,Br_B_Rr_simp.*cos(theta_B_Rr_simp)) %
Simplified Geometry

% Bt and B_theta
figure
subplot(3,1,1)
   plot(theta*(180/pi), B_r,...
```

```
        theta_B_Rr_orig*(180/pi), Br_B_Rr_orig,'--',...
        theta_B_Rr_simp*(180/pi), Br_B_Rr_simp,'--',...
        ...
        theta*(180/pi), Br1_model*cos(theta),... % fundamental
        theta_B_Rr_orig*(180/pi), Br1_FEM_orig*cos(theta_B_Rr_orig),'--',... %
fundamental
        theta_B_Rr_simp*(180/pi), Br1_FEM_simp*cos(theta_B_Rr_simp),'--',... %
fundamental
        'LineWidth',1); grid on
   xlabel('\theta (deg)'); ylabel('B_r (tesla)')
   xlim([0,360])
   legend('Model','FEM original','FEM simplified')
   title('PM Boundary r=Rr')
subplot(3,1,2)
   plot(theta*(180/pi),B_theta,...
        theta_B_Rr_orig*(180/pi), Btheta_B_Rr_orig,'--',...
        theta_B_Rr_simp*(180/pi), Btheta_B_Rr_simp,'--',...
        'LineWidth',1); grid on
   xlabel('\theta (deg)'); ylabel('B_\theta (tesla)')
   legend('Model','FEM original','FEM simplified')
   xlim([0,360])
subplot(3,1,3)
   % Scalar potential phi on boundary of PM as a function of theta
   plot(theta*(180/pi),phi,...
        theta_B_Rr_orig*(180/pi), phi_B_Rr_orig,'--',...
        theta_B_Rr_simp*(180/pi), phi_B_Rr_simp,'--',...
        'LineWidth',1); grid on
   xlim([0,360]); ylim([-55,55])
   xlabel('\theta (deg)'); ylabel('Scalar Potential \phi')
   legend('Model','FEM original','FEM simplified')

% plot(theta*(180/pi),sqrt(B_r.^2+B_theta.^2),'LineWidth',1); grid on
% xlabel('\theta (deg)'); ylabel('|B| (tesla)')
% xlim([0,360])

% Torque Method 1 (General)
T_coil1 = zeros(1,length(beta));
mm=1;
for betaa=beta
    Km = -M*sin(theta-betaa); % Amperian Surface Current Density of PM
    T_coil1(mm) = LL*Rr^2*trapz(theta,Km.*B_r) * 1e3; % m N.m
    mm = mm+1;
end


% Torque Method 2 (Using B1)
T_coil          = pi*Rr^2*LL*M*Br1_model    * sin(beta) * 1e3; % Model, m N.m
T_coil_FEM_orig = pi*Rr^2*LL*M*Br1_FEM_orig * sin(beta) * 1e3; % FEM, Original
Geometry, m N.m
T_coil_FEM_simp = pi*Rr^2*LL*M*Br1_FEM_simp * sin(beta) * 1e3; % FEM,
Simplified Geometry, m N.m


% Coil Plot Torque
figure
plot((180/pi)*beta , T_coil,...
     (180/pi)*beta , T_coil_FEM_orig,'--',...
     (180/pi)*beta , T_coil_FEM_simp,'--',...
      'LineWidth',1); grid on
xlabel('\beta(deg)'), ylabel('Torque (m N.m)')
legend('Model','FEM, Original Geometry','FEM, Simplified Geometry')
ylim([0,1.6])
```

```matlab
%% [5] Vector Fields B and Equipotential Lines phi

% Meshgrid in elliptical coordinates
etaa_mesh = linspace(0,eta0,20);
psii_mesh = linspace(0,2*pi,70);
[eta_mesh,psi_mesh] = meshgrid(etaa_mesh,psii_mesh);

% Elliptical to Cartesian Conversion
x_mesh = c*cosh(eta_mesh).*cos(psi_mesh);
y_mesh = c*sinh(eta_mesh).*sin(psi_mesh);

phi   = zeros(length(psii_mesh),length(etaa_mesh)); % Scalar Potential
Az    = zeros(length(psii_mesh),length(etaa_mesh)); % Vector Potential
B_eta = zeros(length(psii_mesh),length(etaa_mesh)); % B_eta
B_psi = zeros(length(psii_mesh),length(etaa_mesh)); % B_psi

for n=1:2:500
    psii = linspace(pi/2-psi_c/2,pi/2+psi_c/2,10000);
    An   = -(N*ic/Lc)*(2*c./(n*pi*cosh(n*eta0)))...
           *trapz(psii, sqrt(cosh(eta0)^2-cos(psii).^2).*sin(n*psii) );

    phi = phi+An.*cosh(n*eta_mesh).*cos(n*psi_mesh); % Scalar Potential

    Dn  = -u0*An;
    Az  = Az+Dn.*sinh(n*eta_mesh).*sin(n*psi_mesh); % Vector Potential

    ht  = c*sqrt(cosh(eta_mesh).^2-cos(psi_mesh).^2); % Scale factor

    B_eta = B_eta+u0*(-1./ht)*n.*An.*sinh(n*eta_mesh).*cos(n*psi_mesh); % B_eta
    B_psi = B_psi+u0*(1./ht)*n.*An.*cosh(n*eta_mesh).*sin(n*psi_mesh);  % B_psi
end

% Field Vectors B in Cartesian Coordinates
Bx  = imag( (ht./(c*sinh(eta_mesh+j*psi_mesh))) .* (B_psi+j*B_eta)); % Bx
By  = real( (ht./(c*sinh(eta_mesh+j*psi_mesh))) .* (B_psi+j*B_eta)); % By
Bxy = sqrt(Bx.^2+Bx.^2); % Magnitude |B|

% Flux Density Vectors and Equipotential Lines
figure; hold on
quiver(x_mesh,y_mesh,Bx,By) % vectors
contour(x_mesh,y_mesh,phi,21); colormap winter % phi contours
% contour(x_mesh,y_mesh,phi,20,'ShowText','on') % contours
xx = c*cosh(eta0).*cos(psi_mesh); yy = c*sinh(eta0).*sin(psi_mesh);
plot(xx,yy,'k')% Plot Ellipse boundary
hold off; axis equal; axis off

% Flux Density Distribution
figure; hold on
contourf(x_mesh,y_mesh,Bxy,100,'LineStyle','None'); colormap Jet % contours
contour(x_mesh,y_mesh,Az,21,'Linecolor','k','LineWidth',0.7); % Az contours
title('B (Tesla)'); axis equal; axis off
caxis([0,0.2]); hold off

% Distribution of Vector Magnetic Potential Az
figure; hold on
% contour(x_mesh,y_mesh,Az,21,'--','LineWidth',1); colormap cool % Az contours
% title('Az (Wb/m)')
  contour(x_mesh,y_mesh,phi,15); colormap winter % phi contours
% title('psi')
% caxis([-9e-5,9e-5]) % for Az
caxis([-50,50]) % for phi
plot(xx,yy,'k')% Plot Ellipse boundary
```

```
hold off; axis equal; axis off

%% [6] Reluctance Torque by Energy Method

theta_f = 50 *(pi/180); % Angle of Fringing Effect

yr    = linspace(0,Rr,1000); % Integration range of yr on rotor reference frame
thetar = asin(yr/Rr);      % thetar in rotor reference frame

xp1 = zeros(1,length(yr)); yp1 = zeros(1,length(yr)); % Point S1
xp2 = zeros(1,length(yr)); yp2 = zeros(1,length(yr)); % Point S2
Wc_raw  = zeros(1,length(beta)); % co-energy
ii  = 1;

for betaa = beta % Rotor rotaion from 0 to pi [rad/sec]

    % MMF in the loop
    Fm = 2*M*Rr*cos(thetar);

    % length inside magnet
    Lm = 2*Rr*cos(thetar);

    %--------------------[ length Lp1 in airgap ]--------------------
    % Point m1
    xm1 = Rr*cos(betaa+thetar); % xm1 in stationary reference frame
    ym1 = Rr*sin(betaa+thetar); % ym1 in stationary reference frame

    % Polynomial Coefficient
    a4 = (R1^2-R2^2)^2;
    a3 = 2*R2^2*xm1*(R1^2-R2^2);
    a2 = R2^4*xm1.^2+R1^2*R2^2*ym1.^2-R2^2*(R1^2-R2^2)^2;
    a1 = 2*R2^4*xm1*(R2^2-R1^2);
    a0 = -R2^6*xm1.^2;

    for jj=1:length(yr)

        % Calculation of point m1
        roots1 = roots([a4,a3(jj),a2(jj),a1(jj),a0(jj)]); % 4 roots of
polynomial

        % Calculate xp1
        if xm1(jj)>=0 % if xm1>0, so xp1>0
           for kk=1:4 % look in the 4 roots to pick the real positive root
               if isreal(roots1(kk)) && roots1(kk)>=0
                  xp1(jj) = roots1(kk);
               end
           end
        else % if xm1<0, so xp1<0
           for kk=1:4 % look in the 4 roots to pick the real negative root
               if isreal(roots1(kk)) && roots1(kk)<0
                  xp1(jj) = roots1(kk);
               end
           end
        end

        % Calculate ym1 after calculating xm1
        if ym1(jj)>=0 % if ym1>0, so yp1>0
           yp1(jj) =  R1*sqrt(1-xp1(jj)^2/R2^2);
        else % if ym1<0, so yp1<0
           yp1(jj) = -R1*sqrt(1-xp1(jj)^2/R2^2);
        end
    end
```

```
    Lp1 = sqrt((xm1-xp1).^2+(ym1-yp1).^2); % length of Lp1 without fringing

    % Fringing Effect at the Interpolar Region, add quarter curcle: r*pi/4
    correction_Lp11 = zeros(1,length(yr));
    correction_Lp12 =zeros(1,length(yr));
    for jj=1:length(yr)
        % If at top interpolar region, at theta=pi/2
        if abs(thetar(jj)+betaa-pi/2)<theta_c/2 %at distance of theta_c/2 from
pi/2
            correction_Lp11(jj) = theta_f*R1*abs(theta_c/2-
abs(thetar(jj)+betaa-pi/2));
        else
            correction_Lp11(jj) = 0;
        end

        % If at bottom interpolar region, at theta=3pi/2
        if abs(thetar(jj)+betaa-3*pi/2)<theta_c/2 %at distance of theta_c/2
from 3pi/2
            correction_Lp12(jj) = theta_f*R1*abs(theta_c/2-
abs((thetar(jj)+betaa-3*pi/2)));
        else
            correction_Lp12(jj) = 0;
        end

    end

    % Add the extra length for correction
    Lp1 = Lp1 + correction_Lp11 + correction_Lp12;



    %--------------------[ length Lp2 in airgap ]--------------------
    % Point m2
    xm2 = -Rr*cos(betaa-thetar);
    ym2 = -Rr*sin(betaa-thetar);

    % Polynomial Coefficient
    b4 = (R1^2-R2^2)^2;
    b3 = 2*R2^2*xm2*(R1^2-R2^2);
    b2 = R2^4*xm2.^2+R1^2*R2^2*ym2.^2-R2^2*(R1^2-R2^2)^2;
    b1 = 2*R2^4*xm2*(R2^2-R1^2);
    b0 = -R2^6*xm2.^2;

    for jj=1:length(yr)

        % Calculation of point m2
        roots2 = roots([b4,b3(jj),b2(jj),b1(jj),b0(jj)]); % 4 roots of
polynomial

        % Calculate xp2
        if xm2(jj)>=0 % if xm2>0, so xp2>0
           for kk=1:4 % look in the 4 roots to pick the real positive root
               if isreal(roots2(kk)) && roots2(kk)>=0
                  xp2(jj) = roots2(kk);
               end
           end
        else % if xm2<0, so xp2<0
           for kk=1:4 % look in the 4 roots to pick the real negative root
               if isreal(roots2(kk)) && roots2(kk)<0
                  xp2(jj) = roots2(kk);
               end
           end
        end
```

```
        % Calculate yp2 after calculating xp2
        if ym2(jj)>=0 % if ym2>0, so yp2>0
           yp2(jj) =  R1*sqrt(1-xp2(jj)^2/R2^2);
        else % if ym2<0, so yp2<0
           yp2(jj) = -R1*sqrt(1-xp2(jj)^2/R2^2);
        end

    end
    Lp2 = sqrt((xm2-xp2).^2+(ym2-yp2).^2); % length of Lp2 without fringing


    % Fringing Effect at the Interpolar Region, add quarter curcle: r*pi/4
    correction_Lp21 = zeros(1,length(yr));
    correction_Lp22 = zeros(1,length(yr));
    for jj=1:length(yr)
        % If at top interpolar region, at theta=pi/2
        if abs(betaa+pi-thetar(jj)-pi/2)<theta_c/2 %at distance of theta_c/2
from pi/2
            correction_Lp21(jj) = theta_f*R1*abs(theta_c/2-abs(betaa+pi-
thetar(jj)-pi/2));
        else
            correction_Lp21(jj) = 0;
        end

        % If at bottom interpolar region, at theta=3pi/2
        if abs(betaa+pi-thetar(jj)-3*pi/2)<theta_c/2 %at distance of theta_c/2
from 3pi/2
            correction_Lp22(jj) = theta_f*R1*abs(theta_c/2-abs((betaa+pi-
thetar(jj)-3*pi/2)));
        else
            correction_Lp22(jj) = 0;
        end

    end
    % Add the extra length for correction
    Lp2 = Lp2 + correction_Lp21 + correction_Lp22;


    % Total length
    L_DFT = Lp1 + Lm + Lp2;

    %--------------- --[ Flux Density at beta=0 and 90 ]-------------------
    if betaa==0
        B_beta0  = u0*Fm./L_DFT; % B within DFTs
    elseif betaa==pi/2
        B_beta90 = u0*Fm./L_DFT; % B within DFTs
    end

    %--------------------[ Co-energy Calculation ]--------------------
    % Differential co-energy associated with DFT at rotor angle beta
    dWc = 2*(LL*u0/2)*(Fm.^2./L_DFT);
    % Numerical integration to obtain Wc at rotor angle beta
    Wc_raw(ii) = trapz(yr,dWc);
    ii = ii+1; % next rotor position

end

% Numerical derivative to obtain torque
for kk=1:(length(beta)-1)
    T_raw(kk) = (Wc_raw(kk+1)-Wc_raw(kk))/db;
end
```

```
% Flux density distribution
figure
subplot(2,1,1)
    plot([thetar*(180/pi),-
fliplr(thetar*(180/pi))],[B_beta0,fliplr(B_beta0)],'LineWidth',1); grid on
    xlabel('\theta_r(deg)'); ylabel('B (tesla)'); xlim([-90, 90]);
title('\beta=0 deg')
subplot(2,1,2)
    plot([thetar*(180/pi),-
fliplr(thetar*(180/pi))],[B_beta90,fliplr(B_beta90)],'LineWidth',1); grid on
    xlabel('\theta_r(deg)'; ylabel('B (tesla)'); xlim([-90, 90]);
title('\beta=90 deg')

% Lp1 and Lp2
figure
subplot(2,1,1)
   plot(thetar*(180/pi),Lp1,'LineWidth',1)
   xlabel('\theta_r(deg)'; ylabel('Lp1')
subplot(2,1,2)
   plot(thetar*(180/pi),Lp2,'LineWidth',1)
   xlabel('\theta_r(deg)'; ylabel('Lp2')

% Wc
bt  = beta(1:(length(beta)-1));
Wc0 = (2/pi)*trapz(bt,Wc_raw(1:(length(beta)-1))) % DC Component
Wc1 = (2/pi)*trapz(bt,Wc_raw(1:(length(beta)-1)).*cos(2*bt)) % Fundamental
Component
Wc  = Wc0/2+Wc1.*cos(2*bt);
figure; plot(beta(1:(length(beta)-1))*(180/pi),Wc,'LineWidth',1); grid on
xlabel('\beta (degrees)'); ylabel('Wc')

% Reluctance Torque: Tres
bt = beta(1:(length(beta)-1));
Tres1 = (2/pi)*trapz(bt,T_raw.*sin(2*bt))
Tres = Tres1.*sin(2*bt)*1e3; % Fundamental Component
figure; plot(beta(1:(length(beta)-1))*(180/pi),Tres,'LineWidth',1); grid on
xlabel('\beta(deg)')
ylabel('T_r_e_s(m N.m)')



%% [7] Total Torque

Tt          = T_coil          + [Tres,0]; % Model

Tres_FEM = spline(beta_T_FEM_orig, T_res_FEM_orig, beta); % Tres, FEM,
interpolation
Tt_FEM_orig = T_coil_FEM_orig + Tres_FEM; % FEM, Original Geometry
Tt_FEM_simp = T_coil_FEM_simp + Tres_FEM; % FEM, Original Geometry


figure; plot(beta*(180/pi) ,[Tres,0],'b',...
             beta*(180/pi) , Tres_FEM,'r--',...
             theta_Tres_exp, Tres_exp,'k*',...
             ...
             beta*(180/pi), T_coil,'b',...
             beta*(180/pi), T_coil_FEM_orig,'r--',...
             beta*(180/pi), T_coil_FEM_simp,'g--',...
             theta_Tc_exp , Tc_exp,'k*',...
             ...
             beta*(180/pi), Tt,'b',...
             beta*(180/pi), Tt_FEM_orig,'r--',...
             beta*(180/pi), Tt_FEM_simp,'g--',...
```

```
             theta_Tt_exp , Tt_exp,'k*',...
             'LineWidth',1); grid on
xlabel('\beta(deg)'); ylabel('T(m N.m)')
legend('T_r_e_s, Model', 'T_r_e_s FEM', 'T_r_e_s Exp',...
       'T_c_o_i_l, Model','T_c_o_i_l FEM Orig','T_c_o_i_l FEM Simp', 'T_c_o_i_l
Exp',...
       'T_t, Model','T_t, FEM Orig', 'T_t, FEM Simp', 'T_t, Exp')
xlim([1 180])
```

Appendix J

Matlab Code for the Solution of Diffusion Equation

The code is as in below:

```
%-----------------------------------------------------------------------%
%      Diffusion , Eddy-Currents in the Magnet and The Laminations       %
%                Sajjad Mohammadi, EECS, MIT, August 2021               %
%-----------------------------------------------------------------------%


%% Dimensions and Initialization
clc;

L  = 4.191*1e-3; % Axial Length of Actuator [m]
Rr = (3.048/2)*1e-3; % Rotor radius [m]
R1 = 1.71e-3; % semi-major axis of ellipse [m]
R2 = 1.15*1.71e-3; % semi-minor axis of ellipse [m]
Do = 13.716e-3; % Outer diameter of stator [m]
d  = 0.35*1e-3; % Lamination Thickness [m]
m  = 12; % number of laminations
wp = 4.72e-3; % pole width, 4.72mm directly measured from geometry
N  = 100; % Number of turns
Lc0 = 280e-6; % Low-frequency inductance
mu0= 4*pi*1e-7;

% average air-gap length
lg = ((R1-R1)+(R2-Rr))/2 ;
% PM length, square approximation of rectangular cross-section
lm = pi*Rr^2/wp;
% Average iron length
li = (Do/2-wp/4)*pi + (Do/2-wp/4)-(lm+lg)/2 ; % Average length of the iron core
along the flux line

% Effective Permeability
Area = wp*L; % Pole area
Rt0  = N^2/Lc0; % Reluctance seen by stator

mu_eff_i = li /(Rt0*Area); % based on L0
mu_eff_m = lm/(Rt0*Area); % based on L0

% Conductivity, Initial Guess
sigma_m = 0.6*1e6; % conductivity of magnet
sigma_i = 2*1e6; % conductivity of iron

% intial field [T]
B0 = 1;

% Frequency to plot B and J versus dimensions
f = 20000;% frequency [Hz]
omega = 2*pi*f; % rad/sec



%% 2D Diffusion, Eddy-Currents in the Magnet
```

```
% PM dimensions
% b = 0.35e-3; % Lamination thickness

% f = 20000;% frequency [Hz]
omega = 2*pi*f; % rad/sec

a = wp/2; % Rectangle Width=2a
b = L/2; % Rectangle Height=2*b
w = sqrt(4*a*b)/2; % square approximation of the rectangle: side=2*w

scale = 0.97; % scale xy range to avoide overeshoot in quiver plot on
boundaries

phi0 = B0*4*a*b; % Initial flux

% Meshgrid in elliptical coordinates
x_mesh = linspace(-scale*a, scale*a, 15);
z_mesh = linspace(-scale*b, scale*b, 15);
[x,z]  = meshgrid(x_mesh,z_mesh);

By1 = zeros(size(x)); By2 = zeros(size(x));%
phi_m  = 0;
Jx = zeros(size(x)); Jz = zeros(size(x));%

for n=1:2:300
    % k1n and k2n
    k1 = sqrt( (n*pi./(2*b)).^2 + i*omega*mu_eff_m*sigma_m );
    k2 = sqrt( (n*pi./(2*a)).^2 + i*omega*mu_eff_m*sigma_m );

    % Coefficients
    An = B0*(4./(n*pi)) .* sin(n*pi/2);

    % Flux densiyu
    By1 = By1 + An .* cos(n*pi*z/(2*b)) .* ( cosh(k1.*x) ./ cosh(k1*a) );
    By2 = By2 + An .* cos(n*pi*x/(2*a)) .* ( cosh(k2.*z) ./ cosh(k2*b) );

    % Flux
    phi_m  = phi_m  + (8*phi0/(n^2*pi^2)) *( tanh(k1*a)/(k1*a) +
tanh(k2*b)/(k2*b) ); % Exact

    % Current density
    Jx = Jx - (An/mu_eff_m) .* (n*pi/(2*b)) .* sin(n*pi*z/(2*b)) .* (
cosh(k1.*x) ./ cosh(k1*a) )...
            + (An/mu_eff_m)      .* k2      .* cos(n*pi*x/(2*a)) .* (
sinh(k2.*z) ./ cosh(k2*b) );
    Jz = Jz - (An/mu_eff_m)      .* k1      .* cos(n*pi*z/(2*b)) .* (
sinh(k1.*x) ./ cosh(k1*a) )...
            + (An/mu_eff_m) .* (n*pi/(2*a)) .* sin(n*pi*x/(2*a)) .* (
cosh(k2.*z) ./ cosh(k2*b) );
end
By = By1 + By2;

abs(phi_m)

% Flux Density Distribution, abs: magnitude
figure;
contourf(x*1e3 ,z*1e3 ,abs(By),50,'LineStyle','None'); colormap Jet
title('B (Tesla)'); axis equal
% xlabel('x(mm)'); ylabel('z(mm)')
axis off tight;  caxis([0.986 1])

figure;
surf(x*1e3 ,z*1e3 ,abs(By)); colormap Jet % contours
```

```
% xlabel('x(mm)'); ylabel('z(mm)')
% title('B (Tesla)'); axis equal
axis tight;


% Magnitude of J, real: at t=0
J = abs(sqrt((real(Jx)).^2+(real(Jz)).^2));
figure;
contourf( x*1e3 ,z*1e3 ,real(J)*1e-6,1000,'LineStyle','None'); colormap Jet %
contours
xlabel('x(mm)'); ylabel('z(mm)')
title('J (A/mm^2)'); axis equal; axis off
% Current Density Vectors, real: at t=0
% figure;
hold on
quiver( x*1e3, z*1e3, real(Jx)*1e-6, real(Jz)*1e-6) % vectors
xlabel('x(mm)'); ylabel('z(mm)')
axis equal tight


% ------------------------- Plots including time -------------------------
TT = 1/f; % period
timee = 0:TT/8:TT;
mm=1;
figure;
for time = timee % 0, TT/4, TT/2, 3TT/4
    BBy = By.*exp(i*omega*time); % including time
    subplot(3,length(timee),mm)
      contourf(x*1e3 ,z*1e3 ,real(BBy),50,'LineStyle','None');
      title('B (Tesla)'); axis equal
      % xlabel('x(mm)'); ylabel('z(mm)')
      title(['t=',num2str(mm-1),'T/8']); axis equal; axis off
      % caxis([0.95 1])

    JJx = real(Jx.*exp(i*omega*time)); % including time
    JJz = real(Jz.*exp(i*omega*time)); % including time
    subplot(3,length(timee),length(timee)+mm)
      quiver( x*1e3, z*1e3, JJx*1e-6, JJz*1e-6) % vectors
      % xlabel('x(mm)'); ylabel('z(mm)')
      axis equal tight; % xlim([min(x_mesh), max(x_mesh)])
      title(['t=',num2str(mm-1),'T/8']); axis equal; axis off
      caxis([-90,90])


JJ=abs(sqrt((real(Jx.*exp(i*omega*time))).^2+(real(Jz.*exp(i*omega*time))).^2))
; % including time
    subplot(3,length(timee),2*length(timee)+mm)
      contourf( x*1e3 ,z*1e3 ,real(JJ.*exp(i*omega*time))*1e-
6,1000,'LineStyle','None'); colormap Jet % contours
      xlabel('x(mm)'); ylabel('z(mm)')
      % title('J (A/mm^2)'); axis equal; axis off
      title(['t=',num2str(mm-1),'T/8']); axis equal; axis off

    mm = mm+1;
end



%% 1D Diffusion , Eddy-Currents in the The Laminations

omega=2*pi*20000;
alpha = sqrt(i*omega*mu_eff_i*sigma_i);
```

```
phi0_i = B0 * m * d * wp; % Initial Flux

zz = linspace(-d/2, d/2, 1000);

Byy = B0*cosh(alpha*zz)/cosh(alpha*d/2); % Flux density
phi_i = phi0_i*tanh(alpha*d/2)/(alpha*d/2); % Flux
Jxx = B0 * (alpha/mu_eff_i) * sin(alpha*zz)/cosh(alpha*d/2); % Current Density


% ---------------------- Plot of B and J versus y -------------------------
yyaxis left;  plot(zz*1e3,real(Byy),'LineWidth',1)
ylabel('B_y (T)')
yyaxis right; plot(zz*1e3,real(Jxx)*1e-6,'LineWidth',1)
ylabel('J_x (A/mm^2)')
xlabel('z (mm)')
grid on; axis tight


% ------------------ Plot over the lamination surface ---------------------
xx_mesh = linspace(-wp/4, wp/4, 20);
zx_mesh = linspace(-d/2, d/2, 10);
[xx,zz]  = meshgrid(xx_mesh,zx_mesh);

Byy = B0*cosh(alpha*zz)/cosh(alpha*d/2)+0.*xx; % Flux density

Jxx = B0 * (alpha/mu_eff_i) * sin(alpha*zz)/cosh(alpha*d/2)+0.*xx; % Current
Density
Jzz = 0.*xx + 0.*zz; % Current Density

% Flux Density Distribution
figure;
contourf(xx*1e3 ,zz*1e3 ,abs(Byy),50,'LineStyle','None'); colormap Jet
title('B (Tesla)'); axis equal
% xlabel('x(mm)'); ylabel('z(mm)')
caxis([0.994 1])

% Current Density
JJ = abs(sqrt((real(Jxx)).^2+(real(Jzz)).^2));
figure;
contourf( xx*1e3 ,zz*1e3 ,real(JJ)*1e-6,1000,'LineStyle','None'); colormap Jet
% contours
% xlabel('x(mm)'); ylabel('z(mm)')
title('J (A/mm^2)'); axis equal; axis off
caxis([0, 8])
% Current Density Vectors and magnitude at t=0
% figure;
hold on
quiver( xx*1e3, zz*1e3, real(Jxx)*1e-6, real(Jzz)*1e-6) % vectors
% xlabel('x(mm)'); ylabel('z(mm)')
title('J (A/mm^2)'); axis equal; axis off
% caxis([0,5000])


% ------------------------- Plot Including time ---------------------------
TT = 1/f; % period
timee = 0:TT/4:TT;
mm=1;
figure;
for time = timee % 0, TT/4, TT/2, 3TT/4
    subplot(3,length(timee),mm)
    BByy = real(Byy.*exp(i*omega*time)); % including time
    contourf(xx*1e3 ,zz*1e3 ,real(BByy),50,'LineStyle','None');
    title('B (Tesla)'); axis equal
```

```
    % xlabel('x(mm)'); ylabel('z(mm)')
    title(['t=',num2str(mm-1),'T/4']); axis equal; axis off
    % caxis([0.95 1])

    subplot(3,length(timee),length(timee)+mm)
    JJxx = real(Jxx.*exp(i*omega*time)); % including time
    JJzz = real(Jzz.*exp(i*omega*time)); % including time
    quiver( xx*1e3, zz*1e3, JJxx*1e-6, JJzz*1e-6) % vectors
    % xlabel('x(mm)'); ylabel('z(mm)')
    axis equal tight; % xlim([min(x_mesh), max(x_mesh)])
    title(['t=',num2str(mm-1),'T/4']); axis equal; axis off
    caxis([-90,90])

    subplot(3,length(timee),2*length(timee)+mm)
    JJ=abs(sqrt(JJxx.^2 + JJxx.^2)); % including time
    contourf( xx*1e3 ,zz*1e3 ,JJ*1e-6,1000,'LineStyle','None'); colormap Jet %
contours
    xlabel('x(mm)'); ylabel('z(mm)')
    % title('J (A/mm^2)'); axis equal; axis off
    title(['t=',num2str(mm-1),'T/4']); axis equal; axis off

    mm = mm+1;
end



%% The coefficient Reluctances versus frequency
% frequency range to plot Qi and Qm versus frequency
ff = logspace(2,9,1000);% frequency [Hz]
omegaa=2*pi*ff;

% Correction factors for mu*sigma
kk_i = 0.05;
kk_m = 2.15;

% ------------ Flux ratio and reluctances using exact formulas ------------
% phi/Phi0, Exact
phi_phi00_exact  = 1./(1 +0.*omegaa);  % No eddy current

alpha = sqrt(i * omegaa * kk_i * mu_eff_i*sigma_i);
phi_phi0_i_exact = tanh(alpha*d/2)./(alpha*d/2);   % Eddy current in only iron

a=w; b=w; % square
phi_m = zeros(1,length(omegaa));
nn=1;
for omega=omegaa
    phi_mm=0;
    for n=1:2:100
        % k1n and k2n
        k1 = sqrt( (n*pi./(2*b)).^2 + i*omega * kk_m * mu_eff_m*sigma_m );
        k2 = sqrt( (n*pi./(2*a)).^2 + i*omega * kk_m * mu_eff_m*sigma_m );

        % Flux
        phi_mm  = phi_mm  + (8*1/(n^2*pi^2)) *( tanh(k1*a)/(k1*a) +
tanh(k2*b)/(k2*b) ); % Exact
    end
    phi_m(nn) = phi_mm;
    nn=nn+1;
end
phi_phi0_m_exact = phi_m;   % Eddy current in only magnet

phi_phi0_exact   = phi_phi0_i_exact .* phi_phi0_m_exact;% Eddy current in both
iron and magnet
```

```
% Total Reluctance, Exact
Rt00_exact = Rt0 * (1./phi_phi00_exact);  % No eddy current
Rt_i_exact = Rt0 * (1./phi_phi0_i_exact);   % Eddy current in only iron
Rt_m_exact = Rt0 * (1./phi_phi0_m_exact);   % Eddy current in only magnet
Rt_exact   = Rt0 * (1./phi_phi0_exact);% Eddy current in both iron and magnet



% ---- Flux ratio and reluctances using approximation of tanhx=1/(1+x) ----
% Qi, Qm and Q
Q_i = 0.5 * d * sqrt(i*omegaa*mu_eff_i*sigma_i);
% Q_i = (1./phi_phi0_i_exact)-1;

Q_m = (w * sqrt( (pi/(2*w)).^2 + 1i*omegaa*mu_eff_m*sigma_m ) - pi/2) /
(1+pi/2);
% Q_m = (1./phi_phi0_m_exact)-1;

Q  =  Q_i + Q_m;

% phi/Phi0, Approximation of tanhx=1/(1+x)
phi_phi00  = 1./(1 +0*omegaa);  % No eddy current
phi_phi0_i = 1./(1 + Q_i);   % Eddy current in only iron
phi_phi0_m = 1./(1 + Q_m);   % Eddy current in only magnet
phi_phi0   = 1./(1 + (Q_i+Q_m));% Eddy current in both iron and magnet

% Total Reluctance, Approximation of tanhx=1/(1+x)
Rt00 = Rt0 * (1 + 0*omegaa);  % No eddy current
Rt_i = Rt0 * (1 + Q_i);   % Eddy current in only iron
Rt_m = Rt0 * (1 + Q_m);   % Eddy current in only magnet
Rt   = Rt0 * (1 + Q_i+Q_m);% Eddy current in both iron and magnet


% -------------------------------- Plots ---------------------------------
% Plot Rt, Exact formula
% figure
% subplot(2,1,1)
%    semilogx(ff, 20*log10(abs(Rt00_exact)),...
%             ff, 20*log10(abs(Rt_i_exact)),...
%             ff, 20*log10(abs(Rt_m_exact)),...
%             ff, 20*log10(abs(Rt_exact)),...
%             'LineWidth',1); grid
%    xlabel('frequency (Hz)')
%    ylabel('Magnitude (dB)')
%    title('Reluctance, Exact formula')
% subplot(2,1,2)
%    semilogx(ff, (180/pi)*angle(Rt00_exact),...
%             ff, (180/pi)*angle(Rt_i_exact),...
%             ff, (180/pi)*angle(Rt_m_exact),...
%             ff, (180/pi)*angle(Rt_exact),...
%             'LineWidth',1); grid
%    xlabel('frequency (Hz)')
%    ylabel('Angle (deg)')
%    legend('R_t_0','R_t_i','R_t_m','R_t')
%
% % Plot phi/phi0, Exact
% figure
% subplot(2,1,1)
%    semilogx(ff, 20*log10(abs(phi_phi00_exact)),...
%             ff, 20*log10(abs(phi_phi0_i_exact)),...
%             ff, 20*log10(abs(phi_phi0_m_exact)),...
%             ff, 20*log10(abs(phi_phi0_exact)),...
%             'LineWidth',1); grid
```

```
%    xlabel('frequency (Hz)')
%    ylabel('Magnitude (dB)')
%    title('\phi/\phi_0, Exact formula')
% subplot(2,1,2)
%    semilogx(ff, (180/pi)*angle(phi_phi00_exact),...
%              ff, (180/pi)*angle(phi_phi0_i_exact),...
%              ff, (180/pi)*angle(phi_phi0_m_exact),...
%              ff, (180/pi)*angle(phi_phi0_exact),...
%              'LineWidth',1); grid
%    xlabel('frequency (Hz)')
%    ylabel('Angle (deg)')
%    legend('R_t_0','R_t_i','R_t_m','R_t')



% Plot Rt, Approximation of tanhx=1/(1+x)
figure
subplot(2,1,1)
   semilogx(ff, 20*log10(abs(Rt00)),...
            ff, 20*log10(abs(Rt_i)),...
            ff, 20*log10(abs(Rt_m)),...
            ff, 20*log10(abs(Rt)),...
            'LineWidth',1); grid
   ylabel('Magnitude (dB)')
   % title('Reluctance, Appr formula')
   xlim([10^2 10^9]); ylim([148, 200])
   xticks([10^2, 10^3,10^4,10^5,10^6,10^7,10^8,10^9]);
subplot(2,1,2)
   semilogx(ff, (180/pi)*angle(Rt00),...
            ff, (180/pi)*angle(Rt_i),...
            ff, (180/pi)*angle(Rt_m),...
            ff, (180/pi)*angle(Rt),...
            'LineWidth',1); grid
   xlabel('frequency (Hz)'); ylabel('Angle (deg)')
   legend('R_t_0','R_t_i','R_t_m','R_t')
   xlim([10^2 10^9]); ylim([0, 45])
   xticks([10^2, 10^3,10^4,10^5,10^6,10^7,10^8,10^9]); yticks([0, 22.5, 45])


% Plot phi/phi0, Approximation of tanhx=1/(1+x)
figure
subplot(2,1,1)
   semilogx(ff, 20*log10(abs(phi_phi00)),...
            ff, 20*log10(abs(phi_phi0_i)),...
            ff, 20*log10(abs(phi_phi0_m)),...
            ff, 20*log10(abs(phi_phi0)),...
            'LineWidth',1); grid
   xlabel('frequency (Hz)'); ylabel('Magnitude (dB)')
   xlim([10^2 10^9])
   title('\phi/\phi_0, Appr formula')
subplot(2,1,2)
   semilogx(ff, (180/pi)*angle(phi_phi00),...
            ff, (180/pi)*angle(phi_phi0_i),...
            ff, (180/pi)*angle(phi_phi0_m),...
            ff, (180/pi)*angle(phi_phi0),...
            'LineWidth',1); grid
   xlabel('frequency (Hz)'); ylabel('Angle (deg)')
   xlim([10^2 10^9])
   legend('R_t_0','R_t_i','R_t_m','R_t')

% Plot Qm and Qi
% figure
% subplot(2,1,1)
```

```
%    semilogx(ff, 20*log10(abs(Qi)),...
%             ff, 20*log10(abs(Qm))); grid
%    xlabel('frequency (Hz)')
%    ylabel('Magnitude (dB)')
%    title('Q_m=\phi/\phi_0')
%    legend('Q_i','Q_m','Q_i*Q_m')
% subplot(2,1,2)
%    semilogx(ff, (180/pi)*angle(Qi),...
%             ff, (180/pi)*angle(Qm)); grid
%    xlabel('frequency (Hz)')
%    ylabel('Angle (deg)')
%    legend('Q_i','Q_m','Q_i*Q_m')



%%  Electric-Magnetic Coupled Circuit
ff = logspace(0,5,1000);% frequency [Hz]
omegaa=2*pi*ff;

Rc = 1.76; % coil resistance [ohm]
Rs = 0.1; % sense resistor [ohm]
R  = Rc+Rs;
Lc0 = 290e-6; % Low-frequency inductance

% Correction factors for mu*sigma
kk_i = 0.05;
kk_m = 2.15;

% Qi, Qm, Q
Q_i =  sqrt(i*omegaa* kk_i*mu_eff_i*sigma_i)*d/2;
Q_m = 1 * ( w * sqrt( (pi/(2*w)).^2 +  i * omegaa * kk_m*mu_eff_m*sigma_m )-
pi/2)/(1+pi/2);

% Taylor Approximation of Qm with three first for faractional order modeling
aa = (pi/(2*w));
% Q_m = ( w * ( aa + (1/(2*aa)).* i * omegaa * kk_m*mu_eff_m*sigma_m  -
(1/(8*aa^3)).* (i * omegaa *kk_m* mu_eff_m*sigma_m).^2 ) -pi/2)/(1+pi/2);

Q =  Q_i + Q_m;

% Only RL
He = 1./(R+i*omegaa*Lc0);

% RL including eddy effect only in iron
kk_ii = 0.1;
Q_ii =  sqrt(i*omegaa* kk_ii*mu_eff_i*sigma_i)*d/2;
He_eddy_i = (1 + Q_ii)./(R + i*omegaa*Lc0 + R*Q_ii);

% RL including eddy effect
He_eddy = (1 + Q)./(R + i*omegaa*Lc0 + R*Q);

figure
subplot(2,1,1)
   semilogx(ff, 20*log10(abs(He)),...
            ff, 20*log10(abs(He_eddy_i)),...
            ff, 20*log10(abs(He_eddy)),'g',...
            He_appr_exp(:,1), He_appr_exp(:,2),'k--',...
            'LineWidth',1); grid
   xlabel('frequency (Hz)'); ylabel('Magnitude (dB)')
   xticks([10^0, 10^1, 10^2, 10^3,10^4,10^5]); % yticks([-90, -45, 0])
   xlim([10^0 10^5]); ylim([-50 0])
subplot(2,1,2)
   semilogx(ff, (180/pi)*angle(He),...
```

```
            ff, (180/pi)*angle(He_eddy_i),...
            ff, (180/pi)*angle(He_eddy),'g',...
            He_appr_exp(:,1), He_appr_exp(:,3),'k--',...
            'LineWidth',1); grid
   xlabel('Frequency (Hz)'); ylabel('Angle (deg)');
   xticks([10^0, 10^1, 10^2, 10^3,10^4,10^5]); yticks([-90, -45, 0])
   legend('RL Model (2 DoF)','Eddy Model (3 DoF)','Eddy Model (4
DoF)','Experiment')
   xlim([10^0 10^5]); ylim([-90 0])

% Mu-Sigma product
mu_sigma_i_OnlyIron = kk_ii*mu_eff_i*sigma_i % eddy only in iron
mu_sigma_i = kk_i*mu_eff_i*sigma_i % eddy in both iron and magnet
mu_sigma_m = kk_m*mu_eff_m*sigma_m % eddy in both iron and magnet
```

Appendix K

Matlab Code for Modeling of Current-Loop with Non-Ideal and Ideal Op-amp Models

The code is as follows:

```
%-----------------------------------------------------------------------%
%           Current Loop Modeling using ideal and non-ideal Op-Amps       %
%                Sajjad Mohammadi, EECS, MIT, August 2021                 %
%-----------------------------------------------------------------------%

% Including 3 Op-Amps
% Input Block: 1/Z1
% Feed Forward Path: Compensator FF, Power OpAmp, Actuator
% Feedback path: Sensor Resistor Rs, Buffer OpAmp, Compensator FB

% clc; clear;
%% --------------------[ Actuator Gp_exct=Icoil/Vcoil]---------------------
% He_exct:      including back-emf
% He_appr: ignoring back-emf
% Bode Plot of the Plnat C506
% with/without back-emf

% J=1.65e-9; % Inretia/mass with mirror from Solid Works
J  = 1.5077e-09; % Inretia/mass without mirror from Solid Works
kd = 4.4881e-07; % damping
ks = 0.0013; % spring

Rc = 1.76; % coil resistance [ohm]
Rs = 0.1; % sense resistor [ohm]
R  = Rc+Rs;
Lc  = 280e-6; % coil inductance [H]
% kt = 1.836e-3; % torque/force constant, Typical
kt = 1.9063e-3; % Experiment at Pangolin 8-8-2021

He_exct = tf([J kd ks],[Lc*J R*J+Lc*kd R*kd+ks*kd+kt^2 R*ks]); % Icoil/Vcoil
with back emf
He_appr = tf([1],[Lc R]); % Icoil/Vcoil  without back emf
Hm = tf([kt],[J kd ks]); % Torque/Icoil


% Plots
subplot(2,1,1)
   options = bodeoptions;
   options.FreqUnits = 'Hz';
   bode(He_exct,He_appr,Hm,options); title ('Actuator Electrical and mechanical
Part')
   legend('Gp_exct=Icoil/Vcoil  with bemf','Gp_exct=Icoil/Vcoil without
bemf','mechanical G_m=T/Icoil')
subplot(2,1,2)
   step(He_exct,He_appr)
   title ('Step Response, Vcoil to Icoil')
   legend('Model with bemf','Model without bemf (locked rotor)')

figure
```

```
pzmap(He_exct,He_appr,Hm);axis equal; title ('Actuator Electrical and
mechanical Part')
legend('Gp_exct=Icoil/Vcoil  with bemf','Gp_exct=Icoil/Vcoil  without
bemf','mechanical G_m=T/Icoil')



%% ---------------[ Current Sensor Resistor Gcs=Vrs/Icoil]-----------------
% Converting Coil Current to a Voltage to be measured by buffer OpAmp
% Vrs=Rs*Icoil
Rs  = 0.1; % sense resistor
Gcs = Rs; % Gs=Vrs/Icoil;



%% ---------------[ Power OpAmp TF_pAmp_nonideal=Vcoil/Vc]-----------------
% Increasing Compensator Output Voltage Vc to Coil Voltage Vcoil
% PowerOpAmp Modeling, LM3886
% non-ideal OpAmps:  TF_pAmp_nonideal
% ideal OpAmps:      TF_pAmp_ideal

s = tf([1 0],[1]);

% Voltage Divider
R1_pAmp = 64.9e3; %  voltage divider
R2_pAmp = 10e3; %  voltage divider

% Power Op-Amp
Ra_pAmp = 10e3; % feedback
Rb_pAmp = 95.3e3; % feedback

% input lag compensation and input resistance of Op-Amp
Ri_pAmp   = 6.2e3; % input lag compensation
Ci_pAmp   = 470e-12; % input lag compensation
RiCi_pAmp = Ri_pAmp+1/(Ci_pAmp*s); % series Ri and Ci
Zin       = 100e6; % input impedance of Op-Amp
% Zi_pAmp = RiCi_pAmp*Zin/(RiCi_pAmp+Zin);
Zi_pAmp   = RiCi_pAmp;


% Op-Amp Open-Loop Gain Transfer Function A(s), LM3886
GBP_pAmp = 8e6; % Gain-Bandwidth Product [Hz]
Avo_pAmp = 10^(115/20); % Open-Loop DC-gain
f1_pAmp  = GBP_pAmp/Avo_pAmp; w1_pAmp=2*pi*f1_pAmp; % pole 1
% f2_pAmp  = 1.5e6;   w2_pAmp=2*pi*f2_pAmp; % pole 2, usually less than GWB
% f3_pAmp  = 2.9e6;   w3_pAmp=2*pi*f3_pAmp; % pole 3, usually between f2 and
GWB
f2_pAmp  = 3e6;   w2_pAmp=2*pi*f2_pAmp; % pole 2, usually less than GWB
f3_pAmp  = 4e6;   w3_pAmp=2*pi*f3_pAmp; % pole 3, usually between f2 and GWB


A1_pAmp = Avo_pAmp*w1_pAmp /(s+w1_pAmp); % 1st-order model
A2_pAmp = Avo_pAmp*w1_pAmp*w2_pAmp /((s+w1_pAmp)*(s+w2_pAmp)); % 2nd-order
model
A3_pAmp = Avo_pAmp*w1_pAmp*w2_pAmp*w3_pAmp
/((s+w1_pAmp)*(s+w2_pAmp)*(s+w3_pAmp)); % 2nd-order model

A_pAmp  = A3_pAmp; % Order selection

% options.FreqUnits = 'Hz';
%
% figure; bode(A,{1,1e8},options); grid
% title('Open-Loop Gain A')
```

```
% Non-Ideal OpAmp, Uncompensated
FF_pAmp = (R2_pAmp/(R1_pAmp+R2_pAmp)) * A_pAmp; % Feed Forward
FB_pAmp = (Ra_pAmp/(Ra_pAmp+Rb_pAmp)) * ((R1_pAmp+R2_pAmp)/R2_pAmp); % Feedback
LT_pAmp = FF_pAmp*FB_pAmp; % Loop Transmision
TF_pAmp_nonideal = feedback(FF_pAmp,FB_pAmp); % Closed-Loop (internal loop)

% Non-Ideal OpAmp, Compensated with Ri & Ci at input
FF_pAmp_comp = (R2_pAmp/(R1_pAmp+R2_pAmp)) * ( Zi_pAmp/(Zi_pAmp +
(R1_pAmp*R2_pAmp/(R1_pAmp+R2_pAmp)) + (Ra_pAmp*Rb_pAmp/(Ra_pAmp+Rb_pAmp))) ) *
A_pAmp; % Feed Forward
FB_pAmp_comp = (Ra_pAmp/(Ra_pAmp+Rb_pAmp)) * ((R1_pAmp+R2_pAmp)/R2_pAmp); %
Feedback
LT_pAmp_comp = FF_pAmp_comp*FB_pAmp_comp; % Loop Transmision
TF_pAmp_nonideal_comp = feedback(FF_pAmp_comp,FB_pAmp_comp); % Closed-Loop

% DC Gian
DC_gain_pAmp    = (R2_pAmp/(R1_pAmp+R2_pAmp)) *(1+Rb_pAmp/Ra_pAmp)
DC_gain_dB_pAmp = 20*log10((R2_pAmp/(R1_pAmp+R2_pAmp)) *(1+Rb_pAmp/Ra_pAmp))

% Ideal OpAmp
TF_pAmp_ideal   = DC_gain_pAmp;


% Plots
options.FreqUnits = 'Hz';
figure; h=bodeplot(A_pAmp,{1,1e10}); grid title('LM3886 Open-Loop Gain A')
setoptions(h,'FreqUnits','Hz');
title('Power Op-Amp LM3886 Gain A(s)')



ff = logspace(0,10,2000);% frequency [Hz]
omegaa=2*pi*ff;
[mag_pAmp,phase_pAmp,wout] = bode(A_pAmp,omegaa); % calculating magnitude at wc
[mag_Comp,phase_Comp,wout] = bode(A_Comp,omegaa); % calculating magnitude at wc

figure; colororder({'r','b'})
yyaxis left
   semilogx(ff, 20*log10(squeeze(mag_pAmp)),'r','LineWidth',1.2);
   ylabel('Mag (dB)'); title('LM3886 A(s)'); ylim([-250 117])
   % legend('non-ideal OpAmps','ideal OpAmps','Expr')
yyaxis right
   semilogx(ff, squeeze(phase_pAmp),'b','LineWidth',1.1); grid
   xlabel('Frequency (Hz)'); ylabel('Phase (deg)')
   xlim([10^0 10^10]); ylim([-272 2])
   xticks([10^0, 10^2, 10^4,10^6,10^8,10^10])
   legend('Mag', 'Phase')
   % ax = gca; ax.XGrid = 'on';



figure;hold on; bode(LT_pAmp_comp,{10,1e8}); bode(LT_pAmp,{10,1e8});
title('Power OpAmp, Loop Transmision'); legend('Compensated','Uncompensated')

subplot (2,1,1)
   hold on;
bode(TF_pAmp_nonideal_comp,{10,1e8});bode(TF_pAmp_nonideal,{10,1e8}); grid
   title('Power OpAmp, Closed-Loop Bode');
legend('Compensated','Uncompensated')
subplot (2,1,2)
   step(TF_pAmp_nonideal_comp,TF_pAmp_nonideal);
```

```
   title('Power OpAmp, Step Response'); legend('Compensated','Uncompensated')


%% --------[ Compensator 1/Z1, FF_Comp_nonideal, FB_Comp_nonideal ]--------
% C506 Compensator Op-Amp Modeling, OP1652
% Forward Path, non-ideal OpAmp:  FF_Comp_nonideal
% Forward Path, ideal OpAmp:      FF_Comp_ideal
% Feedback Path non-ideal OpAmp:  FB_Comp_nonideal
% Feedback Path ideal OpAmp:      FB_Comp_ideal
% Input Block 1/Z1

s = tf([1 0],[1]);

% Z1 Components
R1_Comp = 5.1e3; % Z1
Z1      = R1_Comp;

% Z2 Components, Lead Compensator
R2_Comp  = 10e3; % Z2, it sets the bandwidth together with R1_Comp

% R2p_Comp = 100;  % Z2, It, together with C2_Comp, sets the Lead
Characteristics, origianl
% C2_Comp  = 2400e-12; % Z2, original
R2p_Comp = 1.1e3;  % Z2, It, together with C2_Comp, sets the Lead
Characteristics
C2_Comp  = 2.2e-09; % Z2

Z2       = R2_Comp*(R2p_Comp*C2_Comp*s+1)/((R2_Comp+R2p_Comp)*C2_Comp*s+1);

% Zf Components, Lag Compensator
% R3_Comp = 2e6; % Zf , large paralle resistor to limit the integrator
 % R3_Comp = 470e3; % Zf , original value, large paralle resistor to limit the
integrator
 R3_Comp = 2e6;

% C3_Comp = 180e-12; % Zf, original
C3_Comp = 100e-12;

Zf      = R3_Comp/(R3_Comp*C3_Comp*s+1); % with parallel R3_Comp, Non-pure
interator
% Zf   = 1/(C3_Comp*s); % without parallel R3_Comp, pure integrator

% Op-Amp Open-Loop Transfer Function A(s), , OP1652
GBP_Comp = 18e6; % Gain-Bandwidth Product [Hz]
Avo_Comp = 10^(114/20); % Open-Loop DC-gain
f1_Comp  = GBP_Comp/Avo_Comp; w1_Comp=2*pi*f1_Comp; % pole 1
f2_Comp  = 1.5e7;   w2_Comp=2*pi*f2_Comp; % pole 2, not found in datasheet
f3_Comp  = 2.9e7;   w3_Comp=2*pi*f3_Comp; % pole 3, not found in datasheet

A1_Comp  = Avo_Comp*w1_Comp /(s+w1_Comp); % 1st-order model
A2_Comp  = Avo_Comp*w1_Comp*w2_Comp /((s+w1_Comp)*(s+w2_Comp)); % 2nd-order
model
A3_Comp  = Avo_Comp*w1_Comp*w2_Comp*w3_Comp
/((s+w1_Comp)*(s+w2_Comp)*(s+w3_Comp)); % 2nd-order model

A_Comp  = A3_Comp; % Order selection

% options.FreqUnits = 'Hz';
% figure; h=bodeplot(A_Comp,{1,1e10}); grid title('Open-Loop Gain A')
% setoptions(h,'FreqUnits','Hz');

% Loop Transmission, Ideal Op-Amp
```

```
FF_Comp_ideal   = Zf;
FB_Comp_ideal   = 1/Z2;
Loop_Comp_ideal = FF_Comp_ideal * FB_Comp_ideal; % Ideal Op-Amp

% Loop Transmission, Non-Ideal Op-Amp
FF_int_Comp      = Zf * ( (Z1*Z2)/(Z1*Z2+Z1*Zf+Z2*Zf) ) * A_Comp; % Feed
Forward, internal OpAmp Loop
FB_int_Comp      = 1/Zf; % Feedback path of internal OpAmp Loop
FF_Comp_nonideal = feedback(FF_int_Comp,FB_int_Comp); % Closed-Loop (internal
loop), FF part of the compensator
FB_Comp_nonideal = 1/Z2; % FB part of the compensator
Loop_Comp        = FF_Comp_nonideal * FB_Comp_nonideal; % Non-Ideal Op-Amp


% Plots
options.FreqUnits = 'Hz';
figure; h=bodeplot(A_Comp,{1,1e10}); grid title('OP1652 Open-Loop Gain A')
setoptions(h,'FreqUnits','Hz');
title('Compensator Op-Amp OP1652 Gain A(s)')

options.FreqUnits = 'Hz';
figure; h=bodeplot(Loop_Comp_ideal,Loop_Comp); grid;
setoptions(h,'FreqUnits','Hz');
title('C506 Compensator Loop Transmission'); legend('ideal','non-ideal')



ff = logspace(0,10,2000);% frequency [Hz]
omegaa=2*pi*ff;
[mag_Comp,phase_Comp,wout] = bode(A_Comp,omegaa); % calculating magnitude at wc

figure; colororder({'r','b'})
yyaxis left
   semilogx(ff, 20*log10(squeeze(mag_Comp)),'r','LineWidth',1.2);
   ylabel('Mag (dB)'); title('LM3886 A(s)'); ylim([-250 117])
   % legend('non-ideal OpAmps','ideal OpAmps','Expr')
yyaxis right
   semilogx(ff, squeeze(phase_Comp),'b','LineWidth',1.1); grid
   xlabel('Frequency (Hz)'); ylabel('Phase (deg)')
   xlim([10^0 10^10]); ylim([-272 2])
   xticks([10^0, 10^2, 10^4,10^6,10^8,10^10])
   legend('Mag', 'Phase')
   % ax = gca; ax.XGrid = 'on';

%% --------[ Current Sensor Buffer OpAmp: TF_buff_nonideal=vs/Vrs ]--------
% C506 Current Sensor Buffer Op-Amp Modeling, OP1652
% Conversing the Voltage of current sense resistor to voltage Vs
% non-ideal OpAmps:  TF_buff_nonideal
% ideal OpAmps:      TF_buff_ideal

s = tf([1 0],[1]);

R1_buff = 1e3;
R2_buff = 10e3;

% Op-Amp Open-Loop Transfer Function A(s), , OP1652
GBP_buff = 18e6; % Gain-Bandwidth Product [Hz]
Avo_buff = 10^(114/20); % Open-Loop DC-gain
f1_buff  = GBP_buff/Avo_buff; w1_buff=2*pi*f1_buff; % pole 1
f2_buff  = 1.5e7;   w2_buff=2*pi*f2_buff; % pole 2, not found in datasheet
f3_buff  = 2.9e7;   w3_buff=2*pi*f3_buff; % pole 3, not found in datasheet

A1_buff  = Avo_buff*w1_buff /(s+w1_buff); % 1st-order model
```

```
A2_buff  = Avo_buff*w1_buff*w2_buff /((s+w1_buff)*(s+w2_buff)); % 2nd-order
model
A3_buff  = Avo_buff*w1_buff*w2_buff*w3_buff
/((s+w1_buff)*(s+w2_buff)*(s+w3_buff)); % 2nd-order model

A_buff   = A3_buff; % Order selection

% options.FreqUnits = 'Hz';
% figure; h=bodeplot(A_buff,{1,1e10}); grid title('Open-Loop Gain A')
% setoptions(h,'FreqUnits','Hz');


% Ideal Op-Amp
TF_buff_ideal = R2_buff/R1_buff; % Ideal Op-Amp

% Loop Transmission, Non-Ideal Op-Amp
FF_int_buff = (R2_buff/(R1_buff+R2_buff)) * A_buff; % Feed Forward, internal
OpAmp Loop
FB_int_buff = R1_buff/R2_buff; % Feedback path of internal OpAmp Loop
TF_buff_nonideal = feedback(FF_int_buff,FB_int_buff);


% Plots
options.FreqUnits = 'Hz';
figure; h=bodeplot(A_buff,{1,1e10}); grid; title('OP1652 Open-Loop Gain A')
setoptions(h,'FreqUnits','Hz');
title('Current Sensor Op-Amp OP1652 Gain A(s)')

options.FreqUnits = 'Hz';
figure; h=bodeplot(TF_buff_nonideal);setoptions(h,'FreqUnits','Hz'); grid;
title('C506 Current Sensor Buffer')

%% -----------[ Model Selection: Model with or without back-emf ]-----------
% Select the Actuator Model?
% Gp=Gp_exct; % 1: Actuator model with back-emf
Gp = He_appr;  % 2:Actuator model without back-emf


%% ---------------------------[ Block Diagram]----------------------------
F  = 1/Z1; % input block

P  = Gp; % Actuator

% C  = FF_Comp_nonideal * TF_pAmp_nonideal_comp; % non-ideal op-amp, Power op-
amp with compensator
C  = FF_Comp_nonideal * TF_pAmp_nonideal; % non-ideal op-amp, Power op-amp
without compensator
Ci = FF_Comp_ideal * TF_pAmp_ideal; % ideal op-amp

H  = Rs * TF_buff_nonideal * FB_Comp_nonideal; % non-ideal op-amp
Hi = Rs * TF_buff_ideal * FB_Comp_ideal; % ideal op-amp


%% ----------------[ Current Loop, Loop Transmission PCH]-------------------

LT_CurrentLoop       = P*C*H;  % Closed-Loop, Non-Ideal OpAmps
LT_CurrentLoop_ideal = P*Ci*Hi;  % Closed-Loop, Ideal OpAmps


% The loop excluding compensator, ideal
LT_CurrentLoop_rest       = P*TF_pAmp_nonideal*TF_buff_nonideal;  % Closed-
Loop, Non-Ideal OpAmps
```

```
LT_CurrentLoop_ideal_rest = P*TF_pAmp_ideal*TF_buff_ideal;  % Closed-Loop, 
Ideal OpAmps


% Plots
% Decomposition of Loop Transmission, non-ideal model of op-amps
figure
options.FreqUnits = 'Hz';
h=bodeplot(Loop_Comp,LT_CurrentLoop_rest,LT_CurrentLoop,{0.1,1e8}); grid;
title('Decomposition of Loop Transmision, nonideal op-amps ');
legend('Compensator','Rest of the Loop','Loop Transmission')
setoptions(h,'FreqUnits','Hz');

% Decomposition of Loop Transmission, ideal model of op-amps
figure
options.FreqUnits = 'Hz';
h=bodeplot(Loop_Comp_ideal,LT_CurrentLoop_ideal_rest,...
           LT_CurrentLoop_ideal,{0.1,1e8}); grid;
title('Decomposition of Loop Transmision, ideal op-amps ');
legend('Compensator','Rest of the Loop','Loop Transmission')
setoptions(h,'FreqUnits','Hz');

figure
subplot(2,1,1)
options.FreqUnits = 'Hz';
h=bodeplot(LT_CurrentLoop,LT_CurrentLoop_ideal,{0.1,1e8}); grid;
title('Loop Transmision Bode ');legend('non-ideal OpAmps','ideal OpAmps')
setoptions(h,'FreqUnits','Hz');

subplot(2,1,2)
nyquist(LT_CurrentLoop,LT_CurrentLoop_ideal);
title('Loop Transmision Nyquist');legend('non-ideal OpAmps','ideal OpAmps')

figure
margin(LT_CurrentLoop); grid;
%% ----------[Gang 1: Closed-Loop Reference Tracking FPC/1+PCH]------------
% Reference tracking PCF/1+PCH

GANG1  = F*P*C/(1+P*C*H);  % Closed-Loop, Non-Ideal OpAmps
GANGi1 = F*P*Ci/(1+P*Ci*Hi);  % Closed-Loop, Ideal OpAmps

DC_gain_CurrentLoop_PureIntegrator = R2_Comp/R1_Comp
DC_gain_dB_CurrentLoop_PureIntegrator = 20*log10(R2_Comp/R1_Comp)

[mag_DC,phase_DC,wout_DC] = bode(GANGi1,0); % calculating magnitude at 0 
rad/sec
DC_gain_CurrentLoop_NonPureIntegrator = mag_DC
DC_gain_dB_CurrentLoop_NonPureIntegrator = 20*log10(mag_DC)


%% -------[Gang 2: Reference to Power Op-Amp output Voltage FC/1+PCH]------

GANG2  = F*C/(1+P*C*H);     % Closed-Loop, Non-Ideal OpAmps
GANGi2 = F*Ci/(1+P*Ci*Hi);  % Closed-Loop, Ideal OpAmps

%% ---------------[Gang 3: Disturbance Rejection  P/1+PCH]-----------------
% Disturbance to plant output
GANG3  = P/(1+P*C*H);    % Closed-Loop, Non-Ideal OpAmps
GANGi3 = P/(1+P*Ci*Hi);  % Closed-Loop, Ideal OpAmps

%% --------------------[Gang 4: Sensitivity 1/1+PCH]-----------------------
% measurement noise to plant output
GANG4  = 1/(1+P*C*H);    % Closed-Loop, Non-Ideal OpAmps
```

```
GANGi4 = 1/(1+P*Ci*Hi);  % Closed-Loop, Ideal OpAmps

%% ------------------[Gang 5: Noise Sensitivity CH/1+PCH]------------------
% Noise to controller (power op-amp) output
GANG5  = C*H/(1+P*C*H);      % Closed-Loop, Non-Ideal OpAmps
GANGi5 = Ci*Hi/(1+P*Ci*Hi);  % Closed-Loop, Ideal OpAmps

%% --------------[Gang 6: Complementary Sensitivity PCH/1+PCH]-------------
% Disturbance to controller (power op-amp) output
GANG6  = P*C*H/(1+P*C*H);     % Closed-Loop, Non-Ideal OpAmps
GANGi6 = P*Ci*Hi/(1+P*Ci*Hi); % Closed-Loop, Ideal OpAmps


%% -----[ FPC/1+PCH, FC/1+PCH, P/1+PCH, 1/1+PCH, CH/1+PCH, PCH/1+PCH]------

% ----- Bode Plot -----

f_range = {10,1e6}; % Frequency range of plots

figure
subplot(3,2,1)
   options.FreqUnits = 'Hz';
   h=bodeplot(GANG1,GANGi1,f_range); grid;
   setoptions(h,'FreqUnits','Hz');
   title('G1: Reference Tracking FPC/1+PCH');
   legend('non-ideal OpAmps','ideal OpAmps')

subplot(3,2,2)
   options.FreqUnits = 'Hz';
   h=bodeplot(GANG2,GANGi2,f_range); grid;
   setoptions(h,'FreqUnits','Hz');
   title('G2: Ref to P-OpAmp Output FC/1+PCH');
   legend('non-ideal OpAmps','ideal OpAmps')

subplot(3,2,3)
   options.FreqUnits = 'Hz';
   h=bodeplot(GANG3,GANGi3,f_range); grid;
   setoptions(h,'FreqUnits','Hz');
   title('G3: Disturbance Rejection P/1+PCH');
   legend('non-ideal OpAmps','ideal OpAmps')

subplot(3,2,4)
   options.FreqUnits = 'Hz';
   h=bodeplot(GANG4,GANGi4,f_range); grid;
   setoptions(h,'FreqUnits','Hz');
   title('G4: Sensitivity 1/1+PCH');
   legend('non-ideal OpAmps','ideal OpAmps')

subplot(3,2,5)
   options.FreqUnits = 'Hz';
   h=bodeplot(GANG5,GANGi5,f_range); grid;
   setoptions(h,'FreqUnits','Hz');
   title('G5: Noise Sensitivity CH/1+PCH');
   legend('non-ideal OpAmps','ideal OpAmps')

subplot(3,2,6)
   options.FreqUnits = 'Hz';
   h=bodeplot(GANG6,GANGi6,f_range); grid;
   setoptions(h,'FreqUnits','Hz');
   title('G6: Compl Sensitivity PCH/1+PCH');
   legend('non-ideal OpAmps','ideal OpAmps')
```

```
% % ----- Magnitude-only Bode Plot -----
% figure
% subplot(3,2,1)
%    options.FreqUnits = 'Hz';
%    h=bodeplot(GANG1,GANGi1,f_range); grid;
%    setoptions(h,'FreqUnits','Hz');
%    setoptions(h,'FreqUnits','Hz','PhaseVisible','off');
%    title('G1: Reference Tracking FPC/1+PCH'); legend('non-ideal
OpAmps','ideal OpAmps')
%
% subplot(3,2,2)
%    options.FreqUnits = 'Hz';
%    h=bodeplot(GANG2,GANGi2,f_range); grid;
%    setoptions(h,'FreqUnits','Hz');
%    setoptions(h,'FreqUnits','Hz','PhaseVisible','off');
%    title('G2: Ref to P-OpAmp Output FC/1+PCH'); legend('non-ideal
OpAmps','ideal OpAmps')
%
% subplot(3,2,3)
%    options.FreqUnits = 'Hz';
%    h=bodeplot(GANG3,GANGi3,f_range); grid;
%    setoptions(h,'FreqUnits','Hz');
%    setoptions(h,'FreqUnits','Hz','PhaseVisible','off');
%    title('G3: Disturbance Rejection P/1+PCH'); legend('non-ideal
OpAmps','ideal OpAmps')
%
% subplot(3,2,4)
%    options.FreqUnits = 'Hz';
%    h=bodeplot(GANG4,GANGi4,f_range); grid;
%    setoptions(h,'FreqUnits','Hz');
%    setoptions(h,'FreqUnits','Hz','PhaseVisible','off');
%    title('G4: Sensitivity 1/1+PCH'); legend('non-ideal OpAmps','ideal
OpAmps')
%
%    subplot(3,2,5)
%    options.FreqUnits = 'Hz';
%    h=bodeplot(GANG5,GANGi5,f_range); grid;
%    setoptions(h,'FreqUnits','Hz');
%    setoptions(h,'FreqUnits','Hz','PhaseVisible','off');
%    title('G5: Noise Sensitivity CH/1+PCH'); legend('non-ideal OpAmps','ideal
OpAmps')
%
% subplot(3,2,6)
%    options.FreqUnits = 'Hz';
%    h=bodeplot(GANG6,GANGi6,f_range); grid;
%    setoptions(h,'FreqUnits','Hz');
%    setoptions(h,'FreqUnits','Hz','PhaseVisible','off');
%    title('G6: Compl Sensitivity PCH/1+PCH'); legend('non-ideal OpAmps','ideal
OpAmps')


% % ----- Pole-Zero Map -----
% figure
% subplot(3,2,1)
%    pzmap(GANG1,GANGi1)
%    title('G1: Reference Tracking FPC/1+PCH'); legend('non-ideal
OpAmps','ideal OpAmps')
% subplot(3,2,2)
%    pzmap(GANG2,GANGi2)
%    title('G2: Ref to P-OpAmp Output FC/1+PCH'); legend('non-ideal
OpAmps','ideal OpAmps')
% subplot(3,2,3)
%    pzmap(GANG3,GANGi3)
```

```
%    title('G3: Disturbance Rejection P/1+PCH'); legend('non-ideal
OpAmps','ideal OpAmps')
% subplot(3,2,4)
%    pzmap(GANG4,GANGi4)
%    title('G4: Sensitivity 1/1+PCH'); legend('non-ideal OpAmps','ideal
OpAmps')
% subplot(3,2,5)
%    pzmap(GANG5,GANGi5)
%    title('G5: Noise Sensitivity CH/1+PCH'); legend('non-ideal OpAmps','ideal
OpAmps')
% subplot(3,2,6)
%    pzmap(GANG6,GANGi6)
%    title('G6: Compl Sensitivity PCH/1+PCH'); legend('non-ideal OpAmps','ideal
OpAmps')


% ----- Step Response -----
figure
subplot(3,2,1)
   step(GANG1,GANGi1)
   title('G1: Reference Tracking FPC/1+PCH');
   legend('non-ideal OpAmps','ideal OpAmps')
   ylabel('Amplitude (A)')

subplot(3,2,2)
   step(GANG2,GANGi2)
   title('G2: Ref to P-OpAmp Output FC/1+PCH');
   legend('non-ideal OpAmps','ideal OpAmps')
   ylabel('Amplitude (Volt)')

subplot(3,2,3)
   step(GANG3,GANGi3)
   title('G3: Disturbance Rejection P/1+PCH');
   legend('non-ideal OpAmps','ideal OpAmps')

subplot(3,2,4)
   step(GANG4,GANGi4)
   title('G4: Sensitivity 1/1+PCH');
   legend('non-ideal OpAmps','ideal OpAmps')

subplot(3,2,5)
   step(GANG5,GANGi5)
   title('G5: Noise Sensitivity CH/1+PCH');
   legend('non-ideal OpAmps','ideal OpAmps')

subplot(3,2,6)
   step(GANG6,GANGi6)
   title('G6: Compl Sensitivity PCH/1+PCH');
   legend('non-ideal OpAmps','ideal OpAmps')
```

Appendix L

Matlab Code for Comparison of Current-Loops by Changing the Location of Lead Compensator

The lead compensator is put in the feedback path, forward path, and then removed. The results are compared. The Matlab code is as follows:

```
%-------------------------------------------------------------------------%
%    Comparison: Lead in Feedback path, Lead in Forward path, No Lead     %
%                Sajjad Mohammadi, EECS, MIT, August 2021                 %
%-------------------------------------------------------------------------%

% C506 Current Loop Modeling using ideal Op-Amps
% Input Block: 1/Z1
% Feed Forward Path: Compensator FF, Power OpAmp, Actuator
% Feedback path: Sensor Resistor Rs, Buffer OpAmp, Compensator FB

% clc; clear;
%% --------------------[ Actuator Gp_exct=Icoil/Vcoil]---------------------
% He_exct:      including back-emf
% He_appr: ignoring back-emf
% Bode Plot of the Plnat C506
% with/without back-emf

% J=1.65e-9; % Inretia/mass with mirror from Solid Works
J  = 1.5077e-09; % Inretia/mass without mirror from Solid Works
kd = 4.4881e-07; % damping
ks = 0.0013; % spring
Rc = 1.76; % coil resistance [ohm]
Rs = 0.1; % sense resistor [ohm]
R  = Rc+Rs;
Lc  = 280e-6; % coil inductance [H]
% kt=1.836e-3; % torque/force constant, Typical
kt = 1.9063e-3; % Experiment at Pangolin 8-8-2021

He_exct = tf([J kd ks],[Lc*J R*J+Lc*kd R*kd+ks*kd+kt^2 R*ks]); % Icoil/Vcoil
with back emf
He_appr = tf([1],[Lc R]); % Icoil/Vcoil  without back emf
Hm = tf([kt],[J kd ks]); % Torque/Icoil


% Plots
subplot(2,1,1)
   options = bodeoptions;
   options.FreqUnits = 'Hz';
   bode(He_exct,He_appr,Hm,options); title ('Actuator Electrical and mechanical
Part')
   legend('Gp_exct=Icoil/Vcoil  with bemf','Gp_exct=Icoil/Vcoil without
bemf','mechanical G_m=T/Icoil')
subplot(2,1,2)
   step(He_exct,He_appr)
   title ('Step Response, Vcoil to Icoil')
   legend('Model with bemf','Model without bemf (locked rotor)')
```

```
figure
pzmap(He_exct,He_appr,Hm);axis equal; title ('Actuator Electrical and 
mechanical Part')
legend('Gp_exct=Icoil/Vcoil  with bemf','Gp_exct=Icoil/Vcoil  without 
bemf','mechanical G_m=T/Icoil')



%% ---------------[ Current Sensor Resistor Gcs=Vrs/Icoil]-----------------
% Converting Coil Current to a Voltage to be measured by buffer OpAmp
% Vrs=Rs*Icoil
Rs=0.1; % sense resistor
Gcs=Rs; % Gs=Vrs/Icoil;



%% ---------------[ Power OpAmp TF_pAmp_nonideal=Vcoil/Vc]-----------------
% Increasing Compensator Output Voltage Vc to Coil Voltage Vcoil
% PowerOpAmp Modeling, LM3886
% non-ideal OpAmps:  TF_pAmp_nonideal
% ideal OpAmps:      TF_pAmp_ideal

s=tf([1 0],[1]);

R1_pAmp=64.9e3; % input voltage divider
R2_pAmp=10e3; % input voltage divider
Ra_pAmp=10e3; % feedback
Rb_pAmp=95.3e3; % feedback

% input lag compensation and input resistance of Op-Amp
Ri_pAmp=6.2e3; % input lag compensation
Ci_pAmp=470e-12; % input lag compensation
RiCi_pAmp=Ri_pAmp+1/(Ci_pAmp*s); % series Ri and Ci
Zin=100e6; % input impedance of Op-Amp
% Zi_pAmp=RiCi_pAmp*Zin/(RiCi_pAmp+Zin);
Zi_pAmp=RiCi_pAmp;

% DC Gian
DC_gain_pAmp = (R2_pAmp/(R1_pAmp+R2_pAmp)) *(1+Rb_pAmp/Ra_pAmp)
DC_gain_dB_pAmp = 20*log10((R2_pAmp/(R1_pAmp+R2_pAmp)) *(1+Rb_pAmp/Ra_pAmp))

% Ideal OpAmp
TF_pAmp_ideal=DC_gain_pAmp;


%% --------[ Compensator 1/Z1, FF_Comp_nonideal, FB_Comp_nonideal ]--------
% C506 Compensator Op-Amp Modeling, OP1652
% Forward Path, non-ideal OpAmp:  FF_Comp_nonideal
% Forward Path, ideal OpAmp:      FF_Comp_ideal
% Feedback Path non-ideal OpAmp:  FB_Comp_nonideal
% Feedback Path ideal OpAmp:      FB_Comp_ideal
% Input Block 1/Z1

s=tf([1 0],[1]);

R1_Comp=5.1e3; % Z1
Z1=R1_Comp;
% Lead (Z2)
% Z2 Components, Lead Compensator
R2_Comp  = 10e3; % Z2, it sets the bandwidth together with R1_Comp
% R2p_Comp = 100;  % Z2, It, together with C2_Comp, sets the Lead 
Characteristics, origianl
% C2_Comp  = 2400e-12; % Z2, original
```

```
R2p_Comp = 1.1e3;  % Z2, It, together with C2_Comp, sets the Lead
Characteristics
C2_Comp  = 2.2e-09; % Z2
Z2 = R2_Comp; % Lead Compensator is in the forward path

% Lag (Zf)
% R3_Comp=470e3; % Zf
R3_Comp = 2e6;
% C3_Comp=180e-12; % Zf
C3_Comp = 100e-12;

% Zf = R3_Comp/(R3_Comp*C3_Comp*s+1); % with parallel R3_Comp, Non-pure
interator
Zf = 1/(C3_Comp*s); % without parallel R3_Comp, pure integrator

% A: Lead Compensator in Feedback Path, Loop Transmission
FF_Comp_ideal_A = Zf;
FB_Comp_ideal_A = (1/Z2) *
((R2_Comp+R2p_Comp)*C2_Comp*s+1)/(R2p_Comp*C2_Comp*s+1);
Loop_Comp_ideal_A = FF_Comp_ideal_A * FB_Comp_ideal_A; % Ideal Op-Amp

% B: Lead Compensator in Forward Path, Loop Transmission
FF_Comp_ideal_B = Zf * ((R2_Comp+R2p_Comp)*C2_Comp*s+1)/(R2p_Comp*C2_Comp*s+1);
FB_Comp_ideal_B = 1/Z2;
Loop_Comp_ideal_B = FF_Comp_ideal_B * FB_Comp_ideal_B; % Ideal Op-Amp

% C: No Lead Compensator, Loop Transmission
FF_Comp_ideal_C = Zf;
FB_Comp_ideal_C = 1/Z2;
Loop_Comp_ideal_C = FF_Comp_ideal_C * FB_Comp_ideal_C; % Ideal Op-Am


options.FreqUnits = 'Hz';
figure; h=bodeplot(Loop_Comp_ideal_A,Loop_Comp_ideal_B,Loop_Comp_ideal_C);
grid;
setoptions(h,'FreqUnits','Hz');
title('C506 Compensator Loop Transmission');
legend('Lead in Feedback Path','Lead in Forward Path', 'No lead')


%% --------[ Current Sensor Buffer OpAmp: TF_buff_nonideal=vs/Vrs ]--------
% C506 Current Sensor Buffer Op-Amp Modeling, OP1652
% Conversing the Voltage of current sense resistor to voltage Vs
% non-ideal OpAmps:  TF_buff_nonideal
% ideal OpAmps:      TF_buff_ideal

s=tf([1 0],[1]);

R1_buff=1e3;
R2_buff=10e3;

% Ideal Op-Amp
TF_buff_ideal = R2_buff/R1_buff; % Ideal Op-Amp


%% -----------[ Model Selection: Model with or without back-emf ]-----------
% Select the Actuator Model?
% Gp=Gp_exct; % 1: Actuator model with back-emf
Gp = He_appr;  % 2:Actuator model without back-emf


%% ---------------------------[ Block Diagram]-----------------------------
F=1/Z1; % input block
```

```
P=Gp; % Actuator

% A: Lead Compensator in Feedback Path
Ci_A = FF_Comp_ideal_A * TF_pAmp_ideal; % ideal op-amp
Hi_A = Rs * TF_buff_ideal * FB_Comp_ideal_A; % ideal op-amp

% B: Lead Compensator in Feedback Path
Ci_B = FF_Comp_ideal_B * TF_pAmp_ideal; % ideal op-amp
Hi_B = Rs * TF_buff_ideal * FB_Comp_ideal_B; % ideal op-amp

% C: Lead Compensator in Feedback Path
Ci_C = FF_Comp_ideal_C * TF_pAmp_ideal; % ideal op-amp
Hi_C = Rs * TF_buff_ideal * FB_Comp_ideal_C; % ideal op-amp


%% ----------------[ Current Loop, Loop Transmission PC]-------------------

LT_CurrentLoop_ideal_A = P*Ci_A*Hi_A;  % Closed-Loop, Ideal OpAmps
LT_CurrentLoop_ideal_B = P*Ci_B*Hi_B  % Closed-Loop, Ideal OpAmps
LT_CurrentLoop_ideal_C = P*Ci_A*Hi_C;  % Closed-Loop, Ideal OpAmps

% Plots
figure
options.FreqUnits = 'Hz';
h=bodeplot(LT_CurrentLoop_ideal_A,LT_CurrentLoop_ideal_B,LT_CurrentLoop_ideal_C
,{10,1e8}); grid;
title('Loop Transmision Bode ')
legend('Lead in Feedback Path','Lead in Forward Path', 'No Lead')
setoptions(h,'FreqUnits','Hz');

% figure
% margin(LT_CurrentLoop_ideal_A,LT_CurrentLoop_ideal_B,LT_CurrentLoop_ideal_C);
grid;

%% ----------[Gang 1: Closed-Loop Reference Tracking FPC/1+PCH]------------
% Reference tracking PCF/1+PCH

GANGi1_A = F*P*Ci_A/(1+P*Ci_A*Hi_A);  % Closed-Loop, Ideal OpAmps
GANGi1_B = F*P*Ci_B/(1+P*Ci_B*Hi_B);  % Closed-Loop, Ideal OpAmps
GANGi1_C = F*P*Ci_C/(1+P*Ci_C*Hi_C);  % Closed-Loop, Ideal OpAmps

DC_gain_CurrentLoop = R2_Comp/R1_Comp
DC_gain_dB_CurrentLoop = 20*log10(R2_Comp/R1_Comp)


%% -------[Gang 2: Reference to Power Op-Amp output Voltage FC/1+PCH]------

GANGi2_A = F*Ci_A/(1+P*Ci_A*Hi_A);  % Closed-Loop, Ideal OpAmps
GANGi2_B = F*Ci_B/(1+P*Ci_B*Hi_B);  % Closed-Loop, Ideal OpAmps
GANGi2_C = F*Ci_C/(1+P*Ci_C*Hi_C);  % Closed-Loop, Ideal OpAmps

%% ---------------[Gang 3: Disturbance Rejection  P/1+PCH]-----------------
% Disturbance to plant output
GANGi3_A = P/(1+P*Ci_A*Hi_A);  % Closed-Loop, Ideal OpAmps
GANGi3_B = P/(1+P*Ci_B*Hi_B);  % Closed-Loop, Ideal OpAmps
GANGi3_C = P/(1+P*Ci_C*Hi_C);  % Closed-Loop, Ideal OpAmps

%% --------------------[Gang 4: Sensitivity 1/1+PCH]-----------------------
% measurement noise to plant output
GANGi4_A = 1/(1+P*Ci_A*Hi_A);  % Closed-Loop, Ideal OpAmps
GANGi4_B = 1/(1+P*Ci_B*Hi_B);  % Closed-Loop, Ideal OpAmps
GANGi4_C = 1/(1+P*Ci_C*Hi_C);  % Closed-Loop, Ideal OpAmps
```

```
%% ------------------[Gang 5: Noise Sensitivity CH/1+PCH]------------------
% Noise to controller (power op-amp) output
GANGi5_A = Ci_A*Hi_A/(1+P*Ci_A*Hi_A);  % Closed-Loop, Ideal OpAmps
GANGi5_B = Ci_B*Hi_B/(1+P*Ci_B*Hi_B);  % Closed-Loop, Ideal OpAmps
GANGi5_C = Ci_C*Hi_C/(1+P*Ci_C*Hi_C);  % Closed-Loop, Ideal OpAmps

%% --------------[Gang 6: Complementary Sensitivity PCH/1+PCH]-------------
% Disturbance to controller (power op-amp) output
GANGi6_A = P*Ci_A*Hi_A/(1+P*Ci_A*Hi_A);  % Closed-Loop, Ideal OpAmps
GANGi6_B = P*Ci_B*Hi_B/(1+P*Ci_B*Hi_B);  % Closed-Loop, Ideal OpAmps
GANGi6_C = P*Ci_C*Hi_C/(1+P*Ci_C*Hi_C);  % Closed-Loop, Ideal OpAmps

%% -----[ FPC/1+PCH, FC/1+PCH, P/1+PCH, 1/1+PCH, CH/1+PCH, PCH/1+PCH]------

% ----- Bode Plot -----
figure
subplot(3,2,1)
   options.FreqUnits = 'Hz';
   h=bodeplot(GANGi1_A,GANGi1_B,GANGi1_C,{10,1e9}); grid;
   setoptions(h,'FreqUnits','Hz');
   title('G1: Reference Tracking FPC/1+PCH')
   legend('Lead in Feedback Path','Lead in Forward Path', 'No Lead')

subplot(3,2,2)
   options.FreqUnits = 'Hz';
   h=bodeplot(GANGi2_A,GANGi2_B,GANGi2_C,{10,1e9}); grid;
   setoptions(h,'FreqUnits','Hz');
   title('G2: Ref to P-OpAmp Output FC/1+PCH')
   legend('Lead in Feedback Path','Lead in Forward Path', 'No Lead')

subplot(3,2,3)
   options.FreqUnits = 'Hz';
   h=bodeplot(GANGi3_A,GANGi3_B,GANGi3_C,{10,1e9}); grid;
   setoptions(h,'FreqUnits','Hz');
   title('G3: Disturbance Rejection P/1+PCH')
   legend('Lead in Feedback Path','Lead in Forward Path', 'No Lead')

subplot(3,2,4)
   options.FreqUnits = 'Hz';
   h=bodeplot(GANGi4_A,GANGi4_B,GANGi4_C,{10,1e9}); grid;
   setoptions(h,'FreqUnits','Hz');
   title('G4: Sensitivity 1/1+PCH')
   legend('Lead in Feedback Path','Lead in Forward Path', 'No Lead')

subplot(3,2,5)
   options.FreqUnits = 'Hz';
   h=bodeplot(GANGi5_A,GANGi5_B,GANGi5_C,{10,1e9}); grid;
   setoptions(h,'FreqUnits','Hz');
   title('G5: Noise Sensitivity CH/1+PCH')
   legend('Lead in Feedback Path','Lead in Forward Path', 'No lead')

subplot(3,2,6)
   options.FreqUnits = 'Hz';
   h=bodeplot(GANGi6_A,GANGi1_B,GANGi1_C,{10,1e9}); grid;
   setoptions(h,'FreqUnits','Hz');
   title('G6: Compl Sensitivity PCH/1+PCH')
   legend('Lead in Feedback Path','Lead in Forward Path', 'No Lead')


% ----- Magnitude-only Bode Plot -----
figure
subplot(3,2,1)
```

```
    options.FreqUnits = 'Hz';
    h=bodeplot(GANGi1_A,GANGi1_B,GANGi1_C,{10,1e9}); grid;
    setoptions(h,'FreqUnits','Hz');
    setoptions(h,'FreqUnits','Hz','PhaseVisible','off');
    title('G1: Reference Tracking FPC/1+PCH')
    legend('Lead in Feedback Path','Lead in Forward Path', 'No Lead')

subplot(3,2,2)
    options.FreqUnits = 'Hz';
    h=bodeplot(GANGi2_A,GANGi2_B,GANGi2_C,{10,1e9}); grid;
    setoptions(h,'FreqUnits','Hz');
    setoptions(h,'FreqUnits','Hz','PhaseVisible','off');
    title('G2: Ref to P-OpAmp Output FC/1+PCH')
    legend('Lead in Feedback Path','Lead in Forward Path', 'No Lead')

subplot(3,2,3)
    options.FreqUnits = 'Hz';
    h=bodeplot(GANGi3_A,GANGi3_B,GANGi3_C,{10,1e9}); grid;
    setoptions(h,'FreqUnits','Hz');
    setoptions(h,'FreqUnits','Hz','PhaseVisible','off');
    title('G3: Disturbance Rejection P/1+PCH')
    legend('Lead in Feedback Path','Lead in Forward Path', 'No Lead')

subplot(3,2,4)
    options.FreqUnits = 'Hz';
    h=bodeplot(GANGi4_A,GANGi4_B,GANGi4_C,{10,1e9}); grid;
    setoptions(h,'FreqUnits','Hz');
    setoptions(h,'FreqUnits','Hz','PhaseVisible','off');
    title('G4: Sensitivity 1/1+PCH')
    legend('Lead in Feedback Path','Lead in Forward Path', 'No Lead')

subplot(3,2,5)
    options.FreqUnits = 'Hz';
    h=bodeplot(GANGi5_A,GANGi5_B,GANGi5_C,{10,1e9}); grid;
    setoptions(h,'FreqUnits','Hz');
    setoptions(h,'FreqUnits','Hz','PhaseVisible','off');
    title('G5: Noise Sensitivity CH/1+PCH')
    legend('Lead in Feedback Path','Lead in Forward Path', 'No Lead')

subplot(3,2,6)
    options.FreqUnits = 'Hz';
    h=bodeplot(GANGi6_A,GANGi6_B,GANGi6_C,{10,1e9}); grid;
    setoptions(h,'FreqUnits','Hz');
    setoptions(h,'FreqUnits','Hz','PhaseVisible','off');
    title('G6: Compl Sensitivity PCH/1+PCH')
    legend('Lead in Feedback Path','Lead in Forward Path', 'No Lead')


% ----- Pole-Zero Map -----
figure
subplot(3,2,1)
    pzmap(GANGi1_A,GANGi1_B,GANGi1_C)
    title('G1: Reference Tracking FPC/1+PCH')
    legend('Lead in Feedback Path','Lead in Forward Path', 'No Lead')
subplot(3,2,2)
    pzmap(GANGi2_A,GANGi2_B,GANGi2_C)
    title('G2: Ref to P-OpAmp Output FC/1+PCH')
    legend('Lead in Feedback Path','Lead in Forward Path', 'No Lead')
subplot(3,2,3)
    pzmap(GANGi3_A,GANGi3_B,GANGi3_C)
    title('G3: Disturbance Rejection P/1+PCH')
    legend('Lead in Feedback Path','Lead in Forward Path', 'No Lead')
subplot(3,2,4)
```

```
   pzmap(GANGi4_A,GANGi4_B,GANGi4_C)
   title('G4: Sensitivity 1/1+PCH')
   legend('Lead in Feedback Path','Lead in Forward Path', 'No Lead')
subplot(3,2,5)
   pzmap(GANGi5_A,GANGi5_B,GANGi5_C)
   title('G5: Noise Sensitivity CH/1+PCH')
   legend('Lead in Feedback Path','Lead in Forward Path', 'No Lead')
subplot(3,2,6)
   pzmap(GANGi6_A,GANGi6_B,GANGi6_C)
   title('G6: Compl Sensitivity PCH/1+PCH')
   legend('Lead in Feedback Path','Lead in Forward Path', 'No Lead')

% ----- Step Response -----
figure
subplot(3,2,1)
   step(GANGi1_A,GANGi1_B,GANGi1_C)
   title('G1: Reference Tracking FPC/1+PCH')
   legend('Lead in Feedback Path','Lead in Forward Path', 'No Lead')
   ylabel('Amplitude (A)')

subplot(3,2,2)
   step(GANGi2_A,GANGi2_B,GANGi2_C)
   title('G2: Ref to P-OpAmp Output FC/1+PCH')
   legend('Lead in Feedback Path','Lead in Forward Path', 'No Lead')
   ylabel('Amplitude (Volt)')

subplot(3,2,3)
   step(GANGi3_A,GANGi3_B,GANGi3_C)
   title('G3: Disturbance Rejection P/1+PCH')
   legend('Lead in Feedback Path','Lead in Forward Path', 'No Lead')

subplot(3,2,4)
   step(GANGi4_A,GANGi4_B,GANGi4_C)
   title('G4: Sensitivity 1/1+PCH')
   legend('Lead in Feedback Path','Lead in Forward Path', 'No Lead')

subplot(3,2,5)
   step(GANGi5_A,GANGi5_B,GANGi5_C)
   title('G5: Noise Sensitivity CH/1+PCH')
   legend('Lead in Feedback Path','Lead in Forward Path', 'No Lead')

subplot(3,2,6)
   step(GANGi6_A,GANGi6_B,GANGi6_C)
   title('G6: Compl Sensitivity PCH/1+PCH')
   legend('Lead in Feedback Path','Lead in Forward Path', 'No Lead')
```

Appendix M

Matlab Code for Comparison of Current-Loops by Changing the Location of Lead Compensator

The Matlab code is given below:

```
%-----------------------------------------------------------------------%
%              Current Loop Modeling including Eddy Current             %
%                         Frequency Domain s=jw                         %
%                    Using ideal and non-ideal Op-Amps                  %
%                Sajjad Mohammadi, EECS, MIT, August 2021               %
%-----------------------------------------------------------------------%

% Including 3 Op-Amps
% Input Block: 1/Z1
% Feed Forward Path: Compensator FF, Power OpAmp, Actuator
% Feedback path: Sensor Resistor Rs, Buffer OpAmp, Compensator FB

%% --------------------[ Actuator Gp_exct=Icoil/Vcoil]---------------------

% Load Experimental data
% run FrequencyTimeResponse_Control_Experiment

% frequency range for plots
ff = logspace(0,7,2000);% frequency [Hz]
omegaa=2*pi*ff;
s = 1i * omegaa;


% J=1.65e-9; % Inretia/mass with mirror from Solid Works
J  = 1.5077e-09; % Inretia/mass without mirror from Solid Works
kd = 4.4881e-07; % damping
ks = 0.0013; % spring
Rc = 1.76; % coil resistance [ohm]
Rs = 0.1; % sense resistor [ohm]
R  = Rc+Rs;
Lc  = 280e-6; % coil inductance [H]
% kt = 1.836e-3; % torque/force constant, Typical
kt = 1.9063e-3; % Experiment at Pangolin 8-8-2021




%% ----------------- [Electrical Dynamic with Eddy Current] ---------------


% from identification, File: Diffusion1D2D
mu_sigma_i = 3.2035;
mu_sigma_m = 2.8227;

d  = 0.35*1e-3; % Lamination Thickness [m]
wp = 4.72e-3; % pole width, 4.72mm directly measured from geometry
L  = 4.191*1e-3; % Axial Length of Actuator [m]
```

```
a = wp/2; % Rectangle Width=2a
b = L/2; % Rectangle Height=2*b
w = sqrt(4*a*b)/2; % square approximation of the rectangle: side=2*w

Rc = 1.76; % coil resistance [ohm]
Rs = 0.1; % sense resistor [ohm]
R  = Rc+Rs;
Lc0 = 295e-6; % Low-frequency inductance

Q_i =  sqrt(i*omegaa* mu_sigma_i)*d/2;
Q_m = ( w * sqrt( (pi/(2*w)).^2 +  i * omegaa * mu_sigma_m )-pi/2)/(1+pi/2);

% Taylor Approximation of Qm with three first for faractional order modeling
% aa = (pi/(2*w));
% Q_m = ( w * ( aa + (1/(2*aa)).* i * omegaa * kk_m*mu_eff_m*sigma_m  -
(1/(8*aa^3)).* (i * omegaa *kk_m* mu_eff_m*sigma_m).^2 ) -pi/2)/(1+pi/2);


Q   =  Q_i + Q_m;

% RL without back-emf (locked)
He = 1./(R+i*omegaa*Lc0);

% RL model with back-emf (unlocked)
% He_exct = tf([J kd ks],[Lc*J R*J+Lc*kd R*kd+ks*kd+kt^2 R*ks]); % Icoil/Vcoil
with back emf
He_exct = (J*s.^2 + kd*s + ks)./( Lc*J*s.^3 + (R*J+Lc*kd)*s.^2 +
(R*kd+ks*kd+kt^2)*s + R*ks );


% RL including eddy effect
He_eddy = (1 + Q)./(R + i*omegaa*Lc0 + R*Q);

% Mechanical Dynamic
Hm = kt./(J*s.^2+kd*s+ks);



figure
subplot(2,1,1)
   semilogx(ff, 20*log10(abs(He)),'--',...      % RL Model without back-emf
            ff, 20*log10(abs(He_exct)),'-.',... % RL Model with back-emf
            ff, 20*log10(abs(He_eddy)),'--',... % Model with eddy
            He_appr_exp(:,1), He_appr_exp(:,2),'k',... % Experiment Locked
            He_exct_exp(:,1), He_exct_exp(:,2),'b--',... % Experiment unlocked
            'LineWidth',1); grid
   xlabel('frequency (Hz)'); ylabel('Magnitude (dB)')
   title('Q_m=\phi/\phi_0')
   % xlim([10^1 10^7])
subplot(2,1,2)
   semilogx(ff, (180/pi)*angle(He),'--',...      % RL Model without back-emf
            ff, (180/pi)*angle(He_exct),'-.',...  % RL Model with back-emf
            ff, (180/pi)*angle(He_eddy),'--',... % Model with eddy
            He_appr_exp(:,1), He_appr_exp(:,3),'k',... % Experiment Locked
            He_exct_exp(:,1), He_exct_exp(:,3),'b--',... % Experiment unlocked
            'LineWidth',1); grid
   xlabel('frequency (Hz)'); ylabel('Angle (deg)')
   legend('RL Model, locked','RL Model, unlocked','Eddy Model','Expr,
locked','Expr, unlocked')
   % xlim([10^1 10^7])

% Plot mechanical dynamic
```

```
figure
subplot(2,1,1)
   semilogx(ff, 20*log10(abs(Hm)),'r',...        %  Model
            Hm_expr(:,1), Hm_expr(:,2),'b--',... % Experiment
            'LineWidth',1); grid
   ylabel('Magnitude (dB)')
   xlim([10^1 10^4])
subplot(2,1,2)
   semilogx(ff, (180/pi)*angle(Hm),'r',...      % Model
            Hm_expr(:,1), unwrap(Hm_expr(:,3)),'b--',... % Experiment
            'LineWidth',1); grid
   xlabel('frequency (Hz)'); ylabel('Angle (deg)')
   legend('Model','Experiment')
   xlim([10^1 10^4])


 % Plot mechanical dynamic WITH fRICTION TESTS
figure
subplot(2,1,1)
   semilogx(Friction_10mv_Bode(:,1), Friction_10mv_Bode(:,2),'--',...
            Friction_20mv_Bode(:,1), Friction_20mv_Bode(:,2),'--',...
            Friction_30mv_Bode(:,1), Friction_30mv_Bode(:,2),'--',...
            Friction_40mv_Bode(:,1), Friction_40mv_Bode(:,2),'g--',...
            Hm_expr(:,1), Hm_expr(:,2),'--r',... % Experiment
            ff, 20*log10(abs(Hm)),'k',...        %  Model
            'LineWidth',0.7); grid
   ylabel('Magnitude (dB)')
   xlim([10^1 10^3]); ylim([-30 17])
subplot(2,1,2)
   semilogx(Friction_10mv_Bode(:,1), Friction_10mv_Bode(:,3),'--',...
            Friction_20mv_Bode(:,1), Friction_20mv_Bode(:,3),'--',...
            Friction_30mv_Bode(:,1), Friction_30mv_Bode(:,3),'--',...
            Friction_40mv_Bode(:,1), Friction_40mv_Bode(:,3),'g--',...
            Hm_expr(:,1), unwrap(Hm_expr(:,3)),'--r',... % Experiment
            ff, (180/pi)*angle(Hm),'k',...      % Model
            'LineWidth',0.7); grid
   xlabel('frequency (Hz)'); ylabel('Angle (deg)')
   legend('10mv, 20mA','20mv, 40mA','30mv, 60mA','40mv, 80mA','60mv, 120mA,
Hm','Model')
   xlim([10^1 10^3]); ylim([-180 0])
   yticks([-180 -90 0])



%% ---------------[ Current Sensor Resistor Gcs=Vrs/Icoil]-----------------
% Converting Coil Current to a Voltage to be measured by buffer OpAmp
% Vrs=Rs*Icoil
Rs  = 0.1; % sense resistor
Gcs = Rs; % Gs=Vrs/Icoil;



%% ---------------[ Power OpAmp TF_pAmp_nonideal=Vcoil/Vc]-----------------
% Increasing Compensator Output Voltage Vc to Coil Voltage Vcoil
% PowerOpAmp Modeling, LM3886
% non-ideal OpAmps:  TF_pAmp_nonideal
% ideal OpAmps:      TF_pAmp_ideal


% Voltage Divider
R1_pAmp = 64.9e3; %  voltage divider
R2_pAmp = 10e3; %  voltage divider
```

```
% Power Op-Amp
Ra_pAmp = 10e3; % feedback
Rb_pAmp = 95.3e3; % feedback

% input lag compensation and input resistance of Op-Amp
Ri_pAmp    = 6.2e3; % input lag compensation
Ci_pAmp    = 470e-12; % input lag compensation
RiCi_pAmp = Ri_pAmp+1./(Ci_pAmp*s); % series Ri and Ci
Zin        = 100e6; % input impedance of Op-Amp
% Zi_pAmp = RiCi_pAmp*Zin/(RiCi_pAmp+Zin);
Zi_pAmp    = RiCi_pAmp;


% Op-Amp Open-Loop Gain Transfer Function A(s), LM3886
GBP_pAmp = 8e6; % Gain-Bandwidth Product [Hz]
Avo_pAmp = 10^(115/20); % Open-Loop DC-gain
f1_pAmp  = GBP_pAmp./Avo_pAmp; w1_pAmp=2*pi*f1_pAmp; % pole 1
f2_pAmp  = 1.5e6;   w2_pAmp=2*pi*f2_pAmp; % pole 2, usually less than GWB
f3_pAmp  = 2.9e6;   w3_pAmp=2*pi*f3_pAmp; % pole 3, usually between f2 and GWB

A1_pAmp = Avo_pAmp.*w1_pAmp ./(s+w1_pAmp); % 1st-order model
A2_pAmp = Avo_pAmp.*w1_pAmp.*w2_pAmp ./((s+w1_pAmp).*(s+w2_pAmp)); % 2nd-order
model
A3_pAmp = Avo_pAmp.*w1_pAmp.*w2_pAmp*w3_pAmp
./((s+w1_pAmp).*(s+w2_pAmp).*(s+w3_pAmp)); % 2nd-order model

A_pAmp  = A3_pAmp; % Order selection


% Non-Ideal OpAmp, Uncompensated
FF_pAmp = (R2_pAmp./(R1_pAmp+R2_pAmp)) .* A_pAmp; % Feed Forward
FB_pAmp = (Ra_pAmp./(Ra_pAmp+Rb_pAmp)) .* ((R1_pAmp+R2_pAmp)./R2_pAmp); %
Feedback
LT_pAmp = FF_pAmp.*FB_pAmp; % Loop Transmision
TF_pAmp_nonideal = FF_pAmp./(1+FF_pAmp.*FB_pAmp); % Closed-Loop (internal loop)

% Non-Ideal OpAmp, Compensated with Ri & Ci at input
FF_pAmp_comp = (R2_pAmp./(R1_pAmp+R2_pAmp)) .* ( Zi_pAmp./(Zi_pAmp +
(R1_pAmp.*R2_pAmp./(R1_pAmp+R2_pAmp)) + (Ra_pAmp.*Rb_pAmp./(Ra_pAmp+Rb_pAmp)))
) .* A_pAmp; % Feed Forward
FB_pAmp_comp = (Ra_pAmp./(Ra_pAmp+Rb_pAmp)) .* ((R1_pAmp+R2_pAmp)./R2_pAmp); %
Feedback
LT_pAmp_comp = FF_pAmp_comp.*FB_pAmp_comp; % Loop Transmision
TF_pAmp_nonideal_comp = FF_pAmp_comp./(1+FF_pAmp_comp.*FB_pAmp_comp); % Closed-
Loop

% DC Gian
DC_gain_pAmp    = (R2_pAmp./(R1_pAmp+R2_pAmp)) .*(1+Rb_pAmp./Ra_pAmp)
DC_gain_dB_pAmp = 20*log10((R2_pAmp./(R1_pAmp+R2_pAmp)) .*(1+Rb_pAmp/Ra_pAmp))

% Ideal OpAmp
TF_pAmp_ideal   = DC_gain_pAmp;



mag_TF_pAmp_nonideal = 20*log10(abs(TF_pAmp_nonideal));
phase_TF_pAmp_nonideal = (180/pi)*unwrap(angle(TF_pAmp_nonideal));

subplot(2,1,1)
   semilogx(ff, mag_TF_pAmp_nonideal,...
            'LineWidth',1); grid
   % xlabel('frequency (Hz)')
```

```
   ylabel('Magn (dB)')
   % set(gca,'xtick',[]);
   % ax = gca; ax.XGrid = 'on'; ax.YGrid = 'on';
subplot(2,1,2)
   semilogx(ff, phase_TF_pAmp_nonideal,...
            'LineWidth',1); grid
   xlabel('Freq (Hz)'); ylabel('Phase (deg)')



%% --------[ Compensator 1/Z1, FF_Comp_nonideal, FB_Comp_nonideal ]--------
% C506 Compensator Op-Amp Modeling, OP1652
% Forward Path, non-ideal OpAmp:  FF_Comp_nonideal
% Forward Path, ideal OpAmp:      FF_Comp_ideal
% Feedback Path non-ideal OpAmp:  FB_Comp_nonideal
% Feedback Path ideal OpAmp:      FB_Comp_ideal
% Input Block 1/Z1

% Z1 Components
R1_Comp = 5.1e3; % Z0
Z1      = R1_Comp;

% Z2 Components, Lead Compensator
R2_Comp  = 10e3; % Z2, it sets the bandwidth together with R1_Comp

% R2p_Comp = 100;  % Z2, It, together with C2_Comp, sets the Lead
Characteristics, origianl
% C2_Comp  = 2400e-12; % Z2, original
R2p_Comp = 1.1e3;  % Z2, It, together with C2_Comp, sets the Lead
Characteristics
C2_Comp  = 2.2e-09; % Z2

Z2       =
R2_Comp.*(R2p_Comp.*C2_Comp.*s+1)./((R2_Comp+R2p_Comp).*C2_Comp*s+1);

% Zf Components, Lag Compensator
% R3_Comp = 2e6; % Zf , large paralle resistor to limit the integrator
 % R3_Comp = 470e3; % Zf , original value, large paralle resistor to limit the
integrator
 R3_Comp = 2e6;

% C3_Comp = 180e-12; % Zf, original
C3_Comp = 100e-12;

Zf      = R3_Comp./(R3_Comp.*C3_Comp.*s+1); % with parallel R3_Comp, Non-pure
interator
% Zf    = 1/(C3_Comp*s); % without parallel R3_Comp, pure integrator

% Op-Amp Open-Loop Transfer Function A(s), , OP1652
GBP_Comp = 18e6; % Gain-Bandwidth Product [Hz]
Avo_Comp = 10^(114/20); % Open-Loop DC-gain
f1_Comp  = GBP_Comp./Avo_Comp; w1_Comp=2*pi*f1_Comp; % pole 1
f2_Comp  = 1.5e7;   w2_Comp=2*pi*f2_Comp; % pole 2, not found in datasheet
f3_Comp  = 2.9e7;   w3_Comp=2*pi*f3_Comp; % pole 3, not found in datasheet

A1_Comp  = Avo_Comp.*w1_Comp ./(s+w1_Comp); % 1st-order model
A2_Comp  = Avo_Comp.*w1_Comp.*w2_Comp ./((s+w1_Comp).*(s+w2_Comp)); % 2nd-order
model
A3_Comp  = Avo_Comp.*w1_Comp.*w2_Comp.*w3_Comp
./((s+w1_Comp).*(s+w2_Comp).*(s+w3_Comp)); % 2nd-order model

A_Comp  = A3_Comp; % Order selection
```

```
% options.FreqUnits = 'Hz';
% figure; h=bodeplot(A_Comp,{1,1e10}); grid title('Open-Loop Gain A')
% setoptions(h,'FreqUnits','Hz');

% Loop Transmission, Ideal Op-Amp
FF_Comp_ideal   = Zf;
FB_Comp_ideal   = 1./Z2;
Loop_Comp_ideal = FF_Comp_ideal .* FB_Comp_ideal; % Ideal Op-Amp

% Loop Transmission, Non-Ideal Op-Amp
FF_int_Comp      = Zf .* ( (Z1.*Z2)./(Z1.*Z2+Z1.*Zf+Z2.*Zf) ) .* A_Comp; % Feed
Forward, internal OpAmp Loop
FB_int_Comp      = 1./Zf; % Feedback path of internal OpAmp Loop

FF_Comp_nonideal = FF_int_Comp./(1+FF_int_Comp.*FB_int_Comp); % Closed-Loop
(internal loop), FF part of the compensator
FB_Comp_nonideal = 1./Z2; % FB part of the compensator
Loop_Comp        = FF_Comp_nonideal .* FB_Comp_nonideal; % Non-Ideal Op-Amp


% ideal
mag_Loop_Comp_ideal = 20*log10(abs(Loop_Comp_ideal));
phase_Loop_Comp_ideal = (180/pi)*unwrap(angle(Loop_Comp_ideal));
% non ideal
mag_Loop_Comp = 20*log10(abs(Loop_Comp));
phase_Loop_Comp = (180/pi)*unwrap(angle(Loop_Comp));


subplot(2,1,1)
   semilogx(ff, mag_Loop_Comp_ideal,...
            ff, mag_Loop_Comp,...
            Bode_Comp(:,1), Bode_Comp(:,2),... % Comp Expr
            'LineWidth',1); grid
   % xlabel('frequency (Hz)')
   ylabel('Magn (dB)')
   % set(gca,'xtick',[]);
   % ax = gca; ax.XGrid = 'on'; ax.YGrid = 'on';
subplot(2,1,2)
   semilogx(ff, phase_Loop_Comp_ideal,...
            ff, phase_Loop_Comp,...
            Bode_Comp(:,1), Bode_Comp(:,3)-180,... % Comp Expr, subtracted by
180
            'LineWidth',1); grid
   xlabel('Freq (Hz)'); ylabel('Phase (deg)')
   title('C506 Compensator Loop Transmission'); legend('ideal','non-ideal',
'Expr')


%% --------[ Current Sensor Buffer OpAmp: TF_buff_nonideal=vs/Vrs ]--------
% C506 Current Sensor Buffer Op-Amp Modeling, OP1652
% Conversing the Voltage of current sense resistor to voltage Vs
% non-ideal OpAmps:  TF_buff_nonideal
% ideal OpAmps:      TF_buff_ideal
R1_buff = 1e3;
R2_buff = 10e3;

% Op-Amp Open-Loop Transfer Function A(s), , OP1652
GBP_buff = 18e6; % Gain-Bandwidth Product [Hz]
Avo_buff = 10^(114/20); % Open-Loop DC-gain
f1_buff  = GBP_buff./Avo_buff; w1_buff=2*pi*f1_buff; % pole 1
f2_buff  = 1.5e7;   w2_buff=2*pi*f2_buff; % pole 2, not found in datasheet
f3_buff  = 2.9e7;   w3_buff=2*pi*f3_buff; % pole 3, not found in datasheet
```

```
A1_buff  = Avo_buff*w1_buff ./(s+w1_buff); % 1st-order model
A2_buff  = Avo_buff.*w1_buff.*w2_buff ./((s+w1_buff).*(s+w2_buff)); % 2nd-order
model
A3_buff  = Avo_buff*w1_buff.*w2_buff.*w3_buff
./((s+w1_buff).*(s+w2_buff).*(s+w3_buff)); % 2nd-order model

A_buff   = A3_buff; % Order selection

% Ideal Op-Amp
TF_buff_ideal = R2_buff./R1_buff; % Ideal Op-Amp

% Loop Transmission, Non-Ideal Op-Amp
FF_int_buff = (R2_buff./(R1_buff+R2_buff)) * A_buff; % Feed Forward, internal
OpAmp Loop
FB_int_buff = R1_buff./R2_buff; % Feedback path of internal OpAmp Loop
TF_buff_nonideal = FF_int_buff./(1+FF_int_buff.*FB_int_buff);

% ideal
mag_TF_buff_nonideal = 20*log10(abs(TF_buff_nonideal));
phase_TF_buff_nonideal = (180/pi)*unwrap(angle(TF_buff_nonideal));

% Plot
subplot(2,1,1)
   semilogx(ff, mag_TF_buff_nonideal,...
            'LineWidth',1); grid
   % xlabel('frequency (Hz)')
   ylabel('Magn (dB)')
   % set(gca,'xtick',[]);
   % ax = gca; ax.XGrid = 'on'; ax.YGrid = 'on';
subplot(2,1,2)
   semilogx(ff, phase_TF_buff_nonideal,...
            'LineWidth',1); grid
   xlabel('Freq (Hz)'); ylabel('Phase (deg)')



%% -----------[ Model Selection: Model with or without back-emf ]-----------
% Select the Actuator Model?
Gp_RL=He; % without eddy. RL Model
Gp = He_eddy;  % with eddy



%% ---------------------------[ Block Diagram]----------------------------
F  = 1./Z1; % input block

P  = Gp; % Actuator
P_RL  = Gp_RL; % Actuator

% C  = FF_Comp_nonideal * TF_pAmp_nonideal_comp; % non-ideal op-amp, Power op-
amp with compensator
C  = FF_Comp_nonideal .* TF_pAmp_nonideal; % non-ideal op-amp, Power op-amp
without compensator
Ci = FF_Comp_ideal .* TF_pAmp_ideal; % ideal op-amp

H  = Rs .* TF_buff_nonideal .* FB_Comp_nonideal; % non-ideal op-amp
Hi = Rs .* TF_buff_ideal .* FB_Comp_ideal; % ideal op-amp



%% ----------------[ Current Loop, Loop Transmission PCH]-------------------
% Loop, non-ideal
LT_CurrentLoop       = P.*C.*H;  % Closed-Loop, Non-Ideal OpAmps
```

```
mag_LT_CurrentLoop = 20*log10(abs(LT_CurrentLoop)); % mag
phase_LT_CurrentLoop = (180/pi)*unwrap(angle(LT_CurrentLoop)); % phase
% The loop excluding compensator, non-ideal
LT_CurrentLoop_rest       = P.*TF_pAmp_nonideal.*TF_buff_nonideal.*Rs;  % 
Closed-Loop, Non-Ideal OpAmps
mag_LT_CurrentLoop_rest = 20*log10(abs(LT_CurrentLoop_rest)); % mag
phase_LT_CurrentLoop_rest = (180/pi)*unwrap(angle(LT_CurrentLoop_rest)); % 
phase

% Loop Transmission, non-ideal, only RL model of electrical dynamic, P=He
LT_CurrentLoop_RL       = He.*C.*H;  % Closed-Loop, Non-Ideal OpAmps
mag_LT_CurrentLoop_RL = 20*log10(abs(LT_CurrentLoop_RL)); % mag
phase_LT_CurrentLoop_RL = (180/pi)*unwrap(angle(LT_CurrentLoop_RL)); % phase

% Loop, ideal
LT_CurrentLoop_ideal = P.*Ci.*Hi;  % Closed-Loop, Ideal OpAmps
mag_LT_CurrentLoop_ideal = 20*log10(abs(LT_CurrentLoop_ideal)); % mag
phase_LT_CurrentLoop_ideal = (180/pi)*unwrap(angle(LT_CurrentLoop_ideal)); % 
phase
% The loop excluding compensator, ideal
LT_CurrentLoop_ideal_rest = P.*TF_pAmp_ideal.*TF_buff_ideal.*Rs;  % Closed-
Loop, Ideal OpAmps
mag_LT_CurrentLoop_ideal_rest = 20*log10(abs(LT_CurrentLoop_ideal_rest)); % mag
phase_LT_CurrentLoop_ideal_rest = 
(180/pi)*unwrap(angle(LT_CurrentLoop_ideal_rest)); % phase

% Plots Non-Ideal
subplot(2,1,1)
   semilogx(ff, mag_Loop_Comp,'m',...
            Bode_Comp(:,1), Bode_Comp(:,2),'k--',...  % Comp Expr,
            ff, mag_LT_CurrentLoop_rest,'g',...
            Bode_LT(:,1), Bode_LT(:,2)+14.6-Bode_Comp(:,2),'k--',... % Rest, 
Expr
            ff, mag_LT_CurrentLoop,'r',...    % Eddy Model
            ff, mag_LT_CurrentLoop_RL,'b',... % RL model
            Bode_LT(:,1), Bode_LT(:,2)+14.6,'k--',... % LT Expr, add by 14.9 
because it was attentuated for measurement
            'LineWidth',1); grid
   % xlabel('frequency (Hz)')
   ylabel('Magn (dB)'); ylim([-40 50]); xlim([10^1 10^5])
   % title('Decomposition of Loop Transmision, nonideal op-amps ');
   xticks([10^1, 10^2 10^3,10^4,10^5])
subplot(2,1,2)
   semilogx(ff, phase_Loop_Comp,'m',...
            Bode_Comp(:,1), Bode_Comp(:,3)-180,'k--',... % Comp Expr, 
subtracted by 180
            ff, phase_LT_CurrentLoop_rest,'g',...
            Bode_LT(:,1), Bode_LT(:,3)-180-(Bode_Comp(:,3)-180),'k--',... % 
Rest, Expr
            ff, phase_LT_CurrentLoop,'r',... % Eddy Model
            ff, phase_LT_CurrentLoop_RL,'b',... % RL Model
            Bode_LT(:,1), Bode_LT(:,3)-180,'k--',... % LT Expr, subtracted by 
180
            'LineWidth',1); grid
   xlabel('Freq (Hz)'); ylabel('Phase (deg)');  ylim([-180 0]); xlim([10^1 
10^5])
   legend('Comp, Model','Comp, Expr','Rest, Model','Rest, Expr','LT, Eddy 
Model','LT, RL Model','LT Expr')
   xticks([10^1, 10^2 10^3,10^4,10^5]); yticks([-180,-90,0])


% Plots Ideal
figure
```

```
subplot(2,1,1)
   semilogx(ff, mag_Loop_Comp_ideal,...
            Bode_Comp(:,1), Bode_Comp(:,2),...  % Comp Expr,
            ff, mag_LT_CurrentLoop_ideal_rest,...
            Bode_LT(:,1), Bode_LT(:,2)+14.6-Bode_Comp(:,2),... % Rest, Expr
            ff, mag_LT_CurrentLoop_ideal,...
            Bode_LT(:,1), Bode_LT(:,2)+14.6,... % LT Expr, add by 14.9 because
it was attentuated for measurement
            'LineWidth',1); grid
   % xlabel('frequency (Hz)')
   ylabel('Magn (dB)')
   title('Decomposition of Loop Transmision, ideal op-amps ');
   legend('Compensator','Compensator Expr','Rest of Loop','Rest of Loop
Expr','Loop Trans','LT Exp')
subplot(2,1,2)
   semilogx(ff, phase_Loop_Comp_ideal,...
            Bode_Comp(:,1), Bode_Comp(:,3)-180,... % Comp Expr, subtracted by
180
            ff, phase_LT_CurrentLoop_ideal_rest,...
            Bode_LT(:,1), Bode_LT(:,3)-180-(Bode_Comp(:,3)-180),... % Rest,
Expr
            ff, phase_LT_CurrentLoop_ideal,...
            Bode_LT(:,1), Bode_LT(:,3)-180,... % LT Expr, subtracted by 180
            'LineWidth',1); grid
   xlabel('Freq (Hz)'); ylabel('Phase (deg)')


% Loop Transmission, ideal and non-ideal op-amps
figure
subplot(2,1,1)
   semilogx(ff, mag_LT_CurrentLoop,...
            ff, mag_LT_CurrentLoop_ideal,...
            Bode_LT(:,1), Bode_LT(:,2)+14.6,... % LT Expr, add by 14.9 because
it was attentuated for measurement
            'LineWidth',1); grid
   % xlabel('frequency (Hz)')
   ylabel('Magn (dB)')
   title('Loop Transmision Bode ');
   legend('non-ideal OpAmps','ideal OpAmps','Expr')
subplot(2,1,2)
   semilogx(ff, phase_LT_CurrentLoop,...
            ff, phase_LT_CurrentLoop_ideal,...
            Bode_LT(:,1), Bode_LT(:,3)-180,... % LT Expr, subtracted by 180
            'LineWidth',1); grid
   xlabel('Freq (Hz)'); ylabel('Phase (deg)')


% Nyquist and sensitivity circle
figure;
plot(real(LT_CurrentLoop),imag(LT_CurrentLoop),'r',...
     real(LT_expr(1:1990)),imag(LT_expr(1:1990)),'k--',...
                  'LineWidth',1.1); grid on
xlabel('real'); ylabel('imaginary')
legend('Model','Expr')
title('Nyquist and sensitivity circle')
axis equal

%% ----------[Gang 1: Closed-Loop Reference Tracking FPC/1+PCH]------------
% Reference tracking PCF/1+PCH

% Eddy Model of Electrical Dynamic, non-ideal op-amps
GANG1  = F.*P.*C./(1+P.*C.*H);  % Closed-Loop, Non-Ideal OpAmps
mag_GANG1 = 20*log10(abs(GANG1));
```

```
phase_GANG1 = (180/pi)*unwrap(angle(GANG1));

% RL Model of Electrical Dynamic, non-ideal op-amps
GANG1_RL  = F.*P_RL.*C./(1+P_RL.*C.*H);  % Closed-Loop, Non-Ideal OpAmps
mag_GANG1_RL = 20*log10(abs(GANG1_RL));
phase_GANG1_RL = (180/pi)*unwrap(angle(GANG1_RL));

% Eddy Model of Electrical Dynamic, ideal op-amps
GANGi1 = F.*P.*Ci./(1+P.*Ci.*Hi);  % Closed-Loop, Ideal OpAmps
mag_GANGi1 = 20*log10(abs(GANGi1));
phase_GANGi1 = (180/pi)*unwrap(angle(GANGi1));

DC_gain_CurrentLoop_PureIntegrator = R2_Comp/R1_Comp
DC_gain_dB_CurrentLoop_PureIntegrator = 20*log10(R2_Comp/R1_Comp)

DC_gain_dB_CurrentLoop_NonPureIntegrator = mag_GANG1(1)
DC_gain_CurrentLoop_NonPureIntegrator = 10^(mag_GANG1(1)/20)


%% -------[Gang 2: Reference to Power Op-Amp output Voltage FC/1+PCH]------

GANG2  = F.*C./(1+P.*C.*H);     % Closed-Loop, Non-Ideal OpAmps
mag_GANG2 = 20*log10(abs(GANG2));
phase_GANG2 = (180/pi)*unwrap(angle(GANG2));

GANG2_RL  = F.*C./(1+P_RL.*C.*H);     % Closed-Loop, Non-Ideal OpAmps
mag_GANG2_RL = 20*log10(abs(GANG2_RL));
phase_GANG2_RL = (180/pi)*unwrap(angle(GANG2_RL));

GANGi2 = F.*Ci./(1+P.*Ci.*Hi);  % Closed-Loop, Ideal OpAmps
mag_GANGi2 = 20*log10(abs(GANGi2));
phase_GANGi2 = (180/pi)*unwrap(angle(GANGi2));


% Lead in Forward Path

FF_Comp_ideal_LF   = (R3_Comp./(R3_Comp.*C3_Comp.*s+1))... % Lag

.*((R2_Comp+R2p_Comp).*C2_Comp*s+1)./(R2p_Comp.*C2_Comp.*s+1);% Lead
FB_Comp_ideal_LF   = 1./R2_Comp;

Ci_LF = FF_Comp_ideal_LF.* TF_pAmp_ideal; % ideal op-amp
Hi_LF = Rs .* TF_buff_ideal.* FB_Comp_ideal_LF; % ideal op-amp

GANGi2_LF = F.*Ci_LF./(1+P.*Ci_LF.*Hi_LF);  % Lead in Forward Path
mag_GANGi2_LF = 20*log10(abs(GANGi2_LF));
phase_GANGi2_LF = (180/pi)*unwrap(angle(GANGi2_LF));


%% ---------------[Gang 3: Disturbance Rejection  P/1+PCH]-----------------
% Disturbance to plant output
GANG3  = P./(1+P.*C.*H);    % Closed-Loop, Non-Ideal OpAmps
mag_GANG3 = 20*log10(abs(GANG3));
phase_GANG3 = (180/pi)*unwrap(angle(GANG3));

GANG3_RL  = P_RL./(1+P_RL.*C.*H);    % Closed-Loop, Non-Ideal OpAmps
mag_GANG3_RL = 20*log10(abs(GANG3_RL));
phase_GANG3_RL = (180/pi)*unwrap(angle(GANG3_RL));

GANGi3 = P./(1+P.*Ci.*Hi);  % Closed-Loop, Ideal OpAmps
mag_GANGi3 = 20*log10(abs(GANGi3));
phase_GANGi3 = (180/pi)*unwrap(angle(GANGi3));
```

```matlab
%% --------------------[Gang 4: Sensitivity 1/1+PCH]----------------------
% measurement noise to plant output
GANG4  = 1./(1+P.*C.*H);     % Closed-Loop, Non-Ideal OpAmps
mag_GANG4 = 20*log10(abs(GANG4));
phase_GANG4 = (180/pi)*unwrap(angle(GANG4));

GANG4_RL  = 1./(1+P_RL.*C.*H);     % Closed-Loop, Non-Ideal OpAmps
mag_GANG4_RL = 20*log10(abs(GANG4_RL));
phase_GANG4_RL = (180/pi)*unwrap(angle(GANG4_RL));

GANGi4 = 1./(1+P.*Ci.*Hi);  % Closed-Loop, Ideal OpAmps
mag_GANGi4 = 20*log10(abs(GANGi4));
phase_GANGi4 = (180/pi)*unwrap(angle(GANGi4));


%% ------------------[Gang 5: Noise Sensitivity CH/1+PCH]------------------
% Noise to controller (power op-amp) output
GANG5  = C.*H./(1+P.*C.*H);      % Closed-Loop, Non-Ideal OpAmps
mag_GANG5 = 20*log10(abs(GANG5));
phase_GANG5 = (180/pi)*unwrap(angle(GANG5));

GANG5_RL  = C.*H./(1+P_RL.*C.*H);      % Closed-Loop, Non-Ideal OpAmps
mag_GANG5_RL = 20*log10(abs(GANG5_RL));
phase_GANG5_RL = (180/pi)*unwrap(angle(GANG5_RL));

GANGi5 = Ci.*Hi./(1+P.*Ci.*Hi);  % Closed-Loop, Ideal OpAmps
mag_GANGi5 = 20*log10(abs(GANGi5));
phase_GANGi5 = (180/pi)*unwrap(angle(GANGi5));


%% --------------[Gang 6: Complementary Sensitivity PCH/1+PCH]-------------
% Disturbance to controller (power op-amp) output
GANG6  = P.*C.*H./(1+P.*C.*H);     % Closed-Loop, Non-Ideal OpAmps
mag_GANG6 = 20*log10(abs(GANG6));
phase_GANG6 = (180/pi)*unwrap(angle(GANG6));

GANG6_RL  = P_RL.*C.*H./(1+P_RL.*C.*H);     % Closed-Loop, Non-Ideal OpAmps
mag_GANG6_RL = 20*log10(abs(GANG6_RL));
phase_GANG6_RL = (180/pi)*unwrap(angle(GANG6_RL));

GANGi6 = P.*Ci.*Hi./(1+P.*Ci.*Hi); % Closed-Loop, Ideal OpAmps
mag_GANGi6 = 20*log10(abs(GANGi6));
phase_GANGi6 = (180/pi)*unwrap(angle(GANGi6));

%% -----[ FPC/1+PCH, FC/1+PCH, P/1+PCH, 1/1+PCH, CH/1+PCH, PCH/1+PCH]------

%% -----[ FPC/1+PCH, FC/1+PCH, P/1+PCH, 1/1+PCH, CH/1+PCH, PCH/1+PCH]------

% ----- Bode Plot -----
% Gang 1
figure; colororder({'r','[0, 0.5, 0]'})
yyaxis left
   semilogx(ff, mag_GANG1,'r',....
            ...% ff, mag_GANGi1,...
            Bode_G1(:,1), Bode_G1(:,2),'k--',... % Experiment
            'LineWidth',1.4);
   % xlabel('frequency (Hz)')
   ylabel('Magn (dB)')
   title('G1: Reference Tracking FPC/1+PCH');
   % legend('non-ideal OpAmps','ideal OpAmps','Expr')
   xticks([10^1, 10^2 10^3,10^4,10^5])
yyaxis right
```

```
   semilogx(ff, phase_GANG1,'g',...
            ...% ff, phase_GANGi1,...
            Bode_G1(:,1), Bode_G1(:,3)-180,'b--',... % Experiment
            'LineWidth',1.1); grid
   xlabel('Freq (Hz)'); ylabel('Phase (deg)')
   xlim([10^1 10^5]); ylim([-180 2])
   xticks([10^1, 10^2 10^3,10^4,10^5])
   legend('Mag, Model','Mag, Expr', 'Phase, Model','Phase, Expr')
   ax = gca; ax.XGrid = 'on';

% Gang 2
figure; colororder({'r','[0, 0.5, 0]'})
yyaxis left
   semilogx(ff, mag_GANG2,'r',...
            ...% ff, mag_GANGi2,...
            Bode_G2(:,1), Bode_G2(:,2),'k--',... % Experiment
            ff, mag_GANGi2_LF,'r',... % Lead in Forward Path
            'LineWidth',1.4); grid
   % xlabel('frequency (Hz)')
   ylabel('Magn (dB)')
   title('G2: Ref to P-OpAmp Output FC/1+PCH');
   % legend('non-ideal OpAmps','ideal OpAmps','Expr')
   % xlim([10^1 10^5]);ylim([10 30]); xticks([10^1, 10^2 10^3,10^4,10^5])
yyaxis right
   semilogx(ff, phase_GANG2,'g',...
            ...% ff, phase_GANGi2,...
            Bode_G2(:,1), unwrap(Bode_G2(:,3))+180,'b--',... % Experiment
            ff, phase_GANGi2_LF,'g',... % Lead in Forward path
            'LineWidth',1.1); grid
   xlabel('Freq (Hz)'); ylabel('Phase (deg)')
   xlim([10^1 10^6]); ylim([-100 100]); xticks([10^1, 10^2 10^3,10^4,10^5,
10^6])
   legend('Mag, Model','Mag, Expr', 'Phase, Model','Phase, Expr')
   ax = gca; ax.XGrid = 'on';

% Gang 3
figure; colororder({'r','[0, 0.5, 0]'})
yyaxis left
   semilogx(ff, mag_GANG3,'r',...
            ...% ff, mag_GANGi3,...
            Freq_G3, Mag_G3,'k--',... % Experiment, G3=P*G4
            'LineWidth',1.4); grid
   % xlabel('frequency (Hz)')
   ylabel('Magn (dB)')
   title('G3: Disturbance Rejection P/1+PCH');
   % legend('non-ideal OpAmps','ideal OpAmps','Expr')
   xlim([10^1 10^6]); ylim([-55 -28]); xticks([10^1, 10^2 10^3,10^4,10^5,
10^6])
yyaxis right
   semilogx(ff, phase_GANG3,'g',...
            ...% ff, phase_GANGi3,...
            Freq_G3, Phase_G3,'b--',... % Experiment, G3=P*G4
            'LineWidth',1.1); grid
   xlabel('Freq (Hz)'); ylabel('Phase (deg)')
   xlim([10^1 10^6]); ylim([-60 90]); xticks([10^1, 10^2 10^3,10^4,10^5, 10^6])
   legend('Mag, Model','Mag, Expr', 'Phase, Model','Phase, Expr')
   ax = gca; ax.XGrid = 'on';

% Gang 4
figure; colororder({'r','[0, 0.5, 0]'})
yyaxis left
   semilogx(ff, mag_GANG4,'r',...
            ...% ff, mag_GANGi4,...
```

```
            Freq_G4, Mag_G4,'k--',...
            'LineWidth',1.4); grid
   ylabel('Magn (dB)')
   title('G4: Sensitivity 1/1+PCH');
   % legend('non-ideal OpAmps','ideal OpAmps','Expr','Expr 2')
   xlim([10^1 10^6]); ylim([-45 3]); xticks([10^1, 10^2 10^3,10^4,10^5, 10^6])
yyaxis right
   semilogx(ff, phase_GANG4,'g',...
            ...% ff, phase_GANGi4,...
            Freq_G4, Phase_G4,'b--',...
            'LineWidth',1.1); grid
   xlabel('Freq (Hz)'); ylabel('Phase (deg)')
   xlim([10^1 10^6]); ylim([-5 160]); xticks([10^1, 10^2 10^3,10^4,10^5, 10^6])
   legend('Mag, Model','Mag, Expr', 'Phase, Model','Phase, Expr')
   ax = gca; ax.XGrid = 'on';

% Gang 5: CH/1+PCH
figure; colororder({'r','[0, 0.5, 0]'})
yyaxis left
   semilogx(ff, mag_GANG5,'r',...
            ...% ff, mag_GANGi5,...
            Freq_G5, Mag_G5,'k--',...
            'LineWidth',1.4); grid
   % xlabel('frequency (Hz)')
   ylabel('Magn (dB)')
   title('G5: Noise Sensitivity CH/1+PCH');
   % legend('non-ideal OpAmps','ideal OpAmps','Expr')
   xlim([10^1 2*10^6]); ylim([0 30]); xticks([10^1, 10^2 10^3,10^4,10^5, 10^6])
yyaxis right
   semilogx(ff, phase_GANG5,'g',...
            ...% ff, phase_GANGi5,...
            Freq_G5, Phase_G5,'b--',...
            'LineWidth',1.1); grid
   xlabel('Freq (Hz)'); ylabel('Phase (deg)')
   xlim([10^1 2*10^6]); ylim([-270 180]); xticks([10^1, 10^2 10^3,10^4,10^5,
10^6])
   legend('Mag, Model','Mag, Expr', 'Phase, Model','Phase, Expr')
   ax = gca; ax.XGrid = 'on';

% Gang 6: PCH/1+PCH
figure; colororder({'r','[0, 0.5, 0]'})
yyaxis left
   semilogx(ff, mag_GANG6,'r',...
            ...% ff, mag_GANGi6,...
            Freq_G6, Mag_G6,'k--',...
            'LineWidth',1.4); grid
   % xlabel('frequency (Hz)')
   ylabel('Magn (dB)')
   title('G6: Compl Sensitivity PCH/1+PCH');
   % legend('non-ideal OpAmps','ideal OpAmps','Expr')
   xlim([10^1 10^5]); ylim([-15 3]); xticks([10^1, 10^2 10^3,10^4,10^5])
yyaxis right
   semilogx(ff, phase_GANG6,'g',...
            ...% ff, phase_GANGi6,...
            Freq_G6, Phase_G6,'b--',...
            'LineWidth',1.1); grid
   xlabel('Freq (Hz)'); ylabel('Phase (deg)')
   legend('Mag, Model','Mag, Expr', 'Phase, Model','Phase, Expr')
   ax = gca; ax.XGrid = 'on';
   xlim([10^1 10^5]); ylim([-150 50]); xticks([10^1, 10^2 10^3,10^4,10^5])


%% ----- Bode Plot -----
```

```
% Gang 1
figure
subplot(2,1,1)
   semilogx(ff, mag_GANG1_RL,'g',... % non-idel op-amo, RL model
            ff, mag_GANG1,'r',... % non-idel op-amo, eddy model
            ...% ff, mag_GANGi1,...
            Bode_G1(:,1), Bode_G1(:,2),'k--',... % Experiment
            'LineWidth',1.1); grid
   ylabel('Magn (dB)')
   title('G1: Reference Tracking FPC/1+PCH');
   legend('RL Model','Eddy Model','Experiment'); xlim([10^1 10^5]); ylim([-35
10])
   xticks([10^1, 10^2 10^3,10^4,10^5])
subplot(2,1,2)
   semilogx(ff, phase_GANG1_RL,'g',... % non-idel op-amo, eddy model
            ff, phase_GANG1,'r',... % non-idel op-amo, RL model
            ...% ff, phase_GANGi1,...
            Bode_G1(:,1), Bode_G1(:,3)-180,'k--',... % Experiment
            'LineWidth',1.1); grid
   xlabel('Freq (Hz)'); ylabel('Phase (deg)')
   xlim([10^1 10^5]); ylim([-200 3])
   xticks([10^1, 10^2 10^3,10^4,10^5])

% Gang 2
figure
subplot(2,1,1)
   semilogx(ff, mag_GANG2_RL,'g',...
            ff, mag_GANG2,'r',...
            ff, mag_GANGi2_LF,'b-.',... % Lead in Forward Path
            ...% ff, mag_GANGi2,...
            Bode_G2(:,1), Bode_G2(:,2),'k--',... % Experiment
            'LineWidth',1.1); grid
   ylabel('Magn (dB)')
   title('G2: Ref to P-OpAmp Output FC/1+PCH');
   legend('RL Model','Eddy Model','Lead in Forward Path','Experiment')
   xlim([10^1 6*10^5]);ylim([-5 40]); xticks([10^1, 10^2 10^3,10^4,10^5,10^6])
subplot(2,1,2)
   semilogx(ff, phase_GANG2_RL,'g',...
            ff, phase_GANG2,'r',...
            ff, phase_GANGi2_LF,'b-.',... % Lead in Forward Path
            ...% ff, phase_GANGi2,...
            Bode_G2(:,1), unwrap(Bode_G2(:,3))+180,'k--',... % Experiment
            'LineWidth',1.1); grid
   xlabel('Freq (Hz)'); ylabel('Phase (deg)')
   xlim([10^1 6*10^5]); ylim([-150 90]); xticks([10^1, 10^2
10^3,10^4,10^5,10^6])

% Gang 3
figure
subplot(2,1,1)
   semilogx(ff, mag_GANG3_RL,'g',...
            ff, mag_GANG3,'r',...
            ...% ff, mag_GANGi3,...
            Freq_G3, Mag_G3,'k--',... % Experiment, G3=P*G4
            'LineWidth',1.1); grid
   ylabel('Magn (dB)')
   title('G3: Disturbance Rejection P/1+PCH');
   legend('RL Model','Eddy Model','Experiment')
   xlim([10^1 10^6]); ylim([-65 -25]); xticks([10^1, 10^2 10^3,10^4,10^5,
10^6])
subplot(2,1,2)
   semilogx(ff, phase_GANG3_RL,'g',...
            ff, phase_GANG3,'r',...
```

```
         ...% ff, phase_GANGi3,...
         Freq_G3, Phase_G3,'k--',... % Experiment, G3=P*G4
         'LineWidth',1.1); grid
   xlabel('Freq (Hz)'); ylabel('Phase (deg)')
   xlim([10^1 10^6]); ylim([-100 55]); xticks([10^1, 10^2 10^3,10^4,10^5,
10^6])

% Gang 4
figure
subplot(2,1,1)
   semilogx(ff, mag_GANG4_RL,'g',...
         ff, mag_GANG4,'r',...
         ...% ff, mag_GANGi4,...
         Freq_G4, Mag_G4,'k--',...
         'LineWidth',1.1); grid
   ylabel('Magn (dB)')
   title('G4: Sensitivity 1/1+PCH');
   legend('RL Model','Eddy Model','Experiment')
   xlim([10^1 10^6]); ylim([-45 5]); xticks([10^1, 10^2 10^3,10^4,10^5, 10^6])
subplot(2,1,2)
   semilogx(ff, phase_GANG4_RL,'g',...
         ff, phase_GANG4,'r',...
         ...% ff, phase_GANGi4,...
         Freq_G4, Phase_G4,'k--',...
         'LineWidth',1.1); grid
   xlabel('Freq (Hz)'); ylabel('Phase (deg)')
   xlim([10^1 10^6]); ylim([-5 130]); xticks([10^1, 10^2 10^3,10^4,10^5, 10^6])

% Gang 5: CH/1+PCH
figure
subplot(2,1,1)
   semilogx(ff, mag_GANG5_RL,'g',...
         ff, mag_GANG5,'r',...
         ...% ff, mag_GANGi5,...
         Freq_G5, Mag_G5,'k--',...
         'LineWidth',1.1); grid
   ylabel('Magn (dB)')
   title('G5: Noise Sensitivity CH/1+PCH');
   legend('RL Model','Eddy Model','Experiment')
   xlim([10^1 2*10^6]); ylim([-20 35]); xticks([10^1, 10^2 10^3,10^4,10^5,
10^6])
subplot(2,1,2)
   semilogx(ff, phase_GANG5_RL,'g',...
         ff, phase_GANG5,'r',...
         ...% ff, phase_GANGi5,...
         Freq_G5, Phase_G5,'k--',...
         'LineWidth',1.1); grid
   xlabel('Freq (Hz)'); ylabel('Phase (deg)')
   xlim([10^1 2*10^6]); ylim([-270 90]); xticks([10^1, 10^2 10^3,10^4,10^5,
10^6])

% Gang 6: PCH/1+PCH
figure
subplot(2,1,1)
   semilogx(ff, mag_GANG6_RL,'g',...
         ff, mag_GANG6,'r',...
         ...% ff, mag_GANGi6,...
         Freq_G6, Mag_G6,'k--',...
         'LineWidth',1.1); grid
   % xlabel('frequency (Hz)')
   ylabel('Magn (dB)')
   title('G6: Compl Sensitivity PCH/1+PCH');
   % legend('non-ideal OpAmps','ideal OpAmps','Expr')
```

```
   legend('RL Model','Eddy Model','Experiment')
   xlim([10^1 10^5]); ylim([-20 3]); xticks([10^1, 10^2 10^3,10^4,10^5])
subplot(2,1,2)
   semilogx(ff, phase_GANG6_RL,'g',...
            ff, phase_GANG6,'r',...
            ...% ff, phase_GANGi6,...
            Freq_G6, Phase_G6,'k--',...
            'LineWidth',1.1); grid
   xlabel('Freq (Hz)'); ylabel('Phase (deg)')
   xlim([10^1 10^5]); ylim([-170 3]); xticks([10^1, 10^2 10^3,10^4,10^5])
```

Appendix N

Matlab Code for Comparison of Current-Loops by Changing the Location of Lead Compensator

The following is the Matlab code implemented using FOMCON toolbox for solving the fractional-order systems. For a part of the results, e.g. step responses it did not work well for my case. Maybe another toolbox can be more helpful.

```
%-------------------------------------------------------------------------%
%            Fractional Order Model, FOMCON toolbox in Matlab             %
%              Current Loop Modeling including Eddy Current               %
%                    Using ideal and non-ideal Op-Amps                    %
%                Sajjad Mohammadi, EECS, MIT, August 2021                 %
%-------------------------------------------------------------------------%

% Including 3 Op-Amps
% Input Block: 1/Z1
% Feed Forward Path: Compensator FF, Power OpAmp, Actuator
% Feedback path: Sensor Resistor Rs, Buffer OpAmp, Compensator FB

%% --------------------[ Actuator Gp_exct=Icoil/Vcoil]---------------------
s=fotf('s'); % Fractional order, Fomcon toolbox in Matlab


% J=1.65e-9; % Inretia/mass with mirror from Solid Works
J  = 1.5077e-09; % Inretia/mass without mirror from Solid Works
kd = 4.4881e-07; % damping
ks = 0.0013; % spring
Rc = 1.76; % coil resistance [ohm]
Rs = 0.1; % sense resistor [ohm]
R  = Rc+Rs;
Lc  = 280e-6; % coil inductance [H]
% kt = 1.836e-3; % torque/force constant, Typical
kt = 1.9063e-3; % Experiment at Pangolin 8-8-2021


%% ----------------- [Electrical Dynamic with Eddy Current] ---------------

%  He_exct = tf([J kd ks],[Lc*J R*J+Lc*kd R*kd+ks*kd+kt^2 R*ks]); % Icoil/Vcoil
with back emf
%  He_appr = tf([1],[Lc R]); % Icoil/Vcoil  without back emf

% From identification, File: Diffusion1D2D
mu_sigma_i = 3.2035;
mu_sigma_m = 2.8227;

d  = 0.35*1e-3; % Lamination Thickness [m]
wp = 4.72e-3; % pole width, 4.72mm directly measured from geometry
L  = 4.191*1e-3; % Axial Length of Actuator [m]
```

```
a = wp/2; % Rectangle Width=2a
b = L/2; % Rectangle Height=2*b
w = sqrt(4*a*b)/2; % square approximation of the rectangle: side=2*w

Rc = 1.76; % coil resistance [ohm]
Rs = 0.1; % sense resistor [ohm]
R  = Rc+Rs;
Lc0 = 295e-6; % Low-frequency inductance

Q_i = (d/2)*(s* mu_sigma_i)^0.5;

% Q_m = ( w * ( (pi/(2*w)).^2 +  S * mu_sigma_m )^0.5 -pi/2)/(1+pi/2);
% Taylor Approximation of Qm with three first for faractional order modeling
aa = (pi/(2*w));
Q_m = ( w * ( aa + (1/(2*aa))* s * mu_sigma_m  -  (1/(8*aa^3))* (s
*mu_sigma_m)^2 ) -pi/2)/(1+pi/2);

Q   =  Q_i + Q_m;

% Only RL
He = 1/(R+s*Lc0);

% RL including eddy effect
He_eddy = (1 + Q)/(R + s*Lc0 + R*Q);

figure;hold on
step(He_eddy,0:0.00001:0.003) % with eddy
step(He,0:0.00001:0.003) % without eddy
xlabel('time (sec)'); ylabel('current (A)')
title('Step Response of He'); legend('with eddy', 'without eddy')
hold off


figure; hold on
bode(He_eddy,logspace(1,6,2000))
bode(He,logspace(1,6,2000))
grid; title('Bode plot of He'); legend('with eddy', 'without eddy')
hold off
h = gcr; setoptions(h,'FreqUnits','Hz')
xlim([10^1 10^5])



%% ---------------[ Current Sensor Resistor Gcs=Vrs/Icoil]-----------------
% Converting Coil Current to a Voltage to be measured by buffer OpAmp
% Vrs=Rs*Icoil
Rs  = 0.1; % sense resistor
Gcs = Rs; % Gs=Vrs/Icoil;



%% ---------------[ Power OpAmp TF_pAmp_nonideal=Vcoil/Vc]-----------------
% Increasing Compensator Output Voltage Vc to Coil Voltage Vcoil
% PowerOpAmp Modeling, LM3886
% non-ideal OpAmps:  TF_pAmp_nonideal
% ideal OpAmps:      TF_pAmp_ideal

% Voltage Divider
R1_pAmp = 64.9e3; %  voltage divider
R2_pAmp = 10e3; %  voltage divider

% Power Op-Amp
Ra_pAmp = 10e3; % feedback
```

```
Rb_pAmp = 95.3e3; % feedback

% input lag compensation and input resistance of Op-Amp
Ri_pAmp    = 6.2e3; % input lag compensation
Ci_pAmp    = 470e-12; % input lag compensation
RiCi_pAmp = Ri_pAmp+1/(Ci_pAmp*s); % series Ri and Ci
Zin        = 100e6; % input impedance of Op-Amp
% Zi_pAmp = RiCi_pAmp*Zin/(RiCi_pAmp+Zin);
Zi_pAmp    = RiCi_pAmp;


% Op-Amp Open-Loop Gain Transfer Function A(s), LM3886
GBP_pAmp = 8e6; % Gain-Bandwidth Product [Hz]
Avo_pAmp = 10^(115/20); % Open-Loop DC-gain
f1_pAmp  = GBP_pAmp/Avo_pAmp; w1_pAmp=2*pi*f1_pAmp; % pole 1
f2_pAmp  = 1.5e6;   w2_pAmp=2*pi*f2_pAmp; % pole 2, usually less than GWB
f3_pAmp  = 2.9e6;   w3_pAmp=2*pi*f3_pAmp; % pole 3, usually between f2 and GWB

A1_pAmp = Avo_pAmp*w1_pAmp /(s+w1_pAmp); % 1st-order model
A2_pAmp = Avo_pAmp*w1_pAmp*w2_pAmp /((s+w1_pAmp)*(s+w2_pAmp)); % 2nd-order
model
A3_pAmp = Avo_pAmp*w1_pAmp*w2_pAmp*w3_pAmp
/((s+w1_pAmp)*(s+w2_pAmp)*(s+w3_pAmp)); % 2nd-order model

A_pAmp  = A3_pAmp; % Order selection

% options.FreqUnits = 'Hz';
%
% figure; bode(A,{1,1e8},options); grid
% title('Open-Loop Gain A')

% Non-Ideal OpAmp, Uncompensated
FF_pAmp = (R2_pAmp/(R1_pAmp+R2_pAmp)) * A_pAmp; % Feed Forward
FB_pAmp = (Ra_pAmp/(Ra_pAmp+Rb_pAmp)) * ((R1_pAmp+R2_pAmp)/R2_pAmp); % Feedback
LT_pAmp = FF_pAmp*FB_pAmp; % Loop Transmision
TF_pAmp_nonideal = FF_pAmp/(1+FF_pAmp*FB_pAmp); % Closed-Loop (internal loop)

% Non-Ideal OpAmp, Compensated with Ri & Ci at input
FF_pAmp_comp = (R2_pAmp/(R1_pAmp+R2_pAmp)) * ( Zi_pAmp/(Zi_pAmp +
(R1_pAmp*R2_pAmp/(R1_pAmp+R2_pAmp)) + (Ra_pAmp*Rb_pAmp/(Ra_pAmp+Rb_pAmp))) ) *
A_pAmp; % Feed Forward
FB_pAmp_comp = (Ra_pAmp/(Ra_pAmp+Rb_pAmp)) * ((R1_pAmp+R2_pAmp)/R2_pAmp); %
Feedback
LT_pAmp_comp = FF_pAmp_comp*FB_pAmp_comp; % Loop Transmision
TF_pAmp_nonideal_comp = FF_pAmp_comp/(1+FF_pAmp_comp*FB_pAmp_comp); % Closed-
Loop

% DC Gian
DC_gain_pAmp    = (R2_pAmp/(R1_pAmp+R2_pAmp)) *(1+Rb_pAmp/Ra_pAmp)
DC_gain_dB_pAmp = 20*log10((R2_pAmp/(R1_pAmp+R2_pAmp)) *(1+Rb_pAmp/Ra_pAmp))

% Ideal OpAmp
TF_pAmp_ideal   = DC_gain_pAmp;


TF_pAmp_nonideal = DC_gain_pAmp; % For simplicity in Fomcon


% bode
figure; bode(TF_pAmp_nonideal,logspace(1,9,2000)); grid
title('Power OpAmp, Closed-Loop Bode')
h = gcr; setoptions(h,'FreqUnits','Hz')
```

```
% Step Response
figure; step(TF_pAmp_nonideal, [0:0.00000001:0.00001]);
title('Power OpAmp, Step Response')



%% --------[ Compensator 1/Z1, FF_Comp_nonideal, FB_Comp_nonideal ]--------
% C506 Compensator Op-Amp Modeling, OP1652
% Forward Path, non-ideal OpAmp:  FF_Comp_nonideal
% Forward Path, ideal OpAmp:      FF_Comp_ideal
% Feedback Path non-ideal OpAmp:  FB_Comp_nonideal
% Feedback Path ideal OpAmp:      FB_Comp_ideal
% Input Block 1/Z1


% Z1 Components
R1_Comp = 5.1e3; % Z1
Z1      = R1_Comp;

% Z2 Components, Lead Compensator
R2_Comp  = 10e3; % Z2, it sets the bandwidth together with R1_Comp

% R2p_Comp = 100;  % Z2, It, together with C2_Comp, sets the Lead
Characteristics, origianl
% C2_Comp  = 2400e-12; % Z2, original
R2p_Comp = 1.1e3;  % Z2, It, together with C2_Comp, sets the Lead
Characteristics
C2_Comp  = 2.2e-09; % Z2

Z2       = R2_Comp*(R2p_Comp*C2_Comp*s+1)/((R2_Comp+R2p_Comp)*C2_Comp*s+1);

% Zf Components, Lag Compensator
% R3_Comp = 2e6; % Zf , large paralle resistor to limit the integrator
 % R3_Comp = 470e3; % Zf , original value, large paralle resistor to limit the
integrator
 R3_Comp = 2e6;

% C3_Comp = 180e-12; % Zf, original
C3_Comp = 100e-12;

Zf      = R3_Comp/(R3_Comp*C3_Comp*s+1); % with parallel R3_Comp, Non-pure
interator
% Zf   = 1/(C3_Comp*s); % without parallel R3_Comp, pure integrator

% Op-Amp Open-Loop Transfer Function A(s), , OP1652
GBP_Comp = 18e6; % Gain-Bandwidth Product [Hz]
Avo_Comp = 10^(114/20); % Open-Loop DC-gain
f1_Comp  = GBP_Comp/Avo_Comp; w1_Comp=2*pi*f1_Comp; % pole 1
f2_Comp  = 1.5e7;   w2_Comp=2*pi*f2_Comp; % pole 2, not found in datasheet
f3_Comp  = 2.9e7;   w3_Comp=2*pi*f3_Comp; % pole 3, not found in datasheet

A1_Comp  = Avo_Comp*w1_Comp /(s+w1_Comp); % 1st-order model
A2_Comp  = Avo_Comp*w1_Comp*w2_Comp /((s+w1_Comp)*(s+w2_Comp)); % 2nd-order
model
A3_Comp  = Avo_Comp*w1_Comp*w2_Comp*w3_Comp
/((s+w1_Comp)*(s+w2_Comp)*(s+w3_Comp)); % 2nd-order model

A_Comp  = A3_Comp; % Order selection

% options.FreqUnits = 'Hz';
% figure; h=bodeplot(A_Comp,{1,1e10}); grid title('Open-Loop Gain A')
% setoptions(h,'FreqUnits','Hz');
```

```
% Loop Transmission, Ideal Op-Amp
FF_Comp_ideal   = Zf;
FB_Comp_ideal   = 1/Z2;
Loop_Comp_ideal = FF_Comp_ideal * FB_Comp_ideal; % Ideal Op-Amp

% Loop Transmission, Non-Ideal Op-Amp
FF_int_Comp      = Zf * ( (Z1*Z2)/(Z1*Z2+Z1*Zf+Z2*Zf) ) * A_Comp; % Feed
Forward, internal OpAmp Loop
FB_int_Comp      = 1/Zf; % Feedback path of internal OpAmp Loop
FF_Comp_nonideal = FF_int_Comp/(1+FF_int_Comp*FB_int_Comp); % Closed-Loop
(internal loop), FF part of the compensator
FB_Comp_nonideal = 1/Z2; % FB part of the compensator
Loop_Comp        = FF_Comp_nonideal * FB_Comp_nonideal; % Non-Ideal Op-Amp


% bode
figure; hold on;
bode(Loop_Comp_ideal,logspace(1,5,2000))
bode(Loop_Comp,logspace(1,5,2000)); grid;
h = gcr; setoptions(h,'FreqUnits','Hz')
title('C506 Compensator Loop Transmission'); legend('ideal','non-ideal')
hold off



%% --------[ Current Sensor Buffer OpAmp: TF_buff_nonideal=vs/Vrs ]--------
% C506 Current Sensor Buffer Op-Amp Modeling, OP1652
% Conversing the Voltage of current sense resistor to voltage Vs
% non-ideal OpAmps:  TF_buff_nonideal
% ideal OpAmps:      TF_buff_ideal


R1_buff = 1e3;
R2_buff = 10e3;

% Op-Amp Open-Loop Transfer Function A(s), , OP1652
GBP_buff = 18e6; % Gain-Bandwidth Product [Hz]
Avo_buff = 10^(114/20); % Open-Loop DC-gain
f1_buff  = GBP_buff/Avo_buff; w1_buff=2*pi*f1_buff; % pole 1
f2_buff  = 1.5e7;   w2_buff=2*pi*f2_buff; % pole 2, not found in datasheet
f3_buff  = 2.9e7;   w3_buff=2*pi*f3_buff; % pole 3, not found in datasheet

A1_buff  = Avo_buff*w1_buff /(s+w1_buff); % 1st-order model
A2_buff  = Avo_buff*w1_buff*w2_buff /((s+w1_buff)*(s+w2_buff)); % 2nd-order
model
A3_buff  = Avo_buff*w1_buff*w2_buff*w3_buff
/((s+w1_buff)*(s+w2_buff)*(s+w3_buff)); % 2nd-order model

A_buff   = A3_buff; % Order selection

% options.FreqUnits = 'Hz';
% figure; h=bodeplot(A_buff,{1,1e10}); grid title('Open-Loop Gain A')
% setoptions(h,'FreqUnits','Hz');


% Ideal Op-Amp
TF_buff_ideal = R2_buff/R1_buff; % Ideal Op-Amp

% Loop Transmission, Non-Ideal Op-Amp
FF_int_buff = (R2_buff/(R1_buff+R2_buff)) * A_buff; % Feed Forward, internal
OpAmp Loop
FB_int_buff = R1_buff/R2_buff; % Feedback path of internal OpAmp Loop
TF_buff_nonideal = FF_int_buff/(1+FF_int_buff*FB_int_buff);
```

```
TF_buff_nonideal = 10; %  % For simplicity in Fomcon

% Plots
figure;
bode(TF_buff_nonideal,logspace(1,11,2000))
grid; title('Bode, sensor buffer')
h = gcr; setoptions(h,'FreqUnits','Hz')
legend('ideal','non-ideal')
hold off


%% -----------[ Model Selection: Model with or without back-emf ]-----------
% Select the Actuator Model
% Gp=He; % without eddy
Gp = He_eddy;  % with eddy


%% ---------------------------[ Block Diagram]----------------------------
F  = 1/Z1; % input block

P  = Gp; % Actuator

% C  = FF_Comp_nonideal * TF_pAmp_nonideal_comp; % non-ideal op-amp, Power op-
amp with compensator
C  = FF_Comp_nonideal * TF_pAmp_nonideal; % non-ideal op-amp, Power op-amp
without compensator
Ci = FF_Comp_ideal * TF_pAmp_ideal; % ideal op-amp

H  = Rs * TF_buff_nonideal * FB_Comp_nonideal; % non-ideal op-amp
Hi = Rs * TF_buff_ideal * FB_Comp_ideal; % ideal op-amp


%% ----------------[ Current Loop, Loop Transmission PCH]-------------------

LT_CurrentLoop       = P*C*H;  % Closed-Loop, Non-Ideal OpAmps
LT_CurrentLoop_ideal = P*Ci*Hi;  % Closed-Loop, Ideal OpAmps


% The loop excluding compensator, ideal
LT_CurrentLoop_rest       = P*TF_pAmp_nonideal*TF_buff_nonideal;  % Closed-
Loop, Non-Ideal OpAmps
LT_CurrentLoop_ideal_rest = P*TF_pAmp_ideal*TF_buff_ideal;  % Closed-Loop,
Ideal OpAmps


% Plots
% Decomposition of Loop Transmission, non-ideal model of op-amps
figure; hold on
bode(Loop_Comp,logspace(1,7,2000));
bode(LT_CurrentLoop_rest,logspace(1,7,2000))
bode(LT_CurrentLoop,logspace(1,7,2000))
grid; h = gcr; setoptions(h,'FreqUnits','Hz')
title('Decomposition of Loop Transmision, nonideal op-amps ');
legend('Compensator','Rest of the Loop','Loop Transmission')
hold off; xlim([10^1 10^5])

% Decomposition of Loop Transmission, ideal model of op-amps
figure; hold on
bode(Loop_Comp_ideal,logspace(1,7,2000));
bode(LT_CurrentLoop_ideal_rest,logspace(1,7,2000))
bode(LT_CurrentLoop_ideal,logspace(1,7,2000))
grid; h = gcr; setoptions(h,'FreqUnits','Hz')
```

```
title('Decomposition of Loop Transmision, ideal op-amps ');
legend('Compensator','Rest of the Loop','Loop Transmission')
hold off; xlim([10^1 10^5])


figure; hold on
bode(LT_CurrentLoop,logspace(1,7,2000));
bode(LT_CurrentLoop_ideal,logspace(1,7,2000))
grid; h = gcr; setoptions(h,'FreqUnits','Hz')
title('Loop Transmision Bode ');legend('non-ideal OpAmps','ideal OpAmps')
hold off; xlim([10^1 10^5])


%% ----------[Gang 1: Closed-Loop Reference Tracking FPC/1+PCH]------------
% Reference tracking PCF/1+PCH

GANG1  = 1/(1+P*C*H)*(F*P*C);  % Closed-Loop, Non-Ideal OpAmps
GANGi1 = F*P*Ci/(1+P*Ci*Hi);  % Closed-Loop, Ideal OpAmps

DC_gain_CurrentLoop_PureIntegrator = R2_Comp/R1_Comp
DC_gain_dB_CurrentLoop_PureIntegrator = 20*log10(R2_Comp/R1_Comp)


%% -------[Gang 2: Reference to Power Op-Amp output Voltage FC/1+PCH]------

GANG2  = (1/(1+P*C*H))*F*C;     % Closed-Loop, Non-Ideal OpAmps
GANGi2 = (1/(1+P*Ci*Hi))*F*Ci;  % Closed-Loop, Ideal OpAmps

%% ---------------[Gang 3: Disturbance Rejection  P/1+PCH]-----------------
% Disturbance to plant output
GANG3  = P/(1+P*C*H);    % Closed-Loop, Non-Ideal OpAmps
GANGi3 = P/(1+P*Ci*Hi);  % Closed-Loop, Ideal OpAmps

%% --------------------[Gang 4: Sensitivity 1/1+PCH]----------------------
% measurement noise to plant output
GANG4  = 1/(1+P*C*H);    % Closed-Loop, Non-Ideal OpAmps
GANGi4 = 1/(1+P*Ci*Hi);  % Closed-Loop, Ideal OpAmps

%% ------------------[Gang 5: Noise Sensitivity CH/1+PCH]------------------
% Noise to controller (power op-amp) output
GANG5  = (1/(1+P*C*H))*(C*H);      % Closed-Loop, Non-Ideal OpAmps
GANGi5 = 1/(1+P*Ci*Hi)*(Ci*Hi);  % Closed-Loop, Ideal OpAmps

%% --------------[Gang 6: Complementary Sensitivity PCH/1+PCH]-------------
% Disturbance to controller (power op-amp) output
GANG6  = P*C*H/(1+P*C*H);     % Closed-Loop, Non-Ideal OpAmps
GANGi6 = P*Ci*Hi/(1+P*Ci*Hi); % Closed-Loop, Ideal OpAmps


%% -----[ FPC/1+PCH, FC/1+PCH, P/1+PCH, 1/1+PCH, CH/1+PCH, PCH/1+PCH]------

% ----- Bode Plot -----
f_range = logspace(1,7,3000); % Frequency range of plots
x_lim = [10^1 10^5];

% Gang 1
figure; hold on
bode(GANG1,f_range)
bode(GANGi1,f_range)
grid; h = gcr; setoptions(h,'FreqUnits','Hz')
title('G1: Reference Tracking FPC/1+PCH')
legend('non-ideal OpAmps','ideal OpAmps')
hold off; xlim(x_lim)
```

```
% Gang 2
figure; hold on
bode(GANG2,f_range)
bode(GANGi2,f_range)
grid; h = gcr; setoptions(h,'FreqUnits','Hz')
title('G2: Ref to P-OpAmp Output FC/1+PCH')
legend('non-ideal OpAmps','ideal OpAmps')
hold off; xlim(x_lim)


% Gang 3
figure; hold on
bode(GANG3,f_range)
bode(GANGi3,f_range)
grid; h = gcr; setoptions(h,'FreqUnits','Hz')
title('Loop Transmision Bode ')
legend('non-ideal OpAmps','ideal OpAmps')
hold off; xlim(x_lim)
title('G3: Disturbance Rejection P/1+PCH');


% Gang 4
figure; hold on
bode(GANG4,f_range)
bode(GANGi4,f_range)
grid; h = gcr; setoptions(h,'FreqUnits','Hz')
title('Loop Transmision Bode ')
legend('non-ideal OpAmps','ideal OpAmps')
hold off; xlim(x_lim)
title('G4: Sensitivity 1/1+PCH');

% Gang 5
figure; hold on
bode(GANG5,f_range)
bode(GANGi5,f_range)
grid; h = gcr; setoptions(h,'FreqUnits','Hz')
title('Loop Transmision Bode ')
legend('non-ideal OpAmps','ideal OpAmps')
hold off; xlim(x_lim)
title('G5: Noise Sensitivity CH/1+PCH');


% Gang 6
figure; hold on
bode(GANG6,f_range)
bode(GANGi6,f_range)
grid; h = gcr; setoptions(h,'FreqUnits','Hz')
title('Loop Transmision Bode ')
legend('non-ideal OpAmps','ideal OpAmps')
hold off; xlim(x_lim)
```

Appendix O

Matlab code for Modeling and Simulation of Position Control, and Initialization for Simulink

The code is given below:

```
%------------------------------------------------------------------------%
%  Position Control Design for Actuator C506 and Simulink Initialization  %
%                 Sajjad Mohammadi, EECS, MIT, August 2021                %
%------------------------------------------------------------------------%

% Note: the file related to the Current loop modeling needs to be run first
% as its transfer functions are empl

% Position Control Design for Actuator C506 and Simulink Initialization
% [1] Motor parameters (SI units)
% [2] Loop Shaping in Frequency Domain
% [3] Pole Placement with Voltage Drive
% [4] Pole Placement with Current Drive
% [5] Nonlinear Control in Frequency Domain
% [6] Nonlinear Control with Pole Placement

% clc; clear; close all

%% ___________________[ Motor parameters (SI units) ]______________________
J  = 1.5077e-09; % Inretia/mass without mirror from Solid Works [kg.m^2]
kd = 4.4881e-07; % damping
ks = 0.0013;  % spring
Krest=ks/2; % spring

Rc = 1.76; % coil resistance [ohm]
Rs = 0.1; % sense resistor [ohm]
R  = Rc+Rs;
Lc  = 280e-6; % coil inductance [H]
% kt = 1.836e-3; % torque/force constant, Typical
kt = 1.9063e-3; % Experiment at Pangolin 8-8-2021
kb = kt;                 % Back-emf Constant [Vs/rad]


% Bandwidth and damping of closed-loop poles
zeta = 0.8; %damping
BW = 500; % bandwidth of Position Controller [Hz]
wn = 2*pi*BW; % Natural frequency of the desired poles
wc = 2*pi*BW; % Crossover frequency of position loop

% Reference Position
f_ref = 20; % Frequency (Hz)
A_ref = 10; % Amplitude (Hz)

% Current Loop Dynamic for Controls with Current drive
% it includes inverse ofits DC gain
G_CurrentLoop = (1/DC_gain_CurrentLoop_NonPureIntegrator) * GANGi1;

% Angular Position Reference
T_ref = 1/f_ref;
t = 0:T_ref/10000:2.5*T_ref;
```

```
theta_ref = A_ref*square(2*pi*f_ref*t);

% Saturation Voltage of Power Op-Amp
V_sat = 21; % volt

s=tf('s');
%% __________________[ Loop Shaping in Frequency Domain ]__________________
% Small-Signal Linear Control System Design using the Linearized Model
% Electrical Dynamic is removed by the haigh bandwidth current loop
% Lead-Lag controller is used
% A low-pass filter is in the DSP after reading the position sensor with ADC
% The sensor function and its inverse are calcelled out
% The DC gain of the current loop and its inverse gian in the DSP are canceled
out
fprintf('Loop Shaping in Frequency Domain')
s=tf('s');


% Mechanical Dynamic:
G_mech = tf([kt],[J kd ks]); % Torque/Icoil

% Lead-Lag Compenstor:  Kp * (1+Ki/s) * (alpha*tau*s+1)/(tau*s+1)
%Lag:
Ki=wc/10 % One decade before wc
C_lg=1+Ki/s; % Lag

% Lead:
alpha=15; % pole-zero ratio to get a phase compensation of 55 degrees
tau=1/(wc*sqrt(alpha))
% tau=1e-4 % rounding
C_ld=(alpha*tau*s+1)/(tau*s+1); % Lead

% Low-Pass Filter
fb_filter=5000; % break frequency Hz
wb=2*pi*fb_filter; % one decade above wc
H_LPF=wb/(s+wb);

% Loop Gain Kp
G_aux = C_lg*C_ld*G_mech; % Loop Transmision excluding Kp
[mag,phase,wout] = bode(G_aux,wc); % calculating magnitude at wc
Kp=1/mag % calculating Kp as the gain required to have unity loop magnitude at
wc

Phase_margin=180+phase % Phase margin

% Position Controller
Cp=Kp*C_lg*C_ld;

% Loop Transmission
LT_p=Cp*G_mech; % Without current loop dynamic
LT_p_CurrentLoop=Cp*G_mech*G_CurrentLoop; % With current loop dynamic


% ----------------------------[ Block Diagram]-----------------------------
F_p=1; % input block
P_p=G_mech; % Mechanical Dynamic, Without current loop dynamic
P_p_CurrentLoop=G_mech*G_CurrentLoop; % Mechanical Dynamic, With current loop
dynamic
C_p = Cp; % Lead-Lag Compensator
H_p = 1; % Low-pass filter


% ----------------[ Current Loop, Loop Transmission PCH]-------------------
```

```
options = bodeoptions;
options.FreqUnits = 'Hz';
bode(G_mech,options); grid; title ('Bode: Mechanical Dynamic H_m')

figure; bode(C_lg,C_ld,C_lg*C_ld); grid
legend('Lag','Lead','Lead-Lag')

figure; bode(LT_p,Cp,G_mech); grid
legend('Loop Tranmission','Compensator C_p','Plant H_m')
title('Bode, Without current loop dynamic')

figure; bode(LT_p_CurrentLoop,Cp,G_mech,G_CurrentLoop); grid
legend('Loop Tranmission','Compensator C_p','Plant H_m','Current Loop')
title('Bode, With current loop dynamic')

% ----------[Gang 1: Closed-Loop Reference Tracking FPC/1+PCH]------------
% Reference tracking PCF/1+PCH
GANG1_p       = F_p*P_p*C_p/(1+P_p*C_p*H_p);  % Closed-Loop
GANG1_p_CurrentLoop       =
F_p*P_p_CurrentLoop*C_p/(1+P_p_CurrentLoop*C_p*H_p);  % Closed-Loop

% -------[Gang 2: Reference to Controller output Voltage FC/1+PCH]------
GANG2_p       = F_p*C_p/(1+P_p*C_p*H_p);  % Closed-Loop
GANG2_p_CurrentLoop       = F_p*C_p/(1+P_p_CurrentLoop*C_p*H_p);  % Closed-Loop

% ---------------[Gang 3: Disturbance Rejection  P/1+PCH]-----------------
% Disturbance to plant output
GANG3_p       = P_p/(1+P_p*C_p*H_p);  % Closed-Loop
GANG3_p_CurrentLoop       = P_p_CurrentLoop/(1+P_p_CurrentLoop*C_p*H_p);  %
Closed-Loop

% --------------------[Gang 4: Sensitivity 1/1+PCH]-----------------------
% measurement noise to plant output
GANG4_p       = 1/(1+P_p*C_p*H_p);  % Closed-Loop
GANG4_p_CurrentLoop       = 1/(1+P_p_CurrentLoop*C_p*H_p);  % Closed-Loop

% ------------------[Gang 5: Noise Sensitivity CH/1+PCH]------------------
% Noise to controller  output
GANG5_p       = C_p*H_p/(1+P_p*C_p*H_p);  % Closed-Loop
GANG5_p_CurrentLoop       = C_p*H_p/(1+P_p_CurrentLoop*C_p*H_p);  % Closed-Loop

% --------------[Gang 6: Complementary Sensitivity PCH/1+PCH]-------------
% Disturbance to controller output
GANG6_p       = P_p*C_p*H_p/(1+P_p*C_p*H_p);  % Closed-Loop
GANG6_p_CurrentLoop       =
P_p_CurrentLoop*C_p*H_p/(1+P_p_CurrentLoop*C_p*H_p);  % Closed-Loop



% -----[ FPC/1+PCH, FC/1+PCH, P/1+PCH, 1/1+PCH, CH/1+PCH, PCH/1+PCH]------

% ----- Bode Plot -----
f_bode=1e5; %frequency range to plot

figure
subplot(3,2,1)
  options.FreqUnits = 'Hz';
  h=bodeplot(GANG1_p,GANG1_p_CurrentLoop,{10,f_bode}); grid;
  setoptions(h,'FreqUnits','Hz');
  title('G1: Reference Tracking FPC/1+PCH')
  legend('Withou current loop dynamic','With current loop dynamic')
```

```
subplot(3,2,2)
   options.FreqUnits = 'Hz';
   h=bodeplot(GANG2_p,GANG2_p_CurrentLoop,{10,f_bode}); grid;
   setoptions(h,'FreqUnits','Hz');
   title('G2: Ref to Controller Output FC/1+PCH')
   legend('Withou current loop dynamic','With current loop dynamic')

subplot(3,2,3)
   options.FreqUnits = 'Hz';
   h=bodeplot(GANG3_p,GANG3_p_CurrentLoop,{10,f_bode}); grid;
   setoptions(h,'FreqUnits','Hz');
   title('G3: Disturbance Rejection P/1+PCH')
   legend('Withou current loop dynamic','With current loop dynamic')

subplot(3,2,4)
   options.FreqUnits = 'Hz';
   h=bodeplot(GANG4_p,GANG4_p_CurrentLoop,{10,f_bode}); grid;
   setoptions(h,'FreqUnits','Hz');
   title('G4: Sensitivity 1/1+PCH')
   legend('Withou current loop dynamic','With current loop dynamic')

subplot(3,2,5)
   options.FreqUnits = 'Hz';
   h=bodeplot(GANG5_p,GANG5_p_CurrentLoop,{10,f_bode}); grid;
   setoptions(h,'FreqUnits','Hz');
   title('G5: Noise Sensitivity CH/1+PCH')
   legend('Withou current loop dynamic','With current loop dynamic')

subplot(3,2,6)
   options.FreqUnits = 'Hz';
   h=bodeplot(GANG6_p,GANG6_p_CurrentLoop,{10,f_bode}); grid;
   setoptions(h,'FreqUnits','Hz');
   title('G6: Compl Sensitivity PCH/1+PCH')
   legend('Withou current loop dynamic','With current loop dynamic')


% ----- Magnitude-only Bode Plot -----
figure
subplot(3,2,1)
   options.FreqUnits = 'Hz';
   h=bodeplot(GANG1_p,GANG1_p_CurrentLoop,{10,f_bode}); grid;
   setoptions(h,'FreqUnits','Hz');
   setoptions(h,'FreqUnits','Hz','PhaseVisible','off');
   title('G1: Reference Tracking FPC/1+PCH')
   legend('Withou current loop dynamic','With current loop dynamic')

subplot(3,2,2)
   options.FreqUnits = 'Hz';
   h=bodeplot(GANG2_p,GANG2_p_CurrentLoop,{10,f_bode}); grid;
   setoptions(h,'FreqUnits','Hz');
   setoptions(h,'FreqUnits','Hz','PhaseVisible','off');
   title('G2: Ref to Controller Output FC/1+PCH')
   legend('Withou current loop dynamic','With current loop dynamic')

subplot(3,2,3)
   options.FreqUnits = 'Hz';
   h=bodeplot(GANG3_p,GANG3_p_CurrentLoop,{10,f_bode}); grid;
   setoptions(h,'FreqUnits','Hz');
   setoptions(h,'FreqUnits','Hz','PhaseVisible','off');
   title('G3: Disturbance Rejection P/1+PCH')
   legend('Withou current loop dynamic','With current loop dynamic')

subplot(3,2,4)
```

```
    options.FreqUnits = 'Hz';
    h=bodeplot(GANG4_p,GANG4_p_CurrentLoop,{10,f_bode}); grid;
    setoptions(h,'FreqUnits','Hz');
    setoptions(h,'FreqUnits','Hz','PhaseVisible','off');
    title('G4: Sensitivity 1/1+PCH')
    legend('Withou current loop dynamic','With current loop dynamic')

subplot(3,2,5)
    options.FreqUnits = 'Hz';
    h=bodeplot(GANG5_p,GANG5_p_CurrentLoop,{10,f_bode}); grid;
    setoptions(h,'FreqUnits','Hz');
    setoptions(h,'FreqUnits','Hz','PhaseVisible','off');
    title('G5: Noise Sensitivity CH/1+PCH')
    legend('Withou current loop dynamic','With current loop dynamic')

subplot(3,2,6)
    options.FreqUnits = 'Hz';
    h=bodeplot(GANG6_p,GANG6_p_CurrentLoop,{10,f_bode}); grid;
    setoptions(h,'FreqUnits','Hz');
    setoptions(h,'FreqUnits','Hz','PhaseVisible','off');
    title('G6: Compl Sensitivity PCH/1+PCH')
    legend('Withou current loop dynamic','With current loop dynamic')


% ----- Pole-Zero Map -----
figure
subplot(3,2,1)
  pzmap(GANG1_p)
  title('G1: Reference Tracking FPC/1+PCH')

subplot(3,2,2)
    pzmap(GANG2_p)
    title('G2: Ref to Controller Output FC/1+PCH')

subplot(3,2,3)
    pzmap(GANG3_p)
    title('G3: Disturbance Rejection P/1+PCH')

subplot(3,2,4)
    pzmap(GANG4_p)
    title('G4: Sensitivity 1/1+PCH')

subplot(3,2,5)
    pzmap(GANG5_p)
    title('G5: Noise Sensitivity CH/1+PCH')

subplot(3,2,6)
    pzmap(GANG6_p)
    title('G6: Compl Sensitivity PCH/1+PCH')


% ----- Step Response -----
figure
subplot(3,2,1)
    % Step Response
    [yy,tt]=lsim(GANG1_p,theta_ref*(pi/180),t);
    [yy2,tt2]=lsim(GANG1_p_CurrentLoop,theta_ref*(pi/180),t);
    plot(tt,theta_ref,'--',tt,yy*(180/pi),tt2,yy2*(180/pi),'LineWidth',1); grid
    xlabel('Time (sec)');ylabel('Position (degree)')
    title('G1: Reference Tracking FPC/1+PCH')

subplot(3,2,2)
    [yy,tt]=lsim(GANG2_p,theta_ref*(pi/180),t);
```

```
    [yy2,tt2]=lsim(GANG2_p_CurrentLoop,theta_ref*(pi/180),t);
    plot(tt,yy,tt2,yy2,'LineWidth',1); grid
    xlabel('Time (sec)');ylabel('i_r_e_f (A)')
    title('G2: Ref to Controller Output FC/1+PCH')

subplot(3,2,3)
    [yy,tt]=lsim(GANG3_p,theta_ref*(pi/180),t);
    [yy2,tt2]=lsim(GANG3_p_CurrentLoop,theta_ref*(pi/180),t);
    plot(tt,yy,tt2,yy2,'LineWidth',1); grid
    xlabel('Time (sec)');ylabel('Amplitude')
    title('G3: Disturbance Rejection P/1+PCH')

subplot(3,2,4)
    [yy,tt]=lsim(GANG4_p,theta_ref*(pi/180),t);
    [yy2,tt2]=lsim(GANG4_p_CurrentLoop,theta_ref*(pi/180),t);
    plot(tt,yy,tt2,yy2,'LineWidth',1); grid
    xlabel('Time (sec)');ylabel('Amplitude')
    title('G4: Sensitivity 1/1+PCH')

subplot(3,2,5)
    [yy,tt]=lsim(GANG5_p,theta_ref*(pi/180),t);
    [yy2,tt2]=lsim(GANG5_p_CurrentLoop,theta_ref*(pi/180),t);
    plot(tt,yy,tt2,yy2,'LineWidth',1); grid
    xlabel('Time (sec)');ylabel('Amplitude')
    title('G5: Noise Sensitivity CH/1+PCH')

subplot(3,2,6)
    [yy,tt]=lsim(GANG6_p,theta_ref*(pi/180),t);
    [yy2,tt2]=lsim(GANG6_p_CurrentLoop,theta_ref*(pi/180),t);
    plot(tt,yy,tt2,yy2,'LineWidth',1); grid
    xlabel('Time (sec)');ylabel('Amplitude')
    title('G6: Compl Sensitivity PCH/1+PCH')



%% __________________[ Pole Placement with Voltage Drive ]_________________
% Small Signal control using Linear Model
% Linearized State Space Model (order: n=3)
% x1= angular pos (theta), x2 = angular velocity (omega), x3 = current(i)
% dX=A3*X+B3*u  , u=coil voltage
% y =C3*X+D3*u
fprintf(['_________________________________________\n\n\n',...
         'Pole Placement with Voltage Drive'])

A3 = [0       1      0
     -ks/J  -kd/J   kt/J
      0     -kb/Lc  -R/Lc];

B3 = [0
      0
      1/Lc];

% all states as output
C3 = eye(3);
D3 = [0; 0; 0];

% Angular Position Tracking
C3_act = [1 0 0];
D3_act = 0;

%Open-Loop System
sys3 = ss(A3,B3,C3,D3);
```

```
% Controllability
Mc3 = ctrb(A3,B3) % Controllability Matrix
Mc3 = [B3 A3*B3 A3^2*B3]

rank_Mc3=rank(Mc3);
if rank_Mc3==3; disp(['It is ontrollable. Rank of Mc is ', num2str(rank_Mc3)])
else; disp('It is NOT ontrollable')
end

% Observability
Mo3 = obsv(A3,C3_act) % Observability Matrix
Mo3 = [C3_act
       C3_act*A3
       C3_act*A3^2]

rank_Mo3=rank(Mo3);
if rank_Mo3==3; disp(['It is observable. Rank of Mo is ', num2str(rank_Mo3)])
else; disp('It is NOT observable')
end


% Pole Placement
% Desired closed-loop poles on a circle with eadius of wn
lambda_d3 = [-zeta*wn+i*wn*sqrt(1-zeta^2), -zeta*wn-i*wn*sqrt(1-zeta^2), -wn];
% Desired characteristic Polynomial
phi_d3 = @(S)(S^2+2*zeta*wn*S+wn^2*eye(size(S)))*(S+wn*eye(size(S)));

% Feedback Gains K3=[k1 k2 k3] by Ackermann's formula
K3 = place(A3, B3, lambda_d3)
K3=[0 0 1]*inv(Mc3)*phi_d3(A3) %  Ackermann's formula

% Untary gain for angular position tracking
G3 = -inv(C3_act*inv(A3-B3*K3)*B3)

%Closed-Loop System
sys3_cl = ss(A3-B3*K3,B3,C3,D3); % Controller



% Full-Order State Observer
% Desired closed-loop poles of the Observer
lambda_e3 = [-10*wn, -10*wn, -10*wn]; % 5 to 10 times faster than controller
% Desired characteristic Polynomial
phi_e3 = @(S)(S+10*wn*eye(size(S)))^3;
% Observer Gains L3=[L1 L2 L3] by Ackermann's formula
L3=acker(A3',C3_act', lambda_e3)' %  with Matlab
L3=phi_e3(A3)*inv(Mo3)*[0 0 1]' %  Ackermann's formula


% Eigenvalues of Controller, Observer and Compensator:
fprintf('Eigenvalues of Controller, Observer and Compensator')
eig_A_BK_3 = eig(A3-B3*K3)
eig_A_LC_3 = eig(A3-L3*C3_act)
eig_A_BK_LC_3 = eig(A3-B3*K3-L3*C3_act)


% Plots
% Open-Loop Responses
figure; step(sys3); grid
title('Step Response (Open-Loop, Voltage Drive)')

figure; pzmap(sys3)
title('Open-Loop A, Voltage Drive')
```

```
figure; bode(sys3); grid
title('Bode (Open-Loop, Voltage Drive)')


% Closed-Loop Responses
% Step Response
[yy3,tt3]=lsim(sys3_cl,G3*theta_ref*(pi/180),t);
u3=G3*theta_ref*(pi/180)-K3*yy3'; % Control signal u=Vref

figure % subplot(4,1,1)
   plot(tt3,theta_ref,'g--',...
        tt3-T_ref, yy3(:,1)*(180/pi),'r',...  % shifted by one period
        Step_theta_VD(:,1)    , Step_theta_VD(:,2),'k',... % Experiment
        'LineWidth',1); grid
   xlabel('Time (sec)');ylabel('Position (degree)')
   xlim([0 0.99*T_ref]); ylim([-5.5 5.5])
   legend('Reference','Model','Experiment')
   title('Step Response (Closed-Loop, Voltage Drive)')

figure % subplot(4,1,2)
   plot(tt3-T_ref, yy3(:,2),'r',...  % shifted by one period
   Step_Velocity_VD(:,1), Step_Velocity_VD(:,2),'k',... % Experiment
   'LineWidth',1); grid
   xlabel('Time (sec)');ylabel('Velocity (rad/sec)')
   legend('Model','Experiment')
   xlim([0 0.99*T_ref]); ylim([-180 180])

figure % subplot(4,1,3)
   plot(tt3-T_ref, yy3(:,3),'r',...  % shifted by one period
        Step_Current_VD(:,1), Step_Current_VD(:,2),'k',... %Experiment
        'LineWidth',1); grid
   xlabel('Time (sec)');ylabel('Current (A)')
   legend('Model','Experiment')
   xlim([0 0.99*T_ref]); ylim([-0.35 0.35])

figure % subplot(4,1,4)
   plot(tt3-T_ref, u3,'r',...  % shifted by one period
   Step_Voltage_VD(:,1), Step_Voltage_VD(:,2),'k',... % Experiment
   'LineWidth',1); grid
   xlabel('Time (sec)');ylabel('V_c (v)')
   xlim([0 0.99*T_ref]); ylim([-1.2 1.2])
   legend('Model','Experiment')


% pole-zero map
figure;
plot(real(eig_A_BK_3),imag(eig_A_BK_3),'x',real(eig_A_LC_3),imag(eig_A_LC_3),'x
',...
             real(eig_A_BK_LC_3),imag(eig_A_BK_LC_3),'x','LineWidth',1)
legend('Controller A-Bk (closed-loop)','Observer A-LC','Compensator A-BK-LC')
xlabel('Real Axis'); ylabel('Imaginary Axis')
title('pole map (Pole Placement, Voltage Dive)')


figure; bode(sys3_cl); grid
title('Bode (Closed-Loop, Voltage Drive)')


% ----------------------[  Frequency Responses ]--------------------------
ff = logspace(1,4,2000);% frequency [Hz]
omegaa=2*pi*ff;
S = 1i * omegaa;
```

```
Ts=1/(160000);


% Loop Transmission
for kk=1:length(S)
    LT3_delay(kk) = exp(-S(kk)*Ts) * K3*inv(S(kk)*eye(3)-A3)*B3; % with delay
    LT3(kk) = K3*inv(S(kk)*eye(3)-A3)*B3;
end

figure
subplot(2,1,1)
   semilogx(ff, 20*log10(abs(LT3_delay)),'g',... % with delay
            ff, 20*log10(abs(LT3)),'r--',... % without delay
            Freq_expr_VD, Mag_LT_VD_expr,'k--',...
   'LineWidth',1.1); grid
   ylabel('Magnitude (dB)')
   xlim([10^1 10^4])
subplot(2,1,2)
   semilogx(ff, (180/pi)*angle(LT3_delay),'g',... % with delay
            ff, (180/pi)*angle(LT3),'r--',... % without delay
            Freq_expr_VD, Phase_LT_VD,'k--',...
            'LineWidth',1.1); grid
   xlabel('frequency (Hz)'); ylabel('Angle (deg)')
   legend('Model with delay','Model','Expr'); title('Loop Transmission')
   xlim([10^1 10^4]); ylim([-180 0]); yticks([-180, -90, 0])


% -------- Gang 1 -----------

for kk=1:length(S)
    G1_VD(kk) = G3*[1 0 0]*inv(S(kk)*eye(3)-(A3-B3*K3))*B3;
    G1_VD_delay(kk) = exp(-S(kk)*Ts)*G3*[1 0 0]*inv(S(kk)*eye(3)-(A3-
B3*K3))*B3;
end

figure
subplot(2,1,1)
   semilogx(ff, 20*log10(abs(G1_VD_delay)),'g',...
            ff, 20*log10(abs(G1_VD)),'r--',...
            Bode_G1_VD(:,1), Bode_G1_VD(:,2),'k--',...
   'LineWidth',1); grid
   ylabel('Magnitude (dB)')
   xlim([10^1 10^4])
subplot(2,1,2)
   semilogx(ff, (180/pi)*unwrap(angle(G1_VD_delay)),'g',...
            ff, (180/pi)*unwrap(angle(G1_VD)),'r--',...
            Bode_G1_VD(:,1), unwrap(Bode_G1_VD(:,3)),'k--',...
            'LineWidth',1); grid
   xlabel('frequency (Hz)'); ylabel('Angle (deg)')
   legend('Model with delay','Model','Expr'); title('Gang 1')
   xlim([10^1 3*10^3])



% -------- Gang 4 -----------
% Loop Transmission
G4_delay = 1./(1+LT3_delay);


figure
subplot(2,1,1)
   semilogx(ff, 20*log10(abs(G4_delay)),'g',... % with delay
```

```
            ff, 20*log10(abs(1./(1+LT3))),'r--',... % without delay
            Freq_expr_VD, Mag_G4_VD,'k--',... % obtained as 1/(1+LT)
   'LineWidth',1.1); grid
   ylabel('Magnitude (dB)')
   xlim([10^1 10^4])
subplot(2,1,2)
   semilogx(ff, (180/pi)*angle(G4_delay),'g',... % with delay
            ff, (180/pi)*angle(1./(1+LT3)),'r--',... % without delay
            Freq_expr_VD, Phase_G4_VD,'k--',...
            'LineWidth',1.1); grid
   xlabel('frequency (Hz)'); ylabel('Angle (deg)')
   legend('Model with delay','Model','Expr'); title('Loop Transmission')
   xlim([10^1 10^4])




%% __________________[ Pole Placement with Current Drive ]_________________
% Small Signal using Linear Model
% Linearized State Space Model (order: n=2)
% x1= angular pos (theta), x2 = angular velocity (omega)
% dX=A2*X+B2*u  , u=coil current
% y =C2*X+D2*u
fprintf(['________________________________________\n\n\n',...
    'Pole Placement with Current Drive'])

    A2 = [0      1
         -ks/J  -kd/J];
    B2 = [0
          kt/J];

% all states as output
    C2 = eye(2);
    D2 = [0
          0];

% Angular Position Tracking
    C2_act = [1 0];
    D2_act = [0];

% Controllability
Mc2 = ctrb(A2,B2) % Controllability Matrix
Mc2 = [B2 A2*B2]

rank_Mc2=rank(Mc2)
if rank_Mc2==2; disp(['It is ontrollable. Rank of Mc is ', num2str(rank_Mc2)])
else; disp('It is NOT ontrollable')
end

% Observability
Mo2 = obsv(A2,C2_act) % Observability Matrix
Mo2 = [C2_act
       C2_act*A2]

rank_Mo2=rank(Mo2)
if rank_Mo2==2; disp(['It is observable. Rank of Mo is ', num2str(rank_Mo2)])
else; disp('It is NOT observable')
end

% Mechanical Dynamic:
G_mech = tf([kt],[J kd ks]); % Torque/Icoil

%Open-Loop System
```

```
sys2=ss(A2,B2,C2,D2);

% Pole Placement
% Desired clodes-loop poles: lambda1, lambda2
% Desired Characteristic Equation: Phi_d=(lambda-lambda1)*(lambda-lambda2)
% Observability Matrix Mc=[B2, A2*B2]
% Ackermann's formula: K=[0 1]*inv(Mc)*Phi_d(A2)

% Desired closed-loop poles on a circle with eadius of wn
lambda_d2 = [-zeta*wn+i*wn*sqrt(1-zeta^2), -zeta*wn-i*wn*sqrt(1-zeta^2)];
% Desired characteristic Polynomial
phi_d2 = @(S)(S^2+2*zeta*wn*S+wn^2*eye(size(S)));

% Feedback Gains K2=[k1 k2] by Ackermann's formula
K2 = place(A2, B2, lambda_d2)
K2=[0 1]*inv(Mc2)*phi_d2(A2) %  Ackermann's formula

% Unitary gain for angular position tracking
G2 = -inv(C2_act*inv(A2-B2*K2)*B2)

%Closed-Loop System
% Without Current Loop Dynamic:
sys2_cl = ss(A2-B2*K2,B2,C2,D2);
% With Current Loop Dynamic:
% calculations: (G=system, H=Current Loop time inverse of DC gain)
% (1) dX=A*X+B*u,y=C*X+D*u => G(s)=X(s)/U(s)=C*inv(sI-A)*B+D => X(s)=G(s)U(x)
% (2) U(s)=H(s)*(R(s)-k*X(s))
% (1)&(2) => X(s)=G(s)*H(s)*(R(s)-k*X(s))=G(s)*H(s)*R(s)-G(s)*H(s)*k*X(s)
% => (I+G(s)H(s)k)*X(s)=G(s)H(s)R(s) => X(s)=inv((I+G(s)H(s)k))*G(s)H(s)R(s)
GG2 = [G_mech ; s*G_mech]; % Mechanical dynamic, input=Ic, outputs=[position,
velocity]
sys2_cl_CurrentLoop = inv(eye(2)+GG2*G_CurrentLoop*K2)*GG2*G_CurrentLoop;

% Full-Order State Observer
% Desired closed-loop poles of the Observer
lambda_e2 = [-10*wn, -10*wn]; % 5 to 10 times faster than controller
% Desired characteristic Polynomial
phi_e2 = @(S)(S+10*wn*eye(size(S)))^2;

% Observer Gains L2=[L1 L2] by Ackermann's formula
L2=acker(A2',C2_act', lambda_e2)' %  with Matlab
L2=phi_e2(A2)*inv(Mo2)*[0 1]' %  Ackermann's formula

% Eigenvalues of Controller, Observer and Compensator:
fprintf('Eigenvalues of Controller, Full-Order Observer and Compensator')
eig_A_BK_2 = eig(A2-B2*K2)
eig_A_LC_2 = eig(A2-L2*C2_act)
eig_A_BK_LC_2 = eig(A2-B2*K2-L2*C2_act)


    A2 = [0      1
         -ks/J  -kd/J];
    B2 = [0
          kt/J];

% Reduced-Order State Observer
% Partitioning of matrix A2 and B2
Ae11 = A2(1,1);
Ae12 = A2(1,2);
Ae21 = A2(2,1);
Ae22 = A2(2,2);

Be1 = B2(1);
```

```
Be2 = B2(2);

% Observability
fprintf('Reduced-Order Observer:')
Mo2_ro = obsv(Ae22,Ae12) % Observability Matrix (Aa=Ae22, C=Ae12)
Mo2_ro = [Ae12]

rank_Mo2_ro=rank(Mo2_ro)
if rank_Mo2_ro==1; disp(['It is observable. Rank of Mo is ',
num2str(rank_Mo2_ro)])
else; disp('It is NOT observable')
end


% Desired closed-loop poles of the Observer
lambda_e2_ro = [-10*wn]; % 5 to 10 times faster than controller
% Desired characteristic Polynomial
phi_e2_ro = @(S)(S+10*wn*eye(size(S)));

% Observer Gains L2=[L1 L2] by Ackermann's formula
L2_ro=acker(Ae22',Ae12', lambda_e2_ro)' %  with Matlab
L2_ro=phi_e2_ro(Ae22)*inv(Mo2_ro)*[1]' %  Ackermann's formula
L2_ro = -lambda_e2_ro-kd/J % Hand calculations


fprintf('Eigenvalues of Controller and Reduced-Order Observer')
eig_A_BK_2 = eig(A2-B2*K2)
eig_A_LC_2_ro = eig(Ae22-L2_ro*Ae12)


% Plots
% Open-Loop Responses
figure; step(sys2); grid
title('Step Response (Open-Loop, Current Drive)')

figure; pzmap(sys2)
title('Open-Loop A, Current Drive')

figure; bode(sys2); grid
title('Bode (Open-Loop, Current Drive)')


% Closed-Loop Responses
% Step Response
% Without Dynamic of Current Loop
[yy2,tt2]=lsim(sys2_cl,G2*theta_ref*(pi/180),t);
u2=G2*theta_ref*(pi/180)-K2*yy2'; % Control signal u=Iref
% With Dynamic of Current Loop
[yy2_CurrentLoop,tt2_CurrentLoop] =
lsim(sys2_cl_CurrentLoop,G2*theta_ref*(pi/180),t);
u2_CurrentLoop = G2*theta_ref*(pi/180)-K2*yy2_CurrentLoop'; % Control signal
u=Iref


% Coil current Ic
% Without Dynamic of Current Loop
[yy_ic_i,tt_ic_i]=lsim((1/DC_gain_CurrentLoop_NonPureIntegrator)*GANGi1,u2_Curr
entLoop,tt2_CurrentLoop);
% With Dynamic of Current Loop
[yy_ic,tt_ic]=lsim((1/DC_gain_CurrentLoop_NonPureIntegrator)*GANG1,u2_CurrentLo
op,tt2_CurrentLoop);

% Coil Viltage
```

```
% Without Dynamic of Current Loop
[yy_vc_i,tt_vc_i]=lsim((1/DC_gain_CurrentLoop_NonPureIntegrator)*GANGi2,u2_Curr
entLoop,tt2_CurrentLoop);
% With Dynamic of Current Loop
[yy_vc,tt_vc]=lsim((1/DC_gain_CurrentLoop_NonPureIntegrator)*GANG2,u2_CurrentLo
op,tt2_CurrentLoop);



figure % subplot(5,1,1)
   plot(tt2, theta_ref,'g--',... % reference
        ...% tt2-T_ref, yy2(:,1)*(180/pi),... % without current loop dynamic
        tt2_CurrentLoop-T_ref, yy2_CurrentLoop(:,1)*(180/pi),'r',... % with
current loop dynamic
        Step_theta_CD(:,1)    , Step_theta_CD(:,2),'k--',... % Experiment,
steady state error=0.005
        'LineWidth',1); grid
   title('Step Response (Closed-Loop, Current Drive)')
   legend('Reference \theta_r_e_f','\theta without current loop dynamicp',...
          '\theta with current loop dynamic','Experiment')
   xlabel('Time (sec)');ylabel('Position (degree)')
   xlim([0 0.99*T_ref]); ylim([-5.5 5.5])


figure % subplot(5,1,2)
   plot(...% tt2-T_ref, yy2(:,2),...
        tt2_CurrentLoop-T_ref, yy2_CurrentLoop(:,2),'r',... % with current loop
dynamic
        Step_Velocity_CD(:,1), Step_Velocity_CD(:,2),'k--',...
        'LineWidth',1); grid
   xlabel('Time (sec)');ylabel('Velocity (rad/sec)')
   legend('Without current loop dynamic','With current loop dynamic',...
           'Experiment')
      xlim([0 0.99*T_ref]); ylim([-270 270])

figure % subplot(5,1,3)
   plot(...% tt2-T_ref, u2,... % without current loop dynamic
        tt2_CurrentLoop-T_ref, u2_CurrentLoop,'r',... % with current loop
dynamic, Iref
        Step_DAC_CD_large10(:,1), Step_DAC_CD_large10(:,2),'k--',... % data for
5deg is missing, so 10 is used with scaling, it is multiplied by Iref=-
(R2/R1)*DAC
        'LineWidth',1); grid
   xlabel('Time (sec)');ylabel('u=i_r_e_f (A)')
   legend('Without current loop dynamic','With current loop
dynamic','Experiment')
   xlim([0 0.99*T_ref]); ylim([-1.4 1.4])

figure % subplot(5,1,4)
   plot(...% tt_ic_i-T_ref,yy_ic_i,... % without current loop dynamic
        tt_ic-T_ref,yy_ic,'r',... % with current loop dynamic, Ic
        Step_Current_CD(:,1) , Step_Current_CD(:,2),'k--',...
        'LineWidth',1); grid
   xlabel('Time (sec)');ylabel('I_c (A)')
   legend('Without current loop dynamic','With current loop
dynamic','Experiment')
   xlim([0 0.99*T_ref]); ylim([-1.4 1.4])

figure % subplot(5,1,5)
   plot(...%tt_vc_i-T_ref, yy_vc_i,... % without current loop dynamic
        tt_vc-T_ref, yy_vc,... % with current loop dynamic
        Step_Voltage_CD(:,1), Step_Voltage_CD(:,2),...
        'LineWidth',1); grid
```

```
   xlabel('Time (sec)');ylabel('V_c (v)')
   legend('Without current loop dynamic','With current loop dynamic')


% pole-zero map
figure;
plot(real(eig_A_BK_2),imag(eig_A_BK_2),'x',real(eig_A_LC_2),imag(eig_A_LC_2),'x
',...
             real(eig_A_BK_LC_2),imag(eig_A_BK_LC_2),'x','LineWidth',1)
legend('Controller A-Bk (closed-loop)','Full-Order Observer A-LC','Compensator
A-BK-LC')
xlabel('Real Axis'); ylabel('Imaginary Axis')
title('pole map (Pole Placement, Voltage Dive)')

figure;
plot(real(eig_A_BK_2),imag(eig_A_BK_2),'x',real(eig_A_LC_2_ro),imag(eig_A_LC_2_
ro)...
             ,'x','LineWidth',1)
legend('Controller A-Bk (closed-loop)','Reduced-Order Observer A-LC')
xlabel('Real Axis'); ylabel('Imaginary Axis')
title('pole-zero map (Pole Placement, Voltage Dive)')

figure; bode(sys2_cl,sys2_cl_CurrentLoop); grid
title('Bode (Closed-Loop, Current Drive)')
legend('Without current loop dynamic','With current loop dynamic')


% Large signal:  -10 to 10 degrees
figure % subplot(5,1,1)
   plot(tt2, theta_ref,'g--',... % reference
        ...% tt2-T_ref, yy2(:,1)*(180/pi),... % without current loop dynamic
        tt2_CurrentLoop-T_ref, yy2_CurrentLoop(:,1)*(180/pi),'r',... % with
current loop dynamic
        Step_theta_CD_large10(:,1)   , Step_theta_CD_large10(:,2),'k--',... %
Experiment, steady state error=0.005
        'LineWidth',1); grid
   title('Step Response (Closed-Loop, Current Drive)')
   legend('Reference \theta_r_e_f','\theta with current loop
dynamic','Experiment')
   xlabel('Time (sec)');ylabel('Position (degree)')
   xlim([0 0.99*T_ref]); ylim([-10.5 10.5])



figure % subplot(5,1,4)
   plot(...% tt_ic_i-T_ref,yy_ic_i,... % without current loop dynamic
        tt_ic-T_ref,yy_ic,'r',... % with current loop dynamic
        Step_Current_CD_large10(:,1) , Step_Current_CD_large10(:,2),'k',...
        'LineWidth',1); grid
   xlabel('Time (sec)');ylabel('I_c (A)')
   legend('Without current loop dynamic','With current loop
dynamic','Experiment')
   xlim([0 0.99*T_ref]); ylim([-2.4 2.4])


% ----------------------[  Frequency Responses ]---------------------------
ff = logspace(1,4,2000);% frequency [Hz]
omegaa=2*pi*ff;
S = 1i * omegaa;

% Loop Transmission
Ts=1/(30e3);
for kk=1:length(S)
```

```
    LT2_delay(kk) = exp(-S(kk)*Ts) * K2*inv(S(kk)*eye(2)-A2)*B2; % with delay
    LT2(kk) = K2*inv(S(kk)*eye(2)-A2)*B2;
end

figure
subplot(2,1,1)
   semilogx(ff, 20*log10(abs(LT2_delay)),'g',... % with delay
            ff, 20*log10(abs(LT2)),'r--',... % without delay
            Bode_LT_CD(:,1), Bode_LT_CD(:,2),'k--',...
   'LineWidth',1.1); grid
   ylabel('Magnitude (dB)')
   xlim([10^1 10^4]); ylim([-30 37])
subplot(2,1,2)
   semilogx(ff, (180/pi)*unwrap(angle(LT2_delay)),'g',... % with delay
            ff, (180/pi)*angle(LT2),'r--',... % without delay
            Bode_LT_CD(:,1), Bode_LT_CD(:,3),'k--',...
            'LineWidth',1.1); grid
   xlabel('frequency (Hz)'); ylabel('Angle (deg)')
   legend('Model with delay','Model','Expr'); title('Loop Transmission')
   xlim([10^1 10^4]); ylim([-220 3])


% -------- Gang 1 -----------
ff = logspace(1,4,2000);% frequency [Hz]
omegaa=2*pi*ff;
S = 1i * omegaa;
Ts=1/(16e3);

    exp(-S(kk)*Ts);

for kk=1:length(S)
    G1_CD(kk) = G2*[1 0]*inv(S(kk)*eye(2)-(A2-B2*K2))*B2;
    G1_CD_delay(kk) = exp(-S(kk)*Ts)* G2*[1 0]*inv(S(kk)*eye(2)-(A2-B2*K2))*B2;
end

figure
subplot(2,1,1)
   semilogx(ff, 20*log10(abs(G1_CD_delay)),'g',...
            ff, 20*log10(abs(G1_CD)),'r--',...
            Bode_G1_CD(:,1), Bode_G1_CD(:,2),'k--',...
   'LineWidth',1); grid
   ylabel('Magnitude (dB)'); xlim([10^1 10^4])
subplot(2,1,2)
   semilogx(ff, (180/pi)*unwrap(angle(G1_CD_delay)),'g',...
            ff, (180/pi)*unwrap(angle(G1_CD)),'r--',...
            Bode_G1_CD(:,1), unwrap(Bode_G1_CD(:,3)),'k--',...
            'LineWidth',1); grid
   xlabel('frequency (Hz)'); ylabel('Angle (deg)')
   legend('Model with delay','Model','Expr'); title('Gang 1'); xlim([10^1
3*10^3])



% -------- Gang 4 -----------
% Loop Transmission
G4_CD_delay = 1./(1+LT2_delay);


figure
subplot(2,1,1)
   semilogx(ff, 20*log10(abs(G4_CD_delay)),'g',... % with delay
            ff, 20*log10(abs(1./(1+LT2))),'r--',... % without delay
            Freq_expr_CD, Mag_G4_CD,'k--',... % obtained as 1/(1+LT)
```

```
   'LineWidth',1.1); grid
   ylabel('Magnitude (dB)')
   xlim([10^1 10^4])
subplot(2,1,2)
   semilogx(ff, (180/pi)*angle(G4_CD_delay),'g',... % with delay
            ff, (180/pi)*angle(1./(1+LT2)),'r--',... % without delay
            Freq_expr_CD, Phase_G4_CD,'k--',...
            'LineWidth',1.1); grid
   xlabel('frequency (Hz)'); ylabel('Angle (deg)')
   legend('Model with delay','Model','Expr'); title('Sensitivity')
   xlim([10^1 10^4])




%% _____________[ Nonlinear Control in Frequency Domain ]___________________
% Feedback Linearization, Current Drive, Frequency Domain
% Nonlinear Model
% dx1 = x2
% dx2 = f(x)+g(x)*u(t) = v    , u=coil current

% Nonlinear Compensation v = f+g*u
% u=(v-f)/g

% Linear Model with input v (compensated with feedback linearization v=f+g*u)
% dx1 = x2
% dx2 = v
% Lead-Lag Control

fprintf(['__________________________________________\n\n\n',...
    'Nonlinear Control in Frequency Domain'])

s=tf('s');

% Mechanical Dynamic:
G_mech_nl = tf([1],[1 0 0]); % Torque/Icoil

% Lead-Lag Compenstor:  Kp * (1+Ki/s) * (alpha*tau*s+1)/(tau*s+1)
%Lag:
Ki_nl=0;%wc/10 % One decade before wc
C_lg_nl=1+Ki_nl/s; % Lag

% Lead:
alpha_nl=10; % pole-zero ratio to get a phase compensation of 55 degrees
tau_nl=1/(wc*sqrt(alpha_nl))
% tau=1e-4 % rounding
C_ld_nl=(alpha_nl*tau_nl*s+1)/(tau_nl*s+1); % Lead

% Loop Gain Kp
G_aux_nl = C_lg_nl*C_ld_nl*G_mech_nl; % Loop Transmision excluding Kp
[mag_nl,phase_nl,wout] = bode(G_aux_nl,wc); % calculating magnitude at wc
Kp_nl = 1/mag_nl % calculating Kp as the gain required to have unity loop
magnitude at wc

Phase_margin_nl =  180+phase_nl % Phase margin

% Position Controller
Cp_nl=Kp_nl * C_lg_nl * C_ld_nl;

% Loop Transmission
LT_nl = Cp_nl * G_mech_nl; % Without current loop dynamic
LT_nl_CurrentLoop=Cp_nl*G_mech_nl*G_CurrentLoop; % With current loop dynamic
```

```
% ---------------------------[ Block Diagram]----------------------------
F_nl = 1; % input block
P_nl=G_mech_nl; % Mechanical Dynamic, Without current loop dynamic
P_nl_CurrentLoop=G_mech_nl*G_CurrentLoop; % Mechanical Dynamic, With current
loop dynamic
C_nl = Cp_nl; % Lead-Lag Compensator
H_nl = 1; % Low-pass filter


% ----------------[ Current Loop, Loop Transmission PCH]-------------------
options = bodeoptions;
options.FreqUnits = 'Hz';
bode(G_mech_nl,options); grid; title ('Bode: Mechanical Dynamic H_m=1/s^2')
title('Nonlinear Control, Frequency Domain')

figure; bode(C_lg_nl,C_ld_nl,C_lg_nl*C_ld_nl); grid
legend('Lag','Lead','Lead-Lag')
title('Nonlinear Control, Frequency Domain')

figure; bode(LT_nl,Cp_nl,G_mech_nl); grid
legend('Loop Tranmission','Compensator C_p','Plant H_m')
title('Bode, Without current loop dynamic')

figure; bode(LT_nl_CurrentLoop,Cp,G_mech_nl,G_CurrentLoop); grid
legend('Loop Tranmission','Compensator C_p','Plant H_m','Current Loop')
title('Bode, With current loop dynamic')


% ----------[Gang 1: Closed-Loop Reference Tracking FPC/1+PCH]------------
% Reference tracking PCF/1+PCH
GANG1_nl        = F_nl*P_nl*C_nl/(1+P_nl*C_nl*H_nl);  % Closed-Loop
GANG1_nl_CurrentLoop =
F_nl*P_nl_CurrentLoop*C_nl/(1+P_nl_CurrentLoop*C_nl*H_nl); % Closed-Loop, with
current-loop dynamic

% -------[Gang 2: Reference to Controller output v(t), FC/1+PCH]------
GANG2_nl        = F_nl*C_nl/(1+P_nl*C_nl*H_nl);  % Closed-Loop
GANG2_nl_CurrentLoop = F_nl*C_nl/(1+P_nl_CurrentLoop*C_nl*H_nl); % Closed-Loop,
with current-loop dynamic

% ---------------[Gang 3: Disturbance Rejection  P/1+PCH]-----------------
% Disturbance to plant output
GANG3_nl        = P_nl/(1+P_nl*C_nl*H_nl);  % Closed-Loop
GANG3_nl_CurrentLoop = P_nl_CurrentLoop/(1+P_nl_CurrentLoop*C_nl*H_nl); %
Closed-Loop, with current-loop dynamic

% --------------------[Gang 4: Sensitivity 1/1+PCH]-----------------------
% measurement noise to plant output
GANG4_nl        = 1/(1+P_nl*C_nl*H_nl);  % Closed-Loop
GANG4_nl_CurrentLoop = 1/(1+P_nl_CurrentLoop*C_nl*H_nl); % Closed-Loop, with
current-loop dynamic

% ------------------[Gang 5: Noise Sensitivity CH/1+PCH]------------------
% Noise to controller  output
GANG5_nl        = C_nl*H_nl/(1+P_nl*C_nl*H_nl);  % Closed-Loop
GANG5_nl_CurrentLoop = C_nl*H_nl/(1+P_nl_CurrentLoop*C_nl*H_nl); % Closed-Loop,
with current-loop dynamic

% --------------[Gang 6: Complementary Sensitivity PCH/1+PCH]-------------
% Disturbance to controller output
GANG6_nl        = P_nl*C_nl*H_nl/(1+P_nl*C_nl*H_nl);  % Closed-Loop
```

```
GANG6_nl_CurrentLoop =
P_nl_CurrentLoop*C_nl*H_nl/(1+P_nl_CurrentLoop*C_nl*H_nl); % Closed-Loop, with
current-loop dynamic



% -----[ FPC/1+PCH, FC/1+PCH, P/1+PCH, 1/1+PCH, CH/1+PCH, PCH/1+PCH]------


% ----- Bode Plot -----
f_bode=1e5; %frequency range to plot

figure
subplot(3,2,1)
   options.FreqUnits = 'Hz';
   h=bodeplot(GANG1_nl,GANG1_nl_CurrentLoop,{10,f_bode}); grid;
   setoptions(h,'FreqUnits','Hz');
   title('G1: Reference Tracking FPC/1+PCH')
   legend('Withou current loop dynamic','With current loop dynamic')


subplot(3,2,2)
   options.FreqUnits = 'Hz';
   h=bodeplot(GANG2_nl,GANG2_nl_CurrentLoop,{10,f_bode}); grid;
setoptions(h,'FreqUnits','Hz');
title('G2: Ref to Controller Output v(t), FC/1+PCH')
legend('Withou current loop dynamic','With current loop dynamic')

subplot(3,2,3)
   options.FreqUnits = 'Hz';
   h=bodeplot(GANG3_nl,GANG3_nl_CurrentLoop,{10,f_bode}); grid;
   setoptions(h,'FreqUnits','Hz');
   title('G3: Disturbance Rejection P/1+PCH')
   legend('Withou current loop dynamic','With current loop dynamic')

subplot(3,2,4)
   options.FreqUnits = 'Hz';
   h=bodeplot(GANG4_nl,GANG4_nl_CurrentLoop,{10,f_bode}); grid;
   setoptions(h,'FreqUnits','Hz');
   title('G4: Sensitivity 1/1+PCH')
   legend('Withou current loop dynamic','With current loop dynamic')

subplot(3,2,5)
   options.FreqUnits = 'Hz';
   h=bodeplot(GANG5_nl,GANG5_nl_CurrentLoop,{10,f_bode}); grid;
   setoptions(h,'FreqUnits','Hz');
   title('G5: Noise Sensitivity CH/1+PCH')
   legend('Withou current loop dynamic','With current loop dynamic')

subplot(3,2,6)
   options.FreqUnits = 'Hz';
   h=bodeplot(GANG6_nl,GANG6_nl_CurrentLoop,{10,f_bode}); grid;
   setoptions(h,'FreqUnits','Hz');
   title('G6: Compl Sensitivity PCH/1+PCH')
   legend('Withou current loop dynamic','With current loop dynamic')


% ----- Magnitude-only Bode Plot -----
figure
subplot(3,2,1)
   options.FreqUnits = 'Hz';
   h=bodeplot(GANG1_nl,GANG1_nl_CurrentLoop,{10,f_bode}); grid;
   setoptions(h,'FreqUnits','Hz');
```

```
   setoptions(h,'FreqUnits','Hz','PhaseVisible','off');
   title('G1: Reference Tracking FPC/1+PCH')
   legend('Withou current loop dynamic','With current loop dynamic')

subplot(3,2,2)
   options.FreqUnits = 'Hz';
   h=bodeplot(GANG2_nl,GANG2_nl_CurrentLoop,{10,f_bode}); grid;
   setoptions(h,'FreqUnits','Hz');
   setoptions(h,'FreqUnits','Hz','PhaseVisible','off');
   title('G2: Ref to Controller Output v(t), FC/1+PCH')
   legend('Withou current loop dynamic','With current loop dynamic')

subplot(3,2,3)
   options.FreqUnits = 'Hz';
   h=bodeplot(GANG3_nl,GANG3_nl_CurrentLoop,{10,f_bode}); grid;
   setoptions(h,'FreqUnits','Hz');
   setoptions(h,'FreqUnits','Hz','PhaseVisible','off');
   title('G3: Disturbance Rejection P/1+PCH')
   legend('Withou current loop dynamic','With current loop dynamic')

subplot(3,2,4)
   options.FreqUnits = 'Hz';
   h=bodeplot(GANG4_nl,GANG4_nl_CurrentLoop,{10,f_bode}); grid;
   setoptions(h,'FreqUnits','Hz');
   setoptions(h,'FreqUnits','Hz','PhaseVisible','off');
   title('G4: Sensitivity 1/1+PCH')
   legend('Withou current loop dynamic','With current loop dynamic')

subplot(3,2,5)
   options.FreqUnits = 'Hz';
   h=bodeplot(GANG5_nl,GANG5_nl_CurrentLoop,{10,f_bode}); grid;
   setoptions(h,'FreqUnits','Hz');
   setoptions(h,'FreqUnits','Hz','PhaseVisible','off');
   title('G5: Noise Sensitivity CH/1+PCH')
   legend('Withou current loop dynamic','With current loop dynamic')

subplot(3,2,6)
   options.FreqUnits = 'Hz';
   h=bodeplot(GANG6_nl,GANG6_nl_CurrentLoop,{10,f_bode}); grid;
   setoptions(h,'FreqUnits','Hz');
   setoptions(h,'FreqUnits','Hz','PhaseVisible','off');
   title('G6: Compl Sensitivity PCH/1+PCH')
   legend('Withou current loop dynamic','With current loop dynamic')


% ----- Pole-Zero Map -----
figure
subplot(3,2,1)
   pzmap(GANG1_nl)
   title('G1: Reference Tracking FPC/1+PCH')
subplot(3,2,2)
   pzmap(GANG2_nl)
   title('G2: Ref to Controller Output v(t), FC/1+PCH')
subplot(3,2,3)
   pzmap(GANG3_nl)
   title('G3: Disturbance Rejection P/1+PCH')
subplot(3,2,4)
   pzmap(GANG4_nl)
   title('G4: Sensitivity 1/1+PCH')
subplot(3,2,5)
   pzmap(GANG5_nl)
   title('G5: Noise Sensitivity CH/1+PCH')
subplot(3,2,6)
```

```
   pzmap(GANG6_nl)
   title('G6: Compl Sensitivity PCH/1+PCH')


% ----- Step Response -----
figure
subplot(3,2,1)
   % Step Response
   [yy_position,tt]=lsim(GANG1_nl,theta_ref*(pi/180),t);

[yy_position_CurrentLoop,tt2]=lsim(GANG1_nl_CurrentLoop,theta_ref*(pi/180),t);
   plot(tt,theta_ref,'--
',tt,yy_position*(180/pi),tt2,yy_position_CurrentLoop*(180/pi),'LineWidth',1);
grid
   xlabel('Time (sec)');ylabel('Position (degree)')
   title('G1: Reference Tracking FPC/1+PCH')
   legend('Withou current loop dynamic','With current loop dynamic')

subplot(3,2,2)
   [yy_v,tt]=lsim(GANG2_nl,theta_ref*(pi/180),t);
   [yy_v_CurrentLoop,tt2]=lsim(GANG2_nl_CurrentLoop,theta_ref*(pi/180),t);
   plot(tt,yy_v,tt2,yy_v_CurrentLoop,'LineWidth',1); grid
   xlabel('Time (sec)');ylabel('v(t)')
   title('G2: Ref to Controller Output v(t), FC/1+PCH')
   legend('Withou current loop dynamic','With current loop dynamic')

subplot(3,2,3)
   [yy,tt]=lsim(GANG3_nl,theta_ref*(pi/180),t);
   [yy2,tt2]=lsim(GANG3_nl_CurrentLoop,theta_ref*(pi/180),t);
   plot(tt,yy,tt2,yy2,'LineWidth',1); grid
   xlabel('Time (sec)');ylabel('Amplitude')
   title('G3: Disturbance Rejection P/1+PCH')
   legend('Withou current loop dynamic','With current loop dynamic')

subplot(3,2,4)
   [yy,tt]=lsim(GANG4_nl,theta_ref*(pi/180),t);
   [yy2,tt2]=lsim(GANG4_nl_CurrentLoop,theta_ref*(pi/180),t);
   plot(tt,yy,tt2,yy2,'LineWidth',1); grid
   xlabel('Time (sec)');ylabel('Amplitude')
   title('G4: Sensitivity 1/1+PCH')
   legend('Withou current loop dynamic','With current loop dynamic')

subplot(3,2,5)
   [yy,tt]=lsim(GANG5_nl,theta_ref*(pi/180),t);
   [yy2,tt2]=lsim(GANG5_nl_CurrentLoop,theta_ref*(pi/180),t);
   plot(tt,yy,tt2,yy2,'LineWidth',1); grid
   xlabel('Time (sec)');ylabel('Amplitude')
   title('G5: Noise Sensitivity CH/1+PCH')
   legend('Withou current loop dynamic','With current loop dynamic')

subplot(3,2,6)
   [yy,tt]=lsim(GANG6_nl,theta_ref*(pi/180),t);
   [yy2,tt2]=lsim(GANG6_nl_CurrentLoop,theta_ref*(pi/180),t);
   plot(tt,yy,tt2,yy2,'LineWidth',1); grid
   xlabel('Time (sec)');ylabel('Amplitude')
   title('G6: Compl Sensitivity PCH/1+PCH')
   legend('Withou current loop dynamic','With current loop dynamic')


% -------------------------------------------------------
% Velocity
% Without Dynamic of Current Loop
Ref2Velocity = s*GANG1_nl;
```

```
[yy_velocity,tt]=lsim(Ref2Velocity,theta_ref*(pi/180),t); % Velocity
% Without Dynamic of Current Loop
Ref2Velocity_CurrentLoop = s*GANG1_nl_CurrentLoop;
[yy_velocity_CurrentLoop,tt2]=lsim(Ref2Velocity_CurrentLoop,theta_ref*(pi/180),
t); % Velocity
% Plot
figure; plot(tt,yy_velocity,tt2,yy_velocity_CurrentLoop,'LineWidth',1); grid
xlabel('Time (sec)');ylabel('velocity(rad/sec)')
title('Nonlinear Control, Frequency Domain')
legend('Withou current loop dynamic','With current loop dynamic')

% Current Reference Iref: u=(v-f)/g
% Without Dynamic of Current Loop
u2nl_Iref = ( yy_v-(1/J)*(-kd*yy_velocity-Krest.*sin(2*yy_position)) )./(
kt*cos(yy_position)/J );

% With Dynamic of Current Loop, Ic=G_CurrentLoop*Iref
u2nl_Iref_CurrentLoop = ( yy_v-(1/J)*(-kd*yy_velocity_CurrentLoop-
Krest.*sin(2*yy_position_CurrentLoop)) )./( kt*cos(yy_position_CurrentLoop)/J
);
[u2nl_Ic,tt]=lsim(G_CurrentLoop,u2nl_Iref_CurrentLoop,tt); % Ic

figure; plot(tt,u2nl_Iref,tt2,u2nl_Iref_CurrentLoop,tt2,u2nl_Ic,'LineWidth',1);
grid
xlabel('Time (sec)');ylabel('Iref, Ic(A)')
title('u=I_r_e_f, Nonlinear Control, Frequency Domain')
legend('Withou current loop dynamic u=Iref=Ic','With current loop dynamic,
u=Iref','With current loop dynamic, Ic')



%% _________________[Nonlinear Control with Pole Placement]________________
% Feedback Linearization, Current Drive, State Space Control
% Nonlinear Model
% dx1 = x2
% dx2 = f(x)+g(x)*u(t) = v    , u=coil current

% Nonlinear Compensation v = f+g*u
% u=(v-f)/g

% Linear Model with input v (compensated with feedback linearization v=f+g*u)
% dx1 = x2
% dx2 = v
fprintf(['________________________________________\n\n\n',...
    'Nonlinear Control with Pole Placement'])

    A2nl = [0  1
            0  0];
    B2nl = [0
            1];

% All states as output
    C2nl = eye(2);
    D2nl = [0
            0];

% Angular Position Tracking
    C2nl_act = [1 0];
    D2nl_act = [0];


% Controllability
```

```
Mc2nl = ctrb(A2nl,B2nl); % Controllability Matrix
rank_Mc2nl=rank(Mc2nl)
if rank_Mc2nl==2; disp(['It is ontrollable. Rank of Mc is ',
num2str(rank_Mc2nl)])
else; disp('It is NOT ontrollable')
end

% Observability
Mo2nl = obsv(A2nl,C2nl); % Observability Matrix
rank_Mo2nl=rank(Mo2nl)
if rank_Mo2nl==2; disp(['It is observable. Rank of Mo is ',
num2str(rank_Mo2nl)])
else; disp('It is NOT observable')
end

%Open-Loop System
sys2nl=ss(A2nl,B2nl,C2nl,D2nl);

% Pole Placement
% Desired clodes-loop poles: lambda1, lambda2
% Desired Characteristic Equation: Phi_d=(lambda-lambda1)*(lambda-lambda2)
% Observability Matrix Mc=[B1nl, A1nl*B1nl]
%  Ackermann's formula: K=[0 1]*inv(Mc)*Phi_d(A2nl)

% Desired closed-loop poles
lambda1=-zeta*wn+i*wn*sqrt(1-zeta^2);
lambda2=-zeta*wn-i*wn*sqrt(1-zeta^2);
lambda_d2nl=[lambda1 lambda2];
% Desired characteristic Polynomial
phi_d2nl = @(S)(S^2+2*zeta*wn*S+wn^2*eye(size(S)));

% Feedback Gains
% K2nl= place(A2nl, B2nl, lambda_d2nl)
K2nl =[lambda1*lambda2  -(lambda1+lambda2)] % Solving equations
K2nl = place(A2nl, B2nl, lambda_d2nl)
K2nl =[0 1]*inv(Mc2nl)*phi_d2nl(A2nl) %  Ackermann's formula


% Unitary gain for angular position tracking
C_act2 = [1 0];
G2nl = -inv(C_act2*inv(A2nl-B2nl*K2nl)*B2nl)

%Closed-Loop System
% Without Current Loop Dynamic:
sys2nl_cl=ss(A2nl-B2nl*K2nl,B2nl,C2nl,D2nl);
% With Current Loop Dynamic:
% calculations: (G=system, H=Current Loop time inverse of DC gain)
% (1) dX=A*X+B*u,y=C*X+D*u => G(s)=X(s)/U(s)=C*inv(sI-A)*B+D => X(s)=G(s)U(x)
% (2) U(s)=H(s)*(R(s)-k*X(s))
% (1)&(2) => X(s)=G(s)*H(s)*(R(s)-k*X(s))=G(s)*H(s)*R(s)-G(s)*H(s)*k*X(s)
% => (I+G(s)H(s)k)*X(s)=G(s)H(s)R(s) => X(s)=inv((I+G(s)H(s)k))*G(s)H(s)R(s)
GG2_nl = [1/s^2 ; 1/s]; % Mechanical dynamic, input=Ic, outputs=[position,
velocity]
sys2nl_cl_CurrentLoop =
inv(eye(2)+GG2_nl*G_CurrentLoop*K2nl)*GG2_nl*G_CurrentLoop;


% Plots
% Open-Loop Responses
figure; step(sys2nl); grid
title('Step Response (Open-Loop, Nonlinear Control by Pole Placement)')

figure; pzmap(sys2nl)
```

```
title('Open-Loop A, Nonlinear Control by Pole Placement')

figure; bode(sys2nl); grid
title('Bode (Open-Loop, Nonlinear Control by Pole Placement)')


% Closed-Loop Responses
% Step Response
% Without Dynamic of Current Loop, u=Iref=Ic
[yy2nl,tt2nl] = lsim(sys2nl_cl,G2nl*theta_ref*(pi/180),t);
v2nl = G2nl*theta_ref*(pi/180)-K2nl*yy2nl'; % v(t)
u2nl_Iref = ( v2nl-(1/J)*(-kd*yy2nl(:,2)'-Krest.*sin(2*yy2nl(:,1)')) )./(
kt*cos(yy2nl(:,1)')/J );
% With Dynamic of Current Loop, u=Iref, Ic=G_CurrentLoop*Iref
[yy2nl_CurrentLoop,tt2nl_CurrentLoop]=lsim(sys2nl_cl_CurrentLoop,G2nl*theta_ref
*(pi/180),t);
v2nl_CurrentLoop=G2nl*theta_ref*(pi/180)-K2nl*yy2nl_CurrentLoop'; % Control
signal u=Iref
u2nl_Iref_CurrentLoop = ( v2nl_CurrentLoop-(1/J)*(-kd*yy2nl(:,2)'-
Krest.*sin(2*yy2nl(:,1)')) )./( kt*cos(yy2nl(:,1)')/J );

[u2nl_Ic_CurrentLoop,tt2nl_CurrentLoop]=lsim(G_CurrentLoop,u2nl_Iref_CurrentLoo
p,tt2nl); % Velocity


% Coil Viltage
% Without Dynamic of Current Loop
[yy_vc_i,tt_vc_i]=lsim((1/DC_gain_CurrentLoop_NonPureIntegrator)*GANGi2,u2nl_Ir
ef_CurrentLoop,tt2nl_CurrentLoop);
% With Dynamic of Current Loop
[yy_vc,tt_vc]=lsim((1/DC_gain_CurrentLoop_NonPureIntegrator)*GANG2,u2nl_Iref_Cu
rrentLoop,tt2nl_CurrentLoop);



figure % subplot(6,1,1)
   plot(tt2nl-T_ref,theta_ref,'g--',...
        ...% tt2nl-T_ref,yy2nl(:,1)*(180/pi),... % withoiut current-loop
dynamic
        tt2nl_CurrentLoop-T_ref,yy2nl_CurrentLoop(:,1)*(180/pi),'r',... % with
current-loop dynamic
        Step_theta_NL_SS10(:,1), Step_theta_NL_SS10(:,2),'k--',...
        'LineWidth',1); grid
   xlabel('Time (sec)');ylabel('Position (degree)')
   title('Step Response (Closed-Loop, Nonlinear Control by Pole Placement)')
   legend('Reference \theta_r_e_f','\theta with current loop dynamic',
'Experiment')
   xlim([0 0.99*T_ref]); ylim([-10.5 10.5])

figure % subplot(6,1,2)
   plot(...% tt2nl-T_ref,yy2nl(:,2),...
        tt2nl_CurrentLoop-T_ref,yy2nl_CurrentLoop(:,2),'r',...
        Step_Velocity_NL_SS10(:,1), Step_Velocity_NL_SS10(:,2),'k--',...
        'LineWidth',1); grid
   xlabel('Time (sec)');ylabel('Velocity (rad/sec)')
   legend('With current loop dynamicu=Iref', 'Experiment')
   xlim([0 0.99*T_ref]); ylim([-550 550])

figure % subplot(6,1,3)
   plot(...% tt2nl-T_ref,u2nl_Iref,...
        tt2nl_CurrentLoop-T_ref,u2nl_Iref_CurrentLoop,'r',...
        Step_DAC_NL_SS10(:,1), (10/5.1)*Step_DAC_NL_SS10(:,2),'k--',... %
Iref=-(R2/R1)*DAC
```

```
        'LineWidth',1); grid
   xlabel('Time (sec)');ylabel('u=Iref, Ic (A)')
   legend('With current loop dynamic, u=Iref', 'Experiment')
   xlim([0 0.99*T_ref]); ylim([-3 3])

figure %    subplot(6,1,4)
   plot(tt2nl_CurrentLoop-T_ref,u2nl_Ic_CurrentLoop,'r',...
        Step_Current_NL_SS10(:,1), Step_Current_NL_SS10(:,2),'k--',...
        'LineWidth',1); grid
   xlabel('Time (sec)');ylabel('u=Iref, Ic (A)')
   legend('Ic With current loop dynamic', 'Experiment')
   xlim([0 0.99*T_ref]); ylim([-3 3])

figure % subplot(6,1,5)
   plot(tt_vc_i-T_ref,v2nl,...
        tt_vc-T_ref,v2nl_CurrentLoop,...
        'LineWidth',1); grid
   xlabel('Time (sec)');ylabel('signal v(t)')
   legend('Without current loop dynamic','With current loop dynamic')

figure % subplot(6,1,6)
   plot(tt2nl-T_ref,yy_vc_i,...
        tt2nl-T_ref,yy_vc,...
        ...%% Experiment includes missing data when saved fromscope
        'LineWidth',1); grid
   xlabel('Time (sec)');ylabel('V_c(t)')
   legend('Without current loop dynamic','With current loop dynamic',
'Experiment')


figure; pzmap(sys2nl_cl); % grid([0.2 0.4 0.6 0.8 1],[wn]); axis equal
title('Closed-Loop A-BK, Nonlinear Control by Pole Placement')


figure; bode(sys2nl_cl,sys2nl_cl_CurrentLoop); grid
title('Bode (Closed-Loop, Nonlinear Control by Pole Placement)')
legend('Without current loop dynamic','With current loop dynamic')




%  ----------------------[  Frequency Responses ]---------------------------
ff = logspace(1,4,2000);% frequency [Hz]
omegaa=2*pi*ff;
S = 1i * omegaa;


% Loop Transmission
Ts=1/(100e3);
for kk=1:length(S)
    LT2_nl_delay(kk) = exp(-S(kk)*Ts) * K2nl*inv(S(kk)*eye(2)-A2nl)*B2nl; %
with delay
    LT2_nl(kk) = K2nl*inv(S(kk)*eye(2)-A2nl)*B2nl;
end

figure
subplot(2,1,1)
   semilogx(ff, 20*log10(abs(LT2_nl_delay)),'g',... % with delay
            ff, 20*log10(abs(LT2_nl)),'r--',... % without delay
   'LineWidth',1.1); grid
   ylabel('Magnitude (dB)')
   xlim([10^1 10^4])
subplot(2,1,2)
```

```
   semilogx(ff, (180/pi)*angle(LT2_nl_delay),'g',... % with delay
            ff, (180/pi)*angle(LT2_nl),'r--',... % without delay
            'LineWidth',1.1); grid
   xlabel('frequency (Hz)'); ylabel('Angle (deg)')
   legend('Model with delay','Model'); title('Loop Transmission')
   xlim([10^1 10^4])


% -------- Gang 1 -----------
ff = logspace(1,4,2000);% frequency [Hz]
omegaa=2*pi*ff;
S = 1i * omegaa;
Ts=1/(22e3);

% double integrator, PD and Loop Transmission and Gang 1 with Model
DI = 1./S.^2;
DI_delay = exp(-S*Ts)./S.^2;
PD = wn^2 + 2*zeta*wn*S; % PD, rest of the loop
LT = DI.*PD;
LT_delay = exp(-S*Ts).*DI.*PD; % LT with delay


for kk=1:length(S)
    G1_nl(kk) = G2nl*[1 0]*inv(S(kk)*eye(2)-(A2nl-B2nl*K2nl))*B2nl;
    G1_nl_delay(kk) = exp(-S(kk)*Ts)* G2nl*[1 0]*inv(S(kk)*eye(2)-(A2nl-
B2nl*K2nl))*B2nl;
end

GG1_delay = exp(-S*Ts).*G2nl.*DI_delay./(1+LT_delay); % Gang 1 with delay = PD
in series with double integrator with delay
GG4_delay = 1./(1+LT_delay); % Gang 4

% Double Integrator, Loop Transmission and Gang 1 with Experiment
% interpolation of double integrator from experiment
Mag_DI_exprr  = interp1(log10(Freq_DI_expr),Mag_DI_expr,log10(ff));
Phase_DI_exprr= interp1(log10(Freq_DI_expr),Phase_DI_expr,log10(ff));
Mag_DI_exprr_abs = 10.^(Mag_DI_exprr/20);
DI_expr = Mag_DI_exprr_abs .*( cosd(Phase_DI_exprr) + 1i* sind(Phase_DI_exprr)
); % complex number by combining angle and phase

LT_expr = DI_expr.*PD; % loop transmission
GG1_expr = G2nl*DI_expr./(1+LT_expr); % Gang 1 = PD in series with double
integrator
GG4_expr = 1./(1+LT_expr); % Gang 1 = PD in series with double integrator


 % remove the problematic element for plots
fff=ff;
fff(1149)=[]; % remove the problematic element
GG1_expr(1149)=[]; % remove the problematic element
DI_expr(1149)=[]; % remove the problematic element
LT_expr(1149)=[]; % remove the problematic element
GG4_expr(1149)=[]; % remove the problematic element


% Gang 1
figure
subplot(2,1,1)
   semilogx(ff, 20*log10(abs(GG1_delay)),'r',... % model with delay
            ...% ff, 20*log10(abs(G1_nl)),'g',...  % model without delay
            fff, 20*log10(abs(GG1_expr)),'k--',...  % experiment
   'LineWidth',1); grid
   ylabel('Magnitude (dB)'); xlim([10^1 3*10^3])
```

```
subplot(2,1,2)
   semilogx(ff, (180/pi)*unwrap(angle(GG1_delay)),'r',...
            ...% ff, (180/pi)*unwrap(angle(G1_nl)),'g',...
            fff, (180/pi)*unwrap(angle(GG1_expr)),'k--',...
            'LineWidth',1); grid
   xlabel('frequency (Hz)'); ylabel('Angle (deg)')
   legend('Model with delay','Model','Experiment'); title('Gang 1')
   xlim([10^1 3*10^3]); ylim([-250 0]); yticks([-180 -90 0])



% Loop Transmission and double integrator
figure
subplot(2,1,1)
   semilogx( ff, 20*log10(abs(DI)),'g',... % double integrator without delay
             ff, 20*log10(abs(DI_delay)),'r',... % double integrator with delay
             fff, 20*log10(abs(DI_expr)),'k--',... % double integrator
experiment
             ...% Bode_DoubleIntegrator_NL_SS(:,1),
Bode_DoubleIntegrator_NL_SS(:,2),'k--',... % Experiment
             ff, 20*log10(abs(PD)),'r',... % PD
             ff, 20*log10(abs(LT_delay)),'r-',... % Loop Transmission
             fff, 20*log10(abs(LT_expr)),'k--',... % Loop Transmission
Experiment
             'LineWidth',1.1); grid on
      xlim([10^1 5*10^3]); ylim([-180 170]);
subplot(2,1,2)
   semilogx(ff, (180/pi)*angle(DI)-360,'g--',...
            ff, (180/pi)*unwrap(angle(DI_delay))-360,'r',...
            fff, (180/pi)*unwrap(angle(DI_expr)),'k--',...
        ...% Bode_DoubleIntegrator_NL_SS(:,1),
unwrap(Bode_DoubleIntegrator_NL_SS(:,3)),'k--',... % Experiment
            ff, (180/pi)*angle(PD),'r',...
            ff, (180/pi)*unwrap(angle(LT_delay)),'r',...
            fff, (180/pi)*unwrap(angle(LT_expr)),'k--',... % Experiment
        'LineWidth',1.1); grid on
        legend('DI','DI with delay', 'DI Expr','PD','LT','LT expr')
   xlim([10^1 5*10^3]); ylim([-270 90]); yticks([-270 -180 -90 0])
   yticks([-270 -180 -90 0 90])

% Gang 4: Sensitivity
figure
subplot(2,1,1)
   semilogx(ff, 20*log10(abs(GG4_delay)),'r',...
            fff, 20*log10(abs(GG4_expr)),'k--',...
   'LineWidth',1); grid
   ylabel('Magnitude (dB)'); xlim([10^2 4.7*10^3]); ylim([-30 5])
   yticks([-30 -20 -10 0 5])
subplot(2,1,2)
   semilogx(ff, (180/pi)*unwrap(angle(GG4_delay))-180,'r',...
            fff, (180/pi)*unwrap(angle(GG4_expr))-180,'k--',...
            'LineWidth',1); grid
   xlabel('frequency (Hz)'); ylabel('Angle (deg)')
   legend('Model with delay','Experiment'); title('Gang 4: Sensitivity')
   xlim([10^2 4.7*10^3]); ylim([-185 0])
   yticks([-180 -90 0])
```

Appendix P

Matlab Code for New Effectiveness Index

The code is given below:

```
% New Effectiveness Index
% Frequency-Domain Analysis of efficiency

% Gp:      including back-emf
% Gp_appr: ignoring back-emf
% Bode Plot of the Plnat C506
% with/without back-emf


J  = 1.5077e-09; % Inretia/mass without mirror from Solid Works
kd = 4.4881e-07; % damping
ks = 0.0013; % spring

Rc=1.76; % coil resistance
Rs=0.1; % sense resistor
R=Rc+Rs;
L=280e-6; % coil inductance
kt = 1.9063e-3; % Experiment at Pangolin 8-8-2021

Gp = tf([J kd ks],[L*J R*J+L*kd R*kd+ks*kd+kt^2 R*ks]); % Icoil/Vcoil  with
back emf
Gp_appr = tf([1],[L R]); % Icoil/Vcoil  without back emf
G_mech = tf([kt 0],[J kd ks]); % Velocity/Icoil

Z_E = tf([kt^2 0],[J kd ks]); % Back-efm impedance

Z_coil = tf([L R],1); % Vcoil/Icoil without back emf

% efficiency=Gp*G_mech*Kf; % efficiency=(T*W)/(V*I)=(kf*I*W)/(V*I)=Kf*W/V
Eff=tf([kt^2 0],[L*J R*J+L*kd R*kd+ks*kd+kt^2 R*ks]); %
efficiency=(T*W)/(V*I)=(kf*I*W)/(V*I)=Kf*W/V

figure;
win=logspace(0,5,1e6);
[mag_Eff,phase_Eff,w] = bode(Eff,win);
Efff = mag_Eff .*( cosd(phase_Eff) + 1i* sind(phase_Eff) ); % Complex number

[mag_Z_E,phase_Z_E,w] = bode(Z_E,win);
Z_EE = mag_Z_E .*( cosd(phase_Z_E) + 1i* sind(phase_Z_E) ); % Complex number

[mag_Z_coil,phase_Z_coil,w] = bode(Z_coil,win);
Z_coill = mag_Z_coil .*( cosd(phase_Z_coil) + 1i* sind(phase_Z_coil) ); %
Complex number


semilogx(win/(2*pi),squeeze(mag_Eff),'LineWidth',1.1); grid on
xlabel('frequency (Hz)'); ylabel('Mag (abs)')
title('efficiency')
xlim([10^0 10^4])

figure;
semilogx(win/(2*pi),20*log10(squeeze(mag_Eff)),'LineWidth',1.1); grid on
xlabel('frequency (Hz)'); ylabel('Mag (dB)')
```

```
xlim([10^0 10^4])

figure
options = bodeoptions;
options.FreqUnits = 'Hz';
bode(Eff,Z_E,Z_coil,Eff,options); grid on
legend('Eff','Z_E','Z_coil','Z_t')
xlim([10^0 10^5])



figure;
subplot(2,1,1)
semilogx(win/(2*pi),(real(squeeze(Efff))),...
         win/(2*pi),(real(squeeze(Z_EE))),...
         win/(2*pi),(real(squeeze(Z_coill))),...
         win/(2*pi),(real(squeeze(Z_EE+Z_coill))),...
         'LineWidth',1.1); grid on
xlabel('frequency (Hz)'); ylabel('Real (abs)')
xlim([10^0 10^4])
xlim([10^0 10^4])

subplot(2,1,2)
semilogx(win/(2*pi),(imag(squeeze(Efff))),...
         win/(2*pi),(imag(squeeze(Z_EE))),...
         win/(2*pi),(imag(squeeze(Z_coill))),...
         win/(2*pi),(imag(squeeze(Z_EE+Z_coill))),...
         'LineWidth',1.1); grid on
xlabel('frequency (Hz)'); ylabel('Imag (abs)')
title('efficiency')
xlim([10^0 10^4])
legend('Eff','Z_E','Z_coil','Z_t')
xlim([10^0 10^4])
```

Appendix Q

Simulink Implementations

Simulink implementation of the models and control system is kind of an alternative to implementation with coding. Each of them has advantages and disadvantages. Coding is better for frequency-domain analysis and time domain analysis without nonlinearities, while Simulink is better for time-domain analysis including nonlinear terms. The Simulink models are given below:

Current Control loop:

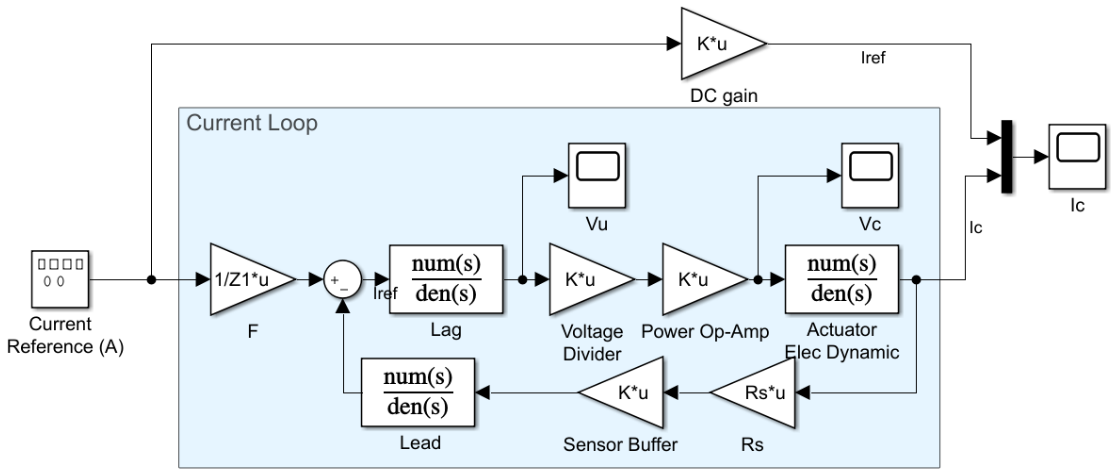

Loop-Shaping Position Control:

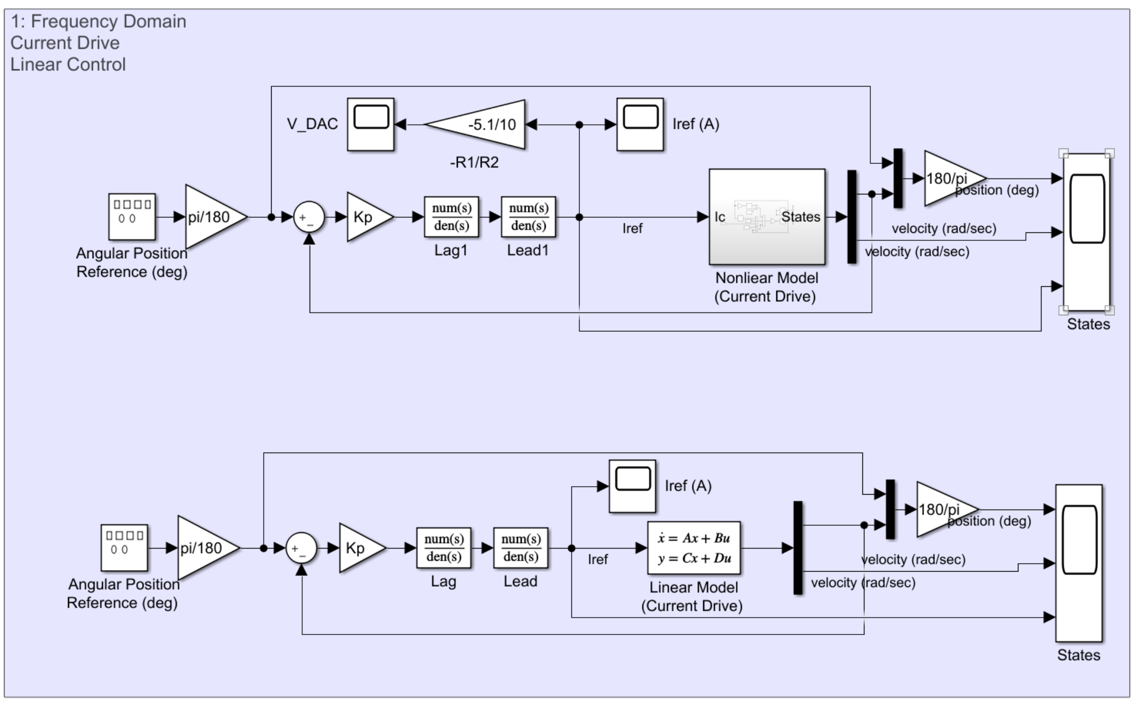

Loop-Shaping Position Control Including Dynamic of Current Loop:

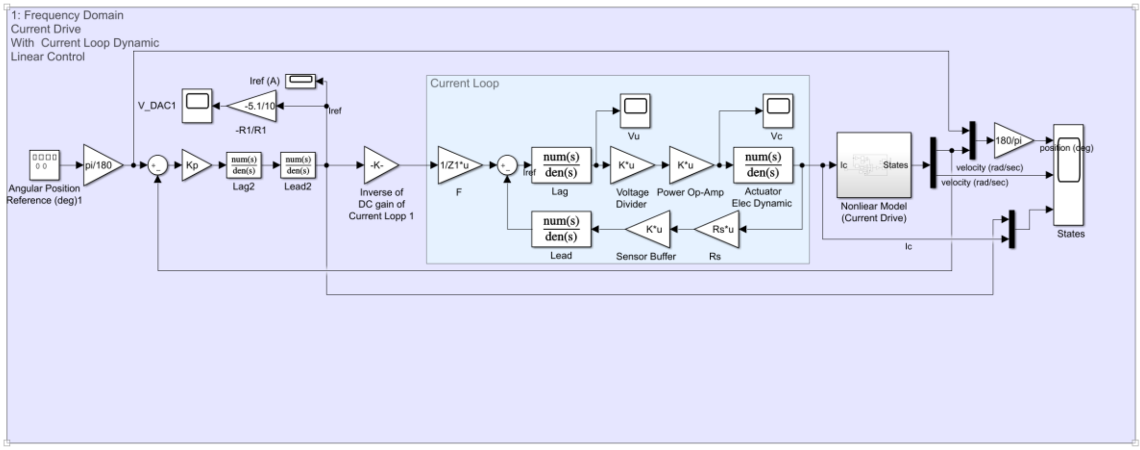

Pole-Placement Position Control with Voltage Drive:

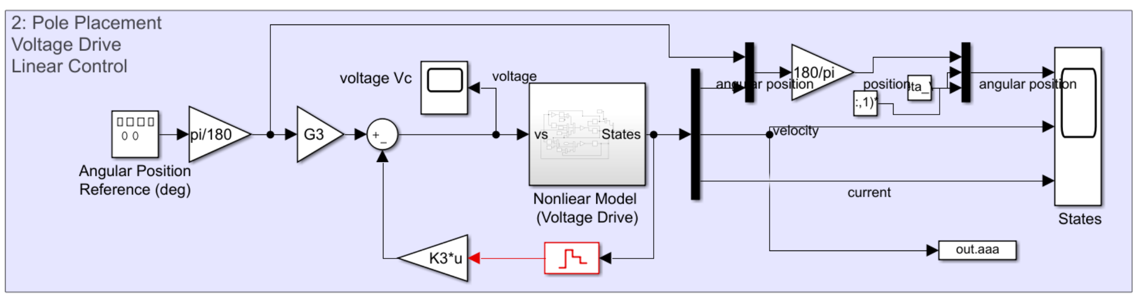

Pole-Placement Position Control with Current Drive

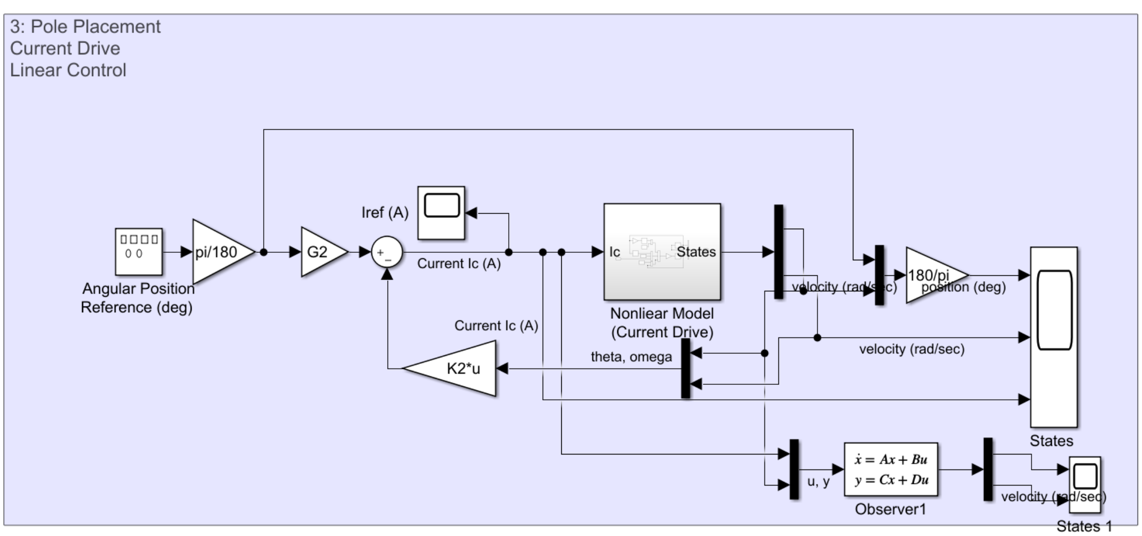

Pole-Placement Position Control with Current Drive Including Current Loop Dynamic:

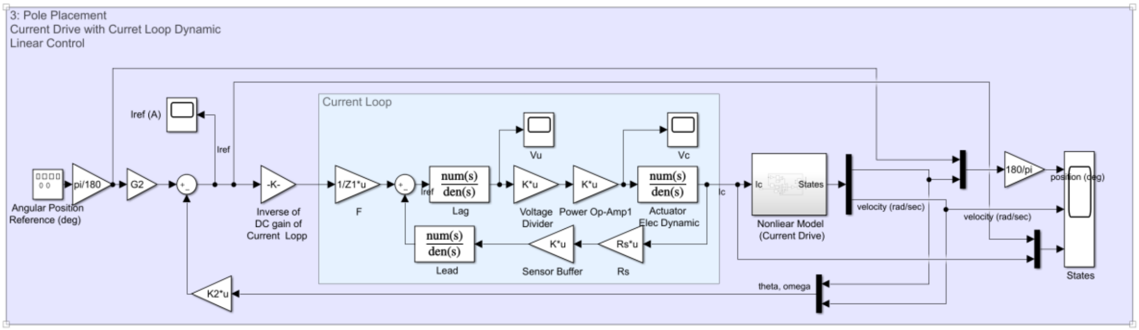

Feedback-Linearization Nonlinear Control with Loop Shaping:

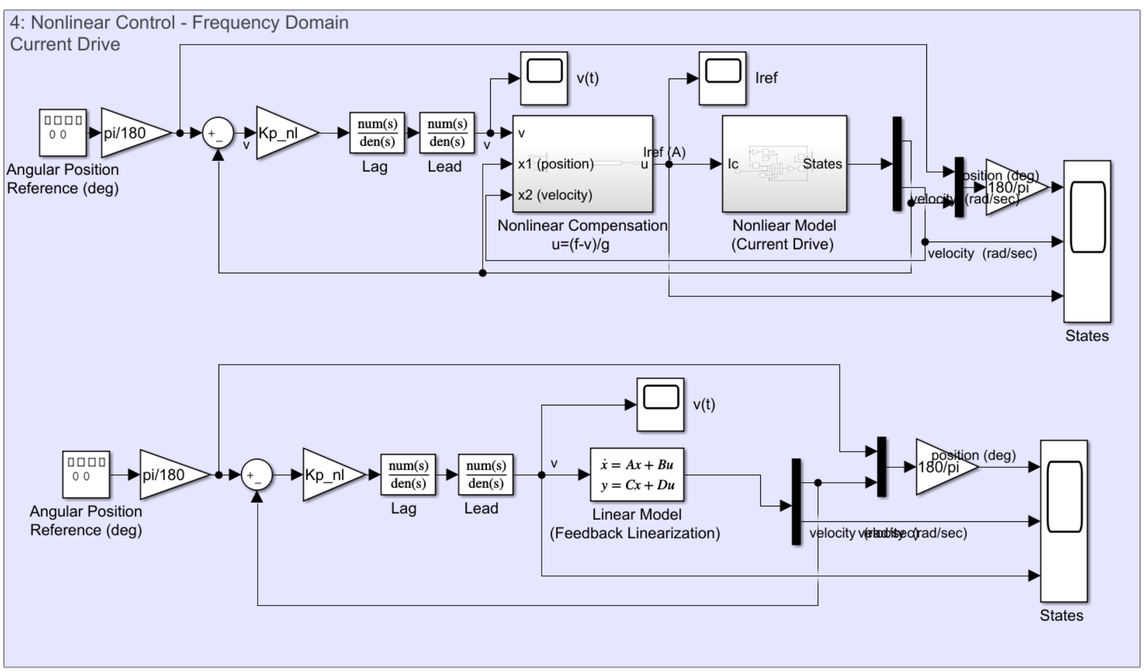

Feedback-Linearization Nonlinear Control with Loop Shaping and Including Current Loop Dynamic

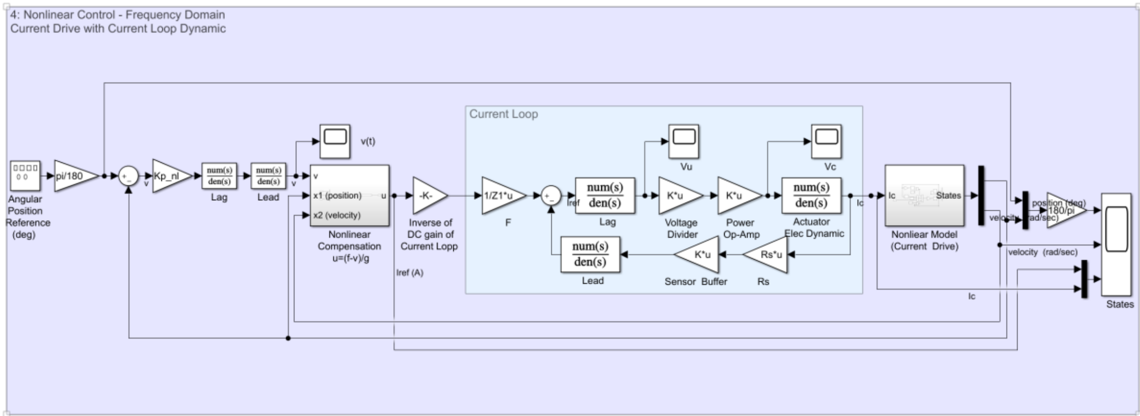

Feedback-Linearization Nonlinear Control with Pole-Placement:

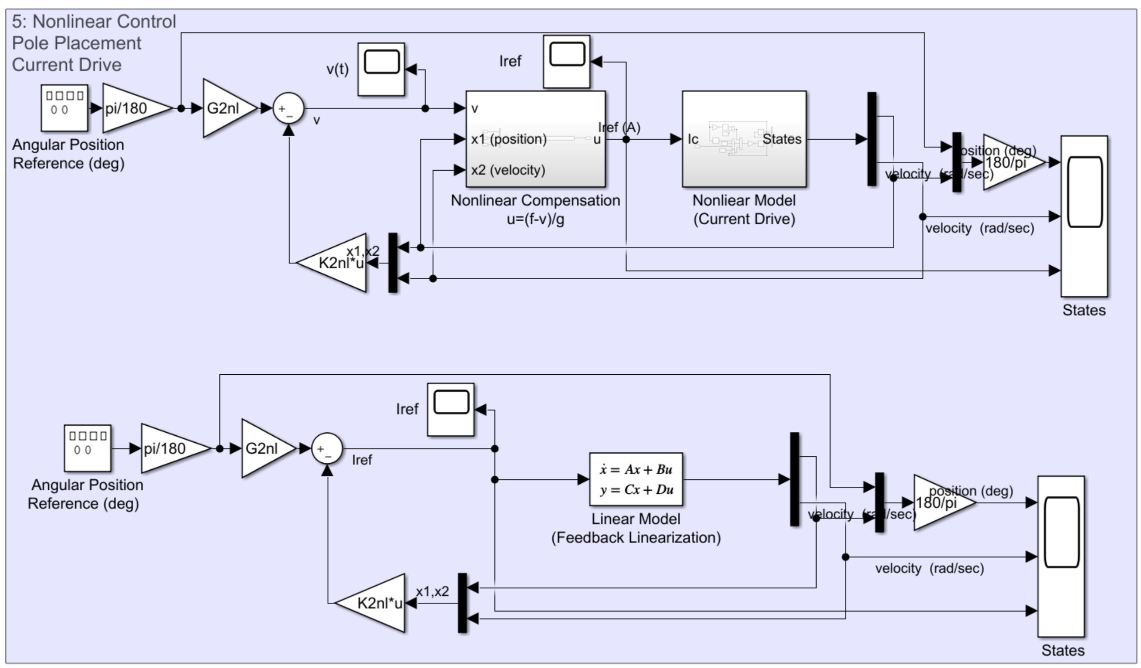

Feedback-Linearization Nonlinear Control with Pole-Placement and Including Current-Loop Dynamic:

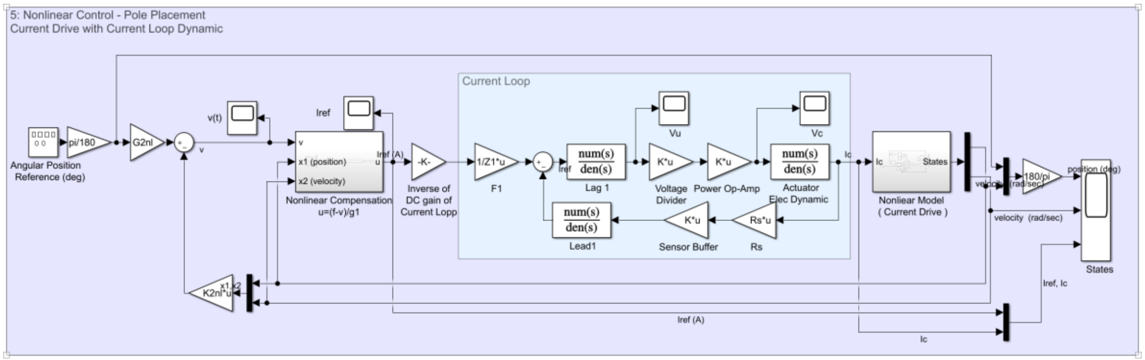

Feedback-Linearization Nonlinear Control with Pole-Placement and Including Current-Loop Dynamic and Delay Terms:

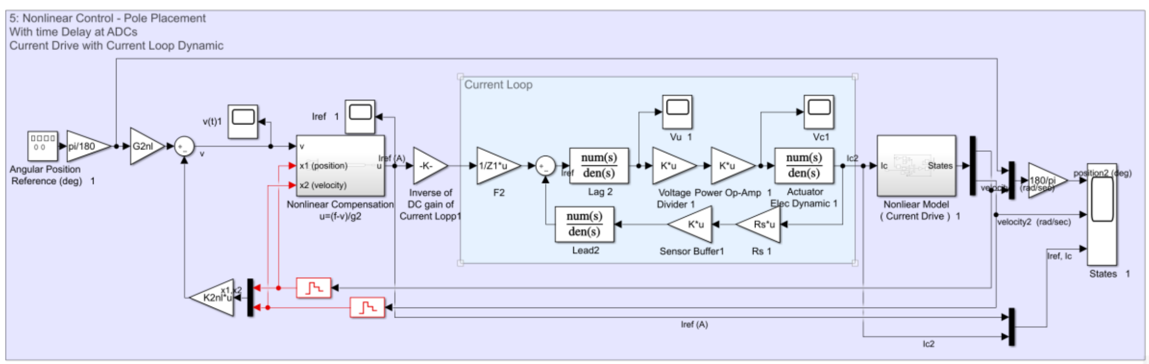

Bibliography

Chapter 1

[1] S. Mohammadi, M. Mirsalim, S. Vaez-Zadeh, and H. A. Talebi, 'Design Analysis of a New Axial-Flux Interior Permanent-Magnet Coupler', *5th Power Electronics, Drive Systems and Tech. Conf. 2014*, Tehran.

[2] S. Mohammadi, M. Mirsalim, S. Vaez-Zadeh, and H. Lesani, 'Sensitivity Analysis and Prototyping of a Surface-Mounted Permanent-Magnet Axial-Flux Coupler', *The 5th Power Electronics, Drive Systems and Tech. Conf. 2014*, Tehran.

[3] S. Mohammadi, M. Mirsalim, M. Niazazari, and H. A. Talebi, 'A New Interior Permanent-Magnet Radial-Flux Eddy-Current Coupler', in *Proc. The 5th Power Electronics, Drive Systems and Tech. Conf. 2014*, Tehran, Iran.

[4] A. Vakilian-Zand, S. Mohammadi, J. S. Moghani, and M. Mirsalim, 'Sensitivity Analysis and Performance Optimization of an Industrial Squirrel-Cage Induction Motor Used for a 150 HP Floating Pump', *5th Power Electronics, Drive Systems and Tech. Conf. 2014*, Tehran.

[5] M. Niazazri, M. Mirsalim, S. Mohammadi, 'Analytical Framework for Analysis and Demagnetization Study of a Slotted Solid-Rotor Line-Start Permanent-Magnet Synchronous Motor', *5th Power Electronics, Drive Systems and Tech. Conf. 2014*, Tehran.

[6] M. Niazazri, M. Mirsalim, and S. Mohammadi, 'Effect of Rotor Slots Parameters on Synchronization Capability of Slotted Solid Rotor Line Start Permanent Magnet Motor', *5th Power Electronics, Drive Systems and Tech. Conf. 2013*, Tehran.

[7] M. Niazazari, M. Mirsalim, S. M. Abedi-Pahnehkolaei, S. Mohammadi, 'Optimum design of a line-start permanent magnet motor with slotted solid rotor using neural network and imperialist competitive algorithm', *IET Electric Power Applications*, vol. 11, no. 1, pp. 1-8, 2017.

[8] Gh. Davarpanah, S. Mohammadi, J. Kirtley, 'A Novel 8/10 Two-Phase Switched Reluctance Motor with Enhanced Performance: Analysis and Experimental Study', *IEEE Transactions on Industry applications*, DOI: 10.1109/TIA.2019.2908952, 2019.

[9] Gh. Davarpanah, S. Mohammadi, J. Kirtley, 'A Novel 8/10 Two-Phase Switched Reluctance Motor with Enhanced Performance', in *53rd IEEE Industry Applications Society Annual Meeting 2018*, Portland, USA.

[10] Gh. Dacarpanah, S. Mohammadi, and J. Kirtley, 'A Self-Starting Technique for Two-Phase Switched Reluctance Motors', *Revised in IEEE Transactions on Energy Conversion*, 2021.

[11] C. Lee, M. Angle, K. Bhalla, M Qasim, J. Mei, S. Mohammadi, K. Iyer, ‘Quantitative Comparison of Vernier Permanent-Magnet Motors with Interior Permanent-Magnet Motor for Hybrid Electric Vehicles’, *Energies*, 2018.

[12] P. Ma, Q. Wang, Y. Li, S. Jiang, and M. Zhao, “Research on Torque Ripple Suppression of the Slotted Limited Angle Torque Motor,” *IEEE Trans. Magn.*, vol. 57, no. 2, pp. 8200106, Feb. 2021.

[13] H. Yu, G. Yu, Y. Xu, and J. Zou, “Torque Performance Improvement for Slotted Limited-Angle Torque Motors by Combined SMA Application and GA Optimization,” *IEEE Trans. Magn.*, vol. 57, no. 2, pp. 8200305, Feb. 2021.

[14] Z. Jibin, Y. Guodong, X. Yongxiang, C. Xia, L. Yong, and W. Qian, “Development of a Slotless Limited-Angle Torque Motor for Reaction Wheels Torque Measurement System,” *IEEE Trans. Magn.*, vol. 50, no. 11, pp. 8204504, Nov. 2014.

[15] Y. Li, P. Ma, Q. Wang, and M. Zhao, “Analysis, Modeling, and Verification of Limited Angle Torque Motors with Irregular Slot Numbers for Performance Improvement, Cost, and Mass,” *IEEE Trans. Energy Convers.*, vol. 35, no. 2, pp. 1004–1013, Jun. 2020.

[16] Y. Guodong, Z. Jibin, X. Yongxiang, L. Yong, H. Jianhui, and W. Qian, “Torque Performance Improvement of a Radial-Flux Slotted Limited-Angle Torque Motor by Tapered Tooth-Tip,” *IEEE Trans. Appl. Supercond.*, vol. 26, no. 7, pp. 0607305, Oct. 2016.

[17] R. M. Fano, L. J. Chu, and R. B. Adler, “Electromagnetic fields, energy and forces,” Jon Wiley and Sons, Inc., 1960.

[18] A. Haus, and J. R. Melcher, “Electromagnetic fields and energy,” Prentice-Hall. Inc., Englewood Cliffs, NJ, 1989.

[19] L. Belguerras, S. Mezani, and T. Lubin, “Analytical Modeling of an Axial Field Magnetic Coupler with Cylindrical Magnets,” *IEEE Trans. Magn.*, vol. 57, no. 2, pp. 8000305, Feb. 2021.

[20] P. Moon, and D. E. Spencer, “Field Theory Handbook,” Springer-Verlag, Berlin, 1988.

[21] P. Schnizer, “Advanced Multipoles for Accelerator Magnets,” Springer, Berlin, 1988.

[22] P. Schnizer, B. Schnizer, P. Akishin, and E. Fischer, “Theory and application of plane elliptic multipoles for static magnetic fields,” *Nuclear Instruments and Methods in Physics Research*, vol. 607, no. 3, pp. 505-516, Aug. 21, 2009.

[23] P. Schnizer, E. Fischer, and, B. Schnizer “Cylindrical Circular and Elliptical, Toroidal Circular and Elliptical Multipoles Fields, Potentials and their Measurement for Accelerator Magnets,” *arXiv: Accelerator Physics*, 2014.

[24] K. Sugahara, “Improvised Asymptotic Boundary Conditions for Magnetostatic Field Problems in Ellipsoidal and Elliptic Cylindrical Domains”, *IEEE Trans. Magn.*, vol. 53, no. 6, pp. 7205604, June 2017.

[25] X. Huang, C. Zhang, J. Chen, and G. Yang, “Modeling of a Halbach Array Voice Coil Actuator via Fourier Analysis Based on Equivalent Structure,” *IEEE Trans. Magn.*, vol. 55, no. 8, pp. 8204006, Aug. 2019.

[26] Y. Guodong, Z. Jibin, X. Yongxiang, W. Qian, W. Baochao, and L. Junlong, “Estimation of Maximum Angular Operation Range for Permanent-Magnet Slotted Limited-Angle Torque Motor,” *IEEE Trans. Magn.*, vol. 51, no. 11, pp. 8205505, Nov. 2015.

[27] S. Mohammadi, M. Mirsalim, S. Vaez-Zadeh, and H.A. Talebi, ‘Analytical Modeling and Analysis of Axial-Flux Interior Permanent-Magnet Couplers’, *IEEE Transactions on Industrial Electronics*, vol. 61, no. 11, pp. 5940-5947, Nov 2014.

[28] S. Mohammadi, M. Mirsalim, and S. Vaez-Zadeh, ‘Nonlinear Modeling of Eddy-Current Couplers’, *IEEE Transactions on Energy Conversion*, vol. 29, no. 1, pp. 224-231, March 2014.

[29] S. Mohammadi, and M. Mirsalim, ‘Double-Sided Permanent-Magnet Radial-Flux Eddy-Current Couplers: Three-Dimensional Analytical Modeling, Static and Transient Study, and Sensitivity Analysis’, *IET Electric Power Applications*, vol. 7, no. 9, pp. 665–679, 2013.

[30] S. Mohammadi, and M. Mirsalim, ‘Design Optimization of Double-Sided Permanent-Magnet Radial-Flux Eddy-Current Couplers’, *Elsevier: Electric Power Systems Research*, vol. 108, pp. 282-292, 2014.

[31] S. Mohammadi, J. Kirtley, and M. Niaz-Azari “Modelling of axial-flux eddy-current couplers,” *IET Elect. Power Appl*., vol. 14, no. 7, pp. 1238-1246, Apr. 2020.

[32] Gh. Davarpanah, S. Mohammadi, and J. Kirtley, “Modelling of switched reluctance machines,” *IET Elect. Power Appl.*, vol. 14, no. 11, pp. 1997-2006, June 2020.

[33] N. K. Sheth, and K. R. Rajagopal, ‘Calculation of the Flux-Linkage Characteristics of a Switched Reluctance Motor by Flux Tube Method’, *IEEE Trans. Magn*., vol. 41, no. 10, pp. 4069–4071, Oct. 2005.

[34] S. Mohammadi, and M. Mirsalim, ‘Analytical Design Framework for Torque and Back-EMF Optimization, and Inductance Calculation in Double-Rotor Radial-Flux Air-Cored Permanent-Magnet Synchronous Machines’, *IEEE Transactions on Magnetics*, vol. 50, no. 1, Jan 2014.

[35] S. Mohammadi, B. Vahidi, M. Mirsalim, and H. Lesani, ‘Simple Nonlinear MEC-Based Model for Sensitivity Analysis and Genetic Optimization of Permanent-Magnet Synchronous Machines’, *COMPEL: The International Journal for*

Computation and Mathematics in Electrical and Electronic Engineering, vol. 24, no. 1, 2015.

[36] S. Mohammadi, "Analytical representation and finite element analysis of magnetically-geared permanent magnet machines," M.Sc Thesis, Massachusetts Institute of Technology, Cambridge, MA, 2019.

[37] M. Johnson, M. Gardner, H. A. Toliyat, "A Parameterized Linear Magnetic Equivalent Circuit for Analysis and Design of Radial Flux Magnetic Gears—Part I: Implementation," *IEEE Trans. Energy Convers.*, vol. 33, no. 2, Jun. 2018.

[38] M. Johnson, M. Gardner, H. A. Toliyat, "A Parameterized Linear Magnetic Equivalent Circuit for Analysis and Design of Radial Flux Magnetic Gears–Part II: Evaluation," *IEEE Trans. Energy Convers.*, vol. 33, no. 2, Jun. 2018.

[39] C. Dawson, and H.R. Bolton, "Performance prediction of Laws's relay actuator," *IEE Proceedings*, vol. 137, Pt. B, no. 1, Jan. 1990.

[40] G. Yu, Y. Xu, J. Zou, L. Xiao, and H. Lan, "Development of a Radial-Flux Slotted Limited-Angle Torque Motor with Asymmetrical Teeth for Torque Performance Improvement," *IEEE Trans. Magn.*, vol. 55, no. 7, pp. 8203305, Jul. 2019.

[41] R. Nasiri-Zarandi, M. Mirsalim, and A. Cavagnino, "Analysis, Optimization, and Prototyping of a Brushless DC Limited-Angle Torque-Motor with Segmented Rotor Pole Tip Structure," *IEEE Trans. Ind. Electron.*, vol. 62, no. 8, pp. 4985–4993, Aug. 2015.

[42] G. Yu, Y. Xu, T. Lin, L. Xiao, J. Zou, and J. Tan, "Nonlinear EMC Modeling and Analysis of Permanent-Magnet Slotted Limited-Angle Torque Motor," *IEEE Trans. Ind. Electron.*, vol. 68, no. 9, pp. 8507–8518, Sep. 2021.

[43] S. Wu, X. Zhao, Z. Jiao, P. C. Luk, and C. Jiu, "Multi-Objective Optimal Design of a Toroidally Wound Radial-Flux Halbach Permanent Magnet Array Limited Angle Torque Motor," *IEEE Trans. Ind. Electron.*, vol. 64, no. 4, pp. 2962–2971, Apr. 2017.

[44] J. Zou, G. Yu, Y. Xu, Y. Wei, and Q. Wang, "Development of a Limited-Angle Torque Motor with a Moving Coil," *IEEE Trans. Magn.*, vol. 52, no. 7, pp. 8203305, Jul. 2016.

[45] C. Dawson, and H.R. Bolton, "Limited motion rotary actuators of the toroidal-stator, permanent-magnet rotor type," *IEE Proceedings*, vol. 129, Pt. B, no. 4, Jul. 1982.

[46] Y. Zhang, I.R. Smith, and J.G. Kettleborough, "Performance Evaluation for a Limited-Angle Torque Motor," *IEEE Trans. Mechatronics*, vol. 4, no. 3, pp. 335-339, Sep. 1999.

[47] I.R. Smith, J.G. Kettleborough, Y. Zhang, "Simplified modelling and dynamic analysis of a Laws' relay actuator," *Elsevier: Mechatronics*, vol. 9, no. 5, pp. 463-475, Aug. 1999.

[48] G. Jang, S. Seo, C. Kim, I. Yoon, and J. Choi, “Self-Aligning Limited-Angle Rotary Torque PM Motor for Control Valve: Design and Experimental Verification,” *IEEE Trans. Appl. Supercond.*, vol. 30, no. 4, pp. 5206005, June 2020.

[49] Y. Zhou, D. Li, L. Huang, and R. Qu, “Design of A Limited-Angle Torque Motor with Magnetic Zero-Returner for Aviation Fuel Valve,” *in Proc. Int. Conf. Electrical Machines (ICEM)*, pp. 654-660, 2020.

[50] W. R. Benner, “High Torque Low Inductance Rotary Actuator,” U.S Patent 9 270 144 B2, Feb. 23, 2016.

[51] W. R. Benner, “Electromechanical Limited Rotation Rotary Actuator,” U.S Patent 9 077 219 B2, Jul. 7, 2015.

[52] W. R. Benner, “Electromechanical Limited Rotation Rotary Actuator And Method Employing Segmented Coils,” U.S Patent 10 734 857, Aug. 4, 2020.

[53] W. R. Benner, “Electromechanical Limited Rotation Rotary Actuator And Method Employing Segmented Coils,” U.S Patent 10 284 038, 2015.

[54] W. R. Benner, “Electromechanical Device And Assembly Method,” U.S Patent 8 963 396, Feb, 2015.

[55] W. R. Benner, “Light Detector Employing Trapezoidal Chips And Associated Methods,” U.S Patent 10,539,433 B2, Jan. 2020.

[56] D. M. Reed, H. F. Hofmann, and J. Sun, “Offline Identification of Induction Machine Parameters with Core Loss Estimation Using the Stator Current Locus,” IEEE Trans. Energy Convers., vol. 31, no. 4, pp. 1549 –1558, Dec. 2016.

[57] E. Levi, and M. Wang, “Online Identification of the Mutual Inductance for Vector Controlled Induction Motor Drives,” IEEE Trans. Energy Convers., vol. 18, no. 2, pp. 229–3055, Jun. 2003.

[58] G. Yu, Y. Xu, T. Lin, L. Xiao, J. Zou, and J. Tan, “Nonlinear EMC Modeling and Analysis of Permanent-Magnet Slotted Limited-Angle Torque Motor,” IEEE Trans. Ind. Electron., vol. 68, no. 9, pp. 8507–8518, Sep. 2021.

[59] O. Bottauscio, A. Manzin, A. Canova, M. Chiampi, G. Gruosso, and M. Repetto, “Field and Circuit Approaches for Diffusion Phenomena in Magnetic Cores,” IEEE Trans. Magn., vol. 40, no. 2, pp. 1322–1325, Mar. 2004.

[60] B. Kou, Y. Jin, H. Zhang, L. Zhang, and H. Zhang, “Analysis and Design of Hybrid Excitation Linear Eddy Current Brake,” IEEE Trans. Energy Convers., vol. 29, no. 2, pp. 496–506, Jun. 2014.

[61] M. K. Kazimierczuk, G. Sancineto, G. Grandi, U. Reggiani, and A. Massarini, "High-Frequency Small-Signal Model of Ferrite Core Inductors," IEEE Trans. Magn., vol. 35, no. 5, pp. 4185–4191, Sep. 1999. (for thesis)

[62] J. R. Nagel, "Finite-Difference Simulation of Eddy Currents in Nonmagnetic Sheets via Electric Vector Potential," IEEE Trans. Magn, vol. 55, no. 12, pp. 6300708, Dec. 2019. (for thesis)

[63] J. J. Feeley, "A Simple Dynamic Model for Eddy Currents in a Magnetic Actuator," IEEE Trans. Magn., vol. 32, no. 2, pp. 453–458, Mar. 1996.

[64] G. Grandi, M. K. Kazimierczuk, A. Massarini, U. Reggiani, and G. Sancineto, "Model of Laminated Iron-Core Inductors for High Frequencies," IEEE Trans. Magn., vol. 40, no. 4, pp. 1839–1845, Jul. 2004.

[65] C. Canudas-de-Wit, H. Olsson, K. J. Astrom, and P. Lischinsky, "A New Model for Control of Systems with Friction," IEEE Trans. Automat. Contr., vol. 40, no. 3, pp. 419 –425, Mar. 1995.

[66] J. Y. Yoon, and D. L. Trumper, "Friction microdynamics in the time and frequency domains: Tutorial on frictional hysteresis and resonance in precision motion systems," Precision Eng., vol. 55, pp. 419 –425, Mar. 1995.

[67] R. H. A. Hensen, M. J. G. van de Molengraft, and M. Steinbuch, "Frequency Domain Identification of Dynamic Friction Model Parameters," IEEE Trans. Control Syst. Technol., vol. 10, no. 2, pp. 191 –196, Mar. 2002.

[68] C. Canudas-de-Wit, "Comments on "A New Model for Control of Systems with Friction"," IEEE Trans. Automat. Contr., vol. 43, no. 8, pp. 1189–1190, Aug. 1998.

[69] M. Noh, W. Gruber, and D. L. Trumper, "Hysteresis Bearingless Slice Motors with Homopolar Flux-Biasing," IEEE/ASME Trans. Mechatronics., vol. 22, no. 5, pp. 2308–2318, Oct. 2017.

[70] L. Zhou, J. Y. Yoon, A. Andriën, M. Imani-Nejad, B. T. Allison, and D. L. Trumper, "FlexLab and LevLab: A Portable Control and Mechatronics Educational System," IEEE/ASME Trans. Mechatronics., vol. 25, no. 1, pp. 305–315, Feb. 2020.

[71] M. Noh, and D. L. Trumper, "Homopolar Bearingless Slice Motor With Flux-Biasing Halbach Arrays," IEEE/ASME Trans. Mechatronics., vol. 67, no. 9, pp. 7757–7766, Sep. 2020.

[72] S. Wu, Z. Jiao, L. Yan, R. Zhang, J. Yu, and C. Chen, "Development of a Direct-Drive Servo Valve with High-Frequency Voice Coil Motor and Advanced Digital Controller," IEEE/ASME Trans. Mechatronics., vol. 19, no. 3, pp. 932–942, Jun. 2014.

[73] Z. Ning, Y. Mao, Y. Huang, and C. Gao, "Robust Current Control of Voice Coil Motor in Tip-Tilt Mirror Based on Disturbance Observer Framework," in IEEE Access, vol. 9, pp. 96814-96822, 2021, doi: 10.1109/ACCESS.2021.3057162. Maybe For thesis

[74] C. Tsai, S. Lin, H. Huang, Y. Cheng, "Design and control of a brushless DC limited-angle torque motor with its application to fuel control of small-scale gas turbine engines," Mechatronics., vol. 19, no.1, pp. 29-41, Feb. 2009. Maybe For thesis

[75] R. T. Ratliff, and P. R. Pagilla, "Design, Modeling, and Seek Control of a Voice-Coil Motor Actuator with Nonlinear Magnetic Bias" IEEE Trans. Magn., vol. 41, no. 6, pp. 2180–2188, Jun. 2005.

[76] R. Oboe, F. Marcassa, and G. Maiocchi, "Hard Disk Drive with Voltage-Driven Voice Coil Motor and Model-Based Control" IEEE Trans. Magn., vol. 41, no. 2, pp. 784–790, Feb. 2005.

[77] D. L. Trumper, S. M. Olson, and P. K. Subrahmanyan, "Linearizing Control of Magnetic Suspension Systems," IEEE Trans. Control Syst. Technol., vol. 5, no. 4, pp. 427 –438, Jul. 1997.

[78] J. Solsona, M. I. Valla, and C. Muravchik, "Nonlinear Control of a Permanent Magnet Synchronous Motor with Disturbance Torque Estimation," IEEE Trans. Energy Convers., vol. 15, no. 2, pp. 163–168, Jun. 2000.

[79] L. Zhou, W. Gruber, and D. L. Trumper, "Position Control for Hysteresis Motors: Transient-Time Model and Field-Oriented Control," IEEE Trans. Ind. Appl., vol. 54, no. 4, pp. 3197–3207, Jul/Aug. 2018.

[80] Y. Zhou, D. Zhang, X. Chen, and Q. Lin, "Sensorless Direct Torque Control for Saliency Permanent Magnet Brushless DC Motors," IEEE Trans. Energy Convers., vol. 31, no. 2, pp. 446–454, Jun. 2016.

[81] C. Garcia, J. Rodriguez, C. Silva, Christian Rojas, P. Zanchetta, and H. Abu-Rub, "Full Predictive Cascaded Speed and Current Control of an Induction Machine," IEEE Trans. Energy Convers., vol. 31, no. 3, pp. 1059 –1067, Sep. 2016.

[82] G. Wang, Z. Li, G. Zhang, Y. Yu, and D. Xu, "Quadrature PLL-Based High-Order Sliding-Mode Observer for IPMSM Sensorless Control with Online MTPA Control Strategy," IEEE Trans. Energy Convers., vol. 28, no. 1, pp. 214–224, Mar. 2013.

[83] F. S. Ahmed, S. Laghrouche, M. El Bagdouri "Analysis, modeling, identification and control of pancake D.C. torque motors: Application to automobile air path actuators," Mechatronics., vol. 22, no. 2, pp. 195–212, 2012.

[84] S. Chen, N. Kamaldin, T. Teo, W. Liang, C. S. Teo, G. Yang, and K. Kiong Tan, "Toward Comprehensive Modeling and Large-Angle Tracking Control of a Limited-Angle Torque Actuator with Cylindrical Halbach," IEEE Trans. Mechatronics., vol. 21, no. 1, pp. 335-339, Feb. 2016.

[85] R. Wang, X. Yin, Q. Wang, and L. Jiang, "Direct Amplitude Control for Voice Coil Motor on High Frequency Reciprocating Rig," IEEE Trans. Mechatronics., vol. 25, no. 3, pp. 1299-1309, June. 2020.

[86] N. Bianchi, 'Electrical Machine Analysis using finite elements', *CRC press*, 2005.

[87] D. C. Hanselman, Brushless Permanent Magnet Motor Design, 2nd ed. USA: Magna Physics Publishing, 2006.

[88] K. J. Astrom, and R. M. Murray, "Feedback Systems: An Introduction for Scientists and Engineers," Princeton University Press, NJ, 2008.